LEVEL

PSI TR-170 A

ANALYSIS OF LASER-TARGET INTERACTION

VOLUME I — THEORY

FINAL REPORT

by

R.G. Root, A.N. Pirri, P.K.S. Wu, and H. Gelman

MARCH 1979

DTIC
ELECTE
SEP 1 7 1980

C

Prepared for:

U.S. Army High Energy Laser Systems Project Office

U.S. Army Missile Research and Development Command
Redstone Arsenal, Alabama 35809

Under Contract No. DAAK40-78-C-0010

REPORT DOCUMENTATION PAGE		READ INSTRUCTIONS BEFORE COMPLETING FORM
1. REPORT NUMBER	2. GOVT ACCESSION NO. AD-A089 ???	3. RECIPIENT'S CATALOG NUMBER
4. TITLE (and Subtitle) ANALYSIS OF LASER-TARGET INTERACTION, VOLUME I, THEORY,		5. TYPE OF REPORT & PERIOD COVERED FINAL REPORT 12/16/77-12/15/78
		6. PERFORMING ORG. REPORT NUMBER PSI-TR-170A-VOL-1
7. AUTHOR(s) R. G. Root, A. N. Pirri, P. K. S. Wu, and H. Gelman		8. CONTRACT OR GRANT NUMBER(s) DAAK40-78-C-0010
9. PERFORMING ORGANIZATION NAME AND ADDRESS PHYSICAL SCIENCES INC. 30 Commerce Way Woburn, MA 01801		10. PROGRAM ELEMENT, PROJECT, TASK AREA & WORK UNIT NUMBERS
11. CONTROLLING OFFICE NAME AND ADDRESS U. S. Army High Energy Laser Systems Proj. Off. U. S. Army Missile Res. & Develop. Command Redstone Arsenal, AL 35809		12. REPORT DATE March 1979
		13. NUMBER OF PAGES 442
14. MONITORING AGENCY NAME & ADDRESS(if different from Controlling Office) Final rept. 16 Dec 77-15 Dec 78,		15. SECURITY CLASS. (of this report) Unclassified
		15a. DECLASSIFICATION/DOWNGRADING SCHEDULE

16. DISTRIBUTION STATEMENT (of this Report)

Approved for public release; distribution unlimited.

17. DISTRIBUTION STATEMENT (of the abstract entered in Block 20, if different from Report)

18. SUPPLEMENTARY NOTES

19. KEY WORDS (Continue on reverse side if necessary and identify by block number)

Pulsed Laser Effects	Laser Coupling to Non-Metals
Dome Materials	Hardening
Laser Coupling to Metals	

20. ABSTRACT (Continue on reverse side if necessary and identify by block number)

This report describes theoretical laser effects research which was performed under Contract DAAK40-78-C-0010 during the period 16 December 1977 to 15 December 1978. This work was divided into three areas: theoretical studies of pulsed laser interaction with metals; theoretical studies of the interaction of repetitively pulsed 10.6 μm lasers with dome materials

DD FORM 1473
1 JAN 73

materials; and first order concepts in the hardening of metals to repetitively pulsed radiation. Therefore, Volume I of this report, in which theoretical models are developed, is divided into three self-contained parts, one for each area. The comparison between the theory and all experimental data obtained in the 1978 JANAF RP VEH Program is deferred to Volume II.

Part I is devoted to theoretical studies of pulsed laser interaction with metals. The model for central thermal coupling to Al2024 targets via plasma reradiation is improved by incorporating axial radiative transport within the plasma. The model is extended to include other metal alloy targets such as SS304, steel 4130 and Ti6Al4V. Based on absorbed fluence, a hierachy is predicted for the metal targets. The model is also adapted to incorporate laser beams incident at oblique angles. The theory predicts substantial thermal and mechanical coupling at large angles of incidence, and the theoretical predictions are verified by the 1978 JANAF data. First order estimates of thermal coupling for pulsed 3.8 μm radiation are made by using the model developed for 10.6 μm modified only to include the correct air absorption coefficient for 3.8 μm radiation.

Part II deals with the interaction of pulsed 10.6 μm radiation with dome materials. First, theoretical models are advanced for the surface interaction of a pulsed laser with dome materials. The predictions of these models are compared to data taken in the 1978 JANAF program to determine the dominant surface interaction physics, and a unified view of the interaction emerges. A model is developed for repetitive pulse damage to fiberglass, based on delamination and the concept of a maximum amount of fluence per pulsed (called residual energy) which can be used to cause delamination. The predictions of the theory are in good agreement with data taken in the 1978 JANAF program.

First order concepts in the hardening of metals to repetitively pulsed radiation are discussed in Part III. A variety of potential hardening schemes is presented and analyzed to determine if they are theoretically feasible. Several attractive hardening approaches are identified.

ABSTRACT

This report describes theoretical laser effects research which
was performed under Contract DAAK40-78-C-0010 during the period
16 December 1977 to 15 December 1978. This work was divided into
three areas: theoretical studies of pulsed laser interaction with
metals; theoretical studies of the interaction of repetitively pulsed
10.6μm lasers with dome materials; and first order concepts in the
hardening of metals to repetitively pulsed radiation. Therefore,
Volume I of this report, in which theoretical models are developed,
is divided into three self-contained parts, one for each area. The
comparison between the theory and all experimental data obtained in
the 1978 JANAF RP VEH Program is deferred to Volume II.

Part I is devoted to theoretical studies of pulsed laser inter-
action with metals. The model for central thermal coupling to Al2024
targets via plasma reradiation is improved by incorporating axial
radiative transport within the plasma. The model is extended to
include other metal alloy targets such as SS304, steel 4130 and Ti6Al4V.
Based on absorbed fluence, a hierachy is predicted for the metal
targets. The model is also adapted to incorporate laser beams
incident at oblique angles. The theory predicts substantial thermal
and mechanical coupling at large angles of incidence, and the theo-
retical predictions are verified by the 1978 JANAF data. First order
estimates of thermal coupling for pulsed 3.8μm radiation are made
by using the model developed for 10.6μm modified only to include the
correct air absorption coefficient for 3.8μm radiation.

Part II deals with the interaction of pulsed 10.6μm radiation with dome materials. First, theoretical models are advanced for the surface interaction of a pulsed laser with dome materials. The predictions of these models are compared to data taken in the 1978 JANAF program to determine the dominant surface interaction physics, and a unified view of the interaction emerges. A model is developed for repetitive pulse damage to fiberglass, based on delamination and the concept of a maximum amount of fluence per pulse (called residual energy) which can be used to cause delamination. The predictions of the theory are in good agreement with data taken in the 1978 JANAF program.

First order concepts in the hardening of metals to repetitively pulsed radiation are discussed in Part III. A variety of potential hardening schemes is presented and analyzed to determine if they are theoretically feasible. Several attractive hardening approaches are identified.

TABLE OF CONTENTS

PART I

THEORY OF REPETITIVELY PULSED 10.6 μm

LASER INTERACTION WITH METALS

TABLE OF CONTENTS (Cont.)

PART II

INTERACTION WITH DOME MATERIALS

TABLE OF CONTENTS (Cont.)

PART III
HARDENING OF METALS TO REPETITIVELY PULSED
10.6 MICRON RADIATION

LIST OF ILLUSTRATIONS

LIST OF ILLUSTRATIONS (Cont.)

LIST OF ILLUSTRATIONS (Cont.)

LIST OF ILLUSTRATIONS (Cont.)

LIST OF ILLUSTRATIONS (Cont.)

LIST OF ILLUSTRATIONS (Cont.)

LIST OF ILLUSTRATIONS (Cont.)

LIST OF ILLUSTRATIONS (Cont.)

LIST OF ILLUSTRATIONS (Cont.)

LIST OF ILLUSTRATIONS (Cont.)

LIST OF TABLES

LIST OF TABLES (Cont.)

PART I

THEORY OF REPETITIVELY PULSED 10.6 μm

LASER INTERACTION WITH METALS

SECTION 1

INTRODUCTION

This part of the report is devoted to theoretical studies of the interaction of the pulsed 10.6μ laser radiation with metal targets. Previously, a model was constructed to describe energy transfer to an aluminum alloy target Al2024 by a plasma ignited over the target surface.[1,2] The model was based upon energy transfer by plasma reradiation and it successfully predicted the fraction of the incident laser energy which is transferred to the center of the target in the regime where this fraction is significantly larger than the intrinsic absorptivity of the target. The optimum laser pulse shape corresponded to an initial spike which ignited the plasma followed by a lower intensity tail which maintained a hot plasma close to the target. It was shown that the radiative transfer mechanism operated most efficiently at intensities where laser supported combustion (LSC) waves were present rather than at intensities where laser supported detonation (LSD) waves persisted. From analysis of radial expansion effects, it was concluded that the optimum pulse length is determined by the time for the radial rarefaction wave to reach the center of the laser spot. The major shortcoming of the previous analysis, when applied to Al2024 targets, is that the simple radiative transfer model which is used breaks down for optically thick plasmas. As a result, the thermal coupling model overestimates the amount of energy transferred whenever thick, one-dimensional LSC waves are produced, such as for large spot size and long pulse time. In addition, the simplicity of the radiative transfer model does not permit the LSC/LSD transition to be treated properly.

This part of the report is devoted to extending the range of applicability of the enhanced thermal coupling model. The basic LSC wave model is improved to include better radiative transfer modeling and a non-uniform temperature profile. This ambitious program also requires improved parameterization of the radiative properties of hot ionized air. The improved laser-

3

supported combustion wave modeling is presented in Section 2 and the improved physical parameters for ionized air are discussed in Appendix A.

The interaction between pulsed lasers and metal targets other than Al2024, such as Ti6Al4V, SS304, and 4130 steel, can also be addressed with this model. Predictions of enhanced thermal coupling to these metals are made in Section 3 by using the LSC wave model to predict radiative emission from the plasma, and the spectral surface absorptivity appropriate for each metal to calculate the fraction of the plasma radiation which is absorbed.

For both Al2024 and the other metal targets listed above, it is assumed the laser is incident perpendicular to the target. However, in many circumstances, the angle of incidence (defined as the angle between the direction of laser beam propagation and the normal to the target surface) may be quite large. It is important, therefore, to investigate the nature of enhanced thermal coupling for oblique angles of incidence. In Section 4, the LSC wave model is modified to incorporate changes required for oblique angles of incidence.

In Section 5, a comparison is made between the available experimental data and the theoretical predictions for (1) the fluence absorbed by metals other than Al2024 and (2) the surface pressure and fluence absorbed by Al2024 for interactions at oblique angles of incidence.

All the interactions described above assume that the laser wavelength is 10.6μ. However, there is also substantial interest in the interaction of pulsed DF lasers ($\lambda = 3.8\mu$) with targets. First order estimates of enhanced thermal coupling have been made for the interaction of a pulsed 3.8μ laser with metal targets by using the LSC wave model designed for 10.6μ, but modified to have the correct laser absorption coefficient for 3.8μ radiation. Typical predictions made with this modification are described in Section 6.

A summary of the conclusions which can be drawn from the theory and from the theory/data comparison is contained in Section 7.

4

SECTION 2
LSC WAVE MODEL

In the previous report,[1,2] a model was advanced in which enhanced thermal coupling of a pulsed laser to a metal target was associated with energy transfer by reradiation from a hot air plasma supported by laser radiation. In the description of the interaction between the plasma and the laser, several regimes were identified: at early times, the plasma motion was perpendicular to a target and all plasma dynamic equations were one-dimensional; at later times, two-dimensional radial expansion became important and plasma motion in three-dimensions had to be considered. An estimate of the time for which the one-dimensional model of the LSC wave is valid can be made as follows: At the start of the laser pulse, the high pressure plasma is created over the entire laser spot area. Expansion of the high pressure plasma into the ambient air in the radial direction occurs immediately at the edges of the plasma. A rarefaction wave moves in from the edge of the plasma towards the center of the laser spot at the speed of sound in the plasma (approximately 4.5×10^5 cm/sec). The arrival of this wave at the center of the target heralds the onset of both the radial expansion and the resultant cooling of the plasma at the center of the target. Effective radiative transfer to the target is curtailed as the plasma temperature falls. Therefore, the one-dimensional LSC wave model cannot be used beyond the two-dimensional relaxation time τ_{2D} which is given by R/a_p where R is the laser spot radius and a_p is the sonic velocity in the plasma. Of course, the one-dimensional laser-supported plasma dynamics is also invalidated if the laser pulse is terminated; the wave no longer has an energy source. Therefore, the one-dimensional LSC wave model is applicable only until a critical time τ_c given by the smaller of τ_p, the laser pulse time, and τ_{2D}, the time characteristic of radial expansion. In order that the laser pulse not be wasted on inefficient plasma heating after effective radiative transfer has ceased, it is important that the non-dimensionalized

parameter $\hat{\tau}$ defined as τ_p / τ_{2D} be less than or approximately equal to one.

The energy transfer from an LSC wave plasma occurs chiefly when the plasma dynamics are one-dimensional. A sketch of this idealized configuration is presented in Fig. 2.1. Throughout the analysis it is assumed that the plasma is an air plasma. A precursor shock propagates into the surrounding air; the LSC wave defines the leading edge of the absorbing plasma and proceeds into the shocked air by thermal conduction and radiative energy transport. The velocity at which the LSC wave propagates into the shocked gas, along with the shock strength, determines the plasma properties and, the intensity of the radiant energy flux to the target from the plasma. The dynamics are unsteady because the LSC wave and the shock have different absolute velocities. Approximate solutions to this problem can be found, however, by searching for quasi-steady solutions which conserve energy. The model developed in the last report[1,2] assumes a simplified configuration wherein the properties are considered uniform in the zone between the shock and the LSC wave and also in the region between the LSC wave and the wall. The gas dynamic relations which govern the motion of the shock and the LSC wave plasma as configured in Fig. 2.1, have been derived in Ref. 1. With reference to the LSC wave, the wall boundary moves at the absolute LSC wave velocity V_{LSC}. Conservation of energy then requires

$$\rho\, V_{LSC} \left(h + \frac{V_{LSC}^2}{2} \right) = \rho_s \left(V_{LSC} - u_s \right) \left[h_s + \frac{\left(V_{LSC} - u_s \right)^2}{2} \right] + I_o - q_r - q_l \ , \quad (2.1)$$

where ρ and h are, respectively, the density and the enthalpy in the plasma (between the LSC wave and the wall), ρ_s is the density between the shock and the LSC wave, u_s is the particle velocity behind the shock, h_s is the enthalpy behind the shock, I_o is the incident laser intensity, q_r is the radiation transferred from the plasma to the target and q_l is the radiation loss in all other
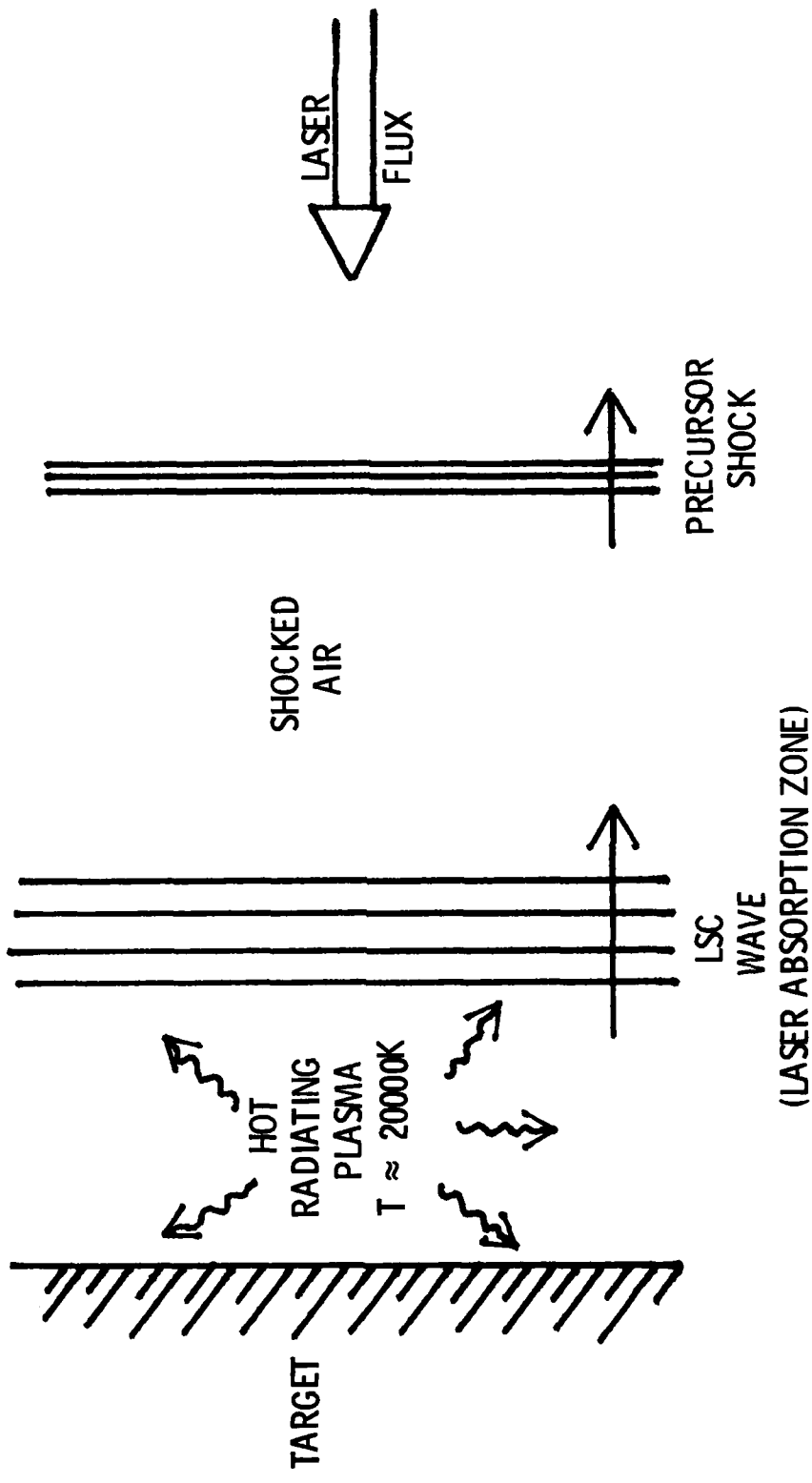
Fig. 2.1 Laser Supported Combustion Wave Plasma in One-Dimension.

directions. It is assumed that all the laser energy is absorbed by the plasma and that conduction losses affect only a small region very close to the surface. Consequently, conduction is neglected in deriving the overall energy balance of Eq. (2.1). In the derivation Eq. (2.1), the LSC wave is treated as a temperature discontinuity and the conditions are taken to be uniform throughout the entire plasma region behind the LSC wave. Similarly, the equations of mass and momentum across the LSC wave are:

$$\rho \, V_{LSC} = \rho_s \left(V_{LSC} - u_s \right), \qquad (2.2)$$

$$p + \rho \, V_{LSC}^2 = p_s + \rho_s \left(V_{LSC} - u_s \right)^2 , \qquad (2.3)$$

where p_s is the pressure behind the shock and p is the pressure in the plasma. In the model presented in Ref. 1, a perfect gas equation of state is used for each region — ambient air, shocked air, plasma — with different values of the effective specific heat ratio, γ, in each region. Therefore, in the plasma regime, the relationship between pressure density and enthalpy can be written as:

$$p = \frac{(\gamma - 1)}{\gamma} \rho \, h , \qquad (2.4)$$

where γ is taken to be 1.2 in the air plasma. Across the shock wave, strong shock relations yield

$$V_s = \frac{(\gamma_s + 1)}{2} u_s , \qquad (2.5)$$

8

$$p_s = \frac{\gamma_s + 1}{2} \rho_o u_s^2 \quad , \tag{2.6}$$

$$\rho_s = \frac{\gamma_s + 1}{\gamma_s - 1} \rho_o \quad , \tag{2.7}$$

where V_s is the shock velocity, γ_s is the specific heat ratio for the shocked air (taken to be 1.4), and ρ_o is the ambient density. It was demonstrated by Thomas[3] that relations similar to Eqs. (2.1) - (2.7) can be manipulated to determine the plasma conditions - temperature, pressure, and enthalpy - in terms of the absorbed laser intensity, I_o, and the velocity, V_{LSC}, of the LSC wave. The shock pressure p_s, particle velocity u_s in the shocked air, plasma pressure ρ, and plasma enthalpy h become

$$p_s = \left[\frac{\gamma_s + 1}{2} \rho_\infty \right]^{1/3} \left[\frac{(\gamma - 1)(\gamma_s - 1) I_p}{(\gamma + W)(\gamma_s - 1 - 2W)} \right]^{2/3} \quad , \tag{2.8}$$

$$u_s = \left[\frac{2(\gamma - 1)(\gamma_s - 1) I_p}{(\gamma_s + 1) \rho_\infty (\gamma + W)(\gamma_s - 1 - 2W)} \right]^{1/3} \quad , \tag{2.9}$$

$$p/p_s = 1 - 2W/(\gamma_s - 1) \quad , \tag{2.10}$$

$$h/u_s^2 = \gamma(1 + W)(\gamma_s - 1 - 2W)/[2(\gamma - 1) W] \quad , \tag{2.11}$$

where I_p is defined to be $I_o - q_r - q_1$ and W is a non-dimensionalized velocity defined as $W = (V_{LSC} - u_s)/u_s$. This velocity is proportional to

9

the particle velocity in a reference frame fixed to the LSC wave. In order to close the system of equations to lead to a unique solution, the LSC wave propagation velocity V_{LSC} must be determined. The speed of the LSC wave can be predicted from a model for LSC wave propagation which was developed in Ref. 4. The model uses radiative transport to control the speed of propagation of the LSC wave. The model, as described in Ref. 4 and used in the previously developed semi-analytic model for enhanced thermal coupling,[1,2] employs a two-band approximation for the radiative properties of air. The radiation corresponding to wavelengths less than 1127A is assumed to contribute to the propagation of the LSC wave, whereas radiation having wavelengths greater than 1127A is treated as a transparent loss term. The solution was obtained by treating the laser intensity as an eigenvalue and integrating throughout the LSC wave the equations describing local energy conservation, mass conservation, and momentum conservation. In a coordinate system attached to the leading edge of the LSC wave and with the distance x being positive toward the surface (see Fig. 2.1), the equations are:

$$\rho_s \ (V_{LSC} - u_s) \left(c_p(T) \ \frac{\partial T}{\partial x} + \left(\frac{\partial h}{\partial p} \right)_T \frac{\partial p}{\partial x} \right) + q(T) - k_L(T) I_o \ e^{-\int_o^x k_L(T)dx}$$

$$= \frac{d}{dx} \left(\lambda(T) \ \frac{dT}{dx} \right) , \qquad\qquad (2.12)$$

$$\frac{\partial \rho u}{\partial x} = 0 , \qquad\qquad (2.13)$$

$$\frac{\partial p}{\partial x} = - \rho u \ \frac{\partial u}{\partial x} \qquad\qquad (2.14)$$

10

where ρ_s is the density behind the precursor shock, T is the temperature, c_p is the specific heat at constant pressure, q(T) is the radiative loss term, k_L(T) is the effective laser absorption coefficient, I_o is the incident laser intensity and λ(T) is the combined thermal and radiative conductivity. As discussed in Ref. 4, it is the nature of Eq. (2.12) - (2.14) that the calculated temperature profile through the LSC wave will correspond to the true profile only if the selected intensity I_o is the correct eigenvalue corresponding to the value of the mass flow through the LSC wave, ρ_s (V_{LSC} - u_s). If I_o is greater than the correct intensity, the temperature profile rapidly decreases towards zero temperature as if there were a heat sink (see Fig. 2.2A), whereas if I_o is less than the correct intensity, the temperature continues to increase rapidly as if there were a heat source (see Fig. 2.2B). Only when I_o is within .01% of the correct intensity (for the corresponding mass flow) will the solution be self-consistent. This extreme sensitivity to the eigenvalue enables a solution to be obtained with only a few iterations. Although the LSC wave code is capable of calculating both the complete temperature profile and the radiation from the LSC wave plasma, in the enhanced coupling model of Refs. 1 and 2 it has not been used in this capacity. Rather, it was used merely to obtain the relationship between mass flow and laser intensity for an LSC wave propagating into shocked air.

In the enhanced coupling model of Refs. 1 and 2, the radiative transfer from the plasma is calculated for an isothermal plasma slab of plasma having constant pressure and a thickness L. The temperature, pressure and thickness are functions of time. The one-sided radiative flux q is given by:

$$q = \epsilon(L, \rho, p) \, \sigma \, T^4, \qquad (2.15)$$

where ϵ(L, ρ, p) is the slab emissivity and σ = 1.03 x 10^5 W/cm^2 - (eV)^4 is the Stefan Boltzmann constant. The functional form of ϵ(L, ρ, p) has been

11
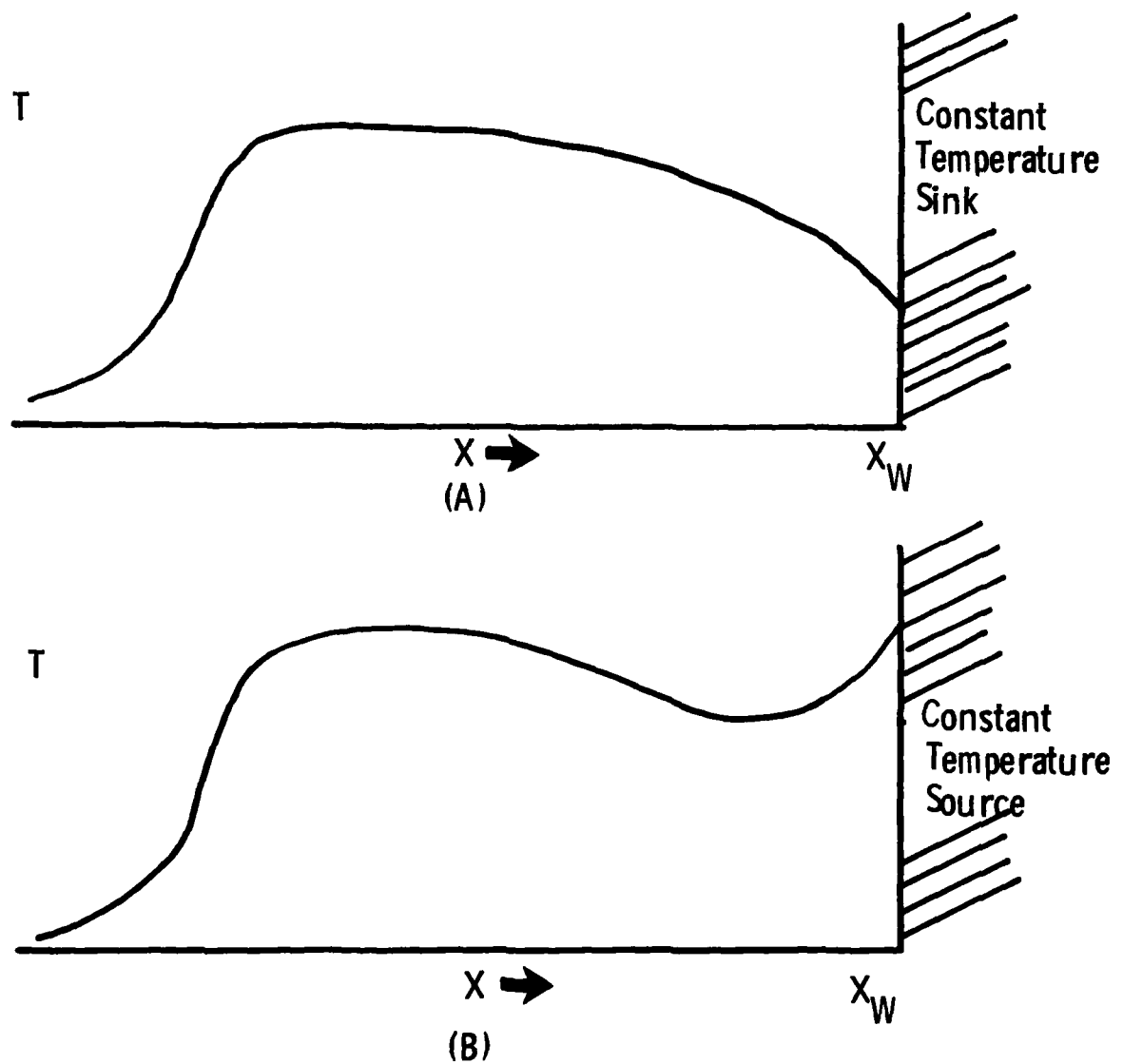
Fig. 2.2   Sketches of Two Pathological Solutions to the LSC Wave
Model, Indicating Possible Physical Circumstances which
Would Lead to Them: (A) Heat Sink at X_w - Solution Valid
Only to X_w; (B) Heat Source at X_w - solution Valid Only
to X_w.

determined by fitting the predictions of Johnston et al.[5] It is assumed that q represents all the radiative losses from the plasma; that is, both the radiative transfer q_r to the target, and the radiative losses, q_l, are contained in q. Then the net radiative energy added per unit time to the plasma, which is denoted by I_p in Eq. (2.8) and (2.9), is equal to $I_p = I_o - q$.

A graph of the one-dimensional radiative flux to the target surface for a given laser intensity can be constructed as follows: First, the pressure behind the precursor shock is estimated for a specific laser intensity I_o; this determines all the conditions in the precursor shock (see Eqs. (2.4) - (2.7)). Given the laser intensity and the precursor shock conditions, the LSC wave model predicts the mass flow into the LSC wave, and the value of the non-dimensionalized velocity W is determined. Equation (2.8) can be used to calculate I_p from the value determined for W and the chosen value of p_s. The LSC wave plasma pressure is determined from Eq. (2.10) and the enthalpy of the LSC wave plasma is given by Eq. (2.11). However, the enthalpy of the plasma has been determined as a function of temperature, pressure, and density by Gilmore,[6] so the value of enthalpy determined from Eq. (2.11) can be used to deduce the plasma temperature. The difference between the incident intensity, I_o, and the net absorbed radiation flux, I_p, is the amount of radiation, q, emitted by the plasma. The plasma radiation is also known as a function of p, ρ and L (see Eq. (2.15)). Since ρ and L are already available from the solution of Eqs. (2.8) - (2.11), the value of q determines the thickness, L, of the LSC wave. The velocity V_{LSC} of the LSC wave with respect to the target is related to W and u_s, both of which are known. Calculations show that the LSC wave velocity does not change much throughout the development of the wave, therefore, the time at which the plasma has the thickness L is approximately $t = L/V_{LSC}$. The sequence of calculations described above is sufficient to define the pressure, velocity, thickness, temperature and radiative flux from the plasma at one value of t and for one

13

specified intensity I_o. By changing the shock pressure by a small amount, these quantities are generated for another value of t. By varying the assumed shock pressure for given fixed incident intensity I_o, we can construct a complete graph of radiative flux to the surface as a function of time which is valid whenever one-dimensional quasi-steady fluid dynamics is appropriate.

Not all the radiation that leaves the plasma is absorbed by the target. As a first order estimate of the amount of radiation which can be easily absorbed by the target, the radiation spectrum is divided into two bands; namely, the band with wavelength less than 1127A, (which is strongly absorbed by the target) and the band having wavelengths greater than 1127A, (which is only 50% absorbed by the target). The short wavelength band is produced by photorecombination of electrons and ions to produce neutral atoms; it has a large absorption coefficient. It is reasonable to model this band as being blackbody limited; that is, its value is given by integrating the Planck blackbody function over the range of wavelengths from 0 to 1127A. This radiation contribution shall be designated as q_{VUV}. Then the remaining contribution of the radiation can be found by merely subtracting q_{VUV} from the total radiation flux q. The total radiation absorbed by the target, q_{ABS}, is given by:

$$q_{ABS} = q_{VUV} + .5 (q - q_{VUV}) . \qquad (2.16)$$

It is assumed that the fraction of the incident radiation flux to the surface which is absorbed remains constant throughout the development of the plasma. Therefore, a coefficient β can be used to represent the fraction q_{ABS}/q for a given laser intensity. The value of β corresponding to incident laser intensities I_o of 1, 4, and 10 MW/cm^2, are, respectively, .7, .6 and .55. The amount of radiative energy from a one-dimensional plasma which is absorbed by a target has been calculated as a function of time for several laser intensities.

14

As soon as the laser pulse is terminated or the radial expansion wave reaches the center of the laser spot, the quasi-steady one-dimensional approximation fails. Expansion effects cause the plasma temperature over the center of the spot to drop rapidly. This temperature decrease is the most crucial feature in determining the radiative transport to the target from the expanding plasma. Therefore, in this regime, it is more important to model the unsteady effect which causes the temperature to drop than to model the details of LSC wave propagation. A simple way of modeling the unsteady effects is to replace the one-dimensional plasma dynamics by blast wave decay laws. The type of decay law used must reflect the geometry of decay; that is, planar or one-dimensional decay laws are appropriate after the laser is turned off but before radial expansion is important, three-dimensional spherical decay laws are appropriate in the regime where the laser is off and radial decay is important, and a powered three-dimensional decay law represents radial expansion which occurs during the laser pulse. The blast wave decay laws give the temperature, pressure, and density of the plasma as a function t/t_{tr} where t is time and t_{tr} is the time at which the decay law first becomes applicable. The radiation from the decaying plasma can be expressed entirely as a function of time by substituting the time dependent value of density, temperature and plasma thickness into the function defining the emissivity. It is assumed that the fraction of the radiation flux which is absorbed remains unchanged during this decay process.

We can now compute the radiation flux absorbed by the surface as a function of time. The one-dimensional approximation applies until such time as unsteady effects become important. Thereafter, the radiation to the surface decays according to blast decay laws. The total coupling to the center of the spot is given by integrating the absorbed radiation flux from the beginning of the laser pulse to infinity. It was shown in the last report [1,2] that this model could predict reasonably well the amount of energy coupled to the center of target by a pulsed $10.6\,\mu$m laser.

There are, however, several circumstances in which the approximations used in the model become inaccurate. For example, the formula used for emissivity is based upon predictions for the emissivity of an isothermal slab that is thin enough for the radiative losses to be mostly transparent. For many of the conditions reached during the laser pulse, this formula predicts emissivities greater than one, a physical absurdity. Whenever this occurs, the model arbitrarily uses the blackbody limit for the radiation flux. Clearly, more accurate radiation models are necessary. Furthermore, it is desirable to partition the radiation more accurately into the various spectral bands, and also to revise the estimates of the spectral absorptivity of the targets.

The SAI numerical simulation [3,6,7] of the laser-supported plasma predicts that for large spot sizes and long pulse times the radiative transport to the target becomes diffusion dominated. As a result, there should be decoupling of the radiating plasma from the surface. This feature can be included in the semi-analytic model described above only if the plasma is allowed to have a non-uniform temperature profile. Comparison of the predictions made with the semi-analytical model to experimental data for large spot sizes and long pulse durations reveal that the predictions fall substantially above the existing data. This discrepancy occurs when thick one-dimensional plasmas are created and the radiation becomes blackbody limited in the semi-analytical model. Under these conditions, radiative diffusion is expected to decouple the plasma from the target as predicted by the SAI numerical simulation.

It is, therefore, important to embark upon a program of improving the PSI semi-analytic model in those areas which it was most deficient, while at the same time retaining its relative simplicity compared to the cumbersome, expensive numerical simulations. Indeed, the great advantage of a semi-analytic approach is that it identifies the dominant physical phenomena, thereby allowing simple scaling laws to be developed to describe a wide range

of interactions. Furthermore, it can be used to study the effect of any particular physical phenomenon in detail.

In the rest of this section we improve the predictive capability of the semi-analytical model and investigate the possibility of axial decoupling through radiative diffusion, while still keeping the model in a reasonably simple form. First, the radiation parameters for hot ionized air are re-examined. The radiation is described by a four-band model rather than the two-band model used previously. The details of the improved modeling of the radiative properties of air are described in Appendix A. Second, radiative transport within the plasma and its effect on the plasma temperature profile are included. The LSC wave model is used not only to predict the propagation speed of the LSC wave, but also to predict the temperature profile and to handle, in detail, the one-dimensional radiative transport within the plasma. In this approach, Eqs. (2.9) through (2.11) are no longer needed since the LSC wave model generates self-consistently the plasma temperature, pressure, wave speed, plasma thickness, and radiation transferred to the target. It is still a quasi-steady approximation, however. We construct a plot of the radiative flux absorbed by the surface as a function of time by calculating the LSC wave configuration and radiation flux for a given steady-state condition and then determining the time required to produce this configuration. That is, the radiation flux as a function of time represents the time evolution through a series of steady-state profiles. It is important to remember that there are many unsteady effects which may become important at high intensity which are not included in this approach. The approach outlined above is sufficient to predict the absorbed intensity of the function of time whenever the plasma is one-dimensional. The description of the plasma after the onset of unsteady effects remains the same as in the simple model; that is, we merely use blast wave decay laws to infer the rate of decay of the radiation flux as a function of time.

17

2.1 Improved Radiation Parameters

As mentioned above, the details of the radiative parameter models are described in Appendix A. However, it is appropriate to review the salient features of the parameterization before we describe, in detail, the model for the laser supported cumbustion wave. It is found that the entire radiation spectrum can be divided into four spectral bands which are designated by the following symbols: EUV, VUV, VUV', and VIS. The bands are chosen to represent faithfully three important radiative characteristics; namely, emission by the hot plasma, absorption by the cooler air in front of the LSC wave, and absorption by the target. A summary of the range of the radiation bands and their qualitative properties are listed in Table 2.1. Although all three of the radiative characteristics mentioned above are important in determining the amount of radiation transferred to the target, two of them can be treated in a very simple manner, whereas one, the plasma radiative emission, must be incorporated into the equations which determine the internal structure of the LSC wave. The target absorptivity merely defines the fraction of the radiation flux incident on the target which is absorbed. The absorption characteristics of the cool air determine the amount of plasma emission which is reabsorbed and contributes to forward propagation of the LSC wave.

The various bands have widely varying radiative capabilities in the plasma regime. For example, the EUV band, which corresponds to photo-recombination into the ground state, has an absorption length of approximately .7 mm under typical conditions (T = 20000K and p = 20 atm.). The next band, VUV, which includes contributions from photo-recombination into states just slightly above the ground state and from overlapping lines, has an absorption length of approximately 1/4 cm; this is almost 4 times that of the EUV band. The other two bands, designated by VUV' and VIS, are rather weak radiators; they have absorption lengths of approximately 5.7 cm.

18

TABLE 2.1

Spectral bands used in radiative transfer modeling of air LSC wave. Emission and absorption characteristics of air and the target are given for these bands.

Band	Range $[eV]$	Range $[\overset{\circ}{A}]$	Plasma Radiation	$\kappa \left[cm^{-1}\right]$ $T = 20000K$ $P = 20$ atm	Wave Front Absorption	Al2024 Absorption
EUV	13.6-∞	0-912	Very Strong	14.6	Strong	95%
VUV	10-13.6	912-1240	Strong	3.7	Strong	90%
VUV'	7-10	1240-1770	Weak	0.18	Strong	50%
VIS	0-7	1770-∞	Weak	0.18	Weak	15%

To determine the most appropriate approximation for modeling radiative transport, it is essential to know the optical thickness of the plasma for each of the bands. For LSC wave plasmas the optical thickness can be estimated by a simple calculation. Recall that the optical thickness τ is given by the product of the absorption coefficient κ and the plasma thickness L;

$$\tau = \kappa L . \tag{2.17}$$

The plasma thickness at the end of the pulse is given by:

$$L = V_{LSC} t_p \tag{2.18}$$

where V_{LSC} is the LSC wave velocity and t_p is the pulse time. For LSC wave plasmas, V_{LSC} is proportional to $(I_o)^{1/3}$ where I_o is the laser intensity. Examination of the temperatures predicted with the isothermal LSC wave model indicate that the plasma temperature is of the order of 20,000 $^{\circ}$K and varies only slowly with intensity. For a constant temperature plasma, the absorption coefficient κ for any band is proportional to the pressure. For an LSC wave plasma, the pressure p varies as $I_o^{2/3}$. Thus, the total optical depth τ obeys the following relationships:

$$\tau = \kappa L$$

$$\sim p \cdot V_{LSC} \cdot t_p \tag{2.19}$$

$$\sim I_o t_p .$$

Therefore, the optical thickness of the plasma is roughly determined by the incident laser fluence F $(F = I_o t_p)$ in J/cm^2 In particular, the following

relationships give reasonable estimates of the optical thickness of any band: (F is measured in J/cm^2):

$$\tau_{EUV} = F, \tag{2.20}$$

$$\tau_{VUV} = F/4, \tag{2.21}$$

$$\tau_{VUV'} = \tau_{VIS} = F/90. \tag{2.22}$$

2.2 Radiative Transport Models

In previous work, two limiting forms of radiation transport models were used, namely, the radiation conduction approximation and the transparent radiator approximation. The radiation conduction approximation[8] is given by

$$S = -\lambda_R \frac{dT}{dx}, \tag{2.23}$$

where S is the radiation flux, and λ_R is the radiation conductivity given by

$$\lambda_R = \frac{4\pi}{3} \int d\omega \frac{B(\omega, T)}{\kappa}. \tag{2.24}$$

In the above equations, κ is the effective absorption coefficient, $B(\omega, T)$ is the Planck spectral blackbody function

$$B(\omega, T) = 2hc^2 \frac{\omega^3}{\exp \frac{h\omega c}{kt} - 1} \tag{2.25}$$

and ω is the wave number. In the definition of the Planck blackbody function, h is the Planck constant, k is the Boltzmann constant, T is the temperature and c is the velocity of light. The limits of integration in the definition of the radiation conductivity are the range of wave numbers covered by the spectral band. The radiation conduction approximation is adequate whenever the plasma thickness is much larger than absorption length for the radiation band in question. On the other hand, if the plasma is optically thin to the radiation band, it is sufficient to treat the radiation as a transparent loss dS/dx which obeys the equation

$$\frac{dS}{dx} = \int 4 \pi \kappa B (\omega, T) d\omega \quad , \tag{2.26}$$

where, as above, S is the radiation flux, κ is the effective absorption coefficient of the band, and B is the Planck spectral blackbody function.

The radiation conduction approximation is expected to be valid if the optical depth τ is much greater than 1, say $\tau \geq 3$. The transparent loss approximation is adequate when τ is much less than 1, say $\tau \leq 1/3$. For optical depths between these values, however, neither approximation is satisfactory. There is a better approximation which is still sufficiently simple to use in the LSC wave model and which can also be used throughout the range $1/3 < \tau < 3$. The approximation is known by a variety of names, but we shall refer to it as the differential approximation. It involves two coupled equations; for planar geometry these equations are written as:[9]

$$\frac{dS}{dx} = \kappa \left[4 \pi \int B \, d\omega - U \right] , \tag{2.27}$$

$$\frac{dU}{dx} = - 3 \kappa S , \tag{2.28}$$

22

where κ, S, and B represent the same variables as in the radiation conduction approximation and U is the radiation intensity density. Using the scaling for optical thickness developed in Subsection 2.1 and the criteria mentioned above, we have constructed in Fig. 2.3 a plot which shows the range of validity of each of the radiation approximations as a function of fluence. The differential approximation is reliable throughout the whole fluence regime, but for the sake of economy and manageability, it is used only when required, that is, in the regime where neither the radiation conduction approximation nor the transparent approximation is valid. LSC waves of practical importance always involve fluences larger than a few J/cm^2; therefore, the radiation conduction approximation can always be used for the EUV band. At early time, when there is only a thin layer of plasma, the differential approximation is used for the VUV band and the transparent loss approximation for the VUV' and VIS band. At later time, when the plasma layer has become thicker, the radiation conduction approximation is used for the VUV band and the differential approximation must now be used for the VUV' and VIS bands.

Axial decoupling of the plasma radiation from the target is expected to commence as the optical thickness τ of the plasma increases. Although no precise value of τ has been associated with the onset of axial decoupling, it is reasonable to expect the phenomena to occur when τ is of the order of one. Therefore, we have plotted in Fig. 2.4, the spot radius which must be used as a function of laser intensity in order to reach the large spot decoupling regime for $\hat{\tau} = 1$. Three lines have been drawn, corresponding to values of 60, 90 and 120 J/cm^2 for the incident fluence. For a 20,000 °K, 20 atm plasma, which typically is produced at an intensity of 2 MW/cm^2, these fluences correspond to optical thicknesses of 2/3, 1 and 4/3. This relationship between fluence and optical thickness (see Eq. (2.22)) has been examined in detail, for other incident intensities by calculating the temperature

23

Incident Fluence [J/cm^2]

Band	1	2	4	8	16	32	64	128
EUV	Differential Approx.			Radiation Conduction				
VUV	Transparent	Differential Approx.		Radiation Conduction				
VUV' VIS	Transparent Losses					Differential Approx.		Radiation Conduction

Fig. 2.3 Fluence Regimes for Radiative Transport Approximations Used in the LSC Wave Model.

24
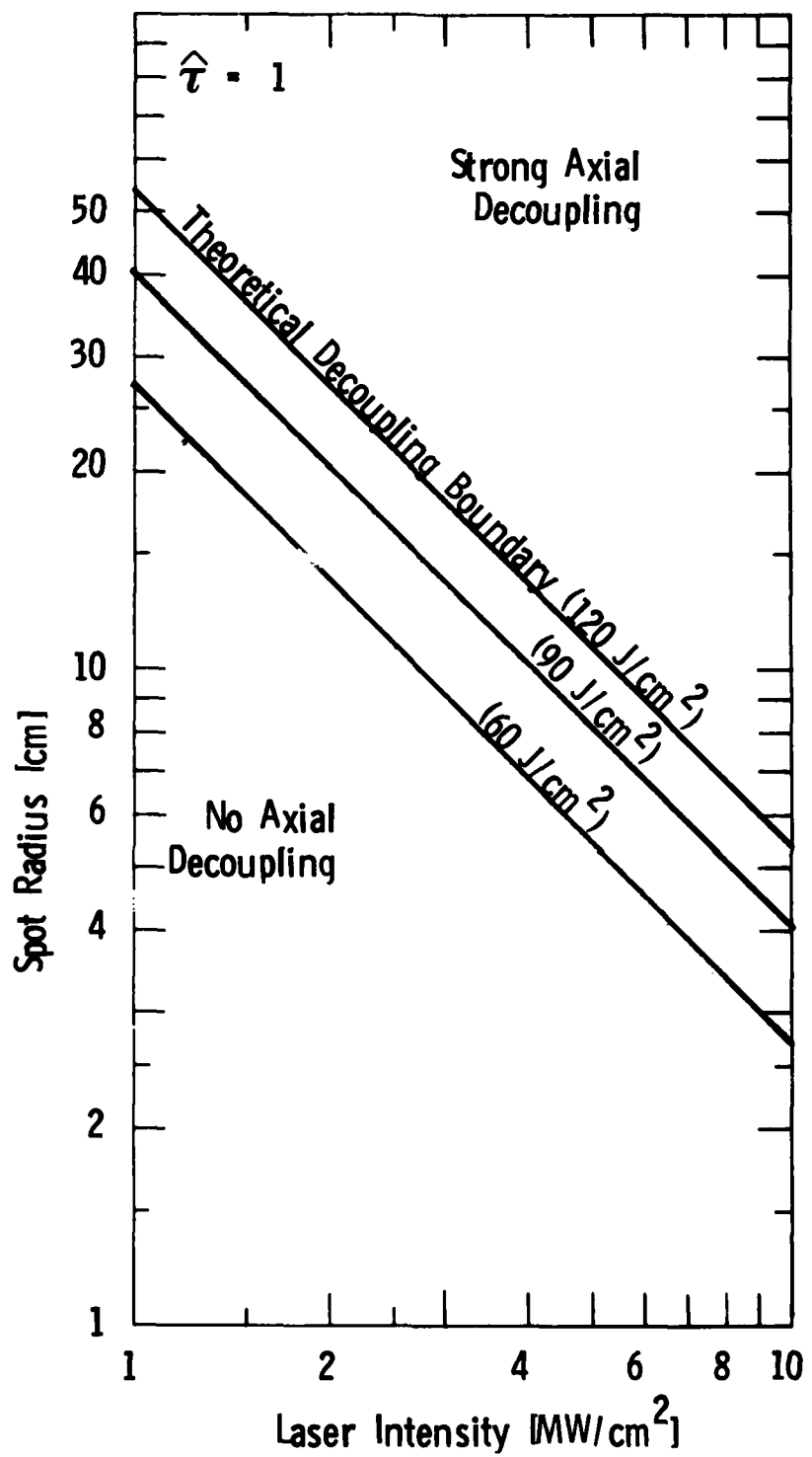
Fig. 2.4 Spot Size Required for Axial Decoupling for
$\widehat{\tau} = 1$ as a Function of Laser Intensity.

and pressure of the LSC wave plasma and then using the air parameters given in Appendix A to determine the absorption coefficient. The relationship (2.22) holds for intensities greater than or equal to 2 MW/cm^2, but at 1 MW/cm^2 the optical thickness of the plasma is given by F/150. The optical density decreases in the low intensity plasma because most of the atoms are ionized at the lower pressure.

To test whether or not strong axial decoupling occurs, the laser is operated at a fixed intensity and the spot size and pulse time are changed, keeping $\hat{\tau}$ = 1, so as to cross the theoretical decoupling boundary. If decoupling occurs, the central coupling coefficient should remain roughly constant below the decoupling boundary and decrease as the radius is increased above the coupling boundary. It is important that the test be made in the above fashion, that is, by changing the spot size and pulse length rather than the intensity, because as the intensity is increased, the coupling may decrease because of the transition from an LSC wave to an LSD wave.

2.3 Improved One-Dimensional LSC Wave Model

Many of the facets of the previous LSC wave model are used in the improved model. The major improvements are better radiation parameters and better radiative transport equations. The method of solution enables us to predict the detailed LSC wave plasma temperature profile in the quasi-steady approximation.

The basic approach used to solve the coupled equations which describe the LSC wave, has been recorded in detail in Ref. 4. In the discussion below, we deal only with the modifications necessary to adapt the LSC wave model to the configuration of shock, plasma and target which exists in the enhanced coupling regime.

At a given point in time, the configuration of the shock and LSC wave are expected to be similar to the sketch in Fig. 2.1. All motion is assumed to

be one-dimensional and typical profiles of the expected temperature T, particle velocity u and pressure p, are illustrated in Fig. 2.5. At the transition from the ambient air into the shocked air there is a jump in the values of all three quantities. Moving through the LSC wave, the temperature rises quickly as the laser energy is absorbed, and then slowly decays because of radiative losses in the tail. The expansion of the gas during the heating phase causes the particle velocity in the laboratory frame to reverse, so that instead of the particle motion being away from the target as it is in the shocked air, the particle motion in the tail of the LSC wave is directed towards the target. At the target, however, the particle velocity must be zero. Similarily, the pressure drops substantially during the high intensity heating in the absorption zones, but in the tail, where there is a radiative cooling, the pressure increases slightly.

The method of solution is similar to the technique used in Ref. 4 to determine the LSC wave profile for a wave propagating in the ambient air with no target. We choose a system of coordinates fixed on the LSC wave; the zero of the x coordinate is chosen to be at a temperature T_i below which laser absorption and radiative losses are unimportant. The equations describing the LSC wave are:

1) Conservation of mass.

$$\frac{d \rho u}{dx} = 0 ,$$

(2.29)

where ρ is the density and u is the particle velocity. Eq. (2.29) can be integrated and written as

$$\rho u = \dot{M} ,$$

(2.30)

where $\dot{M}$ is the constant mass flow through the wave.

27
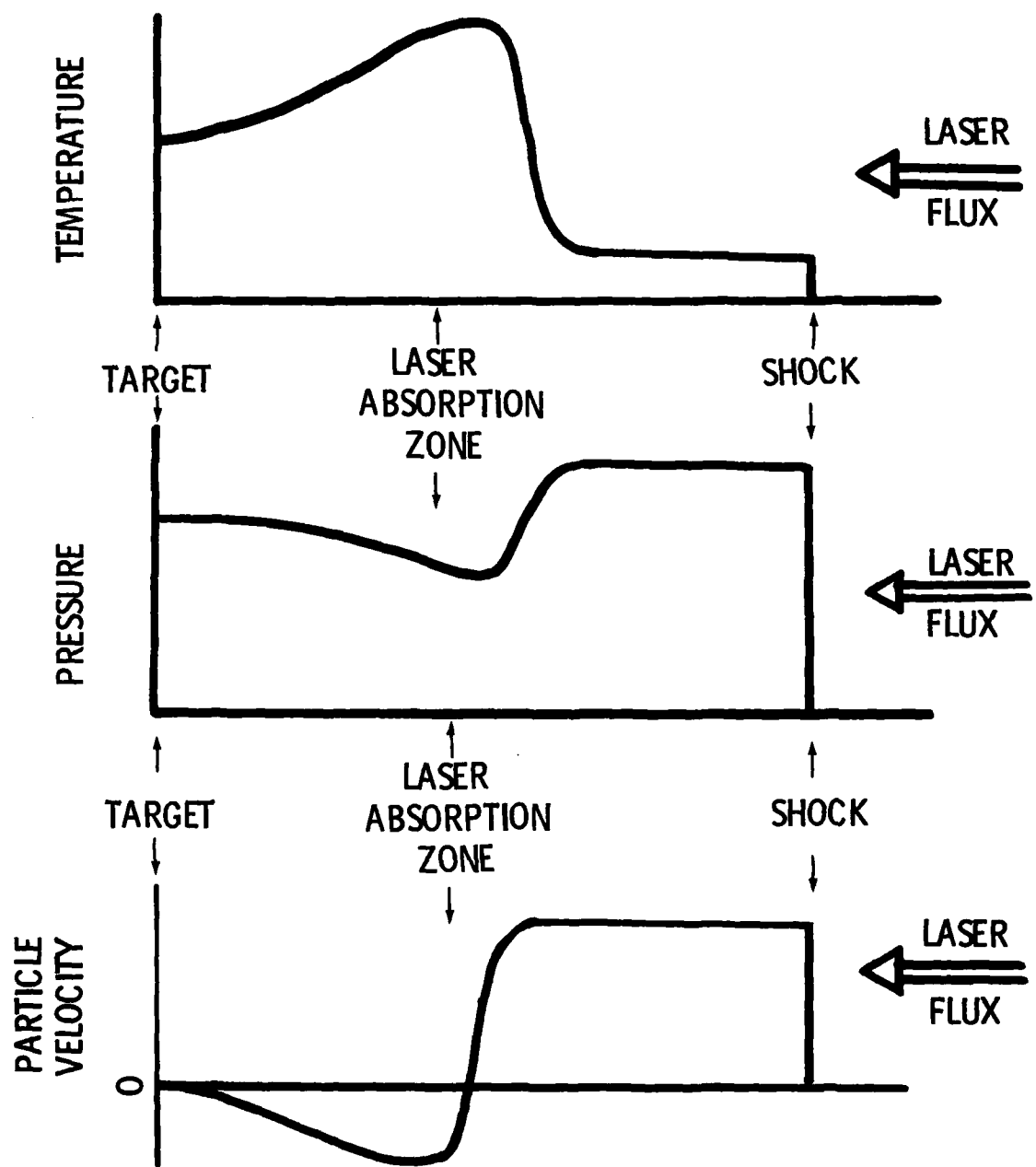
Fig. 2.5 Temperature, Pressure and Particle Velocity Profiles
for One-Dimensional LSC Wave Plasma.

2) The momentum equation.

$$\frac{dp}{dx} = - \frac{\dot{M}du}{dx} \, ,$$ (2.31)

where p is the pressure.   This equation can be integrated to yield

$$p + \dot{M}u = \text{constant.}$$ (2.32)

3) Conservation of energy.

$$\dot{M} \frac{d}{dx}\left(h + \frac{u^2}{2}\right) + \sum_i \frac{dS_i}{dx} + \frac{dI}{dx} = \frac{d}{dx}\left(\lambda \frac{dT}{dx}\right)$$ (2.33)

where h is specific enthalpy, S_i is a radiative flux in the ith band, I is the laser intensity and λ is the thermal conductivity.   Several of the terms in Eq. (2.33) can be rewritten; for example, we have:

$$\frac{dh}{dx} = c_p \frac{\partial T}{\partial x} + \frac{\partial p}{\partial x}\left(\frac{\partial h}{\partial p}\right)_T \, ,$$ (2.34)

and

$$\frac{\dot{M}}{2} \frac{du^2}{dx} = - u \frac{dp}{dx} \, ,$$ (2.35)

by virtue of Eq. (2.31). It is also convenient to write the laser absorption term as

$$\frac{dI}{dx} = - k_L' \, I_o \, e^{-\tau}$$ (2.36)

where k_L' is the effective laser absorption coefficient and τ is the optical depth.

τ obeys the equation:

$$\frac{d\tau}{dx} = k_L' \ .$$

(2.37)

Finally, the radiative flux in each spectral band is described by the appropriate radiative transfer model from the three presented earlier, that is,

$$\frac{dS_i}{dx} = \frac{d}{dx}\left(\lambda_{r_i} \frac{dT}{dx}\right) \qquad \text{(radiation conduction)} \ ,$$

(2.38)

$$\frac{dS_i}{dx} = 4\pi\kappa B_i \qquad \text{(transparent loss)} \ ,$$

(2.39)

$$\frac{dS_i}{dx} = \kappa\left[4\pi B_i - U_i\right]$$

$$\frac{dU_i}{dx} = -3\kappa S_i$$

(differential approximation) ,(2.40)

where λ_{r_i} is the radiation conductivity (see Eq. (2.23)), B_i is the Planck blackbody spectral function integrated over the band (see Eq. (2.25)), κ_i is the absorption coefficient for the given band, and U_i is the radiant energy intensity density for the spectral band of interest. Of course, only one of the three possible radiation models is used to describe the rate of change of flux for a given radiation band at a given position in the wave.

30

We also need the rate of change of pressure in terms of the rate of change of temperature. From Eqs. (2.29) and (2.31) we can solve for the rate of change of pressure as the function of temperature; it is given by:

$$\frac{\partial p}{\partial x} = \frac{\partial T}{\partial x} \left(\frac{\partial \rho}{\partial T}\right)_p \left(1 - \frac{u^2}{\left(\frac{\partial p}{\partial \rho}\right)_T}\right)^{-1} . \tag{2.41}$$

This expression breaks down when the denominator becomes zero, i.e., whenever

$$u^2 = \left(\frac{\partial p}{\partial \rho}\right)_T . \tag{2.42}$$

This corresponds to the particular velocity being equal to the isothermal sound velocity a_T, defined by

$$a_T = \sqrt{\left(\frac{\partial p}{\partial \rho}\right)_T} , \tag{2.43}$$

If this condition occurs during the integration through the wave profile, it is no longer correct to use an unsteady solution; instead a configuration is obtained in which the absorption portion of the wave is unaffected by the unsteady expansion which occurs in the tail of the wave. Equation (2.42) is expected to be satisfied during the transition to an LSD wave. In the calculations performed to model the LSC wave in the enhanced coupling regime, Eq. (2.42) was never satisfied for intensities up to 5 MW/cm^2. Note that the condition is not quite the same as the Chapman-Jouguet condition in that the sound speed we are dealing with is the isothermal sound speed, not the adiabatic sound speed. This is a consequence of having energy addition in the wave.

In addition to the Eqs. (2.29) to (2.41) we also must provide functions defining ρ, h, k_L', λ, and κ_i as a function of temperature and pressure. This is accomplished by the air property code described in Appendix A.

In solving the coupled set of Eqs. (2.29) to (2.41), it is convenient to define a new variable R

$$R = -\left(\lambda + \sum_i \lambda_{r_i}\right)\frac{dT}{dx} , \qquad (2.44)$$

where the sum over i is only over those bands for which the radiation conduction model is used. Then Eq. (2.33) can be used in conjunction with Eqs. (2.41), (2.44) and (2.35) to define dR/dx in terms of T, p and τ. Similarly, Eq. (2.41) expresses dp/dx in terms of R and various thermodynamic quantities. The independent variables in this set of equations are p, T, τ, R, and S_i. The particle velocity u is a dependent variable determined by the constraint Eq. (2.32). There are also two parameters in the series of equations; they are the incident laser intensity I_o and the mass flow $\dot{M}$. The equations which describe the rate of change of the independent variables are Eqs. (2.41), (2.44), (2.37), (2.33) and (2.38)-(2.40) for p, T, τ, R, and the four S_i's, respectively.

As in the previous work,[4] the solution is found by an iterative procedure. First a value of the laser intensity I_o and the mass flow $\dot{M}$ are chosen. We must also choose the initial shock pressure p_s. Using the Hugoniot relations, we can calculate the temperature T_s behind the shock and the particle velocity behind the shock in the lab frame which is denoted by u_s. At the origin of the co-ordinates the temperature is chosen to be $T_i = 10,000\,^{\circ}K$, and the initial value of the optical depth to be 0, since no laser absorption occurs at temperatures below T_i. By virtue of Eq. (2.32), which is valid in the coordinate system fixed on the LSC wave, we find that the

pressure p_i and density ρ_i at the starting point of the integration obey the relationship

$$p_s + \rho_s \left(V_{LSC} - u_s\right)^2 = p_i + \frac{(\dot{M})^2}{\rho_i} . \qquad (2.45)$$

In determining the pressure from Eq. (2.45), it is convenient to use the density corresponding to the temperature T_i and the pressure p_s since the pressure does not change much during the initial heating period. Thus, Eq. (2.45) defines the initial pressure. Conservation of energy gives another constraint on the variables, namely,

$$\left(R + \sum_{i\, =\, (VUV,\ EUV,\ VUV')} S_i\right)_{x\, =\, 0} = \dot{M}\left[h\left(T_i, p_i\right) - h\left(T_s, p_s\right)\right], (2.46)$$

where h is the enthalpy of the air and the sum of fluxes is over the three bands which are absorbed by the shocked air. This equation serves to define the initial condition on R provided we know the initial conditions on the radiative fluxes.

In the radiation modeling it is assumed that the EUV band is always modeled by radiation conduction; therefore, the initial value of S_{EUV} is given by:

$$S_{EUV} = - \lambda_{EUV} \frac{dT}{dx} , \qquad (2.47)$$

where we have now adopted the notation that λ_i represents the radiation conductivity for the band designated by i. The next band, the VUV band,

is described by the differential approximation; therefore, we must specify both the initial flux S_{VUV} and the initial radiation intensity density U_{VUV}. For the thickness of plasmas of interest the VUV band will be optically thick; we can relate S_{VUV} and U_{VUV} by the expression which is appropriate for blackbody radiation; namely,

$$U_{VUV} = 2 \mid S_{VUV} \mid . \qquad (2.48)$$

The initial value of S_{VUV} is still a variable parameter. The integration of Eq. (2.33) is insensitive to the initial values of S_{VUV}, and S_{VIS} since the fluxes are not directly coupled into the energy equation (Eq. (2.33)) at the start of the calculation. Only the rate of change of these fluxes is important and that is defined by Eqs. (2.38) - (2.40). Thus, any reasonable value can be chosen for an initial guess. The above discussion defines the initial conditions for the parameters p, T, τ, R, S_{EUV}, and U_{VUV}. Only two of the parameters remain to be iterated; they are S_{VUV} and $\dot{M}$. The correct values of these parameters are determined by the back boundary conditions.

At the back boundary, the particle velocity must be 0 in the laboratory frame. In the coordinate system in which the LSC wave is at rest, the particle velocity u at the target must be equal to the velocity of the LSC wave in the laboratory system; i.e.,

$$u \text{ (target)} = V_{LSC} . \qquad (2.49)$$

There is also a back boundary condition on the radiative flux in the EUV band; we require that the flux given by radiation conduction approximation be consistent with

the flux which is predicted for the shape of profile near the back boundary. This self-consistency condition must be employed since the radiation conduction approximation breaks down at the target boundary. For a self-consisting condition which conserves energy we choose

$$\left(\lambda + \lambda_{EUV}\right)\left(\frac{dT}{dx}\right)_{Target} = \alpha_{EUV} \ \pi \ B_{EUV} \ \left(T\left(target - \frac{2}{3 \kappa_{EUV}}\right)\right), \quad (2.50)$$

where λ is the thermal conductivity and B_{EUV}, the spectral blackbody function over the EUV band, is evaluated at a temperature corresponding to the temperature of the plasma at distance from the target of 2/3 of an absorption length for EUV radiation, and α_{EUV} is the absorptivity of the target to the EUV radiation. By varying the free parameter M, this back boundary condition can be met for given laser intensity, shock pressure and initial value of S_{VUV}.

The flux S_{VUV} at the target must also be consistent with the value of U_{VUV}. We assume that the relationship between the S_{VUV} and the U_{VUV} is well approximated by using the blackbody relationship which relates the radiative flux and radiation intensity density for a hemispherical distribution.[10] Let S^+ (S^-) and U^+ (U^-) represent the radiative flux and radiative intensity for the hemisphere of radiation directed in the positive (negative) x direction (see Fig. 2.6). For blackbody radiation; that is, isotropic radiation within the hemispheres, the flux is related to the intensity density by

$$2S^+ = U^+,$$

and   (2.51)

$$2S^- = U^- .$$

35
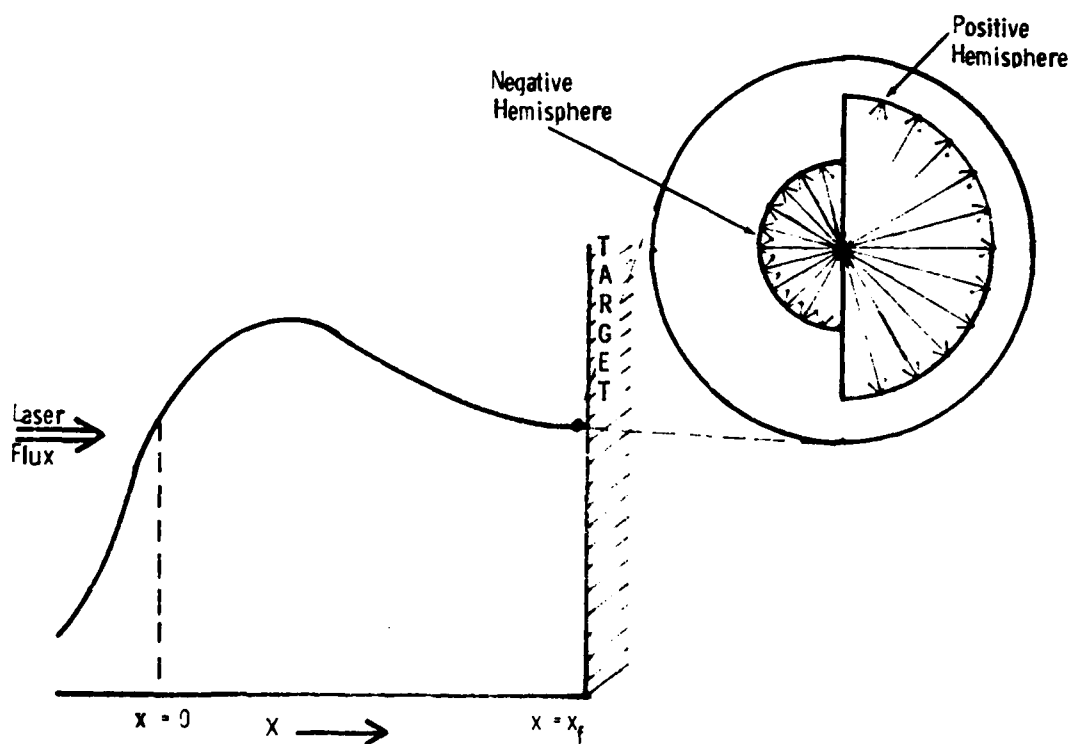
Fig. 2.6 Details of Hemispherical Radiative Distributions Used
for Determining Boundary Conditions.

The total radiation flux S is given by:

$$S = S^+ - S^- ,$$

(2.52)

whereas the total radiation intensity density U is given by:

$$U = U^+ + U^- .$$

(2.53)

At the target, the material absorptivity α relates S^+ to S^- ;

$$S^- = (1 - \alpha) S^+ .$$

(2.54)

From Eqs. (25.1) - (25.4) applied to the VUV band we obtain:

$$S_{VUV} = \frac{\alpha_{VUV} \, U_{VUV}}{2 \, (2 - \alpha_{VUV})}$$

(2.55)

If at the back boundary, as defined by Eq. (2.49), the criterion given in Eq. (2.50) is met by varying $\dot{M}$, the remaining condition, Eq. (2.55), can be satisfied by adjusting the last free parameter - the initial value of S_{VUV}.

There is a systematic way to change the mass flux in order to satisfy Eq. (2.50). If at the back boundary, which is determined by Eq. (2.49) and denoted by x_f, we find

$$\left(\lambda + \lambda_{EUV}\right) \frac{dT}{dx} > \alpha_{EUV} \, \pi B_{EUV} \left(T\left(x_f - \frac{2}{3 \, \kappa_{EUV}}\right)\right) ,$$

(2.56)

then the mass flux $\dot{M}$ is too low, while conversely, if we find

$$\left(\lambda + \lambda_{EUV}\right) \frac{dT}{dx} < \alpha_{EUV} \, \pi B_{EUV} \left(T\left(x_f - \frac{2}{3 \, \kappa_{EUV}}\right)\right) ,$$

(2.57)

the mass flux is too high. Therefore, the direction of the inequality identifies the way in which $\dot{M}$ must be changed.

The above analysis of back boundary conditions assumes that the VUV band is always represented throughout the whole profile by the differential approximation. If, however, the plasma is optically thick to the VUV band, at some position in the wave we must change from the differential approximation to the radiation conduction approximation. The transition must be made without creating an energy source or sink, which can be accomplished only if the flux S_{VUV} can be represented by a radiation conduction term $\lambda_{VUV} \, dT/dx$. Since both S_{VUV} and dT/dx are already determined as a function of distance, it is possible to make the transition only at special points where

$$S_{VUV} = \lambda_{VUV} \frac{dT}{dx} . \qquad (2.58)$$

Another requirement which must be met is that the transition be smooth, that is, during the switch from one description of the radiative transport to another description there must be no change in the derivative of the temperature. This consistency condition replaces the back boundary condition Eq. (2.55) which relates S_{VUV} to U_{VUV}. If the transition is not smooth, i.e., if the slope of the temperature profile changes abruptly during the change from one model of radiative transfer to another, the initial value of S_{VUV} must be changed. The position of the back boundary is still found from Eq. (2.49) and the boundary condition to be satisfied at this point is the analog of Eq. (2.50) in which the total radiative conductivity is self-consistent with the radiation emitted in both the EUV and VUV bands. This equation takes a mathematical form

$$\left(\lambda + \lambda_{VUV} + \lambda_{EUV}\right)\left(\frac{dT}{dx}\right)_{TARGET} = \alpha_{EUV} \, \pi B_{EUV} \left(T\left(x_f - \frac{2}{3\,\kappa_{EUV}}\right)\right)$$

$$+ \quad \alpha_{VUV} \, \pi B_{VUV} \left(T\left(x_f - \frac{2}{3\,\kappa_{VUV}}\right)\right) . \qquad (2.59)$$

For extremely thick plasmas, it is possible for the transparent approximation of the VIS and VUV' bands to become invalid, and the differential approximation must be employed for these bands. At the point where the transition from the transparent approximation to the differential approximation is made, values must be chosen for both the flux and the radiation intensity density of both bands. This is another iterative procedure and the correct choice for S and U at the transition point causes Eq. (2.55) to be satisfied at the target for each of the bands. The values of S and U at the transition can be determined in terms of one unknown function by analysis of the radiation characteristics of the LSC wave. Consider the band radiation into the hemisphere facing downstream which has one-sided flux of S^+ and one-sided radiant energy density U^+ and the radiation into the hemisphere facing upstream which has a one-sided radiation flux denoted by S^- and one-sided radiation intensity density represented by U^-. Then the total flux and total radiant energy density are given by:

$$S = S^+ - S^- \, ,$$

$$U = U^+ + U^- .$$

(2.60)

However, the values of S^+ and U^+ are known as a result of the integration of the LSC wave to the point where the transition is made. Furthermore, the radiation coming from the downstream portion of the plasma is approximately isotropic, so that we may use the requirement

$$U^- = 2S^- \, .$$

(2.61)

Thus, there is only one unknown to be specified at the change-over point and it is uniquely determined by the back boundary condition Eq. (2.55).

39

It is evident that solving for the LSC wave by the technique described above involves a great deal of iteration. However, using previous experience with LSC wave profiles to guide the initial guesses we can minimize the amount of iteration approach.

Plasma profiles for $I = 4 \, MW/cm^2$ are shown in Fig. 2.7 for various times. All the profiles are drawn in the coordinate system at which the LSC wave is at rest and at which the temperature at $x = 0$ is $10,000\,^{\circ}K$. In this coordinate system, the wall appears to move back as time progresses. The peak temperature of the wave remains fairly constant, but the wall temperature drops as time proceeds. Since the temperature of the plasma near the wall controls the bulk of the radiation which is strongly absorbed by the target, this decrease in wall temperature plays an extremely important role. In Fig. 2.8, the intensity absorbed by Al2024 is given as a function of time for three incident laser intensities. In computing the thermal coupling to a target for a given laser intensity and pulse time, we calculate the coupling during the one-dimensional stage merely by integrating the appropriate curve up to τ_c which is defined as the smaller of t_p or τ_{2D} where t_p is the pulse time and τ_{2D} is the time characteristic of radial expansion. The total coupled fluence includes both a contribution from the 1-D LSC wave and a contribution from the decay of the wave after τ_c. The latter contribution is calculated in the same manner as in the previous report,[1,2] i.e., the absorbed intensity is assumed to decrease at a rate determined by the appropriate blast wave decay laws.

Results found by using these improved values of the one-dimensional radiation are shown in Figs. 2.9 and 2.10. In Fig. 2.9, we have plotted the predicted absorbed fluence by an Al2024 target exposed to laser intensity of $2 \, MW/cm^2$. The absorbed fluence is given as a function of spot radius, where it is assumed that the pulse time is designed to keep $\hat{\tau} = 1$.
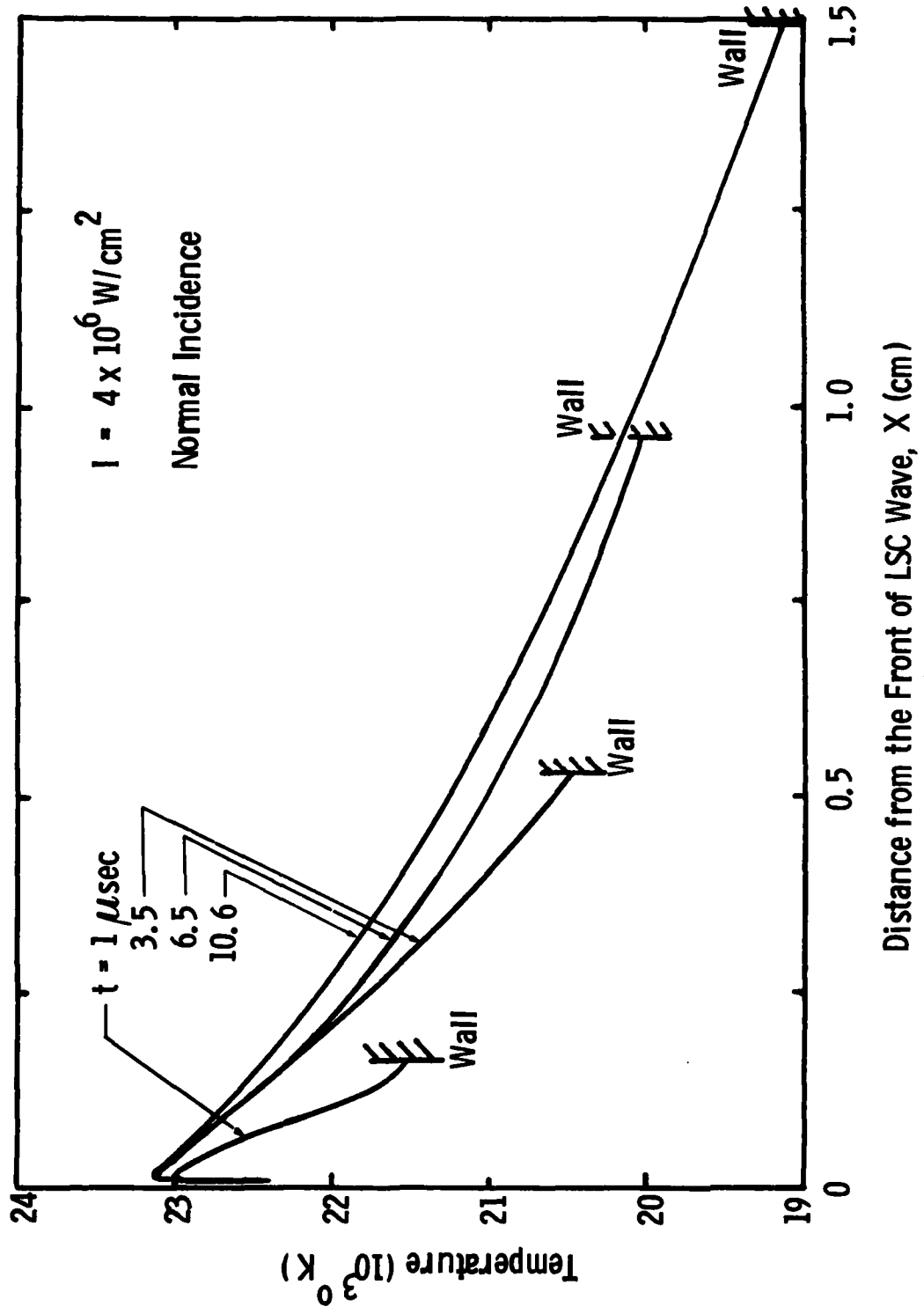
Fig. 2.7 Temperature Profile of One-Dimensional LSC Wave Plasma at Various Times During Laser Pulse.

41
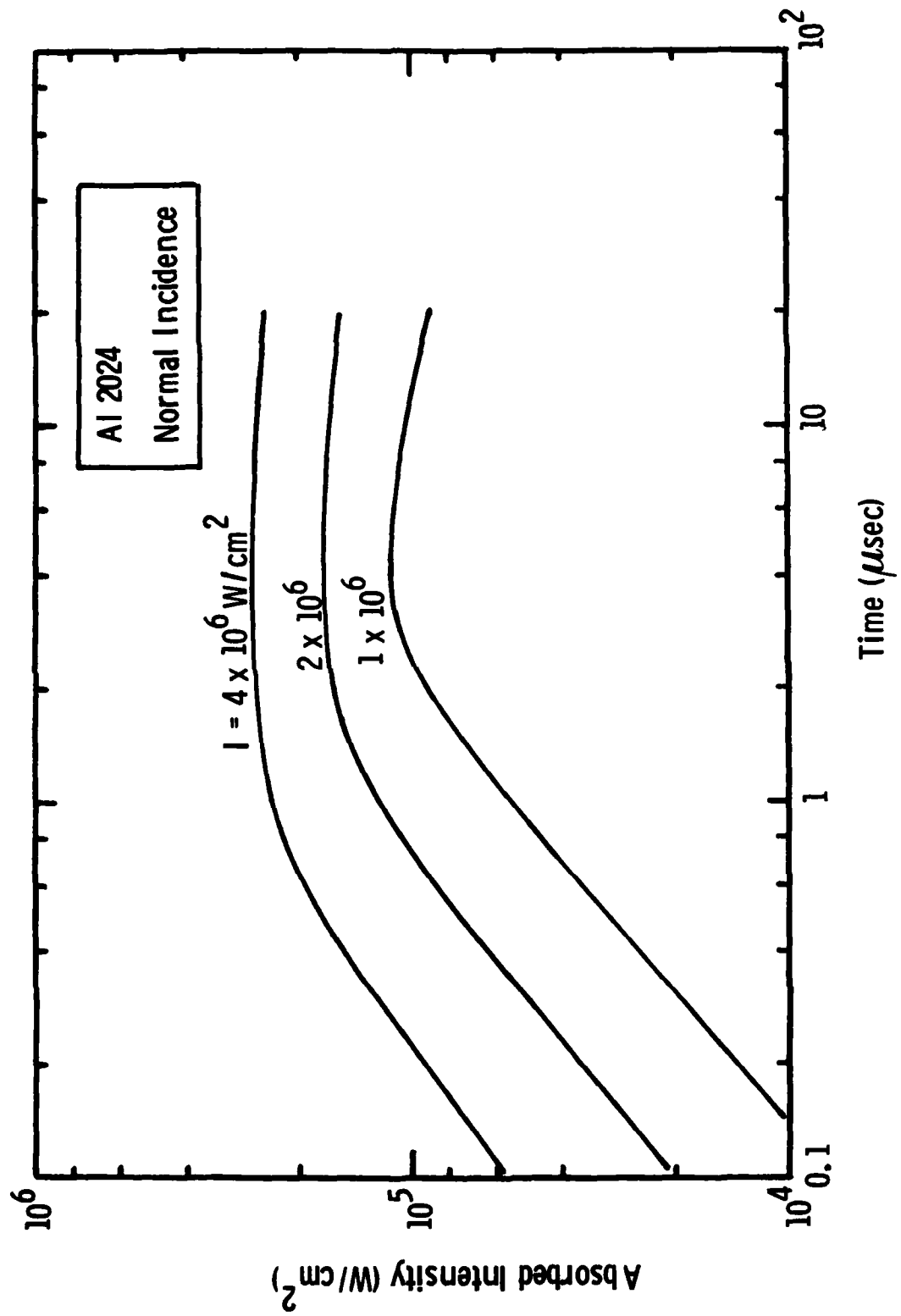
Fig. 2.8 Intensity of One-Dimensional LSC Wave Plasma Radiation Absorbed by Al2024 Target as a Function of Time from Beginning of the Laser Pulse.
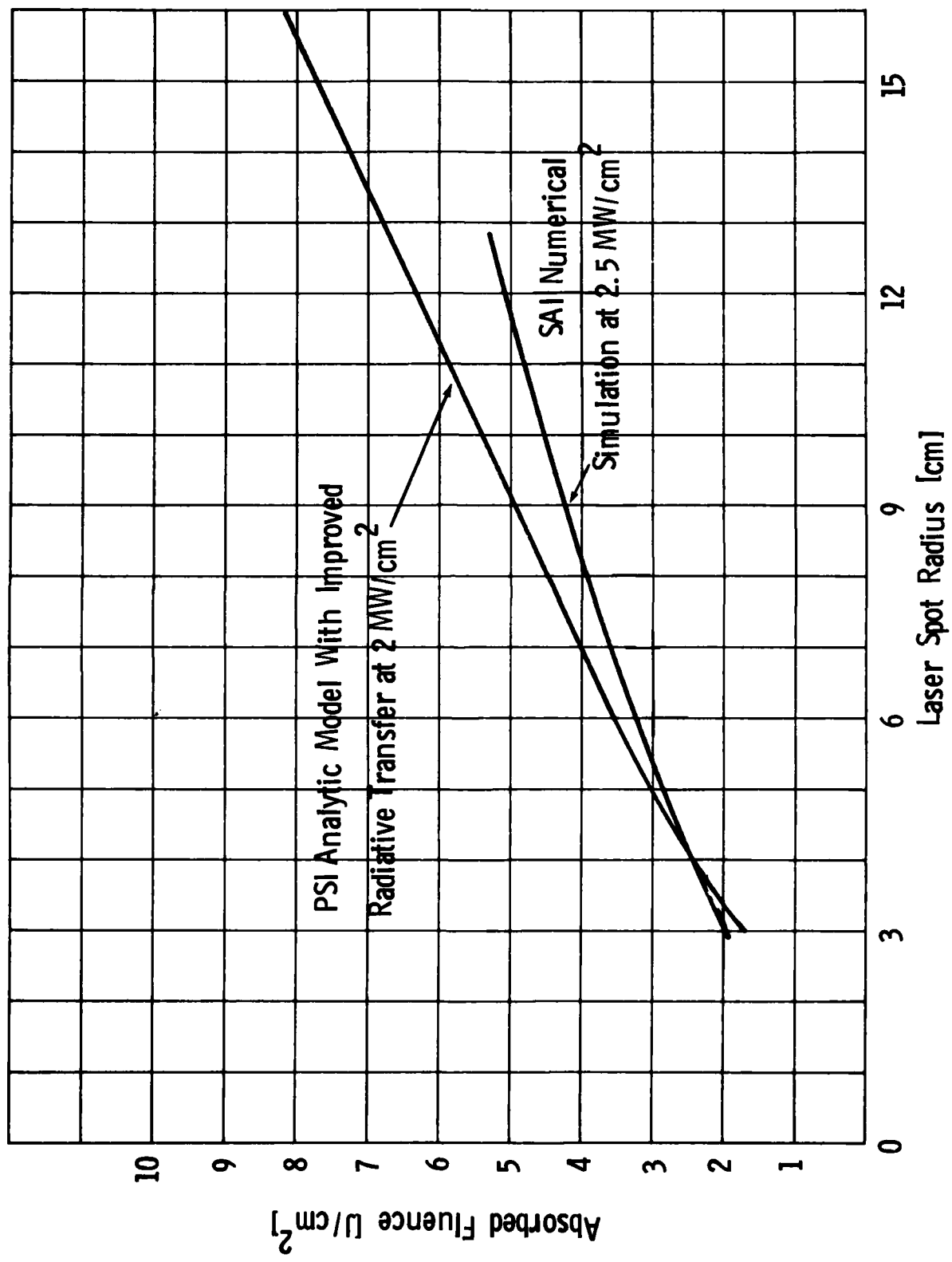
Fig. 2.9 Theoretical Predictions of Fluence Absorbed by Al2024 as Function of Spot Radius for $\hat{\tau} = 1$.

43
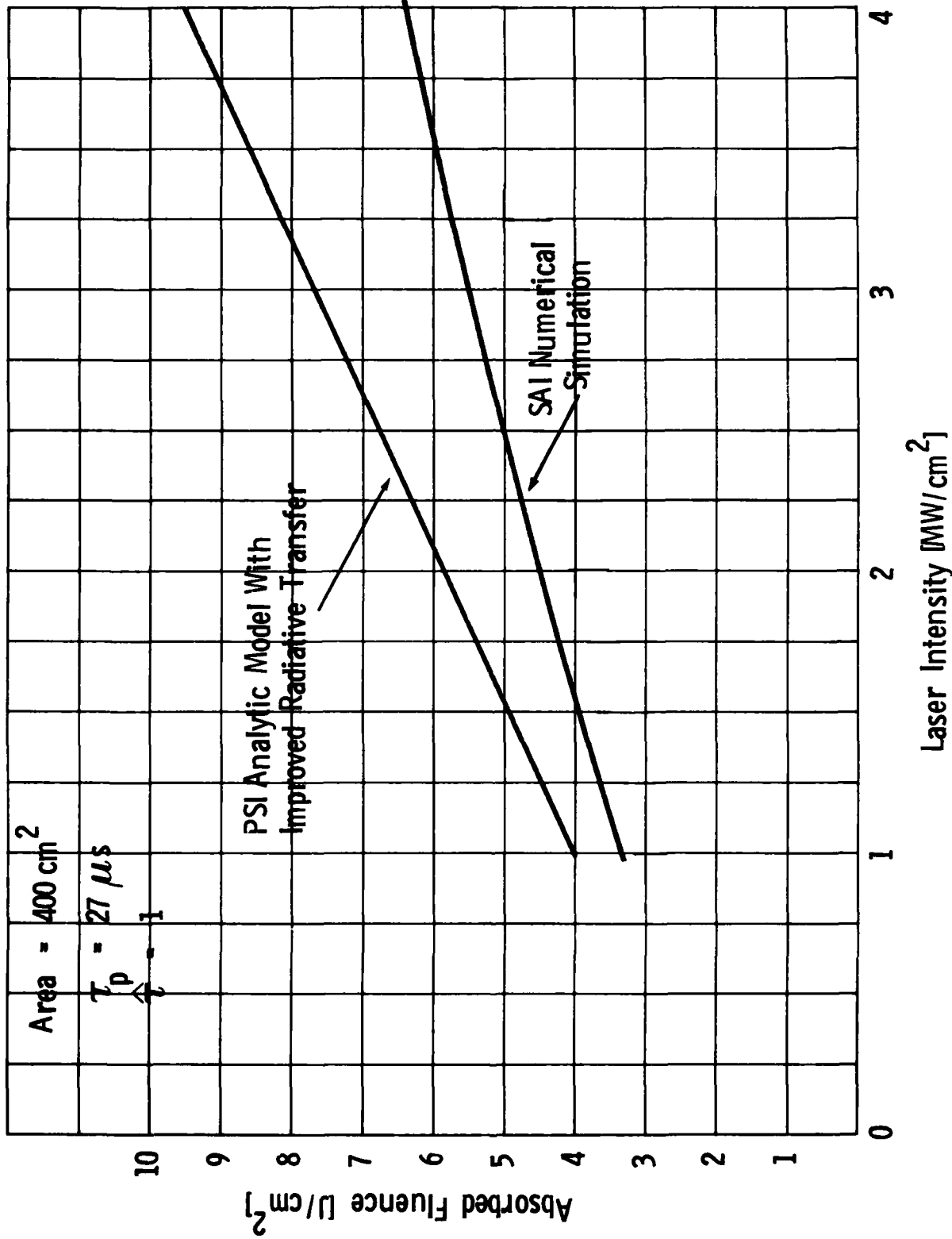
Fig. 2.10 Theoretical Predictions of Fluence Absorbed by Al2024 as Function of Laser Intensity for $\hat{\tau} = 1$.

The figure axes and labels read:

- Y-axis: Absorbed Fluence [J/cm^2]
- X-axis: Laser Intensity [MW/cm^2]
- Area = 400 cm^2
- τ_p = 27 μs
- $\hat{\tau}$ = 1
- PSI Analytic Model With Improved Radiative Transfer
- SAI Numerical Simulation

44

There is no evidence of radial decoupling in these calculations for this low intensity. Also shown on the plot are the new results of the SAI numerical simulation which used the improved radiation parameters given in Appendix A. The numerical simulation includes unsteady effects, but it employs simplified radiative transfer; the radiation is treated either as a transparent loss or as radiative conduction. The predictions of the two models lie extremely close to one another for small spot sizes. As the spot size increases, there is a divergence between the models, but the difference is still not more than 25% for the largest sizes considered. In Fig. 2.10, the predicted absorbed fluence is plotted as a function of intensity for a constant spot size of 400 cm^2 and pulse time of 27 μsec. The PSI model increases almost linearly and has no pronounced saturation effect. For intensities above 4 MW/cm^2, the data on the plasma velocity and plasma pressure indicates that a transition from a LSC wave plasma to an LSD wave plasma occurs. Therefore, the PSI model should not be used beyond 3 to 4 MW/cm^2. The SAI numerical simulation is also shown on this plot. Once again, there is good agreement between the theories at low intensity but the disagreement becomes quite large at high intensity. The shallow slope and apparent saturation observed in the SAI model may be the result of the inclusion of unsteady effects associated with the LSC/LSD wave transition. However, this interpretation is uncertain since the SAI numerical simulation fails to predict the pressure and velocity observed in the transition regime.

In addition to the thermal coupling, the LSC wave model predicts the pressure at the surface at the target as a function of time. For example, in Fig. 2.11, we have plotted the pressure as a function of distance at various times. It can be seen that the pressure drops slowly as time progresses; therefore, there is not a unique surface pressure which can be associated with a given laser intensity. In Fig. 2.12, the surface pressure at approximately 5 μ sec is plotted as a function of laser intensity. The pressure increases in

45
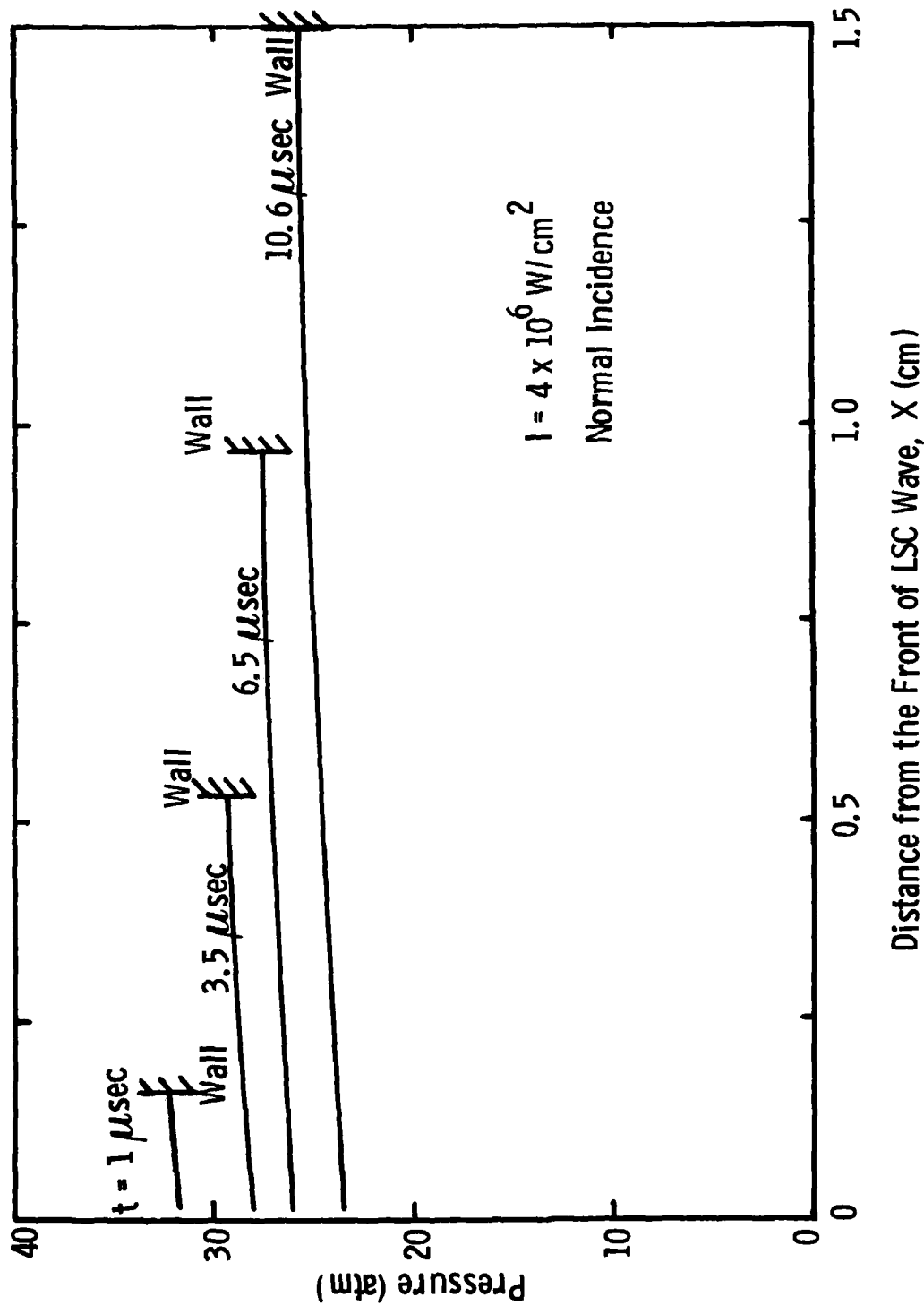
Fig. 2.11 Pressure Profile of One-Dimensional LSC Wave Plasma at Various Times During Laser Pulse.
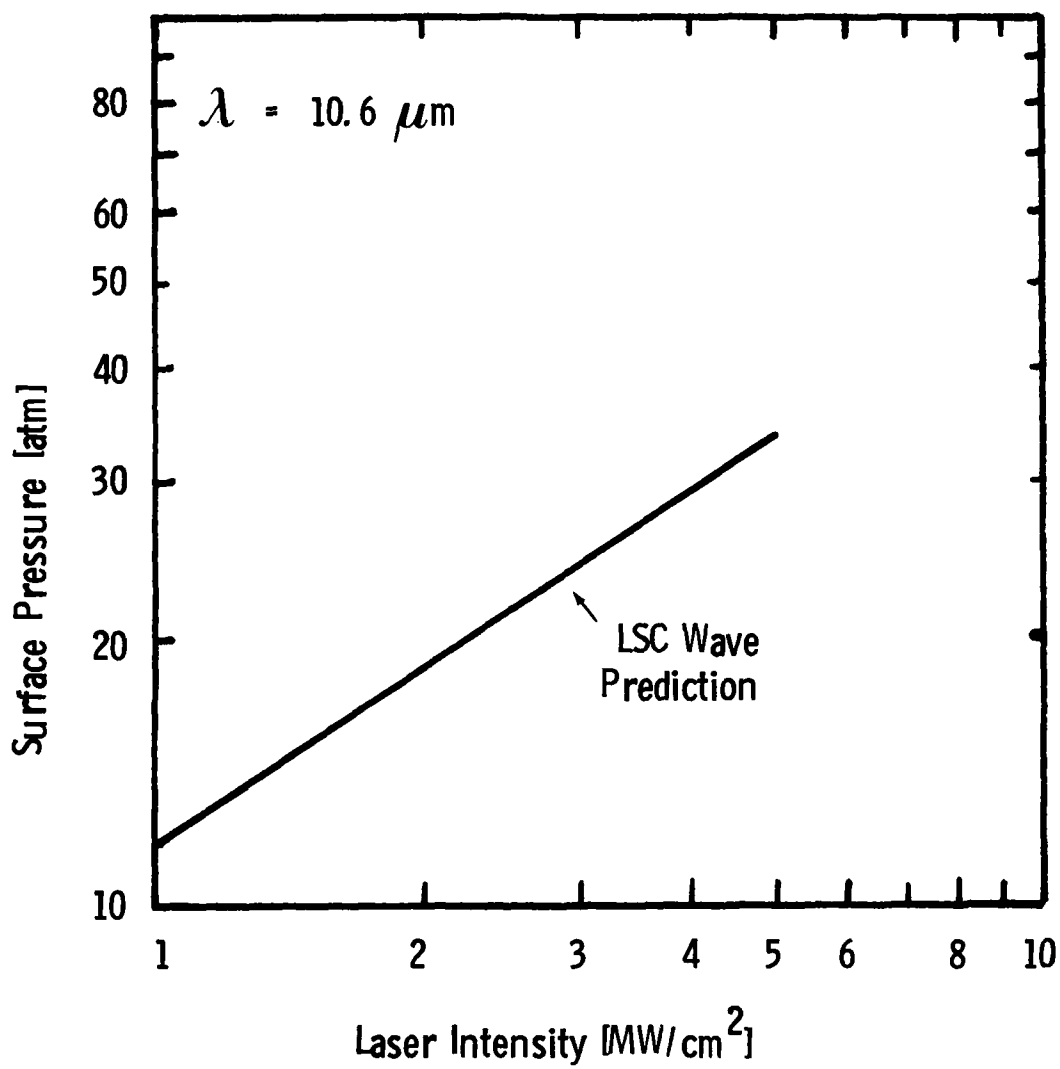
Fig. 2.12 Theoretical Prediction of the Surface Pressure
Produced by One-Dimensional LSC Wave Plasma
as a Function of Laser Intensity. The Predictions
Correspond to 5 μs after the Plasma is Created.

47

proportion to $I_o^{2/3}$ as predicted by the simplified LSC wave theory used in the previous report,[1,2] but the magnitude of the pressure in Fig 2.12 is slightly lower than earlier estimates.

To summarize, an improved version of the LSC wave model has been used to predict the energy transfer via plasma reradiation to the target and the pressure over the target. Predictions made with this improved model indicate that radiative diffusion in the axial direction does not decouple the plasma for fluences less than 100 J/cm^2. The predictions made with this semi-analytical model are in good agreement with the predictions made by the SAI numerical simulation for intensities below 4 MW/cm^2. Above 4 MW/cm^2, the numerical simulation shows a saturation effect, whereas the semi-analytical model does not. It is believed that the LSC/LSD wave transition starts near 4 MW/cm^2 and, therefore, the semi-analytical model is not valid at higher intensities.

SECTION 3

PULSED LASER INTERACTION WITH OTHER METALS

There are other metals of interest besides Al2024; for example, a list of common aerospace metals includes Ti6Al4V, SS304 and 4130 steel. It is important to predict the thermal and mechanical coupling to these materials, as well as to Al2024. These metals have a higher intrinsic absorptivity for 10.6 μm radiation than Al2024; therefore, it is not obvious, a priori, whether or not igniting a plasma enhances the coupling. In this section, we modify the enhanced coupling model discussed in Section 2 to predict the coupling to these other metals. The predicted coupling coefficients are compared to intrinsic absorptivity of the metals and the absorptivities of the various metals are compared to each other for identical laser conditions.

Whenever an air plasma is ignited over a surface, the LSC wave model describes the radiative transfer to the surface. The only dependence of the energy absorbed by the targets on the target composition is through the different spectral absorptivities of the materials. Therefore, for initial estimates of thermal coupling to other metals, it is reasonable to use the air LSC wave model described in Section 2, along with the spectral absorptivities of the various target materials, in order to predict the thermal coupling. Other effects, such as target combustion and the effect of target vapor on the LSC wave properties, have not been incorporated at this stage. The mechanical coupling caused by the air plasma is independent of the target composition; the other metals experience the same pressure and impulse as Al2024.

It is difficult to find reliable experimental values for the spectral absorptivities of the various alloys. The absorptivities depend strongly upon surface preparation; moreover, it is uncommon to measure the spectral absorptivities

of alloys for spectral regimes having wavelengths shorter than 2000 A.

We have, however, constructed an estimate of the spectral absorptivities

for the four alloys of interest; namely, A12024, SS304, steel 4130, and

Ti6A14V, by combining (1) the limited data on the spectral absorptivity

of alloys, [11] which is available for wavelengths $\lambda > 2000$ A, and (2) the

absorptivities measured for the pure metals [12,13,14] (Fe, Al, and Ti)

in the short wavelength, $\lambda < 2000$ A, region of the spectrum. Our best

estimate of the absorptivities are shown in Fig. 3.1.

Examination of Fig. 3.1 shows that, for the spectral region with wave-

lengths less than 1240 A, (wavenumber > 80600 cm^{-1}) the absorptivity is

strong for all metals; whereas in the long wavelength region, $\lambda > 1240$ A,

the absorptivity varies widely from one alloy to another. Under identical

laser conditions, all metals receive the same incident radiation from the

LSC wave plasma. However, based on the spectral absorptivities presented

in Fig. 3.1, we expect to find a hierarchy in the metals based upon absorbed

fluence — the ordering from highest to lowest should be Ti6A14V, steel 4130,

stainless steel 304, and A12024. Moreover, the LSC wave model predicts that

for low intensity and/or small spots, the dominant radiation lies in the spectral

region below 1240 A, where all the alloys absorb strongly, whereas for high

intensities and/or large spots, the radiation in the band having wavelengths

greater than 1240 A becomes equally important. Therefore, it is expected

that the relative differences in absorbed fluence among the various alloys will

increase as the intensity and/or spot size is increased for fixed values of $\hat{T}$.

In order to compute the radiation absorbed by the target, we must

specify the absorptivity of the alloys in the various spectral bands which

are used in the LSC wave model. The recommended values, deduced

from Fig. 3.1, are shown in Table 3.1, along with the values estimated for

SS304 and Ti6A14V for two special surface preparations. The EUV and

VUV bands have essentially the same absorptivity for all six cases, whereas

50
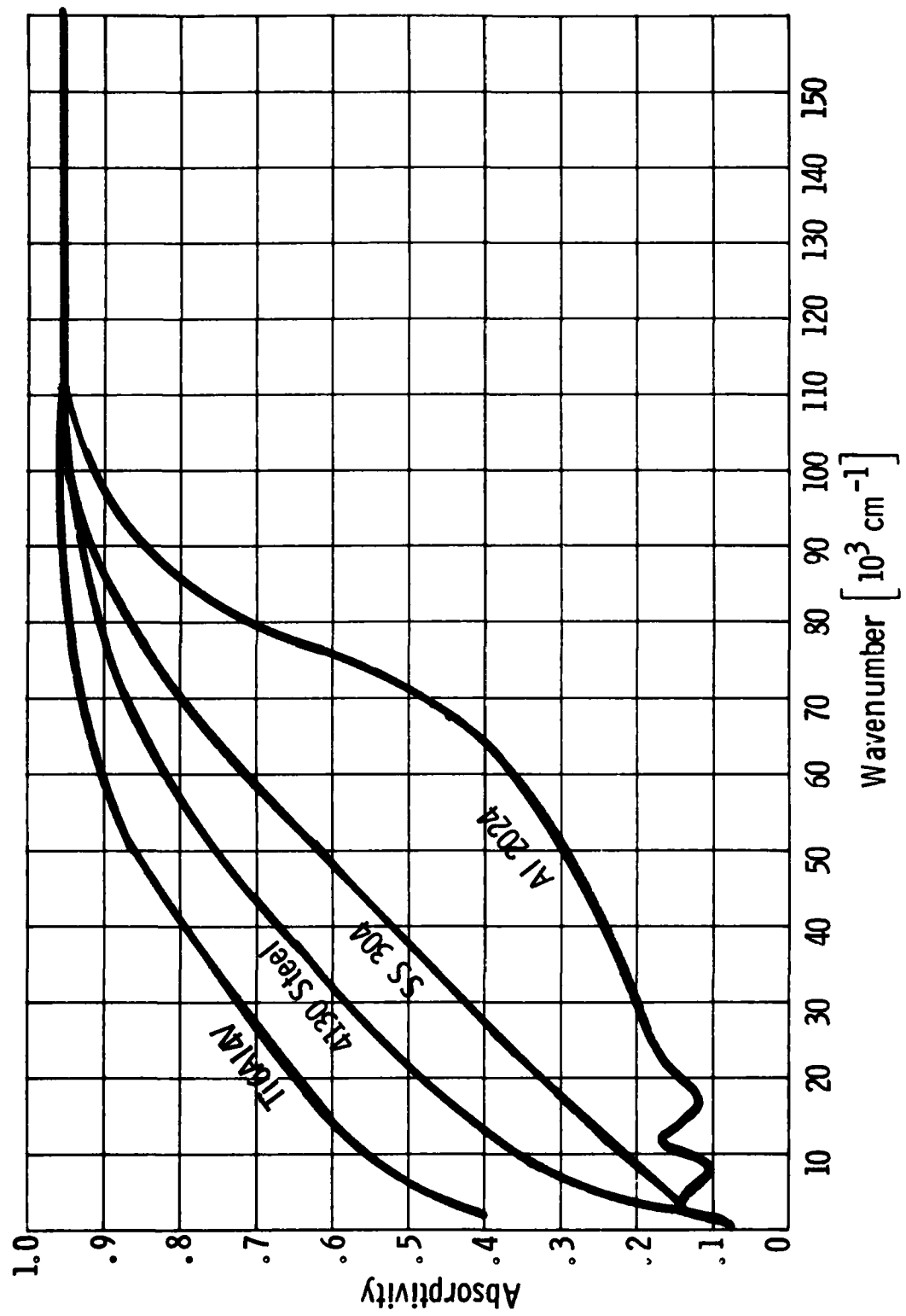
Fig. 3. 1 Spectral Absorptivities of Alloys.

TABLE 3.1

Recommended absorptivities of various alloys for the spectral
bands used in air LSC wave radiation modeling.

Metal	EUV	VUV	VUV'	VIS
Al2024	0.95	0.90	0.50	0.15
SS304	0.95	0.95	0.80	0.40
Steel 4130*	0.95	0.95	0.85	0.50
Ti6Al4V	0.95	0.95	0.90	0.70

*Used Steel Values

SURFACE PREPARATION EFFECTS

SS304 (oxidized)	0.95	0.90	0.90	0.90
Ti6A14V (coated)	0.95	0.95	0.90	0.90

the VUV' and VIS bands have widely varying absorptivities. Furthermore, the oxidized or coated surfaces have the highest absorptivities in the long wavelength regions.

In Figs. 3.2 - 3.4, the intensity absorbed by the three non-aluminum alloys is shown as a function of time. A similar plot for oxidized steel is given in Fig. 3.5. Typical values of the thermal coupling coefficient for the four alloys as a function of the parameter $\hat{\tau}$ are shown in Figs. 3.6 - 3.9 for a spot size of 100 cm^2. For comparison, the intrinsic absorptivities of the materials to 10.6 μm and 3.8 μm radiation are also shown. The simple semi-analytical model breaks down at small $\hat{\tau}$ because the radiation losses during the decay of the plasma are strong enough to affect the temperature of the decaying plasma, but the blast wave decay laws do not include these losses in the determination of the plasma properties. Therefore, the predictions in the small $\hat{\tau}$ regimes are represented by dashed lines to indicate that the theory is only qualitatively correct. It is expected, however, that the coupling coefficient saturates for $\hat{\tau} < 1$, as predicted. In all cases, it is found that the predicted enhanced thermal coupling coefficient for $\hat{\tau} \leq 1$ is larger than the intrinsic absorptivity for 10.6 μm radiation and is at least as large as the intrinsic absorptivity for 3.8 μm radiation. For Ti6A14V, the absorptivity of the alloy at 10.6 μm is uncertain, therefore, a band of representative absorptivities are shown; no value for the intrinsic absorptivity at 3.8 μm is shown.

Theoretical predictions of the fluence absorbed by the various alloys are shown in Fig. 3.10 as a function of laser intensity I for fixed $\tau_p = 10$ μs, $\hat{\tau} = 0.8$, and area of 100 cm^2. The qualitative features which are expected on the basis of the absorptivities of the various alloys are borne out in the quantitative predictions of Fig. 3.9. There is a hierarchy for the alloys
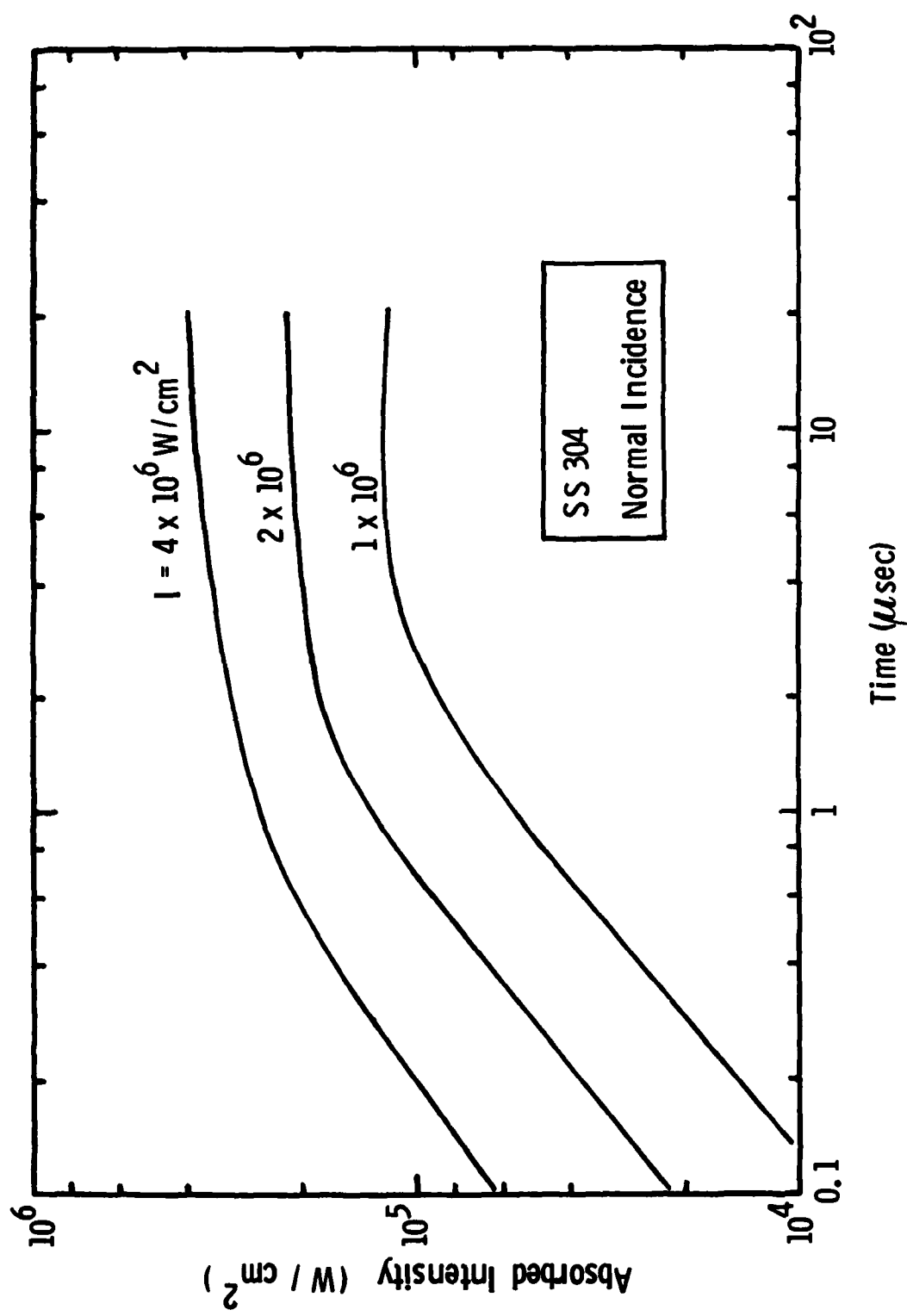
Fig. 3.2 Intensity of One-Dimensional LSC Wave Plasma Radiation Absorbed by SS304 Target.

54
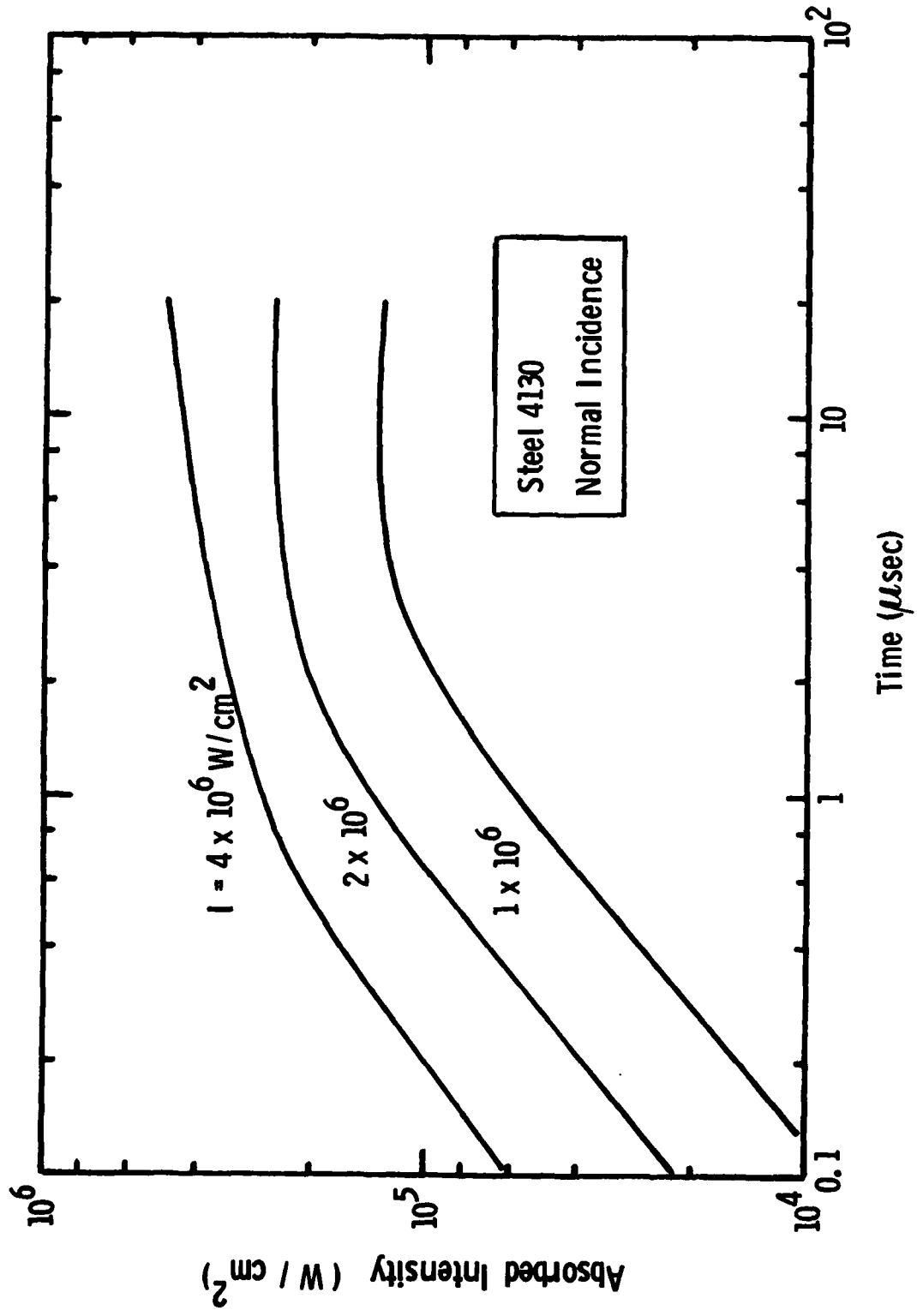
Fig. 3.3 Intensity of One-Dimensional LSC Wave Plasma Radiation Absorbed by Steel 4130 Target.

55
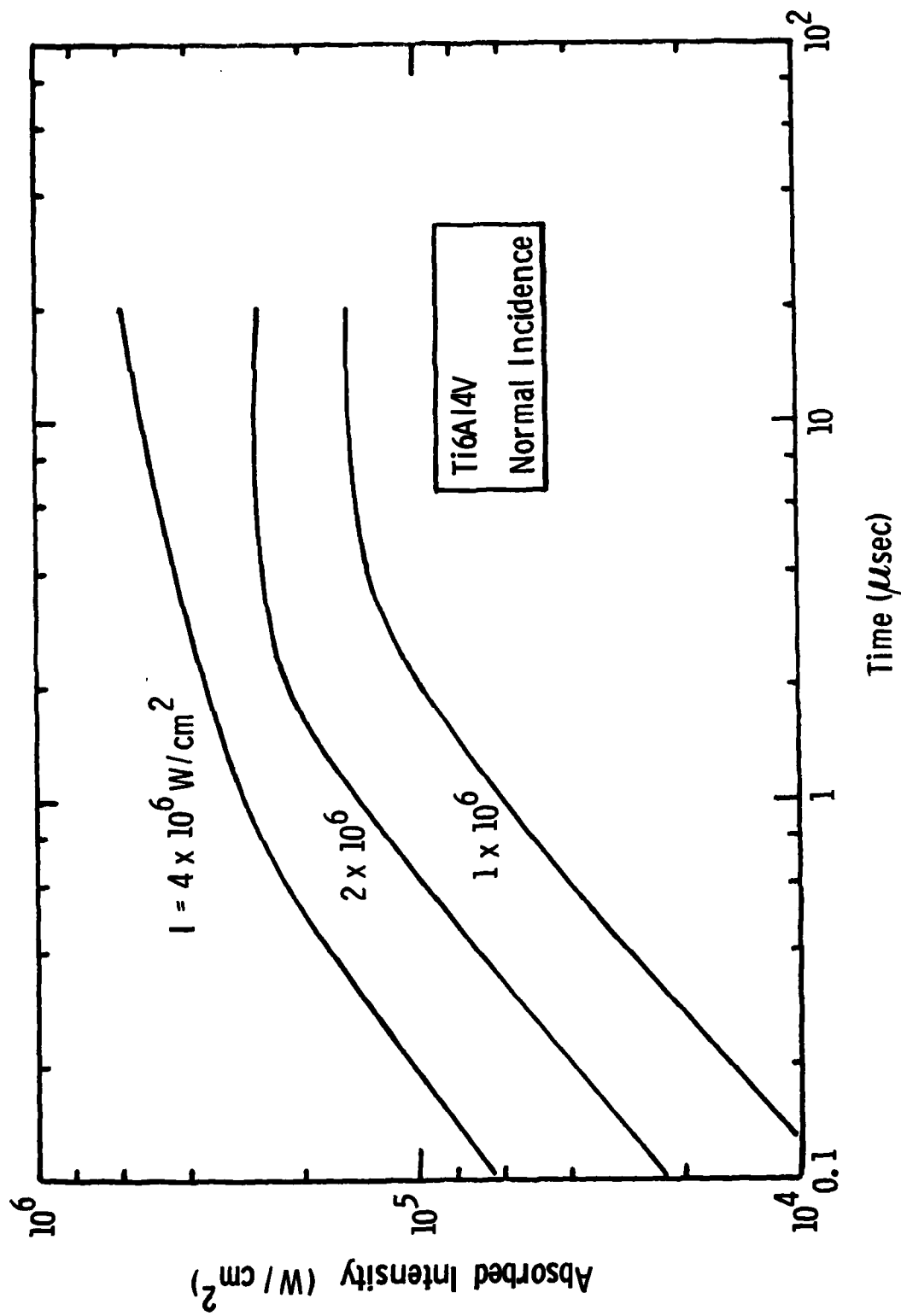
Fig. 3.4 Intensity of One-Dimensional LSC Wave Plasma Radiation Absorbed by Ti6Al4V Target.
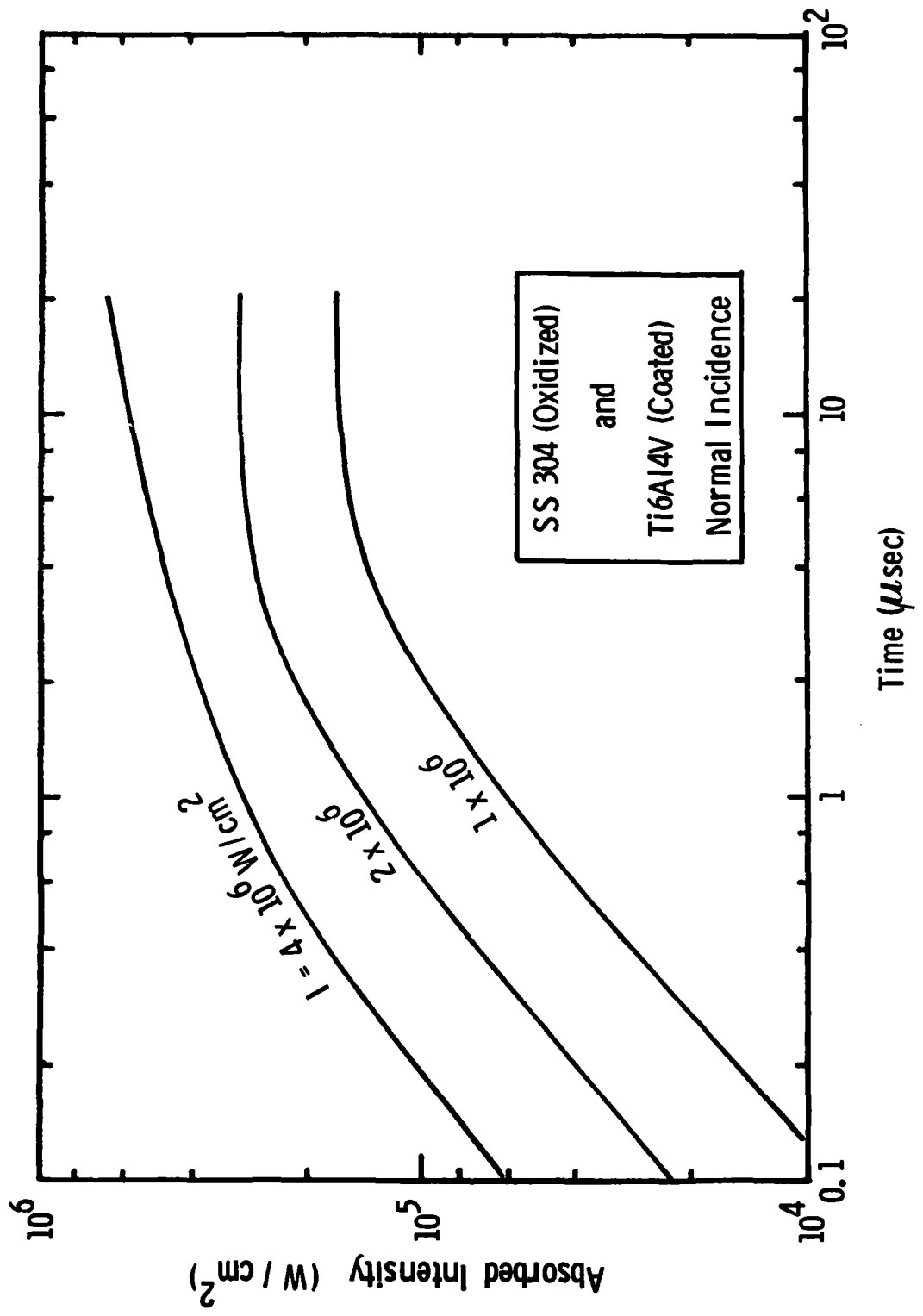
Fig. 3.5 Intensity of One-Dimensional LSC Wave Plasma Radiation Absorbed by Oxidized SS304 Target.

57
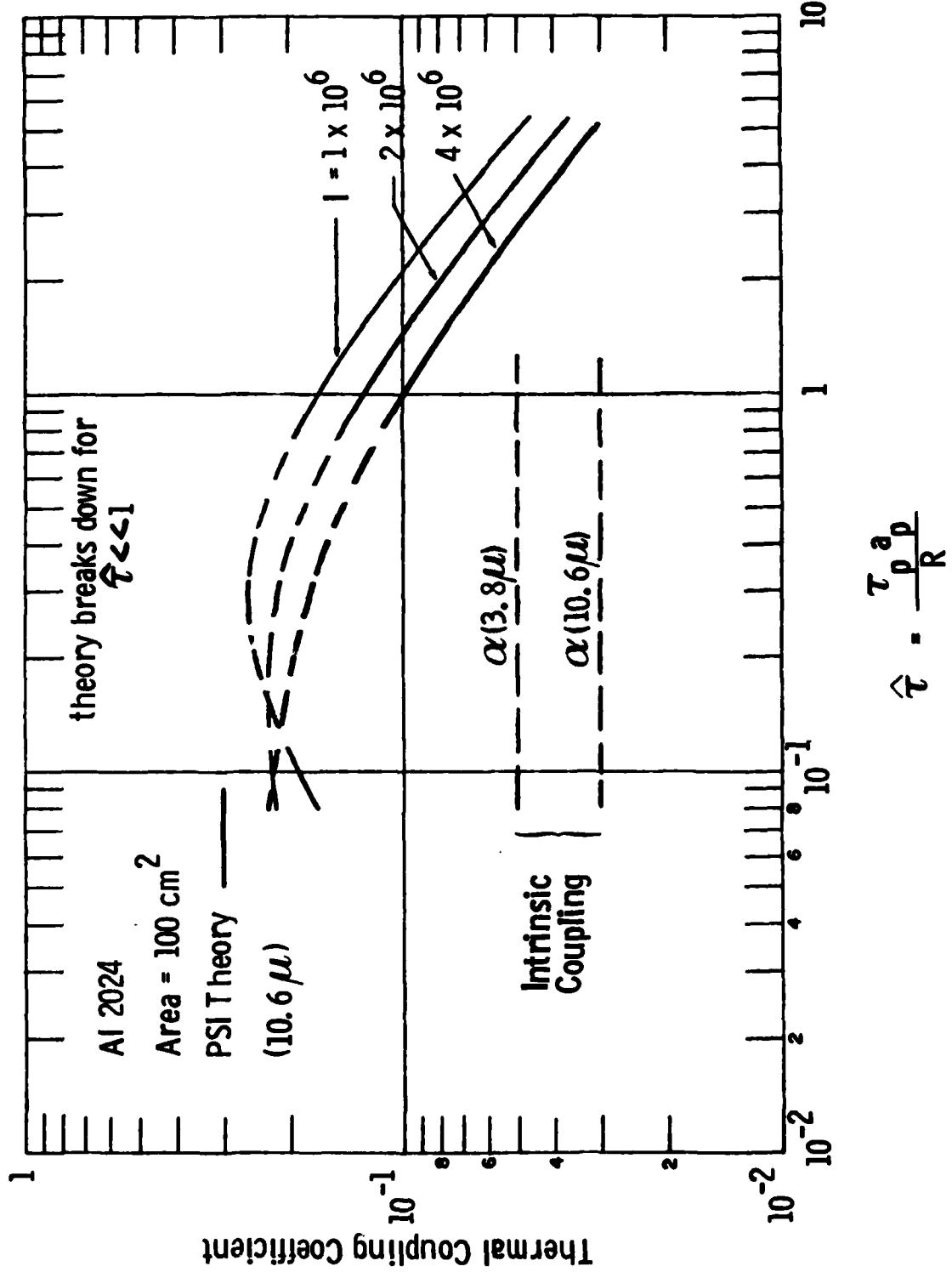
Fig. 3.6 Thermal Coupling Coefficient for Al2024 as Function of Parameter $\hat{\tau}$.

58
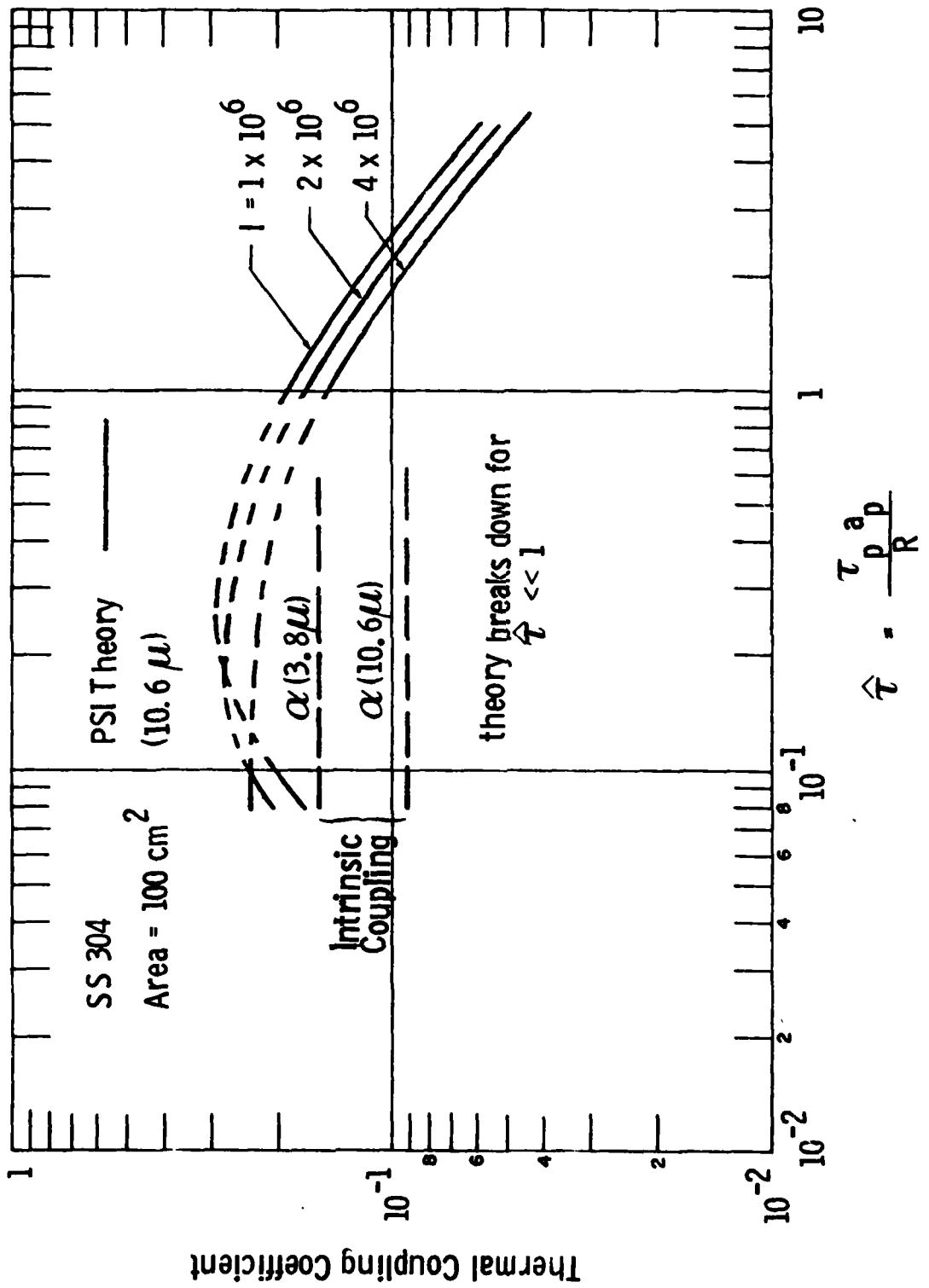
Fig. 3.7 Thermal Coupling Coefficient for SS 304 as Function of Parameter $\hat{\tau}$.

59
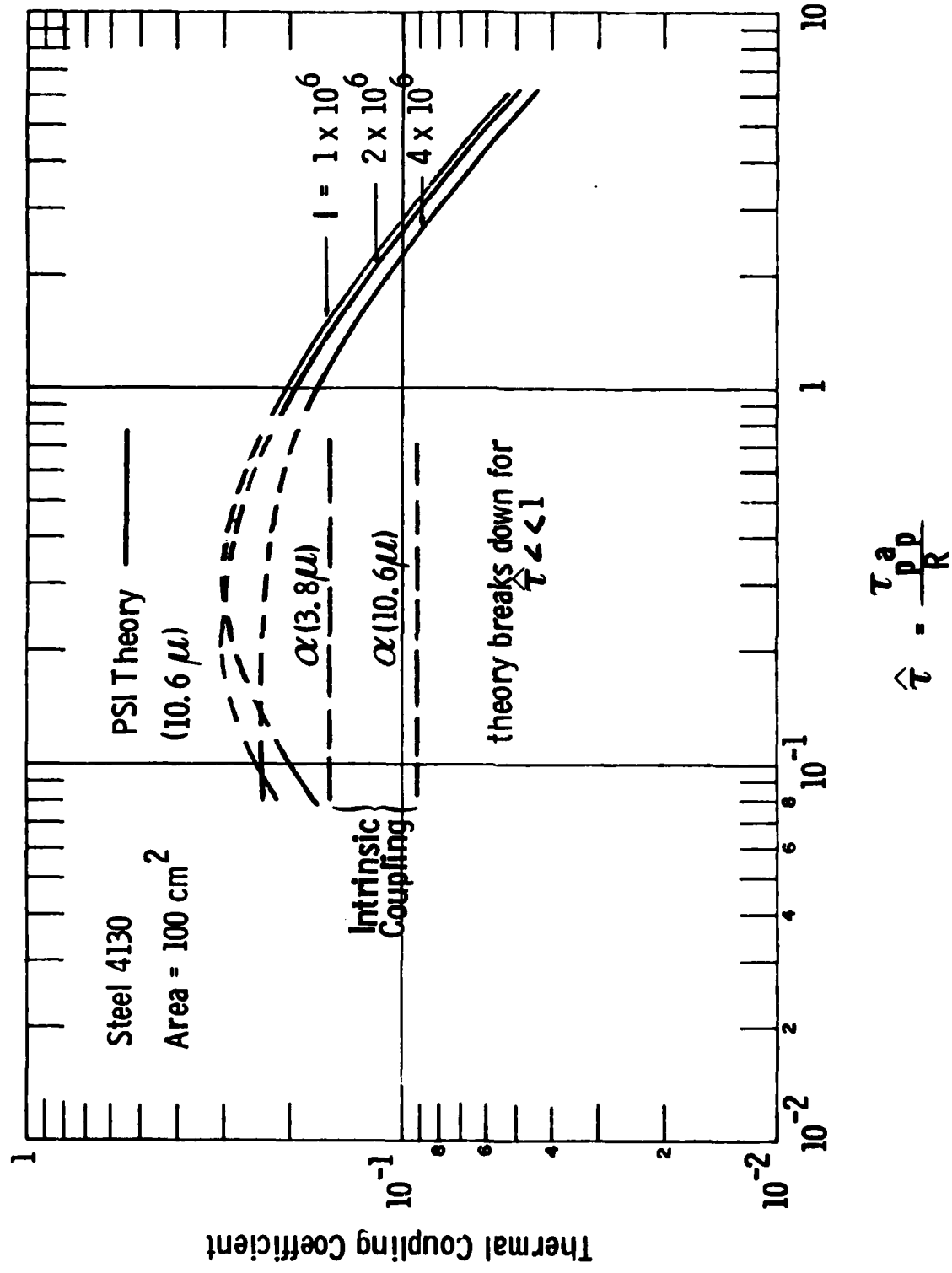
Fig. 3.8 Thermal Coupling Coefficient for Steel 4130 as Function of Parameter $\hat{\tau}$.

$$\hat{\tau} = \frac{\tau \, a}{\rho \, p} \frac{a}{R}$$

Steel 4130
Area = 100 cm^2

PSI Theory ——
(10.6 μ)

α (3.8 μ)

α (10.6 μ)

theory breaks down for
$\hat{\tau} < 1$

Intrinsic
Coupling

$I = 1 \times 10^6$
2×10^6
4×10^6

Thermal Coupling Coefficient
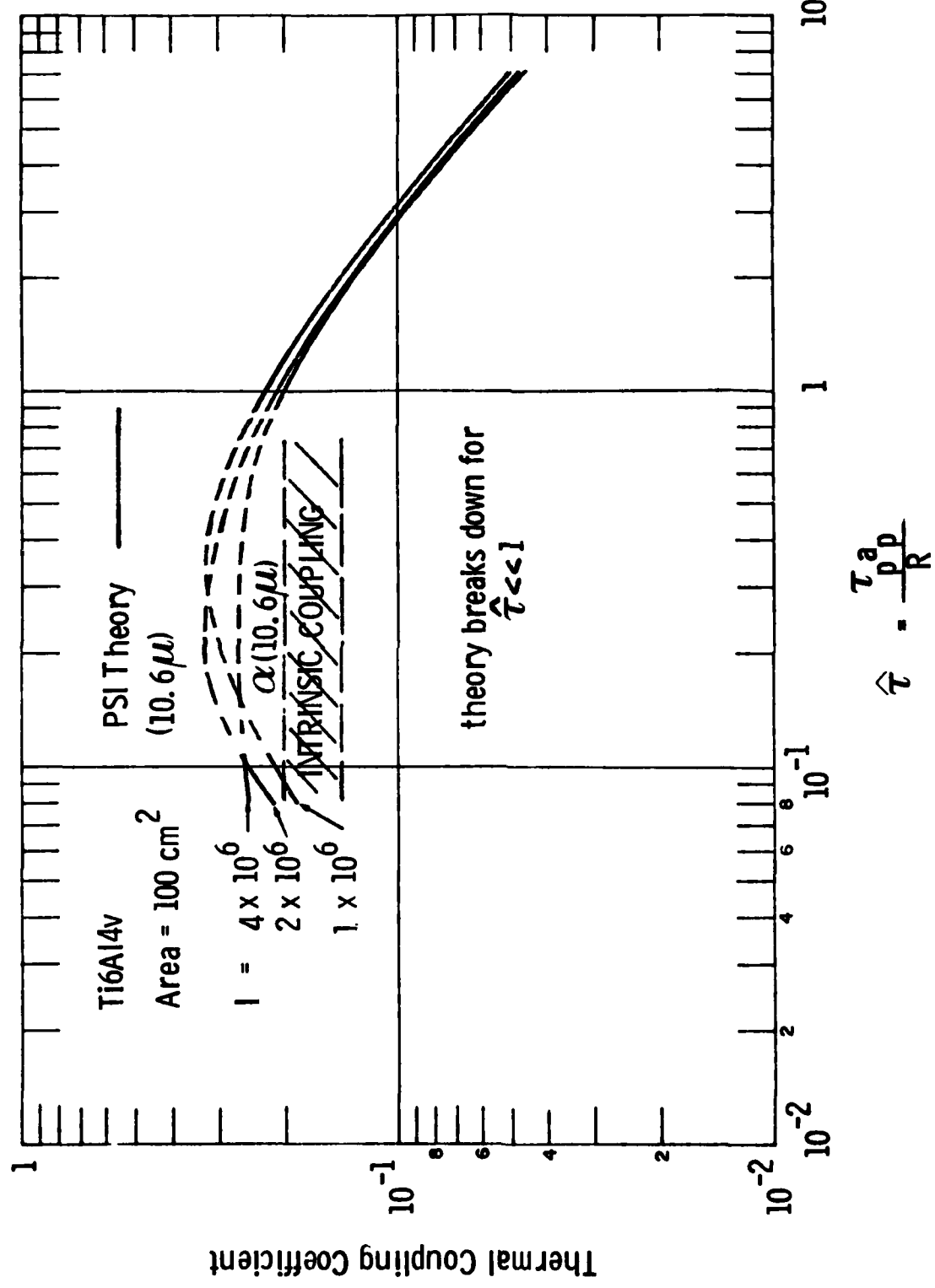
Fig. 3.9   Thermal Coupling Coefficient for Ti6A14V as Function of Parameter $\hat{\tau}$.
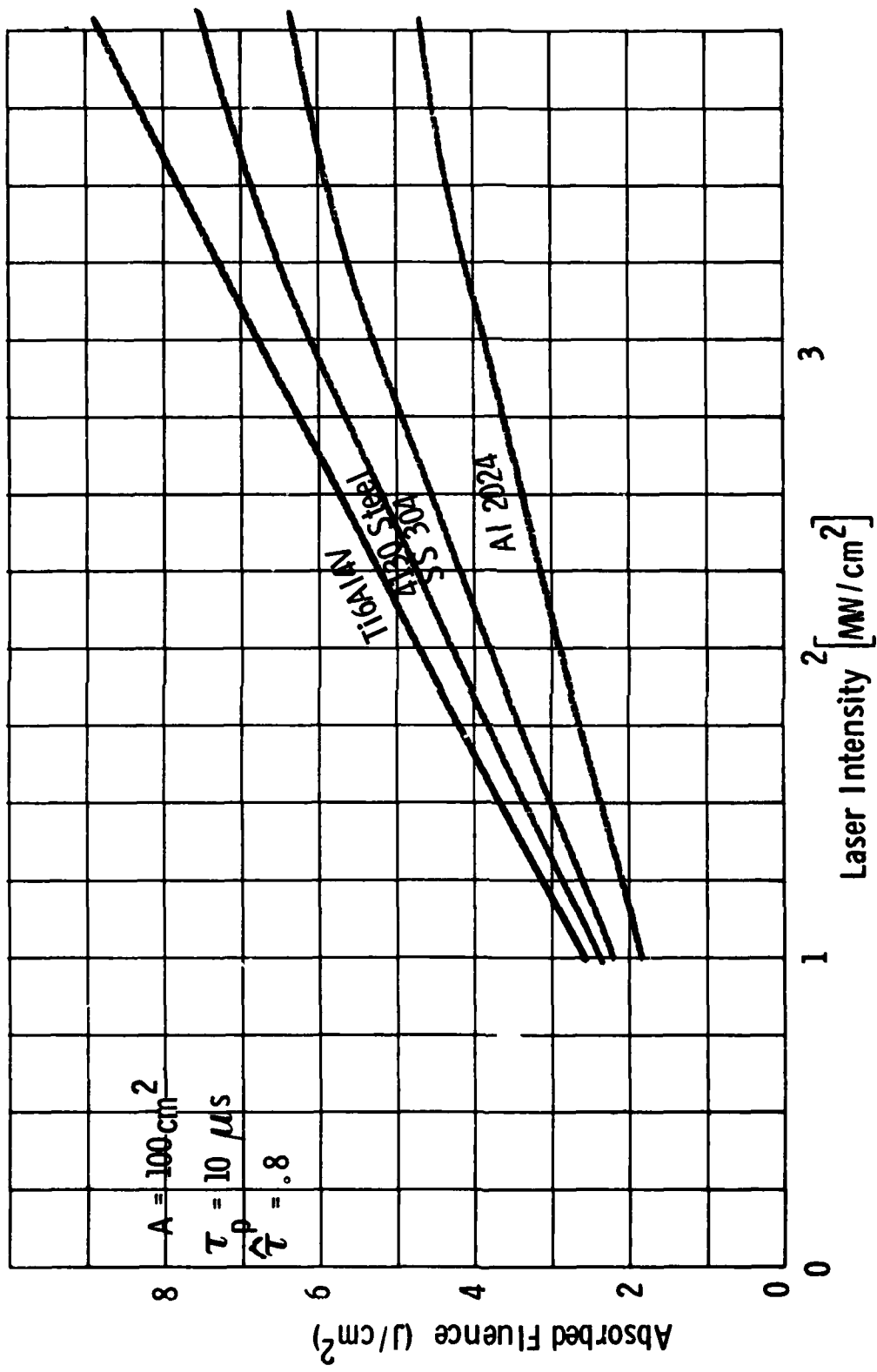
Fig. 3.10 Comparison of Predictions of Fluence Absorbed by Four Alloys as Function of Laser Intensity.

based upon absorbed fluence, and the relative enhancement of the various alloys with respect to Al2024 increases as the intensity increases.

Predictions made with the PSI semi-analytic model for the absorptivity of steel 4130 are compared to the predictions of the SAI numerical code in Figs. 3.11 and 3.12. In both figures the absorbed fluence is plotted as a function of laser intensity for a 170 cm^2 spot. Fig. 3.10 corresponds to a pulse time of 18 μs whereas Fig. 3.11 corresponds to τ_p = 40 μs. The SAI predictions, which are represented by shaded rectangles, are in excellent accord with the PSI predictions for τ_p = 18 μs. For τ_p = 40 μs, the predictions differ by 20% at 2.5 MW/cm^2 and 25% at 5 MW/cm^2. It is expected that unsteady effects have a stronger influence for the longer pulse time. Given the different methods of solution, agreement of the models to better than 30% suggests that the predicted enhanced coupling to steel 4130 is not an artifact of the models but rather represents faithfully the coupling to be expected in the absence of other phenomena such as combustion or vapor effects.

3.1 Vaporization Limits

The energy required per unit mass to penetrate a target at the solidus temperature is given simply by $C_s (T_s - T_o)$ where C_s is the specific heat of the solid, T_s is the solidus temperature and T_o is the initial temperature of the target. However, if penetration is achieved by vaporization, the energy per unit mass, Q^*, required is given by:

$$Q^* = C_s \left(T_s - T_o \right) + C_\ell \left(T_v - T_s \right) + \Delta H_m + \Delta H_v \quad , \text{(3.1)}$$

where ΔH_m is the heat of fusion, ΔH_v is the heat of vaporization, C_ℓ is the specific heat of the liquid, and T_v is the vaporization temperature. It is found that the energy requirements for vaporization are ten to twenty-five

63
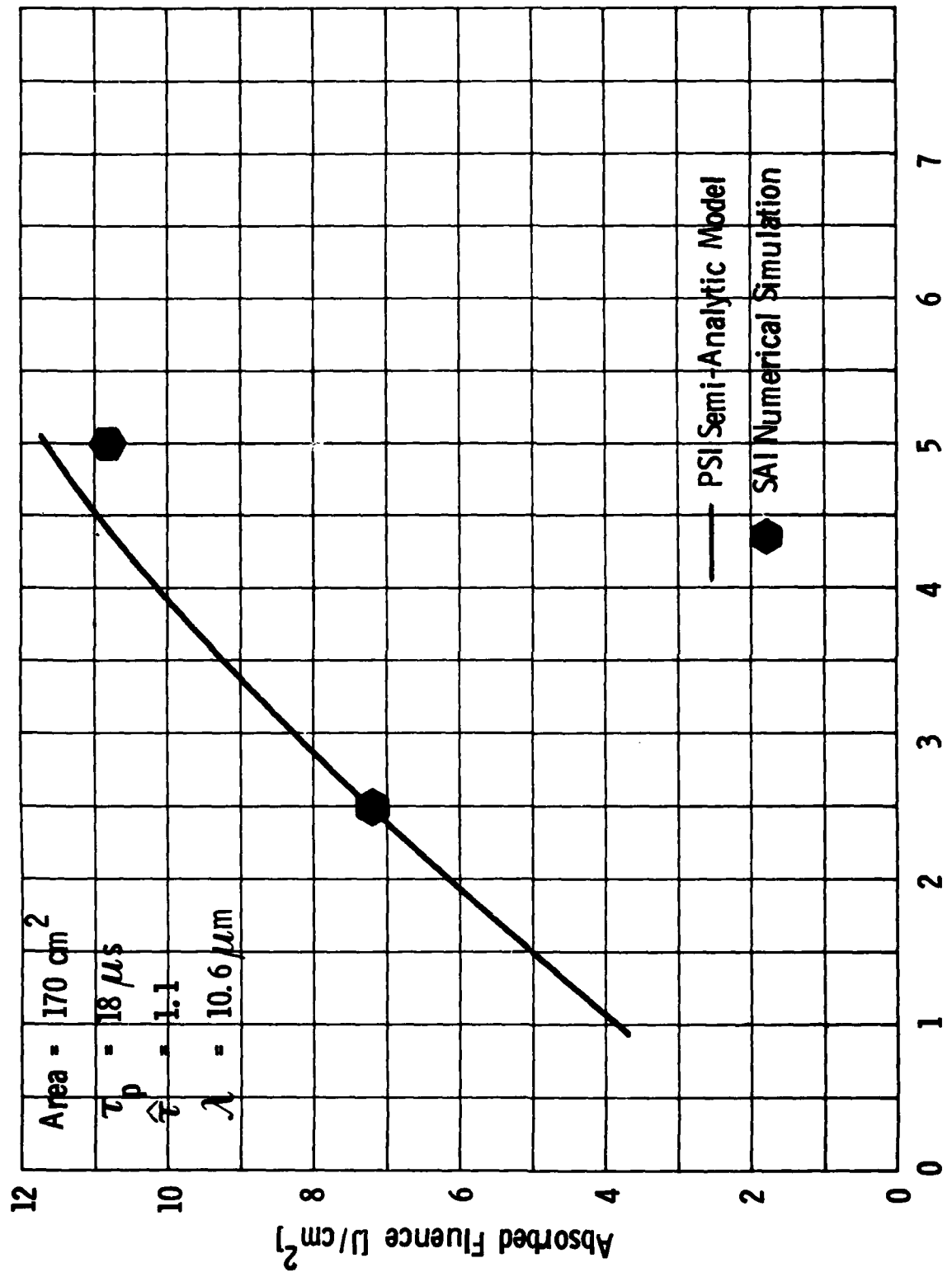
Fig. 3.11 Comparison of Theoretical Predictions for Fluence Absorbed by Steel 4130 as a Function of Intensity.

64
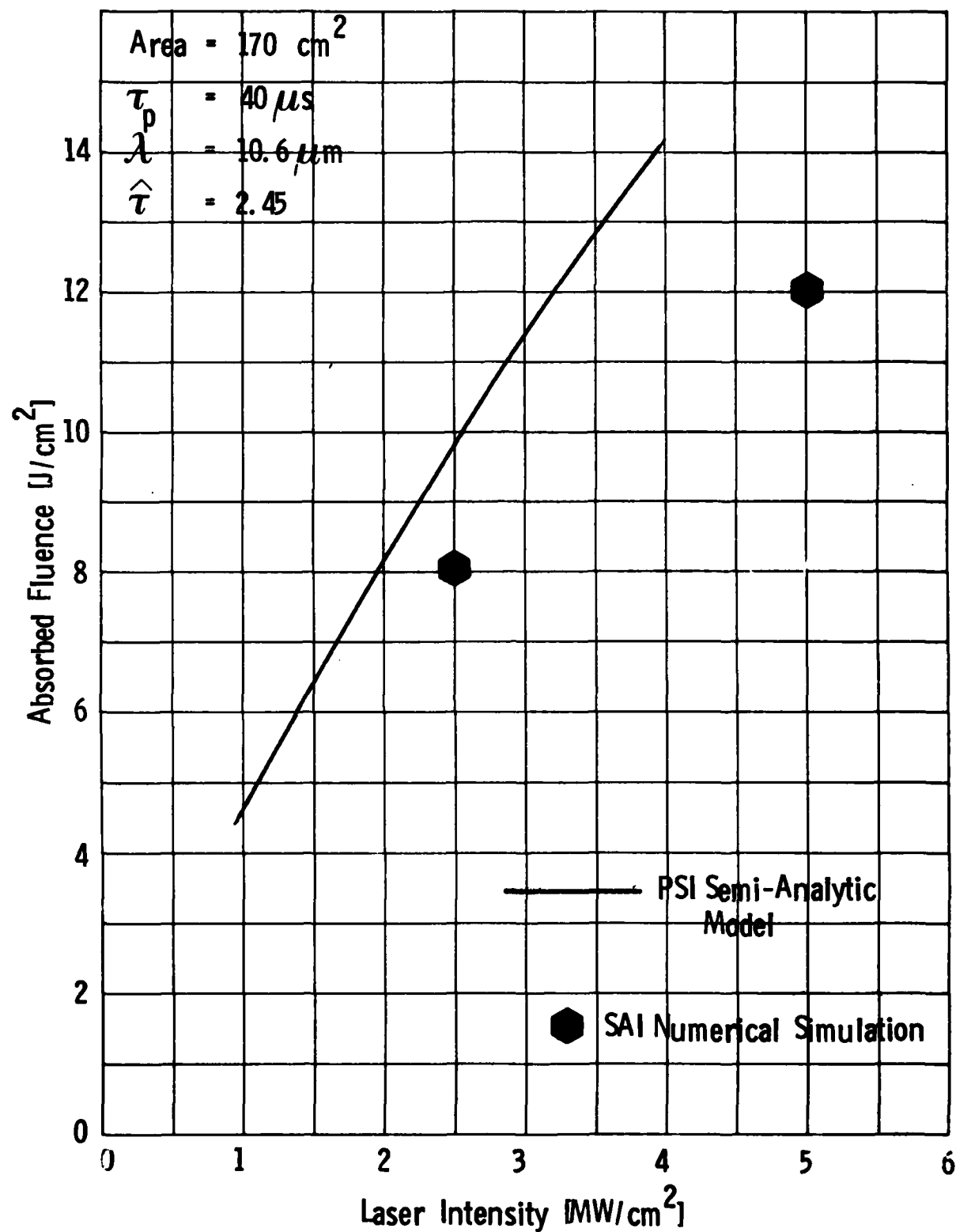
Fig. 3.12 Comparison of Theoretical Predictions for Fluence Absorbed
by Steel 4130 as a Function of Intensity.

times the energy requirements for penetration at solidus. Therefore, vaporization is a very inefficient way to use the incident energy and can effectively be treated as a loss. If vaporization occurs, the absorbed intensity is no longer used in the most efficient manner; if steady state vaporization is achieved all additional absorbed intensity is expended completely in vaporization. It is important, therefore, to determine whether or not vaporization is likely to occur during a repetitively pulsed interaction, and if it does occur, we must properly account for the energy used to supply the heat of vaporization.

If vaporization occurs early in the pulse, the vapor may affect the radiation transport from the air LSC wave to the target. This possibility is not examined here, rather we concentrate on determining the conditions under which vaporization is liable to occur.

Thermal conduction controls the temperature reached by the target surface during the interaction. The time t_v required to reach the vaporization temperature at the surface is given by

$$ t_v = \frac{\pi}{4\kappa} \left(\frac{\lambda (T_v - T_o)}{\alpha I} \right)^2 , \tag{3.2} $$

where κ is the diffusivity, λ is the thermal conductivity, and α is the thermal coupling coefficient. This expression can be rearranged to determine the fluence which can be absorbed at the time the surface reaches the vaporization temperature. In Table 3.2, we have listed for various metals the fluence required to reach the vaporization temperature as a function of laser intensity. For Al2024, the maximum absorbed intensity which is predicted by LSC wave theory is less than .25 MW/cm^2. The absorbed fluence required to achieve vaporization is then (see Table 3.2) calculated to be 100 J/cm^2. Vaporization does not occur for Al2024. For SS304 the

TABLE 3.2

Fluence as a function of absorbed intensity αI required to reach vaporization temperature for various alloys.

Metal	F_v = Fluence Limit J/cm^2	Onset of Vaporization ($\hat{\tau} \sim 1$)
Al2024	$23/\alpha I$	Unlikely
SS304	$8.5/\alpha I$	Marginal
		$I \approx 6\ MW/cm^2; A_s \approx 400\ cm^2$
Ti 6A14V	$6.0/\alpha I$	Possible $13 J/cm^2$
		$I \approx 3\ MW/cm^2; A_s \approx 400\ cm^2$

absorbed intensity is slightly larger but the fluence required to reach vaporization is significantly smaller. However, it is still unlikely that the target can be vaporized. For example, at $I = 6$ MW/cm^2, if $\alpha = .10$ and $\hat{T} = 1$, the vaporization limit could be attained for a 400 cm^2 with $\tau_p = 25 \mu s$. This corresponds to a 50 kJ pulse, so vaporization is expected only for large pulse energies.

For Ti6A14V, however, the vaporization limit may be achieved with moderate energy pulse, since the fluence required to reach vaporization is lower and the expected coupling is higher. For example, it is possible to reach the fluence needed for vaporization with $I = 3$ MW/cm^2, $\alpha = .15$, area = 400 cm^2, and $\tau_p = 25 \mu s$. The absorbed fluence for this example is 13 J/cm^2, and the pulse energy is 30 kJ.

We can also make a crude estimate of the maximum fluence which can be deposited before the onset of steady-state vaporization. Energy deposition after the onset of vaporization is less efficient. The vaporization rate, as a function of time since the onset of vaporization, has been approximated by Pirri[15] by expanding an expression derived by Boley[16]. The vaporization mass flux $\dot{M}$ is given by:

$$\dot{M} = \frac{4 \, (\alpha I)^2 \sqrt{t - t_v}}{\pi^{3/2} \sqrt{\kappa} \, \rho \, c \, H_v \, T_v} , \tag{3.3}$$

where κ is the thermal diffusivity, α is the coupling coefficient, I is the laser intensity, ρ is the target density, c is the target specific heat, T_v is the vaporization temperature, H_v is the heat of vaporization, t is time and t_v is the time at which vaporization commenced. Although, strictly speaking, Eq. (3.3) is valid only near the onset of vaporization, we employ it until steady state vaporization is reached, i. e., until

68

$$\dot{M}(t_{ss}) = \alpha \, I \, / \, H_T \qquad\qquad (3.4)$$

where H_T is the total enthalpy difference required to change the material from a solid at the initial temperature to a vapor at the vaporization temperature. The maximum deposited fluence is then found by integrating the difference between the fluence absorbed and the energy carried away by vaporization. The integration ceases at the time t_{ss} which corresponds to the onset of steady-state vaporization. The expression for the maximum absorbed fluence F_M is:

$$F_M = \alpha I t_v + \int_{t_v}^{t_{ss}} \left(\alpha I - \dot{M} H_T \right) dt \; . \qquad\qquad (3.5)$$

For Ti6A14V, it is found that t_{ss}, as defined by Eq. (3.4), is given by approximately $2.5 \, t_v$, and that the maximum absorbed fluence is given by $9.1/(\alpha I)$ J/cm^2 where I is measured in MW/cm^2. This corresponds to roughly 1.5 times the fluence absorbed at the onset of vaporization. Hence, although the pulse has been on 2.5 times as long as needed to start vaporization, only 1.5 times as much energy is in the target. Clearly, once vaporization begins the effective total coupling becomes quite poor.

3.2 Summary

We have advanced a model for computing thermal coupling to targets such as SS304, steel 4130, and Ti6A14V. The model is based on the model developed previously for A12024; namely, prompt ignition of an air plasma with subsequent energy transfer via plasma reradiation. The difference

between these metals and Al2024 lies mainly in the different spectral absorptivity in the VUV' and VIS band, that is, in the region with wavelengths greater than 1240 A. This model predicts a hierarchy of metals based on absorbed fluence, with Ti6Al4V absorbing the most, followed by 4130 steel, SS304, and finally Al2024 which has the lowest absorbed fluence. Based on the model, it is expected that the relative differences in the absorbed fluence can be enhanced by going to larger spots or to higher intensities. Simple calculations indicate that vaporization is likely to occur only for Ti6Al4V, and then only for large spots and high intensities.

SECTION 4

COUPLING AT OBLIQUE ANGLE OF INCIDENCE

In Sections 2 and 3 of this report, and in Ref. 1 and 2, thermal and mechanical coupling of pulsed 10.6 μm laser radiation to metal targets are calculated for normally incident laser flux. This section extends the methodology of the previous paper to the consideration of non-normally incident laser flux, and reports calculations of the enhanced central thermal coupling and of impulse coupling for that situation.

Insight gained from the previous work (Ref. 1 and 2 and Section 2), is brought to bear in the consideration of non-normally incident laser flux. At normal incidence, the dynamics of the plasma immediately subsequent to its formation was seen to be well described as one-dimensional, and the flux reradiated toward the target surface by the plasma was readily calculated from the one-dimensional model. A time τ_{2D}, equal to the time to transit of an acoustic wave from the edge of the laser spot to the center, was identified as the time interval after which the one-dimensional model could no longer be used. This led to an identification of regimes based on whether the pulse duration was smaller than, or exceeded the acoustic transit time. In all cases in which the time t after the initial plasma-formation was greater than the pulse duration, the acoustic transit time, or both, the reradiated flux toward the surface was calculated on the basis of planar or spherical relaxation laws for the plasma thickness and pressure.

At normal incidence, a laser-supported combustion (LSC) wave is formed when the laser intensity exceeds a plasma threshold value. The wave front then propagates into the air away from the target surface, preceded by a precursor shock. In the one-dimensional model, taken to be valid at early times after plasma formation, the LSC wave front is assumed

71

to be a plane front and the plasma motion just ahead of and just behind the front is assumed to be perpendicular to the target surface.

Figure 4. 1 shows an edge-on view of the target surface and the incident laser flux with the incidence angle $\theta > 0$ with respect to the normal away from the surface. The early-time description of the plasma configuration for this geometry is chosen to be one-dimensional in the same sense that it is one-dimensional at normal incidence. Both the precursor shock and the LSC wave front propagate as planes in the direction normal to the target surface. Furthermore, the particle motion between the precursor and the LSC wave front, and behind the front is one-dimensional in the same direction. This direction is designated as the Z direction in Fig. 4.1. The Y coordinate in that figure is in the plane of the normal and the incident laser flux propagation direction, and is in the target surface. The X axis is perpendicular to the YZ plane. The entire coordinate system is centered at the point O which is the centroid of the laser spot at the instant $t = 0$ at which plasma is formed at the target surface. The point O' is the intersection of the Z axis with the LSC front. The thickness of the plasma, that is, the distance from the LSC front to the target surface, is indicated as L in Fig. 4. 1. If it is assumed that the laser beam cross-section is a circle of radius R, the laser spot on the surface at $t = 0$ is an ellipse with semi-major axis oriented along Y having length $R/\cos \theta$, and semi-minor axis along X having length R. This is shown in Fig. 4. 2 which is a view of the target surface from the half-space of positive Z.

The one-dimensional approximation breaks down near the edge of the beam, such as the areas shown in Fig. 4. 1 as P'PB and RQ'Q. It cannot be determined, a priori, whether plasma is generated in the region RQ'Q as the LSC wave moves away from the surface, or whether plasma is maintained in the region P'PB. It is found that the presence or absence of plasma
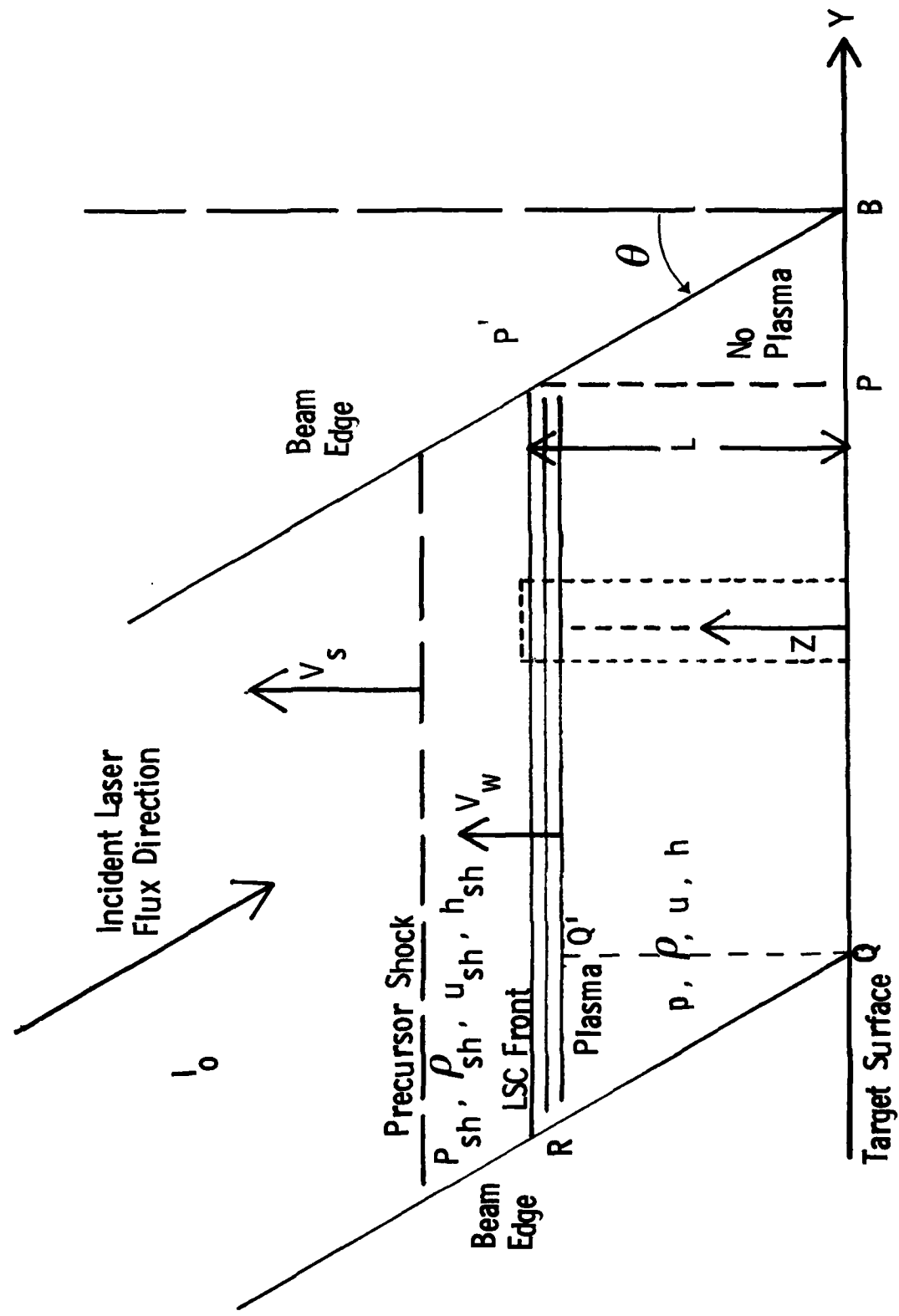
Fig. 4.1 Side Sectional View of Early Time LSC Wave Plasma Configuration for Oblique Angle of Incidence.

73
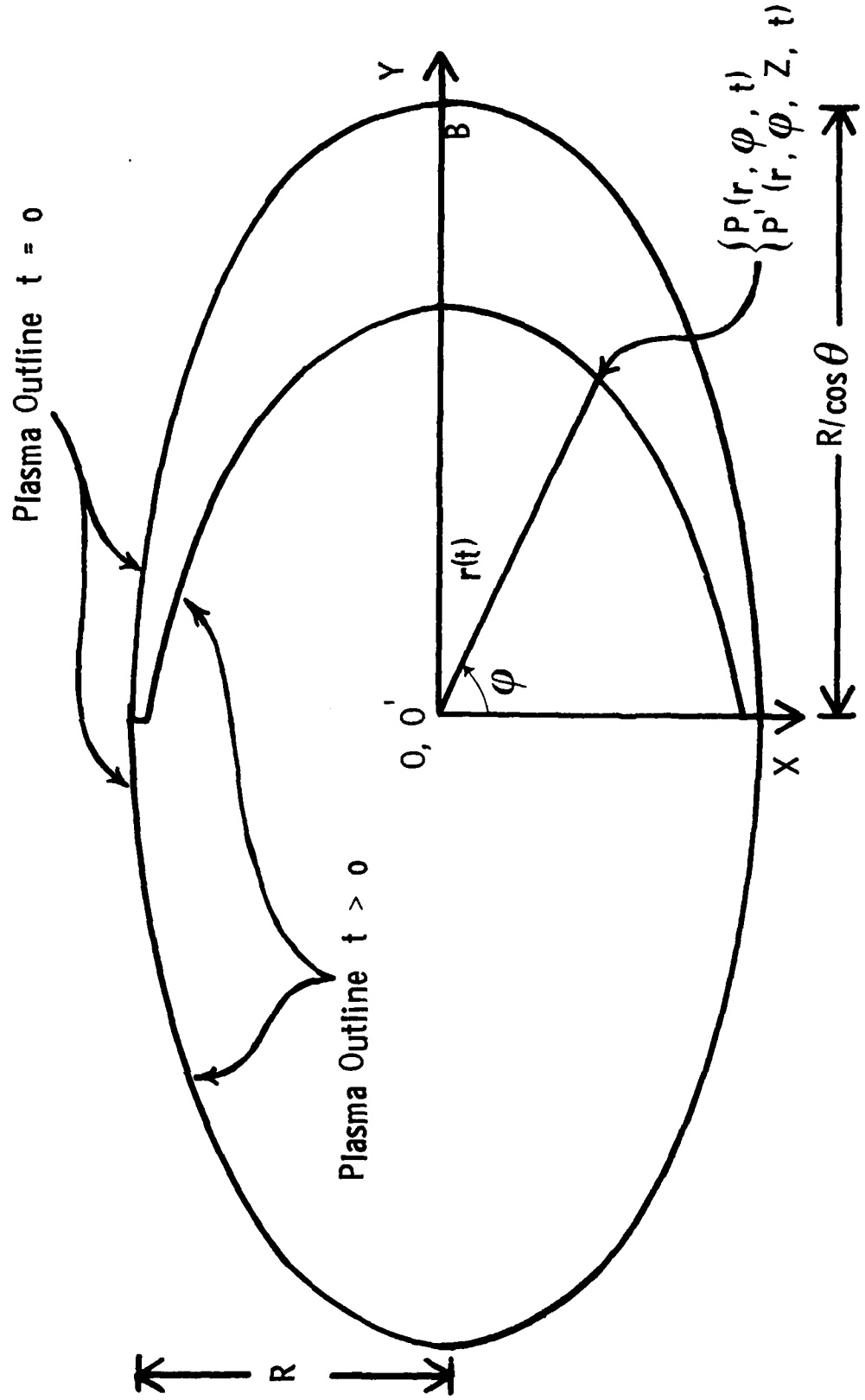
Fig. 4.2 Normal View of Target Surface and Plasma Outlines at t = o and t > o.

74

in the region RQ'Q does not affect the central coupling. The presence or absence of plasma in the region P'PB is found to influence the coupling only in a few special cases, and then the influence is small. However, in order to demonstrate the potential effects of having no plasma in the corner P'PB, we assume that corner to be devoid of plasma. The coupling calculated under this assumption represents a lower bound on the predicted coupling. The line PP' in Fig. 4.1 is thus a plasma boundary which moves toward the Z axis. From the point-of-view of Fig. 4.2 the plasma outline for positive Y, and its projection (trace) in the XY plane, move toward the Z axis.

Although one is concerned with the issue of when the one-dimensional model ceases to be valid, the issue becomes more critical when θ becomes large. At normal incidence, the one-dimensional model ceases to be valid when acoustic disturbances from the plasma periphery reach the center of the spot. For non-normal incidence, the propagation of acoustic disturbances to the center is in competition with the motion of the plasma outline (see Fig. 4.2). If the plasma outline can reach the center of the spot (X = 0, Y = 0, Z = 0) before the earliest acoustic disturbance, then the question of whether or not the corner P'PB has plasma becomes paramount. It is shown in Subsection 4.1, that the plasma outline cannot reach the center in a time τ_{2D}, which is the arrival time of the earliest acoustic disturbance, and that, furthermore, the center is still surrounded by enough plasma at $t = \tau_{2D}$, despite the motion of the plasma outline, that radiation received by the center can be calculated as though it were surrounded by an infinite slab of plasma.

The one-dimensional model is valid up to the time $t = \tau_{2D}$ or the time $t = \tau_p$, where τ_p is the pulse duration, whichever is smaller. Thereafter, blast wave theory, with its accompanying relaxation laws for plasma pressure and thickness, is used to estimate the radiation and impulse reaching

75

the center of the spot. The relaxation laws for normal incidence are planar or spherical. For non-normal incidence, cylindrical relaxation laws need to be introduced to account for the radiation and impulse received between the time that the earliest acoustic wave reaches the center (from along the minor axis), and the time that either an acoustic wave, or the plasma outline, reaches the center from along the major axis. The cylindrical regime is bounded by the time $t = \tau_{3D}$ which is the smaller of the times that either an acoustic wave, or the plasma outline, reaches the center from the major axis direction. For small angles we show that τ_{3D} is the time of arrival of the acoustic wave from the major axis direction. Only for very large angles of incidence does the motion of the plasma outline define τ_{3D}. The time τ_{3D} marks the onset of spherical relaxation.

In Subsection 4.1, the one-dimensional plasma model for early times is developed in detail for non-normal incidence. The time scales which govern the applicability of this model and of the transition to later times are defined. In Subsection 4.2, the late-time model of plasma relaxation is developed and the complete set of relaxation laws for any ordering of the parameters τ_p, τ_{2D}, τ_{3D} (subject to the constraint $\tau_{3D} \geq \tau_{2D}$) is given. In Subsection 4.3, absorbed fluence and the coefficient of enhanced thermal coupling are calculated, and predictions are given for incidence angles of $0°$, $30°$, $60°$, $75°$, and $84°$, and incident laser intensities of $1~MW/cm^2$, $2~MW/cm^2$, $3~MW/cm^2$ and $4~MW/cm^2$. In Subsection 4.4, impulse and the coefficient of impulse coupling are calculated, and predictions are given for various values of the ratio of surface pressure at the time of plasma formation, to a specified "final" pressure. A summary, and some conclusions, are given in Subsection 4.5.

At normal incidence, the LSC wave front moves up the laser beam since that is the direction normal to the surface. Some experiments show

that the absorption wave front moves up the laser beam even at skew incidence. There is, in fact, no conflict between this evidence and the present assumption of a one-dimensional model in which the LSC wave propagates perpendicular to the target surface. The one-dimensional model is an early-time model; whereas the motion of the LSC wave up the laser beam occurs at much later times when practically all of the energy coupling to the surface has already occurred. Furthermore, the absorption waves in the experiment are LSD waves.

4.1 Model of Early-Time Plasma Behavior for Non-Normally Incident Laser Flux

The principal differences between the early-time model described in Ref. 1, Ref. 2 and Section 2 of this report, for normally incident laser flux. and that of the present model for non-normal incidence, are in the description of energy balance and of the absorption of laser flux. In Fig. 4.1, the region D is a cylinder whose generators lie entirely within the laser-induced plasma. The top of the cylinder is just above the LSC front and moves with the speed of the front. The bottom of the cylinder is on the target surface. The volume of this domain changes with time. If h' represents the stagnation enthalpy of the plasma, defined as

$$h' = h + \frac{1}{2} v^2 , \qquad (4.1)$$

where h is the specific enthalpy and $\vec{v}$ is the velocity of the plasma flow-field, the rate of change of h' in a region such as D is described by the kinematic relation

$$\frac{d}{dt} \int_D \rho h' d^3 r = \int_D \rho \frac{dh'}{dt} d^3 r + \int_{A_D} \rho h' (\vec{v} - \vec{V}) \cdot \hat{n} dA , \quad (4.2)$$

in which ρ is the plasma density, d/dt represents the convective time derivative and A represents the area of the surface. In the surface integration, the velocity vector $\vec{V}$ is the local velocity of a surface element and $\hat{n}$ is the outward normal to the surface of D. The entire surface integral represents a rate of change of stagnation enthalpy in D due to the flow of plasma through its moving surface.

The volume integral on the right side of Eq. (4.2) is evaluated from the first law of thermodynamics in the form[17]

$$\rho \frac{dh'}{dt} = \frac{\partial p}{\partial t} - \nabla \cdot \vec{Q} , \qquad (4.3)$$

where p is the plasma pressure, and $\vec{Q}$ is the vector flux of heat <u>leaving</u> a region.

The individual terms in Eq. (4.2) are now evaluated for the region D. A coordinate system fixed in the LSC wave front and moving with it, is adopted. In this system the properties of the plasma appear stationary. Hence the time derivative of pressure in Eq. (4.3) vanishes in this system. In the surface integration over the side surface, the velocity $\vec{v} - \vec{V}$ is perpendicular to the surface normal because $\vec{V}$ is zero (the side surface is not moving), and $\vec{v}$, the plasma velocity as seen in the LSC-fixed coordinate system, is perpendicular to the target surface in the early time model. Hence, the integral over the side surface vanishes. In the integral over that portion of the surface of D that coincides with the target surface, the velocity $\vec{V}$ is $- V_w \hat{z}$, where V_w is the speed of the LSC front and $\hat{z}$ is the unit vector in the Z direction of Fig. 4.1. The plasma is brought to rest at the target in a target-fixed frame by the passage of the LSC front. Then the velocity of the plasma at the target surface is $- V_w \hat{z}$. Hence, the surface integral over the back surface also vanishes.

78

On that part of the surface of D that is located just ahead of the LSC front, the plasma velocity is $u_{sh}\hat{z}$ in the target fixed frame, where u_{sh} is the speed imparted to the plasma by the passage of the precursor shock. Since the surface moves with the LSC wave velocity, the plasma velocity seen in the front-fixed coordinate system is $(u_{sh} - V_w)\hat{z}$. The surface integral over this part of A_D is the total value of the integral over the entire cylinder surface, and is

$$\int_{A_D} \rho h' (\vec{v} - \vec{V}) \cdot \hat{n} dA = A \rho_{sh} (u_{sh} - V_w) \cdot \left[h_{sh} + \frac{(u_{sh} - V_w)^2}{2} \right], \qquad (4.4)$$

where ρ_{sh} and h_{sh} are plasma density and specific enthalpy, respectively, between the precursor shock and the LSC wave, and A is the cross-sectional area of the cylinder.

Since the plasma properties are stationary in the LSC-fixed frame, the left side of Eq. (4.2) has the value

$$\frac{d}{dt} \int_D \rho h' d^3 r = A \rho \left[h + \frac{V_w^2}{2} \right] V_w , \qquad (4.5)$$

where the fact that the plasma behind the LSC wave front is brought to rest in the target-fixed frame is used. The factor V_w which multiplies the square bracket in Eq. (4.5) arises from the fact that the length of the cylinder of integration increases at the LSC wave speed.

The remaining integral in Eq. (4.2) is the one containing the heat flux. This is transformed using the divergence theorem into the surface integral

$$-\int_{A_D} \vec{Q} \cdot \hat{n}dA = -\int_D \nabla \cdot \vec{Q}d^3r \ . \qquad (4.6)$$

The net heat flux $-\vec{Q}$ <u>into</u> the region of integration comes about from three sources;

a)   Laser flux entering D through the top surface. For this source $-\vec{Q} \cdot \hat{n} = I_o \cos \theta$, where I_o is the incident laser flux density.

b)   Plasma reradiation q_ℓ lost through the top and side surfaces of D. For this source, the flux is perpendicular to each surface element of interest so that $-\vec{Q} \cdot \hat{n} = -q_\ell$.

c)   Plasma reradiation q_r toward the target surface (and therefore "lost" through the bottom part of A_D). For this source, $-\vec{Q} \cdot \hat{n} = -q_r$.

In performing the surface integral in Eq. (4.6), one collects the various fluxes just enumerated to arrive at the result:

$$-\int_{A_D} \vec{Q} \cdot \hat{n}dA = \left(I_o \cos \theta - q_r - q_\ell^{(top)}\right)A - q_\ell^{(sides)}LC_A \ , \ (4.7)$$

where L is the plasma length and C_A is the length of the perimeter of the cylinder cross-section. For a truly one-dimensional model $q_\ell^{(sides)} = 0$. This condition also applies in the limit of A tending to zero, for in that limit the ratio C_A/A becomes infinite.

The result of inserting Eqs. (4.4), (4.5), and (4.7) into Eq. (4.2) is the energy equation

80

$$\rho \left[h + \frac{V_w^2}{2} \right] V_w = \rho_{sh} (V_w - u_{sh}) \left[h_{sh} + \frac{(V_w - u_{sh})^2}{2} \right] + I_o \cos \theta - q_r - q_\ell , \quad (4.8)$$

where the designation "top" in q_ℓ has been deleted. This condition is identical to Eq. (4.2) of Ref. 1 except that $I_o \cos \theta$ now replaces I_o.

The conditions for mass and momentum balance for non-normal incidence,

$$\rho_{sh} (V_w - u_{sh}) = \rho V_w , \quad (4.9)$$

$$p + \rho V_w^2 = p_{sh} + \rho_{sh} (V_w - u_{sh})^2 , \quad (4.10)$$

are identical to the respective Eqs. (4.3) and (4.4) of Ref. 1 which describe normal incidence. In the present model, the assumption that the plasma ahead of, and behind the LSC front is described by the appropriate ideal gas law is made, as in the normal incidence situation. It remains only to examine the radiation transport pertinent to the case of non-normal incidence in order to have a closed set of equations.

If δ is a coordinate in the direction of propagation of the incident laser flux, then the absorption is governed by

$$\frac{\partial I_o}{\partial \delta} = - \kappa_L I_o , \quad (4.11)$$

where κ_L is the absorption coefficient appropriate to the laser wavelength. For a one-dimensional plasma model, this absorption condition should be

supplemented by the condition that the laser intensity in the plasma is constant in planes of constant Z. If η is a typical coordinate in a plane of constant Z, then the supplementary condition is:

$$\frac{\partial I_o}{\partial \eta} = 0 .\tag{4.12}$$

From the relations for rotation in a plane, it is easily established that, using the coordinate Y of Fig. 4.1 as a typical η coordinate,

$$\frac{\partial I_o}{\partial \delta} = \frac{\partial I_o}{\partial Y} \sin \theta - \frac{\partial I_o}{\partial Z} \cos \theta .\tag{4.13}$$

When Eqs. (4.11), (4.12), and (4.13) are combined, one arrives at

$$\left(\frac{\partial I_o}{\partial (-Z)}\right) \cos \theta = -\kappa_L I_o ,\tag{4.14}$$

where differentiation with respect to -Z has been indicated to show how the incident laser flux is absorbed as one moves <u>from</u> the LSC front <u>toward</u> the target surface. Equation (4.14) may be written

$$\frac{\partial (I_o \cos \theta)}{\partial (-Z)} = -\frac{\kappa_L}{\cos \theta} (I_o \cos \theta) .\tag{4.15}$$

This shows that the laser absorption for non-normal incidence obeys the same equation as for normal incidence except that $I_o \cos \theta$ replaces I_o, and $\kappa_L / \cos \theta$ replaces κ_L. The change indicated in Eq. (14.15) is the only change in the radiation transport equation necessary for non-normal incidence. Since the only other change in the one-dimensional

radiation-plasma model is the replacement of I_o by $I_o \cos \theta$ in the enthalpy balance condition, one may conclude that the results of the one-dimensional normal incidence model are applicable to non-normal incidence provided the changes in laser intensity and absorption indicated here are made. In particular, techniques for obtaining the LSC wave velocity, and the temperature profile in the plasma behind the LSC wave front for early times, developed for normal incidence, apply as well for non-normal incidence.

The cross-section of the laser beam is assumed to be a circle of radius R. Then the laser spot on the target surface, and the plasma outline at $t = 0$ when laser flux first reaches the target surface, is an ellipse described by

$$\frac{X^2}{R^2} + \frac{Y^2}{(R/\cos \theta)^2} = 1 , \qquad (4.16)$$

whose semi-major axis (along Y) has length $R/\cos \theta$ and whose semi-minor axis (along X) has length R. For large incidence angles, the corner BPP' of Fig. 4.1 is shielded from the incident laser flux by the plasma and itself contains no plasma. The plasma boundary PP' therefore moves to the left in Fig. 4.1 as the LSC wave moves upward. In the view, Fig. 4.2, of the target surface from above, the elliptical plasma outline for $Y > 0$ and its projection onto the X - Y plane move to the left as t increases. The equation of the projection of the plasma in Fig. 4.2 is given, for $Y > 0$ and $t \geq 0$, by the ellipse

$$\frac{X^2}{R^2} + \frac{(Y + Vt \tan \theta)^2}{(R/\cos \theta)^2} = 1 , \qquad (4.17)$$

where the LSC velocity is now designated as V. It is convenient to

parameterize the description of this ellipse by the polar coordinates (r, φ) indicated in Fig. 4.2, and related to X and Y by

$$X = r \cos \varphi , \tag{4.18a}$$

$$Y = r \sin \varphi . \tag{4.18b}$$

The resulting parameteric representation may be solved for r as a function of φ and t. The solution is:

$$r(t) = \frac{R}{k^2} \left[\sqrt{k^2 - (t/t')^2 \cos^2 \varphi} - (t/t') \sin \varphi \cos \theta \right] , \tag{4.19}$$

where k is defined by

$$k = (\cos^2 \varphi + \sin^2 \varphi \cos^2 \theta)^{\frac{1}{2}} = (1 - \sin^2 \varphi \sin^2 \theta)^{\frac{1}{2}} , \tag{4.20}$$

and the time t', by

$$t' = R/(V \sin \theta) . \tag{4.21}$$

This is the time required for the plasma outline to reach the origin, as may be inferred from

$$r(t') = 0. \tag{4.22}$$

As previously stated, the present interest is in the central coupling coefficients; therefore the calcualtion of radiation and impulse received by the target need only be made for the center of the laser spot.

The demarcation between one- and two-dimensional plasma dynamics for normal incidence is the time τ_{2D} after which acoustic disturbance excited in the plasma at the periphery of the laser spot reach the central point. In Ref. 1, the radiation reaching the central point is calculated as though the plasma surrounding that point is an infinite slab, even after the plasma dynamics has become two-dimensional. For non-normal incidence the situation is complicated by the fact that the propagation of acoustic disturbances from the plasma periphery to the central point, which carry the news that the plasma dynamics has undergone a change in dimensionality, is in competition with the actual motion of the periphery toward the center. Further complicating the calculation of central coupling is the fact that the change in dimensionality of the plasma dynamics is communicated to the center at a different time over each direction on the elliptical spot because of the differing distances from the periphery to the center. Nevertheless, the working assumption is adopted here, as for normal incidence, that the radiation reaching the original central point comes from an infinite slab so long as a significant area surrounding it remains covered with plasma. It is now clear that the "early time" restriction in the use of the one-dimensional model for non-normal incidence is that a significant area surrounding the center of the original laser spot should still be covered by plasma at the shortest acoustic transit time to the Z axis.

Assume that as the LSC wave propagates away from the target surface, acoustic disturbances are generated at the intersection points P' of the LSC wave front with the sides of the laser beam. These disturbances propagate in all directions. At any instant t, consider the acoustic wave that propagates from the point P' $(r (t), \varphi)$ in Figs. 4.1 and 4.2 toward the Z axis, that is, toward the point O' in Fig. 4.1. This wave moves with the speed of sound a_p in the plasma and arrives at O' at the time $t_A(t)$ given by

85

$$t_A(t) = t + \frac{r(t)}{a_p} \quad .$$

(4.23)

It is legitimate, although conservative, to regard this time as the earliest time at which an acoustic disturbance from $(r(t), \varphi)$ can influence the dimensionality of the plasma dynamics at the center. A less conservative estimate is the time of travel of the acoustic wave to the center itself although that has not been done here.

For a given θ and a given φ, one may examine the arrival time as a function of the emission time. Special values of arrival time to be noted are the arrival time for acoustic waves leaving the edge of the spot for $t = 0$,

$$t_A(0) = \frac{r(0)}{a_p} = \frac{R}{ka_p} = \frac{\tau_{2D}}{k} \quad ,$$

(4.24)

where τ_{2D}, defined as R/a_p, is the acoustic transit time for normal incidence introduced in Ref. 1, and the value

$$t_A(t') = t' = \tau_{2D} / \left(\frac{V}{a_p} \sin \theta \right),$$

(4.25)

which follows from Eq. (4.22). These values are the arrival times from the extremes of the emission domain. It should be noted that Eq. (4 24) depends on φ whereas Eq. (4.25) does not.

A straightforward investigation of the analytic behavior of $t_A(t)$ for fixed θ and φ, whose details are omitted, shows that the arrival time has four possible forms as a function of emission time. The four

forms arise because t_A may have a maximum in $0 < t < t'$, or not, and that independently, $t_A(0)$ may be larger than t', or smaller. Since the _earliest_ arrival time is desired, it is clear that this time is either $t_A(0)$ or $t_A(t') = t'$. Denoting the earliest arrival time by $\tau_E(\theta, \varphi)$, we may express it as

$$\tau_E(\theta, \varphi) = \text{smaller of} \left[\tau_{2D}/k, \ \tau_{2D} \bigg/ \left(\frac{V}{a_p} \sin\theta \right) \right] . \quad (4.26)$$

It should be emphasized that since the LSC wave speed V is constitutively related to the effective laser intensity reaching the wave front in the normal direction, it is, therefore, a function of θ. The constitutive relation is well approximated by

$$V(\theta) = 10^3 (I_o \cos\theta)^{1/3} , \quad (4.27)$$

where I_o is in watt/cm^2, and V is in cm/sec. The numerical value of a_p used here is 4.5×10^5 cm/sec.

The question of which of the extreme arrival times is actually smaller may be studied graphically. The quantity σ defined as

$$\sigma \equiv \frac{t_A(0)}{t'} = \frac{1}{k} \frac{V}{a_p} \sin\theta , \quad (4.28)$$

is plotted in Figs. 4.3 and 4.4 as a function of φ for specified values of θ and I_o. When $\sigma < 1$, the earliest arrival time is $t_A(0)$, but when $\sigma > 1$, the plasma outline arrival time is the earlier one. It is seen
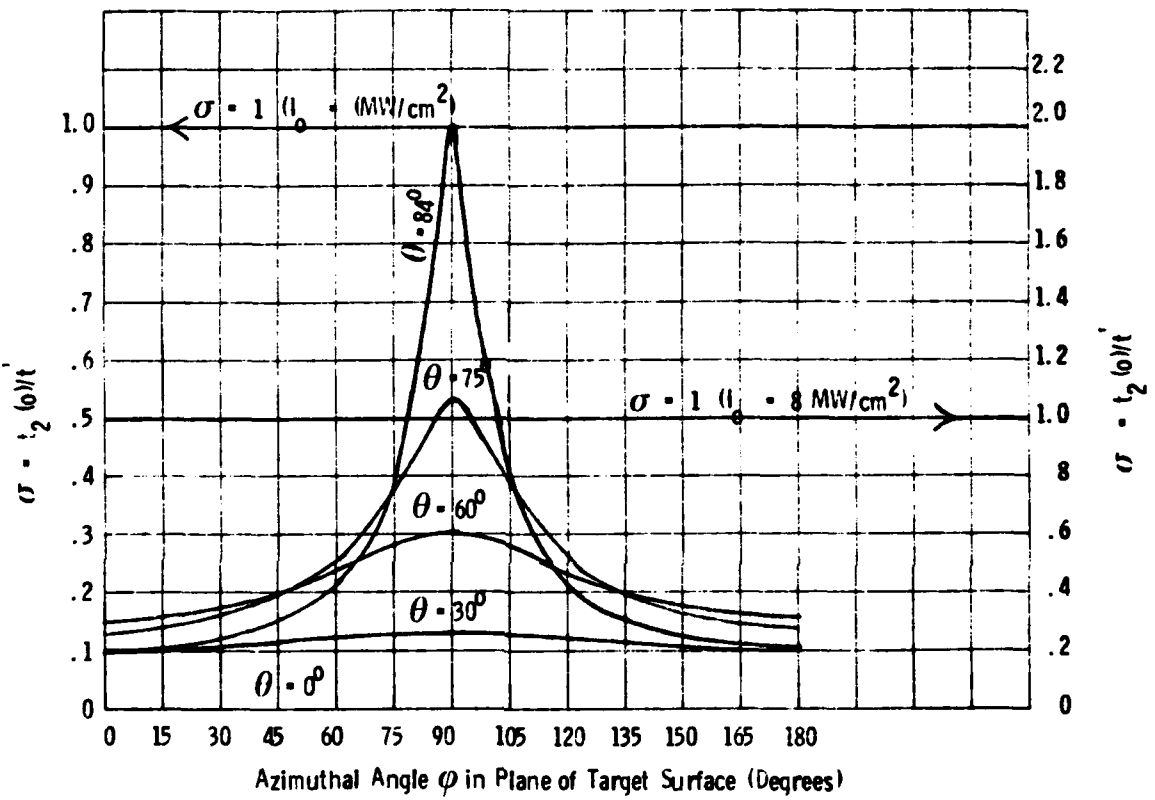
Fig. 4.3 Comparison of Acoustic Arrival Time with Plasma Trace
Arrival Time for Laser Intensities of 1 MW/cm^2 and
8 MW/cm^2.
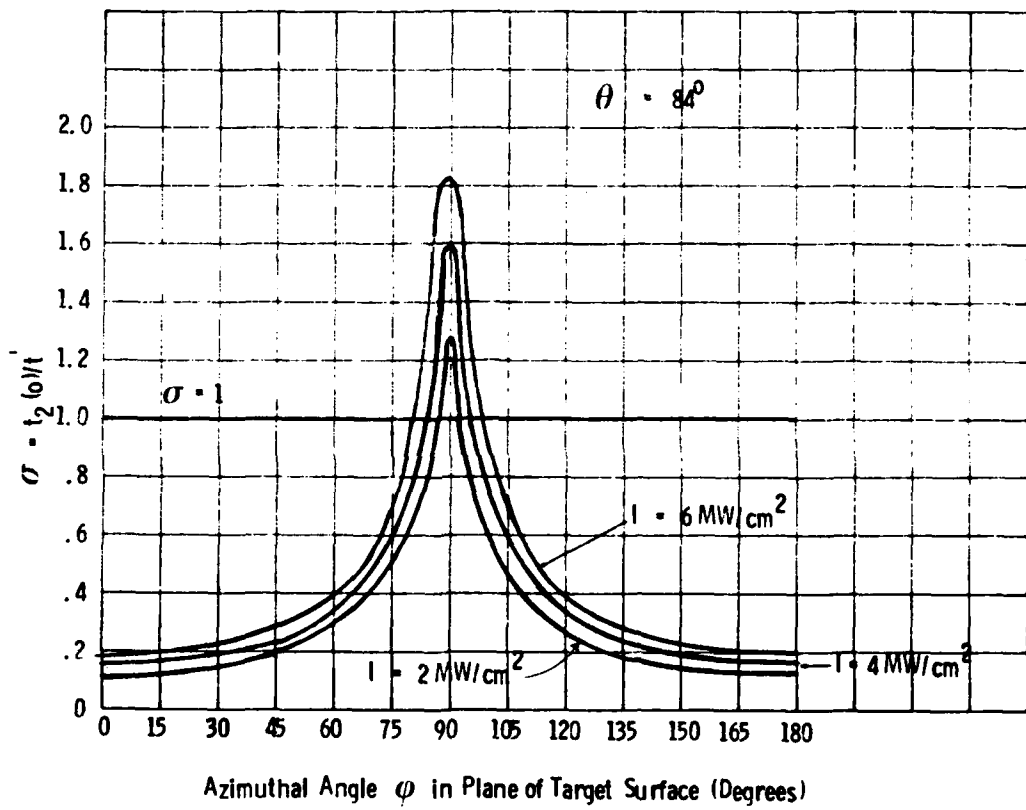
Fig. 4.4 Comparison of Acoustic Arrival Time with Plasma Trace Arrival Time for 84° Flux Incidence.

that at $\varphi = 0$, $t_A(0) = \tau_{2D}$ is always the smaller arrival time but that nearer to $\varphi = 90^o$, the trace arrival time can become the smaller one. The domain of φ for which $\sigma > 1$ is generally concentrated in a narrow band about $\varphi = 90^o$.

The slow variation of σ with φ except in a small domain about $\varphi = 90^o$ suggests that the competition between the acoustic arrival time and the trace arrival time can be approximated by a model in which the full range of variation of τ_E with respect to φ is replaced by _two_ values, those at $\varphi = 0$ and at $\varphi = 90^o$. The arrival time for the minor axis is

$$\tau_E (\theta, 0) = \tau_{2D} \quad , \tag{4.29}$$

while that for the major axis is the new characteristic time

$$\tau_E (\theta, 90^o) \equiv \tau_{3D} = \text{smaller of}$$

$$\left[\tau_{2D} / \cos \theta, \quad \tau_{2D} / \left(\frac{V}{a_p} \sin \theta \right) \right] \quad . \tag{4.30}$$

Since the sound velocity a_p in the plasma is always larger than the velocity V of the LSC wave front, it follows that

$$\tau_{3D} \geq \tau_{2D} \quad , \tag{4.31}$$

and that the equality holds only for normal incidence. This model is equivalent to replacing the original laser spot with a rectangular spot as shown in Fig. 4.5. The right side of the plasma trace moves in the
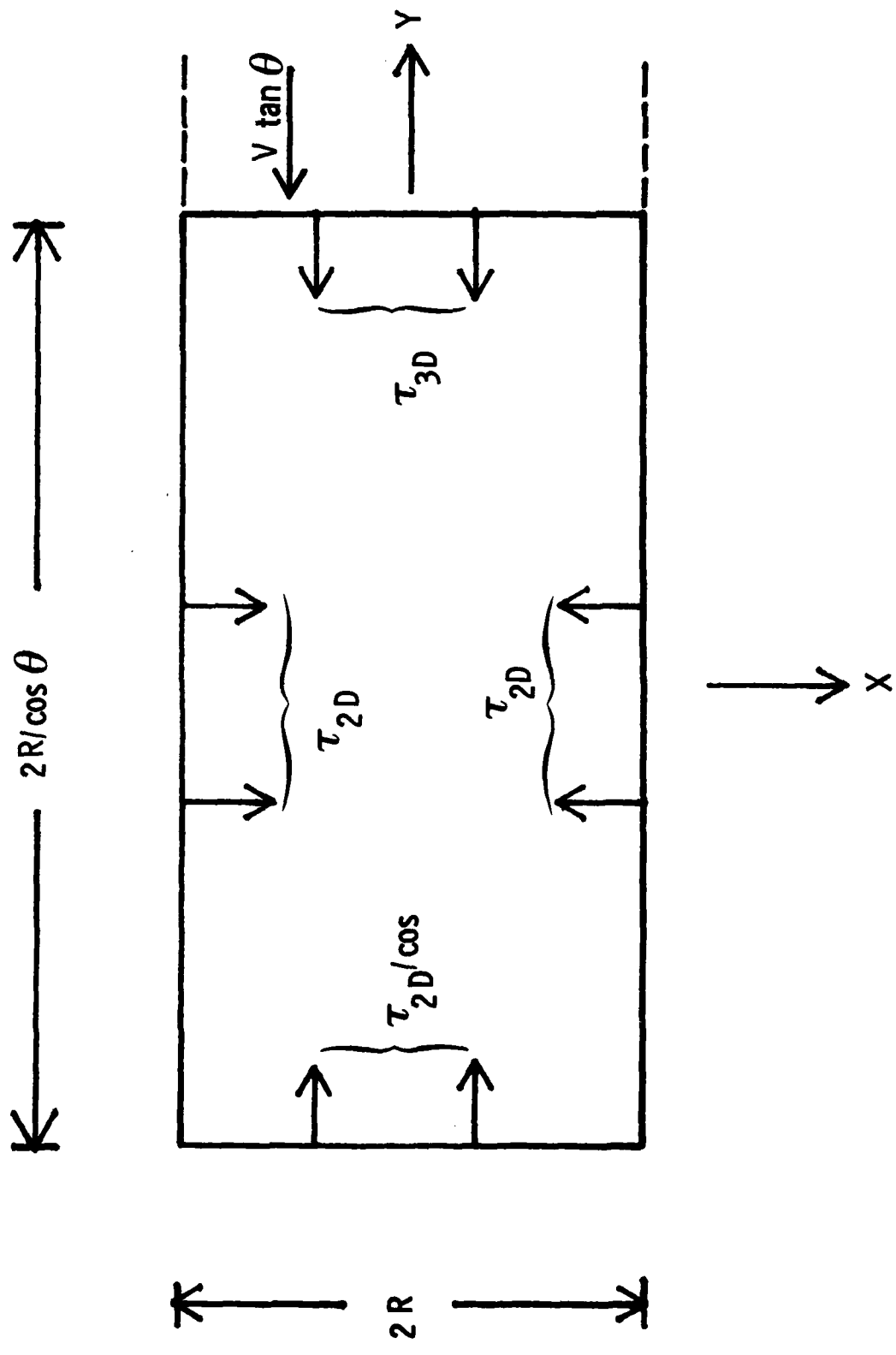
Fig. 4.5 Fictitious Plasma Outline in Two-Time Arrival Model.

negative Y direction. Acoustic propagation takes place only toward the X axis, and toward the Y axis. Propagation toward the Y axis from both the top and bottom sides of the rectangle is included and is governed by τ_{2D}. Propagation toward the X axis from only the right side of the rectangle need be considered since the governing arrival time τ_{3D} is always equal to or less than the arrival time $\tau_{2D}/\cos\theta$ of acoustic waves from the left side of the rectangular periphery. It should be noted that the area of the rectangular spot, $4R^2/\cos\theta$, is greater than that of the elliptical spot, $\pi R^2/\cos\theta$.

The earliest acoustic waves reaching the central spot are those that propagate along the minor axis. Thus, the time τ_{2D} is the earliest time at which the plasma dynamics can change from planar to cylindrical in some direction. One measure of the reliability of the one-dimensional model is the extent to which the center of the laser-irradiated spot is covered with plasma at $t = \tau_{2D}$. Plots of the quantity

$$\frac{r_{2D}}{R} \equiv \frac{r(t = t_{2D})}{R} \tag{4.32}$$

are given in Figs. 4.6 and 4.7 for the intensities 1 MW/cm^2 and 4 MW/cm^2, respectively. It is seen that for all incidence angles considered, the central spot is well covered with plasma and that the calculation of radiation to the center of the spot as though it came from an infinite slab is certainly valid for times up to τ_{2D}.

4.2 Regimes, Cases and Relaxation Laws: The Late-Time Model

The duration of the laser pulse τ_p is the primary time scale in the calculation of thermal and impulse coupling. For normal incidence,

92
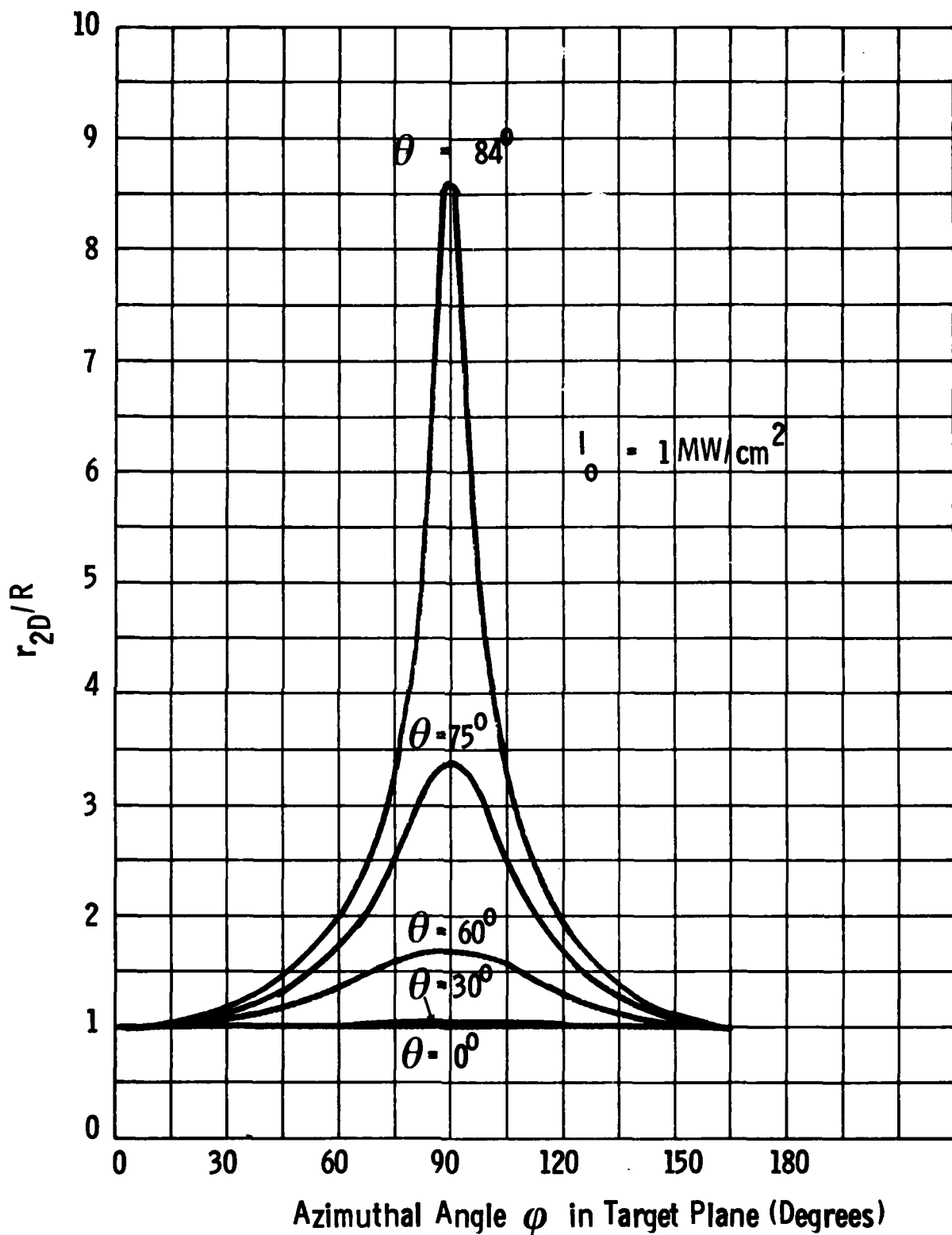
Fig. 4.6 Plasma Coverage of Central Point of Laser Spot at Time τ_{2D} for an Incident Laser Intensity of 1 MW/cm^2.

93
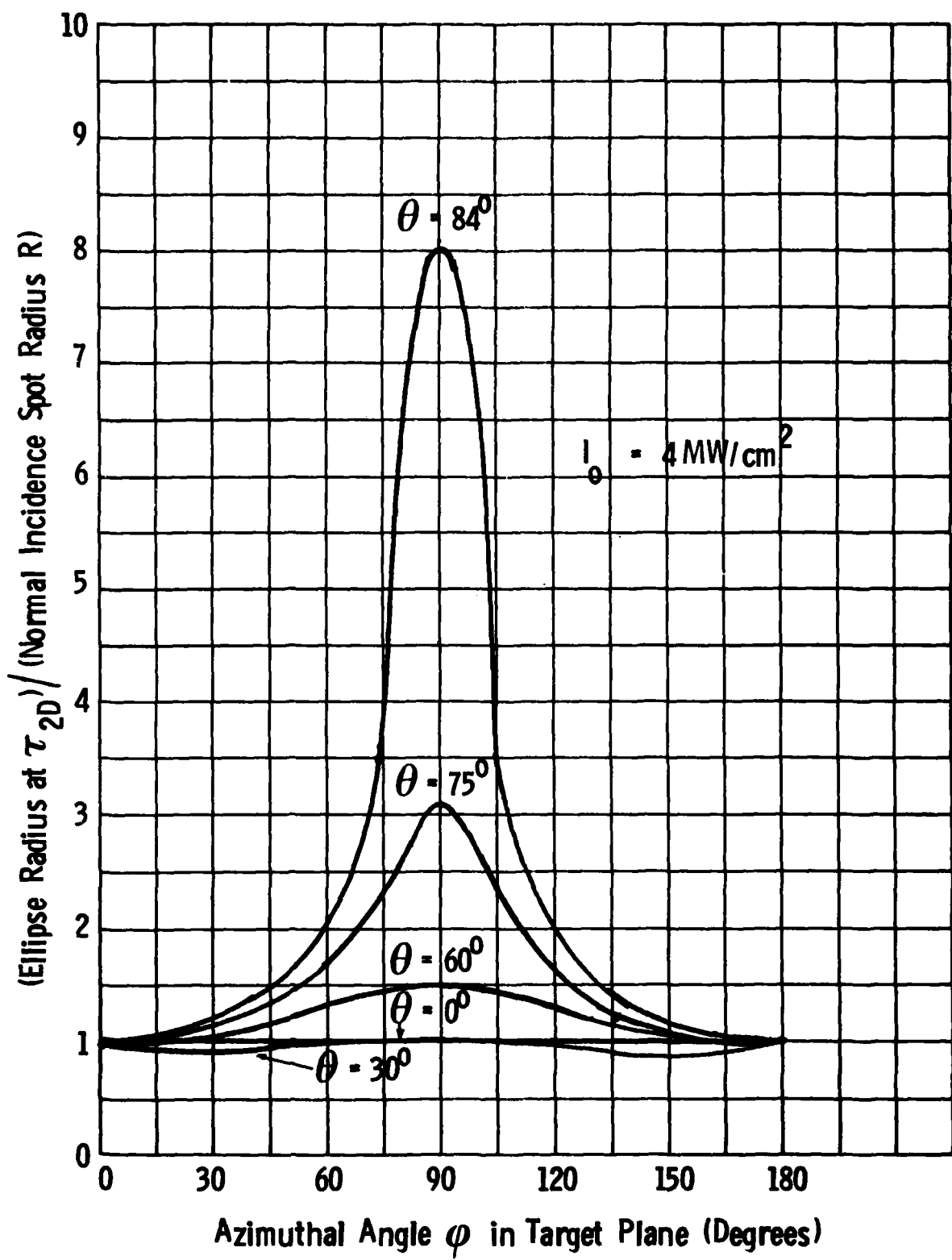
Fig. 4.7 Plasma Coverage of Central Point of Laser Spot at Time τ_{2D} for an Incident Laser Intensity of 4 MW/cm^2.

94

a second time scale is τ_{2D}. The coupling coefficients at normal incidence depend on the interplay of the two time scales. In particular, the dimensionless parameter

$$\hat{\tau} \equiv \tau_p / \tau_{2D} , \tag{4.33}$$

is important in assessing the coupling. For non-normal incidence, the additional time scale τ_{3D} influences the thermal and impulse coupling. It is useful to define a new dimensionless parameter τ_c

$$\tau_c \equiv \tau_{2D} / \tau_{3D} = \text{larger of} \left[\cos\theta, \ \frac{V(\theta)}{a_p} \sin\theta \right] , \tag{4.34}$$

to measure the relative size of τ_{2D} and τ_{3D}. The parameter analogous to $\hat{\tau}$ for τ_{3D} is

$$\tau_p / \tau_{3D} = (\tau_p / \tau_{2D}) (\tau_{2D} / \tau_{3D}) = \hat{\tau} \ \tau_c . \tag{4.35}$$

The inequality, Eq. (4.31), insures that τ_c is always equal to or less than unity, with the equality holding only for normal incidence. The parameter $\hat{\tau}$ may be less than, equal to, or greater than unity. It is thus possible to delineate three <u>regimes</u> based on the relative sizes of τ_p, τ_{2D}, and τ_{3D}. A convenient means of stating the defining relationships of the regimes is in terms of the ratios of the three time scales, to τ_p. Hence, the defining relations for the regimes are:

$$R_1 \quad : \quad 1 \;\leq\; 1/\hat{\tau} \;\leq\; 1/(\hat{\tau}\,\tau_c) \;, \qquad (4.36)$$

$$R_2 \quad : \quad 1/\hat{\tau} < 1 \;\leq\; 1/(\hat{\tau}\,\tau_c) \;, \qquad (4.37)$$

$$R_3 \quad : \quad 1/\hat{\tau} < 1/(\hat{\tau}\,\tau_c) < 1 \;. \qquad (4.38)$$

The convention used for assigning the equalities is that the possible equality of two parameters is always associated with the regime of _lower_ label number.

Radiation fluence and impulse absorbed by the target surface are calculated as integrals with respect to time commencing with $t = 0$. When the regime has been identified, one may then specify how the radiation flux and plasma pressure behave temporally when the time is within a given subrange of a regime. For any given regime, there are four possible subranges of the time variable. Each subrange will be identified as a _case_. Since dimensionless variables have been used in the definitions of the regimes, it is convenient to work with a dimensionless time variable s which represents the time measured in laser pulse durations:

$$s \;\equiv\; t/\tau_p \;. \qquad (4.39)$$

For illustration, the four cases belonging to regime R_1 are now given:

$$R_{11} \quad : \quad s \;\leq\; 1 \;\leq\; 1/\hat{\tau} \;\leq\; 1/(\hat{\tau}\,\tau_c), \qquad (4.40)$$

$$R_{12} : \quad 1 < s \le 1 / \hat{\tau} \le 1 / (\hat{\tau} \tau_c) , \qquad (4.41)$$

$$R_{13} : \quad 1 \le 1 / \hat{\tau} < s \le 1 / (\hat{\tau} \tau_c) , \qquad (4.42)$$

$$R_{14} : \quad 1 \le 1 / \hat{\tau} \le 1 / (\hat{\tau} \tau_c) < s . \qquad (4.43)$$

Case numbers are assigned in increasing sequence as the time variable progresses to the right through a regime. As with regimes, the convention is followed that possible equality between the time variable and any parameter is always associated with the lower case label. The construction of cases for regimes R_2 and R_3 is identical to that for R_1. In general, R_{ij} denotes the j'th case ($j = 1, 2, 3, 4$) of regime i ($i = 1, 2, 3$).

The early time (one-dimensional) model is in force when $s \le 1/\hat{\tau}$. This circumstance is covered by cases R_{11}, R_{21}, and R_{31}. It should be observed that although the early time model is formally valid for case R_{12}, the radiation flux and plasma pressure behave differently with time than they do in case R_{11} since the former case is unpowered, i.e., the laser is off. For this reason, case R_{12} is excluded from the early time model. It and all other cases are the domain of the late-time model.

To specify the late-time model it is necessary to give the temporal behavior of the plasma pressure p(t) at the target surface, and the plasma thickness (the distance L of the LSC front from the target surface in Fig. 4.1). This is shown in Table 4.1 for the nine cases that comprise the late-time model. The behavior of the pressure is needed in the calculation of absorbed impulse (per unit area) while both the plasma

TABLE 4.1

Blast laws for pressure/plasma thickness relaxation.

Relaxation Law	L	P
Planar, Unpowered (One Case) $$\tau_p < t < \tau_{2D} < \tau_{3D}$$	$t^{2/3}$	$t^{-2/3}$
Cylindrical, Unpowered (Two Cases) $$\left\{\tau_p, \tau_{2D}\right\} < t < \tau_{3D}$$	$t^{1/2}$	t^{-1}
Cylindrical, Powered (Two Cases) $$\tau_{2D} < t < \left\{\tau_p, \tau_{3D}\right\}$$	$t^{3/4}$	$t^{-1/2}$
Spherical, Unpowered (Three Cases) $$\left\{\tau_p, \tau_{2D}, \tau_{3D}\right\} < t$$	$t^{2/5}$	$t^{-6/5}$
Spherical, Powered (One Case) $$\tau_{2D} < \tau_{3D} < t < \tau_p$$	$t^{3/5}$	$t^{-4/5}$

pressure and thickness are needed to calculate absorbed fluence.

Of the five distinct relaxation laws given in Table 4. 1, three are already encountered at normal incidence and are used in Ref. 1. These are the unpowered planar law, and the powered and unpowered spherical laws. The relaxation laws specific to non-normal incidence are the powered and unpowered cylindrical laws. These are discussed by Dabora.[18]

For early time, the values of the plasma pressure and radiation flux absorbed by the surface are calculated using the LSC wave model described in Section 2, with the modifications:

$$I_o \rightarrow I_o \cos \theta ,$$

$$\kappa_L \rightarrow \kappa_L /\cos \theta .$$

The target surface pressure is approximately constant throughout the time when the one-dimensional model is valid, thus a constant value can be used to represent p. The calculations reveal that p is essentially a function of $I_o \cos \theta$; this function is plotted in Fig. 4. 8. As in the case of normal incidence we can construct plots of absorbed fluence as a function of time for the one-dimensional model. Typical plots are shown in Fig. 4. 9. When the laser pulse is over, or when the first acoustic wave from the plasma periphery reaches the central spot, the relaxation laws in Table 4. 1 take over and, henceforth, govern the radiation and plasma pressure.

4. 3 Thermal Coupling

The incident laser intensity is assumed to have a rectangular temporal shape. A rectangular pulse of duration τ_p starting at t = 0 may be represented by
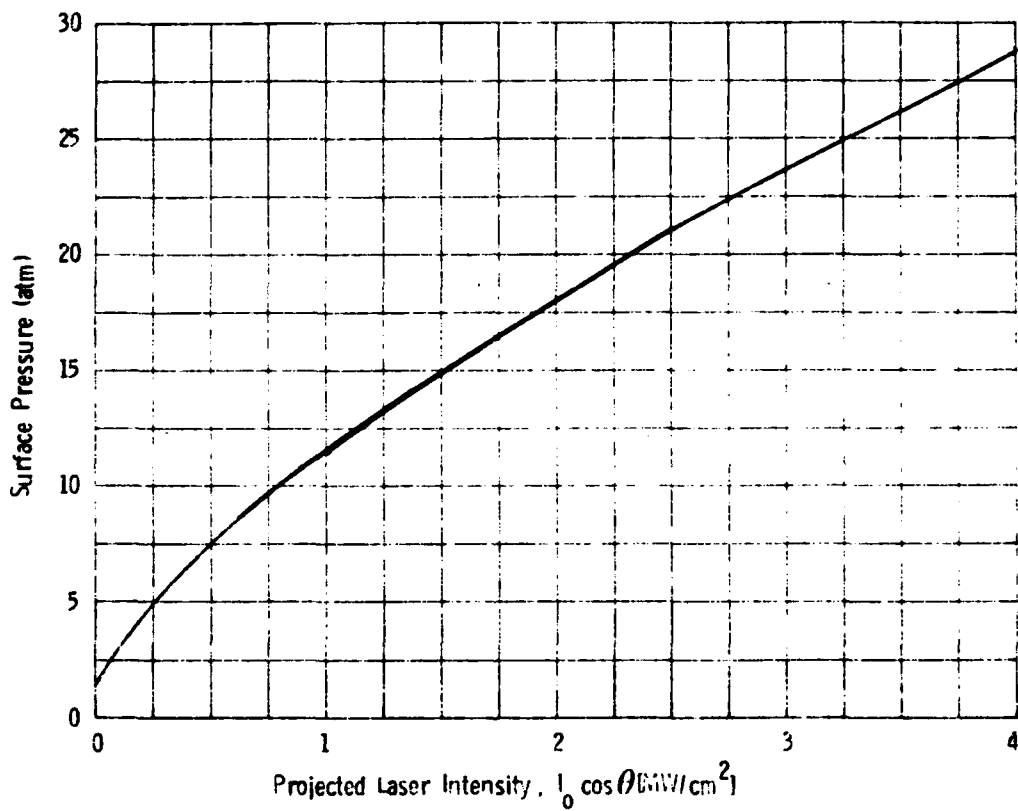
Fig. 4.8   Theoretical Prediction of Surface Pressure Generated
by an LSC Wave as a Function of the Projected Laser
Intensity.
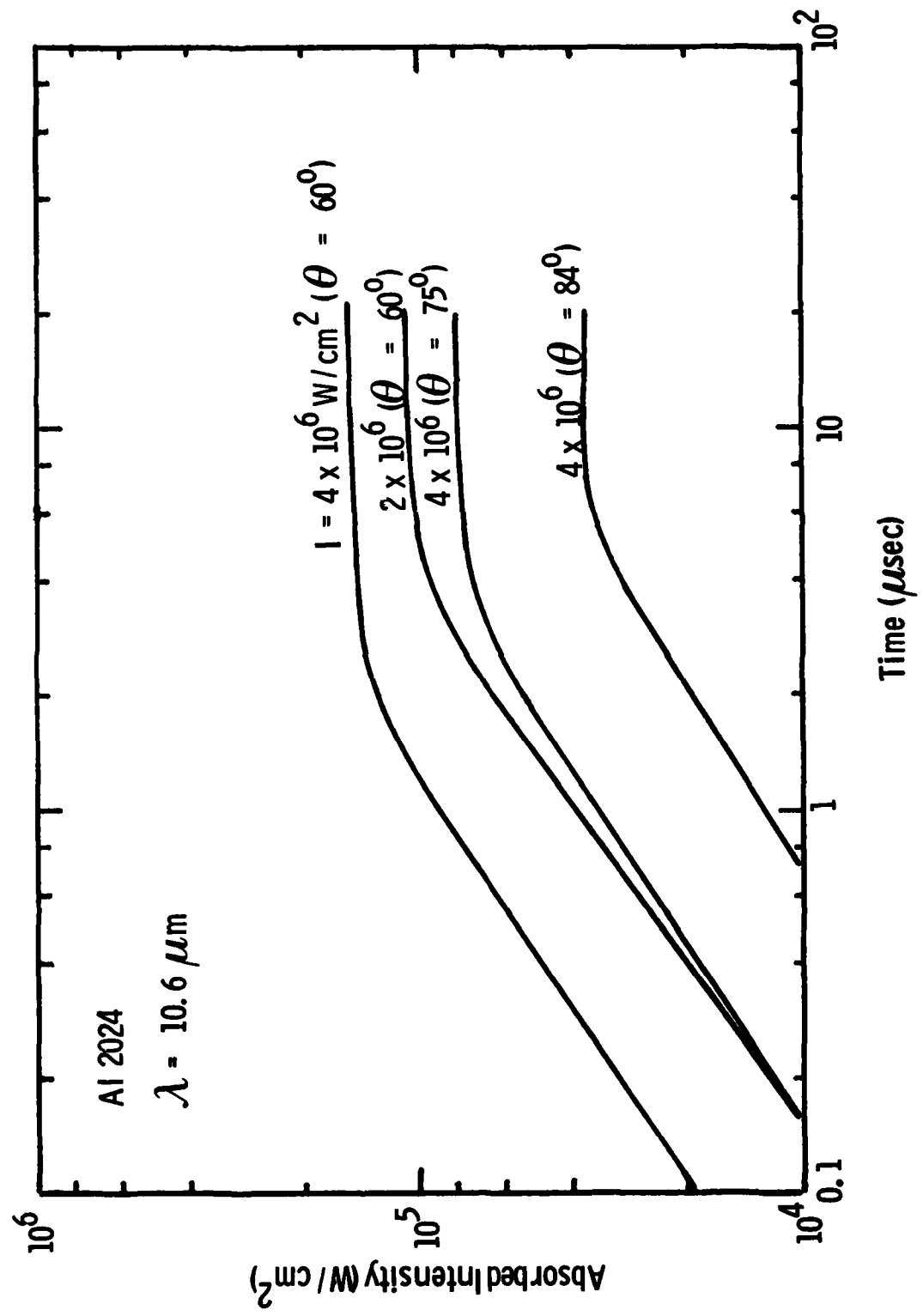
Fig. 4.9 Intensity of One-Dimensional LSC Wave Plasma Radiation Absorbed by Al2024 Target for Laser Beam Incident at Various Oblique Angles.

$$I(s) = (I_o \cos \theta) \left[H(s) - H(s - 1) \right] , \qquad (4.44)$$

where H is the Heaviside step function equal to zero for negative values
of its argument, and equal to unity for positive values.   Plots, such as
Fig. 4.9, define $q_1(t)$, the radiative flux absorbed by the target surface
during the duration of the laser pulse or before the onset of two-dimen-
sional plasma dynamics.   The assumption adopted in Ref. 1, that the
fraction of the plasma radiation flux to the surface that is absorbed re-
mains constant throughout the relaxation of the plasma, is adopted here.
This assumption implies that the spectral content of the radiation flux
in the cylindrical and spherical relaxation cases is the same as in the
planar development case, and that the spectral synthesis of the absorbed
flux need be done explicitly only in the latter case.

For the relaxation cases one resorts to the equations used in Ref. 1
to characterize the absorbed radiation.   The reradiated flux follows the
fourth power law in temperature T,

$$q_r = \sigma \epsilon T^4 , \qquad (4.45)$$

where σ is the Stefan-Boltzmann constant and ϵ is the emissivity.   The
emissivity is expressed in the form

$$\epsilon = \epsilon_o T^F L^G (\rho / \rho_\infty) , \qquad (4.46)$$

where ρ_∞ is the ambient air density, and the exponents and coefficient
are chosen as those appropriate to the range 1.5 e V $\leq$ T $\leq$ 2 eV in the
curve fit[1] of the results of Johnston, Platas, and Tannenwald.[5]   The

exponents are $F = 2.2$, $G = 0.36$, and the coefficient is irrelevant for the present purposes. The Gilmore equation[19] of state,

$$h = h_o p^{-1/9} T^{5/3} , \qquad (4.47)$$

the ideal gas law,

$$h = \frac{\gamma}{\gamma - 1} \frac{p}{\rho} , \qquad (4.48)$$

and the adiabatic assumption,

$$p \rho^{\gamma} = \text{constant}, \qquad (4.49)$$

where γ has the value 1.2, make a closed set of equations with Eqs. (4.45) and (4.46). The absorbed radiation flux is then related to q_r by

$$q(s) = \psi \sigma \epsilon T^4 , \qquad (4.50)$$

where the constant ψ is the fraction of reradiated flux absorbed by the surface.

To utilize the relaxation laws listed in Table 4.1, Eqs. (4.46) through (4.50) are manipulated so that $q(s)$ appears as an explicit function of plasma thickness and pressure. That function is

$$q(s) = C L(s)^G p(s)^\mu , \qquad (4.51)$$

where G, as before, is 0.36, μ has the value 28/15, and C is a constant. This constant subsumes the constants σ, ψ, ϵ_o, h_o, ρ_∞, $\gamma/(\gamma - 1)$, and

the constant in the adiabatic assumption (4.49). Its value is related to the calculated value of $q_1(s)$ at the junction of cases 1 and 2 in each regime by the requirement that $q(s)$ be continuous at this junction. In regime i, the absorbed radiative flux for case $j \geq 2$ has the form

$$q_{ij}(s) = C L_{ij}^G p_{ij}^\mu (s/s_{ij})^{\nu_{ij}} , \qquad (4.52)$$

where L_{ij} and p_{ij} are coefficients for the appropriate thickness and pressure relaxation laws, s_{ij} is the lower bound of s in case j of regime i, and ν_{ij} is calculated from the exponents f_{ij} of the thickness relaxation law and $-n_{ij}$ ($n_{ij} > 0$) of the pressure law in Table 4.2 by the relation

$$\nu_{ij} = Gf_{ij} - \mu n_{ij} . \qquad (4.53)$$

Table 4.2 is a table of the values of ν_{ij}. Upon invoking the continuity requirements one finds the relations

$$q_1(1) = CL_{12}^G p_{12}^\mu , \qquad (4.54)$$

$$q_1(1/\widehat{\tau}) = CL_{22}^G p_{22}^\mu , \qquad (4.55)$$

$$q_1(1/\widehat{\tau}) = CL_{32}^G p_{32}^\mu , \qquad (4.56)$$

for regimes 1, 2 and 3, respectively. Plots such as Fig. 4.9 can be used to determine $q_1(1)$.

TABLE 4. 2

Values of ν_j for relaxation.

Case Regime	2	3	4
1	$- 2/3 (\mu - G)$	$- (\mu - G/2)$	$- 2/5 (3\mu - G)$
2	$- 1/2 (\mu - 3/2 G)$	$- (\mu - G/2)$	$- 2/5 (3\mu - G)$
3	$- 1/2 (\mu - 3/2 G)$	$- 1/5 (4\mu - 3G)$	$- 2/5 (3\mu - G)$

The coefficient of thermal coupling for non-normal laser flux incidence is defined by

$$\alpha(s) \equiv \left[\int_O^S q(s')\, ds' \right] / \int_O^S I(s')\, ds' \ , \qquad (4.57)$$

where $I(s)$ is given by the rectangular shape (4.44). The calculation of α in each case of each regime is a tedious but straightforward exercise whose details are omitted here. The value which characterizes the overall coupling is the final value α_f defined as

$$\alpha_f \equiv \operatorname*{Lim}_{s \to \infty} \alpha(s) \ , \qquad (4.58)$$

and is calculated from the result for case 4 of each regime. The results of the case studies are now summarized. The intensity I which appears is related to the incident intensity I_O and the angle θ by

$$I = I_O \cos \theta \ . \qquad (4.59)$$

Regime R_1

R_{11} : $s \leq 1 \leq 1/\widehat{\tau} \leq 1/(\widehat{\tau}\,\tau_c)$

$$\alpha(s) = \frac{1}{Is} \int_O^S q_1(s')\, ds' \ . \qquad (4.60)$$

R_{12} : $1 < s \leq 1/\widehat{\tau} \leq 1/(\widehat{\tau}\,\tau_c)$

$$\alpha(s) = \alpha(1) + \frac{q_1(1)}{(|\nu_{12}| - 1)\, I} \left[1 - \left(\frac{1}{s}\right)^{|\nu_{12}| - 1} \right] . \qquad (4.61)$$

106

$$R_{13} : 1 \leq 1/\hat{\tau} < s \leq 1/(\hat{\tau}\,\tau_c)$$

$$\alpha(s) = \alpha(1/\hat{\tau}) + \frac{q_1(1)\left(\hat{\tau}^{|\nu_{12}|-1}\right)}{\left(|\nu_{13}| - 1\right)I}\left[1 - \left(\frac{1}{\hat{\tau}\,s}\right)^{|\nu_{13}| - 1}\right]. \quad (4.62)$$

$$R_{14} : 1 \leq 1/\hat{\tau} \leq 1/(\hat{\tau}\,\tau_c) < s$$

$$\alpha(s) = \alpha(1/\hat{\tau}\,\tau_c)$$

$$+ \frac{q_1(1)\left(\hat{\tau}^{|\nu_{12}|-1}\right)\left(\tau_c^{|\nu_{13}|-1}\right)}{\left(|\nu_{14}| - 1\right)I}\left[1 - \left(\frac{1}{\hat{\tau}\,\tau_c\,s}\right)^{|\nu_{14}| - 1}\right]. \quad (4.63)$$

The coefficient of overall coupling is

$$\alpha_f = \alpha(1/\hat{\tau}\,\tau_c) + \frac{q_1(1)\left(\hat{\tau}^{|\nu_{12}|-1}\right)\left(\tau_c^{|\nu_{13}|-1}\right)}{\left(|\nu_{14}|-1\right)I}. \quad (4.64)$$

Regime R_2

$$R_{21} : s \leq 1/\hat{\tau} < 1 \leq 1/(\hat{\tau}\,\tau_c)$$

$$\alpha(s) = \frac{1}{Is}\int_0^s q_1(s')\,ds'. \quad (4.65)$$

R_{22} : $1/\widehat{T} < s \leq 1 \leq 1/(\widehat{T}\,\tau_c)$

$$\alpha(s) = \frac{1}{\widehat{T}s}\,\alpha(1/\widehat{T}) + \frac{q_1(1/\widehat{T})}{(\nu_{22}+1)I}\left[(\widehat{T}s)^{\nu_{22}+1} - 1\right]. \quad (4.66)$$

R_{23} : $1/\widehat{T} < 1 < s \leq 1/(\widehat{T}\,\tau_c)$

$$\alpha(s) = \alpha(1) + \frac{q_1(1/\widehat{T})(\widehat{T}^{\nu}{}_{22})}{(|\nu_{23}| - 1)I}\left[1 - \left(\frac{1}{s}\right)^{|\nu_{23}| - 1}\right]. \quad (4.67)$$

R_{24} : $1/\widehat{T} < 1 \leq 1/(\widehat{T}\,\tau_c) < s$

$$\alpha(s) = \alpha(1/\widehat{T}\,\tau_c) + \frac{q_1(1/\widehat{T})\widehat{T}^{\nu}{}_{22}(\widehat{T}\,\tau_c)^{|\nu_{23}| - 1}}{(|\nu_{24}| - 1)I}$$

$$\left[1 - \left(\frac{1}{\widehat{T}\,\tau_c s}\right)^{|\nu_{24}| - 1}\right]. \quad (4.68)$$

The coefficient of overall coupling is

$$\alpha_f = \alpha(1/\widehat{T}\,\tau_c) + \frac{q_1(1/\widehat{T})(\widehat{T}^{\nu}{}_{22})(\widehat{T}\,\tau_c)^{|\nu_{23}|-1}}{(|\nu_{24}| - 1)I}. \quad (4.69)$$

R_{31} : $s \leq 1/\hat{\mathcal{T}} \leq 1/(\hat{\mathcal{T}} \tau_c) < 1$

$$\alpha(s) = \frac{1}{Is} \int_0^s q_1(s') ds' \quad . \tag{4.70}$$

R_{32} : $1/\hat{\mathcal{T}} < s \leq 1/(\hat{\mathcal{T}} \tau_c) < 1$

$$\alpha(s) = \frac{1}{\hat{\mathcal{T}} s} \alpha(1/\hat{\mathcal{T}}) + \frac{q_1(1/\hat{\mathcal{T}})}{(\nu_{32} + 1) I} \left[(\hat{\mathcal{T}} s)^{\nu_{32} + 1} - 1 \right] . \tag{4.71}$$

R_{33} : $1/\hat{\mathcal{T}} \leq 1/(\hat{\mathcal{T}} \tau_c) < s \leq 1$

$$\alpha(s) = \frac{1}{\hat{\mathcal{T}} \tau_c s} \alpha(1/\hat{\mathcal{T}} \tau_c) + \frac{q_1(1/\hat{\mathcal{T}}) \tau_c^{-\nu_{32}}}{(|\nu_{33}| - 1) I} \left[1 - \left(\frac{1}{\hat{\mathcal{T}} \tau_c s}\right)^{|\nu_{33}| - 1} \right] . \tag{4.72}$$

R_{34} : $1/\tau \leq 1/(\tau \tau_c) < 1 < s$

$$\alpha(s) = \alpha(1) + \frac{q_1(1/\hat{\mathcal{T}}) \tau_c^{-\nu_{32}} (\hat{\mathcal{T}} \tau_c)^{\nu_{33}}}{(|\nu_{34}| - 1) I} \left[1 - \left(\frac{1}{s}\right)^{\nu_{34} - 1} \right] . \tag{4.73}$$

The coefficient of overall coupling is

$$\alpha_f = \alpha(1) + \frac{q_1(1/\hat{\mathcal{T}}) \tau_c^{-\nu_{32}} (\hat{\mathcal{T}} \tau_c)^{\nu_{33}}}{(|\nu_{34}| - 1) I} \quad . \tag{4.74}$$

The absorbed fluence is given in terms of the thermal coupling co-efficient by

$$\tau_p \int_0^s q(s')ds' = \tau_p \left[\int_0^s I(s')ds' \right] \alpha(s) \ ,$$

where the factor τ_p has been inserted in order that the integrals of q and I be with respect to the actual, rather than the dimensionless time.

Figures 4. 10 and 4. 11 are plots of the overall thermal coupling coefficient, and total absorbed fluence, respectively, as functions of cos θ for a pulse duration of 10 μsec, a laser spot area at normal incidence (this determines τ_{2D}) of 40 cm^2, and incident flux densities of 2 MW/cm^2, 3 MW/cm^2, and 4 MW/cm^2. As expected, the absorbed fluence decreases with increasing θ for each laser flux and, for a given θ, increases with increasing laser flux. Even for an incidence angle as large as 84° (cos $\theta \approx 0. 1$), the absorbed fluence is not negligible, being between 0. 3 J/cm^2 and 0. 5 J/cm^2.

The coupling coefficient increases with increasing θ for a given laser flux and, unlike the behavior of absorbed fluence, decreases with increasing laser flux for a fixed angle of incidence. The value of $\hat{\tau}$ for the conditions of Fig. 4. 10 is 1. 26. The values of α predicted by the present theory for normal incidence are between 9% and 12% and are consistent with the predictions of Ref. 1 for the same value of $\hat{\tau}$.

The predictions of this model are compared in Section 5 with recent data taken under the JANAF program on RP laser effects. The comparison shows that theory and data are consistent, and that the modifications of the LSC wave model of enhanced thermal coupling can be confidently applied for non-normal angles of incidence.
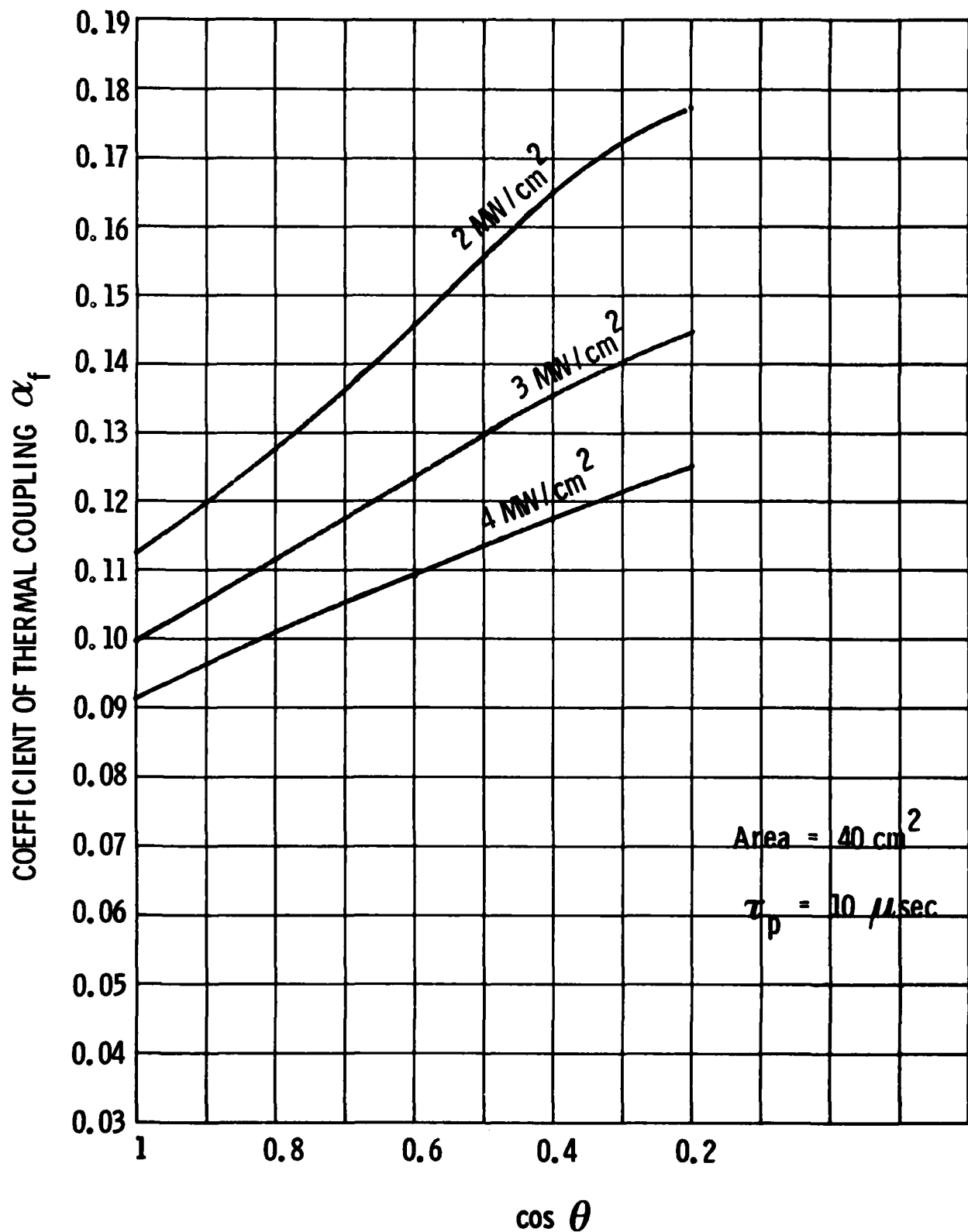
Fig. 4.10 Angular Dependence of Thermal Coupling Coefficient Predicted by an LSC Wave Model.
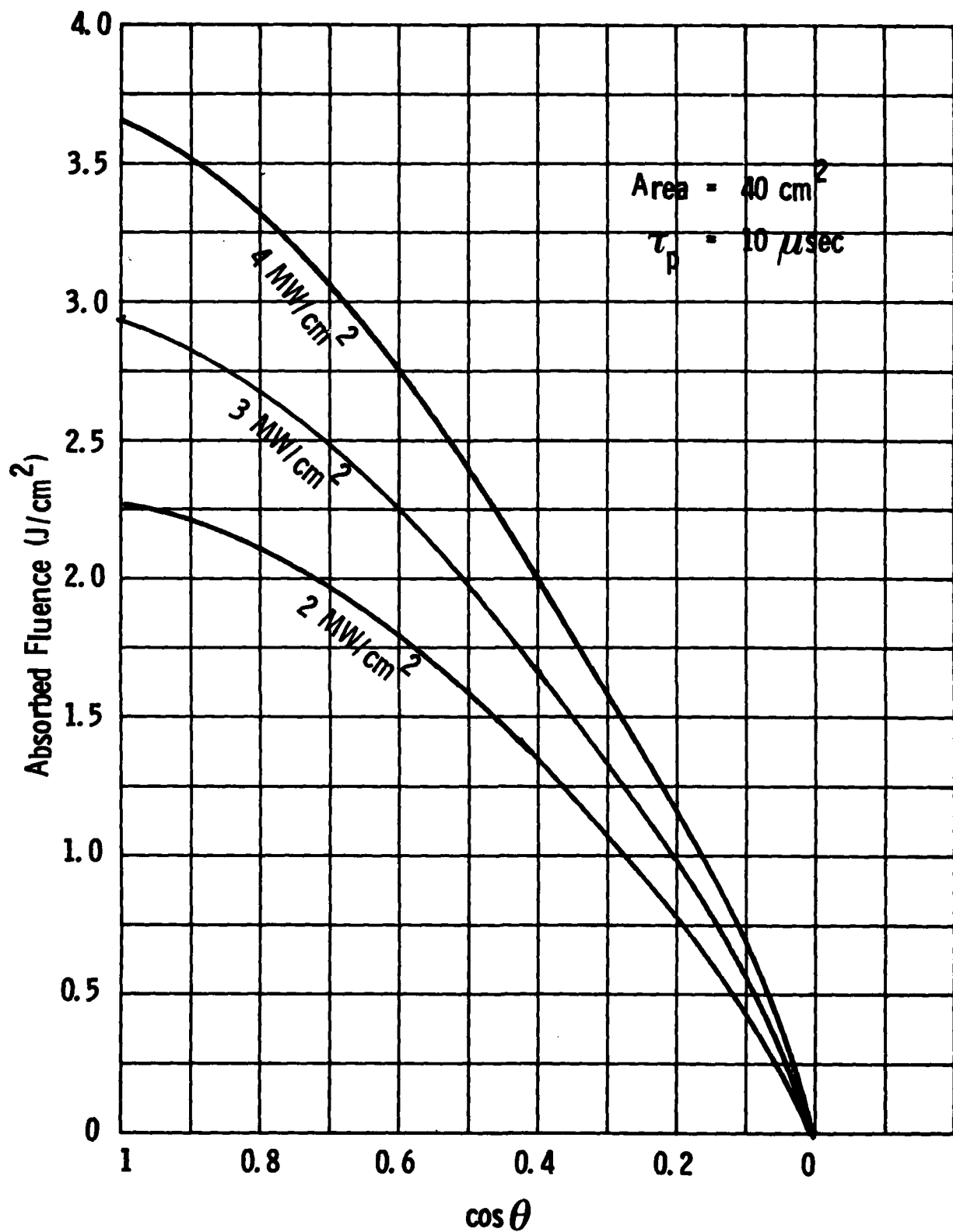
Fig. 4. 11 Theoretical Predictions of Fluence Absorbed by Al2024 as a Function of cos θ Where θ is the Angle of Incidence. Predictions are Shown for Three Laser Beam Intensities.

4.4 Impulse Coupling

The time-integrated plasma pressure at the target surface defines the impulse per unit area. The time history of the surface pressure in the cases of plasma relaxation is given by the dependences in Table 4.1. In case 1 of any regime, the pressure should be approximately constant in time if the early-time one-dimensional model is valid. The corresponding behavior at normal incidence is shown in Fig. 3 of Ref. 1. An expression for the surface pressure p_s for non-normal incidence may be inferred from the one corresponding to normal incidence[2] by replacing I_o by $I_o \cos \theta$. The expression is

$$p_s = \left(\frac{\gamma_{sh} - 1 - 2W}{\gamma_{sh} - 1} \right) \left(\frac{\gamma_{sh} + 1}{2} \rho_\infty \right)^{1/3} \cdot \left[\frac{(\gamma - 1)(\gamma_{sh} - 1) I_p}{(\gamma + W)(\gamma_{sh} - 1 - 2W)} \right]^{2/3} \quad , (4.75)$$

where γ_{sh} is the specific heat ratio between the precursor shock and the LSC front and has the value 1.4, γ is the specific heat ratio in the LSC plasma, with the value 1.2, I_p is the modified intensity

$$I_p = I_o \cos \theta - q_r - q_\ell , \tag{4.76}$$

and W, the dimensionless particle velocity ahead of the LSC wave front is calculated from the LSC wave code (see Section 2) and is well approximated by

113

$$W = 12 \times 10^{-3} (I_o \cos \theta)^{1/2} \quad ,$$

for $I_o \cos \theta$ between 1 MW/cm^2 and 10 MW/cm^2.

For Eq. (4.75), we find that p_s is expected to vary roughly as $I^{2/3}$. Indeed, we find from Fig. 4.8 that the calculated pressure in the one-dimensional LSC wave model can be well represented by

$$p_s \text{ [atm]} = 11.8 [I_o \cos \theta]^{2/3} \tag{4.77}$$

where I_o is measured in MW/cm^2.

A coefficient of impulse coupling $\beta(s)$ may be defined by

$$\beta(s) = \frac{1}{p_s} \int_0^s p(s')ds' \quad , \tag{4.78}$$

where a factor τ_p multiplying p_s is cancelled by the use of the dimensionless time variable in the integration. The absorbed impulse is then given by

$$\tau_p \int_0^s p(s')ds' = \tau_p p_s \beta(s) \quad . \tag{4.79}$$

One may now proceed to calculate the impulse coefficient throughout all regimes, as was done for thermal coupling. A difference arises in specifying a "final" value which characterizes the overall coupling. For thermal coupling, it was sufficient to let s go to infinity and to take the limiting value of α as the overall coupling coefficient. However, impulse measurements are carried out in a different way, which necessitates halting the integration of p at a <u>finite</u> value of time. The

monotonically decreasing pressure at the surface is allowed to decay to a selected final value p_f. The time s_f at which this value is attained is first determined, and the overall coupling coefficient β_f is then defined as

$$\beta_f \equiv \beta(s_f) \ . \tag{4.80}$$

This final value is a function of $\hat{\tau}$, τ_c, and the pressure ratio ξ defined as

$$\xi \equiv p_s / p_f \ . \tag{4.81}$$

In the calculation of thermal coupling, it was necessary to calculate the coefficient in each case for all regimes in order to have the coefficient pertaining to case 4, so that the limit of infinite time could be taken. It is likewise necessary to calculate the coefficient of impulse coupling in each case of all regimes since there is no a priori way to tell in which case of a given regime the final time falls.

As with the calculation of thermal coupling, the details of the impulse calculation are tedious but straightforward, and are omitted. Since the final value of pressure is always chosen to be less than the initial surface value, the final time s_f cannot occur in case 1 of any regime. The unknown coefficients in the pressure relaxation laws are ultimately related to the initial surface pressure by the requirement that the pressure be continuous at the boundary between two contiguous cases.

A summary of the results of the impulse coupling calculations follows. For each case other than case 1 of a regime, a value of s_f is given, and an expression for β_f. The value $p_f = p_s / \xi$ is attained in a given case if the value given for s_f obeys the inequality which would place it in that case.

When the case has been established, the overall coupling is given by the expression for β_f stated for that case. In case 1 of each regime, the expression for $\beta(s)$ is

$$\beta(s) = s .$$ (4.82)

The defining inequalities for each case are given in the summary of the results of the thermal coupling calculation.

Regime R_1

R_{12} : $\beta(s) = \beta(1) + 3(s^{1/3} - 1)$. (4.83)

$$s_f = \xi^{3/2}$$ (4.84)

$$\beta_f = \beta(1) + 3(\xi^{1/2} - 1) .$$ (4.85)

R_{13} : $\beta(s) = \beta(1/\hat{\tau}) + \hat{\tau}^{-1/3} \ln(\hat{\tau}s)$. (4.86)

$$s_f = \hat{\tau}^{-1/3} \xi$$ (4.87)

$$\beta_f = \beta(1/\hat{\tau}) + \hat{\tau}^{-1/3} \ln(\hat{\tau}^{2/3} \xi) .$$ (4.88)

R_{14} : $\beta(s) = \beta(1/\hat{\tau}\tau_c) + 5\hat{\tau}^{-1/3}\left[1 - (\hat{\tau}\tau_c s)^{-1/5}\right]$. (4.89)

$$s_f = \widehat{\tau}^{-4/9} \tau_c^{-1/6} \xi^{5/6} \ . \tag{4.90}$$

$$\beta_f = \beta(1/\widehat{\tau}\tau_c) + 5\widehat{\tau}^{-1/3}\left[1 - (\widehat{\tau}^2 \tau_c^3 \xi^3)^{-1/18}\right]. \tag{4.91}$$

Regime R_2

$$R_{22}: \quad \beta(s) = \beta(1/\widehat{\tau}) + 2\widehat{\tau}^{-1}\left[(\widehat{\tau}s)^{1/2} - 1\right]. \tag{4.92}$$

$$s_f = \widehat{\tau}^{-1} \xi^2 \ . \tag{4.93}$$

$$\beta_f = \beta(1/\widehat{\tau}) + 2\widehat{\tau}^{-1}(\xi-1) \ . \tag{4.94}$$

$$R_{23}: \quad \beta(s) = \beta(1) + \widehat{\tau}^{-1/2} \ell n s \ . \tag{4.95}$$

$$s_f = \widehat{\tau}^{-1/2} \xi \ . \tag{4.96}$$

$$\beta_f = \beta(1) + \widehat{\tau}^{-1/2} \ell n (\widehat{\tau}^{-1/2} \xi) \ . \tag{4.97}$$

$$R_{24}: \quad \beta(s) = \beta(1/\widehat{\tau}\tau_c) + 5\widehat{\tau}^{-1/2}\left[1 - (\widehat{\tau}\tau_c s)^{-1/5}\right]. \tag{4.98}$$

117

$$s_f = \hat{\tau}^{-7/12} \tau_c^{-1/6} \xi^{5/6} \; . \tag{4.99}$$

$$\beta_f = \beta(1/\hat{\tau}\tau_c) + 5\hat{\tau}^{-1/2}\left[1 - (\hat{\tau}\tau_c^2\xi^2)^{-1/12}\right] . \tag{4.100}$$

Regime R_3

R_{32} :

The formulas for this case are identical to the corresponding ones in case R_{22}.

$$R_{33} : \quad \beta(s) = \beta(1/\hat{\tau}\tau_c) + 5(\hat{\tau}^2\tau_c)^{-1/2}\left[(\hat{\tau}\tau_c s)^{1/5} - 1\right] . \tag{4.101}$$

$$s_f = \hat{\tau}^{-1}\tau_c^{-3/8}\xi^{5/4} \; . \tag{4.102}$$

$$\beta_f = \beta(1/\hat{\tau}\tau_c) + 5(\hat{\tau}^2\tau_c)^{-1/2}\left[(\tau_c\xi^2)^{1/8} - 1\right] . \tag{4.103}$$

$$R_{34} : \quad \beta(s) = \beta(1) + 5\hat{\tau}^{-4/5}\tau_c^{-3/10}(1 - s^{-1/5}) . \tag{4.104}$$

$$s_f = \widehat{T}^{-2/3} \tau_c^{-1/4} \xi^{5/6} \ . \tag{4.105}$$

$$\beta_f = \beta(1) + 5\widehat{T}^{-4/5} \tau_c^{-3/10} \left[1 - \widehat{T}^{2/15} \tau_c^{1/20} \xi^{-1/16} \right]. \tag{4.106}$$

The variation of predicted surface pressure as a function of θ is shown in Fig. 4.12. The code results for this figure are for a time $t = 5 \, \mu sec$, early enough to qualify as belonging to the early-time model, and sufficiently removed from $t = 0$ that the details of the plasma ignition process have already occurred. Laser intensities of 2 MW/cm^2 and 4 MW/cm^2 have been used in Fig. 4.12. The behavior is, as expected, that the surface pressure decreases with increasing θ for a fixed laser intensity, and increases with increasing laser intensity at a fixed angle of incidence.

Figures 4.13 and 4.14 show the behavior of the impulse coupling coefficient as a function of $\widehat{T}$ for various values of τ_c. Figure 4.13 is plotted for a final pressure of one-fortieth the initial pressure while Fig. 4.14 represents a final pressure of one-tenth the initial pressure. Although these figures are drawn with the values of τ_c simply given, and not generated from given values of I_o and θ, the table in Fig. 4.14 indicates values of θ which would correspond to the selected values of τ_c (1, 0.5, 0.25, 0.1) for a laser intensity of 2 MW/cm^2, as given by Eq. (4.34). For the values 1, 0.5, and 0.25, the angles θ are those which come from $\cos \theta$. For $\tau_c = 0.1$, the value of θ must be calculated from $V(\theta) \sin \theta / a_p$. This is true for both Figs. 4.13 and 4.14 since the relation of τ_c to I_o and θ is independent of ξ. The impulse coupling coefficient is seen to decrease with increasing $\widehat{T}$.
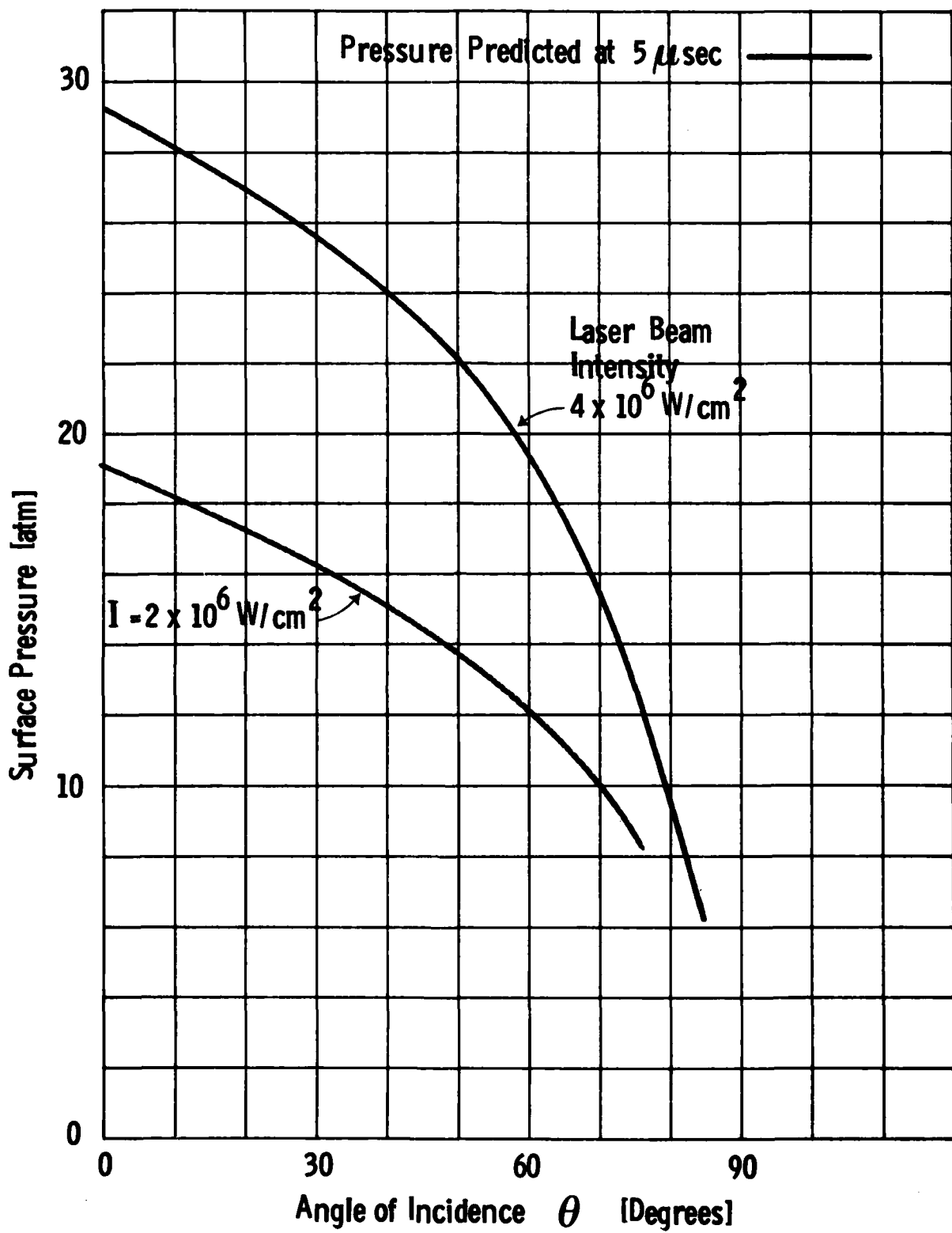
Fig. 4.12 Angular Dependence of Surface Pressure Predicted by LSC Wave Model.

120
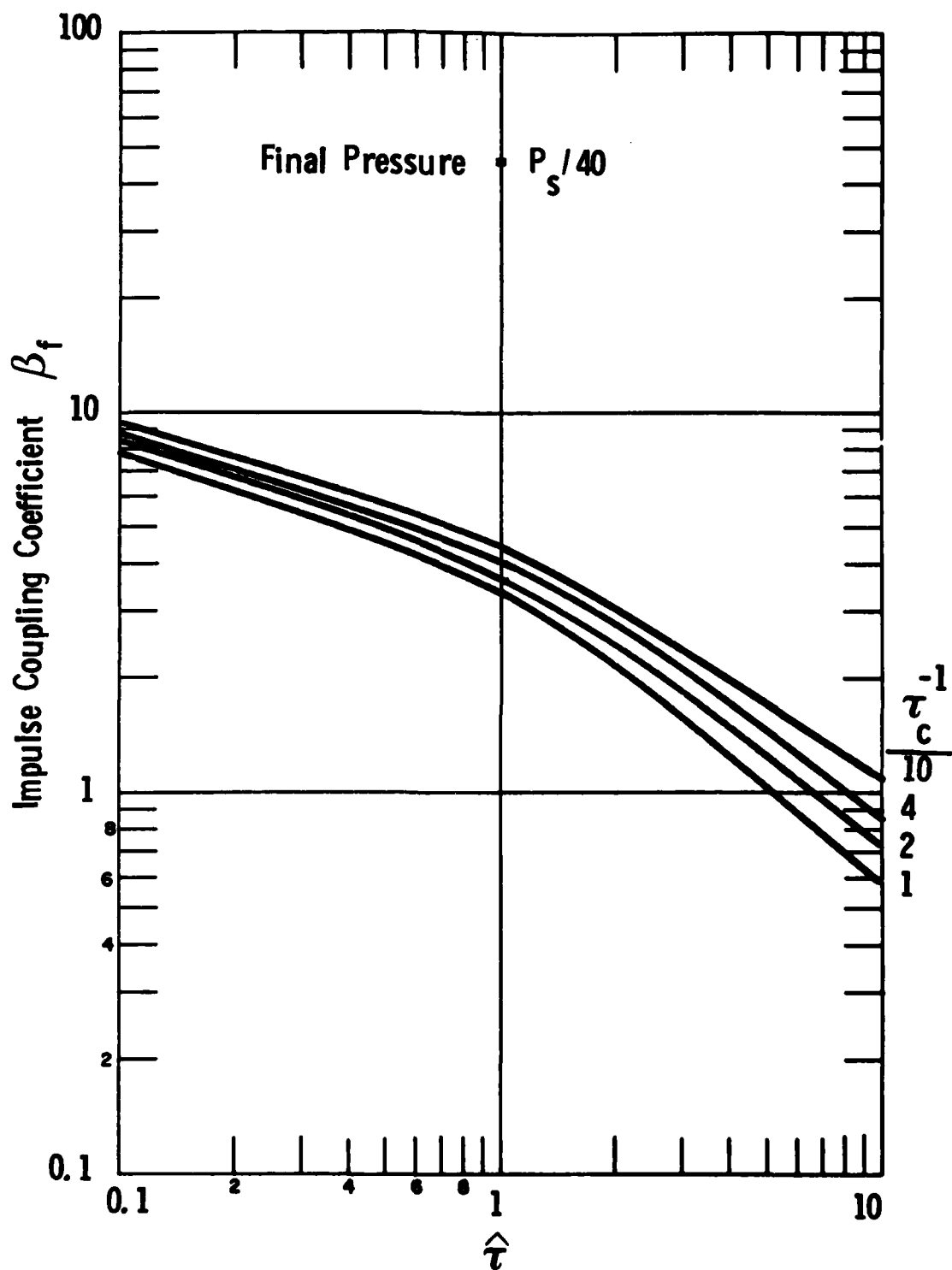
Fig. 4.13 Impulse Coupling Coefficient as a Function of $\hat{\tau}$ for a Final Surface Pressure of $1/40^{th}$ Initial Pressure.
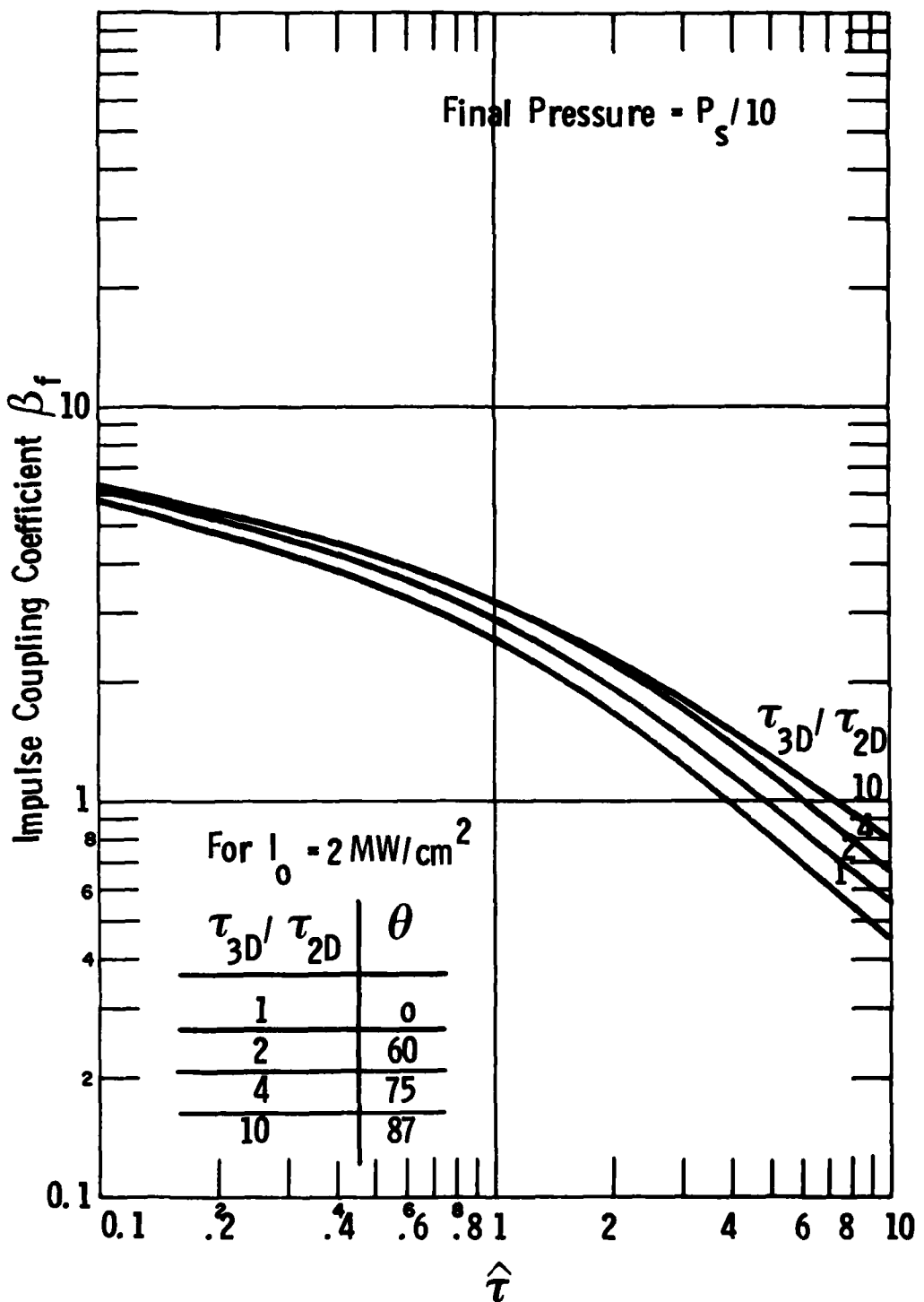
Fig. 4.14 Impulse Coupling Coefficient as a Function of $\hat{\tau}$ for a Final Surface Pressure of One-Tenth the Initial Pressure.

122

The impulse absorbed by a surface is shown in Fig. 4.15 as a function of $\hat{\tau}$, for an incident laser intensity of 4 MW/cm^2, and a beam cross-sectional area of 40 cm^2. Curves are given for $\theta = 0^{\circ}$, 60°, 75°, and 84°. For a given value of $\hat{\tau}$, the absorbed impulse decreases with increasing θ but is still considerable even at 84°, for $\hat{\tau} = 1$.

4.5 Summary and Conclusions

It has been shown that the one-dimensional model of the LSC plasma development for early times at normal incidence is adaptable to describe the early-time development at non-normal incidence by the transformation of replacing I_o by $I_o \cos \theta$, and κ_L (the absorption coefficient for the laser wavelength) by $\kappa_L / \cos \theta$. The resulting model describes the plasma development and the absorption of radiation flux and impulse by the target surface up to the smaller of the times τ_{2D} or τ_p after plasma formation. Even when τ_{2D} exceeds τ_p, the plasma relaxation is planar although unpowered and the plasma development is quasi-one-dimensional. During the planar phase of development radiation reaching the surface is calculated as though it came from an infinite slab of plasma. The validity of this step is attested to by the graphical demonstration that the center of the laser spot is still covered by a significant amount of plasma at $t = \tau_{2D}$, even in the large angle case in which the plasma periphery moves toward the center of the spot.

It has been demonstrated that the description of the arrival of acoustic disturbances at the central point may be simplified to one which utilizes an arrival time for the minor axis of the elliptical spot and one for the major axis. The arrival time for the minor axis is τ_{2D}, which is the arrival time at normal incidence. The arrival time τ_{3D} for the major axis is greater than τ_{2D} and is assignable for all incidence angles. With
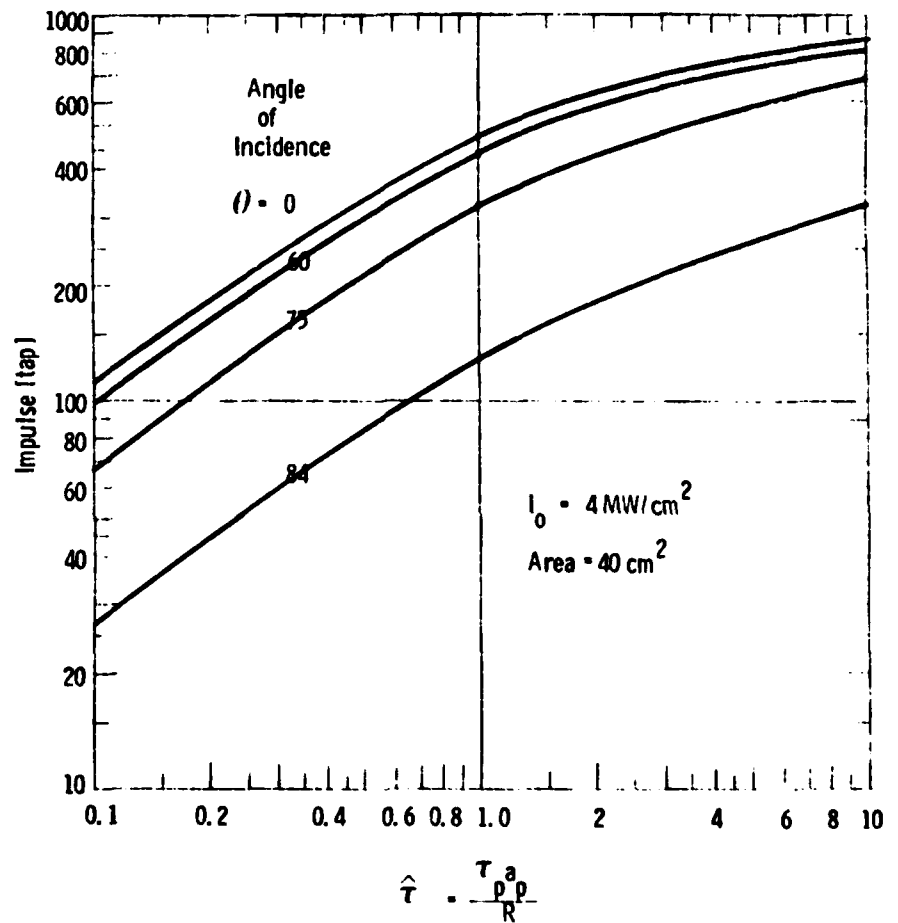
Fig. 4.15 Theoretical Prediction of Impulse Delivered to Target for Several Angles of Incidence.

τ_{3D} modeled by two times, a late time model of plasma development, which takes over from the one-dimensional model at $t = \tau_{2D}$, may be constructed using cylindrical and spherical plasma relaxation laws. Regimes of operation based on the time scales defined by the parameters τ_p, τ_{2D}, and τ_{3D} may be identified and the absorbed fluence, absorbed impulse, and their coupling coefficients readily calculated. Reasonable predicted behavior of these quantities is obtained. The coefficient of impulse coupling turns out to be given by a set of universal expressions which are independent of the initial surface pressure. Code results for the surface pressure show its variation with the two-thirds power of $I_o \cos\theta$, consistent with the behavior predicted from the early--time model.

In Section 5, recent experimental data is compared to the predictions for surface pressure and absorbed fluence. The data and theory are in good agreement, further confirming the applicability of the model described in this section.

SECTION 5

DATA / THEORY COMPARISON

The JANAF RP Laser Effects program has sponsored experiments
at Avco Everett Research Laboratory (AERL) which test the predictions
of the models advanced in the three preceding sections. In this section,
the experimental data are compared with the theoretical predictions and
the validity of the models are evaluated.

5.1 Coupling to Alloys at Normal Incidence

Theoretical predictions of thermal coupling to Al2024, SS304, steel
4130 and Ti6Al4V were made for comparison with experimental data[20]
taken with an E-beam sustained CO_2 laser at AERL. The comparison
has been complicated by three experimental difficulties -- the pulse
energy is not well known, although it is believed to lie between 1 to 1.5
kJ/pulse; the low intensity, large spot shots have sporadic plasma ig-
nition on some targets; and the laser spot was difficult to align, es-
pecially for the smaller spot size, so that the measured coupling may not
be a central coupling. Furthermore, different surface preparations were
used for the targets; for example, the steel 4130 target was sandblasted
prior to irradiation. The state of the surface is expected to affect the re-
sponse. For comparison of the data to the theory, we have shown in Figs.
5.1 to 5.4 the theoretical prediction for two different pulse energies; namely,
1.5 kJ/pulse and 1 kJ/pulse. It is expected that the true laser pulse energy
was approximately 1.2 kJ/pulse. These predictions are made for a pulse
time of 10 μsec and are plotted as a function of the laser target area. The
central coupling data measured in the experiments are indicated by the
circles and squares in the figures. The squares correspond to data having a
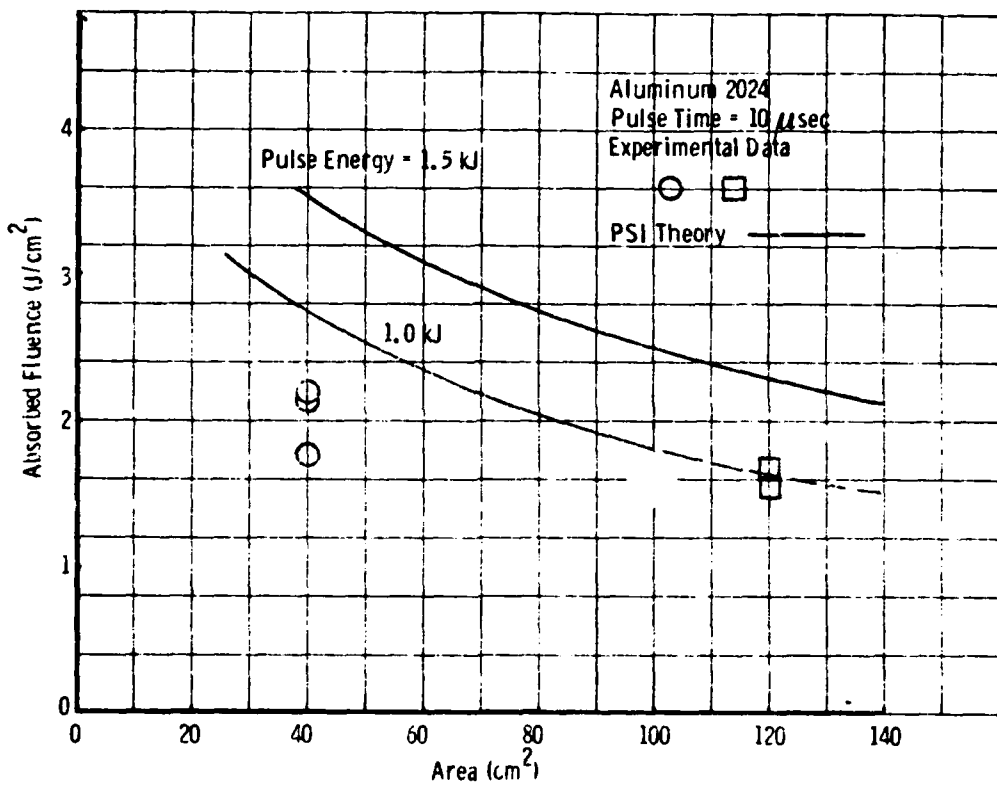
Fig. 5.1 Comparison of Experimental Data and Theoretical
Predictions of Fluence Absorbed by Al2024.
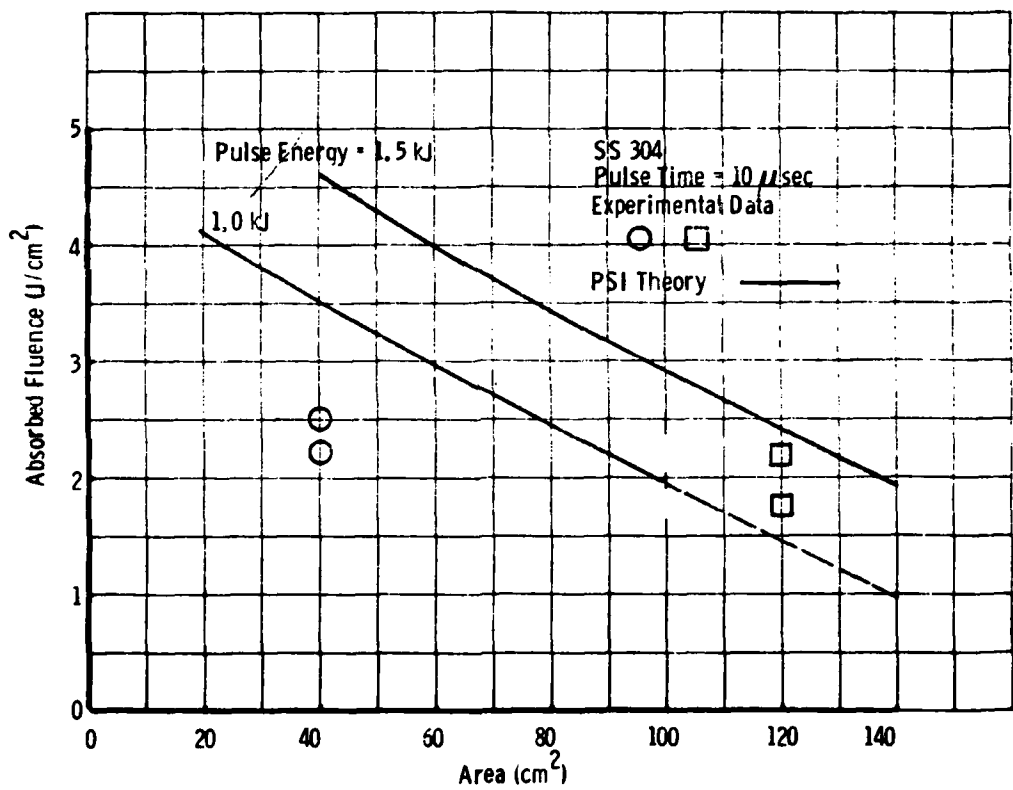
Fig. 5.2 Comparison of Experimental Data and Theoretical
Predictions of Fluence Absorbed by SS 304.

129
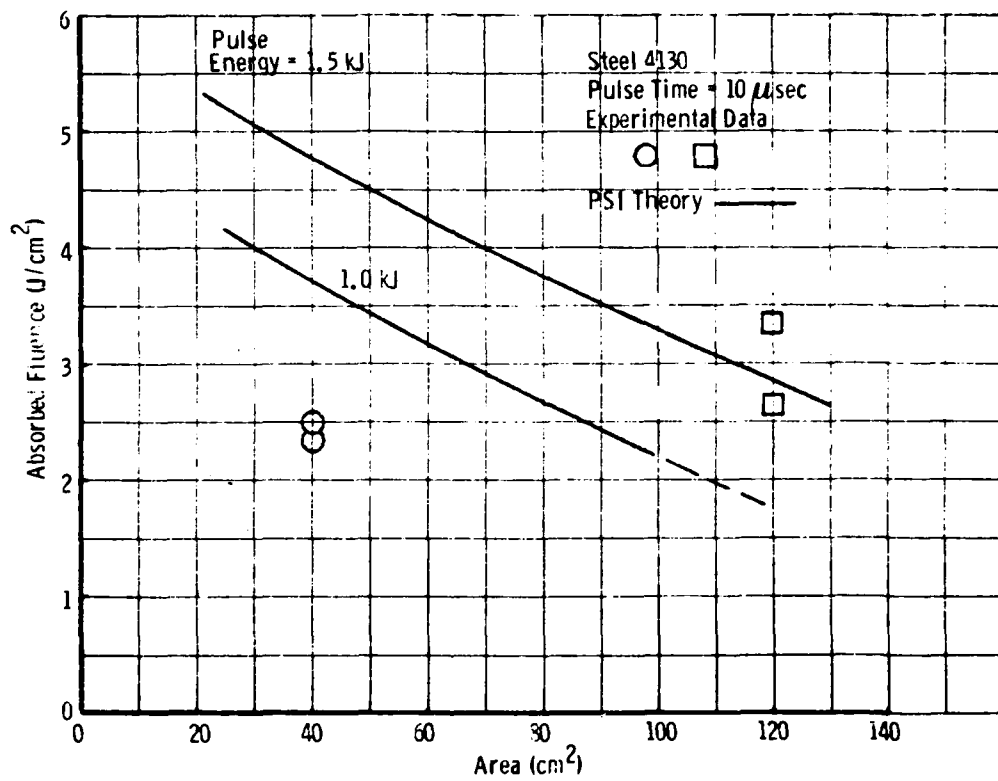
Fig. 5.3 Comparison of Experimental Data and Theoretical
Predictions of Fluence Absorbed by Steel 4130.
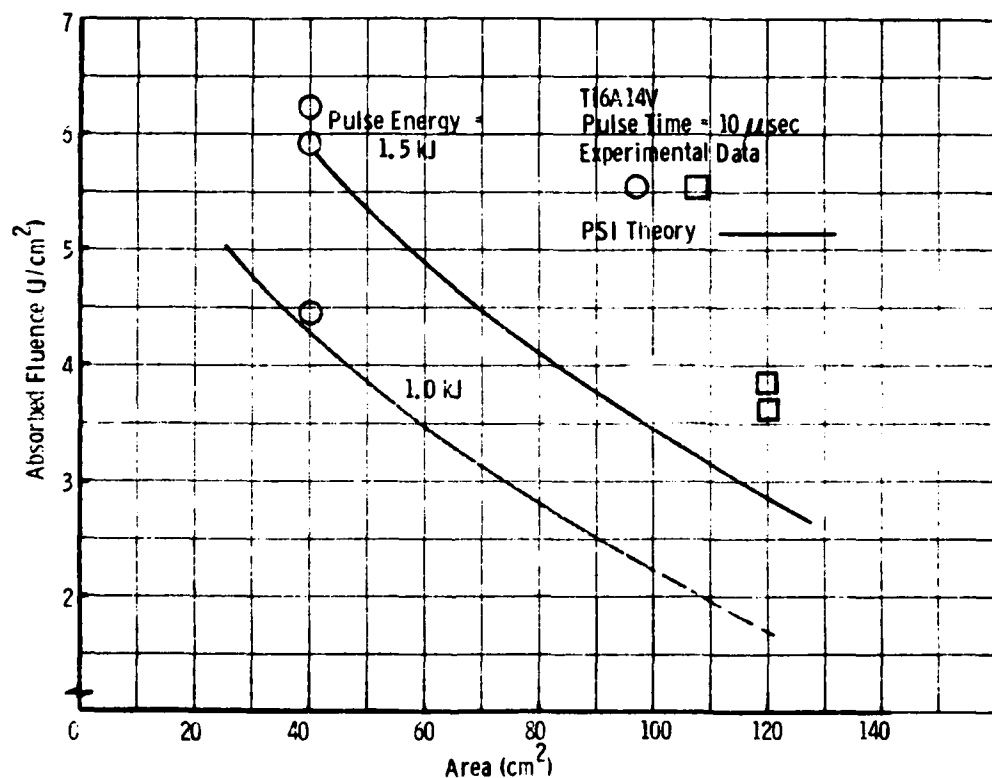
Fig. 5.4 Comparison of Experimental Data and Theoretical
Predictions of Fluence Absorbed by Ti6Al4V.

nominal intensity of 1. 0 MW/cm^2; these shots had sporadic ignition on some of the experiments. The circles correspond to data having a nominal intensity of 3 MW/cm^2. For the high intensity shots the thermocouple which was supposed to lie under the center of the spot had lower readings than the thermocouple at the edge of the spot. The higher reading has been plotted. A further comparison of the experimental data to the theory is contained in Table 5.1, which compares the experimental data with the theoretical prediction at 1.2 kJ/pulse.

The uncertainties in the data make any conclusions about the relationship between theory and data tenuous. Nevertheless, for the larger spot sizes, the theory and data are in reasonable agreement except for Ti6A14V, where the data is 50% higher than the theory. Moreover, the theoretically predicted material hierarchy is obeyed by the data. For the smaller spot size targets, theory predicts significantly higher absorbed fluences than those observed experimentally, except for Ti6A14V. Moreover, experimentally there is found to be no significant increase in the fluence absorbed by the small spots as compared to the large spot size for SS304 and 4130 steel. Indeed, the measured value of fluence absorbed by 4130 steel are lower for the small spot shots than for the large spot shots, contrary to both theoretical predictions and the experimental observation on the other alloy targets. This is believed to be a result of the sandblasting of the target.

The order of magnitude of the predictions agrees with the data and the predicted hierarchy appears to be observed. Given the uncertainties in the data, it is impossible to draw stronger conclusions and the data neither confirms nor refutes the enhanced coupling model. Clearly, more experimental data with fewer uncertainties are required to test the validity of the theory.

TABLE 5.1

Comparison of experimental data and theoretical predictions for fluence absorbed by various alloys.

Target Metal	Absorbed Fluence J/cm²					
	120 cm² spot			40 cm² spot		
	Experiment	Exp Mean	Theory @ 1.2 kJ	Experiment	Exp Mean	Theory @ 1.2 kJ
Al2024	1.5 1.7	1.6 ± 0.1	1.9	1.7 2.1 2.2	2.0 ± 0.2	3.0
SS304	1.8 2.2	2.0 ± 0.2	2.1	2.2 2.5	2.35 ± 0.15	3.85
Steel 4130	2.6 3.3	2.95 ± 0.35	2.3	2.3 2.5	2.4 ± 0.1	4.1
Ti6Al4V	3.6 3.8	3.7 ± 0.1	2.4	4.4 5.9 6.2	5.5 ± 0.75	4.9

Some limited repetitively pulsed data[21] are available and are summarized in Table 5.2. Although the pulse time and intensity are not known precisely, it is believed that the values are close to 10 µsec and 1 MW/cm^2, respectively. There is a significant decrease in coupling between the single shot experiments and repetitively pulsed runs. Data at higher flow rates confirms theoretical calculations that the convective cooling of the target did not account for the difference in the absorbed fluence between single shot and repetitive shot cases. The most plausible explanation is that plasmas were not fully formed over the surface. The tests were run near the plasma threshold intensity, so that plasma ignition is expected to be spotty. In fact, the flight research films confirm the absence of plasma. From Touloukian and Ho,[22] the intrinsic absorptivity of polished targets of SS304 and Ti6A14V (such as these were) is found to be, respectively, 0.10 ± 0.01 and 0.135 ± 0.015. It can be easily seen that the absorbed fluences are consistent with intrinsic absorption of a 10 J/cm^2 laser pulse. Therefore, the interpretation of this repetitively pulsed data as being characteristic of the intrinsic absorptivity is consistent with the available data. Note that the significant enhancement of the single pulse absorbed fluence over the repetitively pulsed value can, therefore, be interpreted as confirmation of the existence of enhanced thermal coupling for metals other than Al2024.

5.2 Coupling to Al2024 at Oblique Incidence

Theoretical predictions of thermal coupling and surface pressure have been made for comparison with experimental data[21] taken with an E-beam sustained CO_2 laser at AERL. It was found that plasmas were ignited at angles of incidence as large as 85° whenever the beam intensity was sufficient to ignite plasmas at normal incidence. The ignition of plasmas is not modeled in Section 4; however, the model for

TABLE 5.2

Absorbed fluence data for repetitive pulse experiments.

Intensity - Near Threshold: $I \sim 1 \text{ MW/cm}^2$

$\tau_\rho \sim 10 \text{ μsec}$

Area - 120 cm^2; First 10 Pulses Only

Target	Single Shot	REP Pulse M = 0.1
SS304	1.8 J/cm^2	1.1 J/cm^2
(15 mil 0.038 cm)	2.2 J/cm^2	1.3 J/cm^2
Ti 6A14V	3.6 J/cm^2	1.3 J/cm^2
(20 mil 0.051 cm)	3.8 J/cm^2	1.4 J/cm^2

thermal coupling developed therein assumes a plasma is ignited. It is an important experimental feature of the interaction that plasmas can be easily ignited at large angles, since this greatly extends the regimes in which enhanced coupling is important.

In Fig. 5. 5 the theoretical calculation of fluence absorbed by Al2024 is shown as a function of the angle of incidence. The laser beam conditions are $I = 1.5$ MW/cm^2; $\tau_p = 10 \mu s$ and area $= 40$ cm^2. Also plotted on the same graph are the measured values of deposited fluence versus angle for a variety of laser intensities near 1.5 MW/cm^2. The agreement between data and theory is remarkably good; the only significant deviation occurs for three data points, marked by a flag, which correspond to an intensity very close to the plasma ignition threshold. Indeed, photographic evidence revealed that there was poor plasma formation on these shots, and, therefore, they are not expected to represent a suitable test of the theory which presupposes good ignition.

A similar comparison of data and theory for $I \approx 3.2$ MW/cm^2 is displayed in Fig. 5. 6. Once again, the data and theory are in good agreement, expecially at large angles of incidence. At normal incidence, the experimental data lies 15% to 30% below the theoretical prediction. This discrepancy is common to all comparisons made at intensities above 3 MW/cm^2; it is believed to be a consequence of the onset of LSD/LSC transition. The error at normal incidence reflects an inadequacy of the LSC wave model at high intensity; it is not a test of the extension of the theory to oblique angles of incidence. The improved agreement at large angles is expected since large angles of incidence correspond to lower projected intensity, and experiments at normal incidence indicate that the theory is more accurate at lower intensities.

The scaling of absorbed fluence with angle for constant intensity, pulse time and spot size is well represented by the theoretical predictions
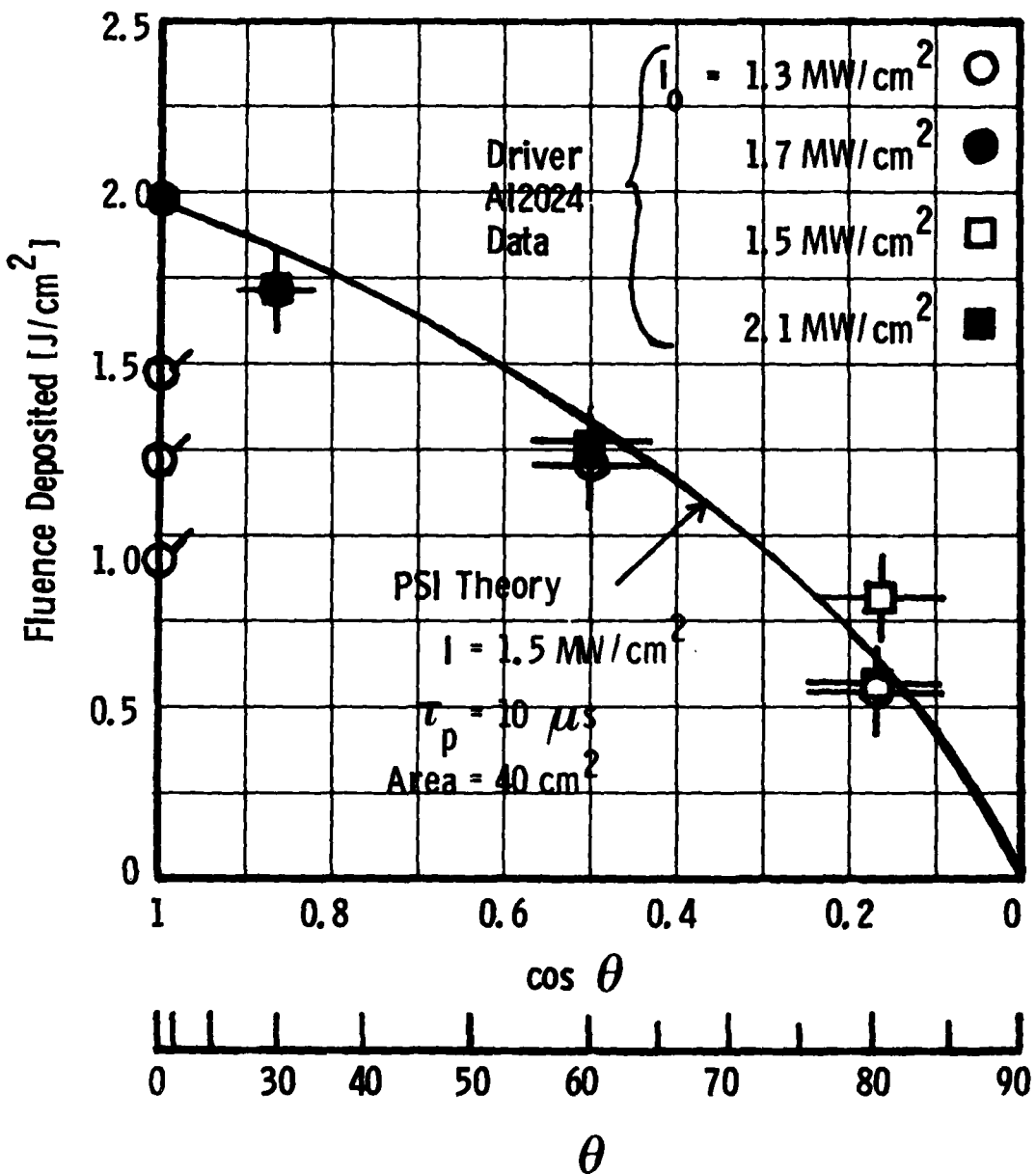
Fig. 5.5 Comparison of Experimental Data and Theoretical
Predictions for Fluence Absorbed by Al2024 as a
Function of the Angle of Incidence.
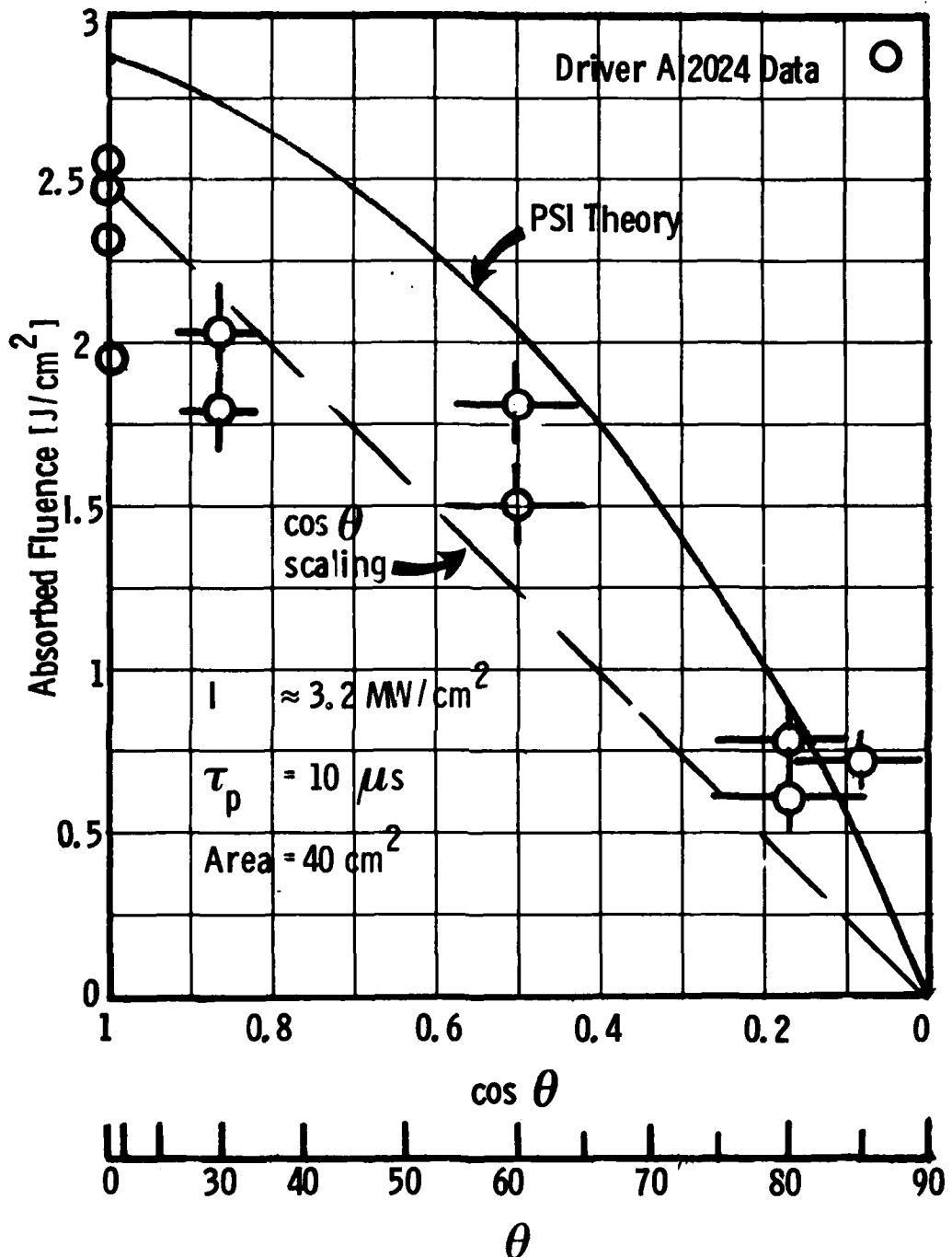
Fig. 5.6 Comparison of Experimental Data and Theoretical
Predictions for Fluence Absorbed by Al2024 as a
Function of the Angle of Incidence.

of the modified LSC wave model. Although the details of the scaling are not significant for small angles, the behavior at large angles is important. Naively, one might scale the normal incidence results by $\cos\theta$ in order to predict coupling at angle of incidence, as sketched in Fig. 5.6. This scaling works well at small angles (of course, the value at normal incidence is chosen to agree with the measured value) but at large angles such as 80° ($\cos\theta = .17$) and 84° ($\cos\theta = .10$) the naive scaling predicts only half of the absorbed fluence which is predicted by the LSC wave theory and which is observed in experiments. The departure from $\cos\theta$ scaling can easily be understood from the discussion in Section 4. The dominant effect of angle of incidence is to change the effective projected intensity in the one-dimensional LSC wave calculation from I_o to $I_o \cos\theta$. (The change in absorption coefficient from κ_L to $\kappa_L/\cos\theta$ makes only a minor change in the propagation velocity of the wave.) Thus, the thermal coupling coefficient, $\alpha(I_o, \theta)$, for oblique angles can be estimated from the coupling coefficient at normal incidence, $\alpha(I, 0)$, by

$$\alpha(I_o, \theta) \approx \alpha(I_o \cos\theta, 0). \qquad (5.1)$$

The naive $\cos\theta$ scaling argument for absorbed fluence would follow if α were independent of laser intensity, but experimental data and our theoretical predictions (see Section 2) demonstrate that α varies approximately inversely as the square root of intensity. Therefore, we conclude that the absorbed fluence F obeys

$$F \approx I_o \cos\theta \; \alpha(I_o \cos\theta, 0) \neq I_o \cos\theta \; \alpha(I_o, 0), \qquad (5.2)$$

and the naive $\cos \theta$ scaling should fail at large angle of incidence. Further-more, if we approximate the thermal coupling coefficient by

$$\alpha (I, 0) = \alpha_0 I^{-\frac{1}{2}} \tag{5.3}$$

where α_0 is a constant, it follows that

$$\alpha (I_0, \theta) \approx \alpha (I \cos \theta, 0) = \alpha (I_0, 0) / \sqrt{\cos \theta}. \tag{5.4}$$

Thus, the thermal coupling coefficient increases as the angle of incidence θ is increased for fixed beam intensity I_0. As a result, there can be significant coupling even at large angle of incidence.

Figure 5.7 shows a comparison of the theoretical predictions of surface pressure with the experimental data. Once again the agreement at oblique angles is remarkable. At normal incidence the data falls below the theoretical predictions. The discrepancy for $I = 3.2$ MW/cm^2 is interpreted as an indication of the onset of LSC/LSD wave transition. The discrepancy for $I = 1.5$ MW/cm^2 is caused by poor plasma ignition.

In Fig. 5.8 all the surface pressure data is plotted against $I_0 \cos \theta$. The data scatters about the theoretical prediction (taken from Fig. 4.9) with the only discrepancy being the flagged data (poor ignition) and the high intensity data (LSC/LSD wave transition). Based on comparisons such as Figs. 5.7 and 5.8, it is concluded the surface pressure is cor-rectly predicted by the modified LSC wave model.

Finally, it should be pointed out that the mechanical coupling, shown in Fig. 4.15, does not diminish appreciably until large angles of incidence, greater than 75°, are reached. For example, for $\hat{T} = 1$, the predictions
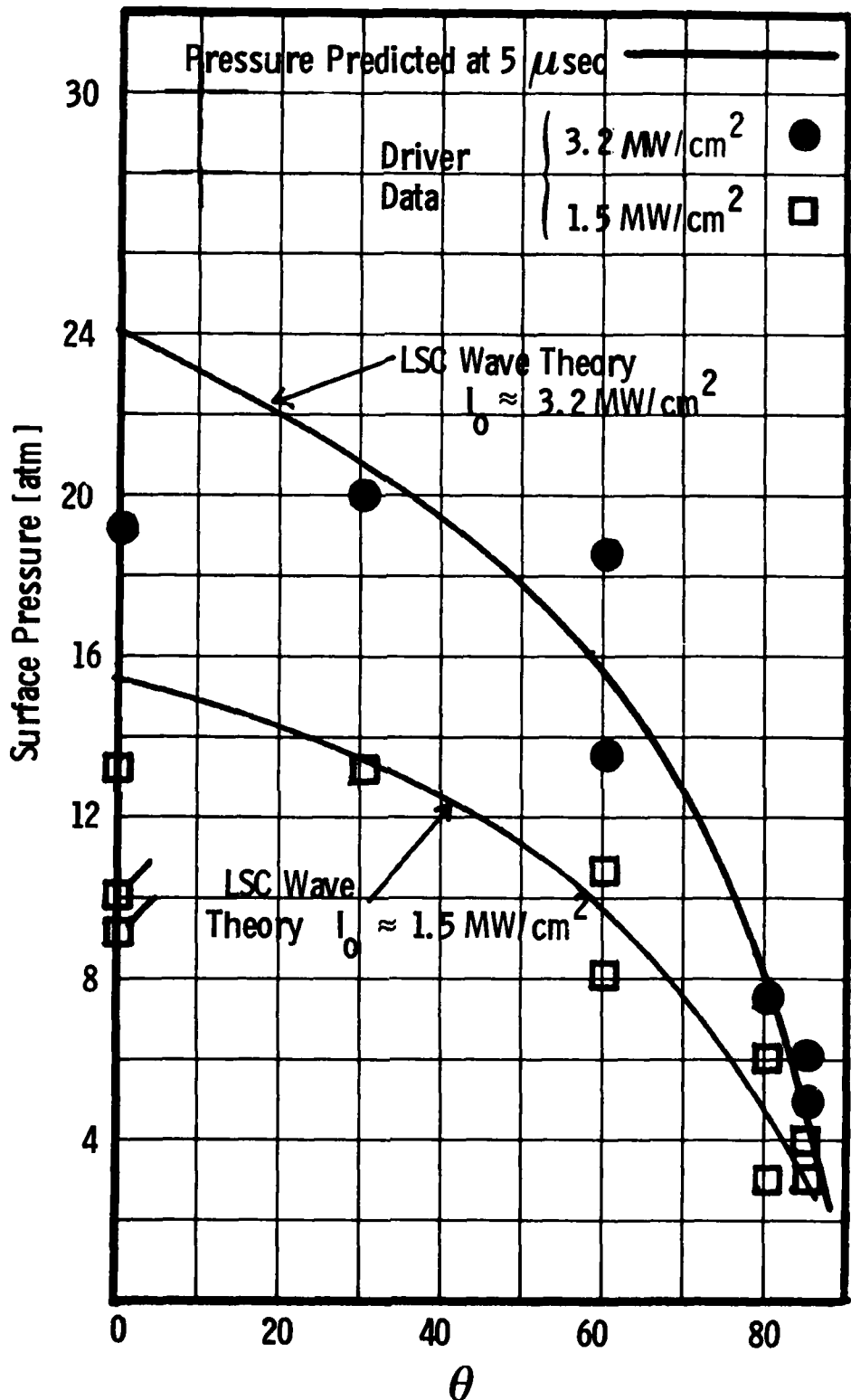
Fig. 5.7 Comparison of Experimental Data and Theoretical
Predictions for Surface Pressure as a Function of
the Angle of Incidence. The Comparison is Made
for Two Different Laser Intensities.

141

SURFACE PRESSURE DATA/THEORY COMPARISON
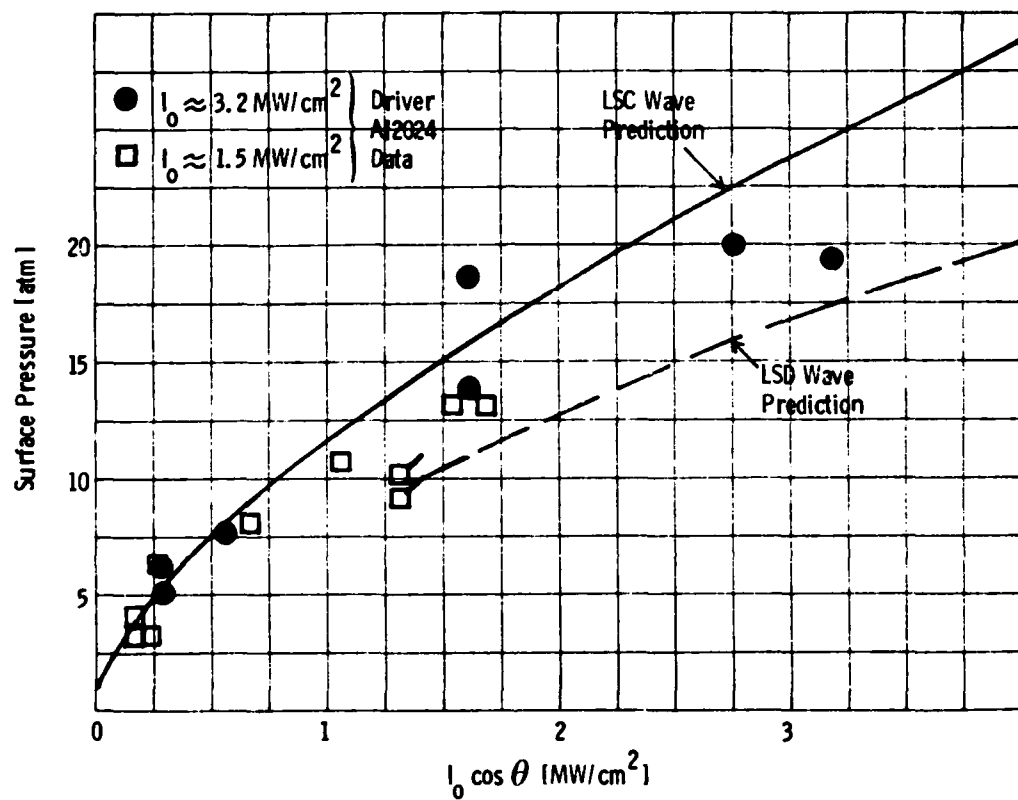
Fig. 5.8 Comparison of Experimental Data on Surface Pressure with
Theoretical Prediction as a Function of the Projected
Intensity.

for impulse generated at 75° is 60% of the value at normal incidence even though the projected intensity is only 25% of the beam intensity. There can be significant mechanical coupling at large angles.

5.3 Summary

Comparison of data and theory for coupling to various alloys reveals that there is no large discrepancy between the two. Furthermore, there appears to be evidence of the predicted hierarchy of metals based on absorbed fluence. However, there are too many uncertainties in the data to enable the theory to be adequately validated or refuted.

The data and theory of thermal coupling and surface pressure for oblique angles of incidence are in excellent accord. The extension of the LSC wave model to oblique angles therefore has a strong empirical backing. It is found that the coupling of both energy and impulse at large angles of incidence can be significantly larger than expected if naive $\cos \theta$ scaling were used.

SECTION 6

APPLICATION OF THEORY TO PULSED LASER INTERACTION
AT 3.8 μm

In the preceding chapters an extensive predictive capability has
been constructed for calculating the coupling of pulsed 10. 6 μm lasers
to metal targets in the presence of an LSC wave plasma. The interaction
of 3. 8 μm pulsed lasers with metal target is also expected to have a
regime where an LSC wave plasma dominates the coupling; however,
various details of the interaction -- such as the plasma ignition require-
ments, the LSC/LSD transition intensity, the possibility of target vapor
formation, and the temporal laser pulse shape -- are expected to the dif-
ferent from the interaction of pulsed 10. 6 μm lasers. However, to
make a first order estimate of the region of laser parameters for which
enhanced coupling via LSC wave formation is expected for pulsed 3. 8 μm
radiation, and to make first order quantitative predictions of the coupling
coefficients, it is appropriate to use the model developed for 10. 6 μm
(see Section 2), modified only to include the correct laser absorption
parameter for 3. 8 μm radiation.

For these calculations, it is assumed that a plasma is ignited
promptly. Furthermore, the temporal history of the laser pulse is
represented by a rectangular pulse which has a length of 6 μs and a
constant intensity. The only change made in the LSC wave computer
code is the replacement of the absorption coefficient k_L (10. 6 μm),
for 10. 6 μm radiation by inverse Bremsstrahlung by the coefficient
k_L (3. 8 μm), for inverse Bremsstrahlung absorption at 3. 8 μm. The
relationship is

$$k_L(3.8 \text{ μm}) = k_L(10.6 \text{ μm}) \frac{(1 - \exp(-14388.3/(3.8T))}{(1 - \exp(-14388.3/(10.6T))} \left(\frac{3.8}{10.6}\right)^3, \quad (6.1)$$

where T is the temperature in K.

The coupling coefficient of 3.8 μm radiation to an aluminum target has been calculated for two intensities, 5 WM/cm^2 and 10 MW/cm^2; the results are shown in Figs. 6.1 and 6.2, respectively. The predicted coupling coefficient for 10.6 μm radiation is also shown in Fig. 6.1 for an aluminum target and I = 5 MW/cm^2. This 10.6 μm prediction represents the gross over-estimate of the actual coupling since this intensity lies close to the LSC/LSD wave transition for 10.6 μm radiation and the semianalytical model is known to break down in the transition region. Nevertheless, we observe that the predicted coupling for 3.8 μm radiation lies well above even the over-estimated value for the 10.6 μm coupling. In Fig. 6.2, the predicted coupling for 10 MW/cm^2 is shown. Since the 10.6 μm calculation is not applicable at these intensities, no comparison is made. Note that the coupling of 3.8 μm radiation at 10 MW/cm^2 is close to the coupling predicted at 5 MW/cm^2 -- the predicted coupling in the LSC wave regime does not decrease rapidly with increasing intensity.

Just as it is possible to define the enhanced coupling region for 10.6 μm radiation in a plot of laser intensity vs $\hat{\tau}$, it is also possible to identify the enhanced coupling region on a similar plot for 3.8 μm radiation. To make the plot, tentative values for the plasma ignition thresholds and the LSC/LSD transition intensity are required. The empirical correlation by Musal[23] suggests that the ignition threshold is in the neighborhood of 8 MW/cm^2.

The 3.8 μm laser pulse is roughly triangular in shape, as sketched in Fig. 6.3. A pulse which has a maximum intensity of 8 MW/cm^2 and a full width at half maximum of approximately 3 μs is approximated as a rectangular pulse having a full width of 6 μs and a constant intensity of 4 MW/cm^2, as shown in Fig. 6.3.
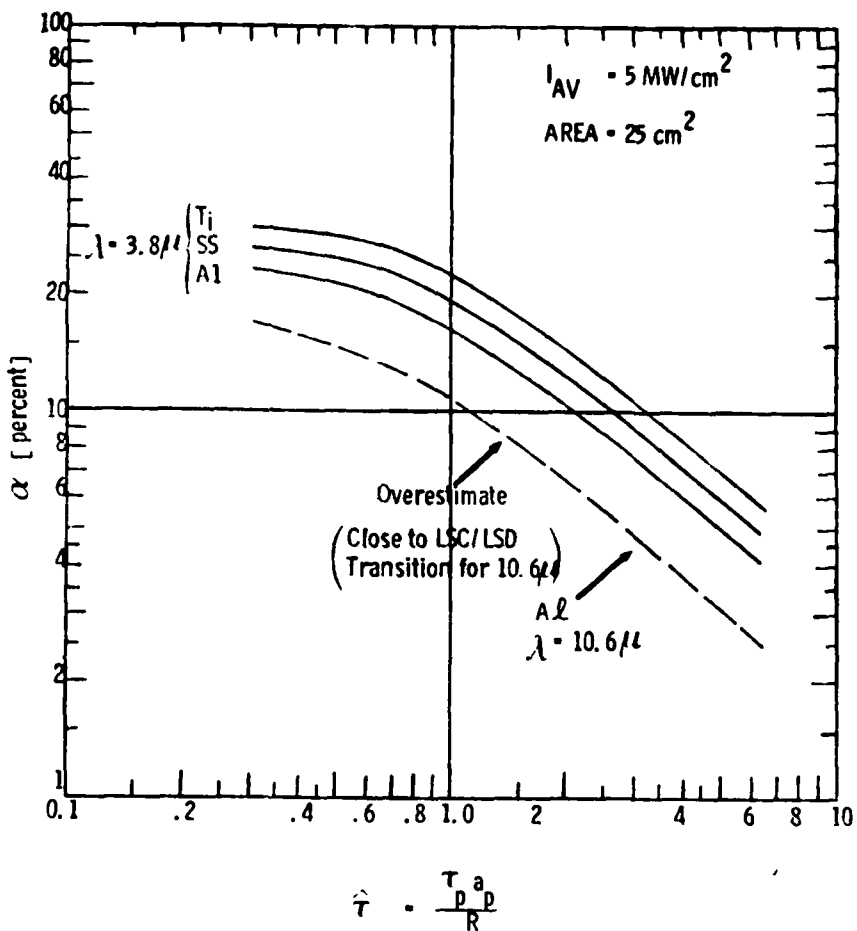
Fig. 6.1 Theoretical Predictions of Central Coupling Coefficient for 3.8 μm Laser Radiation Interacting with Various Alloys. Theoretical Prediction for 10.6 μm is shown for Comparison.
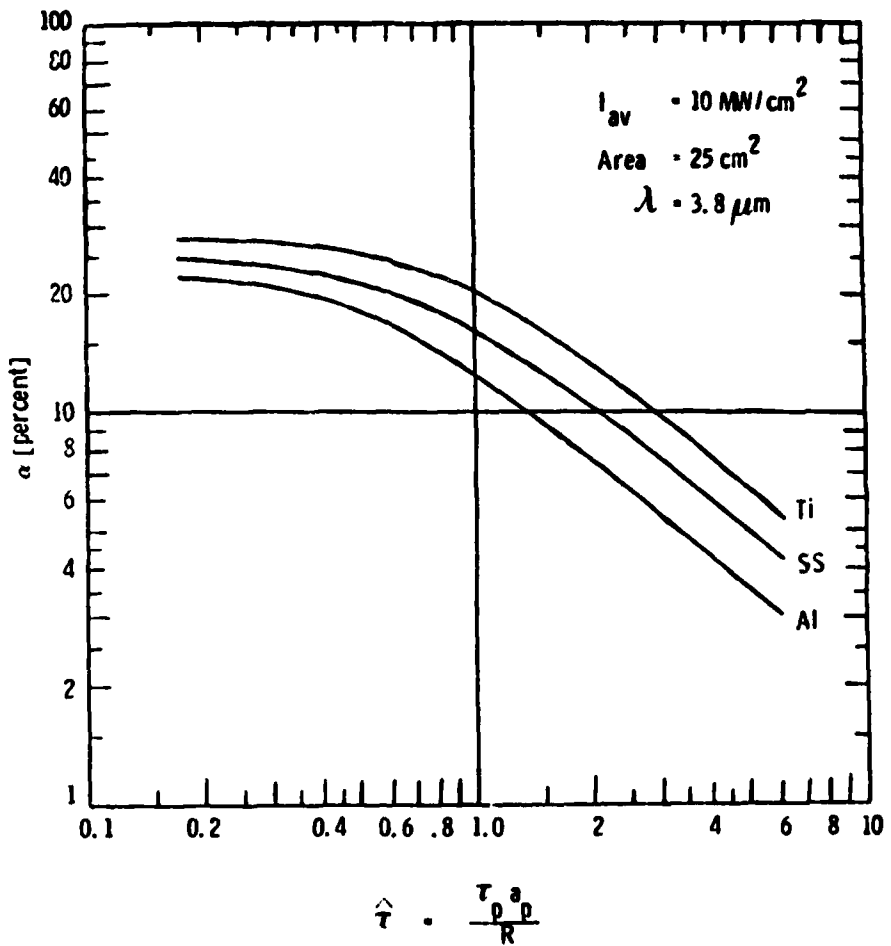
Fig. 6.2 Theoretical Predictions of Central Coupling
          Coefficient for 3.8 μm Laser Radiation
          Interacting with Various Alloys.
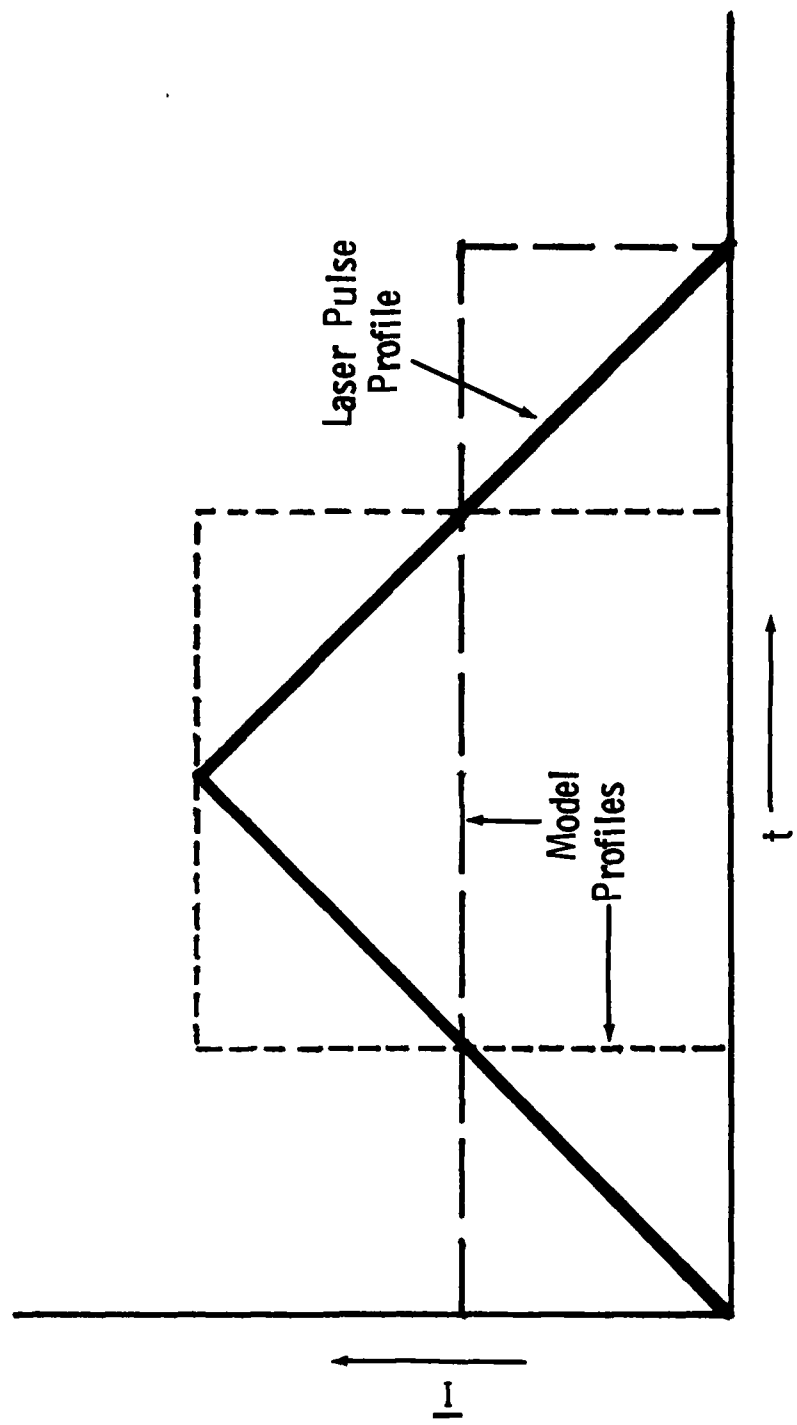
Fig. 6.3 Sketch Showing Triangular Laser Pulse Shape and the Two Different Rectangular Model Pulse Shapes Used to Represent it.

149

Theoretical estimates[24, 25] of the LSC/LSD transition intensity predict a value of approximately 14 MW/cm^2. However, it should be recalled that the predictions for the LSC/LSD transition intensity for 10.6 μm radiation are woefully inadequate. For defining the enhanced coupling regime, it is assumed that the LSC/LSD wave transition is sensitive to the average rectangular intensity rather than the peak triangular intensity. These two intensities, as well as the requirement that $\hat{T}$ be less than 1, define the enhanced coupling region. The enhanced coupling region for 3.8 μm radiation is plotted in Fig. 6.4. Lines corresponding to laser pulses having fixed pulse energy and fixed pulse time are also shown in Fig. 6.4. It is seen that a 150J laser which has a 6 μs pulse length cannot operate in the regime of maximum enhanced coupling. Rather, we require laser pulse energies from 1 to 2 kJ in order to operate in the enhanced coupling region. Also shown in Fig. 6.4 are the predicted absorbed fluences for a 1 and 2 kJ laser at intensities of 5 and 10 MW/cm^2. It should be remembered that these predictions assume prompt ignition of a plasma whereas it is quite possible, especially for the low intensity cases, that plasma ignition occurs only at the peak intensity of the triangular pulse, and, therefore, approximately half of the energy strikes the target without forming a plasma. Improved calculations must include the effect of delayed ignition.

One way of comparing the effectiveness of 10.6 μm laser interactions to 3.8 μm laser interactions is to compare the absorbed fluence at similar pulse energies. A comparison is shown in Fig. 6.5. For 10.6 μm radiation it is important that the laser intensity lie below the LSC/LSD wave transition intensity, and that the pulse be designed to operate in an efficient manner. For these reasons an intensity of 3.2 MW/cm^2 and $\hat{T}$ = 1 are used in the predictions shown in Fig. 6.5. Two predictions are shown for 3.8 μm radiation. It is assumed that the maximum
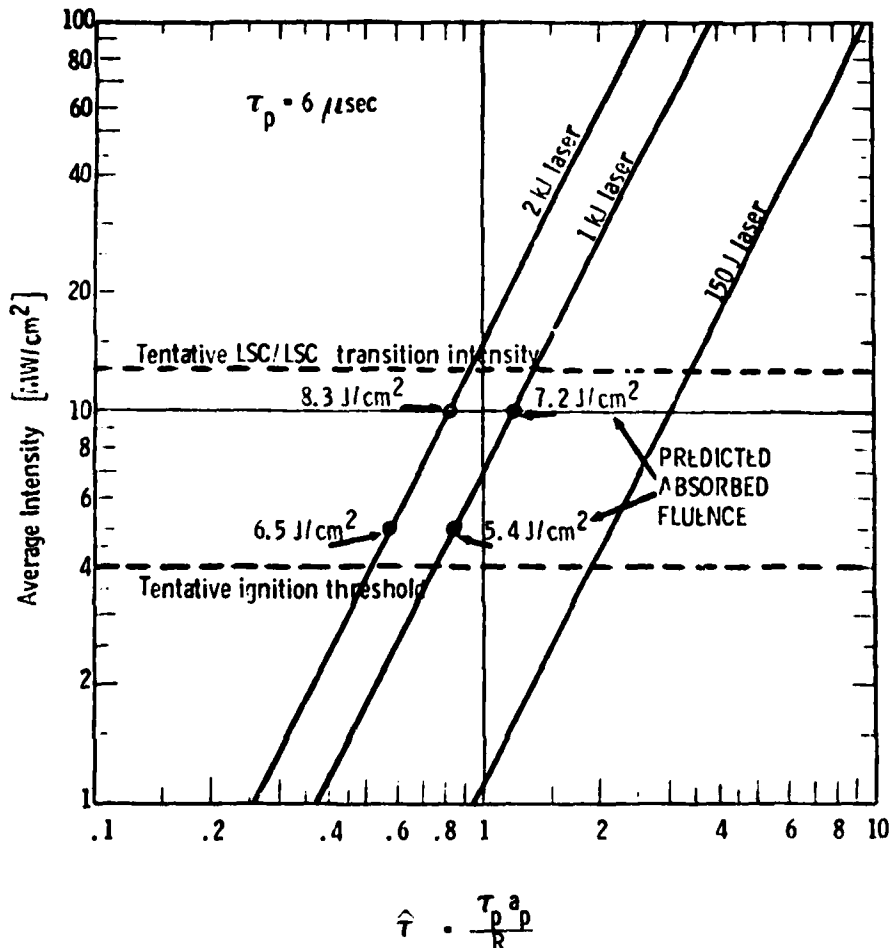
Fig. 6.4 Map Showing Region of Laser Parameters Where Enhanced
Coupling is Expected for 3.8 μm Laser Radiation. Region
Accessible with Various Fixed Energy Laser Having
τ_p = 10 μs are shown. Predicted Values of Fluence
Absorbed by Al2024 are shown for Selected Points.
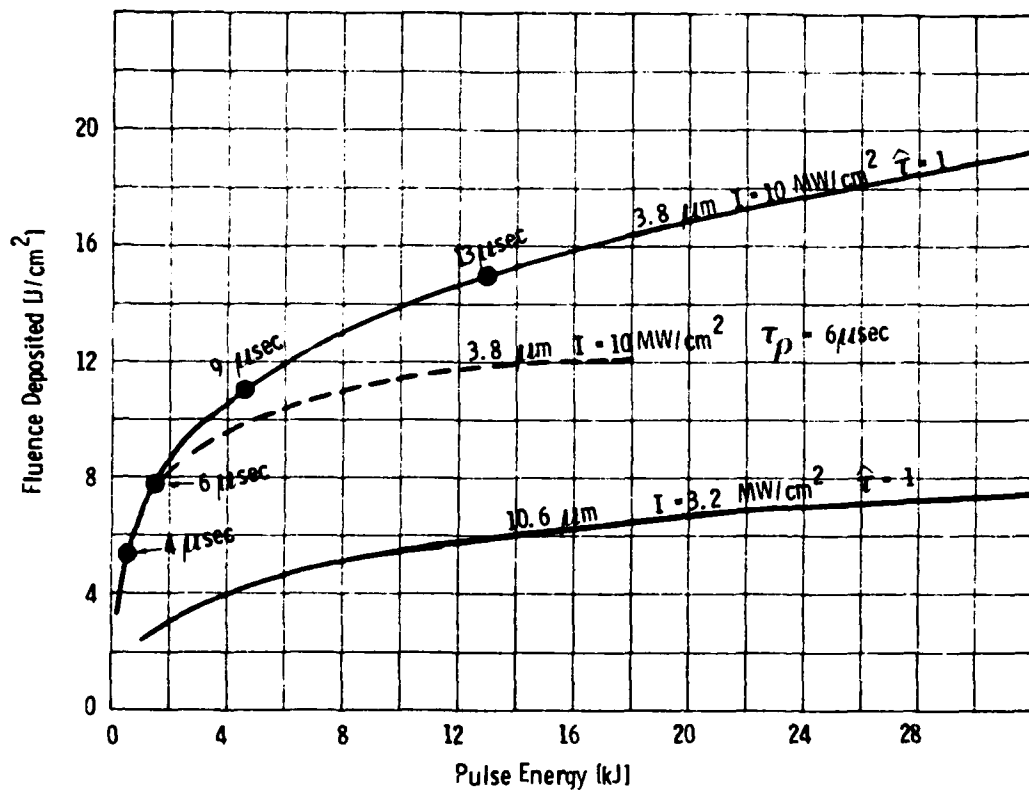
Fig. 6.5 Comparison of Theoretical Predictions of Fluence
Absorbed by Al2024 for 10.6 μm and 3.8 μm Radiation.
Two Predictions are made for 3.8 μm Radiation:
Fixed $\hat{\tau}$ and Fixed Pulse Time.

intensity which can be used is 10 MW/cm^2; higher intensities may have degradation of coupling because of the onset of LSC/LSD wave transition. If the laser pulse length can be extended such that $\hat{\tau} \approx 1$ is maintained, then the deposited fluence is represented by the solid curve in Fig. 6.5. The pulse time required to satisfy $\hat{\tau} = 1$ is shown for various points along this curve. For given laser pulse energy, it is possible to deposit approximately 2.5 to 3 times as much fluence with 3.8 μm radiation as with 10.6 μm radiation. However, this comparison is not strictly valid since it is difficult to make efficient DF lasers with pulse lengths longer than a few microseconds. This limitation is represented by the dashed curve in Fig. 6.5 which has been drawn for a pulse length constrained to be less than 6 μs. The absorbed fluence saturates at approximately 12 J/cm^2, which is only 1.5 to 2 times the fluence which could be deposited by a 10.6 μm laser having 15-30 kJ/pulse. The actual saturation value of the 3.8 μm laser depends crucially upon the maximum intensity which can be used without reaching the LSC/LSD wave transition intensity. For 10.6 μm, it is known that 3.2 MW/cm^2 gives good coupling; however, it is not experimentally known whether or not 10 MW/cm^2 lies below the LSC/LSD wave transition for 3.8 μm radiation.

The LSC wave model also predicts the pressure of the plasma. The surface pressures predicted by LSC wave theory and LSD wave theory are shown in Fig. 6.6. The detailed calculations performed with the LSC wave code for 3.8 μm radiation lie on the LSC wave theory, as expected. The experimentally observed LSC/LSD wave transition for 10.6 μm radiation is shown by the dotted line. The theoretical estimate[24, 25] of the transition is indicated by the X placed on the LSC wave theory line. The prediction is substantially higher than the observed value of the onset of transition at 10.6 μm. Indeed, one might argue that the theoretical prediction is more representative of complete
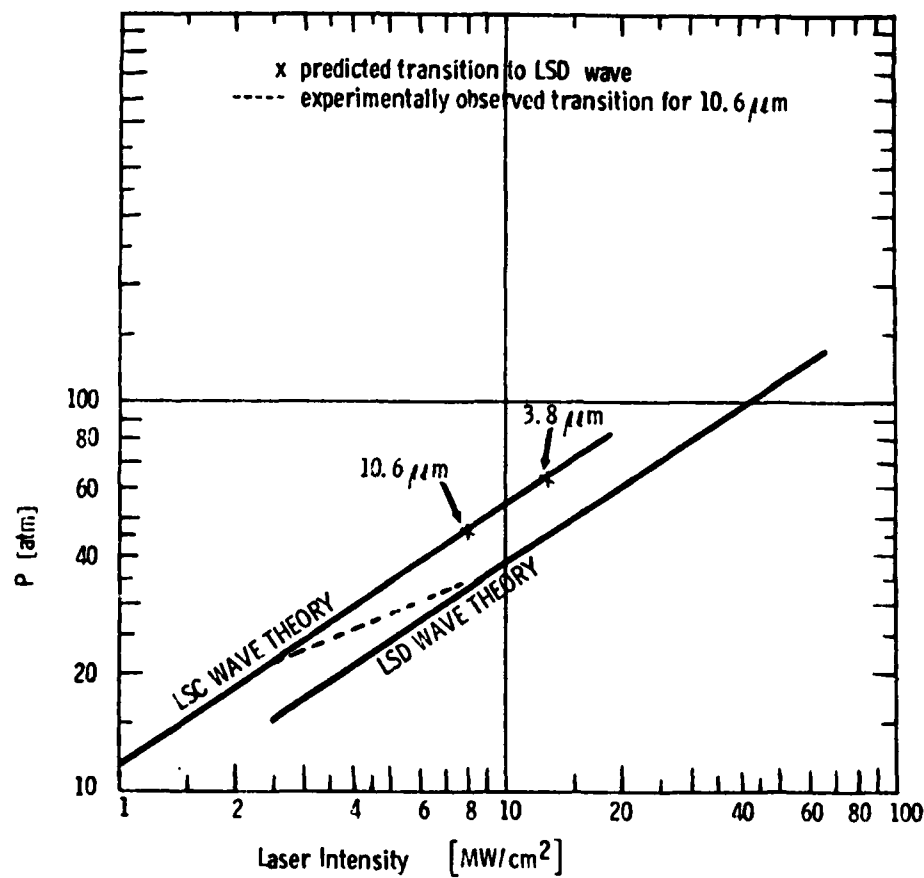
Fig. 6.6 Theoretical Predictions for Surface Pressure Generated
by LSC Waves and LSD Waves. Theoretical Prediction of
Transition Intensity is Shown. Darkened Line Represents
Transition from LSC Wave to LSD Wave Pressure Observed
in Experiments at 10.6 μm.

transition to LSD wave theory rather than the onset of transition. The theoretical value for the LSC/LSD wave transition for 3.8 μm radiation is also shown, however, it is not known whether this is a reliable value. The most important conclusion of Fig. 6.6 is that if the 3.8 μm radiation can maintain an LSC wave configuration at higher intensities than 10.6 μm radiation, it is possible to generate higher surface pressures.

The foregoing calculations and discussions represent only a preliminary examination of the expected coupling of 3.8 μm radiation to metal targets. Nevertheless, these calculations should prove instructive in the preparation of test matrices for the initial experiments of the interaction of 3.8 μm radiation with metals. Based upon the results of these experiments, further theoretical modeling of the interaction should be undertaken. Several issues must be addressed in future modeling; some of them include:

1. Plasma Ignition
    - Intensity and fluence requirements for plasma ignition.
    - Vapor requirements for plasma ignition.
    - Proper incorporation of fluence received prior to ignition.

2. Pulse Shape Effects
    - What important features of the pulse shape must be incorporated into the model pulse shape?

3. LSC/LSD Transition
    - What is the transition intensity?
    - Is the transition controlled by the peak intensity or the average intensity?

4. Vapor Effects
    - Inclusion of the energy required to produce the vapor in the calculation of net absorbed energy.
    - Effects of vapor on radiative transfer.

155

SECTION 7

SUMMARY

The model previously advanced[1,2] to explain enhanced coupling of pulsed laser radiation to metal targets has been improved and extended to provide more accurate predictions over a wider range of circumstances. Significant advances include:

1. Improved, four band, model of air radiation parameters have been developed.

2. Improved radiative transfer models have been used to predict one-dimensional plasma temperature profile and radiative transfer to wall.

3. Thermal coupling predictions have been extended to encompass large spot sizes and the resultant thick plasmas. The calculations show no evidence of axial decoupling for $I = 2$ MW/cm^2 and $\tau_p = 33$ μs.

4. The enhanced coupling model has been adapted to alloy targets other than Al2024. A hierarchy of alloys is predicted, based upon absorbed fluence. Limited experimental data is qualitatively consistent with the predicted hierarchy, but the data is not adequate to test the quantitative predictions.

5. The enhanced coupling model has been extended to oblique angles of incidence. The predictions of both thermal coupling and surface pressure are in excellent agreement with experimental data, which strongly supports the validity of the model.

6.   Both theory and experiment show that the thermal coupling
       coefficient increases as the angle of incidence increases;
       therefore, the coupling at large angles can be significant.
       Theoretical predictions of impulse delivered to target in-
       dicate that the drop in impulse as the angle increases is
       small compared to the drop in projected laser intensity.
       At 75° the predicted impulse is still . 6 of the impulse at
       normal incidence.

7.   The LSC wave model has been modified to give first order
       estimates of the coupling of 3. 8 μm radiation to metal tar-
       gets.   The calculations indicate that a DF laser couples
       more efficiently than a 10. 6 μm laser, provided that a LSC
       wave can be maintained.   The location of the LSD/LSC wave
       transition determines the maximum fluence which can be
       coupled via a DF laser of fixed pulse length.

APPENDIX A

Properties of Air Plasmas

The thermophysical properties of air plasma for temperatures between 10,000 K to 30,000 K and pressures between one to fifty atmospheres have been calculated in the same approximate scheme as in Ref. 4. However, in addition to the thermophysical properties, we have also computed improved radiation parameters for the four spectrals bands used in the LSC wave models. The details of the calculation are presented in the subroutine listing SUBROUTINE SAHA which is duplicated below. The effective absorption coefficients for the EUV, VUV, and VIS bands are denoted as KVUV, KUV and KVIS, respectively. The effective absorption coefficient for the VUV' spectral band is the same as for the VIS spectral band and is therefore also given by KVIS.

```
      SUBROUTINE SAHA(T,P,X0,XP,XPP,XE,N,RHO,H,
     1KVUV,KUV,KVIS)
      IMPLICIT REAL*8(A-H,O-Z)
      REAL*8 I1A,I2A,N,K,ME,MA,KEV,KVUV,KVIS,KUV,N0
      DIMENSION GO(3),WO(3),GOP(3),WOP(3),GN(3),WN(3),
     1GNP(4),WNP(4)
      DATA K/1.3804D-16/,E/4.8029D-10/,ME/9.1083D-28/,
     1HBAR/1.0544D-27/,PI/3.14159/,C/2.997925D10/
      DATA I1A/14.38/,DI1A/.05/,
     1I2A/30.8/,DI2A/.06/,
     2UA/1.405D-11/,KEV/8.6166D-5/,DYNEAT/1.013D6/
     3,MA/2.3952D-23/,ERGEV/1.602D-12/,U/5.11/
      DATA SGVUV/8.333D-18/,SGUV/6.D-18/,SGVIS/8.888D-18/
      DATA TOLD/0.0D0/
C
C STATEMENT FUNCTION DEFINITIONS
C
      FN(XE)=((XE+A)*XE+B)*XE+C
C
      C4=ME*K/(2.*PI*HBAR**2)
C
C EQUATION OF STATE BLOCK
C
      N=P/(K*T)
      IF(T.EQ.TOLD)GO TO 7
C
C SAHA BLOCK - 1
C
C PARTITION FUNCTION FOR O
C
      UOVUV=9.
      UOUV=5.*DEXP(-1.97/(KEV*T))+DEXP(-4.19/(KEV*T))
      UOVIS=8.*DEXP(-9.29/(KEV*T))+24.*DEXP(-10.83/(KEV*T))
     1+144.*DEXP(-12.39/(KEV*T))+306.*DEXP(-13.31/(KEV*T))
      RUOVIS=10.36*DEXP(-9.29/(KEV*T))+10.36*DEXP(-10.83/(KEV*T))
     1+8.18*DEXP(-12.39/(KEV*T))+.56*DEXP(-13.31/(KEV*T))
C
      DUOVUV=0.
      DUOUV=5.*1.97*DEXP(-1.97/(KEV*T))+4.19*DEXP(-4.19/(KEV*T))
      DUOVIS=8.*9.29*DEXP(-9.29/(KEV*T))+24.*10.83*DEXP(-10.83/
     1(KEV*T))+144.*12.39*DEXP(-12.39/(KEV*T))+306.*13.31*
     2DEXP(-13.31/(KEV*T))
C
      UO=UOVUV+UOUV+UOVIS
      PUOPT=DUOVUV+DUOUV+DUOVIS
C
C PARTITION FUNCTION FOR O+
C
```

160

```
      SUBROUTINE SAHA(T,P,X0,XP,XPP,XE,N,RHO,H,

      UOP=4.+10.*DEXP(-3.32/(KEV*T))+6.*DEXP(-5.02/(KEV*T))
C
C PARTITION FUNCTION FOR N
C
      UNVUV=4.
      UNUV=10.*DEXP(-2.38/(KEV*T))+6.*DEXP(-3.58/(KEV*T))
      UNVIS=30.*DEXP(-10.65/(KEV*T))+64.*DEXP(-11.94/(KEV*T))
     1+136.*DEXP(-13.05/(KEV*T))+762.*DEXP(-14.17/(KEV*T))
      RUNVIS=30.*DEXP(-10.65/(KEV*T))+23.3*DEXP(-11.94/(KEV*T))
     1+12.4*DEXP(-13.05/(KEV*T))+2.16*DEXP(-14.17/(KEV*T))
C
      DUNVUV=0.
      DUNUV=10.*2.38*DEXP(-2.38/(KEV*T))+6.*3.58*DEXP(-3.58/
     1(KEV*T))
      DUNVIS=30.*10.65*DEXP(-10.65/(KEV*T))+64.*11.94*
     1DEXP(-11.94/(KEV*T))+136.*13.05*DEXP(-13.05/(KEV*T))+
     2762.*14.17*DEXP(-14.17/(KEV*T))
C
      UN=UNVUV+UNUV+UNVIS
      PUNPT=DUNVUV+DUOUV+DUOVIS
C
C PARTITION FUNCTION FOR N+
C
      UNP=9.+5.*DEXP(-1.9/(KEV*T))+DEXP(-4.05/(KEV*T))
     1+5.*DEXP(-5.85/(KEV*T))
C
C CALCULATE U+/U0
C
    7 UPU0=.21*(UOP/U0)+.79*(UNP/UN)
C
C CALCULATE ALPHA AND BETA
C
      ALPHA=(2./N)*UPU0*(C4*T)**(3./2.)*DEXP(-(I1A-DI1A)/(KEV*T))
      UPPU0=UPU0
      BETA=(2./N)**2*UPPU0*(C4*T)**3*
     1DEXP(-(I1A-DI1A+I2A-DI2A)/(KEV*T))
C
C SAHA BLOCK - 2
C
      SOLVE  XE**3+2.*ALPHA*XE**2-(ALPHA-3.*BETA)*XE-2*BETA=0.

          ALPHA
          BETA-ALPHA
```

```
      FU=FN(XU)
      IF(FD*FU)140,141,142
140   XE=XD-FD*(XU-XD)/(FU-FD)
121   F=FN(XE)
      IF(FD*F)122,15,123
122   XU=XE
      FU=F
      FD=FD/2.
      GO TO 131
123   XD=XE
      FD=F
      FU=FU/2.
131   XE1=XE
      XE=XD-FD*(XU-XD)/(FU-FD)
      IF(DABS((XE-XE1)/XE).LT.1.D-5)GO TO 15
      I=I+1
      IF(I.GT.1000)STOP 2
      GO TO 121
142   STOP 3
141   XE=XD
      IF(FU.EQ.0.D0)XE=XU
 15   CONTINUE
      X0=XE**2*(2.*XE-1.)/(BETA-XE**2)
      XP=ALPHA*X0/XE
      XPP=BETA*X0/XE**2
      RHO=M0*(1.-XE)*N
      PU0PTO=PU0PT
      PU0PTN=PUNPT
      H=N/RHO*(5./2.*K*T+XP*I1A*ERGEV+XPP*(I1A+I2A)*ERGEV+
     1 1./2.*(1.-XE)*UA+X0*(.21/U0*PU0PTO+.79/UN*PU0PTN)*ERGEV)
      N0=X0*N
      KVUV=N0*SGVUV*(.21*(U0VUV+U0UV)/U0+.79*
     1(UNVUV+UNUV)/UN)
      KUV=N0*SGUV*.79*UNUV/UN
      KVIS=N0*SGVIS*(.21*RU0VIS/U0+.79*RUNVIS/UN)
C
C FINISHED
C
      TOLD=T
      RETURN
      END
```

REFERENCES AND FOOTNOTES - PART I

1.   A. N. Pirri, R. G. Root and P. K. S. Wu, "Analytical Laser/
        Material Interaction Investigations," Physical Sciences Inc.,
        Woburn, MA, TR-104, September 1977.

2.   A. N. Pirri, R. G. Root and P. K. S. Wu, "Plasma Energy Trans-
        fer to Metal Surfaces Irradiated by Pulsed Lasers," AIAA Journal,
        16, 1296 (1978).

3.   A. A. Boni, F. Y. Su, P. D. Thomas and H. M. Musal, "Theoretical
        Study of Laser-Target," Sciences Applications Incorporated, La
        Jolla, CA, SAI76-722-LJ, August 1976.

4.   A. N. Pirri, N. H. Kemp, R. G. Root and P. K. S. Wu, "Theoretical
        Laser Effects Studies," Physical Sciences Inc., Woburn, MA,
        TR-89, February 1977.

5.   R. R. Johnston, O. R. Platas and L. M. Tannenwald, "Atomic
        Line Transitions and Radiation from High Temperature Air,"
        Lockheed Palo Alto Research Laboratory, Palo Alto, CA, Re-
        port N-3L-70-1, July 1970.

6.   A. A. Boni, F. Y. Su, P. D. Thomas and H. M. Musal, "Theoretical
        Study of Laser-Target Interactions," Science Applications Incor-
        porated, La Jolla, CA, SAI77-567LJ, May 1977.

7.   A. A. Boni and F. Y. Su, "Numerical Simulation of Thermal Coupl-
        ing for Pulsed-Laser Target Interactions," Science Applications,
        La Jolla, CA, SAI-77-936LJ, November 1977.

8.   Ya. B. Zel'dovich and Yu. P. Raizer, Physics of Shock Waves and
        High-Temperature Hydrodynamic Phenomena, Ed. Wallace D. Hayes
        and Ronald F. Probstein, Vol. I (Academic Press, New York, 1966).
        p. 152.

9.   Ref. 8, p. 145.

10.   Ref. 8., p. 150.

11.   Ed. Y. S. Touloukian and C. Y. Ho, Thermophysical Properties of
        Selected Aerospace Materials, Part I: Thermal Radiative Proper-
        ties (Purdue University, Lafayette, IN, 1976).

REFERENCES AND FOOTNOTES - PART I (Cont.)

12. Bruce H. Billings, "Optics," in American Institute of Physics Handbook, Ed. Dwight E. Gray (McGraw-Hill Book Company, Inc., New York, 1957).

13. George B. Sabine, "Reflectivities of Evaporated Metal Films in the Near and Far Ultraviolet," Phys. Rev. 55, (1939).

14. W. Summer, Ultra-Violet and Infra-Red Engineering, (Interscience Publishers, Inc., New York, 1962).

15. Anthony N. Pirri, "Analytic Solutions for Initiation of Plasma Absorption Above Laser-Irradiated Surfaces," Physical Sciences Inc., Woburn, MA, TR-15, October 1974.

16. B. A. Boley, "A Method of Heat Conduction Analysis of Melting and Solidification Problems," Journal of Mathematical Physics, 40, 300 (1961).

   B. A. Boley, "A General Starting Solution for Melting and Solidifying Slabs," International Journal of Engineering Science, 6, 89 (1968).

17. J. W. Bond, Jr., K. M. Watson and J. A. Welch, Jr., Atomic Theory of Gas Dynamics, (Addison-Welsey Publishing Company Reading, MA, 1965) Sec. 3-2.

18. E. K. Dabora, "Variable Energy Blast Waves," AIAA Journal 10, 1384 (1972).

19. F. R. Gilmore, "Equilibrium Composition and Thermodynamic Properties of Air to 24,000°K," The Rand Corp., Santa Monica, CA, RM-1543, August 1955.

20. R. Stegman, "Single Pulse Test Results," presented to JANAF Pulsed Laser Effects Program Technical Steering Committee Meeting, August 3-4, 1978.

21. R. Stegman, "Repetitive Pulse Test Results," presented at JANAF Pulsed Laser Effects Program Technical Steering Committee Meeting, August 3-4, 1978.

22. Ref. 11.

REFERENCES AND FOOTNOTES - PART I (Cont.)

23.   Ref. 3.

24.   Ref. 1.

25.   A. A. Boni, F. Y. Su, P. D. Thomas and H. M. Musal, "Theoretical Study of Laser-Target Interactions," Science Applications Incorporated, La Jolla, CA, SAI77-567LJ, May 1977.

PART II

INTERACTION WITH DOME MATERIALS

SECTION 8

INTRODUCTION

The theoretical work performed in the last few years has concentrated on the interaction of pulsed 10. 6 μm radiation with metals. The concept of energy transfer via plasma reradiation was advanced two years ago as an explanation of the experimentally observed enhancement of thermal coupling to highly reflective metals in the presence of a plasma. The theory was developed on a quantitative basis in the following year and verified by comparison with experiment.[1] Further modeling of the laser interaction with metals was performed this year and it is presented in Part I of this report. The enhanced coupling theory has been modified to incorporate new predictions for the absorption coefficients of the plasma, and it has been extended to include new scenarios such as coupling at oblique angles of incidence and coupling to metals other than Al2024.

In stark contrast, prior to this year there has been no work, either theoretical or experimental, on the interaction of pulsed 10. 6 μm laser radiation with dome materials. This part of the report presents the results of the first theoretical analysis of this interaction. The approach used herein was deliberately designed to maximize progress; the experimental data developed during the program was used in conjunction with simple theoretical models to suggest the directions in which more intensive theoretical development should concentrate. The algorithm being followed in order to develop a predictive capability for RP laser interaction with domes is outlined below.

1. Compile a list of all possible phenomena
2. Construct simple models and phenomenology maps for the listed phenomena.

3. Compare the model predictions to the experimental data to determine the dominant physics.

4. Compose a synthesized model of the entire interaction sequence.

5. Develop more elaborate models of the various interaction stages used in (4.) in order to provide a predictive capability.

An expanded discussion of how this is implemented follows.

A list of physical phenomena which may be relevant is generated, and very simple theoretical models are devised in order to predict the observable results of these phenomena. Then the experimental data is examined within the framework of these models, and the data is used to choose between competing phenomena. Since the physical and thermal parameters of the materials are not well known, and since only simple, first order models are used, the theoretical predictions cannot reliably select between phenomena which yield results which are fairly close to each other.

The role of experiment is crucial in this program -- it is used to assess which mechanism is most reasonable. Whenever the data is changed, either because of better statistics, correction of systematic errors, or improved reduction and/or interpretation of the data, it is essential to re-examine the comparison between theory and experiment. It is especially important to re-examine mechanisms which are rejected on the basis of the old data, in order to be assured that the original conclusions are still valid. To facilitate this re-examination, all models which are used are recorded in this report; then whenever new or revised data becomes available, all the deductions can be easily re-examined to ascertain if they still are valid.

Once a mechanism has been selected, further modeling can be undertaken to explore the ramifications of the model and to search for observable consequences which can further test the validity of the model.

In this report, most of the effort is being expended on determining the dominant physical phenomena. A synthesized model is advocated, and we are ready to undertake more detailed modeling in order to develop a predictive capability which can then be tested and verified by experiment.

The discussion of the modeling of the interaction of pulsed laser radiation with dome materials is organized as follows. In Section 9, the material properties of the targets -- or more precisely, the material properties used in the theoretical models of the targets -- are presented. It should be emphasized that the properties which were assigned to the materials were often those of superficially similar materials which had better documented properties. The properties are subject to revision as more data becomes available, and as the type of targets are better characterized. In Section 10, the theoretical models for the surface interaction of a pulsed laser with dome materials are reviewed. In Section 11, the predictions of these models are compared to the data taken to determine surface interaction physics and a unified view of the surface interaction physics emerges. In Section 12, both the theory and experimental data for the damage mechanisms in repetitive pulse runs are discussed, and the dominant mass removal mechanism is successfully modeled. If the same physical phenomena dominate the interaction at other conditions, implications for repetitive pulse interactions can be made. They are discussed in Section 13, and the main conclusions of this part of the report are also summarized.

SECTION 9

PROPERTIES OF DOME MATERIALS

There are several materials which are of use in the manufacture of radomes and irdomes. Those considered herein, listed in order of decreasing importance for this program, are: fiberglass, pyroceram, and slip-cast fused silica. Unfortunately, these materials are not uniquely specified by the above names and there are wide variations in the preparation of the materials depending upon their ultimate use. Furthermore, the samples used in the tests were not always well specified or documented, and some of the important properties, such as absorption depth for $10.6\,\mu m$ radiation, are not commonly measured for any specimens. The following approach for determining appropriate properties was adopted. For properties which are well documented, a variety of similar materials which fall within one of the general categories mentioned above were examined, and a typical value was chosen for use in the theoretical models. If data were not available for a material within these categories, the properties for related materials, which fall outside the categories, were examined to provide an estimate of the value of the property for the target material. If no data exist, even for related materials, the experiments on the laser/surface interaction physics were used to suggest the value of the property. That is, the interpretation of an experimental result often depended on the value of some parameter; the value which best fit the data for one experiment would be employed in predictions of results of subsequent experiments.

Within the general classes of materials mentioned above, there are several subdivisions. For example, three types of fiberglass were used in the experiments and potentially interesting target materials include several other types. Pyroceram can have different surface preparations.

It is assumed that the pyroceram of interest is fortified, but it is not known if the material properties that were gathered were for fortified or unfortified pyroceram. The slip-cast fused silica targets were prepared in two different ways, some were impregnated with silicone resin whereas others were not. In the following subsections the properties used for each of the general classes are given; but the variation of the properties within the classes is not discussed.

9.1 Slip-cast Fused Silica

Several materials were used to compile the properties of slip-cast fused silica. Some of the properties were found for slip-cast fused silica, other properties were estimated by using the available properties of vitreous silica, quartz, fused silica glass, and fused quartz.

The density of slip-cast fused silica is listed in Ref. 2 as 2.0 g/cm^2; whereas fused silica glass as listed in Ref. 3 has a density of 2.2g/cm^2. The specific heat of slip-cast fused silica[2] and silicon dioxide[4] are plotted in Fig. 9.1. The values for the two materials are in good agreement except for the α - β transition in SiO_2. At room temperature the specific heat is approximately .7J/g-K whereas an average value between 300 to 1500K is 1.12J/g-K. Thermal conductivity for slip-cast fused silica[2] is shown in Fig. 9.2. The conductivity of SiO_2 is also shown[4]; it lies significantly higher. For slip-cast fused silica, the thermal conductivity is approximately 9.1 x 10^{-3}W/cm-K at room temperature, with an average value of 1.2 x 10^{-2}W/cm-K throughout the temperature range from 300 to 1400K. The thermal diffusivity of slip-cast fused silica can be calculated from the values given above for the density, specific heat and thermal conductivity. The results are plotted in Fig. 9.3, along with measured values for clear fused quartz and silica brick.[4] For slip-cast fused silica, the room temperature value is approximately 6.8 x 10^{-3} cm^2/sec and the average value between 300 and 1400K is 5.7 x 10^{-3} cm^2/sec. It is believed that the reason
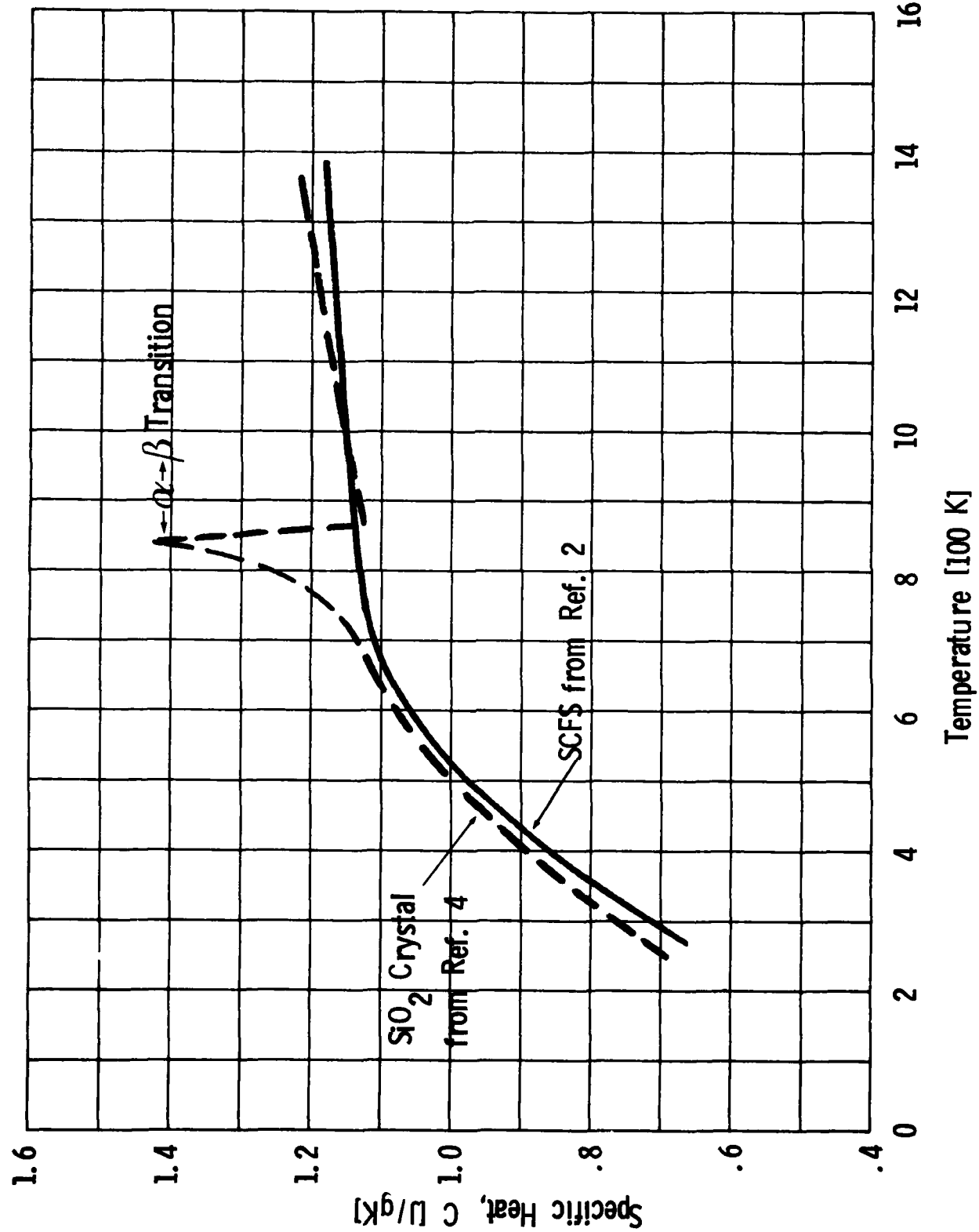
Fig. 9.1 Specific Heat of Slip Cast Fused Silica and Silicon Dioxide.

175
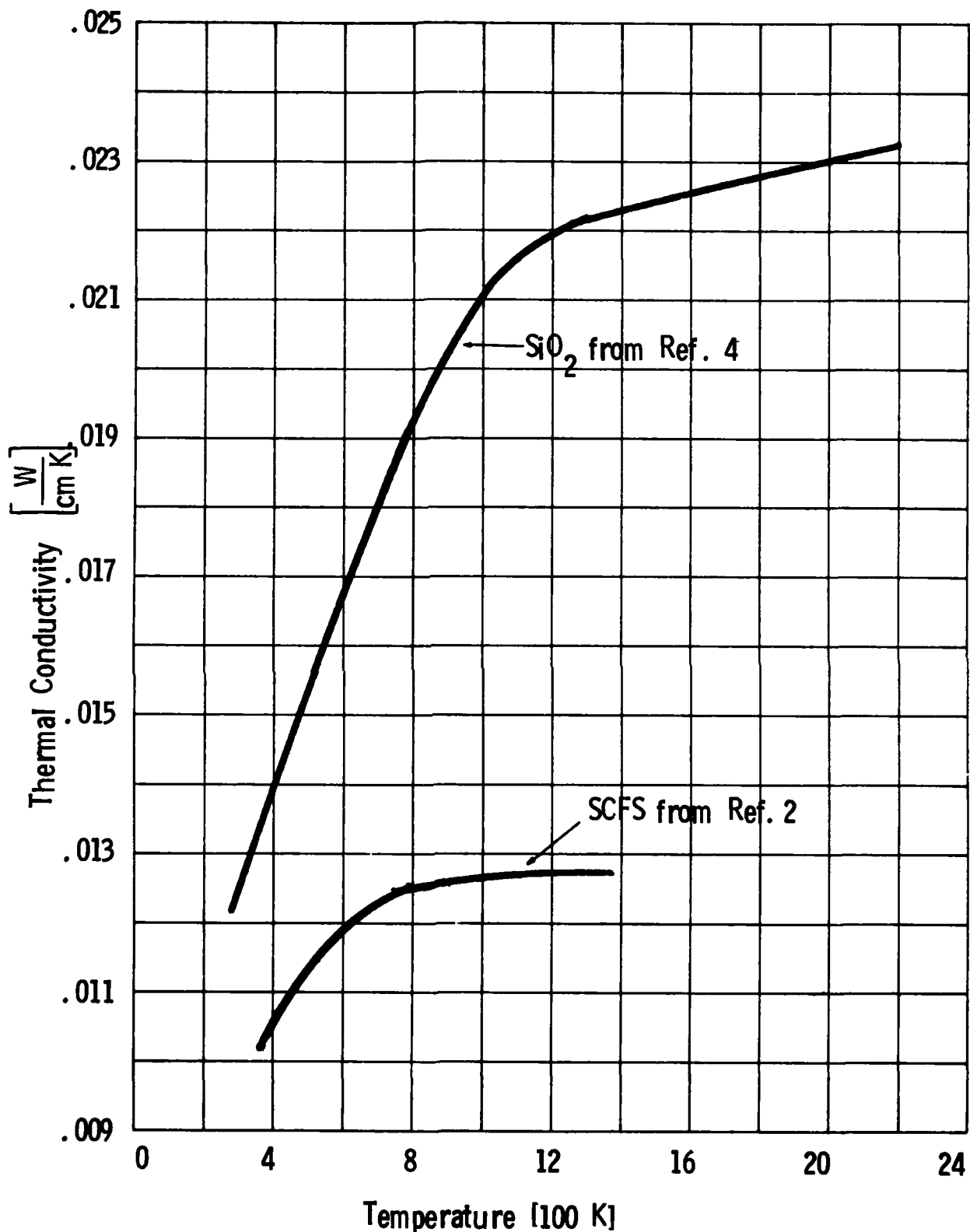
Fig. 9.2 Thermal Conductivity of Slip Cast Fused Silica and SiO_2.
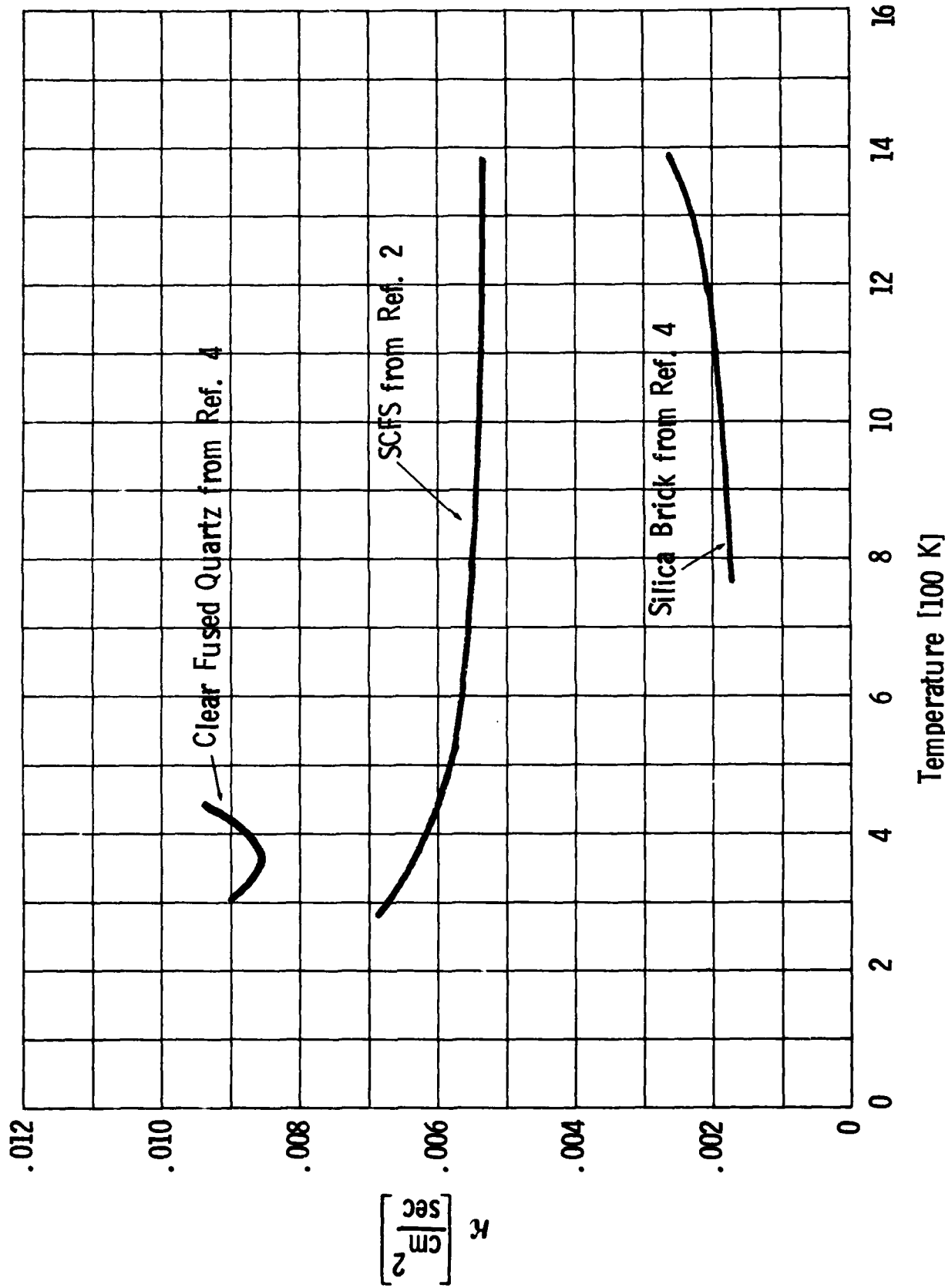
Fig. 9.3 Thermal Diffusivity of Slip Cast Fused Silica, Silica Brick and Clear Fused Quartz.

177

that the density, thermal conductivity, and thermal diffusivity differ for slip-cast fused silica and fused silica, whereas the specific heat is the same, is that slip-cast fused silica has voids in its structure which reduce the density and thermal conductivity.

The vapor pressure and heat of vaporization has been calculated by determining the equilibrium vapor composition of SiO_2 as a function of temperature. In this calculation, the partition functions of the various species, namely SiO_2 liquid and gases of SiO_2, SiO, Si_2, Si_3, O, O^-, O_2, O_2^-, Si, Si^+, O^+, O_2^+, SiO^+ and electrons, were taken from the JANAF tables.[5] The results are shown in Fig. 9.4. The normal boiling point is 3130K and the heat of vaporization is 12500 J/g of SiO_2.

The remaining quantities needed to determine the deposition of laser energy in slip cast fused silica are the reflectivity and absorption depth for 10.6 μm radiation. Values of the refractive index of fused silica can be found in Touloukian and Ho.[6] The real part is $n_1 = 2.05 \pm .1$ whereas the imaginary part n_2 has measured values of .175, .123, .121 and .04. The reflectivity R at a planar boundary is given by

$$R = \frac{(n_1-1)^2 + n_2^2}{(n_1+1)^2 + n_2^2} = .12 \qquad (9.1)$$

and this calculated value falls within the range of values measured experimentally.[6] The bulk absorptivity of silica is given by

$$k = \frac{4\pi n_2}{\lambda} \qquad (9.2)$$

where λ is the wavelength of the radiation. The values of k corresponding to the values of n_2 quoted above are 2075, 1458, 1434, and 500 cm^{-1}, which correspond to absorption depths of 4.8, 6.9, 7.0 and 20 μm, respectively. Clearly, if k is an important parameter in the theoretical models, it must be determined more accurately.
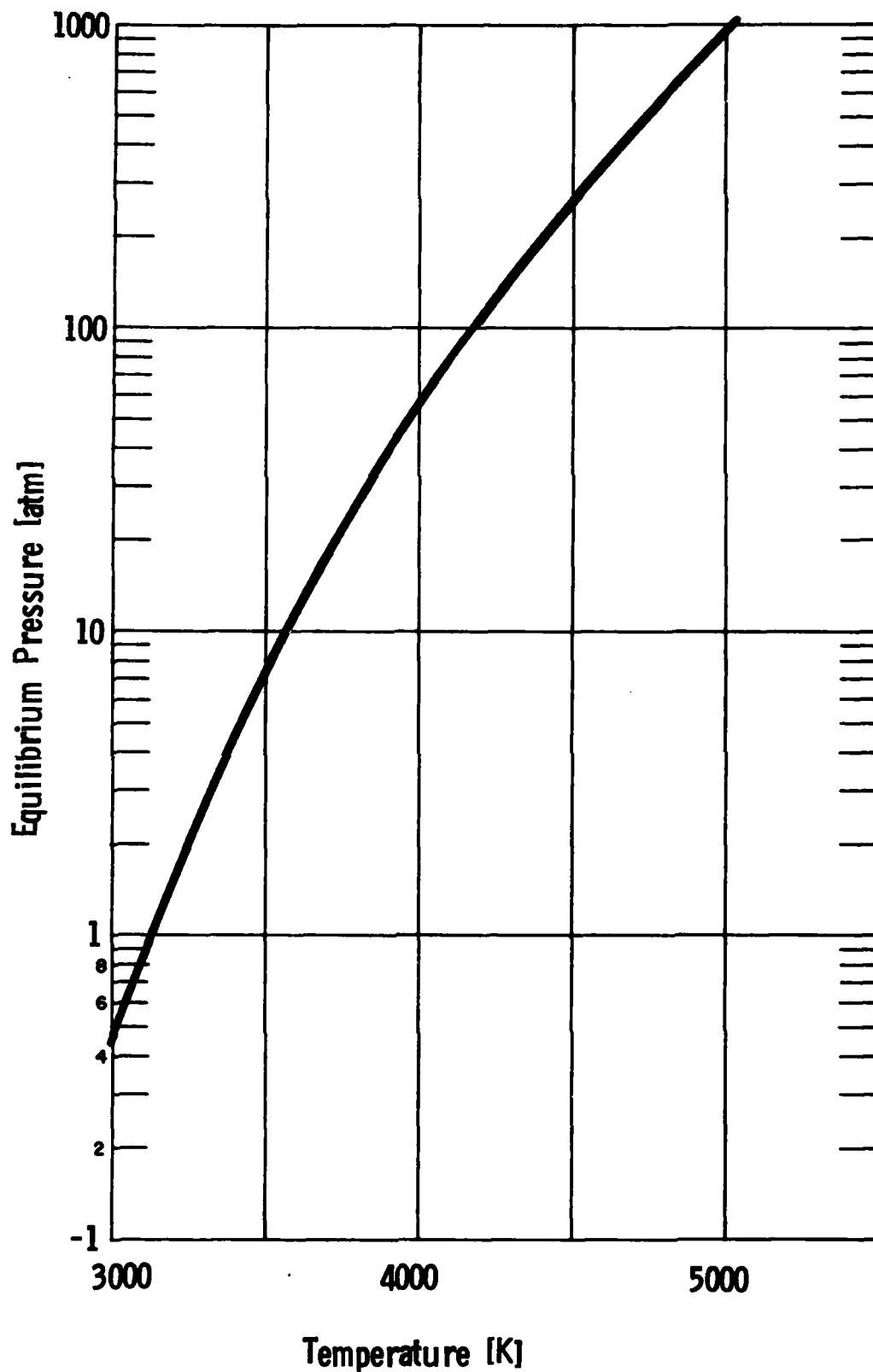
Fig. 9.4 Pressure of Vapor in Equilibrium with Liquid SiO_2 as a Function of Temperature.

9.2 Pyroceram 9606

Pyroceram 9606 is a glass ceramic used in radomes. It is approximately, by weight, 56% SiO_2, 20% Al_2O_3 and 15% MgO with 9% TiO_2 added to control crystalization. The structure of the crystals is $5SiO_2 \cdot 2Al_2O_3 \cdot 2MgO$. The density is 2.6 g/cm^2 and the specific heat, thermal conductivity and diffusivity are given in Fig. 9.5, 9.6 and 9.7, respectively. The values given by Ref. 2 and Ref. 7 are in good agreement.

The softening point[7] of pyroceram 9606 is 1623K. The vapor pressure has been estimated by treating pyroceram as an ideal mixture of five parts SiO_2, 2 parts Al_2O_3 and 2 parts MgO. An ideal mixture is a mixture in which the partial pressure of the products of a given component is given by multiplying the partial pressure of the pure component by the mole fraction of mixture which consists of that component. Equilibrium vapor compositions of liquid SiO_2, Al_2O_3 and MgO have been constructed from an equilibrium code which solves the law of mass action and the partition functions given by the JANAF tables.[5] A plot of vapor pressure versus temperature for SiO_2, Al_2O_3, MgO and pyroceram 9606 is shown in Fig. 9.8. It is clear that SiO_2 dominates the vapor pressure of pyroceram. The normal boiling point is calculated to be 3200K and the heat of vaporization is 11100 J/g.

The absorption characteristics of pyroceram are not known. Since SiO_2 is a major component of pyroceram, the absorption length is expected to be dominated by silica and to lie in the range from 4 to 20 μm. Al_2O_3 absorption properties have also been studied;[8] the absorption coefficient increases an order of magnitude as the temperature is raised from room temperature to 1723K. The high temperature absorption depth is 4.2 μm. The Al_2O_3 in pyroceram is expected to reduce the absorption depth for pyroceram to a value of the order of 5 to 10 μm.
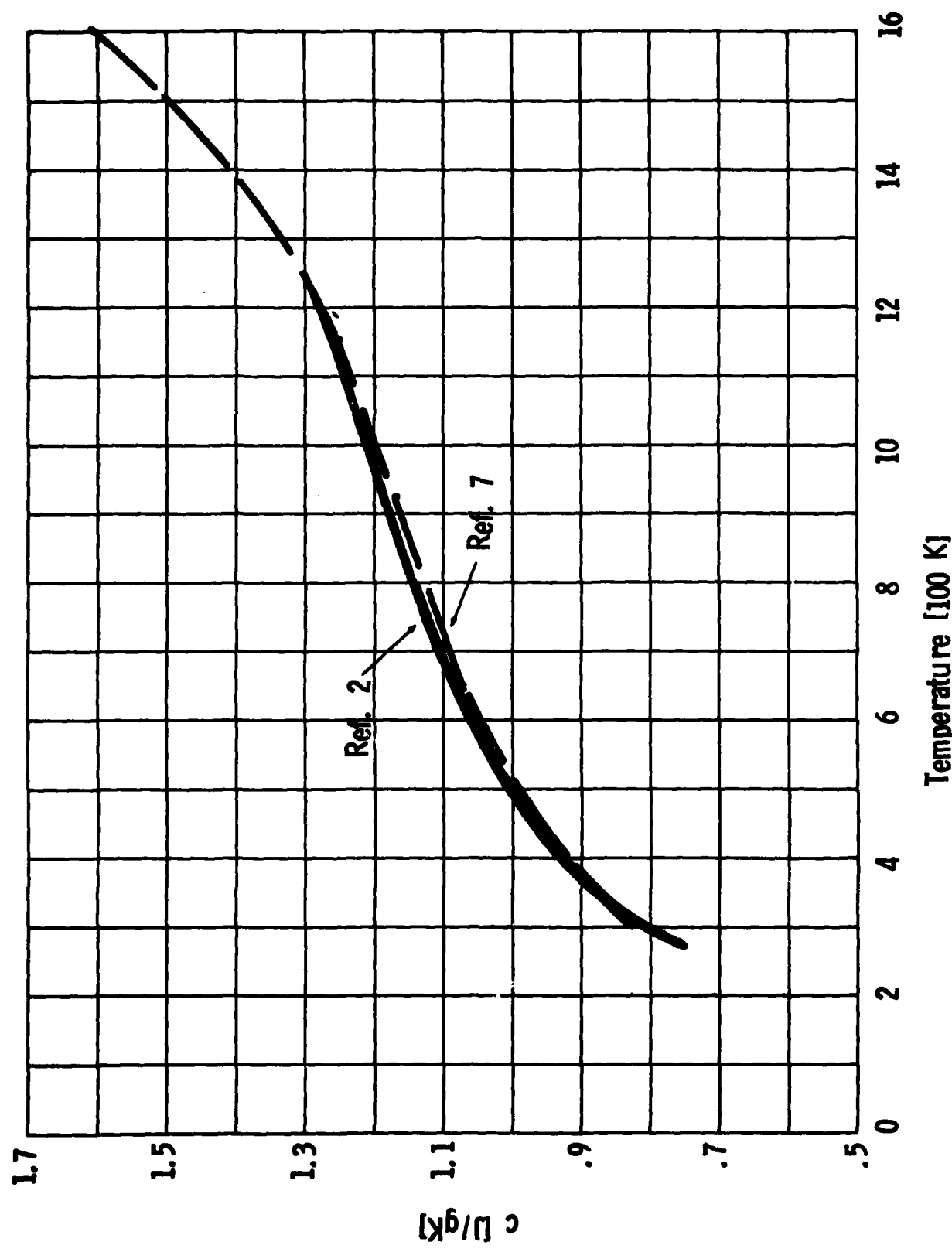
Fig. 9 5 Specific Heat of Pyroceram 9606 as a Function of Temperature
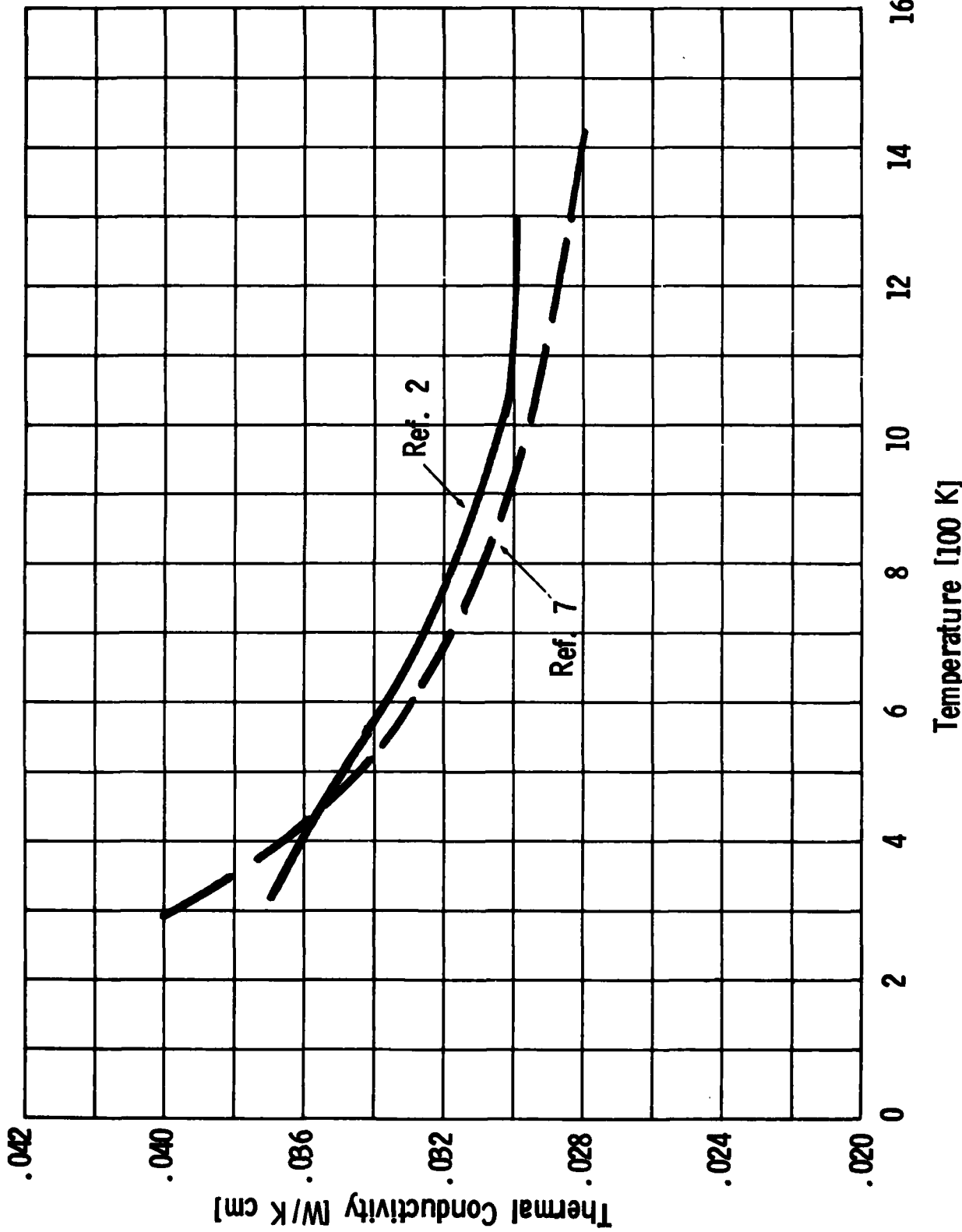
Fig. 9. 6 Thermal Conductivity of Pyroceram 9606 as a Function of Temperature.
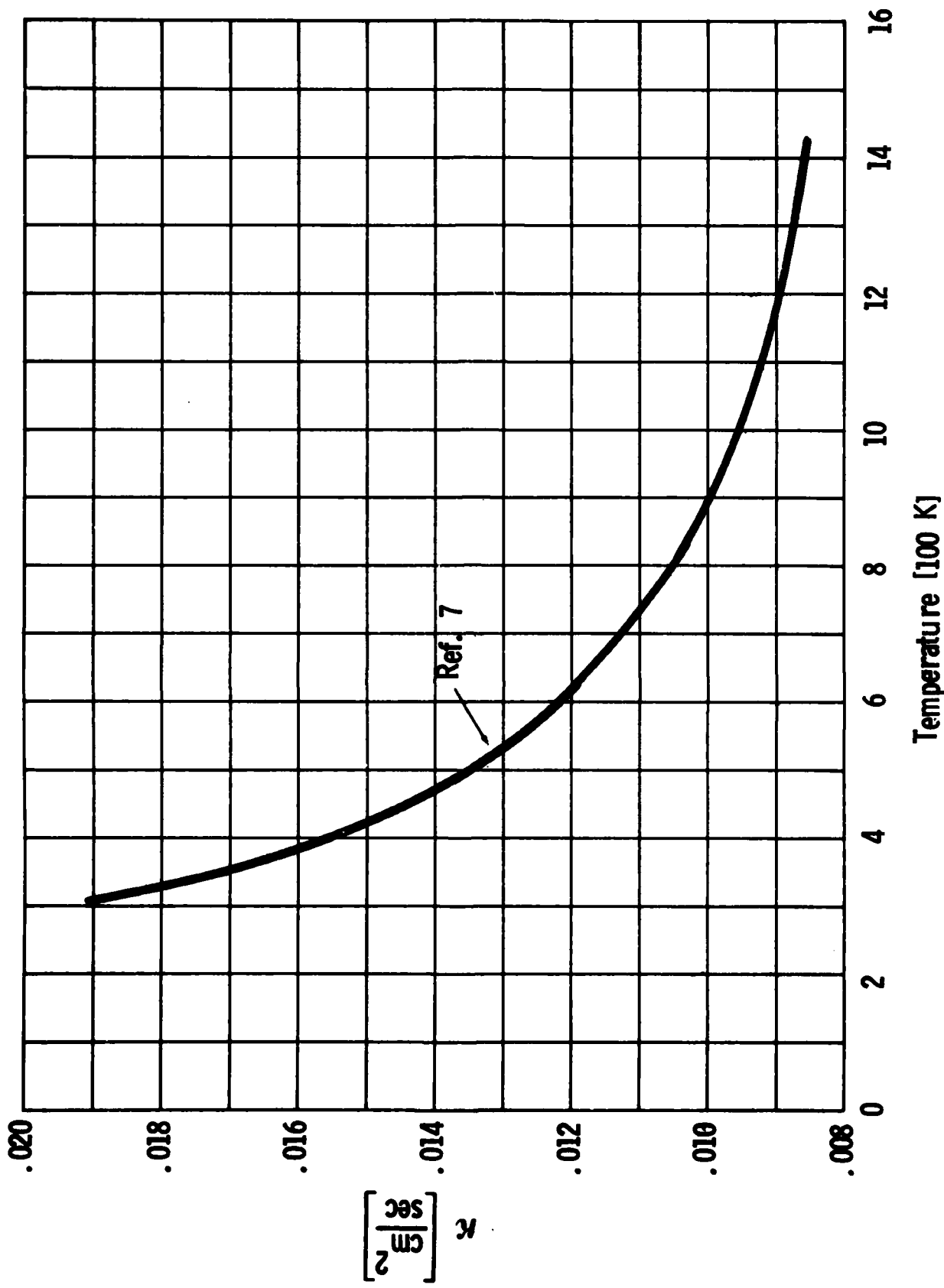
Fig. 9.7 Thermal Diffusivity of Pyroceram 9606 as a Function of Temperature
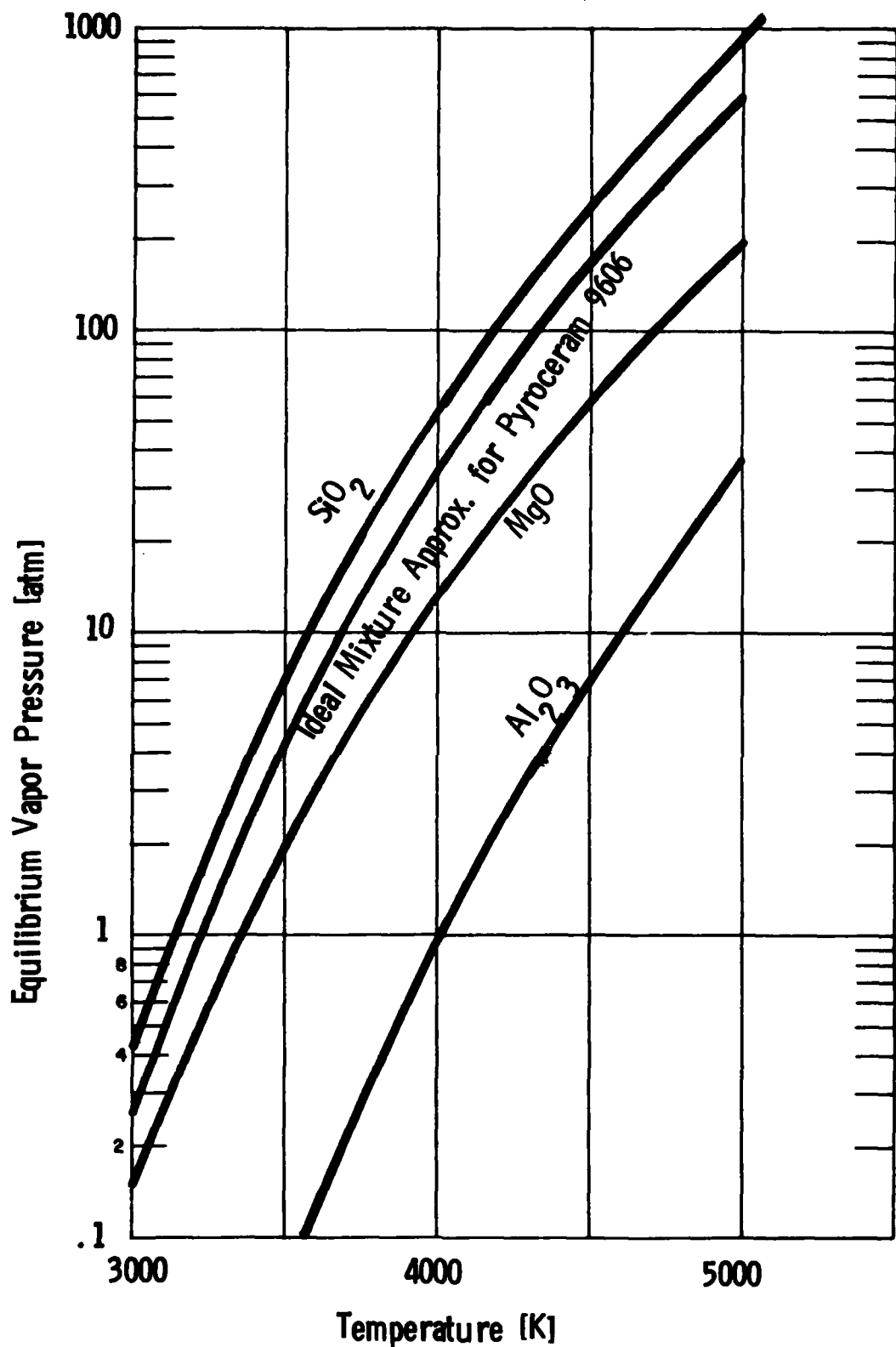
Fig. 9.8 Pressure of Vapor in Equilibrium with Liquid SiO_2, Liquid MgO, Liquid Al_2O_3 and Liquid Pyroceram 9606 as a Function of Temperature.

9.3 Fiberglass

Fiberglass is a composite material consisting of glass fibers and resin. Three types of fiberglass were used in the experiments:

1. Cordopreg - A clear stabilized epoxy resin and a E-glass fiber reinforcement.

2. Polyimide resin and E-glass reinforcement.

3. E-glass - a type of fiberglass made by AMMRC especially for these experimental tests. An epoxy resin and an E-glass reinforcement.

Since other types of resins and glass may be of interest later on, the discussion is not confined to the above resins and glasses although they are given special emphasis.

Fiberglass, or glass fiber reinforced resins, come in a wide variety of forms depending upon the eventual use of the product. The fibers[9] are employed primarily to improve the mechanical properties of the composite; that is, to make it stronger, stiffer, more resistant to impact, etc. The resin is used to make the composite light in weight and give it desirable properties (such as the correct dielectric constant).

Glass fibers are vastly stronger than bulk glass; this added strength is used to advantage in fiberglass composites. But high strength fibers are brittle and can abrade each other thus reducing their strength. Resin provides protection from this type of degradation. Furthermore, the resin has high shear strength and can transfer loads around broken fibers giving the structure high impact resistance. To perform these tasks effectively, there must of course be a strong adhesive bond between the resin and the fibers. Thermosetting resins such as phenolic, epoxy and polyimide are commonly used in fiberglass.

Fiberglass has its greatest strength in directions parallel to the fibers. Perpendicular to the fiber direction, the structure is only as strong as the resin. Under a tensile load perpendicular to the fibers a unidirectional fiber-glass composite can withstand only 5000 psi compared to a load 10 times as large in a direction parallel to the fibers.

This problem is solved by having the fibers run in two directions. Two methods of accomplishing this are used in the targets; one method, used in Cordopreg, is to weave the glass into a cloth so that each layer has fibers in both directions (see Fig. 9.9a); the other way is to build layers of unidi-rectional fibers with the fibers of alternate plies being at right angles (see Fig. 9.9b), much akin to the construction of plywood.

The glass cloth technique has a larger percent of resin in it than the parallel fiber technique. A ply of Cordopreg is .025 cm thick, has a density of 1.8 g/cm^2, and has a resin content of approximately 34 percent by weight.

The unidirectional ply technique is employed in the target composed of epoxy resin and E-glass reinforcement. Often in constructing fiberglass structures in this manner, the fiberglass comes in the form of preimpregnated tapes in which all the fibers lie in a single direction. A ply or a laminate layer can then be constructed with one or more layers of these tapes. Typically, two to three layers may be used to form a ply; each layer being about 100 μm thick. Fiberglass laminates made with unidirectional layers can be constructed with a larger mass fraction of glass than can fiberglass made from glass cloth.

Two types of glass fibers are commonly used in the construction of composites for aerospace purposes; they are E-glass and S-glass. E-glass is a low-alkali, lime-alumina-borosilicate which is relatively inexpensive to produce and has good electrical properties. The composition of E-glass is not rigidly controlled but may vary within the range listed in Table 9.1. Also listed in Table 9.1 are various physical properties of E-glass. [10]

186
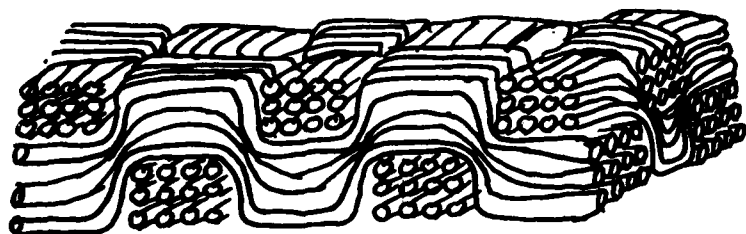
(a)
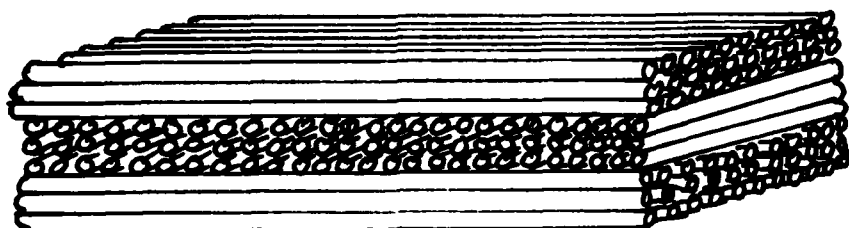
(b)

Fig. 9.9 (a) Sketch of Ply of Fiberglass Formed by Weaving
Bundles of Glass Fibers. (b) Sketch of Three Plies
of Fiberglass, Each Ply Composed of Unidirectional
Fibers.

TABLE 9.1

Typical Properties of E and S Glass.   From Ref. 10.

Property	E Glass	S Glass
Composition	% by Weight	% by Weight
SiO_2	52-56	65
Al_2O_3	12-16	25
CaO	16-25	--
MgO	0-6	10
B_2O_3	8-13	--
Na_2O and K_2O	0-3	--
TiO_2	0-0.4	--
Fe_2O_3	0.05-0.4	--
F_2	0-0.5	--
Physical Properties*		
Specific gravity	2.54	2.49
Mechanical Properties*		
Virgin tensile strength at 72°F	500,000 psi	665,000 psi
Yield strength at 1000°F	120,000 psi	275,000 psi
Ultimate strength at 1000°F	250,000 psi	350,000 psi
Modulus of elasticity at 72°F	10,500,000 psi	12,400,000 psi
Modulus of elasticity at 72°F (after heat compaction)	12,400,000 psi	13,500,000 psi
Modulus of elasticity at 1000°F (after heat compaction)	11,800,000 psi	12,900,000 psi
Elastic elongation at 72°F	4.8%	5.4%
Thermal Properties**		
Coefficient of thermal expansion	2.8 in/in$^{\circ}$F x 10^{-6}	1.6 in/in/$^{\circ}$F x 10^{-6}
Specific heat at 75°F	0.192	0.176
Softening point	1.555°F	1778°F
Strain point	1.140°F	1400°F
Annealing point	1.215°F	1490°F
Electrical Properties**		
Dielectric constant at 72°F, 10^6Hz	5.80	4.53
Dielectric constant at 72°F, 10^{10}Hz	6.13	5.21
Loss tangent at 72°F, 10^6 Hz	0.001	0.002
Loss tangent at 72°F, 10^{10} Hz	0.0039	0.0068
Acoustical Properties*		
Velocity of sound (calculated)	17,500 ft/sec	19,200 ft/sec
Velocity of sound (measured)	18,000 ft/sec	
Optical Properties**		
Index of refraction	1.547	1.523

*Properties measured on glass fibers.
**Properties measured on bulk glass.

S-glass is an expensive glass fiber with carefully controlled composition which has been developed by Owens-Corning Corporation for structural purposes. It has unusually high strength. Its properties are listed in Table 9.1.

In the popular fiberglass materials there are several types of resin. In aerospace uses, thermosetting plastics are regularly used. Several types are common - phenolics because they are cheap, epoxies because they are strong, and more recently, polyimides because they can survive higher temperatures. Although epoxy is the resin used in the two basic targets of the 1978 JANAF pulsed effects test series, and polyimide is the resin employed in the third target, we shall, nevertheless, also examine some of the properties of phenolic. Pyrolysis of the resin is an important phenomenon in the interaction of a laser with fiberglass, and phenolic has the best characterized pyrolysis properties because of its prevalence in re-entry applications.

From the previous discussion it should be evident that fiberglass has many variable quantities, e.g., type of glass, type of resin, layup, ratio of glass to resin - so that it is difficult to characterize the thermal and physical properties. The properties discussed below have been garnered from a variety of sources[2, 7, 11, 12, 13] and represent values for typical fiberglasses rather than any specific fiberglass. In Fig. 9.10 - 9.12, specific heat, thermal conductivity and thermal diffusivity are shown as a function of temperature. The values of the specific heat are seen to vary strongly with resin content. At room temperature Cordopreg and silica phenolic have nearly identical values of 1.05 J/g-$^\circ$K. The thermal conductivity of Cordopreg at room temperature agrees with the values quoted by Ref. 7. For both specific heat and conductivity, the curves end at 400 to 500K because the resin starts to decompose. The experimental values of thermal diffusivity for a fiberglass laminate and a fiberglass mat (no resin) are shown in Fig. 9.12. The values for Cordopreg and silica phenolic are found to lie above the measured value. The measured diffusivity of the glass mat depends upon the gas pressure, indicating that the hot gas plays a role in the
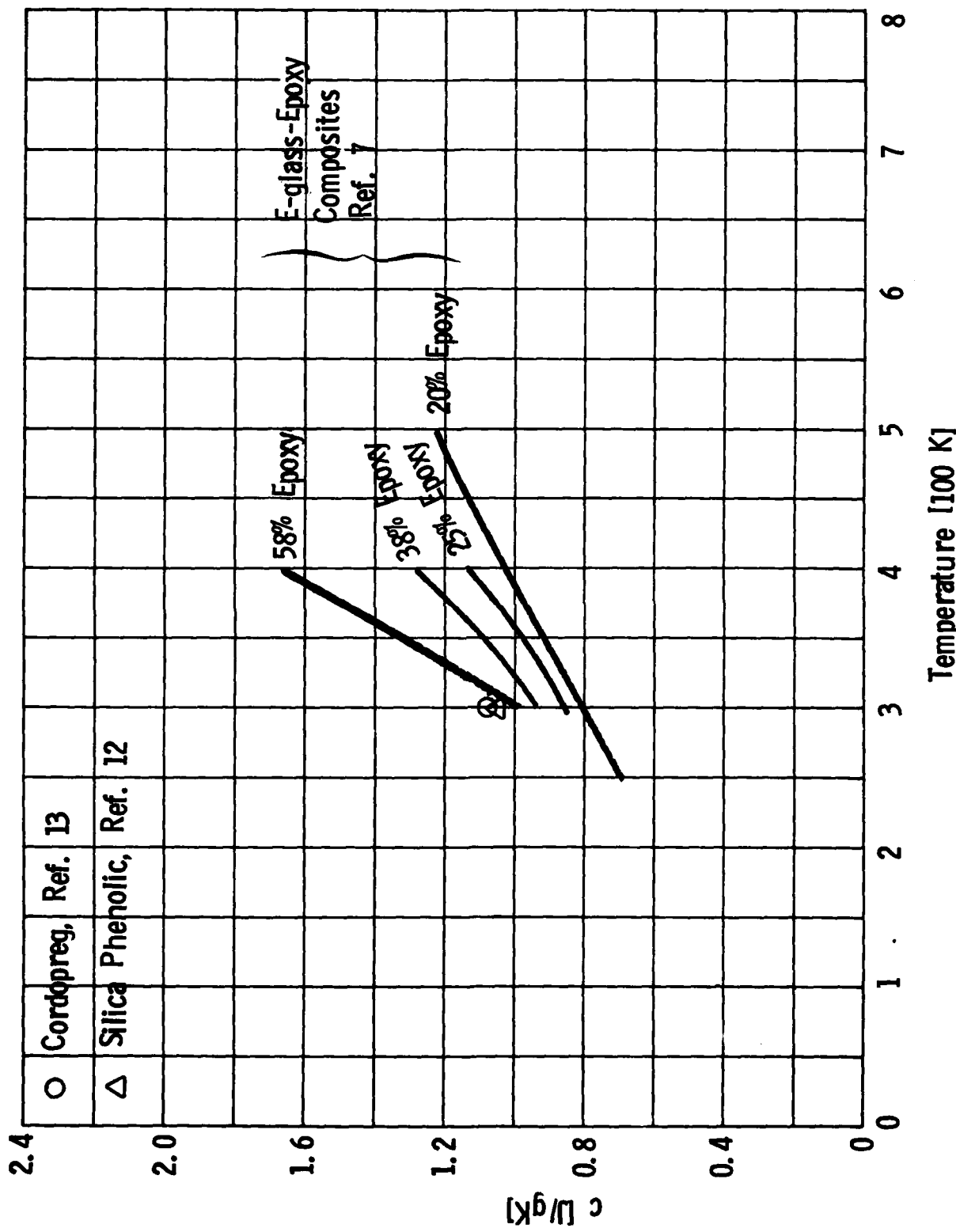
Fig. 9.10 Specific Heat of a Variety of Fiberglasses.

Fig. 9.11 Thermal Conductivity of Fiberglass.

191
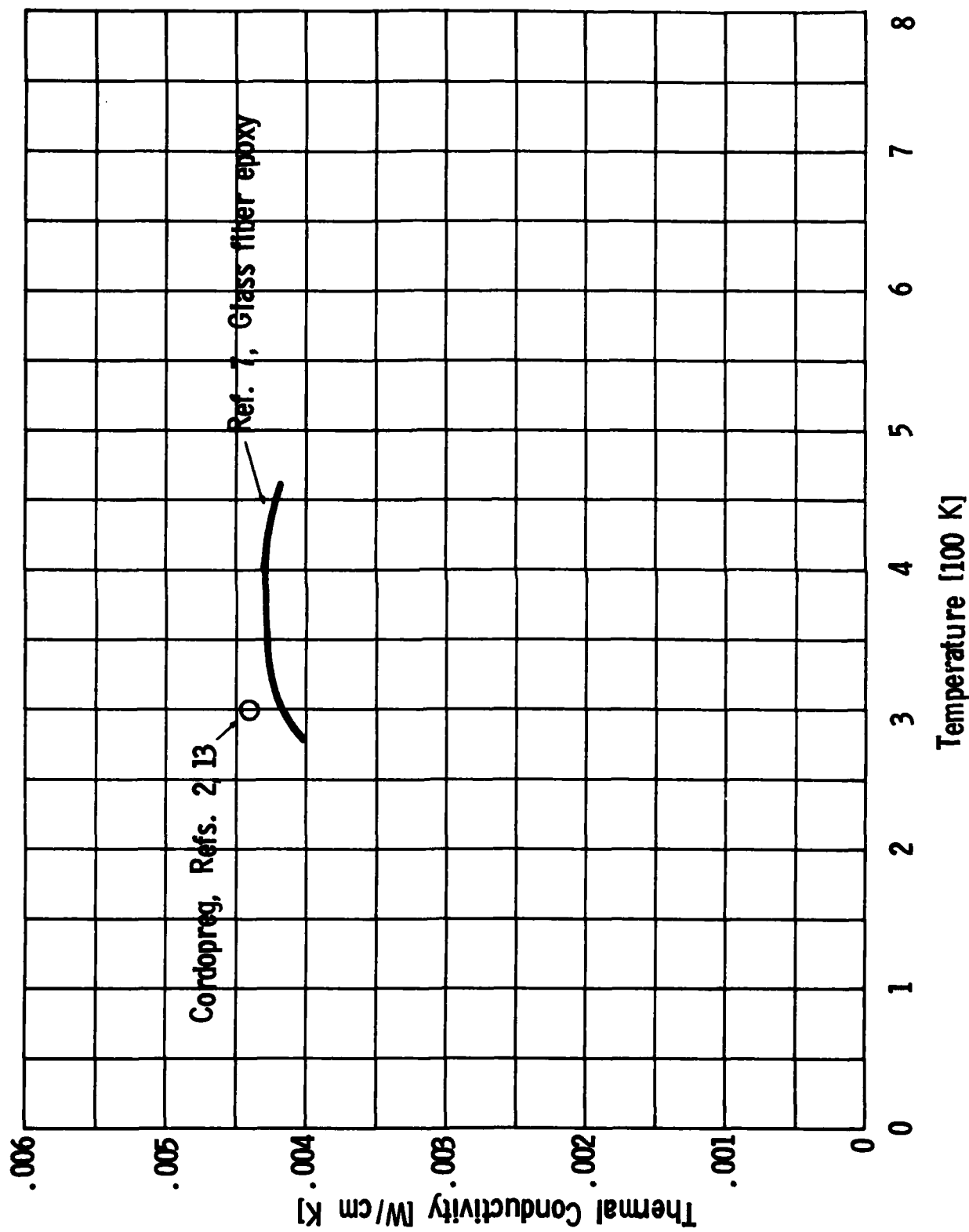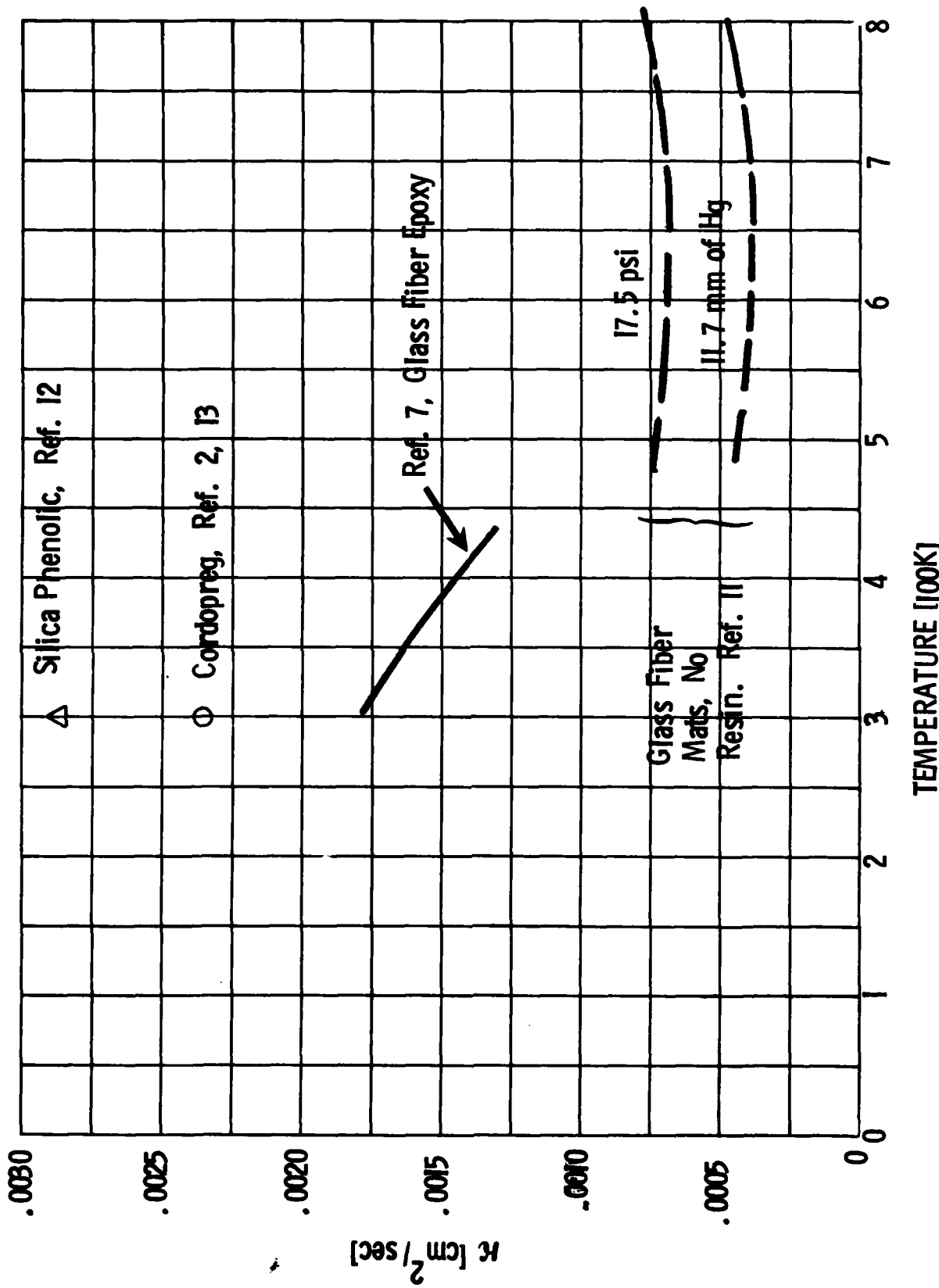
Fig. 9.12 Thermal Diffusivity of Several Fiberglasses as a Function of Temperature.

heat transport. As a first approximation, the properties of Cordopreg,[2] as listed in Table 9.2, are used for all temperatures throughout the interaction.

During the laser pulse it is possible that high surface temperatures will be attained and the glass will vaporize. As a first approximation to the behavior of glass at high temperatures, we use the properties of silica. Silica melts at 1996K, boils at 3130K, and has a heat of vaporization of 12500 J/gm. The energy required to take silica from a solid at room temperature to a melt at 2000K is 2156J/g, and it requires 3770 J/g to reach 3130K (liquid).

Resin does not melt or vaporize, rather it undergoes an irreversible decomposition reaction called pyrolysis. It is common to fit the observed pyrolysis rates with an Arrenhius type equation

$$\frac{\partial \rho}{\partial t} = - A\rho^n \exp (-B/T) \qquad (9.3)$$

where p is the resin density, T is the temperature, and A, B and n are constants. A time τ_{pyro}, which is characteristic of decomposition of a virgin resin at temperature T, is defined by

$$\tau_{pyro} = \rho / \left(\frac{\partial \rho}{\partial t}\right) = \frac{\rho^{1-n} \exp (B/T)}{A} . \qquad (9.4)$$

The pyrolysis time, as defined by Eq. 9.4, is plotted in Fig. 9.13 for a variety of resins, matrices, and heating rates.[12, 14, 15, 16, 17] This plot is not to be used as a source of detailed rates; rather, it is shown to demonstrate that the empirically deduced pyrolysis time is not only a function of temperature, but also a function of resin, matrix, heating rate and type of experiment.

However, despite the large discrepancies in the pyrolysis times a few conclusions can be drawn. Vaporization of glass occurs at a rapid rate at

TABLE 9.2

Properties used to model Cordopreg.

density	=	1.8 g/cm^3
thermal conductivity	=	4.4×10^{-3} W/K-cm
specific heat	=	1.05 J/g-K
thermal diffusivity	=	2.3×10^{-3} cm^2/sec

194
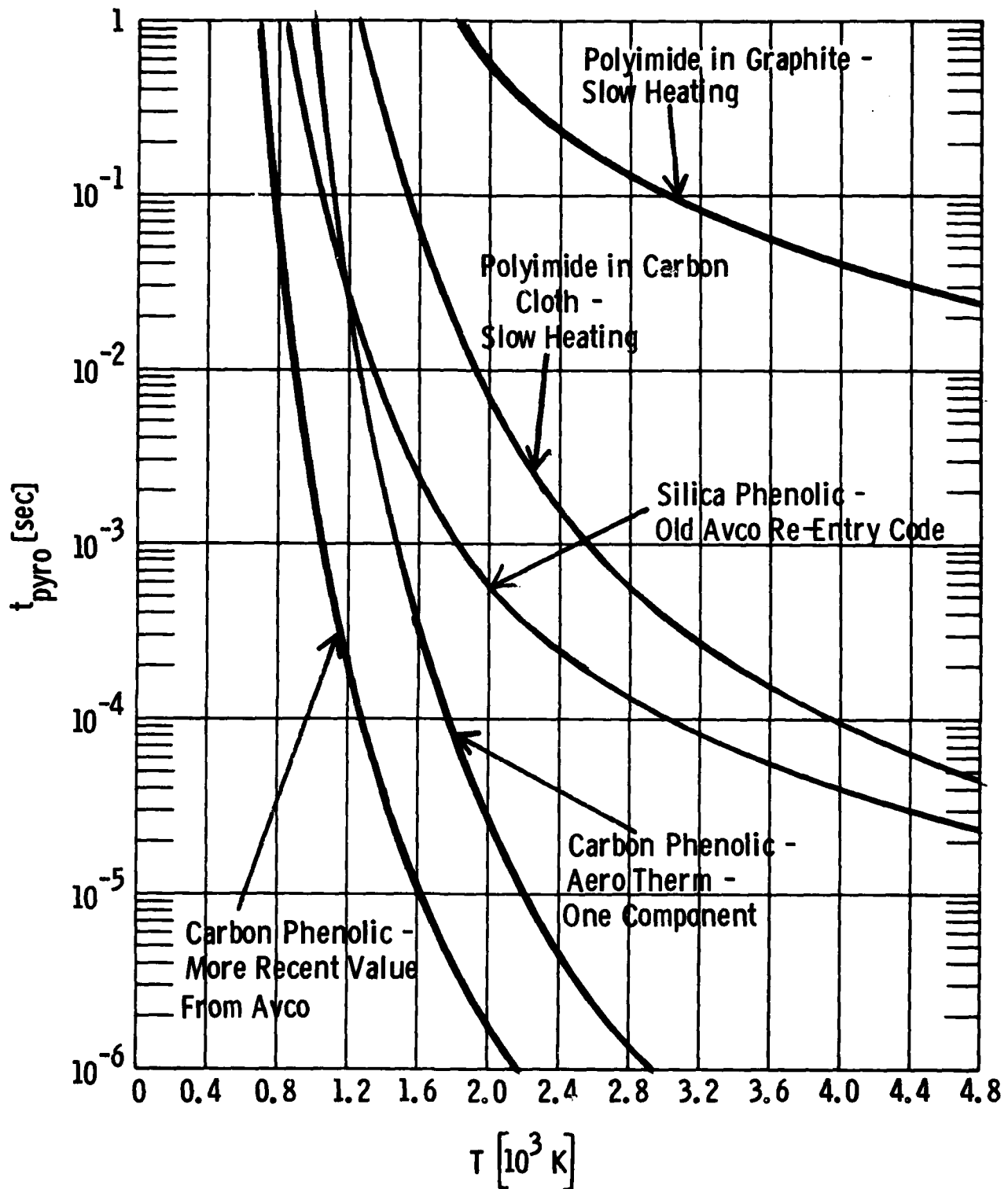
Fig. 9.13 Characteristic Time for Pyrolysis as a Function of
Temperature for Various Conditions.

195

3130K. If the target temperature is well below 3130K, say 2000K, all but
one of the curves shows that pyrolysis cannot occur on the time scale of
the pulse (10^{-5} sec). In fact, it is unlikely that any pyrolysis can occur
during the laser pulse unless temperatures are reached which are high
enough to cause vaporization of the glass. However, pyrolysis is predicted
by three of the curves to occur on the time scale of the interpulse time
(.1 sec) at modest temperatures such as 800 - 1100K. It seems likely,
therefore, that pyrolysis during the laser pulse coincides with glass vapor-
ization whereas pyrolysis between laser pulses is characterized by a
temperature near 950K.

The last property needed to describe fiberglass is the heat of pyrolysis
of the resin. The values listed in Ref. 12 for epoxy and phenolic are 1160 J/g
and 2210 J/g respectively. A more detailed analysis of the heat of pyrolysis
of silica phenolic[18] reveals that the heat of pyrolysis and the relative production
of volatiles and char varies with temperature. Some results of Ref. 17 are
summarized in Table 9.3.

This completes the discussion of the properties of dome materials. It
is clear that considerably more detailed and reliable values are needed before
accurate predictions of material response can be made, however, the values
discussed in the foregoing section are sufficient for constructing first order models
of the interaction.

TABLE 9.3

Thermochemistry of Pyrolysis (from Ref. 18).

Property	Temperature of Pyrolysis, K		
	672	872	1155
Virgin resin			
Standard heat of formation, ΔH_f (298°K)			
J/gm -2442			
Products of pyrolysis			
Fraction of resin volatilized, f	0.107	0.377	0.494
Volatiles			
Average molecular weight M g/mole	26.2	26.0	15.4
Average specifc heat, C_p, J/g-°C	1.97	1.93	2.18
Average heat of vaporization, cal/g	1210	444	193
Average standard heat of formation, ΔH_f (298°K)			
kcal/mole	-58.1	-23.9	-14.6
J/g	-9275	-3841	-3966
Resin char			
Standard heat of formation, ΔH_f			
J/g	-656	+295	+245
Standard heat of pyrolysis, $\Delta H_{298}^{°}{}_{py}$ (T)			
J/g resin	+862	+1176	+1724

SECTION 10

SINGLE PULSE INTERACTION - THEORY

The ability of a repetitively pulsed laser to penetrate a target can be studied in two sequential steps. First, the physics of the surface interaction must be understood; that is, a model must be developed which is capable of predicting the amount of thermal and mechanical energy transferred to the target. In the second step, the response of the target to the delivered energy is assessed. Since the first step deals with the interaction which occurs between the laser and the target on each pulse, the first investigations of this phenomenon need use only single pulse experiments.

There are several potential interactions between the laser radiation and the target; for example, the target may absorb the laser radiation directly, and mechanical coupling may occur as a result of vaporization of target material, or the laser may ignite a laser supported combustion wave which then transfers both thermal energy and impulse to the target. As discussed in the introduction, the properties of the various targets are not known well enough to allow a unique determination, on theoretical grounds alone, of the nature of the interaction. Instead, we adopt the approach of developing simple models to describe the effects expected under a variety of possible laser conditions, and then compare the theoretical predictions to experimental data in order to select the correct model. In this process, we also gain some information about the physical properties of the material.

In this section the various models of the surface interaction are developed in the following order: pressure response in absence of plasma, plasma ignition, pressure response after prompt air plasma ignition, pyrolysis contribution to pressure, energy requirements for mass removal, and limits on the fluence remaining in the material (hereafter called residual energy).

199

10.1   Pressure Response - No Plasma

When there is no plasma in front of the target, the only source of pressure is the vaporization of the target material. For a given surface temperature it is possible to make an estimate of the pressure exerted on the surface, but the relationship between the temperature, the absorbed intensity and the time depends upon the nature of the absorption process. We first develop the theory for surface vaporization following the approach of Pirri.[19] Studying this process will enable us not only to estimate time scales but also to determine the pressure as a function of temperature.

A simplified model for the vaporization of a surface irradiated by a high power laser in an air environment is illustrated in Fig.10.1. The target will be considered to be semi-infinite, and the laser pulse is specified as a step function in time. If the absorption is assumed to take place in a thin layer near the surface, the time to raise the surface to its vaporization temperature becomes[20]

$$\tau_v = \frac{\pi}{4} k_s \rho_s c_s \left(\frac{T_v - T_o}{I_s} \right)^2 \tag{10.1}$$

where k_s is the thermal conductivity, ρ_s is the solid density, c_s is the specific heat of the solid, T_v is the vaporization temperature, T_o is the initial surface temperature and I_s is the absorbed laser flux. For dome materials, which typically have absorptivities of .9 or greater, and a vaporization temperature of approximately 3100K, we find the following time scales, τ_v, for reaching the vaporization temperature using the average properties listed in Section 9.

$$
\begin{aligned}
&\text{pyroceram 9606} &&\tau_v = .7/I^2 \\
&\text{slip cast fused silica} &&\tau_v = .2/I^2 \\
&\text{fiberglass} &&\tau_v = .06/I^2
\end{aligned}
\tag{10.2}
$$
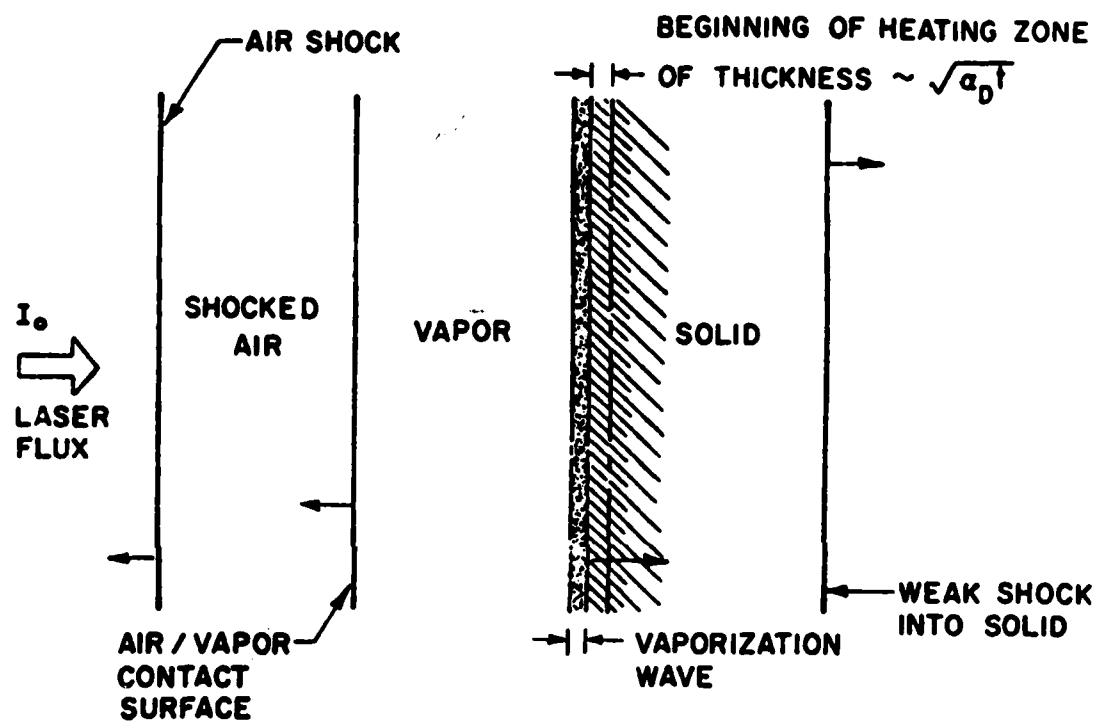
Fig. 10.1   Schematic of Model Used to Determine the Initial Vapor
Properties.   From Ref. 19.

where τ_V is given in microseconds and the incident laser intensity I is measured in MW/cm^2. These are very short times compared to the pulse length; vaporization should commence immediately for surface absorption.

Once the surface begins to vaporize, there is a characteristic time for the vaporization rate to approach its steady-state value. This time has been calculated by Landau[21] for the case of a solid that is melting due to a heat flux at the boundary. After this time the conditions at the surface are no longer affected by heat conduction. This time scale can also be estimated to be the time after which the surface recession velocity is approximately equal to the thermal diffusion velocity u_D ($u_D \sim \sqrt{K/t_s}$, where K is the thermal diffusivity and t_s is the time since the onset of vaporization). If the steady-state vaporization rate is estimated by

$$\dot{m} = \frac{I_s}{\Delta H_V} \tag{10.3}$$

where ΔH_V is the heat of vaporization ($H_V \sim 12500$ J/g), then steady-state vaporization is approached on the following times scales:

fiberglass	$t_s \approx 1.4/I^2$	
slip-cast fused silica	$t_s \approx 4./I^2$	(10.4)
pyroceram	$t_s \approx 9/I^2$	

where t_s is measured in microseconds and I in MW/cm^2. If the laser pulse time is greater than t_s, the maximum pressure on the surface is characteristic of steady-state vaporization. For ten microsecond pulse lengths, fiberglass and slip-cast fused silica should reach steady state vaporization for intensities greater than .6MW/cm^2, whereas pyroceram reaches steady state only for intensities above 1 MW/cm^2.

For times much less than t_s, the vaporization rate as a function of time can be estimated from an unsteady vaporization model which is presented later in this subsection.

After steady-state is reached, the vaporization of the surface is considered to take place across a "vaporization wave" which propagates into the solid (Fig. 10.1). The concept of a vaporization wave has been utilized by several authors,[22,23,24] and is more appropriate at much higher laser intensities where conduction is unimportant. However, once steady-state is attained, this phase change model is assumed, and the conduction effects serve as a precursor to the wave. The rapid evaporation of material drives a shock wave into the air, and a contact surface divides the shocked air from the vapor (Fig. 10.1). The solution for the vapor properties is obtained by satisfying conservation of mass, momentum and energy across each of the discontinuities.

Since the recession velocity of the solid surface (equal to the vaporization wave velocity) is much less than the vapor velocity, conservation of energy and momentum across the vaporization wave can be written

$$\rho u \left(h + \frac{u^2}{2} + H_v \right) = \alpha_s I \qquad \text{(energy)} \qquad (10.5)$$

$$p + \rho u^2 = P_s \qquad \text{(momentum)} \qquad (10.6)$$

where ρ, u and h are the vapor density, velocity and enthalpy, respectively, α_s is the surface absorptivity at the particular laser wavelength, I is the incident laser intensity, p is the pressure in the vapor and P_s is the surface pressure. Pressure and velocity are constant across the air/vapor contact surface, and the vapor velocity and pressure can be related using one-dimensional shock dynamics[25]

$$u = \frac{a_\infty}{\gamma_\infty} \left(\frac{p}{p_\infty} - 1 \right) \sqrt{\frac{2 \, \gamma_\infty / (\gamma_\infty + 1)}{\frac{p}{p_\infty} + \frac{(\gamma_\infty - 1)}{(\gamma_\infty + 1)}}} \qquad (10.7)$$

where a_∞, γ_∞ and ρ_∞ are the ambient sound speed, specific heat ratio and pressure, respectively. Since the vapor velocity will not exceed the vapor sound speed, Eq. (10.7) will only be utilized until $u = a$ where a is the sound speed. For these calculations, a simple state equation is used to relate the pressure, density and enthalpy of the vapor.

Equations (10.5) - (10.7) and the state equation yield a system of four equations for five unknowns. In addition, Vilenskaia and Nemchinov[22] and Thomas and Musal[23] assume that the vapor temperature and pressure can be related by a phase equilibrium expression, i.e., the vapor is assumed to be in local phase equilibirium on the vapor side of the vaporization wave. Kucherov and Rikenglaz[26] and Anisimov[27] have examined the vaporization kinetics in more detail, and they conclude that the equilibrium vapor temperature and the surface temperature are different. Anisimov relates the two temperatures using kinetic theory for the case of evaporation into a vacuum environment. He assumes that it is the surface temperature that can be related directly to the surface saturated vapor density. Therefore, it is assumed that phase equilibirum exists in vapor at some point close to the solid side of the vaporization wave and

$$p_s = p_m \exp\left(-H_v / R T_s \right) \qquad (10.8)$$

where p_m is a constant, R is the vapor gas constant and T_s is the surface temperature. Since energy is conserved throughout the vaporization wave, the surface temperature is assumed to be related to the equilibrium vapor temperature by

$$h\,(T)\ +\ \frac{u^2}{2}\ =\ h_s\ (T_s) \qquad\qquad (10.9)$$

where h_s is the vapor enthalpy at the surface temperature. Equation (10.9) is obtained by integrating the Clausius-Clapeyron equation. It can be shown by writing the rate equation for the evaporation process that using the phase equilibrium expression is a reasonable approximation provided $u < \beta a$, where β is the surface accommodation coefficient.

Equations (10.7) - (10.9) plus the vapor state equation can now be solved simultaneously to get the initial vapor properties and surface temperature as a function of the absorbed laser intensity I_s ($I_s = \alpha_s I$).

The steady-state surface pressure as a function of laser intensity has been calculated for a generic dome material, and is shown in Fig. 10.2. The pressure of the expanded vapor is also shown since it is used to determine the initial conditions for the plasma ignition studies of subsection 10.2. For the generic dome material, a normal boiling point of 3130K is assumed. The heat of vaporization for use in Eq. (10.8) is taken to be 12600 J/g and the value of R is .211 J/K; these values are designed to fit the pressure curve predicted by the equilibirium code (see Fig. 9.8). The value of γ_∞ is 1.4. The surface absorptivity of .85 has been used in the calculations shown in Fig. 10.2. It should be noted that if the actual vaporization temperature and heat of vaporization are less than the estimates used here, the correct surface pressure lies above the prediction shown in Fig. 10.2. The observed pressure should lie below the predictions only if steady-state vaporization has not been achieved.

In the above calculation, the vapor properties were calculated based upon the assumption that the vaporization rate has reached its steady-state value. It has been noted that the time scale for approaching the steady value is usually of the order of the time to raise the surface to its vaporization
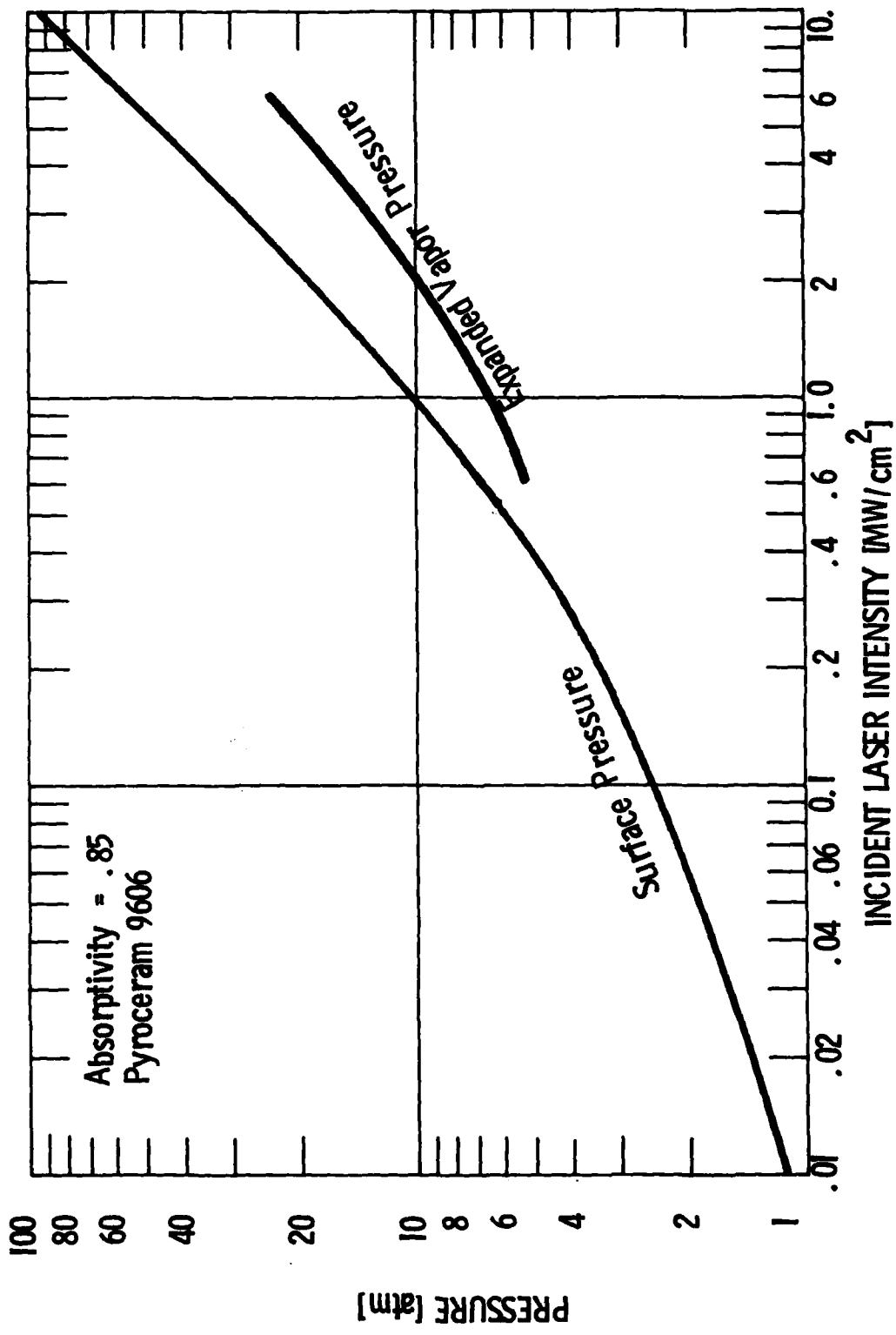
Fig. 10.2   Predictions of Steady State Surface Pressure and Pressure of Expanded Vapor for Pyroceram 9606 as a Function of Laser Intensity.

206

temperature (see Eq. 10.4). It is useful to estimate the time dependent properties more carefully.

In order to obtain the time dependent vaporization rate and the vapor/ solid thermodynamic state from the time when the laser pulse begins, it is necessary to solve the unsteady heat conduction equation with moving boundaries and a time varying surface radiation flux. One such detailed surface melting and vaporization computer code has been developed by Nash and McGill.[28] Such a code could be utilized to obtain the unsteady vaporization rate, but it was pointed out by Nash[29] that the asymptotic solutions of Boley[30,31] yield excellent agreement with numerical results.

Boley's asymptotic relations[30,31] will be used to obtain the vapor removal rate ρu as a function of absorbed laser intensity and time. For a step laser pulse in the limit of no melt layer formation and $(t - \tau_v) \to 0$, the first term result for the vaporization rate becomes[30]

$$\rho u = \frac{4 I_s^2 (t - \tau_v)^{1/2}}{\pi^{3/2} \kappa^{1/2} \rho_s c_s H_v T_v} \tag{10.10}$$

where I_s is the absorbed intensity, ρ_s is the target density, c_s is the target specific heat, H_v is the heat of vaporization, T_v is the steady-state vaporization temperature, and τ_v is the time required to reach the steady-state vaporization temperature in the absence of vaporization losses. Eq. (10.10) replaces Eq. (10.5) when the properties of the vapor are calculated as a function of time. It can be shown that the pressure, vapor temperature, velocity and density are only a function of the vaporization rate. If this early time expression for the vaporization rate is used to determine when steady-state vaporization is achieved, we find that the mass flux from Eq. (10.10) reaches the steady-state value of

$$\rho u = \frac{I_s}{c_s T_v + H_v} \tag{10.11}$$

at a time given by

$$t_s = \tau_v \left[1 + \left(\frac{\pi H_v}{2(c_s T_v + H_v)} \right)^2 \right] \approx 2.6\, \tau_v \,. \qquad (10.12)$$

The steady-state times defined by Eq. (10.12) are:

$$\text{pyroceram} \qquad t_s = 1.8/I^2$$

$$\text{slip-cast fused silica} \qquad t_s = .5/I^2 \qquad (10.13)$$

$$\text{fiberglass} \qquad t_s = .16/I^2$$

where t_s is measured in microseconds and I is measured in MW/cm^2. The times listed as Eqs. (10.13) are substantially shorter than those listed as Eqs. (10.4). The values listed as Eqs. (10.13) are believed to underestimate the onset of steady-state -- based on simple arguments they correspond to a mass flux of approximately half the steady-state value. The times listed as Eqs. (10.4) overestimate the time to achieve a substantial fraction of the steady-state mass flux. The experiments measure the peak pressure observed during the laser target interaction and therefore are sensitive to the mass flux rather than the details of how the steady-state temperature profile is attained; the characteristic time for the production of a substantial fraction of the steady-state pressure lies between the two estimates listed as Eq. (10.4) and Eq. (10.13).

For fiberglass and slip-cast fused silica, the steady-state pressure is reached within ten microseconds for laser intensities above .4 MW/cm^2 and .6 MW/cm^2, respectively. For pyroceram, the steady-state pressure is reached within ten microseconds only at intensities above 1 MW/cm^2, but half of the steady-state pressure can be produced within 10 μ sec. at intensities of only .4 MW/cm^2. For 20 μ sec. pulses, the intensities required to reach a given fraction of the steady-state pressure are .707

of the intensities required for a 10 μ sec pulse. Based upon the above cal-
culations, the steady-state pressure shown in Fig. 10.2 is representative
of the peak pressure expected as the result of surface absorption of laser
energy by dome materials.

In Section 9, it was mentioned that measured values of the absorp-
tion depth of 10.6 μm radiation in silica range from 4 μm to 20 μm.
The thermal depth of typical dome materials after a ten microsecond pulse
is only 1.5-3 μm. If the absorption depth of silica is typical of the absorp-
tion depth of the dome materials, absorption of the laser occurs in-depth,
and the character of the pressure onset is changed dramatically. No bulk
vaporization can occur before enough energy has been deposited to heat the
surface to the vaporization temperature (or higher). Thus, a threshold for
vaporization occurs as a function of fluence (the product of laser intensity
I and time t);

$$ It \geq \frac{\rho_s \Delta H}{\kappa_L} \approx \frac{\rho_s c_s \Delta T}{\kappa_L} \qquad (10.14) $$

where κ_L is the absorption coefficient at $\lambda = 10.6$ μm, ρ_s is the density,
c_s is the specific heat, ΔT is the temperature difference between room
temperature and the vaporization temperature T_v, and ΔH is the enthalpy
change of the material as the temperature is raised to T_v. (If there are
phase changes between room temperature and T_v, it is important to use the
enthalpy difference.)

From the properties given in Section 9, the product $(\kappa_L It)$ required
to reach 3130K is 5.3, 6.3 and 9.5 kJ/cm^3 for fiberglass, slip-cast fused
silica, and pyroceram, respectively. For an assumed absorption depth of
6 μm, the threshold fluences become 3.2, 3.8 and 5.7 J/cm^2, respectively.

Rapid vaporization does not begin immediately after the temperature
reaches the vaporization point; the heat of vaporization must also be supplied.

The vaporization mass flux can approach the steady-state vaporization limit only after both the heat of vaporization H_v and the enthalpy difference ΔH required to reach T_v are supplied locally; that is,

$$\kappa_L It \geq \rho \ (\Delta H + H_v). \tag{10.15}$$

For the dome materials of interest, the local deposition of energy must exceed $25 kJ/cm^3$ (fiberglass), $26 kJ/cm^3$ (slip-cast fused silica), and $29 kJ/cm^3$ (pyroceram) in order to reach steady-state vaporization. In these estimates the normal boiling temperature has been used. At high intensities the temperature for steady-state vaporization is somewhat higher and therefore more energy must be deposited to reach steady-state vaporization, however, the change in enthalpy is small so that Eq. (10.15) serves as a suitable first order estimate.

Note that the time difference between the onset of vaporization and the onset of steady-state vaporization is large -- a factor of three to five. For the expected values of the in-depth absorption coefficient (4 to 20 μm), typical fluences required to reach steady-state vaporization are 10 to 60 J/cm^2. Therefore, if in depth absorption does occur, the pressure as a function of absorbed fluence should lie below the steady-state value calculated earlier until fluences of 10 - 60 J/cm^2 are reached. These are within the range of fluences used in the experiments and therefore, a threshold behavior should be seen if the absorption of the laser occurs in-depth.

There is a large fluence regime between the start of vaporization, when the front surface reaches T_v, and the onset of steady-state vaporization. Vaporization kinetics are fast enough to permit the steady-state vaporization rate to be attained instantaneously, but local energy conversation must be satisfied and it controls the approach to steady-state. As a first estimate of the rate of increase of the pressure we assume that some of the energy absorbed behind the surface is transferred to the surface by thermal conduction. The energy expended at the surface to vaporize the material acts

as a heat sink; therefore, the surface temperature stays close to the vaporiz-
ation temperature while the temperature of the material immediately
behind the surface is increasing. The temperature profile close to the
surface shortly after the start of vaporization is sketched in Fig. 10.3. The
depth of the thermal wave is approximately $\sqrt{\kappa\,(t-t_v)}$, where κ is the thermal
diffusivity and t_v is the time at which the surface reaches T_v (see Eq. (10.14)).
The rate of laser energy deposition into the region occupied by the thermal
wave is approximately $\kappa_L\,I\,\sqrt{\kappa\,(t-t_v)}$ where κ_L is the absorption coeffi-
cient and I is the absorbed laser intensity. If all the energy absorbed in the
thermal depth is available for supporting vaporization, the relationship
between laser intensity, time and mass flux becomes

$$\rho\,u\left(\frac{u^2}{2} + H_v\right) = \kappa_L\,I\,\sqrt{\kappa\,(t-t_v)}\ . \qquad (10.16)$$

This expression replaces Eq. (10.5) and is used only until the thermal
depth reaches the absorption depth or local energy absorption is sufficient
to vaporize the surface (see Eq. 10.15). Thereafter, steady-state vaporization
commences. (The onset of steady-state vaporization is usually determined
by Eq. 10.15 rather than the thermal depth reaching the absorption depth.)
For an assumed absorption depth of 17 microns, the pressure predicted by
in-depth absorption by fiberglass for 10 and 20 microsecond pulses are
shown in Fig. 10.4. The steady-state prediction is also shown.
Note that at low intensity the predictions using in-depth absorption depart
significantly from the steady-state pressures. Since the predictions made
assuming surface absorption lie on the steady-state curve for intensities
above .4 MW/cm^2, experimental measurements of the pressure should
permit a determination of the correct absorption mechanism.
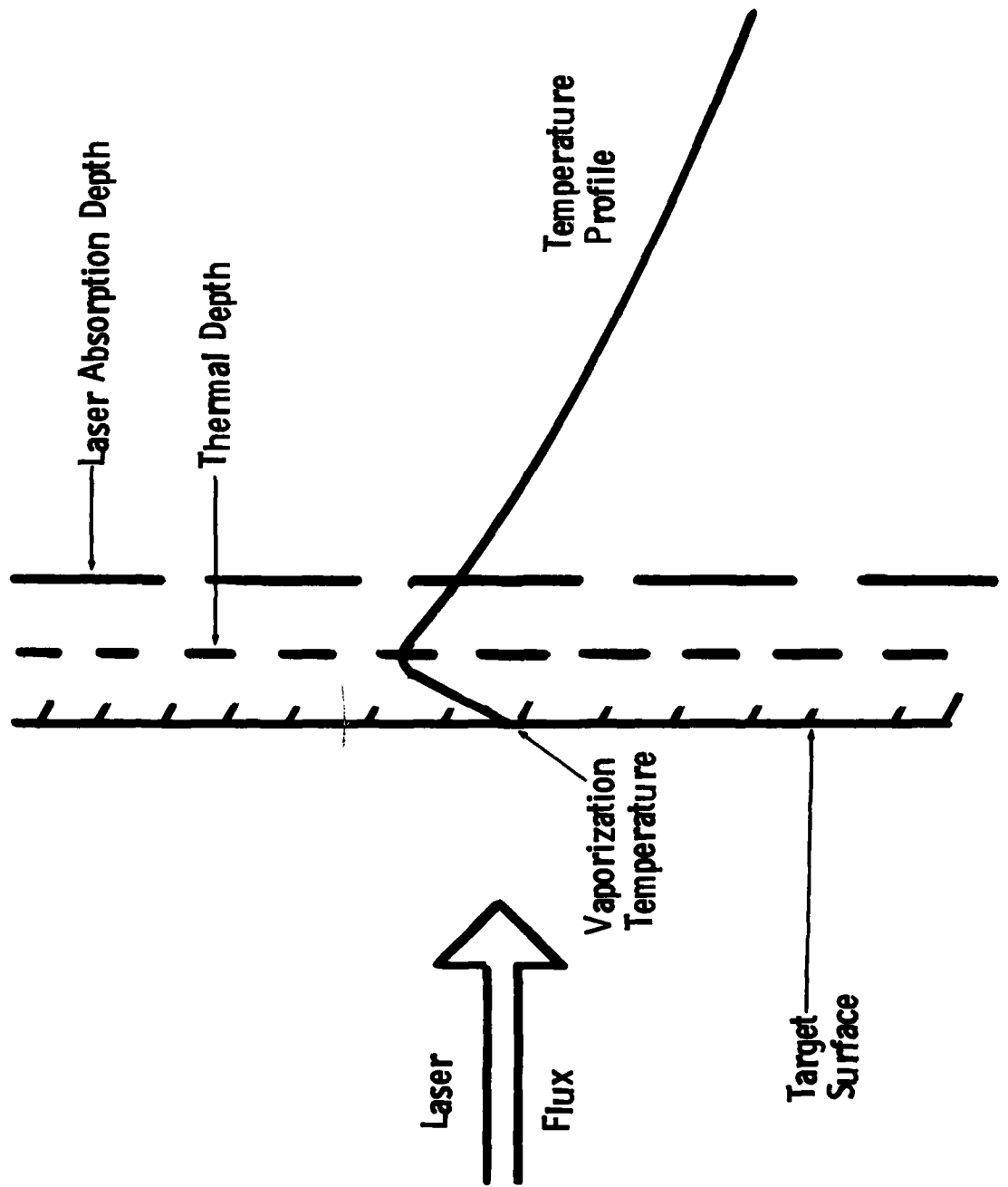
Fig. 10.3 Sketch of Temperature Profile in Target Which Absorbs in Depth Shortly After Vaporization Commences.

212
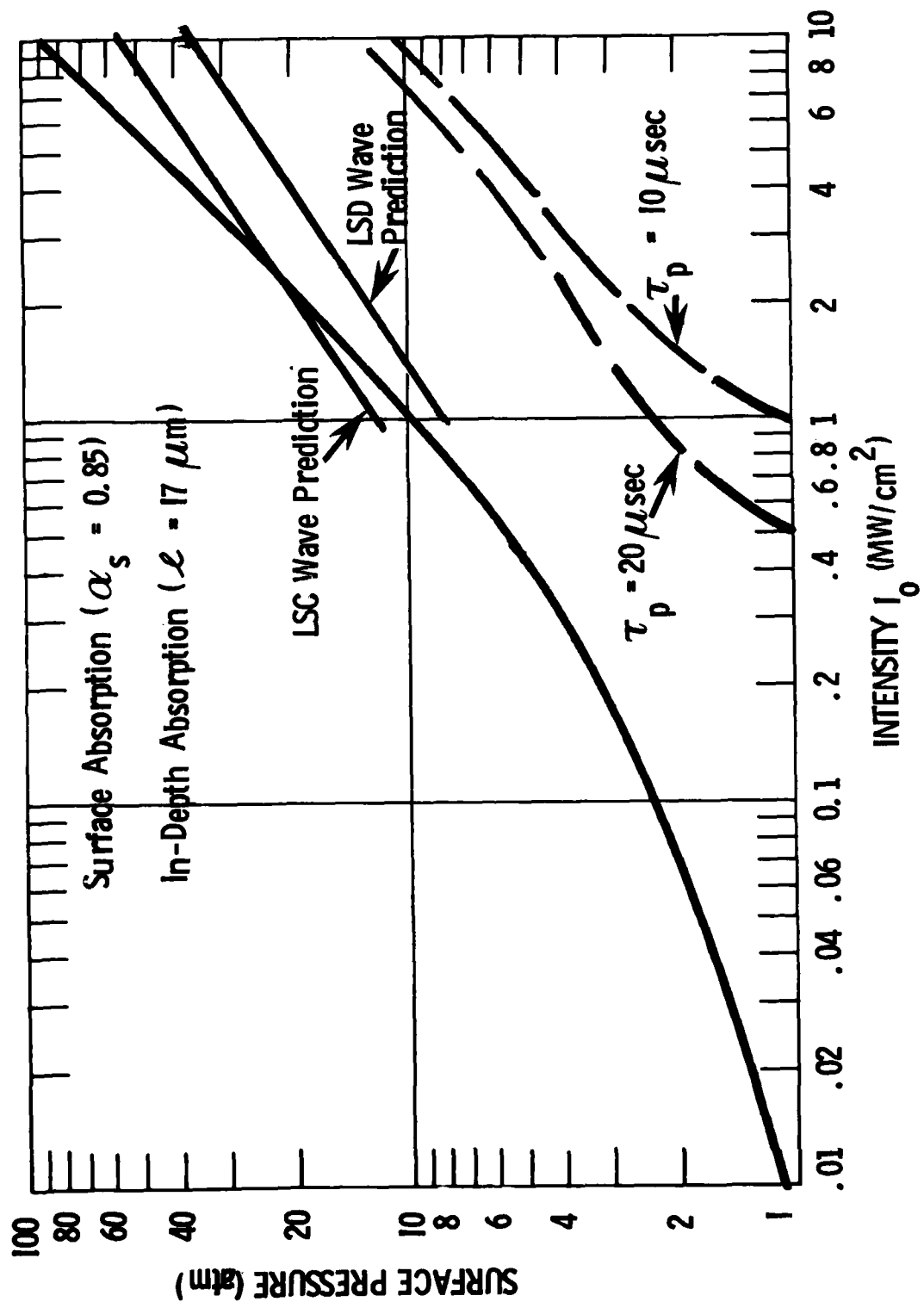
Fig. 10.4   Surface Pressure Predictions for Fiberglass.

213

10.2   Plasma Ignition

In the study of metals it was found that plasmas could be ignited
by two competing routes -- prompt ignition during the gain switch spike
caused by surface defects, and plasma ignition in the products of bulk
vaporization. Prompt ignition is the result of surface defects; it is expected
to depend on details, which are not known at present, of the microscopic
structure of the surface. However, prompt ignition is easy to identify in
that it occurs quickly, and it does not require the bulk production of vapor.
Difficulty in separating prompt ignition from bulk vapor ignition arises only
if bulk vaporization occurs during the gain switch spike. Vapor dominated
ignition is the result of heating the bulk vapor in thermodynamic equilibrium
until such time as the vapor becomes sufficiently ionized to absorb the
laser radiation strongly. (There are also regimes of intensity where the
heating of the vapor may create a difference between the electron
temperature and the vapor temperature, but at low laser intensities the
temperature difference is negligible and equilibrium vapor heating
adequately describes the ignition process.)

In principle, the heating of the bulk vapor in equilibrium is easy to
model. The effective absorption coefficient k_L' for laser radiation is a
unique function of pressure and temperature, as are the density ρ and heat
capacity at constant pressure c_p. It is assumed that the heating occurs slow
enough to maintain constant pressure. The temperature T of the gas is
then governed by the equation

$$\rho \, c_p \, \frac{dT}{dt} = k_L' \, I \qquad\qquad (10.11)$$

where I is the laser intensity. Therefore, for fixed initial temperature
T_o the temperature of the vapor can be given as a function of the laser
fluence:

$$\int_{T_o}^{T} \frac{\rho \, c_p \, dT}{k_L'} = It \quad .$$

<div align="right">(10.18)</div>

The determination of the initial conditions and of the laser absorption coefficient requires detailed knowledge of the vapor composition. As a specific example, consider the ignition of a plasma by heating the vapor products of pyroceram 9606 with an incident laser intensity of 5 MW/cm^2. Pyroceram contains a large fraction of Al_2O_3, and AlO, which is present in the vapor, is known to be a strong absorber of 10.6 μm radiation. Moreover, as mentioned in Section 9, the compositions of pyroceram and E-glass are fairly similar, although the nature of the solid, that is presence and absence of crystals, is substantially different. Equilibrium calculations of the vapor of SiO_2 (slip-cast fused silica) indicate that the number of free electrons is negligible and that the oxide SiO is not a strong absorber of 10.6 μm radiation. Therefore, the calculation of vapor ignition for pyroceram should also be representative of E-glass and sets a lower limit on plasma ignition in the vapor from slip-cast fused silica.

The first step is to determine the composition and density of the vapor from the target. Pyroceram does not correspond to a single unit or molecule, so the vapor pressure of the various "elements" of the composition must be determined. As discussed in Subsection 10.1, we treat liquid pyroceram as an ideal liquid of five parts SiO_2, three parts Al_2O_3 and two parts MgO. The equilibrium vapor compositions of liquid SiO_2, Al_2O_3 and MgO are obtained from an equilibrium code which solves the law of mass action and uses the partition functions given by the JANAF tables[5]. The curve of vapor pressure versus temperature is shown in Fig. 9.8. The composition of the pyroceram vapor has been calculated as a function of vapor temperature for two different initial conditions: (1) equilibrium heating of the vapor at a constant surface pressure corresponding to steady-state ablation induced by the absorption of 5 MW/cm^2, and (2) equilibrium heating of the expanded vapor which

has left the surface. This expansion occurs during the acceleration of the vapor products to the sonic choking velocity and is accompanied by cooling of the vapor. The details of how both the surface pressure and the expanded vapor pressure are determined are discussed in the Subsection 10.1 .

The composition of pyroceram vapor at 68 atm. pressure is shown as a function of temperature in Fig. 10.5. The relative abundance of the various atomic species is determined by demanding that the vapor be in equilibirum with the liquid at 4200K.

Once the composition of the vapor is known, the laser absorption co-efficient can be calculated. Several processes contribute to the absorption: molecular absorption by SiO_2 and AlQ neutral inverse Bremsstrahlung in which the electron collides with a neutral heavy particle, and ion Bremss-trahlung in which the electron collides with an ion. Neutral inverse Bremss-trahlung dominates ion inverse Bremsstrahlung unless the ion concentration exceeds about one percent of the neutral concentration. For purposes of dis-cussion it is convenient to separate the total laser absorption coefficient k_L' into two terms -- one representing the inverse Bremsstrahlung contribution, k_{IB}', and one representing molecular absorption, k_{MOL}':

$$k_L' = k_{IB}' + k_{MOL}' .$$

(10.19)

The effective absorption coefficient for inverse Bremsstrahlung, in-cluding the effect of stimulated emission, has the form

$$k_{IB}' = \left(1 - e^{-\frac{hc}{\lambda k T}}\right) n_e \sum_i n_i Q_i$$

(10.20)

216
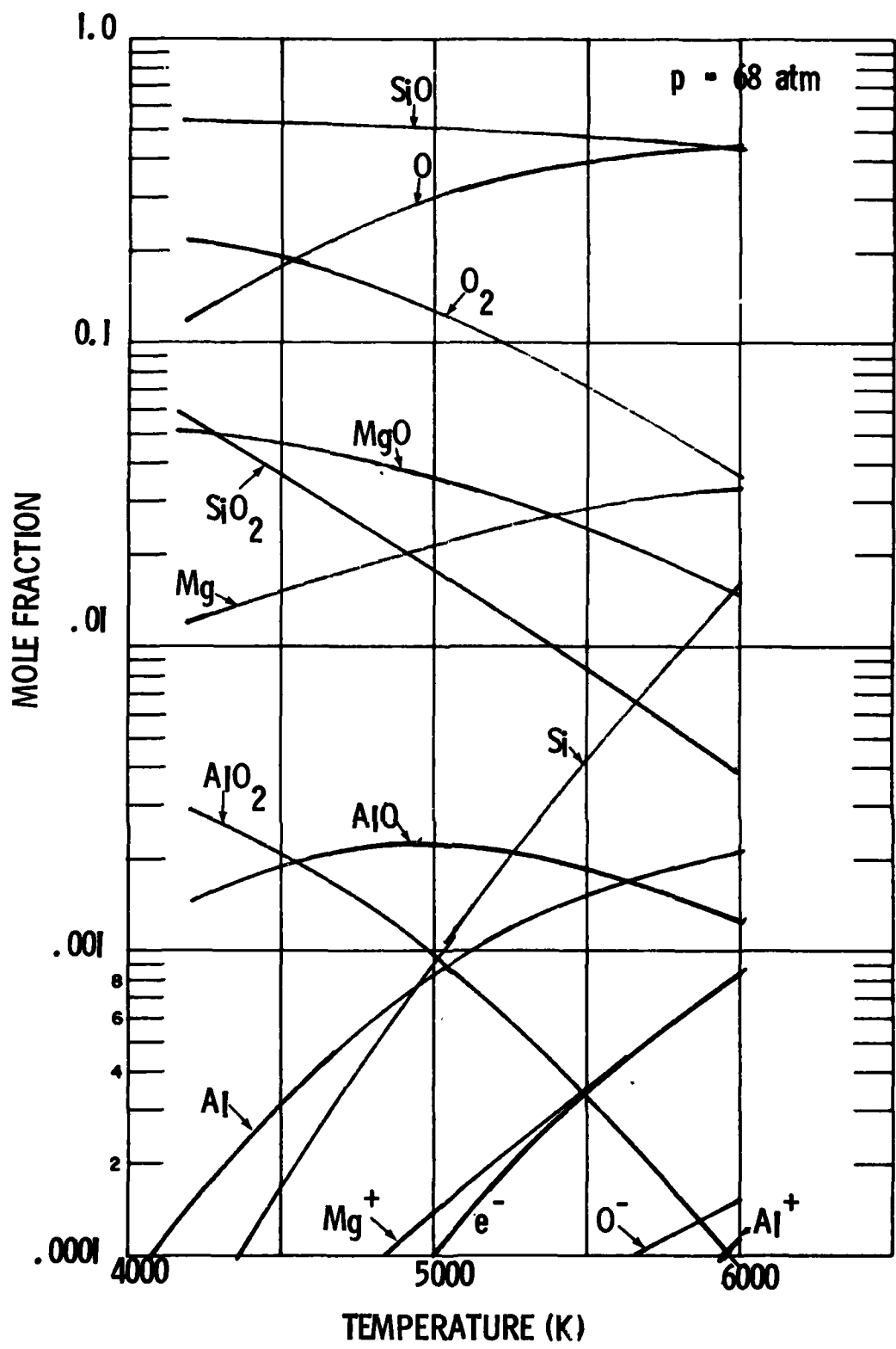
Fig. 10.5 Composition of Pyroceram 9606 Vapor as a Function of
Temperature for a Vapor Pressure of 68 atm. Original
Composition Chosen to be in Equilibrium with Liquid at
4200K and 68 atms.

217

where k is the Boltzmann constant, h is the Planck constant, c is the velocity of light, λ is the laser wavelength, T is the vapor temperature, n_i is the concentration of the species i (e is used for electrons), and Q_i is the cross-section for inverse Bremsstrahlung absorption by an electron colliding with species i.

The species considered are Al, Mg, Si, O, e, AlO, Al_2O, Al_2O_2, MgO, SiO, O_2, SiO_2, O_3, Si_2, Si_3, Al, AlO^+, Al_2O^+, $Al_2O_2^+$, Mg^+, O^+, SiO^+, O_2^+, SiO_2^+, Si^+, O^-, O_2^- and AlO_2^- . The cross-sections for neutral inverse Bremsstrahlung are not well known, but generally their magnitude is approximately .01 of the cross-section for ion inverse Bremsstrahlung. In the calculations discussed here, the cross-sections listed in Table 10.1 have been used, - they represent a synthesis of experimental results, such as those of Taylor and Caledonia,[32] of theoretical models, such as that of Hyman and Kivel,[33] and order of magnitude estimates in the case of molecules for which no information is available. The cross-section for electron-ion inverse Bremsstrahlung also is listed in Table 10.1.

Molecular absorption involves detailed calculations of the position and the width of lines corresponding to transitions between different vibrational levels. Metal oxides often have rotational-vibrational bands in the neighborhood of 10.6 μm. Detailed examination reveals that the spectral band for MgO does not include 10.6 μm; only the tail of the SiO band overlaps 10.6 μm; and AlO has a large cross-section which has previously been calculated.[34]

The SiO contribution was taken from the calculations by Boni and Tripplett[35] which use an overlapping line model. The collision broadening of the lines is substantial at the high pressures expected in the vapor and the use of an overlapping line approximation is justified. From Fig. 23 of Ref. 35, the absorption coefficient is found to be 2.5×10^{-4} $(atm\ -cm)^{-1}$ where the pressure refers to the total pressure of all the components of equilibrium SiO_2 vapor. Since SiO constitutes approximately .6 of the

TABLE 10.1

Inverse Bremsstrahlung Cross-Sections.

Species	$Q\,[\text{cm}^{-5}]$
positive ion	$\dfrac{1.63 \times 10^{-32}}{\sqrt{T[K]}}\; g$ for $g = 1.25$
Al	$6.4 \times 10^{-40}\; T[K]$
Mg	$7.2 \times 10^{-40}\; T[K]$
Si	$5.0 \times 10^{-40}\; T[K]$
O	3×10^{-36}
O_2	1.2×10^{-35}
AlO SiO MgO	6×10^{-36}

total vapor pressure, the effective absorption coefficient of SiO is 4.2×10^{-4} $(atm-cm)^{-1}$ where the pressure now refers only to the partial pressure of SiO.

The molecular absorption by AlO has been calculated in great detail in Ref. 34. The collision broadening at the expected pressure is so large that the predicted absorption is insensitive to the exact value of the collision broadening parameter. One modification was made to the calculation presented in Ref. 34 -- an improved value of the oscillator strength of the vibrational-rotational transitions were used. This value, deduced by Sulzmann,[32] is 3.22×10^{-5}. A plot of the calculated laser absorption coefficient corresponding to the compositions shown in Fig. 10.5, is shown in Fig. 10.6. The molecular absorption contribution and the inverse Bremsstrahlung contribution are also given.

In Fig. 10.7 the vapor temperature is shown as a function of fluence for two initial conditions. In the expanded vapor, which is at 27 atm., heating to a modest temperature of 4700K (the temperature at which strong inverse Bremsstrahlung absorption can rapidly heat the vapor to high temperatures) requires a fluence of $400 J/cm^2$. For an incident laser intensity of 5 MW/cm^2, this corresponds to an 80 microsecond pulse. At an initial vapor pressure sixty-eight atmospheres, a fluence of approximately $50 J/cm^2$ is needed to obtain a fully ionized plasma. For a laser intensity of 5 MW/cm^2, this corresponds to a ten microsecond delay after steady-state vaporization commences. This long delay permits vapor dominated ignition to be distinguished from prompt ignition during the gain switched spike. Furthermore, bulk vapor ignition is not expected except for long laser pulses at high intensity.

If the experiments indicate that plasma ignition occurs in the bulk vapor, calculations must be done for other laser intensities. Furthermore, the role of the non-equilibrium effects, such as the electrons having a temperature different from the vapor temperature, must be examined in detail, and the initial conditions of the vapor must be more accurately specified.

220
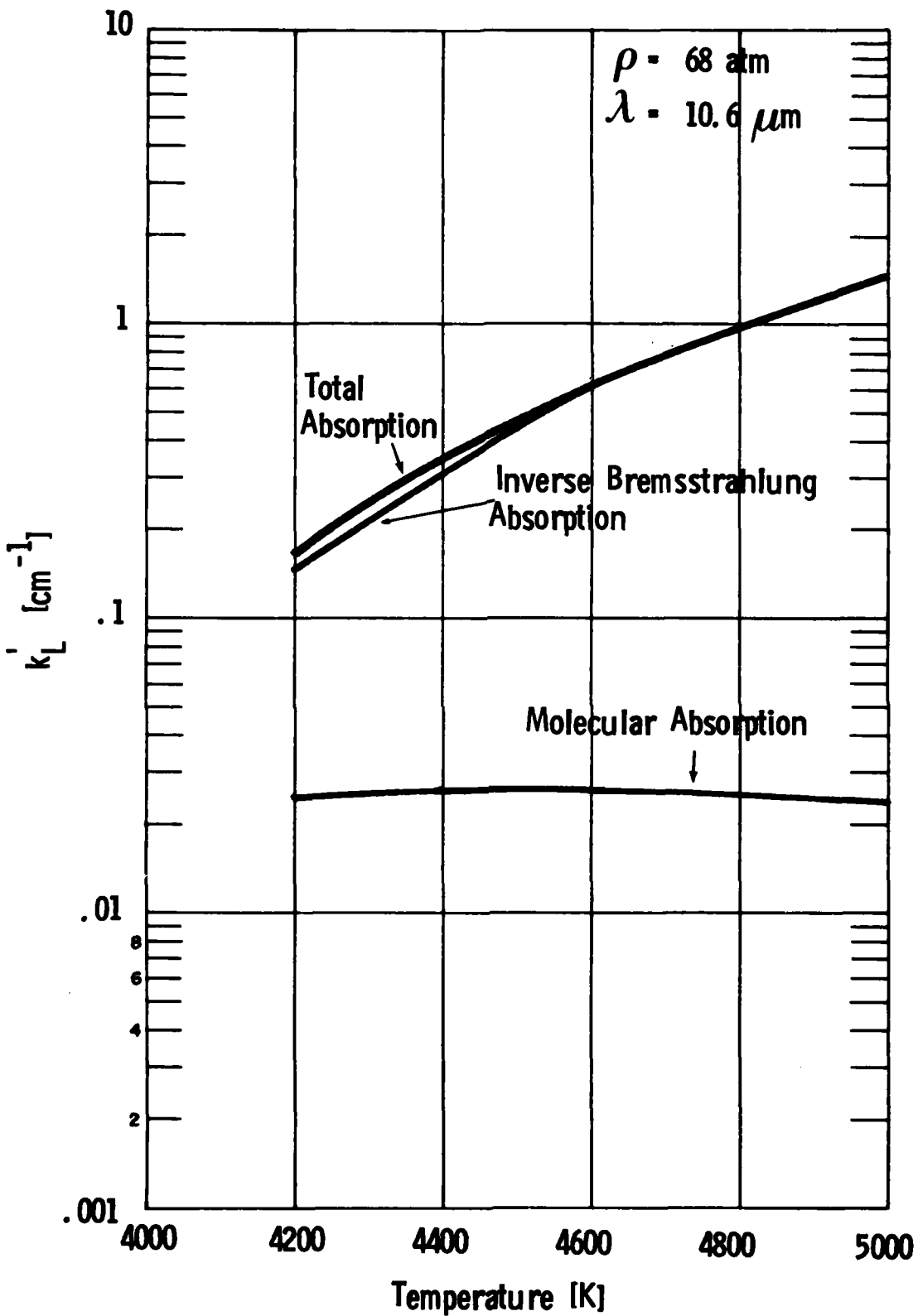
Fig. 10.6   Effective Absorption Coefficient for 10.6μm Laser Radiation
            for Pyroceram Vapor at 68 atm.
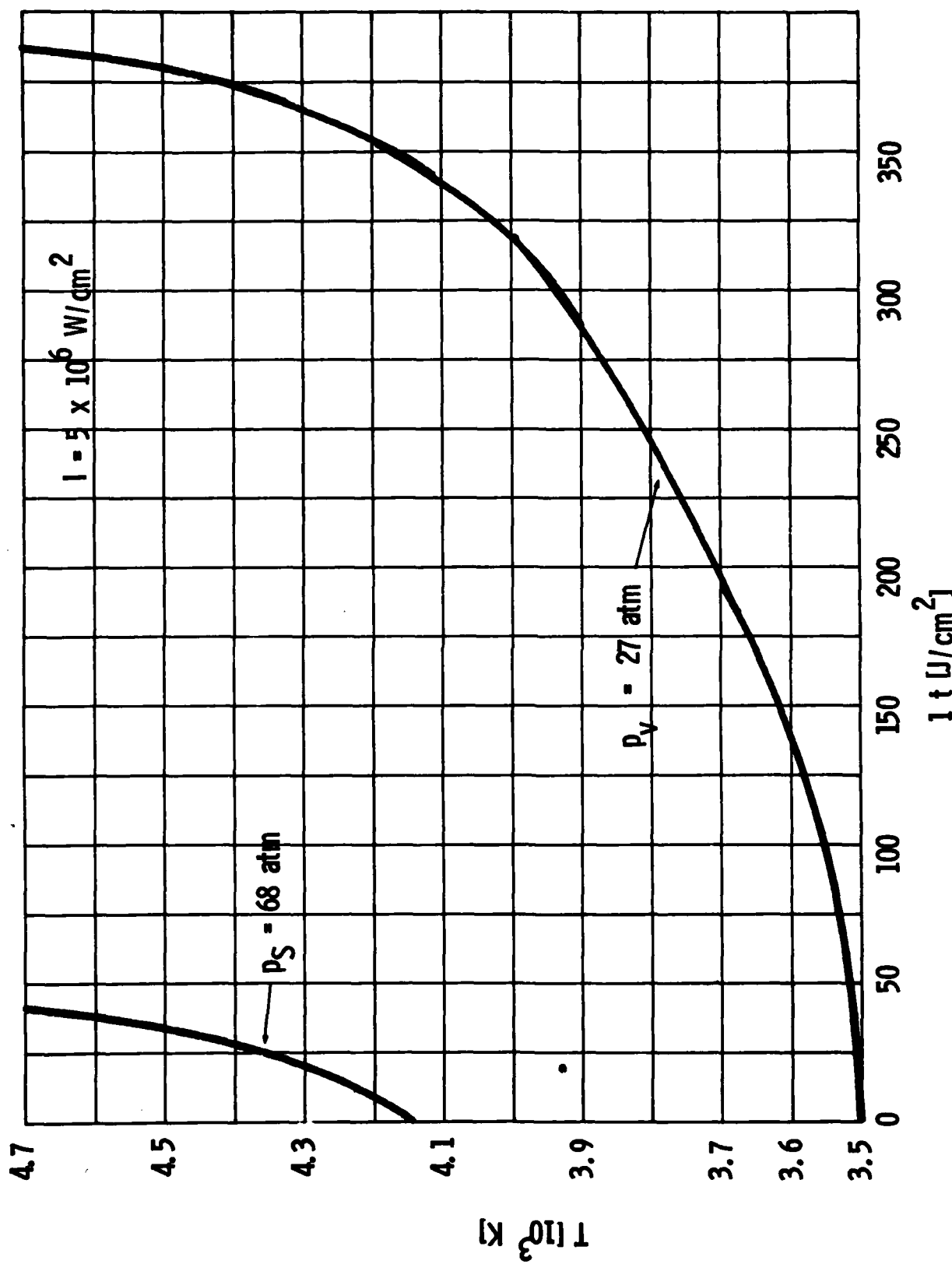
Fig. 10 7 Temperature of Pyroceram Vapor Heated at Constant Pressure by 10 6μm Radiation Two Initial Vapor Pressures are Shown and the Temperature is Plotted as a Function of Incident Laser Fluence.

10.3 Pressure Response -- Plasma Ignited

If a plasma is created by spike ignition from defects or highly absorbing sites, the plasma is an air plasma and is well described by the analysis of laser supported combustion waves in Part I of this report. The pressure response is expected to be identical to the response observed over metal targets; it is given by LSC wave theory at low intensities (below 3 to 4 MW/cm^2) and LSD wave theory at high intensities (above 8 MW/cm^2) with a transition zone in between. These predictions are also plotted in Fig. 10.4 for comparison with the "no plasma" predictions. Note that the predictions for LSC wave plasma and for steady-state vaporization are equal in the region near 1-2 MW/cm^2, and can be distinguished only at higher intensity. Furthermore, the onset of the LSC/LSD wave pressure is rapid; it occurs on a time scale of approximately one microsecond. Time resolved pressure histories can distinguish between prompt plasma ignition and vaporization as a result of in-depth absorption.

The above calculations were made assuming that no vaporization occurred as a consequence of the radiative transfer from the plasma to the target.

The effect of vaporization on the surface pressure can be ascertained as follows. Assume that a fraction of the incident laser energy is coupled into the target by plasma reradiation. The steady-state surface pressure can be estimated by using the model for steady-state vaporization presented in Subsection 10.1, but with the modification that the ambient pressure be replaced by the pressure of the laser absorption wave. In Fig. 10.8 the predicted pressure for an incident laser intensity of 2 MW/cm^2 is shown as a function of the thermal coupling coefficient. The mass flux is also shown. The pressure is only minimally above the value expected if there were no vaporization, even for thermal coupling coefficients as large as .6.
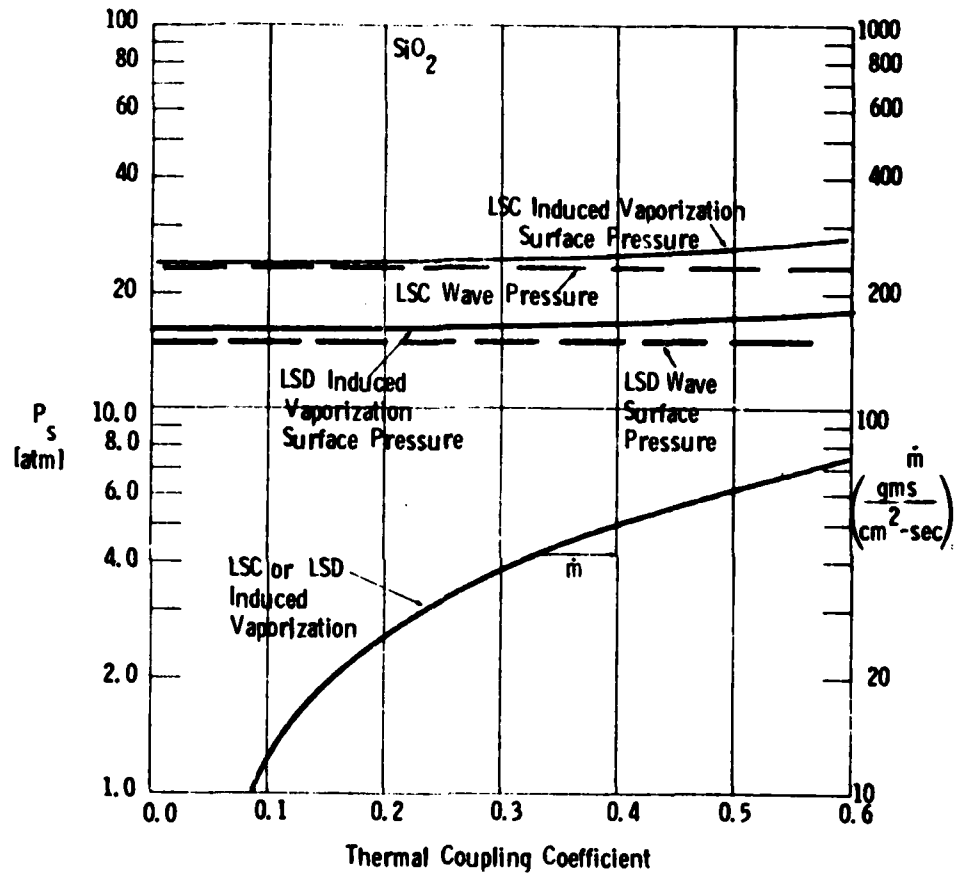
Fig. 10.8 Effect of Vaporization Induced by Plasma Reradiation
on the Surface Pressure and Mass Loss Rate of SiO_2.

The time integrated thermal coupling coefficient is expected to be less than
.3, and the instantaneous coupling is usually less than .1 (see Part I). Vapor-
ization into the high pressure plasma does not enhance the surface pressure
significantly unless the vaporization rate is high enough to produce, in one
atmosphere background gas, pressures of the order of the LSC wave pres-
sure. Even with 30 percent coupling, the mass flux in the LSC wave regime is
too low to lead to a substantial pressure increase, as can be seen from
Fig. 10.4 by comparing the LSC wave pressure corresponding to an
intensity I with the steady-state vaporization pressure corresponding to
an intensity of .3I. In the LSD wave regime, the thermal coupling
coefficient falls far below .3, and the radiation induced pressure is much
less than the LSD wave pressure. Therefore, the pressure predicted
for an LSC wave or LSD wave with radiation induced vaporization is
essentially the same as for the laser absorption wave without vaporization.

It is also possible that vaporization begins first and that a plasma is
subsequently ignited in the vapor. This ignition process has been
examined in Subsection 10.2. It was found that vapor dominated plasma
ignition is improbable except at intensities greater than 5 MW/cm^2, and
there is a detectable delay time. In order to predict the plasma pressure,
the structure of the vapor absorption wave must be modeled. This
possibility is not pursued here; it is merely noted that since this
mechanism first requires that a vapor be produced, and since there is
a delay between vapor production and plasma ignition, if this occurs, the
pressure history at early times must be consistent with the vaporization
model (with no plasma).

10.4 Pressure Caused by Pyrolysis

In addition to the pressure produced by uniform vaporization of the dome materials, which is discussed in Subsection 10.1, fiberglass may exhibit anomolous behavior because of the pyrolysis of resin. The vapor production by pyrolysis generally proceeds at a rate limited by the kinetics of the decomposition reaction rather than at the rate controlled by equilibrium considerations as is the case in vaporization. Furthermore, pyrolysis can occur at much lower temperature than vaporization, although the rate is quite slow. As mentioned in Subsection 9.4, for the values of pyrolysis rates, which we have available, rapid pyrolysis can only occur at temperatures so high that glass vaporization is also predicted. However, if the fluence is insufficient to reach these high temperatures, the only mass loss mechanism available is pyrolysis. Moreover, pyrolysis may persist long after the pulse has terminated, since the time for the temperature of the material to cool to half of its initial value is approximately ℓ^2 / κ, where κ is the thermal diffusivity and ℓ is the larger of the absorption depth for the laser radiation and the thermal conduction depth at the end of the laser pulse. A typical value for the former is 5-20 μm; for the latter, 2-4 μm. The characteristic time for cooling then ranges from 0.1-2.0 milliseconds.

A first estimate of the pressure contribution due to pyrolysis has been made by using an existing ablation code. The code uses the standard formulation for ablation models developed for re-entry problems. The effect on in-depth, rate-limited pyrolysis is included, but the energy absorbed by the target is deposited at the surface rather than in-depth. The treatment is entirely one-dimensional since the conduction depth at the end of a few milliseconds is much less than the laser spot radius. The governing equation is

$$\rho_s c_s \frac{\partial T}{\partial t} = \frac{\partial}{\partial x}\left(k \frac{\partial T}{\partial x}\right) + \left(c_p\right)_g \dot{m}_g \left(\frac{\partial T}{\partial x}\right) + Q_g W_g \quad (10.21)$$

226

where ρ_s is the density of the target; c_s is the specific heat of solid; T is
the temperature; t is the time; $(c_p)_g$ is the specific heat of pyrolysis gas;
$\dot{m}_g$ is the mass flux of pyrolysis gas; Q_g is the enthalpy of pyrolysis per
unit mass of gas generated; W_g is the rate of gas generation per unit
volume and k is the thermal conductivity of fiberglass. The last two terms
represent the energy transfer due to internal gasification (pyrolysis) of
the resin. Equation (10.21) has been solved by an explicity forward-march-
ing technique in finite difference form with the initial condition

$$T(x, t = o) = T_o \tag{10.22}$$

and the boundary conditions for $t > 0$

$$\left\{ \begin{array}{l} -k \dfrac{\partial T}{\partial t} = I - \dot{m} H_v - \epsilon \sigma T^4 - \dfrac{\rho_s c_s \Delta T}{\Delta t} \dfrac{\Delta x}{2}, \quad x = 0 \qquad (10.23) \\[3mm] \dfrac{\partial T}{\partial x} = 0 \qquad\qquad\qquad\qquad\qquad\qquad x = L \end{array} \right.$$

where L is the target thickness; $\dot{m}$ is the vaporization rate at the surface; H_v is
the heat of vaporization; ϵ is the emissivity; σ is the Stefan-Boltzmann
constant; and I is the laser flux. As discussed in Subsection 9.3, the pyrol-
ysis reaction rate can be expressed

$$W_g = A \left(\rho_r \right)^n \exp \left(-\frac{E}{RT} \right) \tag{10.24}$$

where A and n are constants; ρ_r is the resin density; E is the activation
energy of pyrolysis; and R is the gas constant. The resin density is given
by

$$\rho_r = \rho_{r_0} - \int_0^t W_g \, dt \qquad (10.25)$$

where ρ_{r_0} is the resin density of the virgin fiberglass; and the gaseous mass loss due to pyrolysis is

$$\dot{m}_g = \int_0^L W_g \, dy \qquad (10.26)$$

where L is the target thickness. Finally, the recession rate is parameterized as

$$\dot{m} = \beta_1 \, \rho \left(T_s \right)^{\beta_2} \exp \left(- \frac{\beta_3}{T_s} \right) \qquad (10.27)$$

where the β's are constants and T_s is the surface temperature. For a first order estimate of the potential effect of pyrolysis, calculations were made for silica phenolic with the properties listed in Table 10.2. The properties in the left hand column are taken from Ref. 14. Since there is a great deal of uncertainty associated with the pyrolysis rate (Fig. 9.13), calculations were also performed with values of the pyrolysis parameters listed in the right hand column. These parameters are chosen to fit the pyrolysis rate for the fast component in Ref. 15.

The prediction of pyrolysis mass loss rate, using the two different expressions for the pyrolysis decomposition rate, are shown in Fig. 10.9 and Fig. 10.10. The change in pyrolysis rate strongly affects the maximum mass loss rate. The maximum surface temperature in the two calculations is approximately the same but the local pyrolysis rate varies by a factor of seven. Note that the pyrolysis rate has a maximum which occurs before

228

TABLE 10.2

Thermodynamic Properties.

Property		Silica Phenolic	
Symbol	Units	Ref. 14	Ref. 15
ρ	gm/cm^3	1.63	
ρ_{r_o}	gm/cm^3	.32	
C_p	J/gm^oK	$.234 + .523\rho$	
K	$J/sec\text{-}cm^oK$	$-2.77 \times 10^{-4} + 3.24 \times 10^{-3}\rho$	
ϵ		.5	
ΔH	J/gm	14,500	
β_1	$cm/sec^oK^{\beta_2}$	4.2×10^{10}	
β_2		-.5	
β_3	^oK	64,444	
$(C_p)_g$	J/gm^oK	1.76	
Q_g	J/gm	2.210	
A	sec^{-1}	7 for T < 525 K; 9×10^8 for T > 525 K	3.415×10^8
E/R	^oK	5200 for T < 525 K; 15000 for T > 525 K	20440
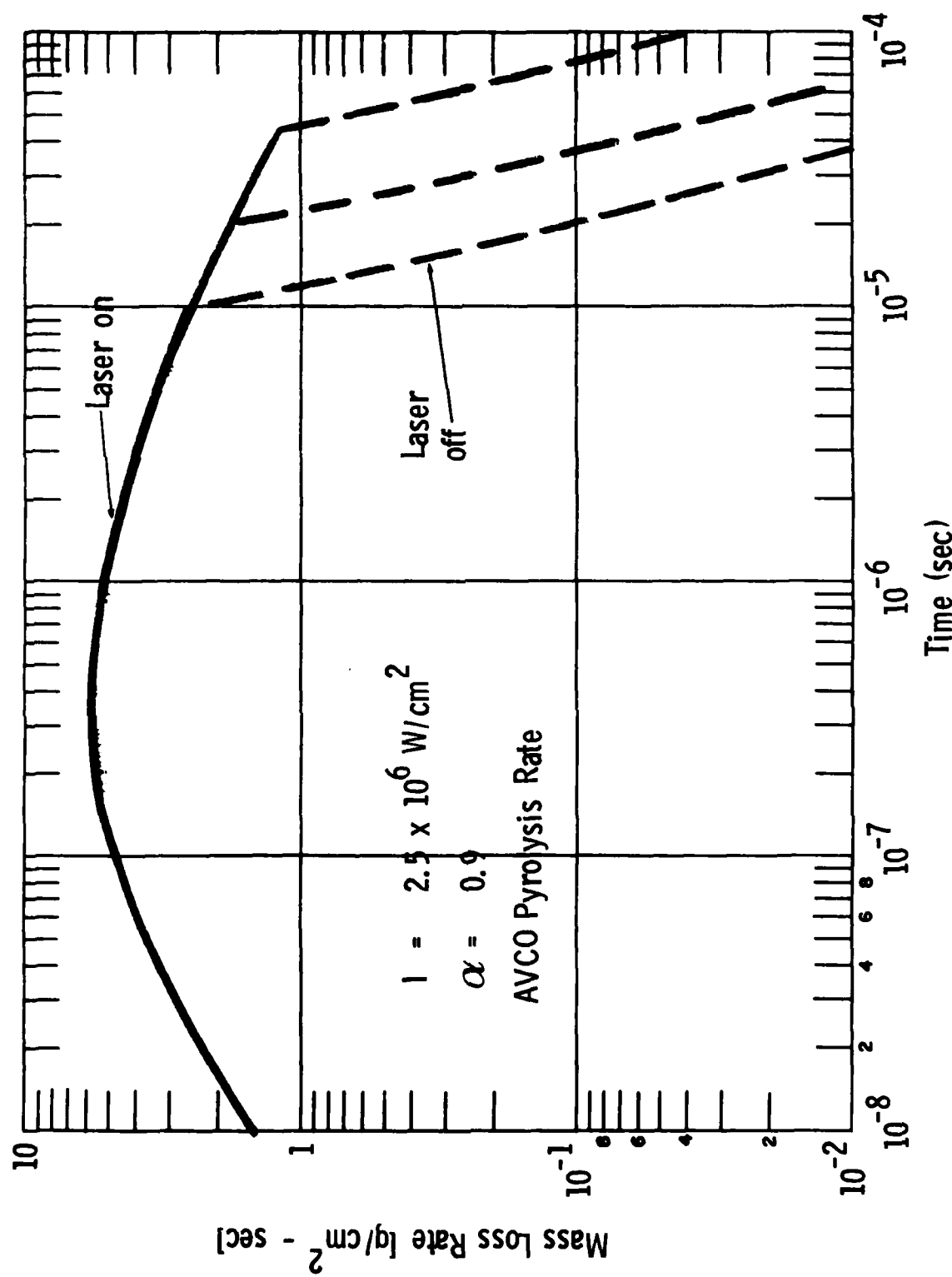
Fig. 10.9 Pyrolysis Mass Loss Rate of Silica Phenolic.

230
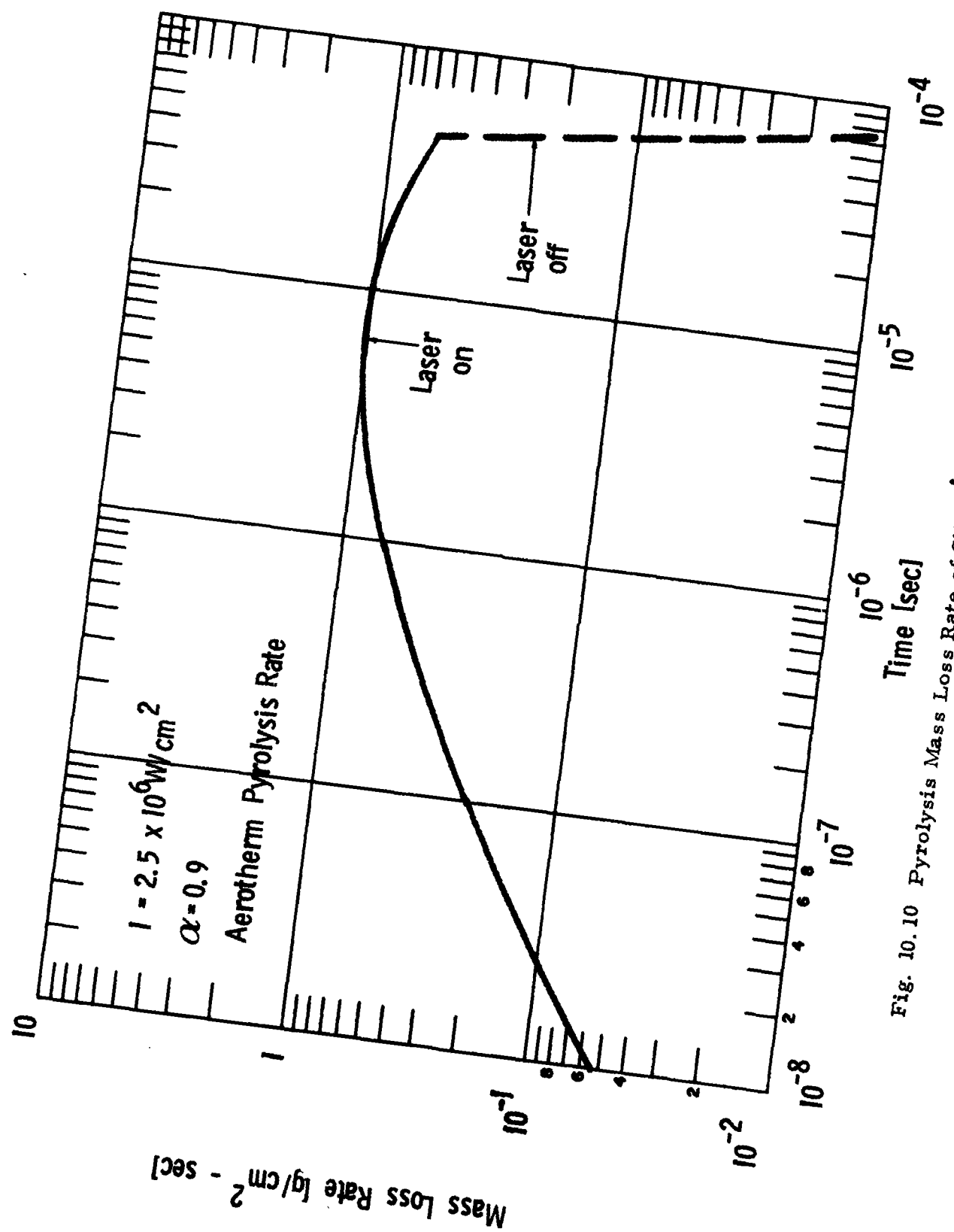
Fig. 10.10 Pyrolysis Mass Loss Rate of Silica Phenolic.

231

uniform ablation is substantial. As ablation becomes increasingly more important, the time available for pyrolysis is decreased, with the result that the mass loss attributable to pyrolysis (without accompanying vaporization of the silica) is decreased. In the Fig. 10.9, the decay of the pyrolysis rate after the pulse is terminated is shown for three different pulse times. In all three examples, post-pulse pyrolysis accounts for almost a third of the total mass loss caused by pyrolysis.

The contribution of the pyrolysis gases to the pressure can be estimated by multiplying the mass loss rate by a typical sonic velocity, say 10^5 cm/sec. Thus, the peak pressure attributable to pyrolysis alone is estimated to be .6 atm. for the example shown in Fig. 10.9 and only .1 atm. for the example shown in Fig. 10.10.

The above calculations suggest that pyrolysis can cause a mass loss, but the accompanying pressure is small since the mass loss occurs over a long period of time. If vaporization occurs, the pressure from vaporization clearly dominates the pyrolysis contribution.

10.5 Energy Requirements for Mass Removal

The following discussion of mass removal mechanism concentrates on fiberglass targets since the possible mass loss mechanisms for pyroceram and slip-cast fused silica are a subset of the ones for fiberglass. Some of the more obvious mass loss schemes are: uniform vaporization of glass and resin; pyrolysis with no glass removal; pyrolysis accompanied by delamination or melt removal or aerodynamic removal. More exotic methods of removal include the removal of individual fibers by the pressure of escaping pyrolysis gases, shattering of the fiber by thermal stresses, and individual fiber removal caused by laser radiation being focused by the glass fiber onto the back of the fiber, thereby initiating vaporization and the resultant pressure. It is worthwhile to remember that such exocitic

mechanisms are possible; but until experimental data indicates their presence, it is appropriate to confine the discussion of energy requirements to the obvious mass removal mechanisms.

The energy requirements for mass removal can be expressed in terms of Q^*, the amount of energy needed to remove one gram of material.

Herein, uniform ablation is defined to be the removal of glass and resin in the proportion they are present in the virgin target. The energy requirement, ignoring any losses due to conduction into the target (convective cooling is insignificant for a single pulse) is given simply by the heat of vaporization of the glass, the heat of pyrolysis of the resin and the sensible heat required to raise both glass and resin to the vaporization temperature. Because the heat of vaporization of the glass is so large, it dominates energy requirements; the additional sensible heat required to correctly account for departures of the vaporization temperature from the normal boiling point of glass is small. For a fiberglass which is 80% glass and 20% epoxy by weight, the energy required for uniform vaporization corresponds to $Q^* \approx 13.5$ kJ/g. For 66% glass and 34% epoxy, the energy required is given by $Q^* \approx 11.5 - 12.0$ kJ/g.

If pyrolysis of pure epoxy were to occur, the energy requirements, assuming high temperature pyrolysis at 3000K, correspond to $Q^* \approx 3.7$ kJ/g. This value might be expected experimentally when a layer of resin covers the fiberglass, as in E-glass.

However, if the resin is imbedded in fiberglass, the fibers retain most of the heat and the value of Q^* depends strongly on whether or not the fibers are moved with the resin. For delamination, in which the glass fibers are removed after the resin has pyrolyzed, the estimated value of Q^* for 20% epoxy and 80% glass is 900 J/g, whereas for 34% epoxy and 66% glass the required energy is 1050 J/g. (Remember that

no losses by convection or conduction into the target are included in these estimates.) It is possible the glass fibers can be removed by aerodynamic shear or by the pressure of escaping pyrolysis products if the glass reaches a temperature of 1500K (the working point of typical borosilicate glasses) or 2000K (the melting point of high cristobalite (SiO_2)). Pyrolysis and melt removal corresponding to these temperatures have Q^*'s, respectively, of approximately 1.45 kJ/g and 2.0 kJ/g for 20% epoxy and 1.6 kJ/g and 2.1 kJ/g for 34% epoxy. Although these values of Q^* are twice the value of delamination, they are still energy efficient mass removal schemes compared to vaporization.

If pyrolysis occurs without any glass removal, the value of Q^* becomes quite high -- just as much energy is required for pyrolysis at 950 K as for delamination but only a small fraction of the mass is removed. For epoxy, which has an estimated heat of pyrolysis of 1100 J/g, the energy required to remove a gram of resin at a temperature of 950K without removing any glass is 4.5 kJ/g for 20% epoxy and 3.1 kJ/g for 33% epoxy. If the resin forms a char, as phenolic does, the value of Q^* to remove a gram of material more than doubles because less than 50% of the pyrolyzed resin escapes. The values of Q^* can be as high as 12-13 kJ/g for pyrolysis accompanied by char formation. Thus pyrolysis of resin imbedded in fiberglass is an inefficient method of mass removal compared to delamination or melt removal. It should be remembered, however, that delamination and melt removal are removal mechanisms which are expected only in repetitive pulse interactions, whereas pyrolysis with no fiber removal is anticipated only in single pulse interactions.

By summary, any method which removes glass fibers without vaporizing them is very efficient compared to removal by vaporization. In single pulse experiments, resin can be pyrolyzed without fiber removal.

The energy costs for pyrolysis, unaccompanied by glass removal, vary from moderate (for pure resin or no char information) to exorbitant (for pyrolysis with char formation).

The above estimates of the energy required to remove material, are lower limits; it is assumed that none of the energy is expended in other purposes such as heating excess parts of the target (by conduction) and convective losses. Conduction losses are negligible in a repetitive pulse interaction in which penetration is achieved, but they can be extremely important in single shot experiments or in repetitive pulse experiments which do not achieve penetration.

10.6 Residual Energy

The energy absorbed by the target during a laser pulse can be expended in two ways -- it can be used for rapid mass removal on the time scale of the laser pulse, or it can remain behind in the target as heat. The portion which remains behind as heat, hereafter denoted as residual energy, can be combined with the residual energy deposited on subsequent pulses and thereby cause the bulk target to heat to temperatures high enough for delamination or melt removal or other efficient mass removal mechanisms to occur. In light of the wide disparity in energy efficiency of vaporization and the other mass removal mechanisms, it is worthwhile to separate the energy absorbed during the pulse into (1) the component which is expended on vaporization and (2) the residual energy which is available for more efficient mass removal.

In the calculation of residual energy, it is important that long-term pyrolysis, that is pyrolysis which does not occur at high temperatures on time scales equivalent to the pulse length, be included in the residual energy even though the energy may be carried from the target by the escaping gases. The

235

removal of resin without glass vaporization contributes to the low Q^* mechanisms. Furthermore, unless uniform vaporization is the only mass loss mechanism, the pyrolysis zone will progress farther into the material than the laser absorption depth. The long time pyrolysis that occurs is then a result of slow thermal heating of the target and, therefore, must be properly included as a target heating phenomenon rather than a phenomenon induced by an individual laser pulse.

It is demonstrated in Subsection 10.1 that if there is surface absorption of the laser radiation, steady-state vaporization is expected to be attained well within the laser pulse time. An upper limit can then be placed on the residual energy for surface absorption by calculating the sensible heat stored in the temperature profile corresponding to the steady-state vaporization. For steady-state recession, the solution to the conduction equation is

$$T = T_v \, e^{-x/x_o} \tag{10.28}$$

where T_v is the vaporization temperature and x_o is a constant length parameter determined by the recession rate. The recession rate is given by

$$\alpha I = \dot{m} \left(H_v + c_s T_v \right) \tag{10.29}$$

where α is the absorptivity, $\dot{m}$ is the mass flux, I is the incident laser intensity, H_v is the heat of vaporization, and c is the heat capacity of the target. The spatial temperature derivative at the surface is given by

$$- k_s \frac{\partial T}{\partial x} = \dot{m} \, c_s T_v \tag{10.30}$$

236

where k is the thermal conductivity. Therefore, the distance x_o is given by

$$x_o = \frac{\left(H_v + c_s T_v\right) k_s}{\alpha I c_s} \qquad (10.31)$$

and the integrated energy in the target is

$$\rho_s c_s T_v x_o = \frac{k_s \rho_s T_v \left(H_v + c_s T_v\right)}{\alpha I} \qquad (10.32)$$

where ρ_s is the target density. The expressions for the residual energy E_r, as determined by Eq. (10.32) and the properties given in Sec. 9, are

$$\text{fiberglass} \qquad E_r = .3/\alpha I$$

$$\text{slip-cast fused silica} \qquad E_r = 1./\alpha I$$

$$\text{pyroceram} \qquad E_r = 3/\alpha I$$

where E_r is given in J/cm^2 and I is measured in MW/cm^2. For fiberglass, the dome material of primary interest, the residual energy is miniscule. For pyroceram it is appreciable.

In Subsection 10.1, it is pointed out that in-depth absorption is likely to occur. Rough limits on the residual energy for in-depth absorption can be calculated from the target temperature profile. In the absence of conduction, the enthalpy profile for in-depth absorption is given by

$$H(x) = \Delta H \, e^{-x/\ell}$$

where ℓ is the absorption depth and ΔH is the enthalpy increase of the front surface. The amount of energy contained in the profile is given by

$$E_r = \int \rho\, H(x)\ dx$$

where ρ is the target density. At the time that the front surface first reaches the vaporization temperature (see Fig. 10.11a), the residual energy E_r, given in J/cm^2, can be expressed in terms of the absorption depth ℓ (measured in μm) as .6 ℓ for fiberglass targets and 1.0 ℓ for pyroceram targets. At the onset of steady-state vaporization (see Fig. 10.11b), the residual energy is estimated as 2.4 ℓ and 3.9 ℓ for fiberglass and pyroceram, respectively. The two calculations of the residual energy serve as limits on the maximum residual energy per pulse, but the range between them is rather large. More detailed estimates of the residual energy require an estimate of the fraction of the energy stored in the steady-state profile which can later be used for post pulse vaporization. A compromise value can be estimated by calculating the residual energy in the profile shown in Fig. 10.11c, in which it is assumed that all energy in the steady profile which exists as sensible heat at temperatures in excess of the vaporization temperature (but without the necessary heat of vaporization), is eventually lost to post pulse vaporization. This profile leads to an estimated value for the residual energy in J/cm^2, of 1.4 ℓ for fiberglass and 2.4 ℓ for pyroceram.

The foregoing estimates are applicable when no plasma is created. When a plasma is formed, it is first necessary to estimate the amount of radiation which is emitted from the plasma, and then to estimate the spectral absorption coefficient of the target. The LSC wave model can be used to compute the radiative emissions from an air plasma. For a first order estimate of the absorption characteristics, the spectral absorption depth of a typical glass can be used as typical of all the dome materials. The absorption curve of a typical glass[37] is given in Fig. 10.12. In the short wavelength region, approximately λ <2500A, the absorption depth is small, .01 microns, and glass acts as a surface absorber. In the wavelength region λ >1μm, the absorption depth is of the order of a few microns, consistent with the estimates in Section 9 and 10.6 μm radiation, but this

238

(a) Onset of Vaporization

T_V

$T\uparrow$

Temperature Profile $T = T_V e^{-X/\ell}$

$E_R = \rho \int H dx = \rho c\, T_V \ell$

$X \longrightarrow$

(b) Steady State Vaporization

$H_V + cT_V$

$H\uparrow$

Enthalpy Profile $H = (H_V + cT_V) e^{-X/\ell}$

$E_R = \int \rho H\, dx = \rho c\, (H_V + cTv)\ell$

$X \longrightarrow$
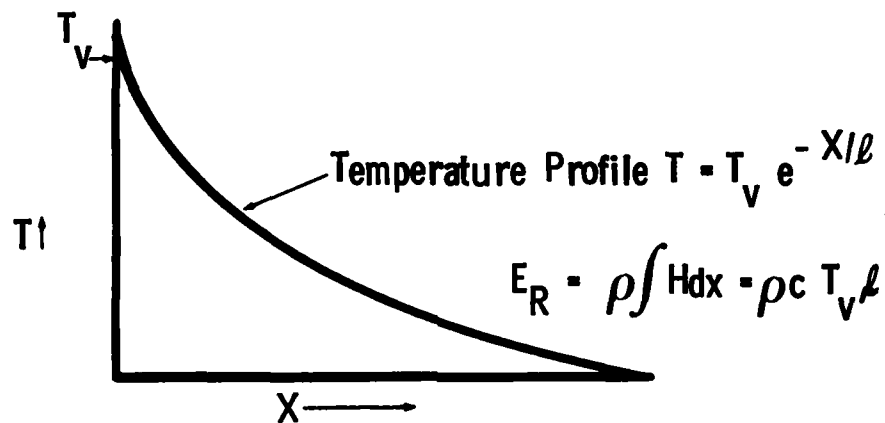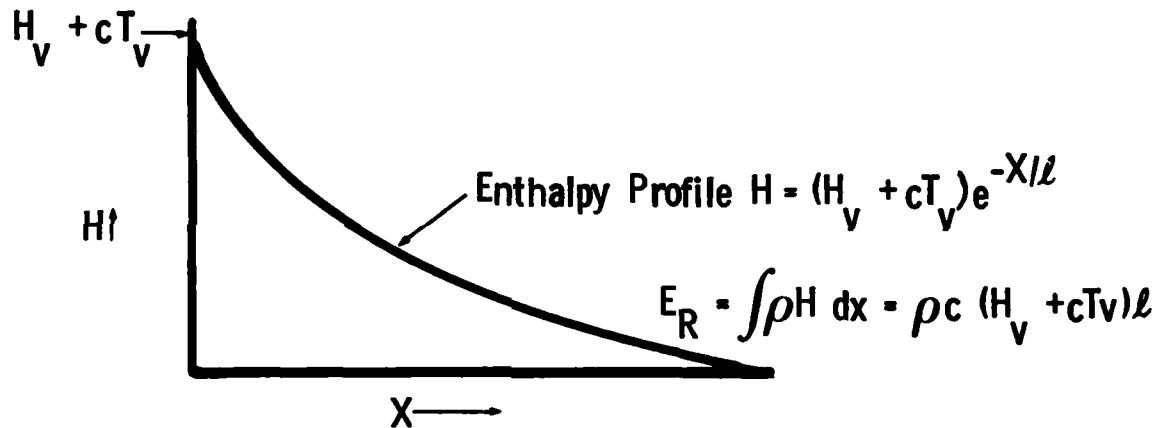
(c) Possible Profile After Post Pulse Vaporization

$H_V + cT_V$

Enthalpy Profile $H = (H_V + cT_V) e^{-X/\ell}$

$E_R = \rho \cdot$ (unshaded area)

cT_V

$H\uparrow$

$$= \rho c T_V \ell \left[1 + \ell n \left(\frac{H_V + cT_V}{cT_V} \right) \right]$$

$X \longrightarrow$
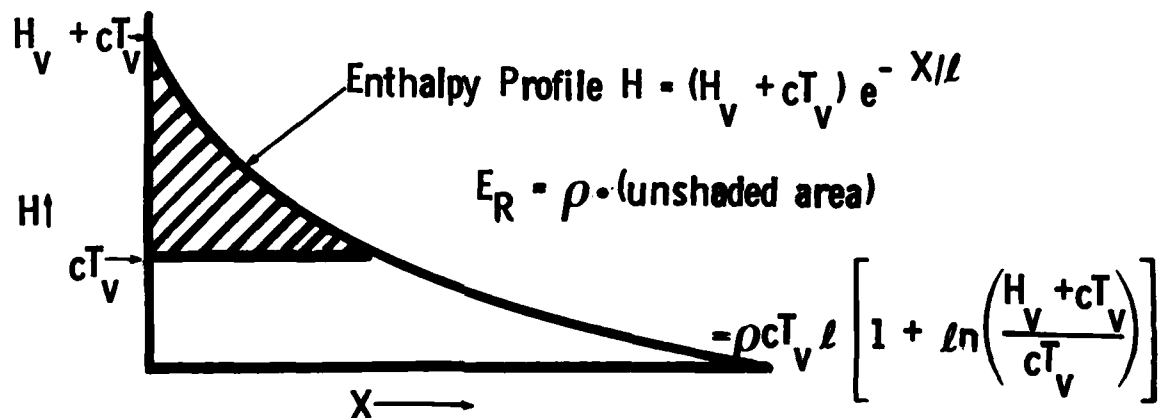
Fig. 10.11   Sketches of Temperature and Enthalpy Profiles Used to Determine Residual Energy Under Three Different Assumptions.
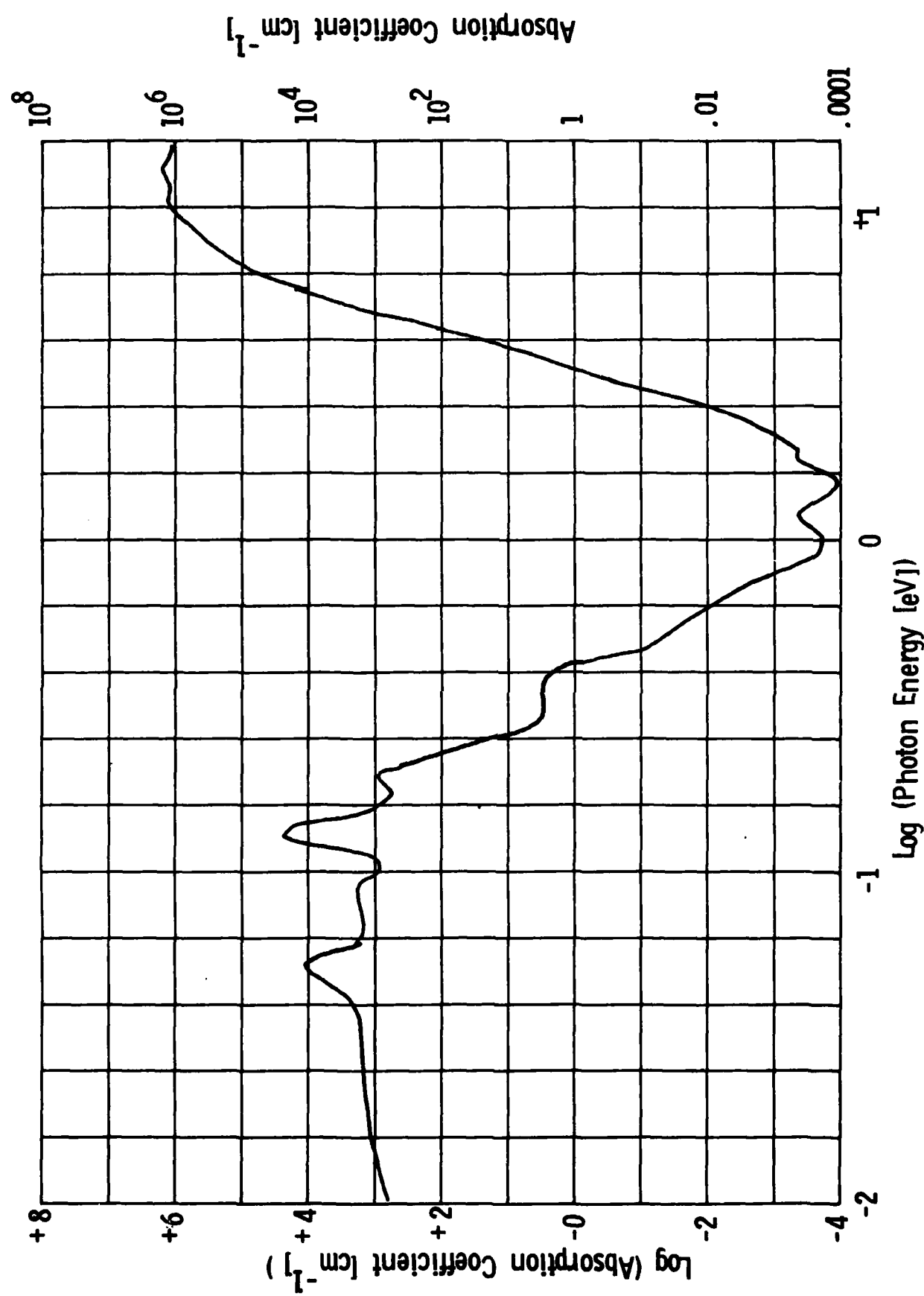
Fig. 10.12 Absorption Coefficient of a Typical Glass Fiber Used in Fiber Optics. From Ref. 37.

spectral region is not important because there is little radiative transport from the plasma in this spectral regime. In the intermediate wavelengths, $.25 \mu m < \lambda < 1 \mu m$, the absorption depth is very large -- and the depth depends crucially on the purity of the glass, and the lack of imperfections. The wavelength corresponding to the transition from surface absorption to in-depth absorption is, likewise, very sensitive to the nature of the glass. However, the error in identifying the wavelength of the transition is small compared to the width of the spectral band which has large in-depth absorption. Thus, as a first approximation, it is appropriate to model dome materials as surface absorbers for $\lambda < .25 \mu m$ and in-depth absorbers for $\lambda > .25 \mu m$.

The expressions developed earlier for the residual energy limits for surface and in-depth absorbers are applicable here. It is found that the plasma radiative emission from the LSC wave is strong in the short wavelength band, so that the surface absorption limit on the residual energy is achieved. Thus, vaporization is always present for laser interactions in which a plasma is created. The short wavelength contribution to the residual energy is insensitive to the incident laser intensity. About 1 J/cm^2 is expected as the residual energy contribution from the short wavelengths for fiberglass.

In the long wavelength region, the precise value of the absorption depth is unimportant as long as it is greater than a few microns. Indeed, because of the small size of both the fibers in fiberglass and the crystal structure in pyroceram, the huge absorption depths shown in Fig. 10.12 are gross overestimates because other effects, such as scattering, dominate. As a conservative estimate, consider an absorption depth of 20 μm. From the discussion of in-depth absorption earlier in this subsection, the maximum residual energy expected for fiberglass with $\ell \approx 20 \mu m$ is at least 12J/cm^2 and probably 28 J/cm^2. But the total fluence emitted by an LSC wave plasma in the spectral band with wavelengths greater than 2500A is limited to less than 15J/cm^2 for even the largest pulses which are presently practical, so we consider the long wavelength band to be fluence limited rather than vaporization limited. Plots of the residual energy predicted from LSC

wave theory are shown in Fig. 10.13 and Fig. 10.14. In Fig. 10.13 the predictions for residual energy contribution from each band are shown. Note that the short wavelength region is vaporization limited, whereas the long wavelength region is fluence limited. For purposes of this plot the plasma threshold has been assumed to be 1.5 MW/cm^2 -- experimental evidence as to the threshold laser intensity for plasma ignition is presented in Sec. 11. The predictions should not be extended to higher than 4 MW/cm^2 since the LSC wave is believed to degenerate into an LSD wave above this intensity. The combined residual energy from both bands is plotted in Fig. 10.14. Lines of constant residual energy are shown for varying values of $\hat{\tau}$ and the laser intensity. A spot area of 250 cm^2 is used in the plot, but the results can be roughly scaled to other spot sizes by multiplying the residual energy predicted in the plot (for the appropriate intensity and $\hat{\tau}$) by the square root of the ratio of the actual area to the nominal area of 250 cm^2. In this plot the predictions for intensities above 4 MW/cm^2 have been adjusted to compensate for the transition to an LSD wave.

In the estimates of the residual energy in the presence of a plasma, it is assumed that a plasma opaque to laser radiation is formed instantaneously. However, should the development of the plasma require a formation time of the order of a microsecond, a considerable amount of energy can be deposited by the laser directly into the target before the plasma shields the surface. This contribution has not been included in the calculations.

10.7 Energy Available for Ablation

In a single pulse interaction the main method of removing material is to ablate or vaporize the surface. In the analysis of the surface interaction, it is useful, therefore, to estimate the amount of energy available for ablation. If no plasma is formed, the amount of energy available for ablation is simply given by taking the total energy (fluence) absorbed, and then subtracting the energy which is left in the target as residual energy. This approach should also be valid for a typical pulse in a string of independent pulses irradiating the same spot.

242
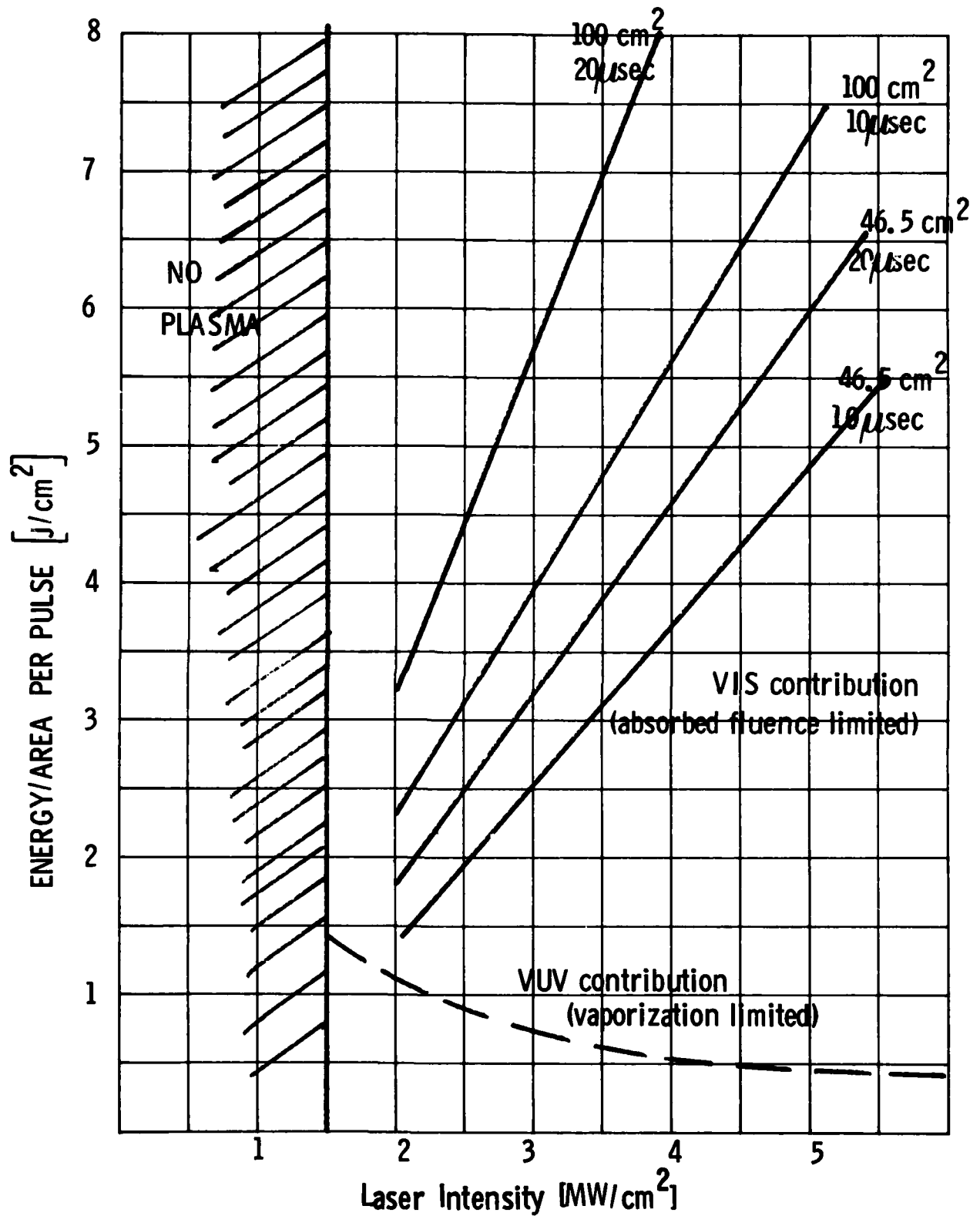
Fig. 10 13 Predictions of Contributions to Residual Energy Per Pulse
when an LSC Wave Plasma is Ignited.

243
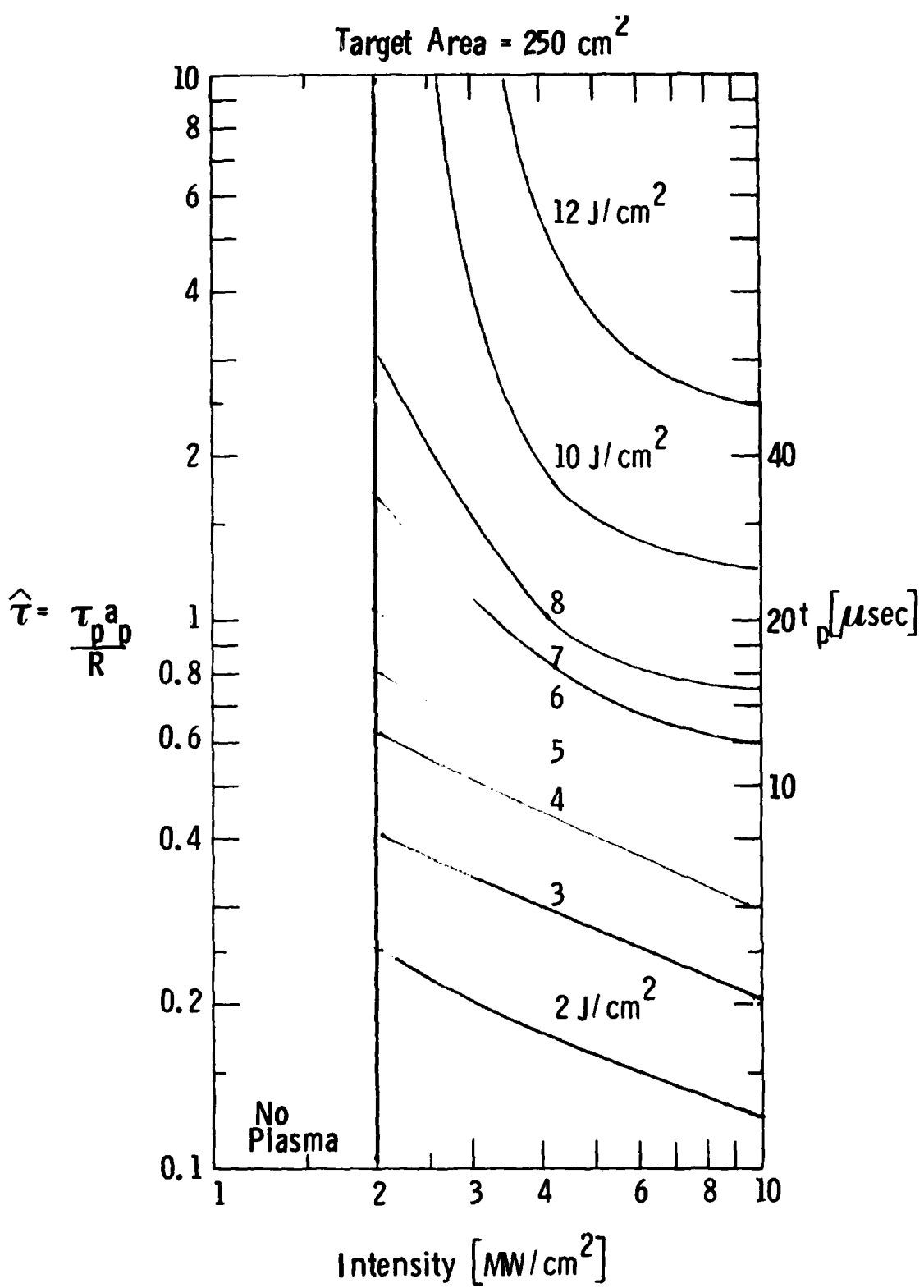
Fig. 10.14   Map Showing Residual Energy Predictions As a Function
of Laser Intensity and $\hat{\tau}$ for an Air LSC Wave Plasma.

However, for the first pulse on a virgin target, the residual energy may cause post-pulse pyrolysis as the residual energy diffuses into the material. Moreover, the surface preparation may result in a layer of resin coating the surface. For first pulse analysis in Sec. 11, we shall neglect the residual energy estimate and assume that all the absorbed fluence goes into ablation. (This interpretation may lead to overestimates of Q^*.)

In cases where a plasma is ignited, the energy available for ablation is dominated by the energy transferred to the surface in the band $\lambda < .25 \, \mu m$. This contribution can be calculated from the LSC wave model. Estimates of the fluence available for ablation in the presence of a plasma are shown for a typical spot area of 250 cm^2 in Fig. 10.15. As in the case of Fig. 10.14, the results of this figure can be roughly scaled to other spot sizes by multiplying the prediction at the appropriate intensity and $\hat{\tau}$ by the square root of the ratio of the actual area to the nominal area of 250 cm^2.
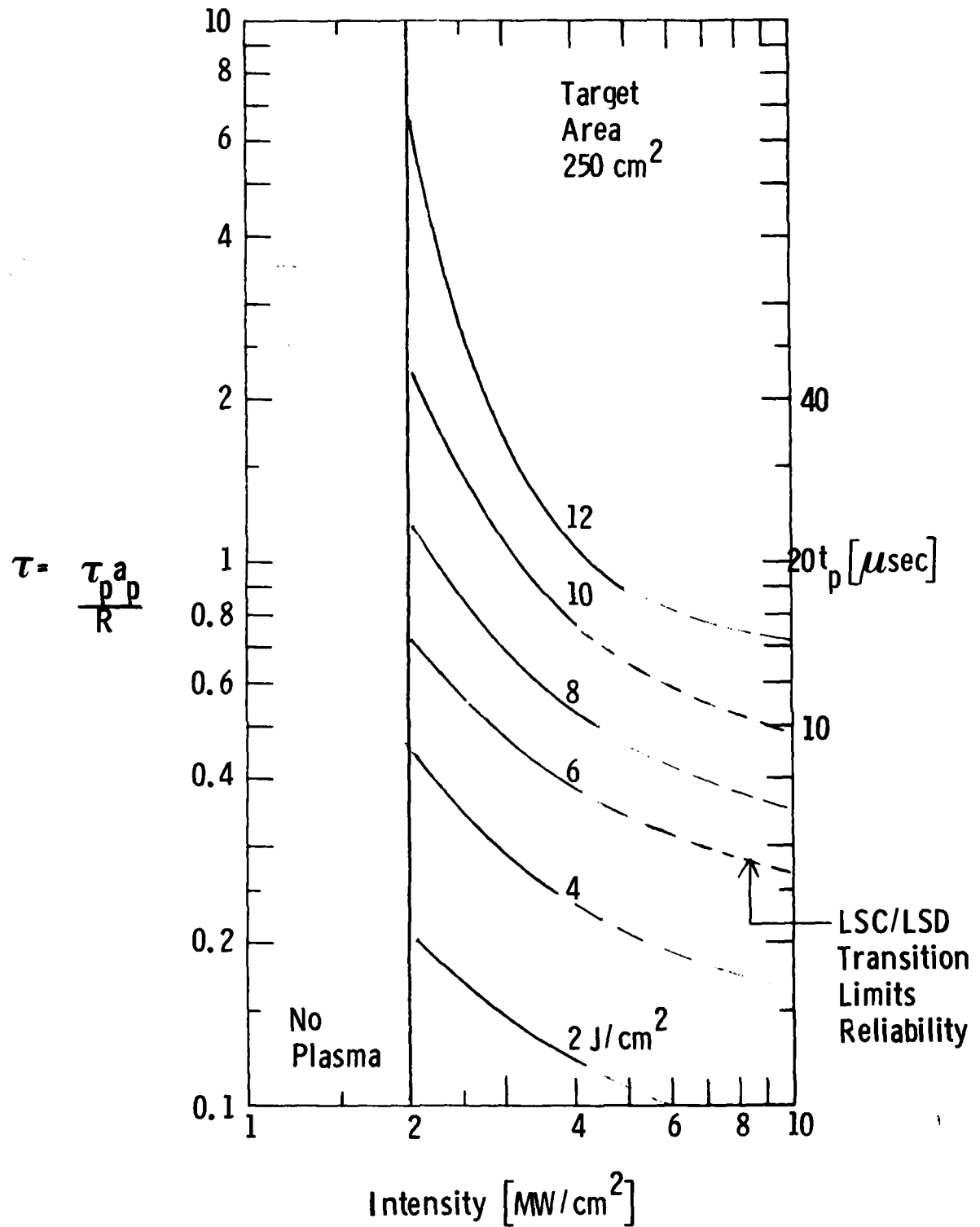
Fig. 10.15 Map Illustrating Prediction of Energy Available for Ablation when an Air LSC Wave Plasma is Ignited.

SECTION 11

SINGLE PULSE DATA/THEORY COMPARISON

In the previous section the types of phenomena which may occur during single pulse interaction were investigated, and the results one might expect were detailed. In this section, we shall analyze the single pulse data[38,39] taken as part of the JANAF program on pulsed laser effects, and compare it to the theoretical predictions in order to infer which physical phenomena are important and which ones are unimportant.

11.1 Radiative Emissions

During the experiments performed on single pulse irradiation of dome materials,[38] it was found that at the low intensities of 1 MW/cm^2 no luminous clouds were observed whereas above intensities of ~ 2 MW/cm^2 extremely bright clouds were found. In the region intermediate between 1 and 2 MW/cm^2, there was a transition region characterized by spotty intermittent production of luminous clouds. The extreme brightness of the cloud for intensities above 2 MW/cm^2 is almost certainly the result of plasma ignition. The interpretation of the transition region is somewhat ambiguous, however. The luminousity could be the result either of spotty plasma ignition or of production of a luminous vapor cloud. The difference between the two possibilities could presumably be ascertained by examination of the spectral radiation from the cloud; however, this has not been recorded in the present experiments.

There are two tentative conclusions which can be drawn from these observations. If the emission in the transition zone is the result of hot vapor, then the lack of luminous clouds at intensities below 1 MW/cm^2 indicates that no vapor is formed. Since surface absorption is inconsistent with the absence of vapor at intensities just below 1 MW/cm^2, the laser must be absorbed in depth. On the other hand, if the emission is the result

of plasma formation, then the plasma must be formed by site ignition since a fluence well in excess of the incident fluence used during the experiments is required to produce vapor dominated plasma ignition.

11.2 Pressure Response

The data on the surface pressure response[39] for the single pulse interaction with dome materials are shown in Figs. 11.1 - 11.5, where the surface pressure is plotted against the laser intensity. The duration of the pulse is indicated by the shading of the data point. For comparison, several theory lines are drawn, such as the laser supported combustion wave plasma pressure, the laser supported detonation wave plasma pressure, the steady-state surface pressure, and the surface pressure predicted for a prescribed absorption depth for pulse times of 10 to 20 microseconds.

The limited data[39] on pyroceram is shown in Fig. 11.1. The in-depth absorption curves are drawn for an absorption depth of 8 μ. It is seen that the data at roughly 1.8 MW/cm^2 with a 19 μsec. pulse length agrees with both the laser supported plasma pressure predictions and the steady-state plasma predictions. However, the data at .67 MW/cm^2 with a 17 μsec. pulse length falls far below the steady-state plasma pressure predictions. Under these conditions surface absorption by pyroceram should produce the steady-state pressure; therefore, we conclude that in-depth absorption must occur. Using the in-depth absorption model developed in Section 10.1, we find that an absorption depth of 8 microns is capable of fitting the data for pyroceram at both .67 MW/cm^2 and 1.8 MW/cm^2.

As mentioned, the high intensity pyroceram data (I $\sim$ 1.8 MW/cm^2) can be explained by either having a plasma or by having in-depth absorption. Neither the maximum surface pressure observed nor the fact that a luminous cloud is produced is capable of distinguishing between the two explanations. This issue is resolved in Subsection 11.3.
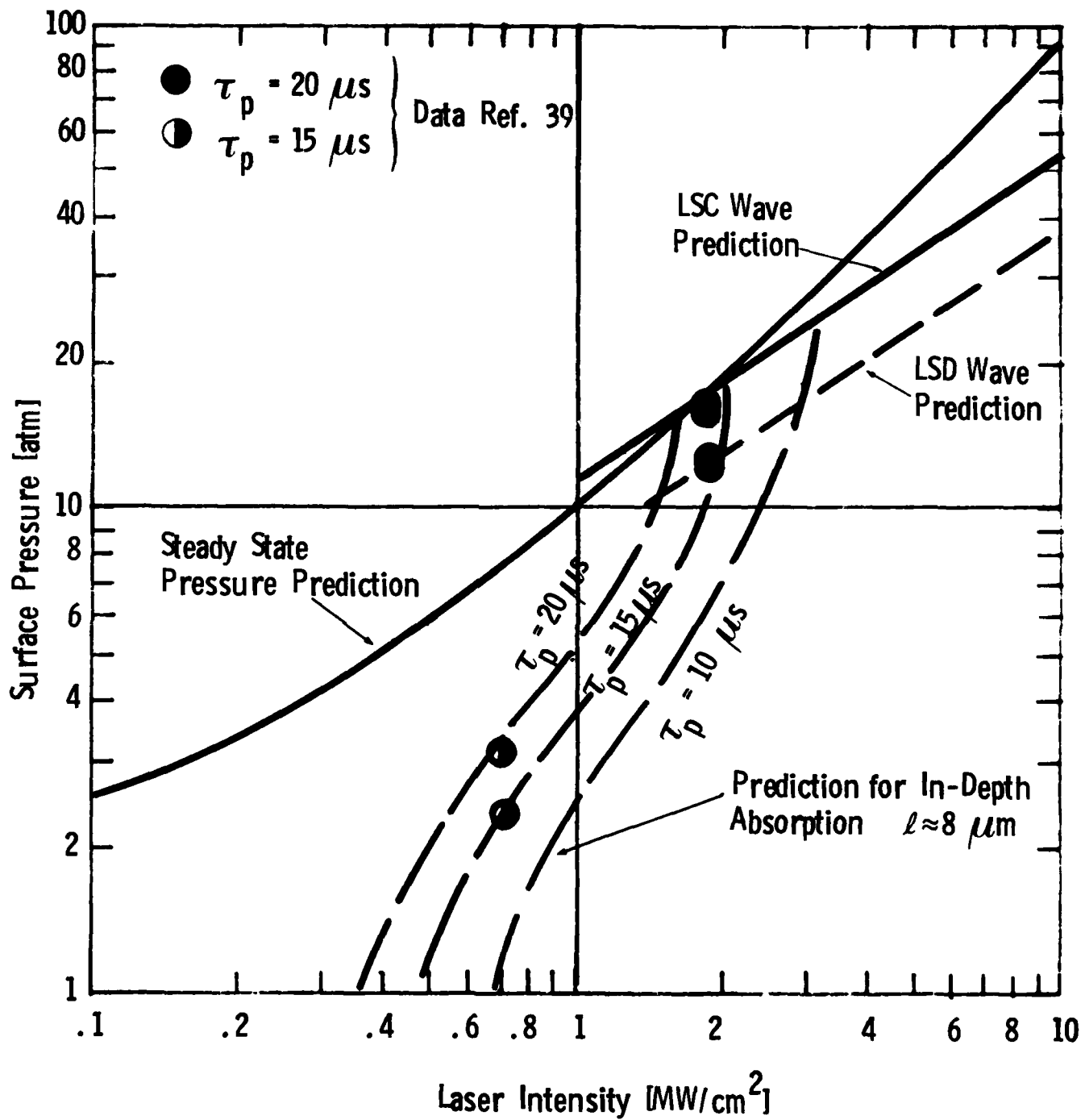
Fig. 11.1 Comparison of Data and Theory for Surface Pressure Generated
by 10.6μm Pulsed Laser Interacting with Pyroceram 9606.
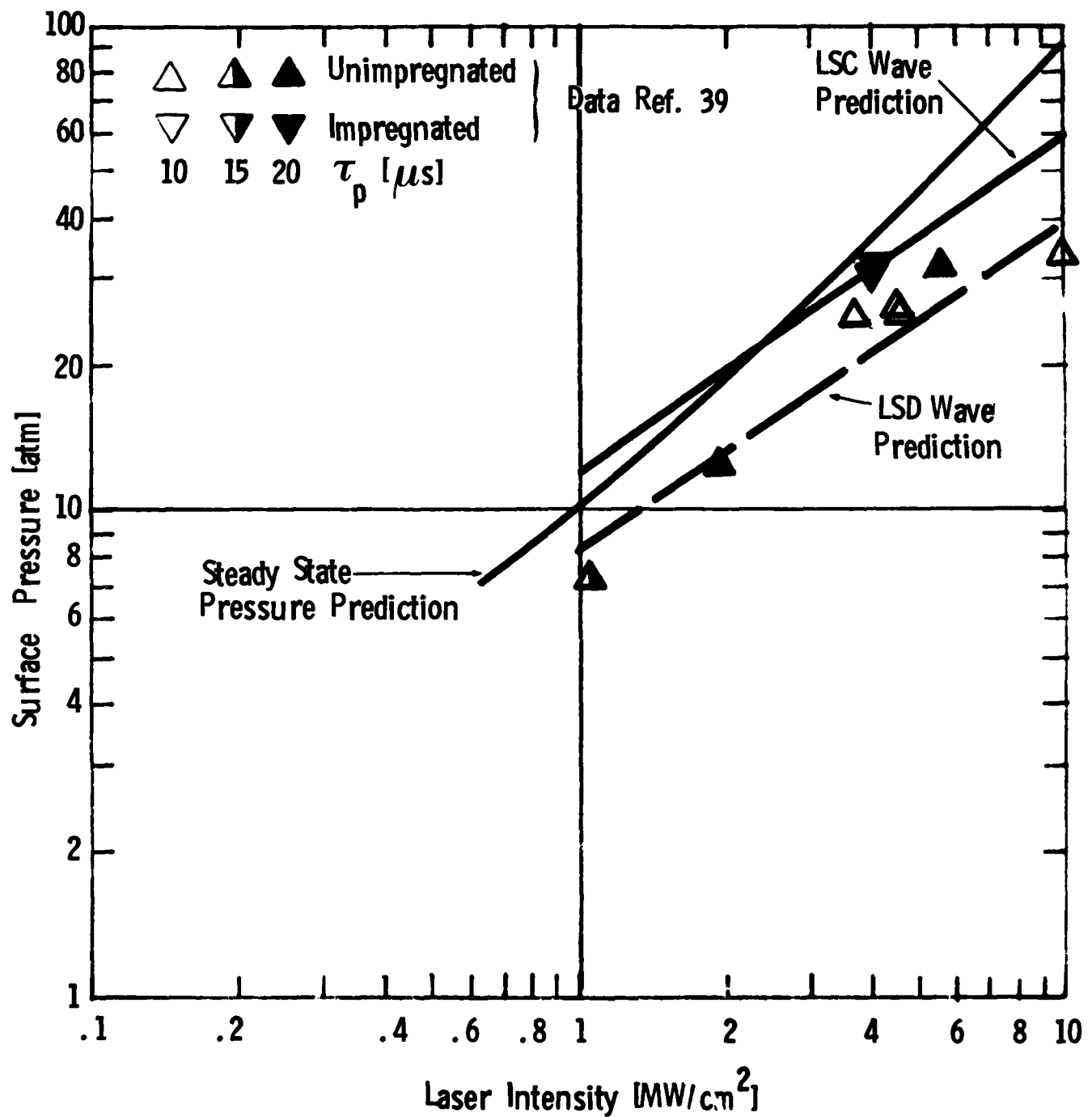
Fig. 11.2 Comparison of Data and Theory for Surface Pressure Generated by 10.6μm Pulsed Laser Interacting with Slip Cast Fused Silica.
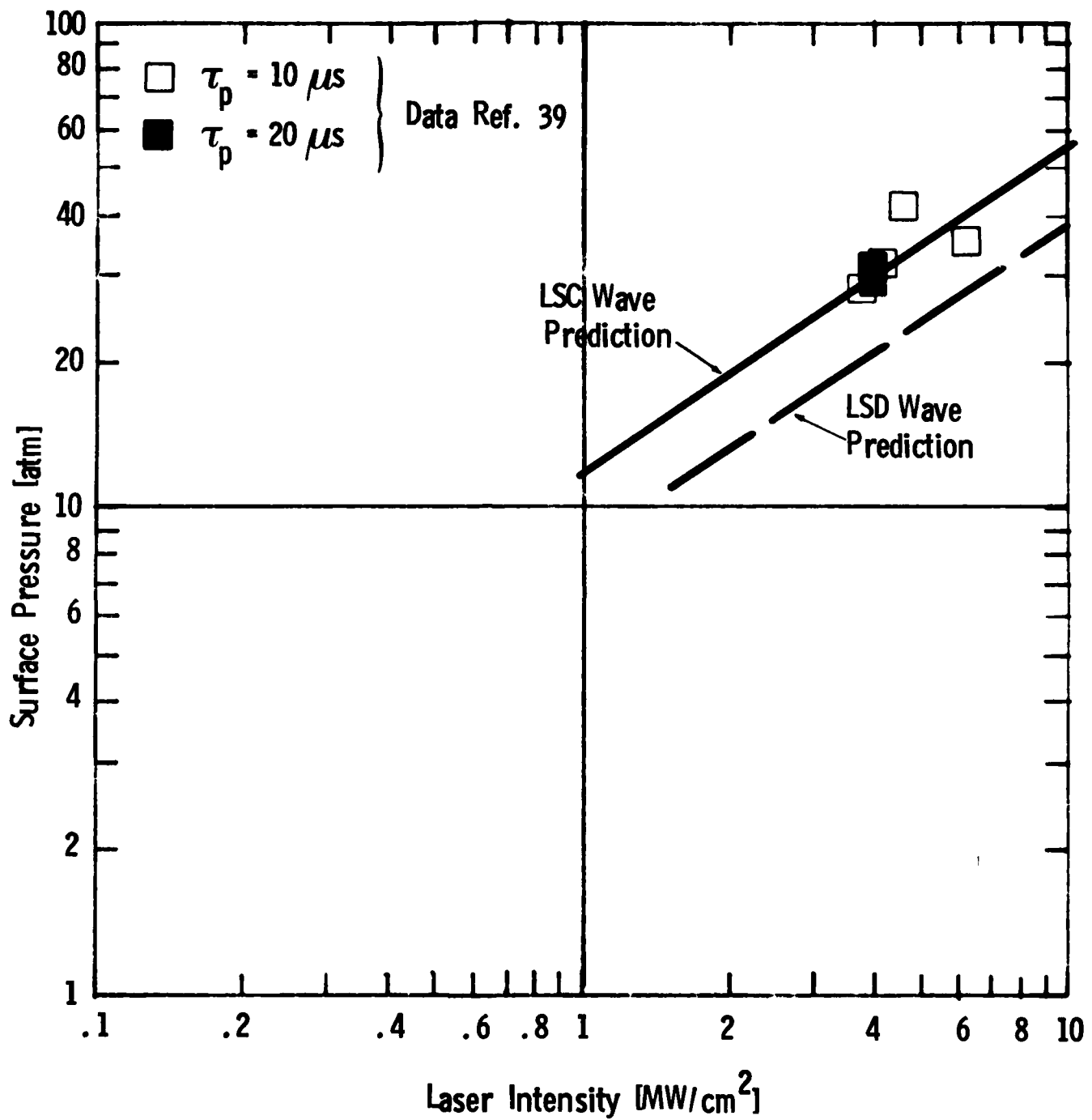
Fig. 11. 3   Comparison of Data and Theory for Surface Pressure Generated
by 10. 6μm Pulsed Laser Interacting with E-glass Fiberglass.
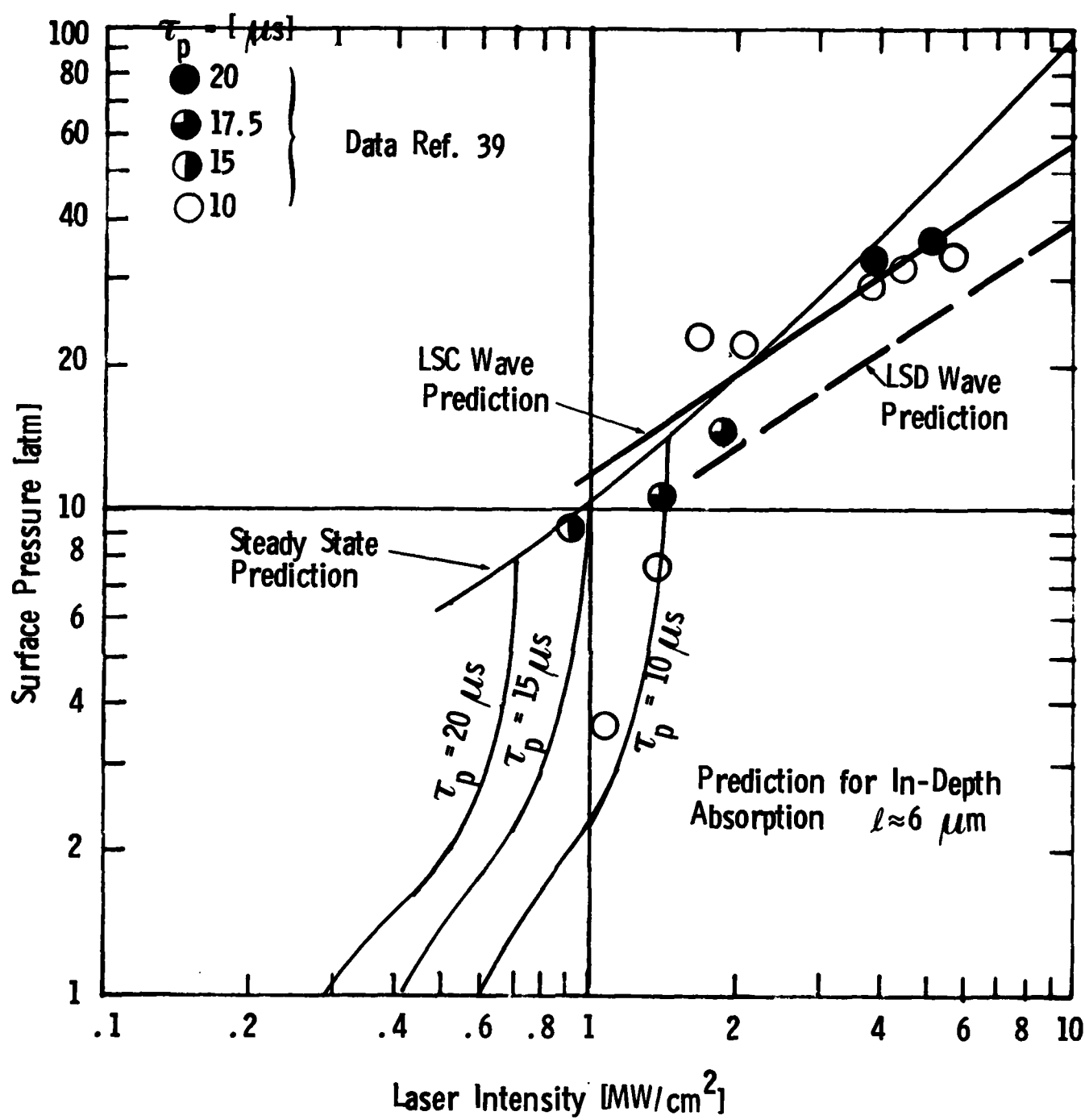
Fig. 11.4 Comparison of Data and Theory for Surface Pressure Generated by 10.6μm Pulsed Laser Interacting with Cordopreg.
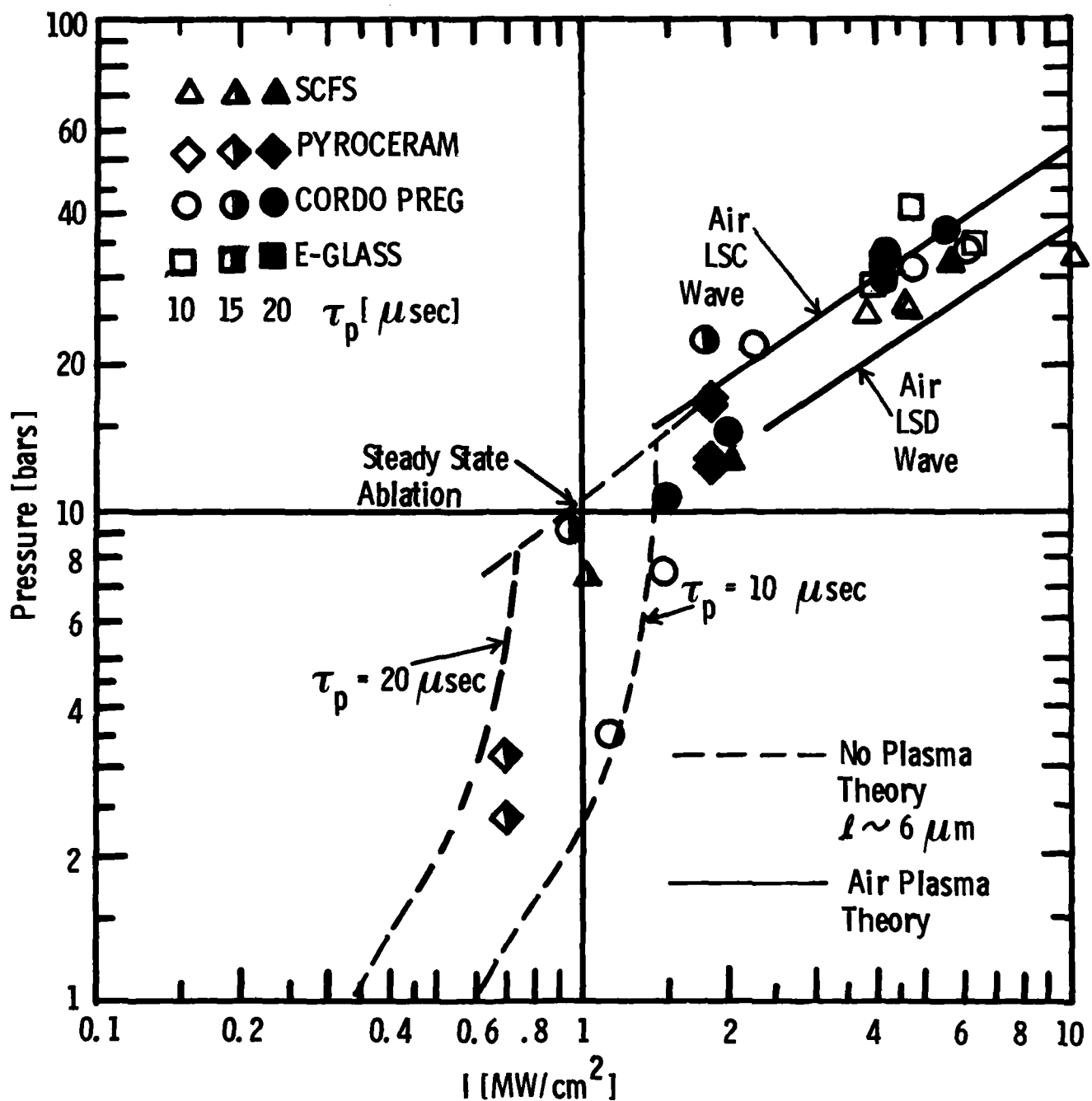
Fig. 11.5 Comparison of Data of Ref. 39 with Theoretical Predictions of Pressure Generated by 10. 6μm Pulsed Laser Interacting with Non-metal Targets.

The maximum surface pressure during the single pulse physics of interaction experiments[39] on slip-cast fused silica is shown in Fig. 11.2. Most of the data was taken in the plasma regime and falls between the pressure predicted for a laser supported combustion wave above a surface and the pressure predicted for a laser supported detonation wave above a surface. There are indications of a transition from the laser supported combustion wave pressure to the laser supported detonation wave pressure in the region above 4 MW/cm^2. (One must be extra careful in interpreting the data since two types of slip-cast fused silica were used; one type was impregnated with silicone resin; the other type was unimpregnated. The attitude of the triangles marking the data in Fig. 11.2 distinguishes the two types. The few data points corresponding to samples with silicone resin lie above the other points.)

At lower intensities, approximately 1 to 2 MW/cm^2, the pressure lies 50% below the predicted LSC wave pressure. Although these pressures correspond to LSD wave pressures, it is not expected that an LSD wave can be maintained at such low intensities. It is possible, rather, that these points represent steady-state vaporization with a heat of ablation slightly higher than that used in the theoretical curves.

The experimental results[39] for surface pressure for experiments using E-glass targets are shown in Fig. 11.3. Note that these are all high intensity experiments and that the data is well represented by the LSC wave pressure predictions. Only one point is peculiar in that it lies above the predicted LSC wave value. This point is discussed later in Subsection 11.3. The other point which does not lie on the LSC wave prediction is consistent with the transition to an LSD wave.

The surface pressure[39] observed during the interaction of the laser beam with a Cordopreg target is shown in Fig. 11.4. Once again, the high intensity data, around 5 MW/cm^2, is in good agreement with the LSC wave pressure prediction. At 1 MW/cm^2, the pressure for short pulse times, such as 10 microseconds, lies well below the predicted steady-state pressure. If the laser were absorbed at the surface, the steady-state value of the pressure is predicted; therefore, this indicates that in-depth absorption occurs. The theoretical predictions for in-depth absorption with an absorption depth of 6 microns are also shown in Fig. 11.3 and they are consistent with the data. In particular, the point at approximately .9 MW/cm^2, which has a pulse length of 15 microseconds, lies above the pressure observed at 1.1 and 1.5 MW/cm^2 because the low intensity point corresponds to a larger fluence. Only the point at 1.75 MW/cm^2, which lies considerably above the LSC wave prediction, is at variance with the predictions based on in-depth laser absorption below plasma threshold and LSC wave plasma ignition above plasma threshold. From this data the *exact point of plasma ignition cannot be ascertained,* although the fact the pressure for one data point at 1.5 MW/cm^2 lies considerably below the LSC wave prediction suggests that, in Cordopreg at least, one must exceed 1.5 MW/cm^2 in order to ignite an LSC wave plasma. The data points near 2 MW/cm^2 are consistent both with steady-state vaporization and the ignition of an LSC wave plasma.

In order to show the best theory/data fit, we have plotted in Fig. 11.5 the surface pressure data for all four targets. In general, the surface pressure appears to be independent of the detailed nature of the target for a given intensity. Above 2 MW/cm^2 the surface pressures are in general agreement with the laser supported combustion wave plasma prediction with the transition from LSC wave to LSD wave occurring above 4 MW/cm^2. Below approximately 1.5 MW/cm^2, the surface pressure predictions are in general agreement with an in-depth absorption model having an absorption

depth of approximately 6 microns. The region between 1.5 MW/cm^2 and 2 MW/cm^2 is consistent with both the LSC wave interpretation and the steady-state vaporization interpretation. This data does not resolve the issue of the precise threshold for plasma ignition.

11.3 Temporal Surface Pressure History

SRI measured not only the maximum surface pressure but also the entire temporal response of a pressure gauge on the back surface of the target[39]. The interpretation of this data is somewhat clouded by the fact that there is a time delay between the pressure being imparted to the surface and the response of the detector. The delay obstructs absolute measurements of the onset time of the pressure. However, the qualitative nature of the curve can give us an indication as to whether the pressure was imparted promptly or whether it occurred with a gradual buildup. Sketches of a variety of reduced pressure traces from SRI are shown in Figs. 11.6 - 11.9.

In Fig. 11.6, the pressure response is plotted for an aluminum target (for reference) with an intensity of approximately 3.9 MW/cm^2, and an E-glass target with an intensity of 4.7 MW/cm^2. The pulse time in both cases is approximately 10 microseconds. It is well known that there is a plasma over the aluminum surface at these intensities. The aluminum pressure trace rises abruptly to approximately 25 bars which is consistent with the predictions based on laser absorption wave theory. Both the rapid pressure rise and the sawtooth nature of the earlier time pressure response are typical of measurements of surface pressure produced by plasmas. (The sawtooth nature of the pressure response may be an artifact of the transducer response to rapid pressure increases, rather than an accurate representation of the surface pressure. Even if it is only an artifact, it can still provide information about qualitative changes
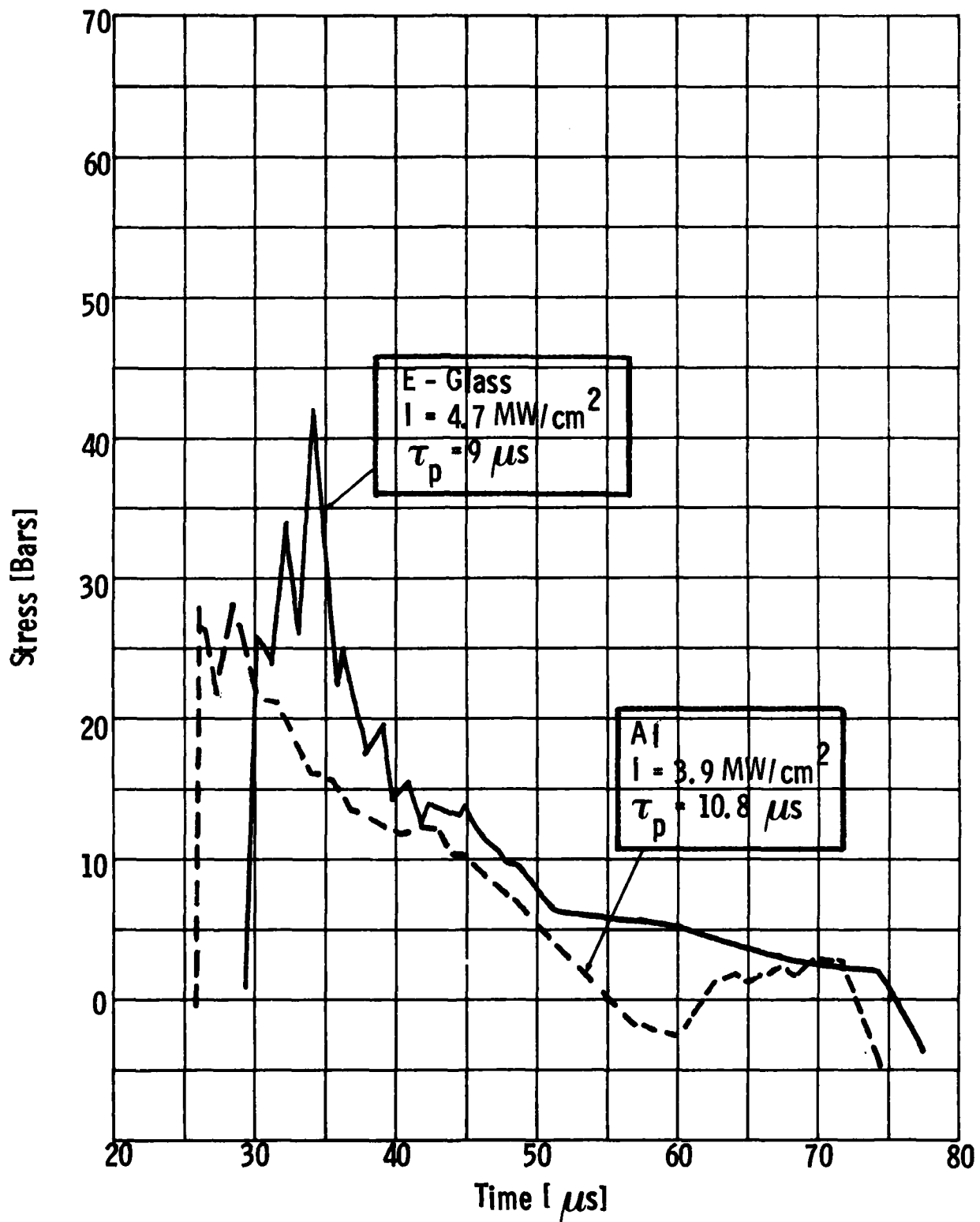
Fig. 11.6 Surface Pressure as a Function of Time. From Ref. 39.
Comparison of Response of E-glass Target and Al Target.

257
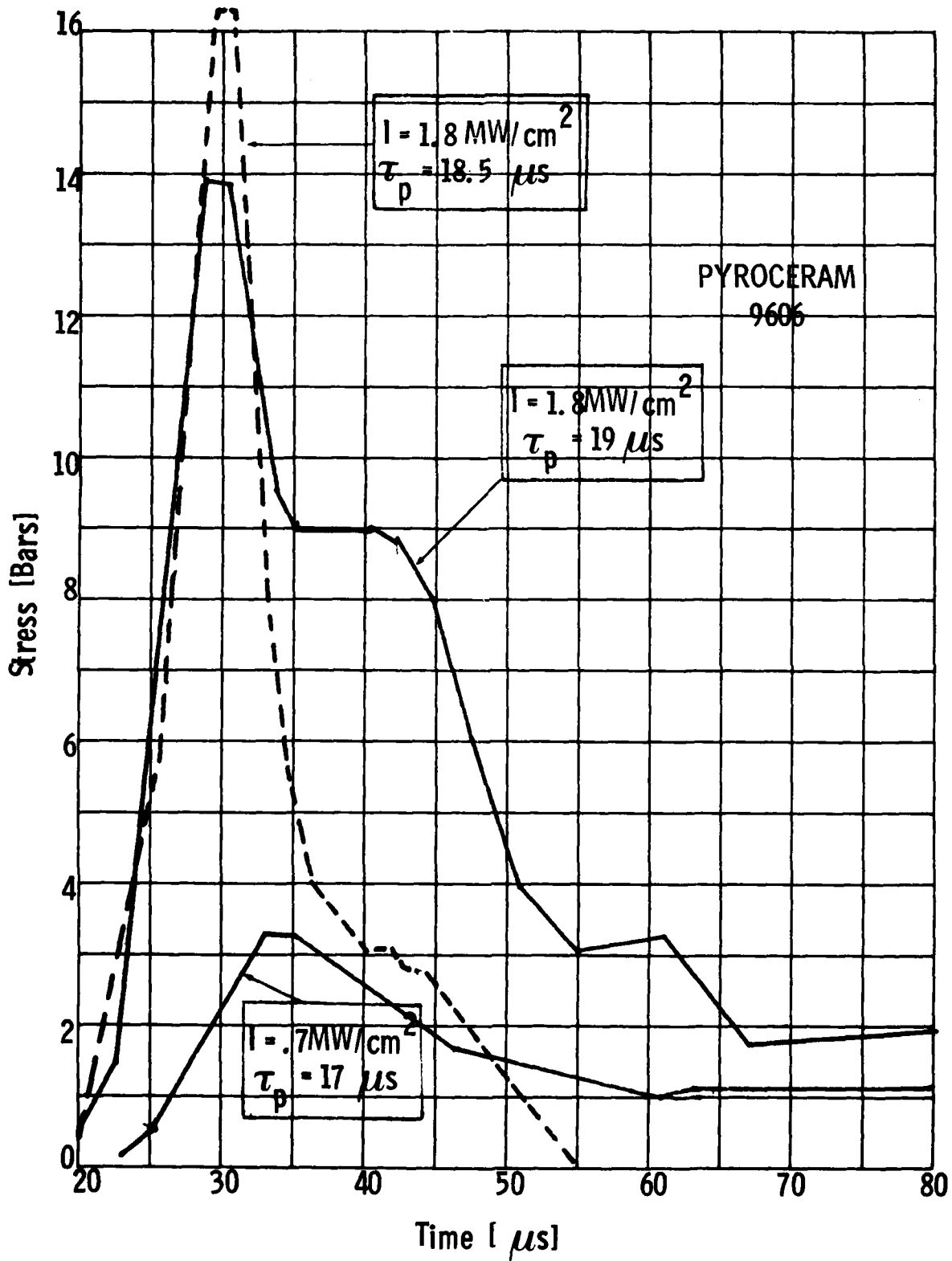
Fig. 11.7 Surface Pressure on Pyroceram Target as a Function of Time. From Ref. 39.
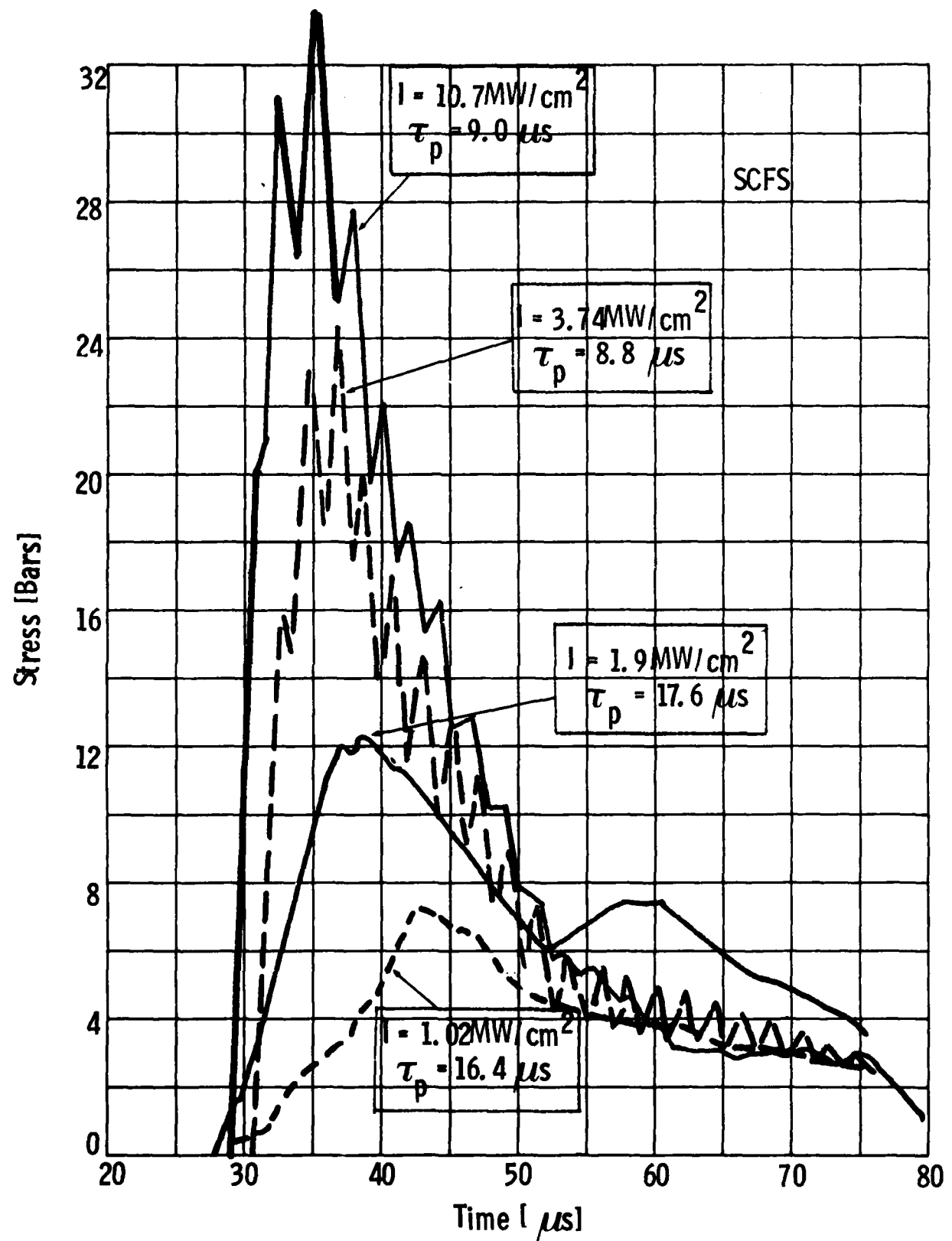
Fig. 11.8 Surface Pressure on Slip Cast Fused Silica as a Function of Time. From Ref. 39.
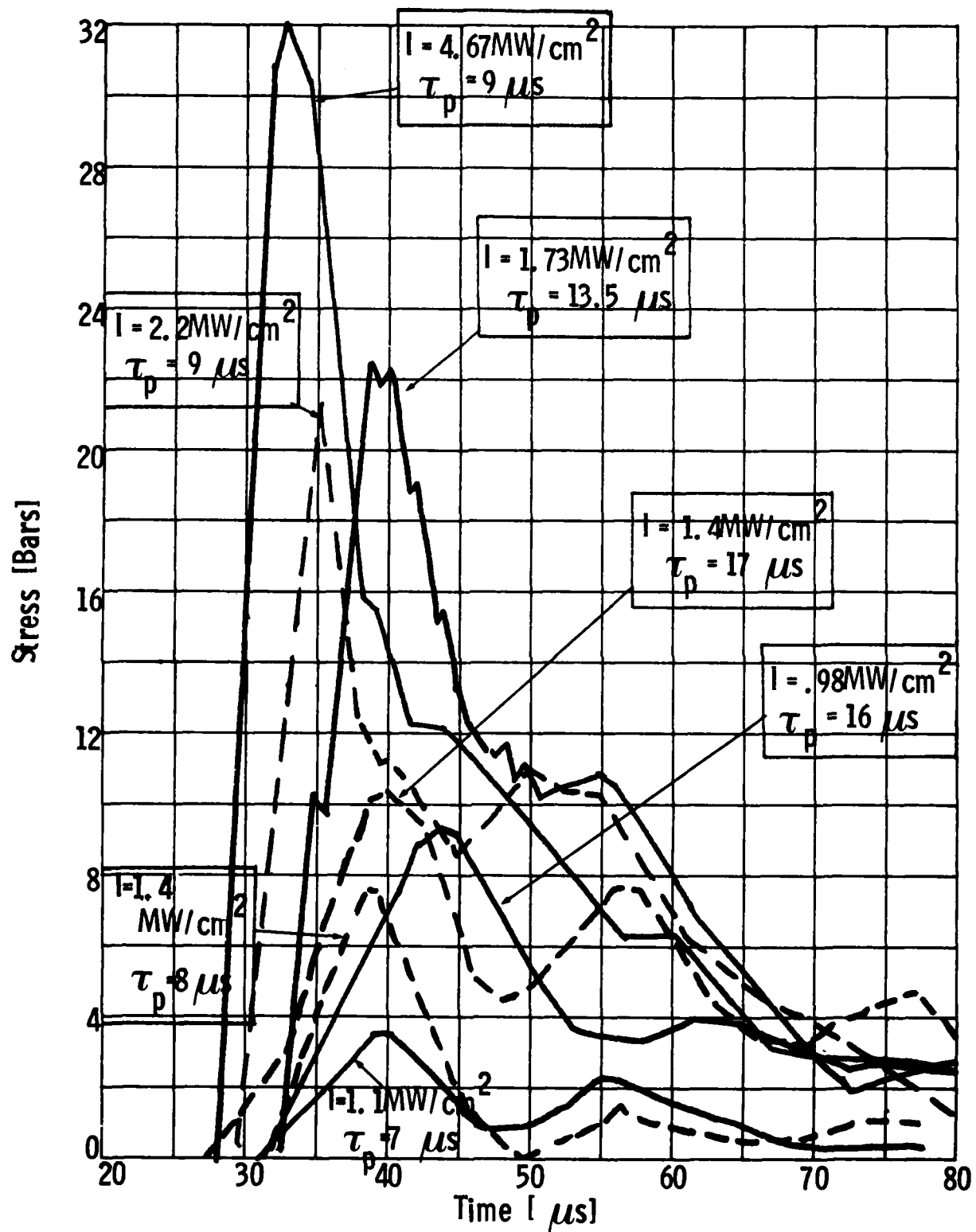
Fig. 11.9 Surface Pressure on Cordopreg Targets as a Function of Time. From Ref. 39.

in the character of the pressure response because the surface interaction
at laser intensities where the response is jagged must differ from the
interaction at laser intensities where the response is smooth.) The E-glass
example similarly exhibits an abrupt pressure response rising to
approximately 25 bars immediately. The jagged structure of the pres-
sure response in this case is extreme with a peak value of roughly 42 bars
being given. This is the value which is plotted in Fig. 11.3. However,
the pressure that is predicted by laser supported absorption wave theory
is a time-average value over the plateau pressure of the laser pulse. For
this E-glass example a more reasonable pressure is approximately 30
bars, which is consistent with the other pressure measurements shown in
Fig. 11.3. Normally, the saw-tooth nature is not so extreme, and the differ-
ence between the peak pressure, which is plotted in Figs. 11.1 - 11.5, and the
average pressure of the plateau is only a few bars. This example was singled
out to show how some of the unusual points can be understood by detailed ex-
amination of the pressure trace. Furthermore, it shows that the character
of the pressure response over the E-glass at an intensity of 4.7 MW/cm^2
is similar to that of aluminum, in that the pressure response is abrupt and
the plateau has a sawtooth character.

The traces for three shots on pyroceram are shown in Fig. 11.7. The
intensities of these shots are .7 MW/cm^2 and 1.8 MW/cm^2. The initial
pressure onset in all three cases is much slower than it was for the
aluminum shot in Fig. 4.6. This behavior is consistent with in-depth
absorption, but it cannot be unambiguously determined whether the response
of 1.8 MW/cm^2 is indeed the result of in-depth absorption or rather the
result of poor plasma ignition. One would speculate, however, from the
data above, that in-depth absorption is the more likely reason.

The traces for four shots on slip-cast fused silica are shown in Fig. 11.8. The low intensity shot at an intensity of 1.02 MW/cm^2 has a very slow rise in pressure consistent with in-depth absorption. The rise for an intensity of 1.9 MW/cm^2 is also quite slow and is suggestive of in-depth absorption. For an intensity of 3.74 MW/cm^2, however, there is an abrupt pressure rise and the jagged structure characteristic of the measurement of an LSC wave. The same nature is evident in the trace for the shot at 10.7 MW/cm^2. These results suggest that in-depth absorption and poor plasma formation are present below 2 MW/cm^2 for slip-cast fused silica, but at a higher intensity there is abrupt formation of a plasma.

Several traces are plotted for Cordopreg in Fig. 11.9. The lowest intensity case, .98 MW/cm^2, exhibits the slow onset of pressure characteristic of in-depth absorption with no plasma formation. The same character persists at intensities of 1.1 MW/cm^2 and 1.4 MW/cm^2. However, at an intensity of 1.73 MW/cm^2 the pressure tends to rise more quickly and to show the beginning of the jagged peaks associated with the measurement of pressures produced by LSC waves. At even higher intensities the pressure rise is still quite steep taking only of the order of a few microseconds, but the pressure trace is smoother than the 1.73 MW/cm^2 case. Nevertheless, it is believed that above 1.73 MW/cm^2 there is indeed an LSC wave plasma formed. The analysis of the pressure traces for Cordepreg suggest that no plasma is formed below 1.5 MW/cm^2 but plasma is formed above 1.73 MW/cm^2. We do not know, however, whether or not plasma is formed at intensities between 1.5 MW/cm^2 and 1.7 MW/cm^2.

As mentioned above, the interpretation of these pressure traces is very tenuous, both because the absolute time scale is not known and because there are substantial variations in the pressure about the constant slowly changing values predicted by theory. However, certain qualitative trends persist and can be used to justify the conclusion that, for the first laser pulse, plasmas are not formed over dome materials until an intensity of 1.7 to 2 MW/cm^2 is achieved.

11.4 Q^* in Single Pulse Experiments

The values of Q^* measured in the single pulse physics of interaction experiments[38] for Cordopreg and E-glass are shown in Figs. 11.10 and 11.11. Because of the large amount of scatter in the Q^* data, it is impossible to use the Q^* data above to deduce the nature of the surface interaction. Since we have already used the pressure data to infer the nature of the interaction, we now examine the Q^* data to ascertain if it is consistent with the conclusions derived from the pressure data. In other words, the detailed examination of the Q^* data discussed below, strives to demonstrate that the Q^* data is consistent with the model developed to explain the pressure data; it does not attempt to prove that the Q^* data can be explained only by this model.

The data in Fig. 11.10 represents the Q^* for Cordopreg alone. At first sight it may appear that a good fit to the data is to draw a straight line starting from the point at .78 MW/cm^2, extending through the bulk of the data between 1 and 2 MW/cm^2, and finally ending roughly in the middle of the scattered data points around 4 to 6 MW/cm^2. However, this approach to correlating the data is at variance with the known physics. It is believed, as has been discussed earlier in this section, that below 1.5 to 2 MW/cm^2 there is no plasma formation whereas above 2 MW/cm^2 the interaction is surely dominated by the formation of a laser supported combustion wave. The amount of energy transferred to the surface by these two different types of interactions is expected to differ widely. Therefore, one does
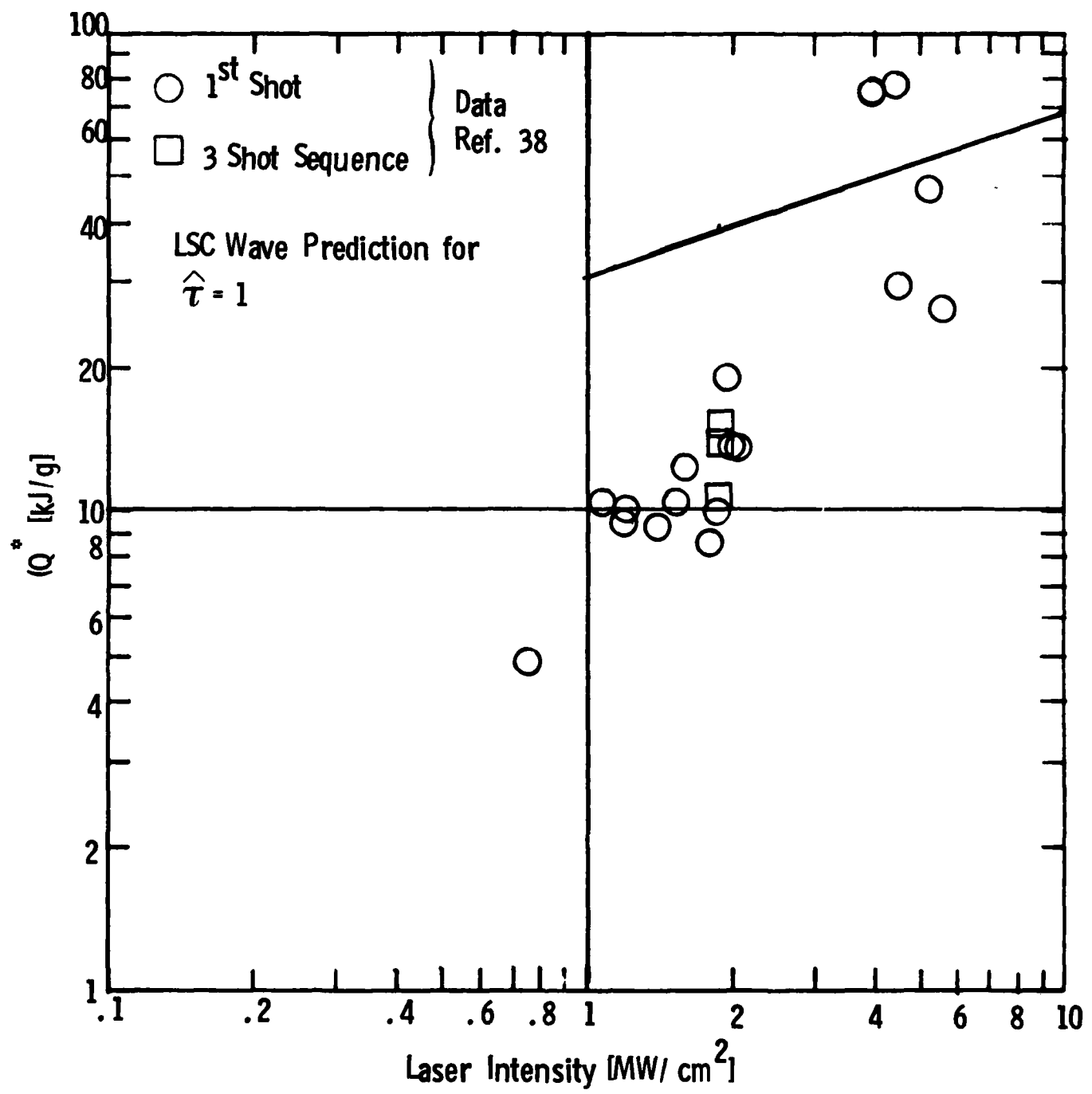
Fig. 11.10 Data Showing Q* for Cordopreg as a Function of Laser Intensity.
Theoretical Prediction for Q* for LSC Wave Plasma at $\tau = 1$
is Shown Assuming All Plasma Radiation to Target is Absorbed.
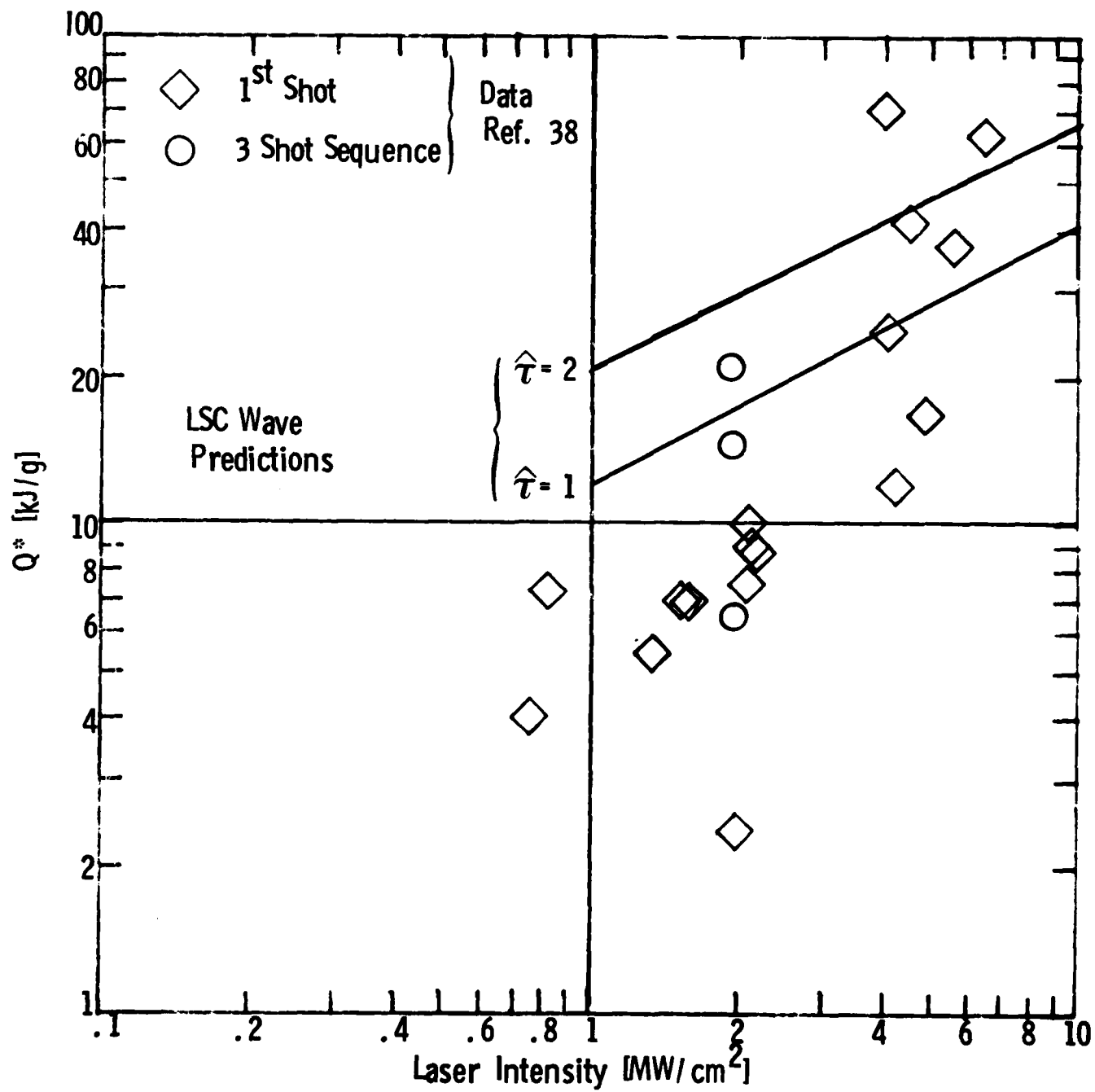
Fig. 11.11 Data Showing Q^* for E-glass as a Function of Laser Intensity.
Theoretical Predictions for Q^* for LSC Wave Plasma at $\hat{\tau} = 1$
and $\hat{\tau} = 2$ are Shown Assuming All Plasma Radiation to the
Target is Absorbed.

not expect a single straight line to be a true representation of the physics underlying the mass removable mechanisms in both regimes. Instead, both regimes must be treated separately.

The measurement[38] of Q^* was complicated by the presence of grease on the back surface of the fiberglass targets. This grease was needed to make the good contact with the pressure transducers on the back surface, but it had to be removed in order to make a measurement of Q^*. As a result, it is possible that some grease was left in some measurements and erroneously low values of Q^* were reported. The value of Q^* for .78 MW/cm^2 in Fig. 11.10 is such a possible case. We will ignore that point.

The value of Q^* between 1 and 1.6 MW/cm^2 falls in the range between 9 and 10 kJ/g. This is interpreted as being the Q^* for vaporization. As we move to higher intensities, near 2 MW/cm^2, this trend persists, but there also are some points which have considerably higher values of Q^*. Two possible explanations of this behavior are: (1) spotty plasma ignition occurs at these intensities and therefore the energy is not used as efficiently as one approaches 2 MW/cm^2; or (2) there is a small amount of resin on the surface and that the first shot does not truly represent vaporization of an almost homogeneous material, but rather represents first removal of resin layer at low Q^* followed by uniform ablation which has a higher Q^*. This latter explanation is favored by the three data points represented in Fig. 11.10 by squares. They represent three subsequent irradiations of the same spot. The first irradiation has a Q^* of about 10.5 kJ/g which is consistent with the Q^* measured in the region between 1 and 2 MW/cm^2. The second and third shots on the same spot, however, show higher value of Q^*; namely, 13.5 kJ/g and 14.5 kJ/g. This sequence of three shots indicates that a lower Q^* mechanism operates for at least part of the first pulse. (It is possible to explain this behavior as being the result of plasma ignition only if the plasma ignition threshold changes between the

266

first and second pulse.) It is claimed, therefore, that the data between 1 and 2 MW/cm^2 can be understood as a result of mass removal by ablation without the formation of a plasma. The typical value of Q^* in this regime for multiple pulse experiments (where first pulse effects are minimized) is expected to be roughly 13.5 kJ/g as long as there are no additional mass removal mechanisms present in multiple pulse experiments.

The data between 4 and 6 MW/cm^2 lies considerably above the data between 1 and 2 MW/cm^2. This is consistent with the interpretation of the formation of a plasma, followed by ablation of material due to the energy transfer by reradiation from the plasma. A theoretical prediction for the value of Q^* corresponding to energy transfer from an air plasma is shown in the dashed line labeled $\hat{\tau} = 1$. This line is drawn assuming that a Q^* of 10 kJ/g, the value that fits the below plasma data, is appropriate for characterizing mass removal by the energy which reaches the surface. The LSC wave theory of Part I for the energy radiated from the air plasma was used. All radiated energy was assumed to be absorbed by surface. The difference between the $\hat{\tau} = 1$ line and the $Q^* = 10$ kJ/g line is the result of the inefficiency of coupling the energy into the surface through a plasma. The data was taken for values of $\hat{\tau}$ ranging from 1.3 to 3; therefore, one would expect that the results should fall above the $\hat{\tau} = 1$ line.

It should be noted, however, that there is substantial scatter in the data at high laser intensity. In fact, for one typical example, a shot at 4.7 MW/cm^2, two widely different values of Q^* were found on two identical experiments on fresh targets. One value gave Q^* of 28 kJ/g whereas the other gave a Q^* of 72 kJ/g. Thus, the scatter represents experimental uncertainties in data rather than the effect of changing laser pulse parameters.

These uncertainties are expected for two reasons: only small amounts of mass are being removed and, therefore, it takes only small variations in the amount of mass removed to lead to large variations in Q^*; and the presence of grease, which may not be as important when large amounts of mass are removed, becomes extremely important for the small amounts of mass removed here. It is not the purpose, however, of this analysis to try to explain all the details of the data. Rather, it is to indicate that the gross features of the data can be understood considering mass removal by vaporization. In summary, we find for intensities below 2 MW/cm^2 no plasma is created, and the value of Q^* experimentally observed in approximately 10 kJ/g (for the first pulse). For intensities above 2 MW/cm^2, air plasmas are ignited and the data, which has a large amount of statistical uncertainty, does not contradict the notion of vaporization induced by radiative transfer from the plasma.

In Fig. 11.11 a similar plot of Q^* data is shown for E-glass. It should be noted that E-glass has a rather large layer of resin over the surface, estimated to be roughly 10 microns thick. The data for E-glass once again has roughly the same character as for Cordopreg. Below 2 MW/cm^2 the data falls roughly on a flat line around 6 J/cm^2. At 2 MW/cm^2, there is substantial variation in the values of Q^*. Above 2 MW/cm^2, in the plasma regime, the value of Q^* is significantly higher than the average value of 2 MW/cm^2. Because of the large scatter in the data and the existence of a variety of phenomena such as the removal of the resin overcoat and the substantial variation in Q^* for a sequence of three pulses on the same target, the data interpretation is explained in more detail below.

At an intensity of approximately .75 MW/cm^2, there are two data points taken under similar conditions. They vary substantially; one value is 4 kJ/g whereas the other is 8 kJ/g. Since there is no reason to favor one of these points over the other, for purposes of data interpretation they can be considered as statistical scatter about an average value of 6 kJ/g. Then the data in the range of intensities between .75 MW/cm^2 and 1.5 MW/cm^2 are consistent with a constant value of Q^*. Moreover, all these data points correspond to the same incident laser fluence of approximately 15 J/cm^2. It is possible, then, to interpret the low constant value of Q^* as the result of first removing the resin coating, and then ablating some of the fiberglass. We assume that the pure resin can be removed with a Q^* of 3.5 kJ/g, whereas uniform ablation requires the expenditure of 13.5 kJ/g (see Subsection 10.5). It then requires 4 J/cm^2 to remove the resin coating before uniform fiberglass ablation occurs. The average value of Q^* predicted for a 15 J/cm^2 pulse is approximately 7.5 kJ/g which is in reasonable agreement with the data.

At an intensity of approximately 2 MW/cm^2, there is a large amount of scatter in the data. Although it is possible that this scatter is caused by intermittent plasma ignition, it is also consistent with the model used between .75 MW/cm^2 and 1.5 MW/cm^2. First note that the lowest value and the two highest values of Q^*, corresponding to the round circles, represent a three shot sequence on the same target. They illustrate the increase in Q^* as the resin overcoat is removed; they are not analyzed further. The remaining data represents an average value of 8.5 kJ/g, approximately 30% higher than the constant value observed between .75 MW/cm^2 and 1.5 MW/cm^2. However, the data at 2 MW/cm^2 represents an incident laser fluence of approximately 30 J/cm^2. The average value of Q^* for this fluence, as predicted by the model used to explain the lower fluence data, if 9.8 kJ/g, which is 30% higher than the lower fluence prediction. Thus, the 2 MW/cm^2 data is consistent with the explanation of the lower intensity data.

At intensities above $2\,MW/cm^2$ there is no apparent correlation of the data. However, two pairs of data points can be identified in which each of the pair of points were measured under similar conditions. The wide discrepancy between the measured values of Q^* under similar laser conditions indicate that the observed scatter of the data at high laser intensity is the result of experimental uncertainty. For example, at $4\,MW/cm^2$ there are extremely wide variations in the values of Q^*; one measurement gives 12 kJ/g whereas another gives 72 kJ/g. If the values are averaged, however, the experimental data falls close to the theoretical predictions for Q^* for $\hat{\tau} = 1$ and $\hat{\tau} = 2$.

The theoretical values of Q^* for E-glass shown in Fig. 11.11, are lower that those for Cordopreg (Fig. 11.10) in the plasma regime. It is assumed that the plasma radiation ablates material with the same efficiency as the laser radiation. Thus, since the measured value of Q^* below plasma threshold for E-glass is approximately 6.5 kJ/g, which is 35% below the value measured for Cordopreg, the predicted value of Q^* above plasma threshold is also 35% lower for E-glass than for Cordopreg.

As a result of the analysis of Q^* on the single pulse, physics of interaction experiments, we find further confirmation for the view that below $2\,MW/cm^2$ there is no plasma (or at least the interaction is not dominated by the presence of a plasma), whereas above $2\,MW/cm^2$ the interaction is controlled by the presence of a laser supported combustion wave.

11.5 Model for Laser -Target Surface Interactions

As a result of the comparison of the theory and data for single pulse interactions of 10.6 μm radiation with dome materials, a picture of the interaction has emerged in which two regimes exist where different phenomena control the physics of the interaction. At high intensity the interaction proceeds via the prompt ignition of an air LSC wave. The pressure and radiative transport to the surface of the target can be computed from the LSC wave theory developed in Part I of this report. The plasma radiation is absorbed at the surface of the target for wavelengths less than .25 μm and is absorbed in-depth for wavelengths greater than .25 μm. Target vaporization, caused by the absorption of the plasma radiation, has little effect on the surface pressure. The intensity threshold above which plasma effects dominate the surface interaction has been determined to be 2 MW/cm^2, at least for single pulse experiments. This is not to say that plasma ignition never occurs at intensities below 2 MW/cm^2 but only that it does not dominate the single pulse interaction with virgin targets.

At low intensities, below 2 MW/cm^2, the laser target interaction is dominated by the direct absorption of the laser. This absorption occurs in-depth with an absorption depth estimated to be 6 μm for fiberglass and 8 μm for pyroceram. Pressure is generated only as a result of vaporization of the target. Theoretical calculations indicate that the absorbed energy is partitioned into a portion which vaporizes the target and a portion, called residual energy, which remains in the target as heat. The residual energy contribution is limited by the onset of vaporization; for an absorption depth of 6 μm, it is estimated that the residual energy per pulse is limited to a maximum value of the order of 8-14 J/cm^2.

SECTION 12

REPETITIVE PULSE INTERACTION WITH FIBERGLASS

In the two preceding sections it has been shown that mass removal of fiberglass during a typical pulse in a train of pulses is characterized by a value of Q^* of approximately 13.5 kJ/g. (The first pulse, of course, exhibits a somewhat lower value of Q^*.) If vaporization during the pulse is the only method by which mass is removed, the fluence required to penetrate a thick target can be easily estimated. For example, to penetrate a 25 ply target of Cordopreg requires a total fluence of 15.2 kJ. Since this fluence must be supplied at intensities below the plasma threshold, say 1.5 MW/cm^2, it requires over 500 twenty microsecond pulses to penetrate the target.

There may be, however, other mechanisms which can enhance mass removal. It is possible that after sufficient ablation the impulse generated by ablation may punch through the target. However, from experiment,[40] it is known that the impulse generated in the interaction can not destroy a virgin target with more than two plies. Therefore, impulse alone can not be expected to significantly decrease the requirements for penetration of a thick target.

The above discussion assumes that each pulse operates independently and there is no effect on the target other than immediate target material removal.[41] Since the energy and pulse requirements for ablative penetration of a target are prohibitive, it is worthwhile to investigate other mass removal mechanisms which are more energy efficient. It was noted in Subsection 10.5 that any mechanism which does not vaporize the glass fibers can provide substantial benefits in terms of energy efficient mass removal. Delamination presents an extremely efficient method of removing material; it can result from the gradual build-up of energy in the target over a

273

series of pulses. Moreover, delamination was observed in the early scoping experiments with fiberglass targets.[42] Thus, we concentrate, in this section, on developing a first order analytic model for laser induced delamination of fiberglass. In addition, we estimate the potential effect of combustion of the pyrolysis products on mass removal for fiberglass. These models are then compared to the available data.

12.1 Delamination Model

Delamination is the removal of an entire ply of fiberglass rather than some intermediate amount of material. The role of resin in fiberglass has been mentioned earlier -- it protects the fibers from rubbing against one another and breaking, and it transmits shear across a broken fiber. It is plausible, therefore, that the disappearance or degrading of the resin throughout the whole thickness of a ply, is a necessary condition for delamination. The mechanism by which the resin is likely to be removed or degraded is pyrolysis caused by heating of the target. From our earlier analysis of laser absorption, it was determined that the laser is absorbed within 6-8 μm of the surface. Since a ply of Cordopreg is approximately .025 cm thick, the energy required to pyrolyze the resin must be transferred to the rear surface of the ply by conduction. Furthermore, only the energy which remains in the target after the pulse is terminated, that is, the residual energy defined in Subsection 10.6, is useful in heating the target. The energy expended in vaporization is carried away from the target and can not contribute to delamination.

From the above observations, a first order model of delamination can be constructed. The target heats as a result of the residual energy flux. The energy which is deposited near the surface is transported into the target by thermal conduction, and a temperature profile similar to the one sketched in Fig. 12.1 is obtained. Pyrolysis occurs as the resin is heated. Although the pyrolysis commences at low temperatures, it
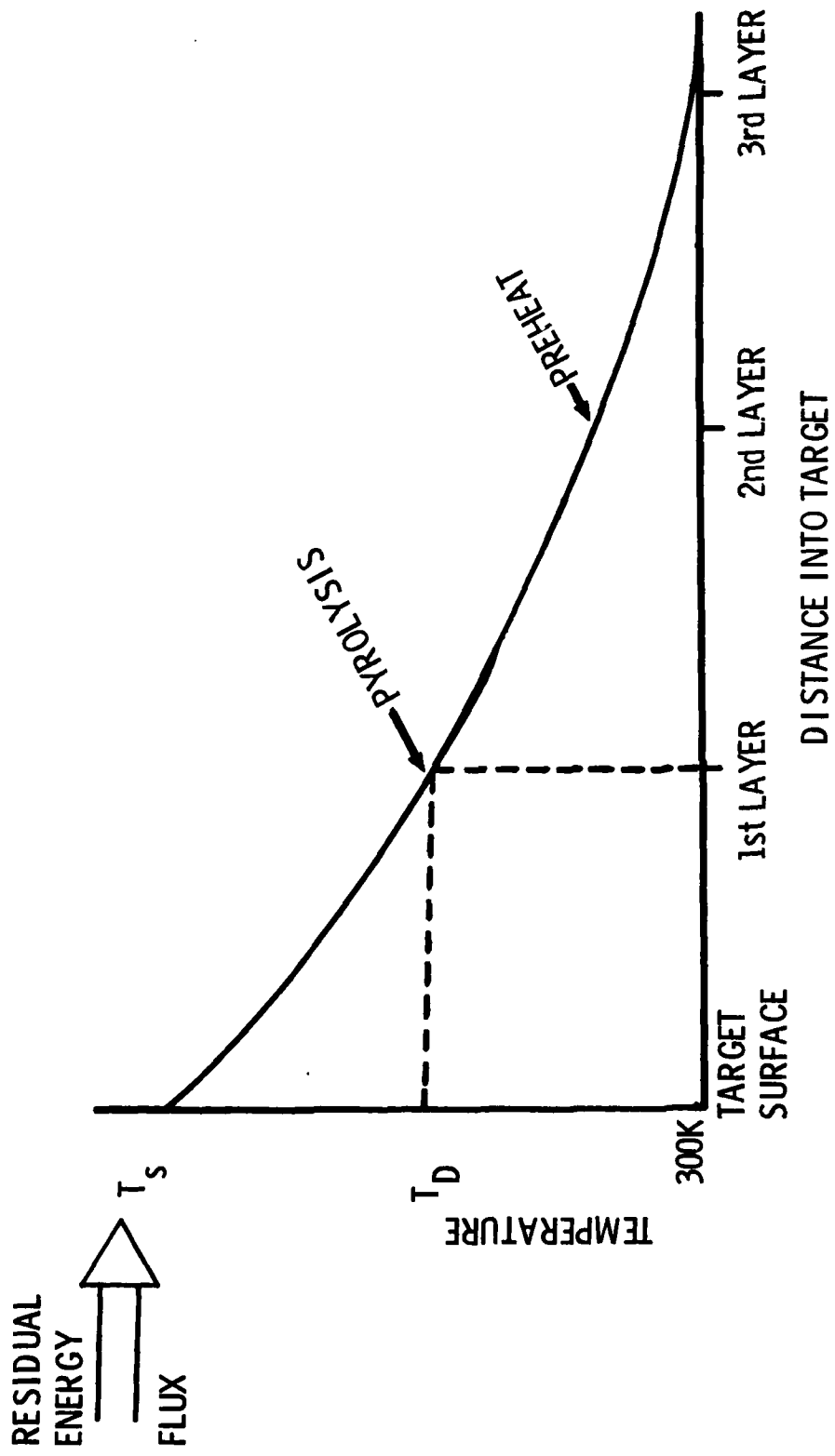
Fig. 12. 1 Sketch Showing Temperature Profile in Fiberglass Target Just Prior to Delamination of First Ply.

becomes significant on the time scale of the pulse repetition period only when a temperature of the order of 950K is reached. (See the discussion in Sec. 9.3.) The criteria for delamination is that enough energy be conducted to the back of the ply to heat the fiberglass to a temperature close to 950K and to provide the heat of pyrolysis. If the conduction of the heat into the target is approximated by analytic solutions of the conduction equation, the heat of pyrolysis must be incorporated into the model by adjusting either the specific heat of the material or the "delamination" temperature which is denoted by T_D. The latter method is used in the model detailed below, and delamination occurs when the temperature at the back interface of the ply reaches the delamination temperature, as illustrated in Fig. 12.1.

As a first approximation, it can be assumed that the residual energy E_R is deposited near the surface of the target in a profile corresponding to in-depth absorption with an absorption coefficient k_L; that is, the initial temperature profile immediately after the laser pulse ends is given by

$$T(x) = \frac{E_R}{\rho_s c_s} e^{-k_L x} \qquad (12.1)$$

where ρ_s is the target density and c_s is the specific heat. The conduction of energy into the target during the interpulse time is controlled by the usual conduction equation

$$\rho_s c_s \frac{\partial T}{\partial t} = k_c \left(\frac{\partial^2 T}{\partial x^2} \right) \qquad (12.2)$$

where k_c is the thermal conductivity. The solution for the temperature profile $T(x,t)$ of the target, at a time t after the profile given in Eq. (12.1) is imposed on the target is given by

$$T(x,t) = \frac{E_R k_L}{2 \rho_s c_s} \exp\left(\frac{-x^2}{\sqrt{4\kappa t}}\right) \left| F\left(k_L\sqrt{\kappa t} + \frac{x}{\sqrt{4\kappa t}}\right) + F\left(k_L\sqrt{\kappa t} \frac{-x}{\sqrt{4\kappa t}}\right) \right| \qquad (12.3)$$

where κ is the thermal diffusivity, $(\kappa \equiv k_c / (\rho_s c_s))$. In Eq. (12.3) the function $F(y)$ is defined by

$$F(y) = \frac{2e^{y^2}}{\sqrt{\pi}} \int_x^\infty e^{-z^2} dz \qquad (12.4)$$

The temperature at any point x after a series of pulses is found by summing the contributions from each individual pulse, using the appropriate delay time. A typical plot of the surface temperature divided by E_R is shown in Fig. 12.2 for a ten Hertz rep rate. The temperature at the rear of the first ply, x = .025 cm, is shown for three values of the absorption depth ℓ ($\ell \equiv 1/k_L$). The temperature history at the rear of the second ply (x = .05 cm) is illustrated for one absorption depth. If the absorption depth is small compared to the ply thickness, an increase in the absorption depth results in a small increase in the temperature at the back of the first ply for a fixed number of pulses. For absorption depths of the order of the ply thickness the trend is reversed, and the temperature at the back of the ply decreases with increasing absorption depth. The large values of the absorption depth are of interest only for radiation emitted by the plasma in the wavelength band $\lambda > 2500A$. Direct laser absorption has an absorption depth of 6-8 μm. The temperature history is insensitive to such small uncertainties in the absorption depth, so we shall restrict further discussion to a nominal absorption depth of 8 μm.

Enough energy must be transported to the back of the first ply to heat the fiberglass to a temperature of the order of 950K and to supply the heat of pyrolysis. For a heat of pyrolysis of 1000J/g, and a resin content in the range from 20-30%, the temperature difference equivalent to this heat content is approximately 850-975K. The precise values for the heat of pyrolysis and the delamination temperature depend on the details of the material. Note that the number of pulses to reach the delamination
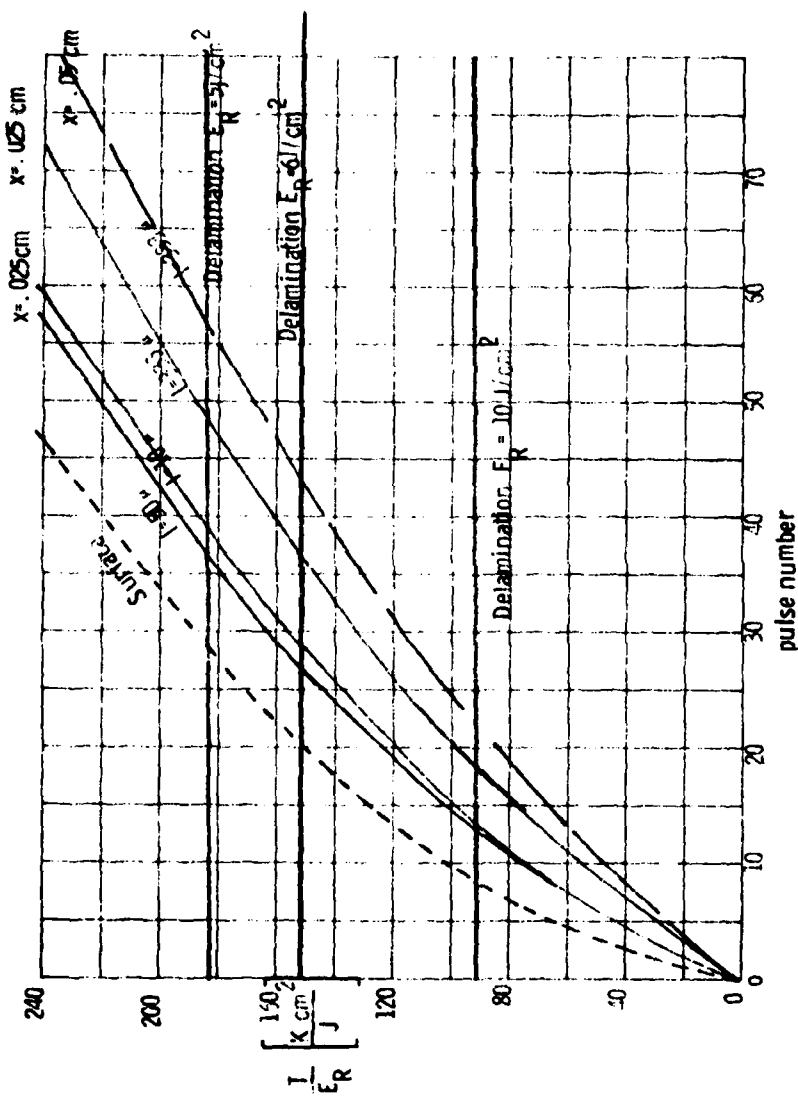
Fig. 12.2 Fiberglass Temperature, Normalized by Residual Energy Per Pulse, as a Function of Pulse Number. Temperature is Shown for Several Depths in Target and Several Absorption Depths.

temperature is sensitive to the value of E_R. Lines corresponding to delamination at a heat content equivalent to a temperature difference of 910K are shown in Fig. 12.2 for three values of E_R. First ply delamination is predicted in 13 pulses for $E_R = 10$ J/cm^2, 28 pulses for $E_R = 6$ J/cm^2, and 38 pulses for 5 J/cm^2.

A considerable amount of heat is transported into the second ply before the first ply delaminates. This energy preheats the ply and, therefore, fewer pulses are needed between first and second ply delamination.

The approximation we have used is a simple analytical model to describe the complex process of heat conduction within a material which contains a resin. Pyrolysis is somewhat akin to a change of phase and can not in general, be modeled analytically. The conduction solution described above is not reliable for estimating the amount of energy conducted past the pyrolysis zone into the depths of the material. However, as a first order estimate, the conduction solution can be used to model the preheat if the residual energy in Eq. (12.3) is replaced by an effective value E_r' which is designed to compensate for the fact that less energy traverses the pyrolysis zone than is predicted by a pure conduction model. The value of E_r' is determined empirically in Subsection 12.3.

The delamination of subsequent plies can now be estimated. First the rear surface temperature of a freshly exposed ply must be calculated. This can be computed from Fig. 12.3 which gives the ratio of T/E_r' for the rear surface of the second ply (x = .05 cm.) at the number of pulses corresponding to the delamination of the first ply. For simplicity, it is assumed that this contribution to the heat (temperature) does not change appreciably before delamination occurs. The number of pulses to delaminate the second ply is then found from Fig. 12.3 by locating the number of pulses needed to

279
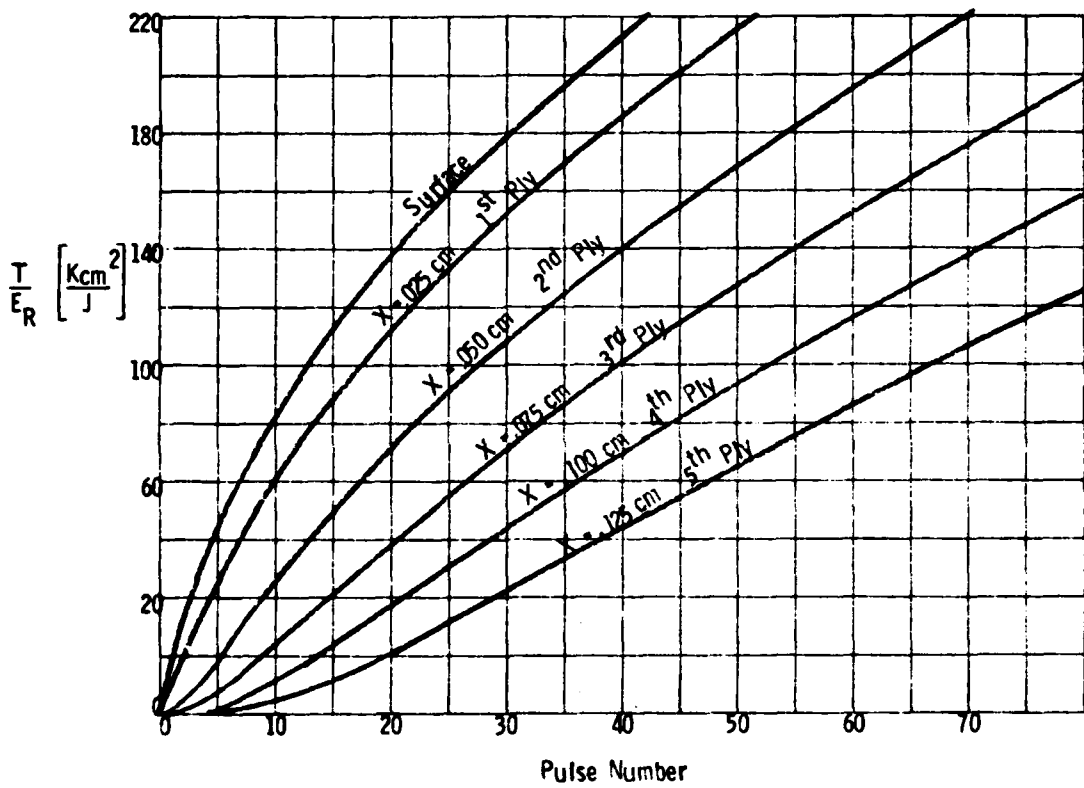
Fig. 12.3   Fiberglass Temperature, Normalized by Residual Energy,
at the Surface and at the Rear of the First Five Plies
of Cordopreg, as a Function of Pulse Number.

increase the temperature, at a depth of .025 cm., from the preheated value to the delamination value. For third ply delamination there are two contributions to preheat -- heating of the third interface (x = .075 cm) until first ply delamination occurs and heating of the second interface (x = .05 cm) for the number of pulses between first and second ply delamination. The number of pulses between second and third ply delamination is again identified as the number required to raise the temperature at x = .025 cm from the preheated value to the delamination value.

Predictions for the delamination of fiberglass have been made for the following conditions: ρ_s = 1.8 g/cm^3, c_s = 1.05 J/g-k, κ = 2.3 x 10^{-3} cm^2/sec, E_R = 5.6 J/cm^2, E_r' = 1.8 J/cm^2 and a delamination temperature difference of 880K (this corresponds to a real temperature of approximately 850-950K when corrected for pyrolysis. For these values, the temperature difference at the front surface and at the rear of several plies is shown as a function of pulse number in Fig. 12.4. The plot of number of pulses versus plies delaminated is shown in Fig. 12.5 with a smooth line through the predicted delamination pulse numbers. Note that there is considerable acceleration in the ply delamination rate. The available data for Cordopreg is also shown.[42] It is required that the target have at least six plies so that acceleration effects caused by the finite thickness of the target can be ignored. The theoretical delamination rate saturates at approximately one ply per 13 pulses if the predictions are extended past four plies.

281

TEMPERATURE DIFFERENCE [K]
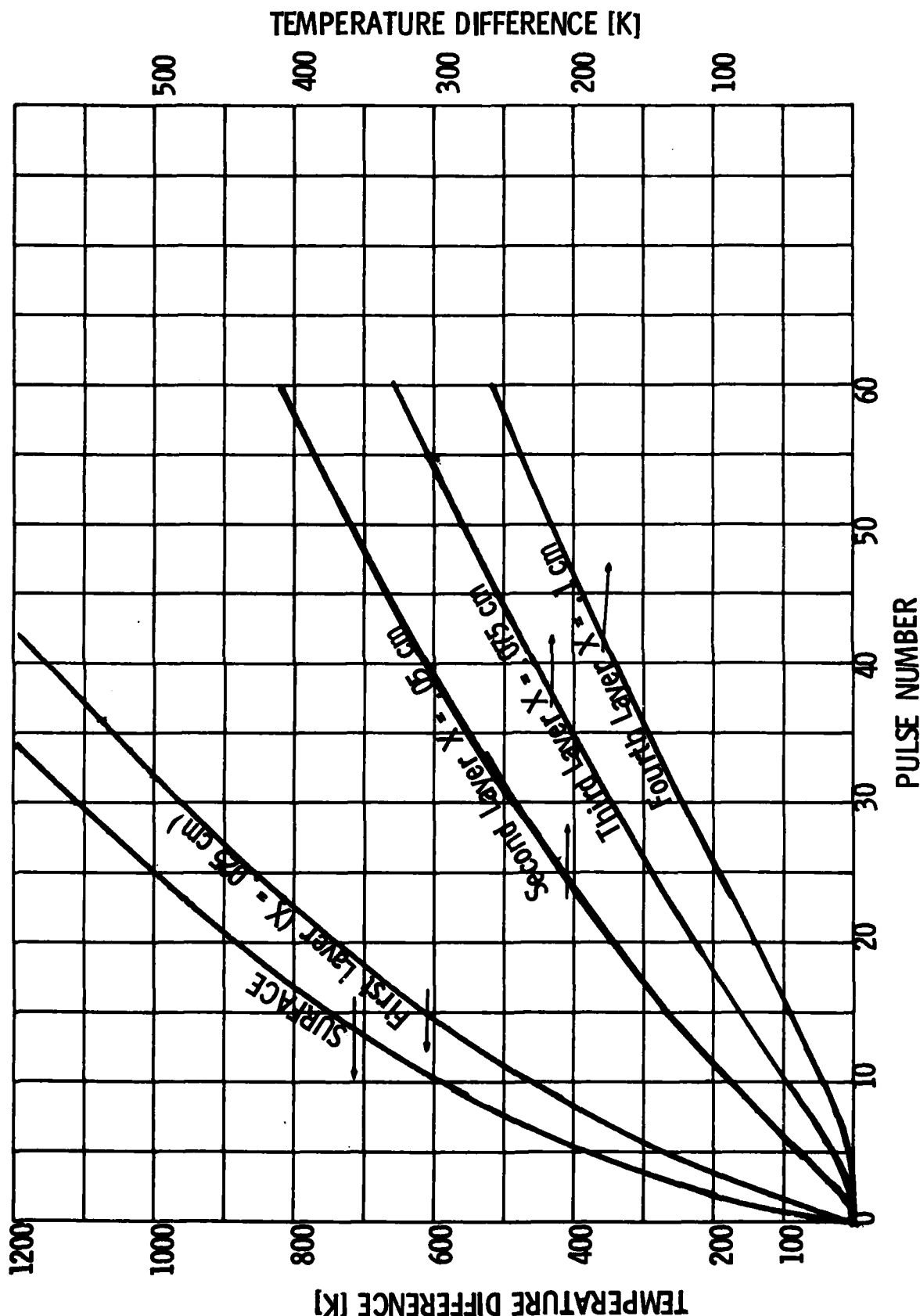
Fig. 12.4 Fiberglass Temperature as a Function of Pulse Number for the Surface and Rear of First Four Plies. The Residual Energy is 5.6 J/cm^2 and the Preheat Value is 1.8 J/cm^2.

282
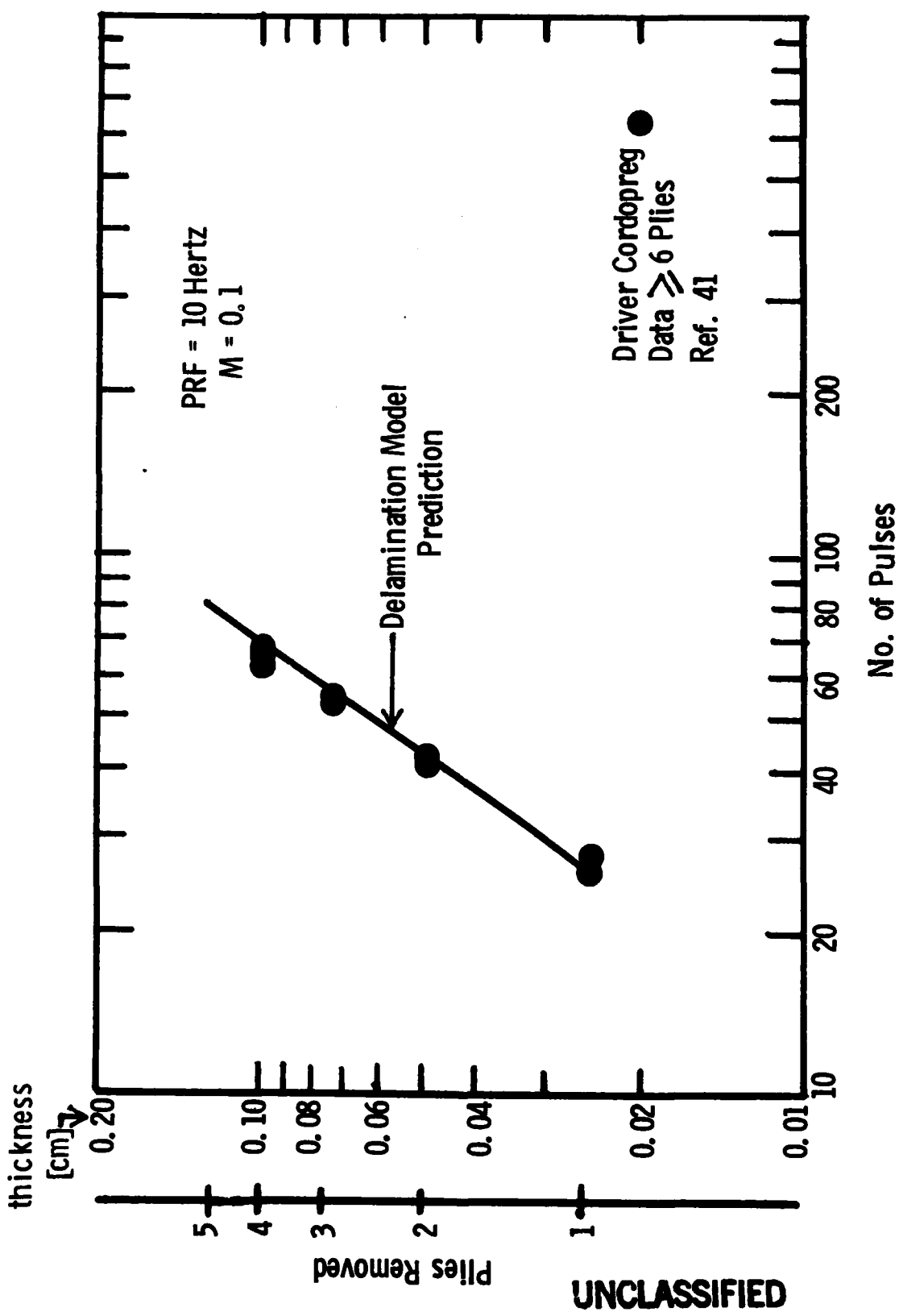
Fig. 12.5 Comparison of Data and Delamination Model Prediction for Number of Plies Removed as a Function of Pulse Number.

UNCLASSIFIED

283

Considering the simplicity of the model, the agreement between theory and the experimental data is remarkable. (Of course, the value of E_R, E_r' and T_D are free parameters in the model; but the values used in the comparison are based upon empirical evidence and theoretical calculations. The permissible values of these parameters are discussed in Subsection 12.3.)

In the experiments, it was necessary to have a flow of air across the surface to remove debris and to improve the beam propagation. Another effect of the air is to cool the target. Experiments performed with flat metal plates and the same wind tunnel indicate that the convective cooling rate is approximately given by

$$\dot{q} \approx .08 \, (M)^{.8} \, \Delta T \, [W/cm^2] \qquad (12.5)$$

where M is the Mach number of the flow and ΔT is the temperature difference between the target surface and the ambient air. This paramaterization is consistent with theoretical calculations.[43] Delamination can not occur unless the front surface temperature is sufficiently hot to cause conduction to transport energy back into the pyrolysis zone which is at a temperature of approximately 900K. As a first estimate, a surface temperature of 1050K is used to estimate the convective cooling losses. (It is realized that the surface is not at this temperature throughout the entire pulse sequence, but it must be at temperatures of this order for a substantial fraction of the pulse sequence.) For a ten Hertz pulse repetition frequency, the convective losses estimated from Eq. (12.5) are $6 \, (M)^{.8} \, J/cm^2/pulse$. For a flow of M = 0.1, the losses per pulse are $.9 \, J/cm^2$; for M = 0.3, $2.2 \, J/cm^2$; and for M = 0.9, $5.3 \, J/cm^2$. If the residual energy per pulse is approximately $7 \, J/cm^2$, it is clear that the convective losses at 10 pps can be important as the flow is increased beyond M = 0.1. The predictions for first ply delamination, for an initial residual energy of $6.5 \, J/cm^2$ before convective losses are subtracted, is presented in Fig. 12.6. Note that as the flow is increased, it rapidly becomes impossible to delaminate any plies in less than 50 pulses. The data points[42] corresponding to M = 0.0 and 0.1 are also shown; they are consistent with theoretical expectations.

284
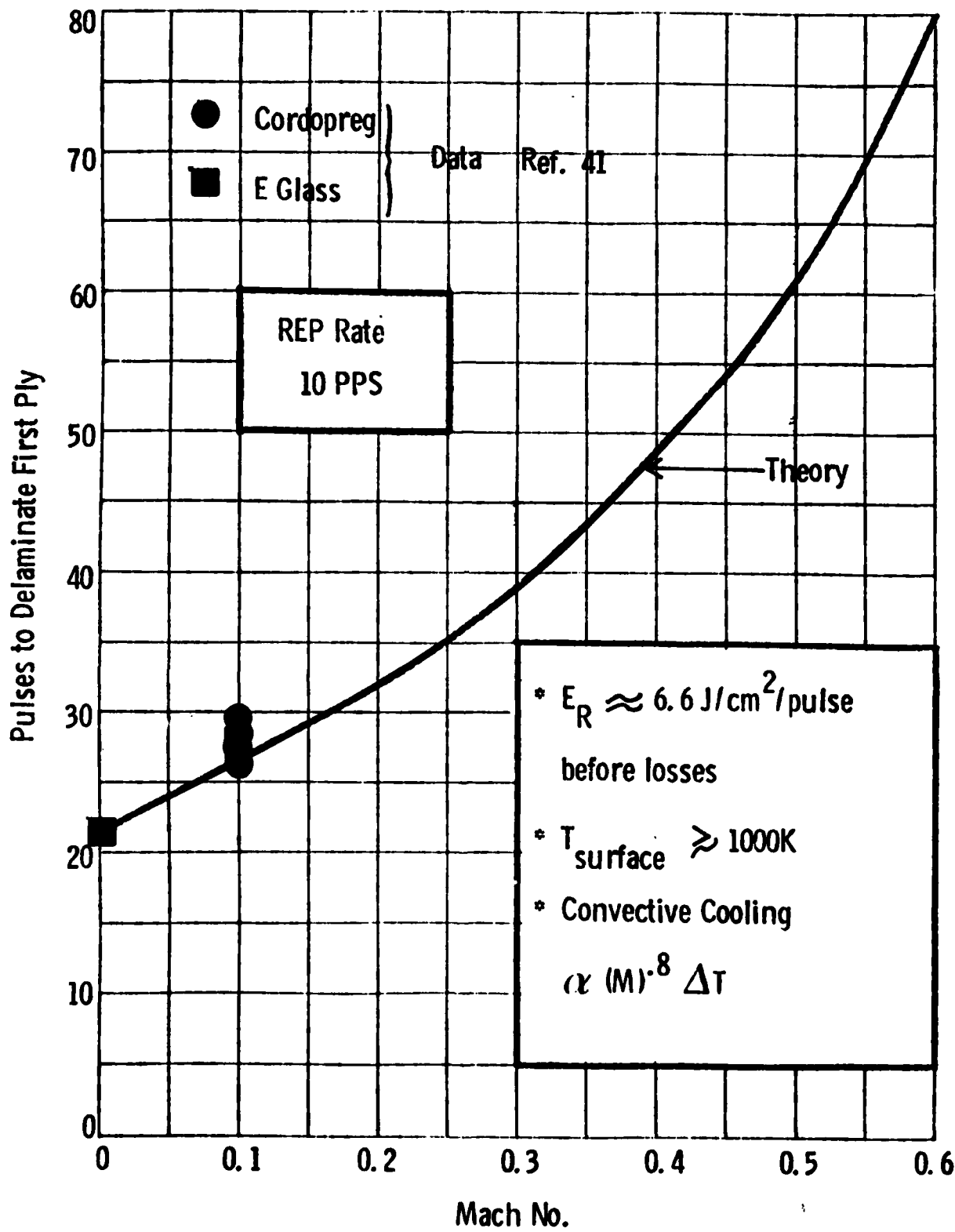
Fig. 12.6 Comparison of Data and Theory for the Effect of Convective Cooling on Number of Pulses to First Ply Delamination.

285

The role of Q^* as a meaningful quantity is in dispute for repetitively pulsed fiberglass experiments since it is possible for mass to be removed from outside the target areas. Nevertheless, it is worthwhile to compute the value of Q^* predicted by the delamination model. For an interaction which removes 4 plies in 70 pulses, with an incident fluence per pulse of 6.5 J/cm^2, the local value of Q^* is 2.5 kJ/g. This value is in agreement with the values observed for the whole target of 2.3 - 2.7 kJ/g. Thus, the value of Q^* predicted by the delamination model is consistent with the observations. It should be noted, however, that, as a result of mass removal outside the spot, this low value of Q^* is sometimes observed for interactions wherein the pulse fluence is approximately 14 J/cm^2. The delamination model predicts a Q^* of 5.4 kJ/g for these cases.

12.2 Combustion Estimates

In many of the repetitive pulse experiments, substantial amounts of combustion are observed in front of the target. Since the repetitive pulsed experiments also demonstrate low values of Q^*, such as 2.7 kJ/g, it has been suggested that the energy produced by the combustion of the pyrolysis products may account for the difference between the single pulse values of Q^* (approximately 13.5 kJ/cm g) and the repetitive pulse values.

In order to assess the potential of combustion to reduce Q^* by virtue of the energy supplied by combustion, consider a situation in which mass is being removed uniformly, such as in a steady-state process, so that the amount of resin pyrolyzed is related to the amount of glass removed. The effect of combustion on Q^* can be estimated by computing the amount of energy available as the result of burning the volatile pyrolysis products of the resin in a gram of fiberglass. We assume that all the energy released in combustion

is recovered by the target, which is at the temperature associated with pyrolysis (this is the lowest target temperature consistent with pyrolysis, and it gives the most efficient transfer of energy to the target), For purposes of this calculation, we assume that the resin is phenolic and it is pyrolyzing at 872K, because the pyrolysis products are well identified for this situation and the energy of formation of the resin and energy of pyrolysis are known[18]. Then the heat liberated by a stoichiometric mixture of volatiles and air is given by the difference between the energy required to form a gram of resin and the energy required to form the combustion products, char $(CO_2$, and H_2O) and to heat the required amount of air to 872K. In terms of the mass m_i of the species i, $\Delta H (i)$, the heat of formation of species i, and $c_p \Delta T$, the enthalpy difference required to heat air from 300K to 872K, the heat liberated, ΔQ, is

$$\Delta Q = \Delta H (resin) - m_{char} \Delta H (char) - m_{CO_2} \Delta H (CO_2) - m_{H_2O} \Delta H (H_2O)$$

$$- m_{air} c \Delta T . \tag{12.6}$$

The required values for the mass of the products and the heats of formation can be found in Ref. 18 and Ref. 5, and are listed in Table 12.1. In these calculations it is assumed that the difference in the heat of formation of the species is relatively insensitive to temperature. Pyrolysis and combustion of a gram of resin imbedded in fiberglass releases approximately 6kJ/g. In terms of the typical fiberglass which has only .2 - .33 grams of resin per gram of fiberglass, the heat released is only 1.2 - 2 kJ/g of fiberglass. The difference between the values of Q^* with and without combustion, denoted by Q^*_{com} and $Q^*_{n.c.}$, respectively, is given by

$$Q^*_{com} = Q^*_{n.c.} - \Delta Q - m_r \Delta H_p \tag{12.7}$$

TABLE 12.1

Concentration and heats of formation of the species involved in burning the pyrolysis products of 1g phenolic at 872 K.

Species i	Amount m_i	Heat of Formation $\Delta H_f(i)$
CO_2	1.536×10^{-2} moles	-94.054 k cal/mole
H_2C	1.712×10^{-2} moles	-57.79 k cal/mole
O_2 required	.0239 moles	$C\Delta T = 4.6$ k cal/mole
N_2 required	.0957 moles	$C\Delta T = 4.355$ k cal/mole
Char	.623 g	295 J/g
Resin	1 g	-2442 J/g

where ΔH_p is the heat of pyrolysis (1176 J/g for phenolic at 872K) and m_r is the fraction of the fiberglass mass which is resin. For the typical fiberglasses mentioned above, the difference between the two values of Q^* is 1.4 - 2.4 kJ/g.

This model grossly overestimates the actual heat contribution of combustion since it assumes that all the energy is recovered. Nevertheless, even this overestimate is incapable of explaining the difference between the single shot values of Q^* and the repetitive pulse values. We must look into other mass removal mechanisms such as delamination, to explain the difference. It should be commented, however, that combustion may still play an important role in mass removal by methods such as delamination; we have shown only that as a pure energy source it can not reduce Q^* more than 1.4 - 2.4 kJ/g.

12.3 Empirical Determination of Parameters for Delamination Model

The amount of residual energy expected per pulse has been modeled in Subsection 10.6. For intensities where plasmas are created, the value predicted depends on the details of the laser pulse and varies from 4 to 7 J/cm^2/pulse. At intensities below the plasma threshold, the residual energy is the smaller of the incident fluence and the maximum value determined by in-depth absorption. For the absorption depth of 6 μm, determined by the pressure response analysis of subsection 11.2, the theoretical value of the residual energy lies between 3.6 and 14.1 J/cm^2. The most reasonable model advanced in Sec. 10.6, predicts 8.4 J/cm^2 for the residual energy corresponding to a 6 μm absorption depth. Moreover, if the average temperature of the target is 700K (rather than 300K), the predicted value of E_R is reduced to 7.5 J/cm^2.

The number of pulses required to delaminate the first ply[42] is shown in Fig. 12.7. As the fluence increases, the number of pulses to first ply delamination decreases until a constant value of approximately 26 pulses is attained. The pulse fluence at which the constant value is reached is interpreted as the maximum residual energy which can be deposited per pulse. The value of the residual energy indicated by the data is somewhat ambiguous because the limiting number of pulses was observed at 4 J/cm^2 but not at 5.25 J/cm^2. Both of these points correspond to interaction with E-glass targets which does not exhibit the clean delamination observed with Cordopreg. Cordopreg delaminates in clean layers and all the energy transport within the target is due to conduction. E-glass appears to be able to delaminate in "tapes" which are approximately .01 cm thick, and radiative transport aids conduction in transferring energy into the target. It is further possible that E-glass and Cordopreg have different limits on the residual energy. For these reasons we discount the data point at 4 J/cm^2 and claim Fig. 12.7 reveals that the maximum fluence which can be left in the target as residual energy is approximately 6-7 J/cm^2.

Lockheed recorded the radiation emitted from the front surface of the target in a band from three to five microns.[44] For a typical run the temperature history is shown in Fig. 12.8. Two histories are shown because the emissivity ϵ of the fiberglass is uncertain; virgin targets have an emissivity of .87 but, some charred targets exhibit emissivities as low as .405. The rapid drop in front surface temperature, which starts after the thirtieth pulse, is associated with delamination. The temperature of the uncovered ply is 1070K for ϵ = .87 and 1240K for ϵ = .405. Also shown in Fig. 12.8 is the predicted front surface temperature from the delamination model with E_R taken to be 5.6 J/cm^2. The general trends predicted by the theory are in agreement with the data. Moreover, if the temperature criterion for delamination is adjusted to correspond to the observed temperature of 1070K, the theory predicts that delamination occurs on the 33rd
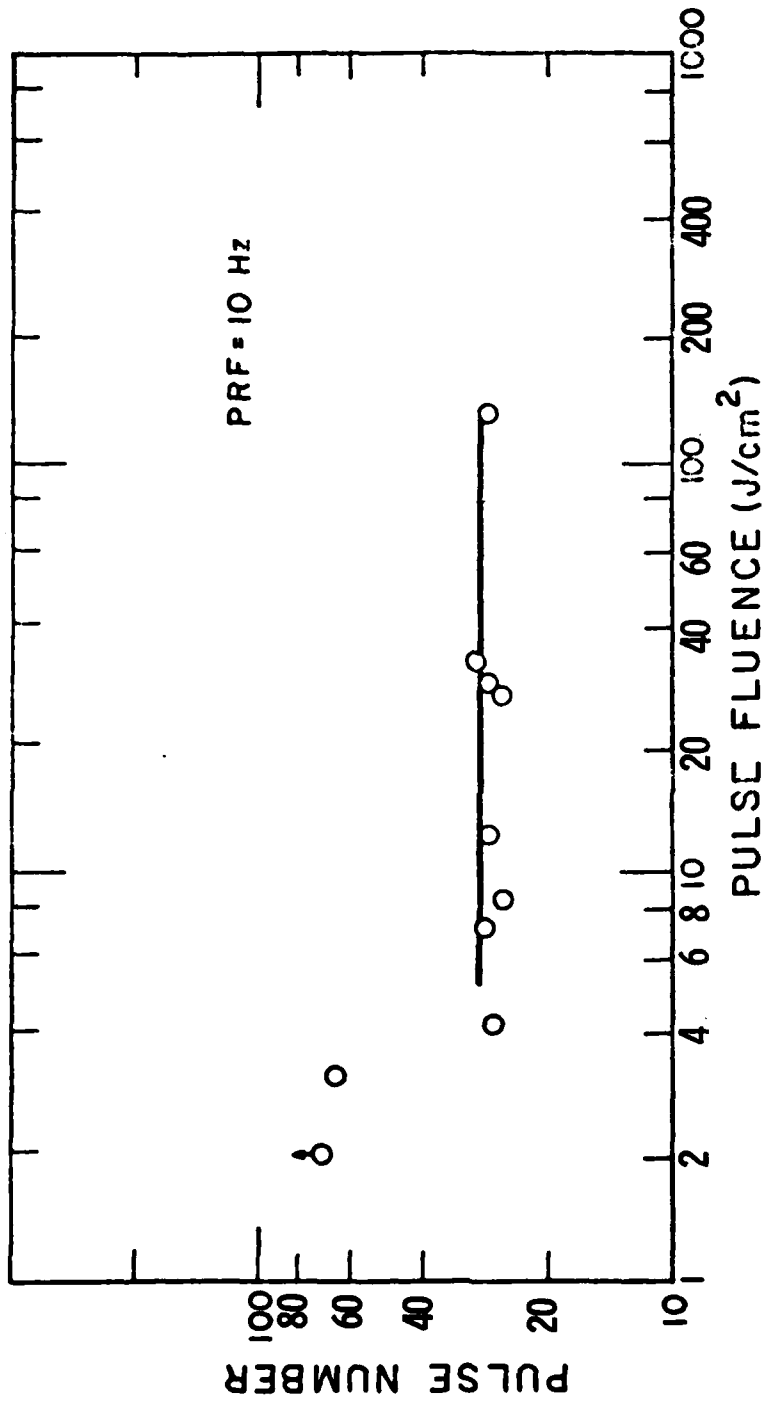
Fig. 12.7 Number of Pulses to Remove First Fiberglass Layer Vs. Pulse
Laser Fluence - Mach 0.1 Flow From Ref. 42.
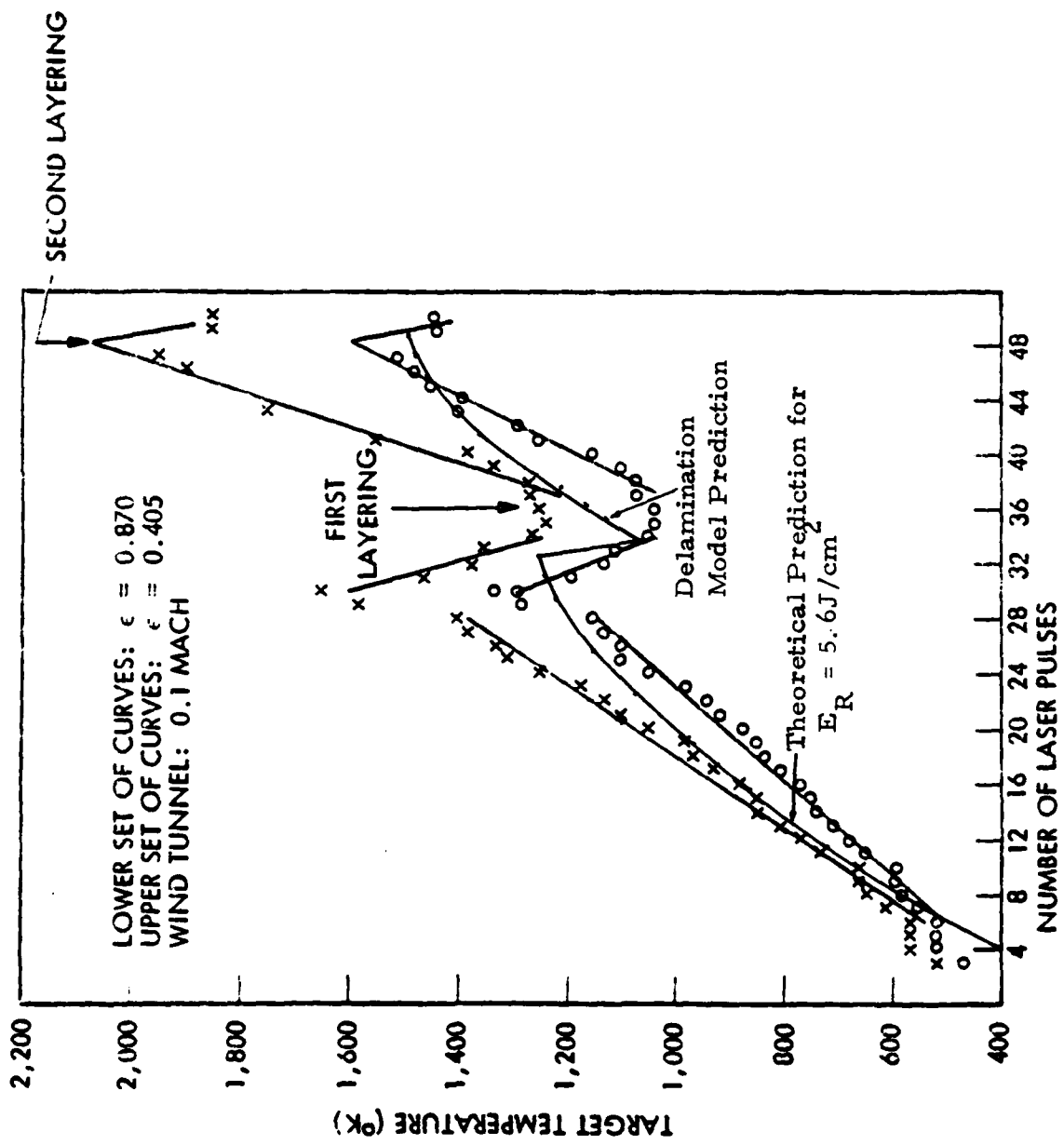
Fig. 12.8 Front Surface Temperature of Cordopreg Target as Measured by Radiometry, Ref. 44. Also Shown is Prediction of Temperature from Delamination Model.

pulse, which is close to the observed delamination time. The agreement between data and theory is further support for a value of residual energy of 6-7 J/cm^2 per pulse. (Convective cooling losses per pulse are estimated as being .9 J/cm^2; therefore, a net residual energy of 5.6 J/cm^2 corresponds to an initial absorbed residual energy of 6.5 J/cm^2.)

Both theory and empirical evidence consistently indicate a value of the residual energy per pulse of 6-7 J/cm^2. For the purposes of making predictions, the value of residual energy has been fixed at 6.5 J/cm^2, as indicated by the analysis of the Lockheed radiometric data,[44] and the correction for convective cooling is determined by Eq. (12.5).

Another parameter which appears in the delamination model is the delamination temperature, T_D. In the analysis of the pyrolysis rates in Subsection 9.3, it was deduced that pyrolysis on the time scale of the interpulse time occurs at a target temperature between 850K and 1150K. Ref.2 quotes a value of 925K as the delamination temperature for Cordopreg. Finally, the Lockheed radiometric data, Fig. 12.8, supports a delamination temperature of 1050K. (It is assumed that the freshly exposed surface has the high value of the emissivity.) Thus, there are three independent pieces of evidence in favor of a delamination temperature cf 850K to 1050K.

Thermocouple measurements of the temperature deep within the target have been made by SRI.[45] Two typical traces of reduced data are shown in Fig. 12.9 and Fig. 12.10 for E-glass and Cordopreg, respectively. In the E-glass curve an inset shows the response during the interpulse period. Note that an immediate temperature rise occurs which indicates that energy is being transferred by some mechanism other than conduction. (It is speculated that radiative transport is the mechanism, although no plasma is believed to be formed. The hot surface itself can radiate and E-glass fiberglass is translucent to the radiation.) For the Cordopreg shots no such immediate response was observed; the long term response may well be dominated by thermal conduction. The best fit of a conduction
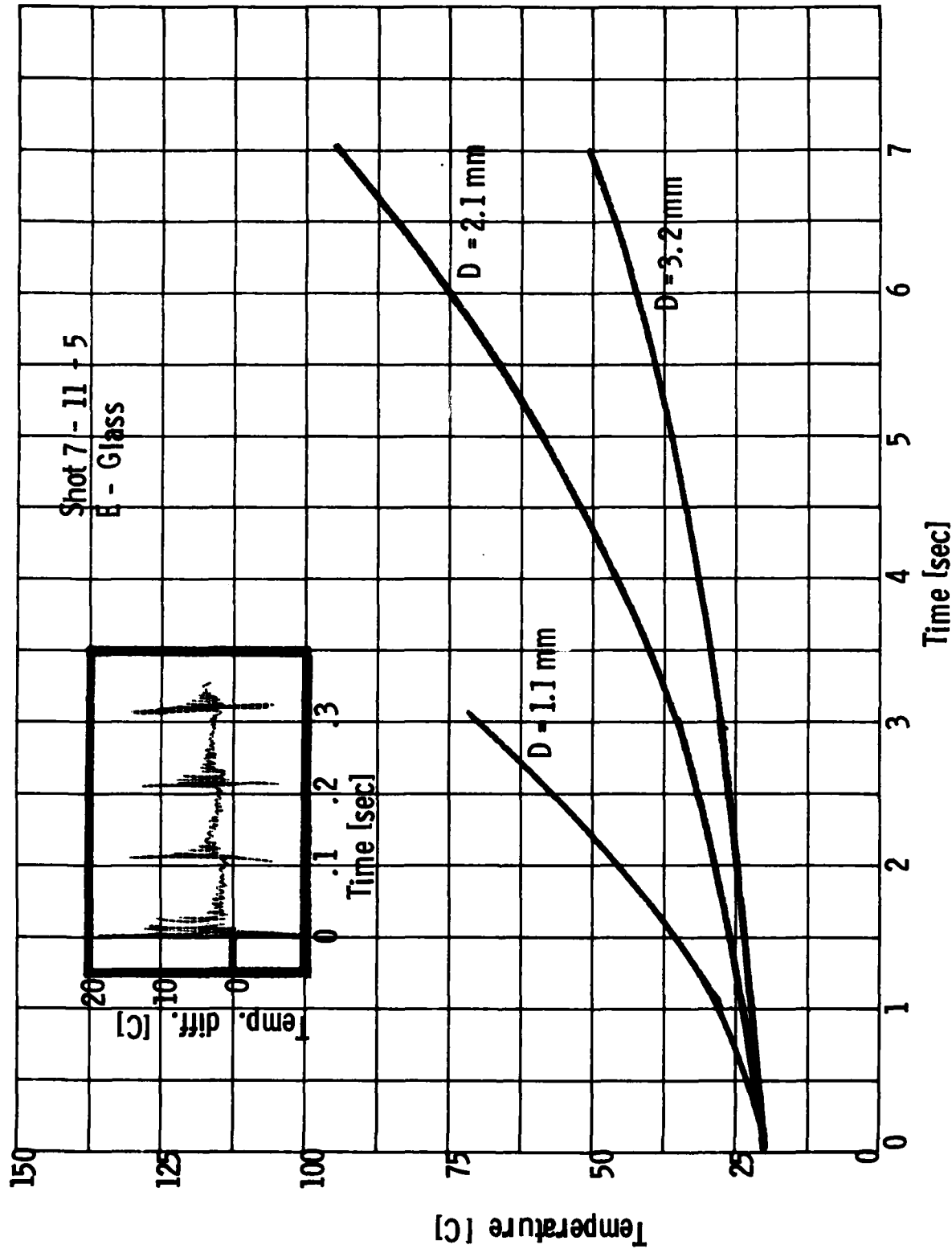
Fig. 12.9 Temperature in E-Glass at Depth D in Target Measured by Thermocouples (Ref. 45) Insert Shows Abrupt Temperature Response After First Pulse.
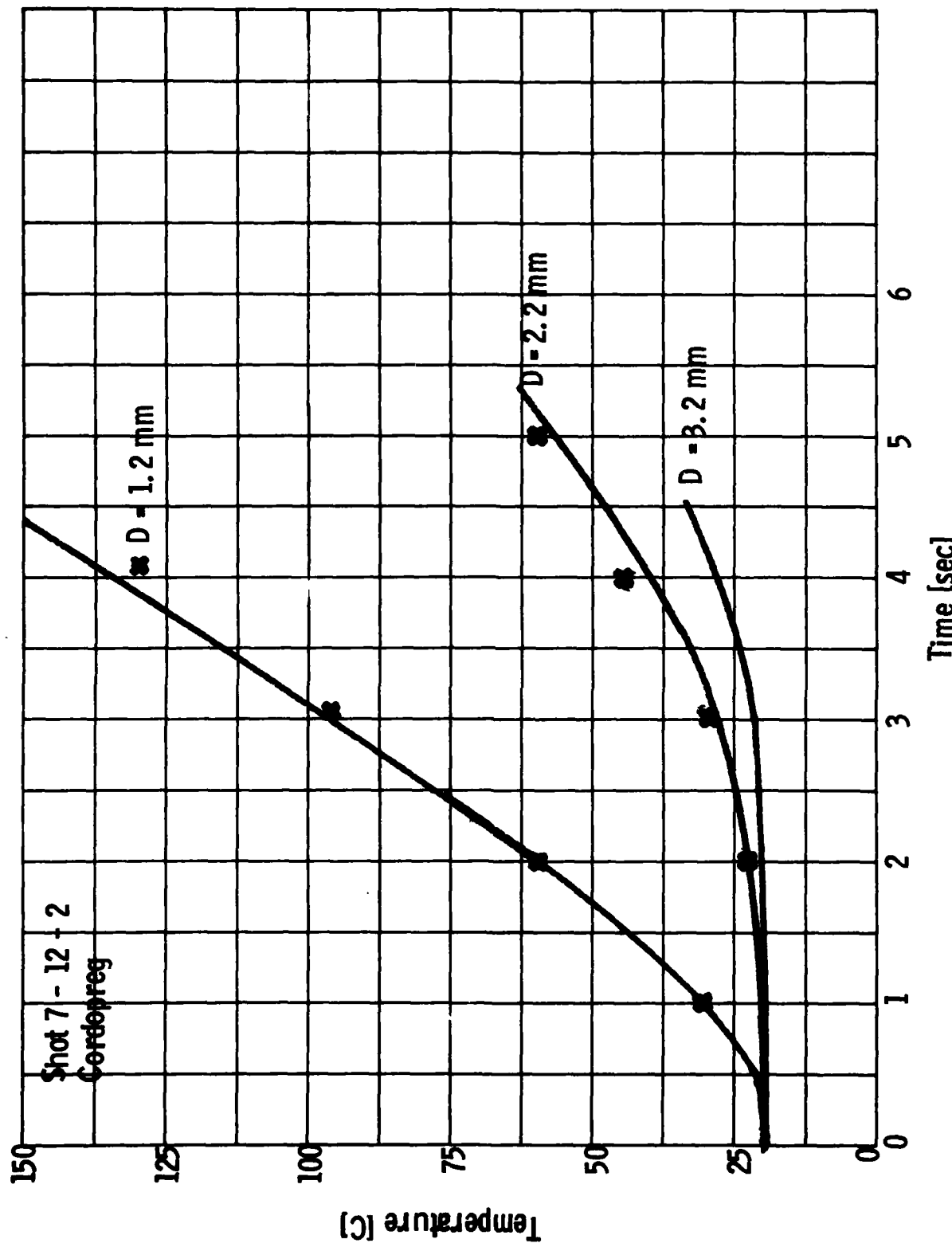
Fig. 12.10 Temperature of Cordopreg Target at Depth D as Measured by Thermocouple, (Ref. 45).Predictions of Conduction Model for E_r = 1.8J/cm^2 are Shown by ▓.

solution to the Cordopreg curve is also shown. There is reasonable agreement between the data and theory despite the fact that pyrolysis and temperature dependent physical parameters are known to exist. The value of residual energy needed to reproduce the curve is 1.6 J/cm^2. Similar calculations on other runs also lead to residual energy estimates in the range from 1.5 - 2 J/cm^2. This is inconsistent with the other estimates of residual energy. It is believed that the in-depth temperature response is sensitive to the amount of energy which passes through the pyrolysis zone on each pulse.

It is possible that other effects, such as temperature dependent physical properties, affect the transport of energy deep into the target. Therefore, despite the good agreement between the data and theory for Cordopreg, shown in Fig. 12.10, another analysis of the thermocouple data has been performed. Deep inside the material the temperature does not respond to the intensity profile of the individual pulses, but instead to the time averaged flux of residual energy. Therefore, consider the case of a constant flux on the surface given by $F_0 \equiv 10 \, E_r'$. The temperature as history in the target is given by [46]

$$T = \frac{2F_o}{k_c} \int_x^\infty \mathrm{erfc}\left(\frac{x}{\sqrt{4\kappa t}}\right) \, dx \qquad (12.8)$$

296

where κ is the diffusivity, T is temperature, t is time, x is position, erfc is the complimentary error function, and k_c is the thermal conductivity. The derivative of the temperature with respect to time obeys the equation

$$\frac{dT}{dt} = \frac{F_o}{k_c} \sqrt{\frac{\kappa}{\pi t}} \exp \left(-\frac{x^2}{4\kappa t}\right) .$$ (12.9)

Therefore, the quantity $\ln\left(\sqrt{t}\,\frac{dT}{dt}\right)$ can be expressed as a linear function of $1/_t$:

$$\ln \left(\sqrt{t}\,\frac{dT}{dt}\right) = \ln \left(\frac{F_o}{k_c}\sqrt{\frac{\kappa}{\pi}}\right) - \frac{x^2}{4\kappa t} .$$ (12.10)

A plot in $\ln\left(\sqrt{t}\,\frac{dT}{dt}\right)$ versus $(1/t)$ for a constant position x should be a straight line if the conduction model is correct. The slope of the curve is given by $x^2/4\kappa$, so that the diffusivity can be determined. If the conductivity is assumed, the value of the intercept of the straight line with the origin $(1/t = 0)$ can be used to determine the residual energy flux.

Plots of these quantities for the E-glass and Cordopreg curves are shown in Fig. 12.11 and Fig. 12.12. The data points tend to have large errors because the derivatives were evaluated from taking differences from the data presented in the graphical form of Fig. 12.9 and Fig. 12.10. The E-glass curve, for x = .2 cm can not be represented by a straight line, which is consistent with the expectation that radiative transport is important. For Cordopreg, however, the data for the two values of x gives consistent intercepts and can be easily represented by straight lines. The
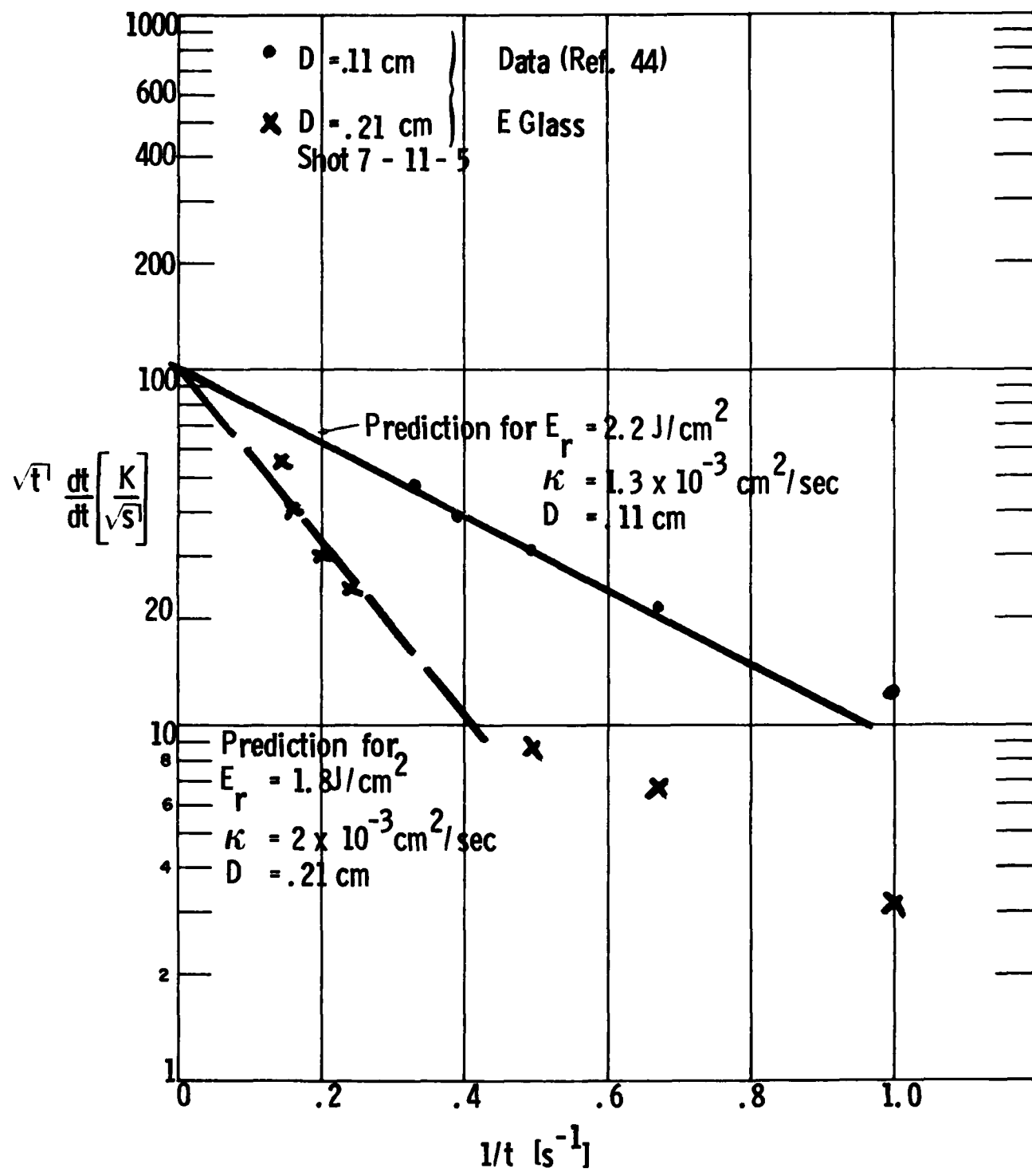
Fig. 12.11 Analysis of Thermocouple Data of Ref. 45. Data for
D=.21 cm Cannot be Fit by Conduction Solution.
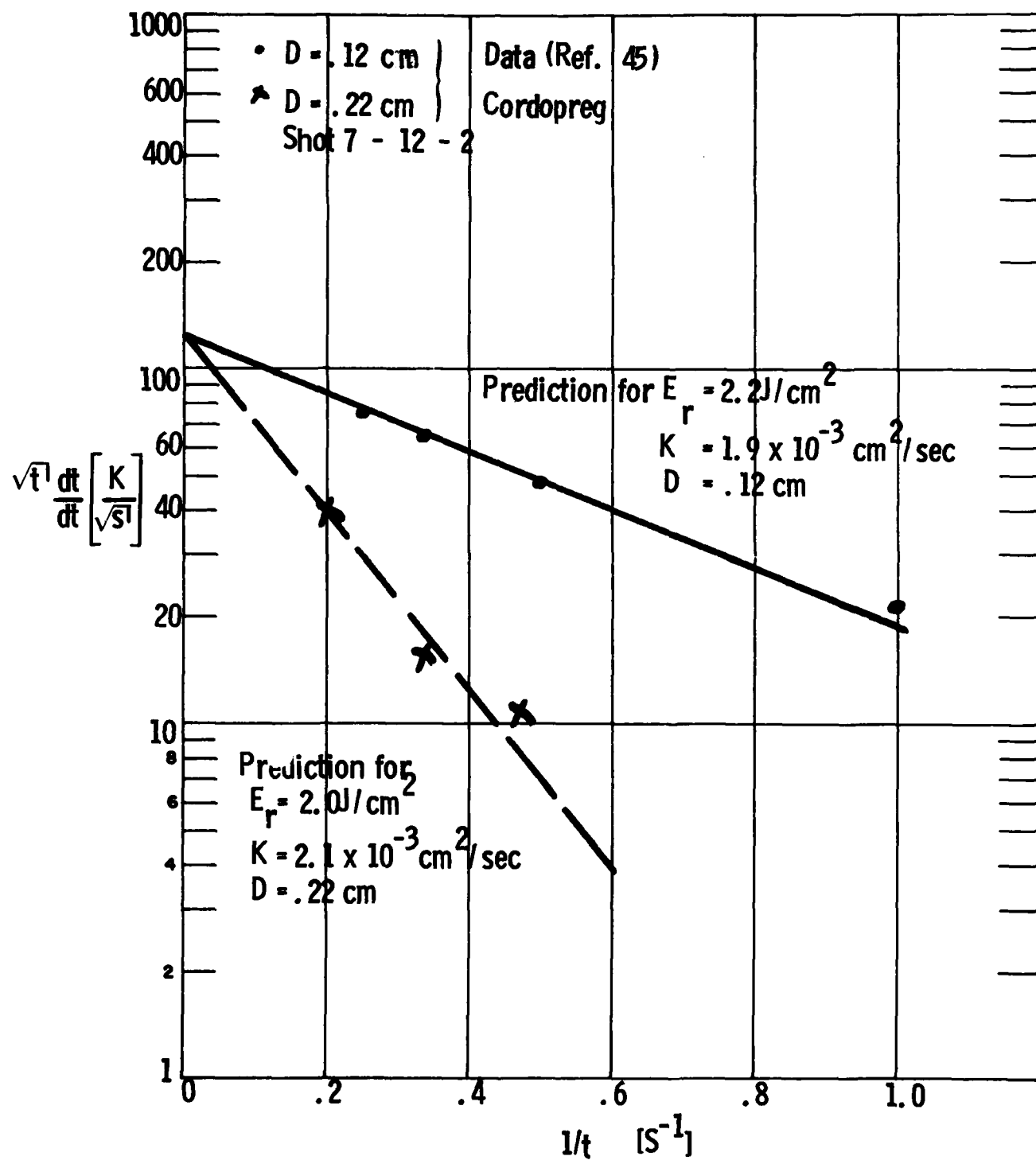
Fig. 12.12 Analysis of Thermocouple Data of Ref. 44.

values of κ and E_r' are found to be approximately $2 \times 10^{-3} \mathrm{cm}^2/\mathrm{sec}$ and 1.8 J/cm^2, respectively. This value of the diffusivity is close to the quoted value of $2.3 \times 10^{-3} \mathrm{cm}^2/\mathrm{sec}$ at 300K for Cordopreg; and therefore, the corresponding value of 1.8 J/cm^2 for E_r' is used to represent the heat flux contributing to the preheat of the target.

12.4 Summary of Repetitive Pulse Mass Removal of Fiberglass

A model for delamination has been advanced based on the following assertions: (1) Delamination is associated with the pyrolysis of resin at the rear of the ply to be delaminated, and the pyrolysis can be associated with a local temperature criterion; (2) Only the residual energy portion of the absorbed laser energy can contribute to delamination. The residual energy is deposited near the front of the target; (3) Thermal conduction is responsible for the transport of the residual energy deep into the target where it pyrolyzes the resin.

This model correctly predicts the delamination of Cordopreg targets in a Mach 0.1 air flow as the result of the interaction with 10.6 μ radiation which is repetitively pulsed at 10 Hertz. It also can be used to estimate the effect of convective cooling on the delamination rate. It is believed, of course, that there are many necessary conditions for delamination, but the good agreement between theory and experiment indicates that, in the present experiments[42] at least, all the other conditions are fulfilled before the resin pyrolysis condition.

SECTION 13

SUMMARY AND CONCLUSIONS

As a result of the comparison between the theory and data for single pulse interaction of 10.6 μm radiation with dome materials, a picture of the interaction has emerged in which two regimes exist where different phenomena control the physics of the interaction. At high intensity the interaction proceeds via the prompt ignition of an air LSC wave. The pressure and radiative transport to the surface of the target can be computed from the LSC wave theory developed in Part I of this report. The plasma radiation is absorbed at the surface of the target for wavelengths less than .25 μm and is absorbed in-depth for wavelengths greater than .25 μm. Target vaporization, caused by the absorption of the plasma radiation, has little effect on the surface pressure. The intensity threshold above which plasma effects dominate the surface interaction has been determined to be 2 MW/cm^2, at least for single pulse experiments. This is not to say that plasma ignition never occurs at intensities below 2 MW/cm^2; but only that it does not dominate the interaction.

At intensities below 2 MW/cm^2, the laser target interaction is dominated by the direct absorption of the laser radiation. This absorption occurs in-depth with an absorption depth estimated to be 6 μm for fiber-glass and 8 μm for pyroceram. Pressure is generated only as a result of vaporization of the target. Theoretical calculations indicate that the absorbed energy is partitioned into a portion which vaporizes the target and a portion, called residual energy, which remains in the target as heat. The residual energy contribution is limited by the onset of vaporization. For an absorption depth of 6 μm, it is estimated that the residual energy per pulse is limited to a maximum value of the order of 8 - 14 J/cm^2.

A model for delamination has been advanced based on the following assertions: (1) delamination is associated with the pyrolysis of resin at the rear of the ply to be delaminated, and the pyrolysis can be associated with a local temperature criterion; (2) only the residual energy portion of the absorbed laser energy can contribute to delamination. The residual energy is deposited near the front of the target; (3) thermal conduction is responsible for the transport of the residual energy deep into the target where it pyrolyzes the resin.

This model correctly predicts the delamination of Cordopreg targets in a Mach 0.1 air flow as the result of the interaction with 10.6 μm radiation which is repetitively pulsed at 10 Hertz. It also can be used to estimate the effect of convective cooling on the delamination rate. It is believed, of course, that there are many necessary conditions for delamination, but the good agreement between theory and experiment indicates that, in the present experiments at least, all the other conditions are fulfilled before the resin pyrolysis condition.

The foregoing discussion of repetitive pulse phenomena leads to a simple model for the interaction of a repetitively pulsed laser (λ = 10.6 μm, pulse repetitive frequency = 10 Hertz) with fiberglass. The most energy efficient mechanism for removing mass is delamination. Only the residual energy is effective in producing delamination; therefore, the most efficient removal of mass occurs when the pulse fluence is channeled entirely into residual energy. This is accomplished by keeping the intensity below the plasma threshold intensity and limiting the pulse fluence to less than 6.5 J/cm^2, which is the value deduced for the maximum residual energy. Exceeding this limit of the pulse fluence or laser intensity does not increase the number of pulses required for delamination; it increases only the amount of energy expended. Decreasing the pulse fluence below the residual energy maximum does not decrease the energy efficiency of penetrating a target by

delamination, but it does increase the number of pulses required to delaminate a typical layer. It also increases the amount of energy which must be deposited in the target before steady-state delamination can be reached.

Vaporization, which can occur during the laser pulse, is another mass removal mechanism. With a $Q^*_{VAP} \approx 13.5$ kJ/g, it is much less efficient than delamination, $Q^*_{Delam} \approx 2.3$ kJ/g. Therefore, vaporization does not compete with delamination unless the pulse fluence greatly exceeds the residual energy maximum. Only when the intensity is below plasma threshold and the pulse fluence exceeds approximately

$$\left(\frac{Q^*_{VAP}}{Q^*_{Delam}} \right) E_R = 38 \text{ J/cm}^2$$

is vaporization expected to compete with delamination.

REFERENCES AND FOOTNOTES - PART II

1. A. N. Pirri, R. G. Root and P. K. S. Wu, "Analytical Laser/
    Material Interaction Investigations," Physical Sciences Inc.,
    Woburn, MA, TR-104, September 1977.

2. AFWL - TR-72-94, Vol. 1.

3. J. R. Hutchins, III and R. V. Harrington, "Glass," in Kirk-
    Othmer Encyclopedia of Chemical Technology, Vol. 10.
    (John Wiley & Sons, Inc., 1966), p. 598.

4. Y. S. Touloukian, Thermophysical Properties of High Tem-
    perature Solid Materials, Vol. 4: Oxides and Their Solutions
    and Mixtures, Part I (The Macmillan Company, New York).

5. D. R. Stull and H. Prophet, Ed. JANAF Thermochemical
    Tables, 2nd ed., (NSRDS--NBS 37, 1971).

6. Y. S. Touloukian and C. Y. Ho, Ed. Thermophysical Pro-
    perties of Selected Aerospace Materials, Part I; Thermal
    Radiative Properties, (Purdue University, Lafayette, IN,
    1976).

7. Y. S. Touloukian and C. Y. Ho, Ed. Thermophysical Pro-
    perties of Selected Aerospace Materials, Part II: Thermo-
    physical Properties of Seven Materials, (Purdue Univer-
    sity, Lafayette, IN, 1977).

8. R. G. Root, P. K. S. Wu and A. N. Pirri, "Theoretical Study
    of Laser-Induced Breakdown in Particle-Contaminated Air,"
    Physical Sciences Inc., Woburn, MA, TR-91, May 1977.

9. "Reinforced Plastics" by Donald V. Rosato, in Encyclopedia
    of Polymer Science and Technology, Volume 12, (John Wiley
    and Sons, Inc., New York, 1970).

10. David G. Mettis, "Glass Fibers," in Handbook of Fiberglass
    and Advanced Plastics Composites, Ed. George Lubin, (Van
    Nostrand Reinhold Company, New York, NY, 1969).

11. Y. S. Touloukian, Ed. Thermophysical Properties of High
    Temperature Solid Materials, Vol. 6, Intermetallics, Cer-
    mets, Polymers, and Composite Systems, Part II, (The
    Macmillan Company, New York).

REFERENCES AND FOOTNOTES - PART II (Cont.)

12.   G. A. Weber and R. R. Bartle, "Thermal Design Properties Handbook," AVCO/MSP, Wilmington, MA, KHDR-AVMSD-68-3 May 1978.

13.   "Cordopreg E-293," Ferro Corporation Pamphlet, April 1968.

14.   L. A. Young and S. Glickler, "High Altitude Phenomenology," in Avco Everett Research Laboratory, Final Report, "Research in Re-entry Physics (U)," SAMSO-TR-76-66, June 1976, (Confidential).

15.   H. Tong and K. E. Suchsland, "Material Response to High Intensity Laser Radiation," Aerothem Division, Acurex Corporation, Mountain View, CA, Order No. RJ-57047, January 1972.

16.   R. W. Farmer, "Phenolic Resin Char-Formation During Hyper-thermal Ablation," Reprint from Thermochim. Acta, $\underline{4}$, 223 (1972).

17.   R. W. Farmer, "Thermogravimetry of Thermally Stable Aromatic and Heterocyclic Polymers," Reprint from Thermochim. Acta, $\underline{4}$, 203 (1972).

18.   Michael Ladacki, Janet V. Hamilton and Samuel N. Cohz, "Heat of Pyrolysis of Resin in Silica-Phenolic Ablator," AIAA Journal, $\underline{4}$, 1798 (1966).

19.   Anthony N. Pirri, "Analytic Solutions for Initiation of Plasma Absorption Above Laser-Irradiated Surfaces," Physical Sciences Inc., Woburn, MA, TR-15 October 1974.

20.   H. S. Carslaw and J. C. Jaeger, Conduction of Heat in Solids, (The Clarendon Press, Oxford, England, 1947).

21.   H. G. Landau, "Heat Conduction in a Melting Solid, Quarterly Journal of Applied Mathematics, $\underline{8}$, 81 (1950).

22.   G. G. Vilenskaia and I. V. Nemchinov, "Numerical Analysis of the Motion and Heating, by Laser Radiation, of a Plasma Being Formed in an Absorption Flare in the Vapors of a Solid," Prikl, Mekh. i. Tckh. Fiz., $\underline{6}$, 3 (1969).

REFERENCES AND FOOTNOTES - PART II (Cont.)

23.   S. L. Gralnick, "Solid Deuterium Evaporation in a Fusion Plasma;
        Nuclear Fusion, 13, 703 (1973).

24.   C. Fauquiquon and F. Floux, "Hydrodynamic Behavior of Solid
        Deuterium Under Laser Heating, " Physics of Fluids, 13, 386
        (1970).

25.   H. W. Liepmann and A. Roshko, Elements of Gasdynamics,
        (Wiley, New York, 1957).

26.   R. Y. Kucherov and L. E. Rikenglaz, "On Hydrodynamic Boun-
        dary Conditions for Evaporation and Condensation, " Soviet
        Physics-JETP, 37, 88 (1960).

27.   S. I. Anisimov, "Vaporization of Metal Absorbing Laser Radi-
        ation, " Soviet Physics - JETP, 27, 182 (1968).

28.   G. E. Nash and R. E. McGill, "ZAP: A Computer Code for
        Solving One Dimensional Heat Conduction Problems Involving
        Melting and Vaporization, " NRL report.

29.   G. E. Nash, presentation at the NRL Pulsed Effects Workshop,
        June 1974; also private communication.

30.   B. A. Boley, "A Method of Heat Conduction Analysis of Melt-
        ing and Solidification Problems," Journal of Mathematical
        Physics, 40, 300 (1961).

31.   B. A. Boley, "A General Starting Solution for Melting and
        Solidifying Slabs, " International Journal of Engineering Science,
        6, 89 (1968).

32.   R. L. Taylor and G. Caledonia, "Experimental Determination of
        the Cross-Sections for Neutral Bremsstrahlung -- II. High Tem-
        perature Air Species -- O, N and N_2, " Journal of Quantitative
        Spectroscopy and Radiative Transfer, 9, 681 (1969).

33.   H. A. Hyman and B. Kivel, "A General Formula for Free-Free
        Absorption on Highly Polarizable Neutral Atoms, " J. Q. S. R. T.
        13, 699 (1973).

REFERENCES AND FOOTNOTES - PART II (Cont.)

34. R. G. Root, P. K. S. Wu and A. N. Pirri, "Theoretical Study of Laser-Induced Breakdown in Particle-Contaminated Air, " Physical Sciences Inc., Woburn, MA, TR-91, May 1977.

35. A. A. Boni, F. Y. Su and J. R. Triplett, "A Theoretical Description of the Interaction of an Intense Laser Beam with a Solid Target, " Systems, Science and Software, La Jolla, CA, SSS-R-1510, January 1973.

36. K. G. P. Sulzmann, "Shock-Tube Measurements of the f-Number for the Fundamental Vibration-Rotation Bands of A10 in the $X^2\Sigma^+$ Electronic Ground-State, " J. Quant. Spectrosc. Radiat. Transfer, $\underline{15}$, 313 (1975).

37. B. G. Bagley, E. M. Vogel, W. G. French, G. A. Pasteur, J. N. Gan and J. Tauc, "The Optical Properties of a Soda-Lime-Silica Glass in the Region from 0.006 to 22 eV, " Jour. Non-Crystalline Solids, $\underline{23}$, 423 (1976).

38. Ralph Rudder, "Overview of Non-Metals Experiments, " presented at JANAF RP Vulnerability, Effects and Hardening Program Technical Steering Committee Meeting, June 6-7, 1978.

39. B. S. Holmes, "Pressure Response Data and Interpretation, " presented at JANAF RP Vulnerability, Effects and Hardening Program Technical Steering Committee Meeting, June 6-7, 1978.

40. B. S. Holmes, "Thermomechanical Tests, " presented at Vulnerability, Effects and Hardening Panel of the High Energy Laser Review Group, Naval Research Lab., Washington, D. C., Dec. 6-7, 1978.

41. An alternative model of multiple pulse fiberglass removal has been presented by A. Ballantyne of AVCO Everett Research Laboratory. The model includes pyrolysis, vaporization, conduction and convective losses during a single pulse. For multiple pulse engagements, the effect of the shielding of the resin by an overlying fiber mat is included. See A. Ballantyne, "Rep-Pulsed Laser Fiberglass Mass Removal, " presented at JANAF RP VEH Program Technical Steering Committee Meeting, September 20-21, 1978.

42. R. R. Rudder, personal communication, March 1978;

    R. R. Rudder, "Overview of Failure Mechanisms II and Radome Experiments, " presented at JANAF RP VEH Program Technical Steering Committee Meeting, September 20-21, 1978.

43. N. H. Kemp, Physical Sciences Inc., personal communication.

REFERENCES AND FOOTNOTES - PART II (Cont.)

44.   J. Horwith, M. Bina and H. Norris, "Pulsed Laser Target
        Radiometric Temperature Measurements, Part III," Lockheed
        Missiles and Space Company, Inc., Sunnyvale, CA, LMSC-
        D563648 (CONFIDENTIAL).

45.   B. S. Holmes, "Fiberglass Thermal Deposition Measurements,"
        presented at Non-Metals Workshop of JANAF RP VEH Program,
        AFWL, Kirtland AFB, NM, Nov. 6-7, 1978.

46.   Ref. 20.

PART III

HARDENING OF METALS TO REPETITIVELY PULSED

10. 6 MICRON RADIATION

SECTION 14

INTRODUCTION

In part one of this report, the theory of thermal and mechanical coupling to metals has been discussed and compared to data. It was found that significant enhancement of the coupling could be achieved if the laser pulse was designed to create a hot radiating laser supported combustion wave adjacent to the target surface. In this part of the report, first order concepts in the hardening of metals to repetitively pulsed radiation are developed; that is, ideas are advanced and analyzed whose purpose is to defeat or inhibit the enhanced coupling phenomenon described in Part I. First, a variety of hardening schemes is presented; then each of these is analyzed in order to discover if there are any reasons why the proposed schemes will not perform in the manner postulated. This should be, of course, only the first step in the development of a reliable countermeasure. It should be followed with experimental investigations and more detailed theoretical modeling.

The main objective of the theoretical effort in this report is to determine what criteria must be met for a hardening approach to perform effectively and/or what further experimental information is required to identify such criteria. It is not the purpose of this study to pass final judgment on the practicality of the suggested methods from the standpoint of cost and of material properties. Of course, if it is clear that a proposed scheme cannot meet the various criteria, it will be rejected. However, some approaches may survive the analysis in this report and later be rejected when more detailed material properties are known or when other factors, such as cost, are considered.

In order to propose a number of reasonable hardening approaches, it is important to first review the nature of the phenomena which contribute to enhanced coupling. After having identified the important stages of the coupling phenomenon, the physical processes which are essential to the coupling mechanism can then be isolated. Approaches which inhibit these processes can be suggested at this point. This program for investigating hardening approaches is implemented as follows: the basic physical concepts underlying coupling theory are discussed in Section 15 and a list of possible hardening approaches is advanced. The approaches are grouped into three categories: ignition inhibition, plasma detachment and laser supported detonation wave ignition. These groups are analyzed respectively in Sections 16, 17, and 18. The conclusions on the analysis are summarized in Section 19.

SECTION 15

POTENTIAL HARDENING SCHEMES

In order to propose methods of defeating enhanced coupling to metals, one must first understand the essential aspects of the phenomenon. The theory is developed in Part I of this report; energy transport to the target surface is accomplished by radiative transport from a hot, laser-created plasma, and mechanical coupling occurs by virtue of the presence of this high pressure plasma adjacent to the surface. Several criteria must be met for the efficient thermocoupling by this mechanism: a plasma must be ignited; the plasma must radiate profusely in the spectral regime which is strongly absorbed by the target; the radiation produced by the plasma must reach the target without undue attenuation; and the above conditions must prevail throughout the entire laser pulse time. For mechanical coupling, a high pressure plasma must be ignited adjacent to the surface and the pressure must be maintained throughout the entire laser pulse. The criteria can be met by tailoring the pulse shape both spatially and temporally.

The theory of enhanced thermal coupling is based upon energy transfer via plasma re-radiation. The optimum pulse shape[1,2] for efficient energy transfer has the following characteristics: There should be an initial spike whose purpose is to ignite the plasma, followed by a lower intensity plateau which maintains a hot plasma close to the surface. It is found that the radiative transfer mechanism operates most effectively at lower intensities where laser supported combustion (LSC) waves exist instead of at higher intensities where laser supported detonation (LSD) waves persist. Since, for a given laser, the intensity of the spike is related to the intensity of the plateau, it is possible to define both upper and

315

lower limits on the plateau intensity. The lower limit is the lowest intensity sufficient for the corresponding spike to ignite the plasma (it is found that the plateau intensity required to maintain an LSC wave is lower than the plateau intensity associated with a spike capable of igniting a plasma), and an upper limit is the highest intensity which does not support an LSD wave. If radial expansion occurs during the pulse, strong plasmadynamic cooling occurs which curtails the radiative transport. Thus, efficient coupling requires that the laser pulse time be short compared to the characteristic time for two-dimensional expansion, τ_{2D}. This time is approximately given by R/a_p where R is the laser spot radius and a_p is the speed of sound in the plasma ($a_p = 4.5 \times 10^5$ cm/sec for LSC wave plasmas). In a plot of intensity versus the ratio of the pulse time to the radial relaxation time, hereafter denoted as $\hat{\tau}$ ($\hat{\tau} \equiv \tau_p / \tau_{2D}$), the above mentioned limits can be plotted to define the region of efficient thermal coupling. Hereafter, this region is referred to as the enhanced coupling region, and it is sketched in Fig. 15.1.

An effective hardening approach should alter the boundaries of the enhanced coupling region such that the region is reduced to negligible size. It may not be necessary to completely eliminate the efficient coupling region; rather, it may be sufficient merely to shrink the size such that in realistic engagement scenarios it becomes impossible to couple efficiently for more than a few pulses. In this report, however, methods of defeating the enhanced coupling mechanism will be sought which virtually eliminate the enhanced coupling region. In the analysis in the subsequent sections, it is assumed, of course, that the laser pulse parameters are designed to fall in the enhanced coupling region. First, the various stages of the enhanced coupling mechanism must be reviewed. Plasmas are ignited over the surface by the gain-switched spike which precedes the main laser pulse. It is known that the ignition process cannot be bulk vaporization of the target, since there is insufficient fluence for bulk vaporization to commence within

316
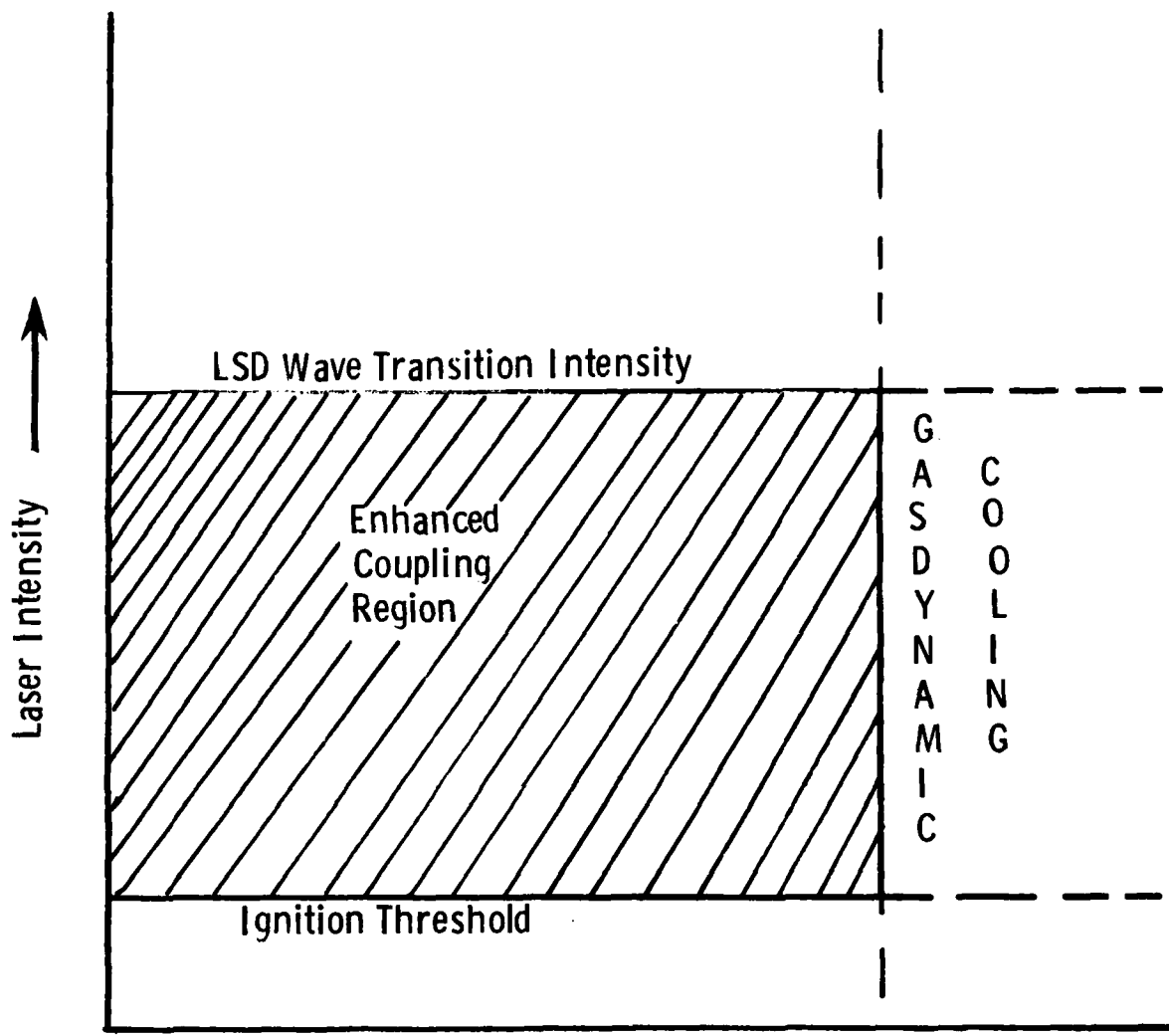
$$\hat{\tau} = \frac{\tau_\rho \, a_\rho}{R}$$

Fig. 15. 1 Sketch of the Region of Enhanced Thermal Coupling.

317

the time scale on which ignition is actually observed to occur. The exact mechanism of prompt ignition is not understood in complete detail, but it is believed thermally insulated flakes present on the target surface are essential to the breakdown process. They are the source of the initial electrons, produced either by thermionic emission, electric field-induced emission, or vaporization. Once the electrons are produced, a cascade breakdown then proceeds either in the air or in the vapor cloud, if present. The ignition process can be inhibited either by preventing the defects from providing the initial electrons or by causing the cascade breakdown itself to be curtailed.

Approaches, which are directed to the ignition stage of enhanced coupling, are classified as ignition inhibition schemes and are discussed in Section 16. Note that ignition inhibition schemes eliminate mechanical coupling entirely. In terms of the enhanced coupling region, ignition inhibition is equivalent to raising the plasma ignition threshold above the LSD wave transition threshold, as illustrated schematically in Fig. 15. 2a.

To achieve efficient coupling, however, it is not sufficient merely to ignite a plasma; rather, the plasma must be the highly radiating LSC wave type. As mentioned above, it is assumed that the laser parameters are chosen so that, in lieu of any countermeasures, the plasma formed by the interaction would indeed be the highly radiating LSC wave. A conceivable method of hardening is to induce the plasma to form in the poorly radiating LSD wave configuration. Approaches which employ poorly radiating LSD waves are classified as LSD wave ignition schemes, and are discussed in Section 18.

LSD wave ignition approaches reduce mechanical coupling but do not eliminate it entirely. The effect of LSD wave ignition schemes can be visualized in the plot of the enhanced coupling region as the lowering of the LSD

318

Plasma Ignition Threshold

LSD Wave Transition

Plasmadynamic Cooling

$\hat{\tau} \rightarrow$ 1

Fig. 15.2a

Ignition Inhibition:

Ignition threshold raised above LSD wave transition intensity.
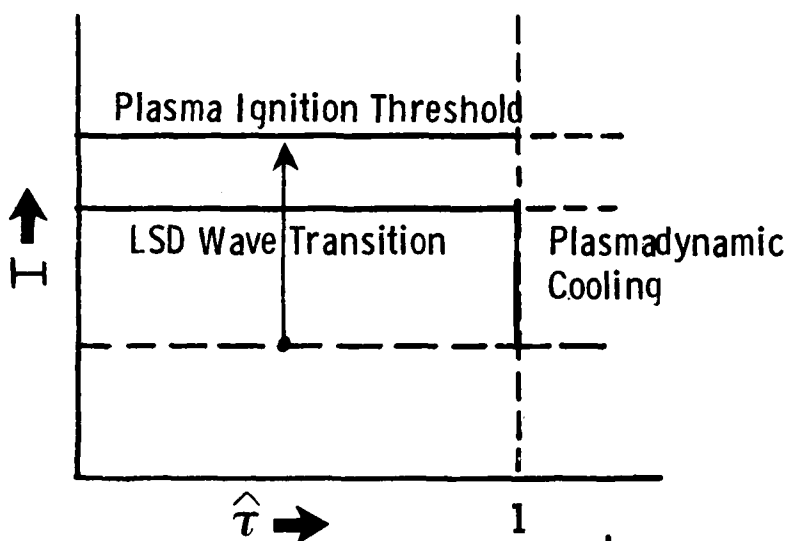
Fig. 15.2b

LSD Wave Ignition:

LSD wave transition intensity lowered below prompt ignition threshold.

Plasma-Dynamic Cooling

Plasma Ignition Threshold

LSD Wave Transition

$\hat{\tau} \rightarrow$ 1

LSD Wave Transition

Plasma-Dynamic Cooling

Plasma Ignition Threshold

Fig. 15.2c

Plasma Detachment:

Shorten onset of plasma-dynamic cooling.

$\hat{\tau} \rightarrow$ 1
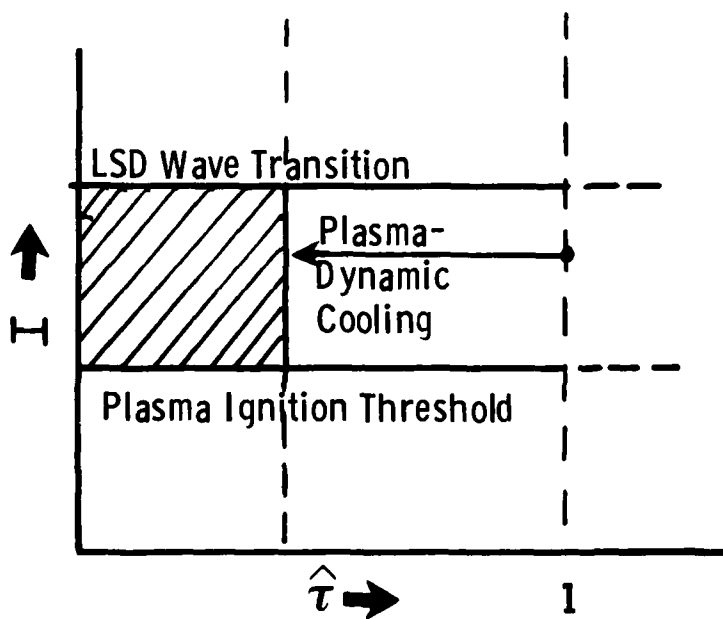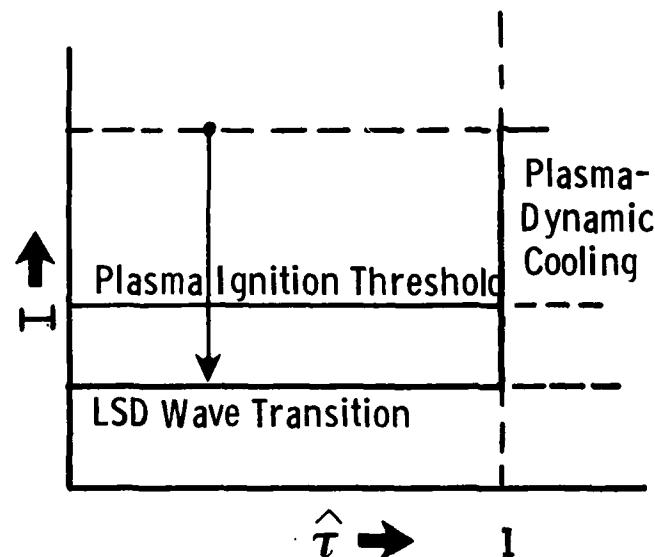
wave transition intensity to the plasma ignition intensity, as illustrated in Fig. 15. 2b.

Even if a hot LSC wave can be produced, the radiation must reach the target surface, and the LSC wave configuration must be maintained throughout the entire pulse. It is important for transfer of the radiation to the target surface that the plasma remain adjacent to the surface; an intervening layer of cold air absorbs the radiation emitted in the spectral regime which is preferentially absorbed by the target. For thin intervening layers (a few absorption lengths), it may be possible for the radiation from the plasma to heat the intervening gas between the plasma and the target to temperatures high enough for the important radiation to be transmitted. For thick layers, however, the radiation is absorbed very quickly by the cold gas and the radiant energy transport into the cold gas then becomes similar in nature to thermal conduction. It takes a long time for the thermal wave to travel many absorption lengths. Thus, the thickness of the intervening layer controls the effectiveness of the shielding. A reasonably thick layer cannot be quickly heated by the diffusion-limited energy transport mechanism, but a thinner layer could be heated so quickly that it would be indistinguishable from the original plasma.

As an added benefit of interposing cold gas between the plasma and the target, the plasma can expand in two directions - toward the laser and toward the target. The plasma cannot be maintained at as high a pressure as the plasma which expands in only one direction, and some of the plasma energy is expended in the backward expansion, thereby reducing the plasma temperature. This behavior is qualitatively similar to the radial expansion of the plasma for large values of $\hat{\tau}$. Countermeasures which are expected to employ the features described above are denoted hereafter as detached plasma schemes and are discussed in Section 17.

Detaching the plasma has two effects; it destroys the radiative transport and it enhances plasmadynamic cooling. This latter effect can be illustrated on the plot of the enhanced coupling region as the movement of the plasmadynamic cooling boundary towards lower values of $\widehat{T}$ (see Fig. 15.2c).

Based on the motivations presented above, a partial list of potential hardening approaches has been compiled. They are listed below, grouped according to the mechanism they are expected to employ.

1. Ignition inhibition

    a. *Elimination of defects*

        1) Mechanical polishing

        2) Chemical polishing

        3) Surface melting

        4) Defect-free metal coating

        5) Transparent coating

    b. Elimination of cascade breakdown

        1) Electron attaching gas in boundary layer

2. Detached plasma

    a. Surface dimpling to focus beam above target

    b. Debris injection

    c. Electron injection

3. LSD wave ignition

    a. Flow easily ionized gas in boundary layer

    b. Seed easily ionized materials in ablative coating

The potential performance of these approaches shall be analyzed in detail in the next three sections.

SECTION 16

IGNITION INHIBITION APPROACHES

In this section we analyze the effectiveness of the methods listed in Section 15 for inhibiting ignition of the plasma. Two possible ways of preventing ignition are suggested; namely elimination of the ignition sitee, and curtailing the nonequilibrium cascade breakdown. In order to analyze critically the effectiveness of the proposed schemes, it is essential to investigate in detail the plasma ignition process.

16.1 Plasma Initiation Theory

The following discussion of the creation of an LSC wave is confined to a specific model of the initiation process. Although it is the presently favored explanation of prompt ignition, it has not been conclusively established as the correct model. In the model the initial electrons are provided by the heating of thermally insulated flakes. The flakes must be thermally insulated in order to reach high temperatures which could not possibly be achieved if thermal conduction into the target were present. As will be shown below, the thickness of the flake is the crucial parameter in determining whether the flake reaches high temperatures, and, as a result, the flake thickness also controls the fluence required for breakdown to proceed.

The flake temperature can be determined from the absorbed fluence. Since aluminum has high thermal diffusivity ($K \approx .6$ cm^2/sec), a thermal wave can penetrate roughly $\sqrt{Kt} = 2.5$ microns within the duration of the gain switch spike ($t \approx .1$ microsecond). Therefore, for flakes less than a micron thick, conduction equilibrates the temperature across the flake within the time of interest, and a single temperature characterizes the flake. The temporal history of the temperature is then given by the solution to

$$\alpha(T) \, I = \rho \ell \, \frac{dh(T)}{dt} \, , \tag{16.1}$$

where $\alpha(T)$ is the absorptivity, I is the incident laser intensity, T is the flake temperature, ρ is the density of aluminum, ℓ is the thickness of the flake, and $h(T)$ is the enthalpy of aluminum. In terms of the specific heats, c_s and c_1, of the solid aluminum and liquid aluminum, respectively, and the latent heat of fusion, $H_m = 397 \text{ J/g}$, the incident laser fluence F required to reach a temperature T (assumed to be above the melt temperature) is given by

$$F = \rho \ell \left\{ c_s \int_{T_i}^{T_m} \frac{dT}{\alpha(T)} + \frac{H_m}{\alpha(T_m)} + c_1 \int_{T_m}^{T} \frac{dT}{\alpha(T)} \right\} \, , \tag{16.2}$$

where T_i is the initial temperature and T_m is the melting temperature. For aluminum, typical values of T_i and T_m are 300°K and 900°K respectively. The actual value of T_m for an alloy lies between 775 and 911°K, but for a rough estimate of F the value of $T_m = 900^\circ\text{K}$ is sufficiently accurate. The temperature, as a function of the fluence received per unit thickness, is plotted in Fig. 16.1 using the following choice for the intrinsic absorbtivity of the aluminum target:

$$\alpha(T) = .03 + (T-300) \, 5 \times 10^{-5} \quad 300\text{K} \le T < 900\text{K} \; ;$$

$$\tag{16.3}$$

$$\alpha(T) = .09 + (T-900) \, 5 \times 10^{-5} \quad 900\text{K} < T \; .$$
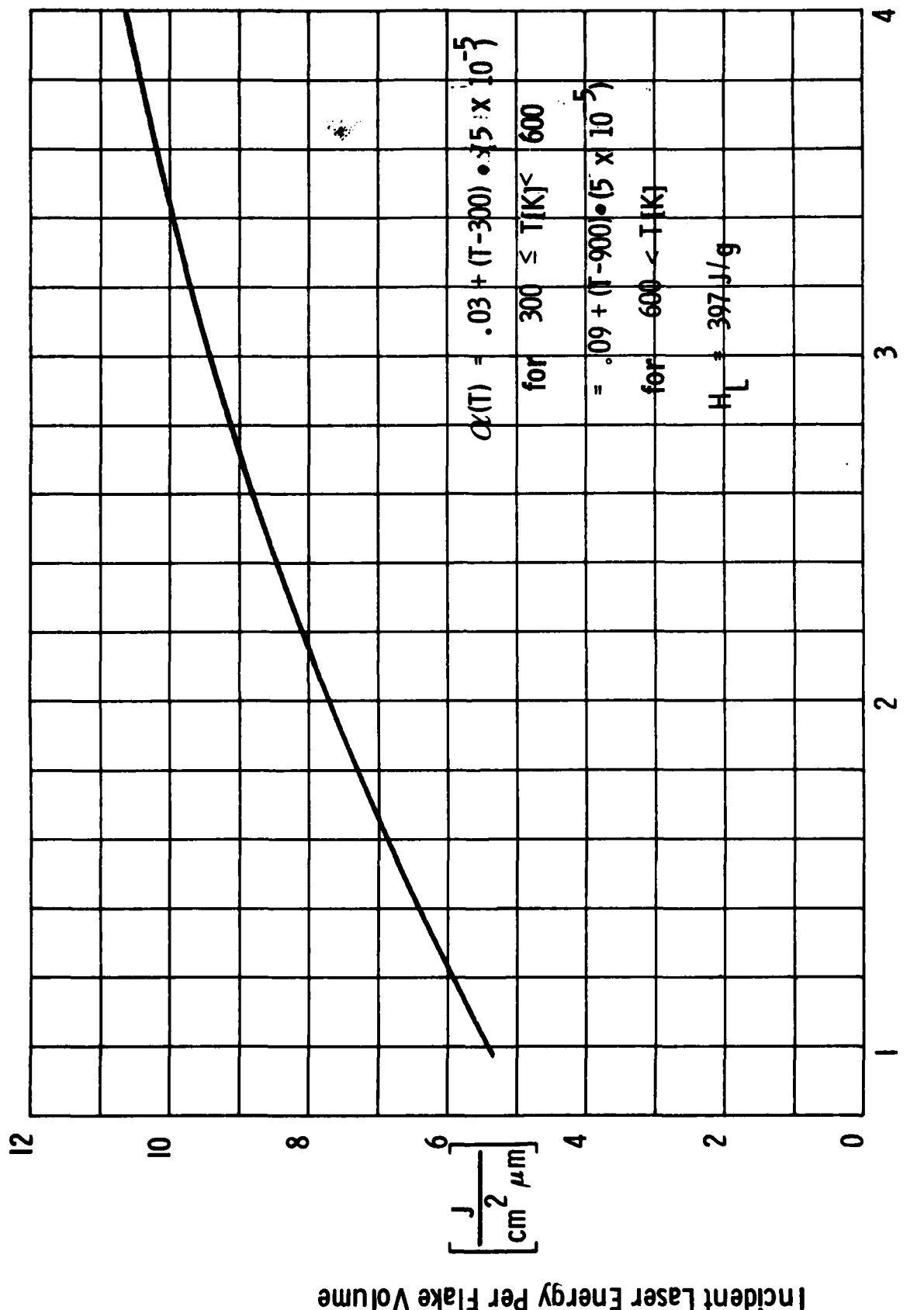
Fig. 16.1 Fluence Requirements to Heat Insulated Flake.

The figure contains the following annotations:

$$\alpha(T) = .03 + (T-300) \cdot (5 \times 10^{-5})$$

$$\text{for } 300 \leq T[K]^{<} 600$$

$$= .09 + (T-900) \cdot (5 \times 10^{-5})$$

$$\text{for } 600 < T[K]$$

$$H_L = 397 \text{ J/g}$$

FLAKE TEMPERATURE T [10^3K]

Incident Laser Energy Per Flake Volume $\left[\dfrac{J}{cm^2 \, \mu m}\right]$

This temperature dependence has been suggested by Thomas and Musal[3], and an abrupt increase is also included at T_m since the DC conductivity, which is related to the absorptivity, also has an abrupt change[4]. The important feature of Fig. 16.1 is that while it takes 6.7 J/cm^2 - μm to reach 2000°K, it requires only 10.6 J/cm^2 - μm to reach 4000°K if vaporization is not permitted. The difference between heating a flake to 2000°K and 4000°K can be compensated for by reducing the thickness of the flake by only 30%. Therefore, the fluence requirements for breakdown are insensitive to the final temperature which must be attained by the flake, and are instead determined by the thickness of the flake.

Walters, et al.[5] found a correlation between the breakdown time and the fluence received. Breakdown corresponded to roughly 1.67 J/cm^2 being incident. Identifying this fluence with the time to heat the flake to a high temperature, say 2700°K, we deduce that the thickness of the flakes must be approximately .2 μm. This justifies the use of the uniform flake temperature.

At the present time, it has not been established whether the heated flake initiates breakdown by virtue of thermionic emission of electrons from the heated flake or by actual vaporization of the flake. Both possibilities will be considered here.

The maximum current density j available from thermionic emission is given by the Richardson equation[6]

$$j = A(1-r) \ T^2 \ \exp(-\varphi/kT) \ , \qquad (16.4)$$

where A is a constant numerically equal to 120 amps/cm^2/degree^2, r is a reflection coefficient, typically of the order of .05, T is the temperature in °K, k is the Boltzmann constant, and φ is the work function. The value of φ is not well known for aluminum. For example, the Chemical Rubber

Company Applied Engineering Sciences Handbook[7] lists the following values in electron volts: 2.98, 3.43, 4.18, 4.2, 4.36 for the photoelectric work function; 3.38 and 4.25 for the work function determined from the contact potential method; and no values for the thermionic work function. In their analysis of flake initiated breakdown, Thomas, Musal and Chou[8] used a value of 3.74 eV for the work function. Since the work function appears in the exponential in Eq. (16.4), the uncertainty in the work function can cause very large uncertainties in the thermionic current. In Fig. 16.2 we have plotted the predicted current for thermionic emission from aluminum for various values of the work function.

According to Thomas and Musal[9], the thermionic emission rapidly becomes space charge limited and the maximum electron density can be estimated for plane geometry as

$$n_{max} [cm^{-3}] = .35 [j]^{2/3} , \tag{16.5}$$

and the total number of electrons, N, is given by

$$N = 500 [j]^{1/3} \sqrt{E} , \tag{16.6}$$

where j is the current density from Eq. 16.4 and E is the electron energy in eV. In Table 16.1 the values of n_{max}, N, and the distance x, characteristic of the thickness of the zone containing the emitted electrons ($x \equiv N/n_{max}$), are listed for various values of current densities. Also given is the time N/j which it would require for a target at temperature T to reach the space charge limited number of electrons, assuming that the current was unaffected by space charge limitations.

Observe that the space charge limited electron density remains small unless high current densities are attained. The lower limit on the number of electrons required to initiate breakdown at intensities of interest is discussed later
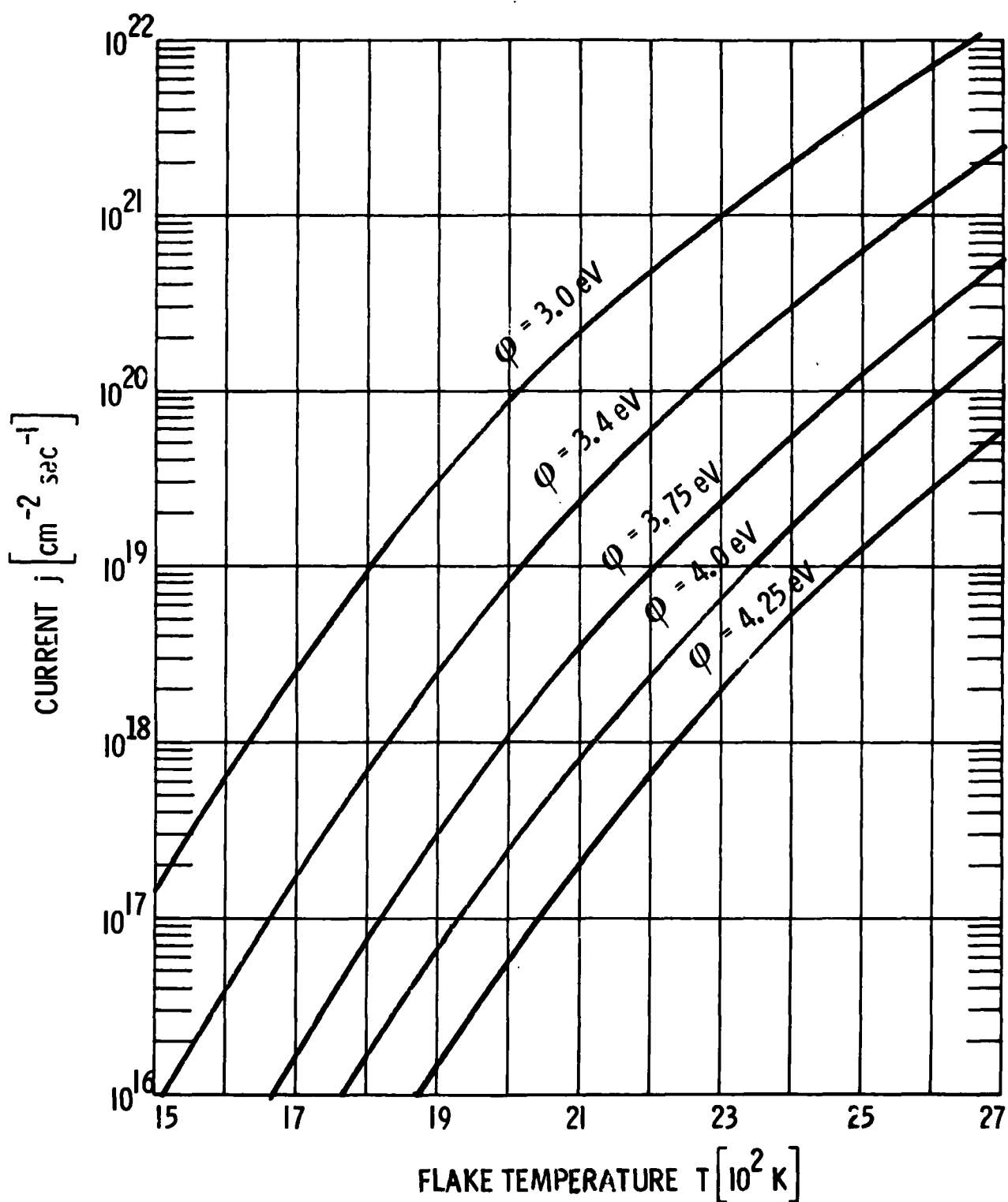
Fig. 16.2   Thermionic Emission Current Versus Temperature for Several
Values of Work Function.

TABLE 16.1

Space–Charge Limited Electron Concentration as Function
of Current Density.

J $[cm^{-2}\ sec^{-1}]$	n_{MAX} $[cm^{-3}]$	$N_{TOT}[cm^{-2}]$	$X[cm] = \dfrac{N_{TOT}}{n_{MAX}}$	t $[s]$
10^{15}	3.5×10^9	2.41×10^7	6.9×10^{-3}	2.4×10^{-8}
10^{16}	1.63×10^{10}	$5.2 \times 10^{+7}$	3.2×10^{-3}	5.2×10^{-8}
10^{17}	7.54×10^{10}	1.12×10^8	1.49×10^{-3}	1.12×10^{-9}
10^{18}	3.5×10^{11}	2.41×10^8	6.9×10^{-4}	2.41×10^{-10}
10^{19}	1.6×10^{12}	5.2×10^8	3.2×10^{-4}	5.2×10^{-11}
10^{20}	7.54×10^{12}	1.12×10^9	1.5×10^{-4}	1.12×10^{-11}
10^{21}	3.5×10^{13}	2.41×10^9	6.9×10^{-5}	2.41×10^{-12}
10^{22}	1.63×10^{14}	5.2×10^9	3.2×10^{-5}	5.2×10^{-13}
10^{23}	7.54×10^{14}	1.12×10^{10}	1.5×10^{-5}	1.12×10^{-13}

in this section and is shown to be quite large, approximately 10^{17} cm^{-3}. However, to obtain even low densities such as 10^{12} electrons per cm^3, current densities of the order of 10^{19} electrons/ cm^2-s are required. From Fig. 16.2 it is seen that even for the lowest work functions, high temperatures of the order of 1800°K must be reached in order to achieve the required current densities. For a work function of 3.75 eV, the temperature must exceed 2200°K. However, in the discussion of Fig. 16.1, it was pointed out that only minor changes in the incident fluence are required to raise the temperature from 2000°K to 4000°K. Therefore, it is likely that either the flake temperature remains too low for thermionic emission or else the flake partially vaporizes.

Rapid vaporization can commence as soon as the flake temperature reaches the vaporization temperature, 2767°K, and a portion of the energy absorbed by the flake can then be partitioned into vaporization rather than flake heating. Simple models can be used to relate the surface temperature T_s to the mass loss rate $\dot{m}$. The surface pressure p_s as a function of temperature is given by

$$p_s = p_o e^{-H_v/RT_s} , \qquad (16.7)$$

where H_v is the heat of vaporization, R is the ideal gas constant divided by the atomic weight of the vapor and p_o is a constant which can be determined from the normal boiling point. It is found that the pressure is related to the mass loss rate $\dot{m}$ and the sonic velocity of the vapor,

$$V_s = \sqrt{\gamma R T_s} , \qquad (16.8)$$

by

$$p_s = \dot{m} \, V_s \, . \tag{16.9}$$

In the above equations γ is the ratio of the specific heats C_p / C_v, and A is the atomic weight of aluminum.

For aluminim, we find

$$\dot{m} \approx \frac{p}{V_s} \approx \frac{p_o \, e^{- H_v/RT_s}}{\sqrt{\gamma RT_s}} \, , \tag{16.10}$$

with the following values of the parameters: $H_v = 10770$ J/g, $p_o = 3.1 \times 10^{11}$ dynes/ cm^2, $\gamma = 5/3$, and R = .308 J/g. The energy carried away by vaporization is denoted by $\dot{E}_v = H_v \dot{m}$, and is plotted as a function of temperature in Fig. 16.3. The incident intensity I_s required to sustain this vaporization rate is also shown in Fig. 16.3 where the absorptivity used in the calculation is that given in Eq. (16.3). It is clear from Fig. 16.3 that the flake continues to heat rapidly even after the start of vaporization, since I_s is much less than the expected values of the incident laser intensity. At an intensity of 10 megawatts/cm^2, (a lower limit for the gain switched spike) a temperature close to 4000 ^{o}K could be achieved before vaporization losses equal the absorbed flux, provided the spike duration is sufficient.

Although the onset of vaporization occurs when the flake temperature exceeds 2767°K, the whole flake cannot be vaporized without a substantial increase in the fluence above the amount required to initiate vaporization. For an absorbtivity of 18% at a temperature of 2767°K, it takes 16J/cm^2- μm to vaporize the aluminum flake. This is 1.8 times the fluence required to reach 2767°K. We conclude, therefore, that, while partial vaporization is quite likely to occur, complete vaporization is not likely.

331
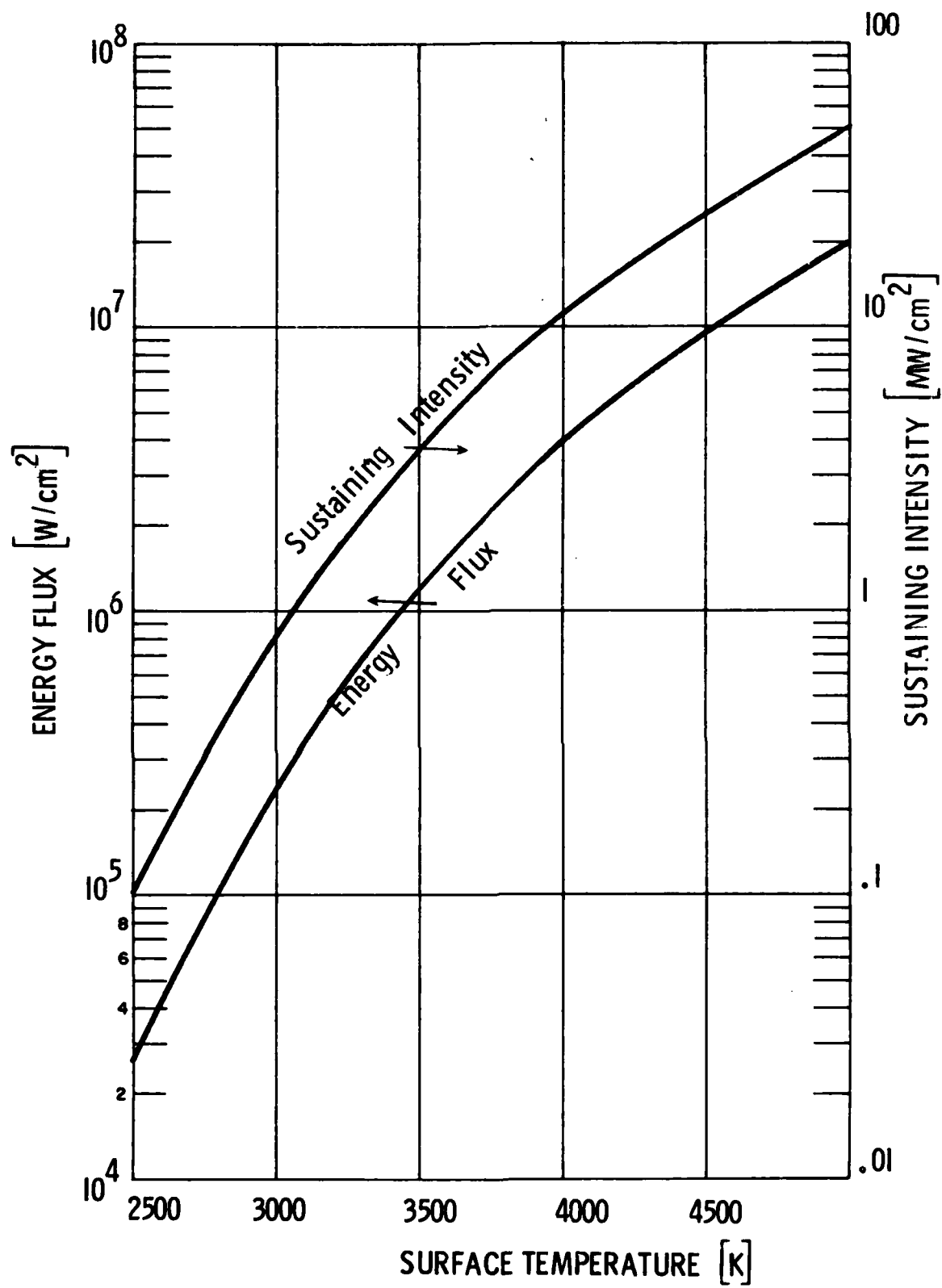
Fig. 16.3 Energy Flux Carried Away by Vaporization of Al, as a Function of Surface Temperature. Laser Intensity Required to Sustain Vaporization is Also Plotted.

In order for an LSC wave plasma to be created, more than a few initial electrons are required. A cascade breakdown must occur. In the calculations of Walters et al.[10] and Thomas and Musal,[11] in which it was shown that thermionic emission could provide sufficient electrons to account for the observed attenuation of the incident laser beam, it was specifically assumed that all of the absorbed energy was available for producing new electrons. This hypothesis will be examined further.

The threshold intensity for breakdown of clean air can be calculated by employing a simple extension of microwave theory.[12] The estimates made in this manner are in good agreement with the observed thresholds for both clean air and for noble gases. It is assumed that the electrons initially absorb energy much faster than they can transfer energy to the heavy particles, although they do transfer energy among themselves efficiently enough to define an equilibrium temperature, T_e. As the electron temperature increases because of the laser absorption, the rate of energy transfer to the heavies also increases. Eventually the electrons reach a high enough temperature that the average rate of energy absorption per electron is equal to the average rate of energy lost to the heavies. For a given electron temperature, the rate of energy lost to the heavies can be roughly calculated as

$$\left.\frac{d\epsilon}{dt}\right)_{loss} = \nu_\mu \epsilon , \tag{16.11}$$

where ϵ is the electron energy and ν_μ is the inelastic collision frequency. The inelastic collision frequency has been determined by Hake and Phelps[13] in the presence of a DC electric field. The effect of using AC electromagnetic fields, such as laser beam, can only be incorporated either by obtaining new experimental information or by employing the cross-sections derived by Hake

and Phelps[13] in conjunction with the numerical solution to the Boltzmann equation. These solutions are beyond the scope of the simple approach used here, but the model we use is justified in that the calculation method predicts the correct breakdown threshold for pure air. The rate of energy lost per electron found by using the data of Hake and Phelps and Eq. (16.11) is shown in Fig. 16.4.

There are two ways to calculate the rate of energy absorption per electron. According to the microwave analog, the rate of energy absorption is given by

$$\left.\frac{d\epsilon}{dt}\right)_{absorbed} = \frac{e^2}{m_e}\left(\frac{\nu_c E_o^2}{\nu_c^2 + \omega^2}\right) = \frac{4\pi e}{m_e c}\left(\frac{I_o \nu_c}{\nu_c^2 + \omega^2}\right), (16.12)$$

where ω is the radial frequency of the laser radiation, ν_c is the momentum transfer frequency, m_e is the mass of an electron, c is the speed of light, e is the charge of an electron, E_o is the rms electric field and I_o is the laser intensity. The absorption rate per electron, found by using Eq. (16.12) and the data of Hake and Phelps[13] for DC fields, is plotted in Fig. 16.5 for a laser intensity of 10 megawatts/cm^2. Absorption rates for other intensities can be determined by simply scaling the rate of energy absorption with the incident laser intensity.

Another method for calculating the absorption rate is to use the measured[14] inverse Bremsstrahlung cross-sections Q_{O_2} and Q_{N_2} for oxygen and nitrogen, respectively, which are listed in Table 16.2. The expression for the absorption per electron for inverse Bremsstrahlung is

$$\left.\frac{d\epsilon}{dt}\right)_{abs} = \left(1 - e^{-h\nu/kT}\right)\left[Q_{O_2} \cdot N_{O_2} + Q_{N_2} \cdot N_{N_2}\right] I_o, (16.13)$$
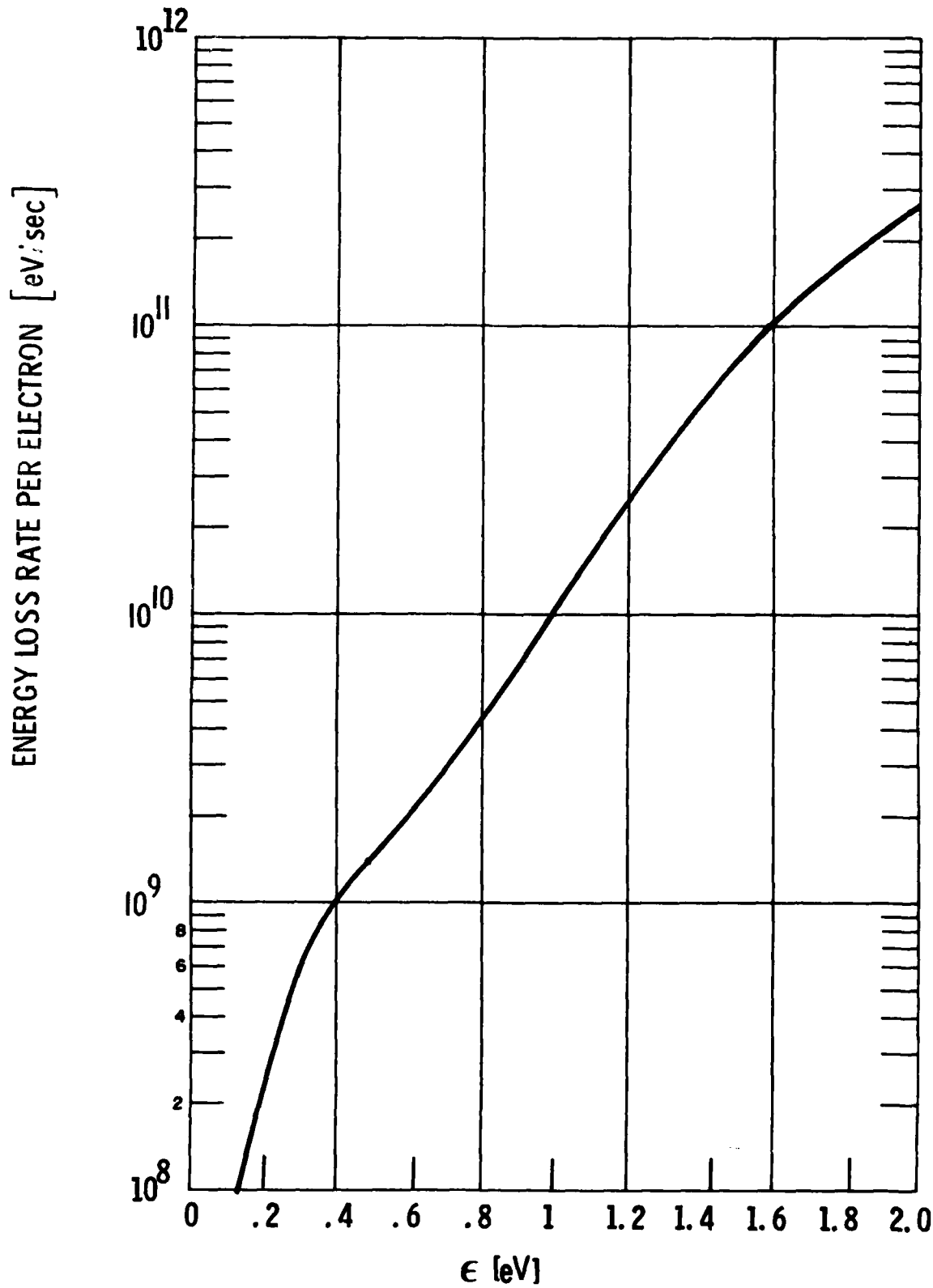
Fig. 16.4 Energy Transfer per Electron of Characteristic
Energy ε to Air at 293 K.

335
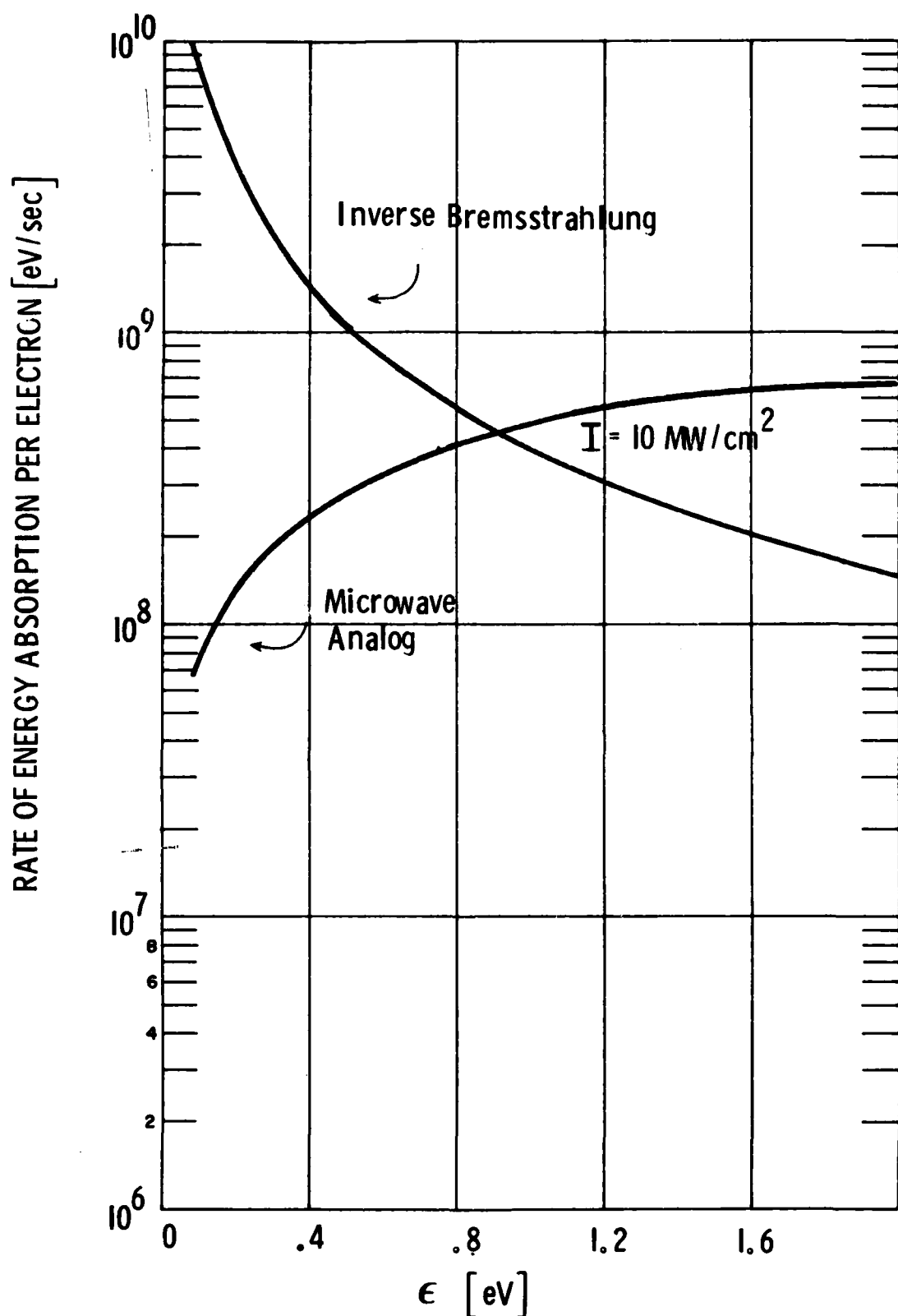
Fig. 16.5 Rate of Energy Absorption by Electron of Characteristic
Energy ϵ in 10 MW/cm^2 Laser Beam (λ = 10.6 μm) at T = 293 K
in Air Using Two Methods of Predictions – Inverse Bremss-
trahlung and Microwave Analog.

TABLE 16.2.

Cross-Sections for Inverse Bremsstrahlung

$$Q_i \approx 1.37 \times 10^{-35} \quad \frac{\lambda^3 \ [\mu] \ z_i^2}{\sqrt{T \ [K]}}$$

$$z_i^2 = a \ \lambda \ [\mu]^b$$

	a	b
N_2	.053	- .75
O_2	.094	- .36

where I_o is the laser intensity, k is the Boltzmann constant, T is the temperature, h is the Planck constant, ν is the laser frequency, and N_{O_2} and N_{N_2} are the concentrations of oxygen and nitrogen, respectively. The first term in the product in Eq. (16.13) represents the effect of stimulated emission. The absorption rate calculated by using Eq. (16.13) is also plotted in Fig. 16.5 for a laser intensity of 10 megawatts/cm^2. It is evident that there are some qualitative differences between the two methods of calculating laser absorption, but the most important feature is that the energy absorption rate in both methods of calculation is small compared to the collisional losses for electron energies above .5 eV. To illustrate this fact more clearly the energy loss rate from Fig. 16.4 and the energy absorption from Fig. 16.5 are both plotted in Fig. 16.6 on the same scale. Several other laser intensities are also shown. Observe that for the intensities anticipated in the gain switched spike, namely 10 and 100 MW/cm^2, it is impossible for the electron energy to exceed 1 eV. (The purpose of showing the energy absorption rate calculated in two different ways is not to compare the two methods nor to show which method is in better agreement with observed threshold intensities, but rather to demonstrate that the electron temperature cannot exceed 1 eV, even if the microwave analog is abandoned and inverse Bremsstrahlung absorption is used to calculate the absorption rate.) This electron energy is insufficient to produce significant ionizing collisions. Indeed, it can be seen from Fig. 16.7, which is taken from Ref. 12, that the electron temperature must exceed 2 eV in order for the electron production rate to overcome the electron attachment rate to oxygen molecules. A similar conclusion could be reached by using the analysis of Thomas and Musal.[15] For laser intensities below 10^8 W/cm^2, cooling caused by collisions which excite vibrational modes of N_2 prevents the electrons from reaching the high temperatures necessary for ionization to be the major energy loss. Therefore, we conclude that cascade breakdown cannot occur in cold air at the laser intensities expected in the gain switched spike.
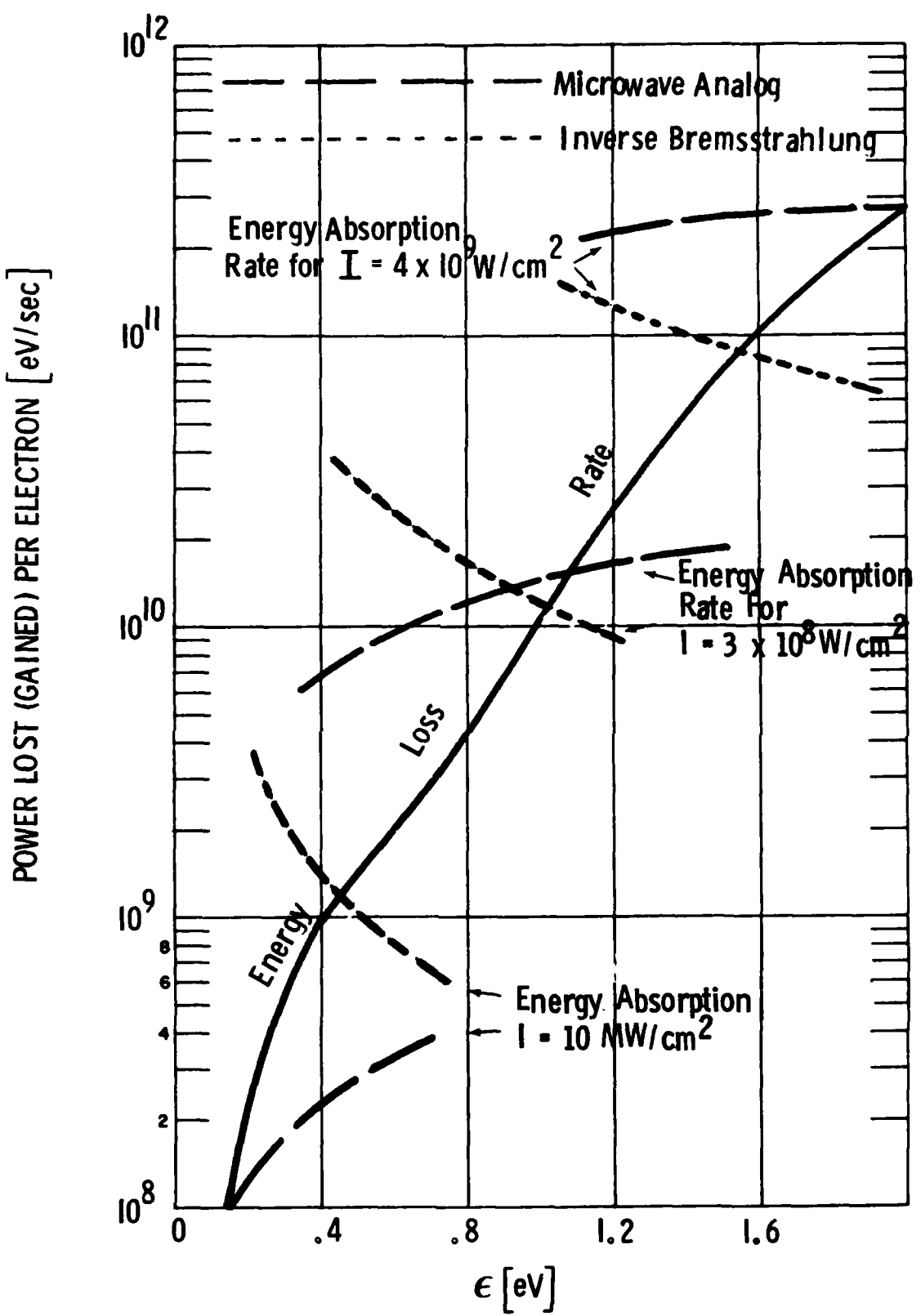
Fig. 16.6 Determination of Equilibrium Temperature Attained
by Laser Heated Electrons.
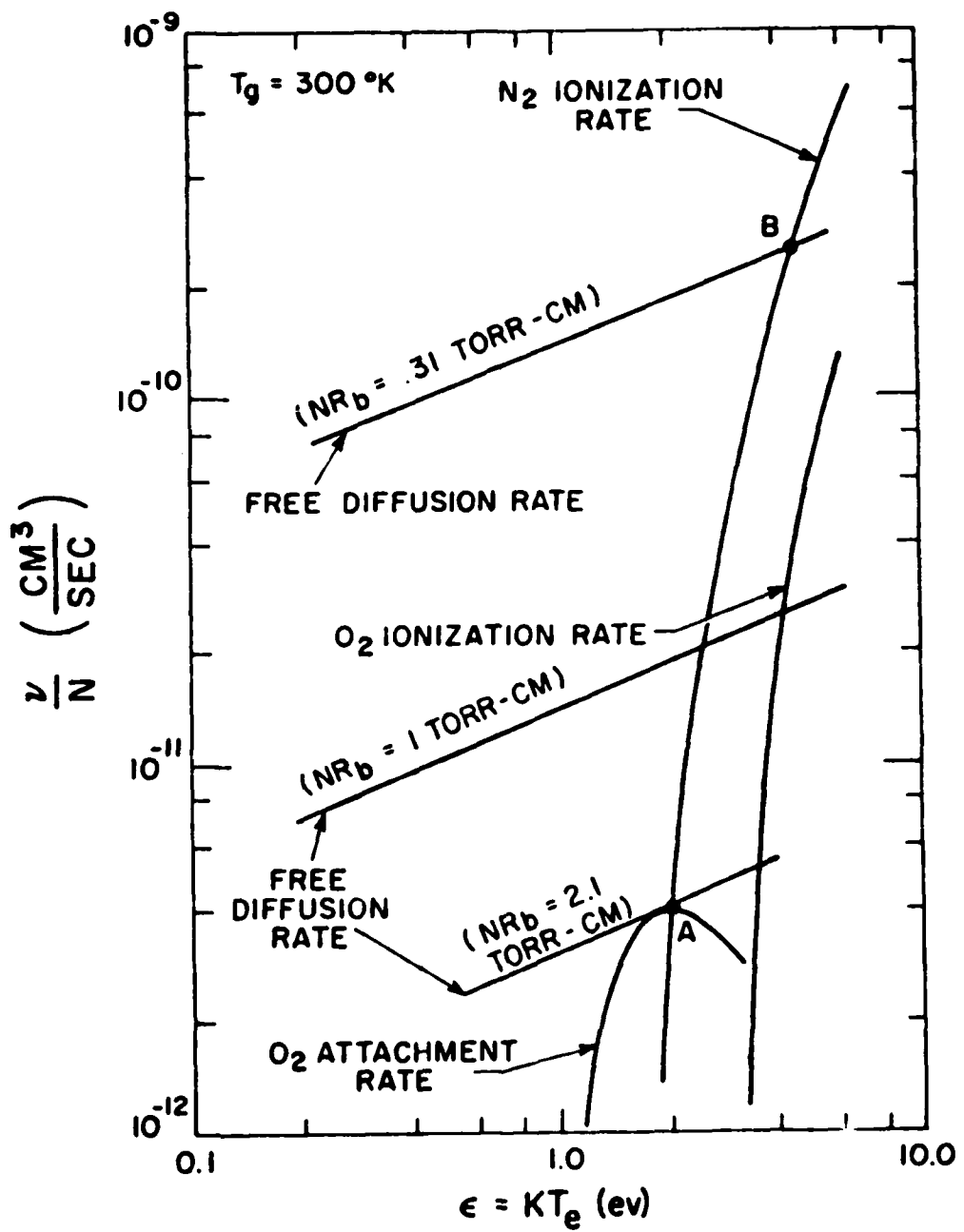
Fig. 16.7 Rate of Ionizing Collisions of Electrons with
N_2 and O_2 and Electron Attachment to O_2.
Taken from Ref. 12.

This conclusion cannot be averted by invoking absorption by electron-ion inverse Bremsstrahlung unless the concentration of electrons is enormous. Electron-ion inverse Bremsstrahlung is unimportant compared to electron-neutral inverse Bremsstrahlung as long as the concentration of ions (which equals the concentration of electrons) is less than one percent of the concentration of neutrals. For cold air this requires approximately 10^{17} electrons, far above the concentration expected by thermionic emission.

As a consequence of the above analysis we are led to suggest that indeed a small cloud of vapor is produced. There are numerous advantages of aluminum vapor insofar as cascade breakdown is considered, some of which are, low ionization potential, no cooling caused by excitation of vibrational states, and a high pressure, high temperature vapor which acts as a source of electrons. We do not have the data to perform a detailed analysis of the cascade breakdown in aluminum vapor, but a few calculations suffice to indicate the plausibility of this process. The neutral inverse Bremsstrahlung absorption coefficient, k_L', for 10.6 μm radiation and aluminum vapor has been estimated in Ref. 16 to be

$$k_L' \, [\text{cm}^{-1}] = \left(1 - e^{-1357.4/T}\right) n_{Al} n_e \, 6.4 \times 10^{-4} \, T[K] \quad , \quad (16.14)$$

where T is the temperature, and n_e is the concentration of electrons, and n_{Al} is the number density of neutral aluminum atoms. Under the assumption that most of the energy absorbed by the electron goes into creating new electrons, an assumption which is likely to be true for aluminum since there are no vibrational states to be excited, the rate of increase of the electron density obeys the following equation:

$$\frac{dn_e}{dt} = \frac{k'_L}{n_e} \frac{I_o}{I_p} , \qquad (16.15)$$

where I_o is the laser intensity and I_p is the ionization potential of aluminum which is approximately 6 eV. For $T = 4000\,^\circ K$, which corresponds to an aluminum vapor pressure of 48 atmospheres according to Eq. (16.7), the electron concentration can be increased an order of magnitude with a fluence of 2.4×10^{-2} J/cm^2. For an intensity of 10^7 watts/cm^2 in the gain switched spike this corresponds to 2.5 nanoseconds, which is comparable to the expansion time of the plasma bubble 2.5 μm in diameter. It is plausible, therefore, that a cascade breakdown can occur in the high pressure plasma vapor.

Even if the complete cascade does not occur in the high pressure plasma bubble, it is possible that after the vapor has expanded to 1 atmosphere, the electrons have not had enough time to recombine completely. They can still participate in a non-equilibrium cascade, although their absorption coefficient is approximately 40 times smaller; the breakdown times are, however, much longer; say 100 nanoseconds. Musal[17] has made an empirical correlation of breakdown thresholds for various radiation wavelengths and target materials. His results suggest that cascade breakdown will progress in target vapor at intensities as low as 1 megawatt/cm^2. Thus, if a vapor pocket at one atmosphere is formed, the cascade breakdown can even be completed by the plateau of the laser pulse, if necessary. It can be concluded, therefore, that the plasma initiation process probably requires that a small amount of vapor be produced by the target.

The preceding analysis suggests that breakdown in vapor pockets should occur at a plateau intensity of $1 MW/cm^2$, even in the absence of a high intensity spike. The spike is required, however, to produce the vapor cloud. The assertion that the flake is insulated from the bulk material is an approximation which is valid only if the heating is sufficiently rapid. In reality, the flake is joined to the bulk material at an edge, as illustrated in Fig. 16.8. In order to absorb the laser energy the flake must have a length a of at least a quarter wavelength. To prevent a substantial portion of the absorbed energy from being conducted into the target, the thickness of the thermal wave, $\sqrt{Kt}$, must be much less than the flake size a. For a ~ 2.5 µm and $K = .6 cm^2/sec$, the flake must start vaporizing within 100 nsec. However, to deliver $1.67 J/cm^2$, the experimentally observed fluence required for breakdown,[5] within 100 nsec, the intensity must be $16.7 MW/cm^2$.

Another estimate of the intensity needed to offset conduction losses can be made by comparing the thermal conduction flux through an edge to the rate of laser absorption, that is

$$\frac{k \Delta T}{\Delta X} \, \ell a = \alpha I a^2 , \qquad (16.16)$$

where ℓ is the thickness of the flake, α is the absorptivity, k is the coefficient of thermal conductivity, ΔT represents the flake temperature and ΔX is a measure of the thickness of the thermal wave. An appropriate value of ΔX is the smaller of $\sqrt{Kt}$ and a. Evaluating Eq. (16.16) with $\Delta T = 2400°C$, $\lambda = 1.7 \frac{W}{cm-sec}$, a = 2.5 µm, $\ell = .2$ µm and α (2700) = 18, we find $I = 7 MW/cm^2$. Of course, these are only crude estimates; for example, the flake size and number of thermally connected edges must be different. However, these estimates are sufficient to illustrate that thermal conduction requires a minimum intensity of the order of $10 MW/cm^2$ in the gain switched spike if the flake is to be vaporized.
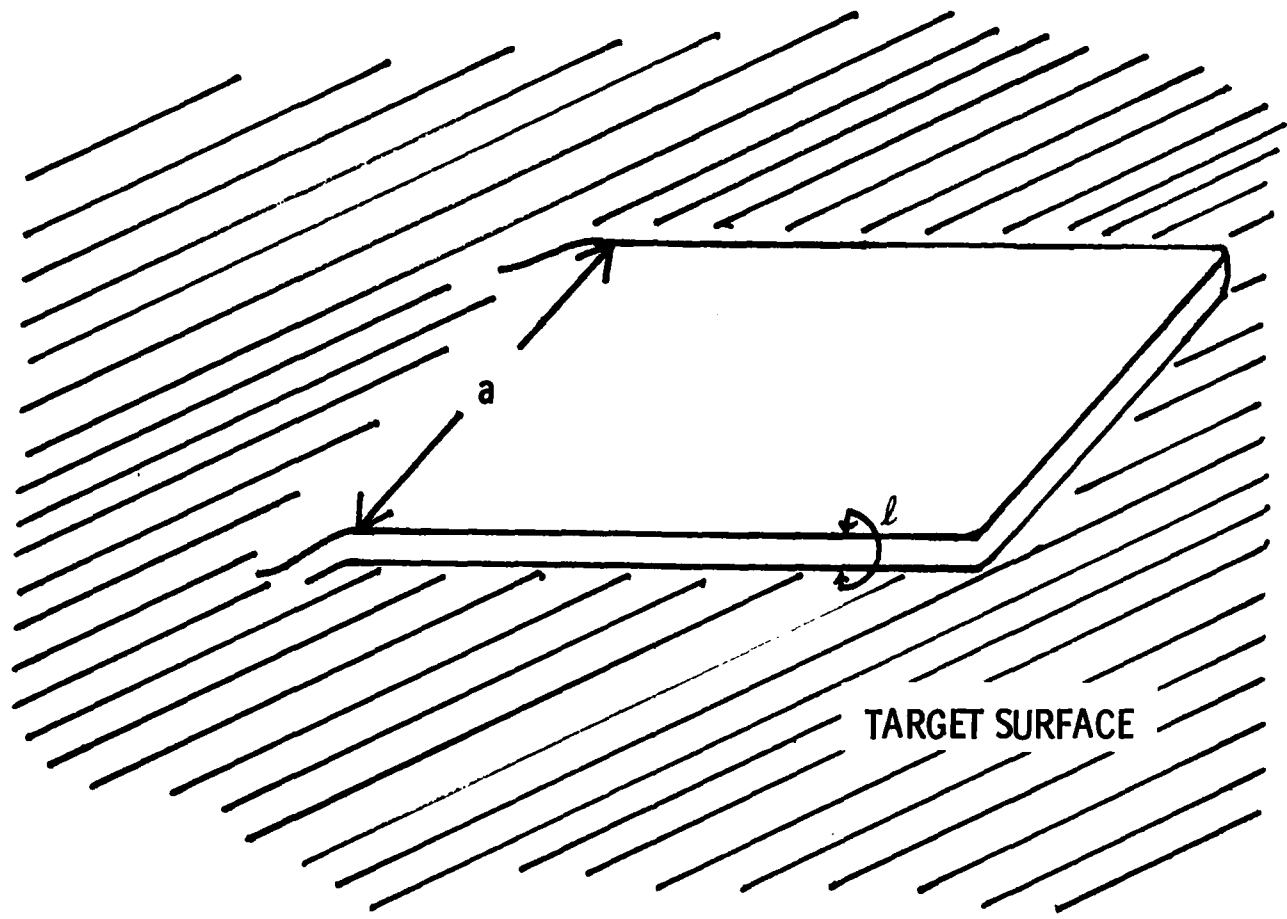
Fig. 16.8 Sketch of Flake.

The foregoing analysis of defect initiated air breakdown is not a thorough examination of all the intricacies involved in the breakdown process; rather it is merely an investigation of one popular model, in order to establish what the limiting physical steps are likely to be. Reliable models of ignition deserve far more theoretical attention. Having examined the breakdown mechanism, we can now evaluate the methods suggested in Section 15 for inhibiting ignition. First, methods which eliminate the defect sites required for prompt ignition are examined; then methods of preventing the cascade breakdown are analyzed.

16.2 Mechanical Polishing

Over a highly reflective surface such as aluminum, it is sufficient merely to eliminate the plasma since the intrinsic absorptivity of the target is small. Unfortunately, the tendency of mechanical polishing is to reduce the scale of the defects rather than eliminate the smallest ones. However, in the ignition model discussed above, the defects are already assumed to be thin and they are unlikely to be eliminated by mechanical polishing. Therefore, based on the proposed method of ignition, mechanical polishing is not expected to prevent ignition.

16.3 Chemical Polishing

Another method of hardening aluminum is to polish the target by using chemical agents to attach the defects. This method of polishing preferentially attacks small particles and edges and, for that reason, it may be superior to mechanical polishing for prevention of ignition. There is a minor piece of evidence supporting this approach to hardening. Some samples of Ti6A14V targets were chemically treated prior to irradiation in repetitive

pulse runs. These targets showed substantially poorer coupling than the single pulse interactions. It is believed that the poorer coupling was a consequence of poor plasma formation. Since plasma is believed to have been present in the single shot experiments performed at the same intensity, it is possible that the surface preparation may have been responsible for the difference. However, this conclusion is by no means certain since the details of the spike may have been significantly different between the repetitive pulse runs and the single pulse runs.

It is not clear if chemical polishing can completely remove all the defects, especially pit type defects which are speculated to have no edges. It is plausible, therefore, that chemical polishing can raise the ignition threshold by virtue of the elimination of the smallest defects, but the threshold may still lie below the LSD wave transition intensity. This behavior is anticipated because large defects become more important as the laser intensity is increased, and large defects are difficult to remove by chemical polishing. The utility of this approach may well depend upon the incident intensities expected. In summary, chemical polishing is a more attractive hardening approach than mechanical polishing but it may have only limited applicability.

16.4 Surface Melting

Another potential method of eliminating defects in aluminum is to melt the surface to a depth of a few microns in hope that the solid layer reforms without any defects. Quite apart from the question of defect formation, however, a potential drawback of this procedure is that aluminum oxide can form as the metal is heated, and the oxide has substantially higher intrinsic absorptivity that the untreated targets. Therefore, this approach

may necessitate heating in an inert atmosphere which may be prohibitively expensive. This approach appears to be cumbersome and its potential depends upon unknown features such as whether the defects are removed and whether aluminum oxide forms. These uncertainties are best resolved by experiments.

16.5 Highly Reflective Metal Coating

This approach can be employed with any metal, whether highly reflective or not. The target is covered with a thin layer of high-purity, defect-free, highly reflective metals such as aluminum or copper. The coating cannot have any (many) defects, otherwise the coating itself will ignite the LSC wave and its purpose is defeated. Moreover, the coating must be strongly bonded to the underlying substrate such that it can withstand mechanical and thermal loads.

Not all coatings meet these criteria. For example, plasma sprayed aluminum does not meet the first criteria - absence from defects. Electron scanning micrographs of a plasma sprayed surface reveal a wealth of structure in the surface[18] which, it is speculated, leads to enhanced plasma ignition. This hypothesis is consistent with the experimental observation that plasma sprayed aluminum absorbs more of the laser energy than untreated aluminum targets do.[18] Conversely, in the same experiments, diffusion bonded coatings absorb less energy than the untreated targets, and photographs indicated that few plasmas were ignited. In the analysis in the remainder of this subsection, it is assumed that plasmas are not ignited and that the coating is strongly bonded to the substrate.

Two different situations are considered. In the first, a layer of pure aluminum is bonded to an aluminum alloy substrate; this is representative of a coating covering a substrate with high thermal conductivity. In the second case highly reflective metals such as aluminum or copper cover poorly conducting targets such as SS304 and Ti6A14V.

For an aluminum target over an aluminum alloy, the substrate and the coating can be treated as having the same material properties - the effect of the coating is merely to eliminate defects and thereby prevent plasma ignition. The surface temperature is found by solving the heat conduction equation

$$\rho c \frac{\partial T}{\partial t} = \frac{\partial}{\partial x} \left(k \frac{\partial T}{\partial x} \right) ,$$ (16. 17)

where ρ is the density, c is the specific heat, and k is the thermal conductivity, with the boundary condition at the surface being

$$\alpha I = -k \left(\frac{\partial T}{\partial x} \right) ,$$ (16. 17)

where α is the absorptivity and I is the incident laser flux.

The absorptivity of the aluminum increases with temperature. Below the melting temperature the absorption coefficient can be represented by (see Eq. 16. 3)

$$\alpha(T) = \alpha_o + \alpha' (T-300) ;$$ (16. 19)

$$\alpha_o = .03, \alpha' = 5 \times 10^{-5} [K^{-1}] ,$$

where T is the temperature in $^{\circ}$K. The solution for surface temperature, when the absorptivity is a linear function of the surface temperature, has been derived by Thomas and Musal.[19] They find the difference between the surface temperature T_s and the initial target temperature T_o obeys

348

$$T_s - T_o = \frac{\alpha_o}{\alpha'} \left(2e^{x^2} - 1 - e^{x^2} \operatorname{erfc} x \right) , \qquad (16.20)$$

where x is defined by

$$x \equiv \alpha' I \sqrt{\frac{t}{k\rho c}} . \qquad (16.21)$$

In the above equation, ρ is the density; c is the specific heat; k is the thermal conductivity, and t is time. A plot of the front surface temperature as a function of the parameter x is given in Fig. 16.9.

An average absorptivity for heating to a given temperature can be defined by comparing Eq. (16.20) to the solution for the front surface temperature at a constant flux, namely,

$$T - T_o = 2\alpha I \sqrt{\frac{t}{k\rho c\pi}} . \qquad (16.22)$$

It is found that the time to reach the melting temperature can be calculated by using Eq. (16.22) and an average absorptivity of 0.05. The definition of an equivalent average absorptivity for a target heated to the vaporization temperature is ambiguous, since there is an abrupt jump in the absorptivity at the melt temperature. The result depends upon how this jump is incorporated into an expression for $\alpha(T)$ which is linear in T; the equivalent average absorptivity for heating to the vaporization temperature can range from a low of 0.11 to a high of 0.15 depending upon the approximation used.

$$\alpha(T) = \alpha_0 + \alpha' \Delta T$$
$$\Delta T = T - 300K$$
$$\alpha' = 5 \times 10^{-5} \ K^{-1}$$
$$\alpha_0 = .03$$

Bulk Vaporization of Aluminum

Aluminum Melts

$$X = \sqrt{\frac{\alpha'}{\kappa \rho_c}} \ \sqrt{FI}$$
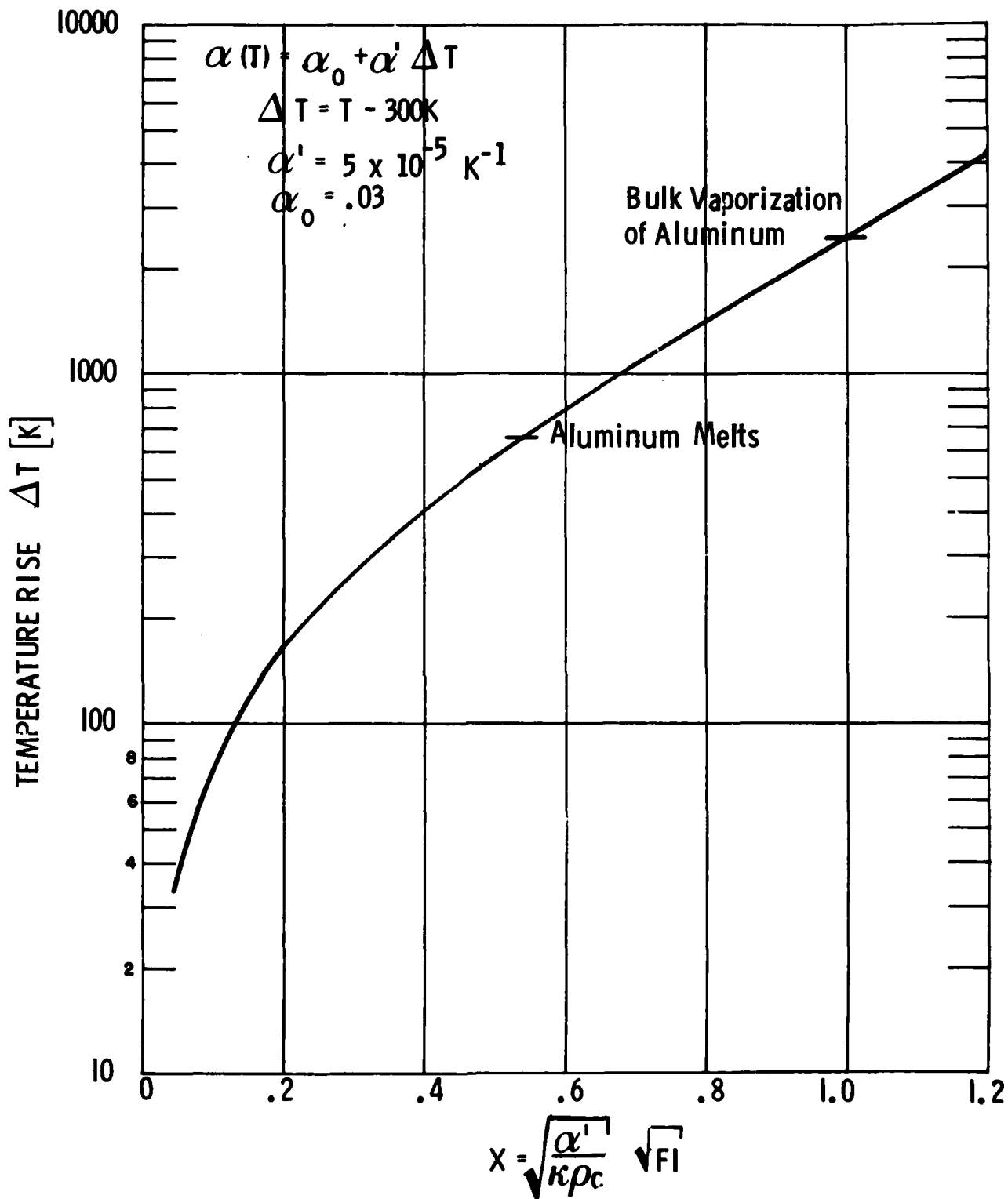
Fig. 16.9   Front Surface Temperature for Linearly Increasing Absorbed
Heat Flux.

In Fig. 16.10, a plot has been constructed to show the relationship between the fluence and the intensity necessary to reach both the melting temperature and the vaporization temperature of aluminum, where Eq. (16.19) has been used for the absorptivity all the way to the vaporization temperature. The fluence delivered by laser pulses 10, 20 and 40 μsec in duration is also shown. As can be clearly seen, it is virtually impossible to vaporize the surface with a reasonable length laser pulse - it requires 10 MW/cm^2 for 20 μsec. It is possible, however, to melt the surface with only 5 MW/cm^2 for 20 μ sec; but at this intensity, the coupling via a plasma is approximately the same as the expected intrinsic coupling. Since the surface must melt before any mass removal can occur, (the bonding to the substrate is assumed to be strorg), the fluence required for melting is a conservative lower limit on the fluence needed to defeat a protective coating with a long series of pulses. Therefore, the aluminum coating should protect the aluminum target from enhanced thermal coupling, as long as the laser pulse train is not adjusted to operate against the coating for the first few pulses and to operate in the enhanced coupling regime for the remaining pulses. Note, however, that in this approach up to 5 percent of the energy may be coupled to the target by virtue of the intrinsic absorptivity.

The second configuration to be examined is a highly reflective coating of aluminum or copper bonded to a poorly conducting substrate such as Ti-6Al4V or SS304. The energy requirements for removal of the coating can be calculated in several approximate methods. One model is to assume that the coating has essentially no thermal capacity. Then the surface temperature reached by the coated metal is controlled by Eq. (16.20) with the thermal properties being those of the substrate and the absorption characteristics being those of the coating. Two temperatures which characterize potential critical temperatures are the melting temperature of the coating material which may correspond to the destruction of the bond between the coating and
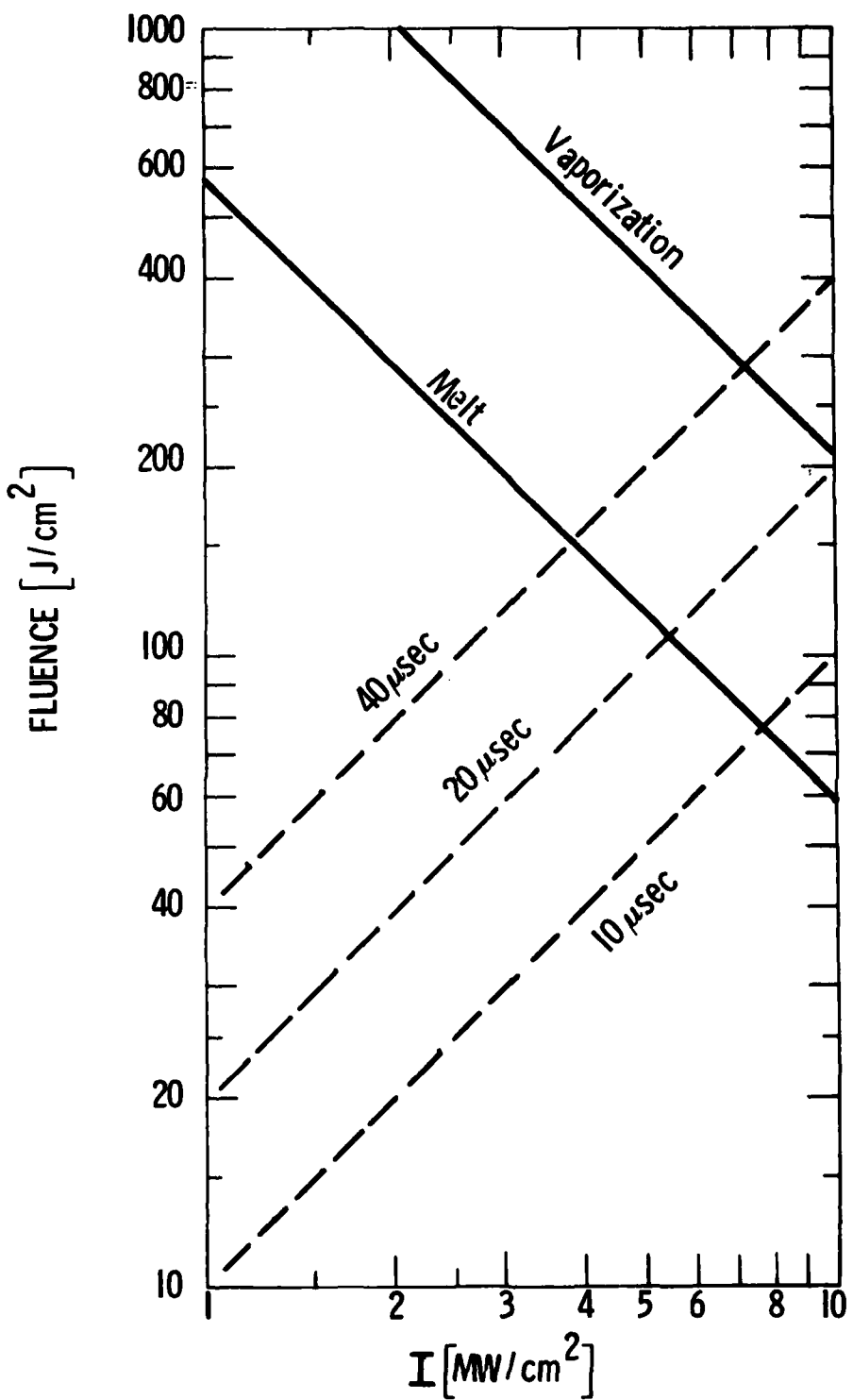
Fig. 16. 10 Fluence as a Function of Intensity Required to
Raise Thin Coat of Aluminum on Al2024 Substrate
to Melting and Vaporization Temperature. Dashed
Lines Show Fluence Delivered by Lasers of Fixed
Pulse Time.

the substrate, and the vaporization temperature of the coating, which is the temperature at which the coating can certainly be removed by a sequence of pulses. In Table 16.3, the thermal properties of Ti6A14V and SS304 are given, along with the absorptivities used for aluminum and copper and the product of fluence times intensity which is associated with the surface reaching both the melting temperature and the vaporization temperature. The predictions for the removal of thin layers are plotted in Fig. 16.11 for aluminum coatings and in Fig. 16.12 for copper coatings. It is clear that, if the coated layer has no thermal capacity, it is possible to melt the aluminum coating with modest laser pulse requirements.

As the thickness of the layer increases the thermal capacity of the coating becomes significant. For example, a one mil thick coating of aluminum has a thermal capacity of 4.5 J/cm^2 for a change in temperature of 630K. For an average surface absorptivity of 0.05, an additional incident fluence of 90 J/cm^2 is required. In this example, the thermal capacity of the coating exceeds the amount of energy conducted into the substrate.

When the coating is thick enough to have significant thermal capacity, both the thermal capacity of the coating and the energy diffused into the substrate must be accounted for in the model. As a first order estimate the temperature and energy contained in the substrate are calculated assuming that a constant flux of heat I' is transferred into the substrate (see Fig. 16.13). In order to attain a temperature T_i at the interface, the fluence F' into the substrate is related to the intensity I' by

$$F' I' = \frac{\pi \rho_s c_s k_s T_i^2}{4} , \qquad (16.23)$$

where ρ_s, c_s, and k_s are the density, specific heat, and thermal conductivity of the substrate, respectively. Because of the high thermal conductivity of the coating, the temperature profile within the coating can be

TABLE 16.3

Data Used to Evaluate Effect of Defect-Free Coatings.

	Ti6Al4V	SS 304
k	.1 W/cm-K	.19 W/cm-K
ρ	4.45 g/cm^3	7.9 g/cm^3
c	.6 J/g-K	.56 J/g-K
FI (T_m) (Al)	$32 \frac{MW-J}{cm^4}$	$102 \frac{MW-J}{cm^4}$
FI (T_m) Cu	$280 \frac{MW-J}{cm^4}$	$870 \frac{MW-J}{cm^4}$
FI (T_v) Al	$118 \frac{MW-J}{cm^4}$	$371 \frac{MW-J}{cm^4}$
FI (T_v) Cu	$667 \frac{MW-J}{cm^4}$	$2101 \frac{MW-J}{cm^4}$

	Al	Cu
T_m	933 K	1358 K
T_v	2767 K	2845 K
α_o	.03	.016
α' [K^{-1}]	5 x 10^{-5}	1.7 x 10^{-5}
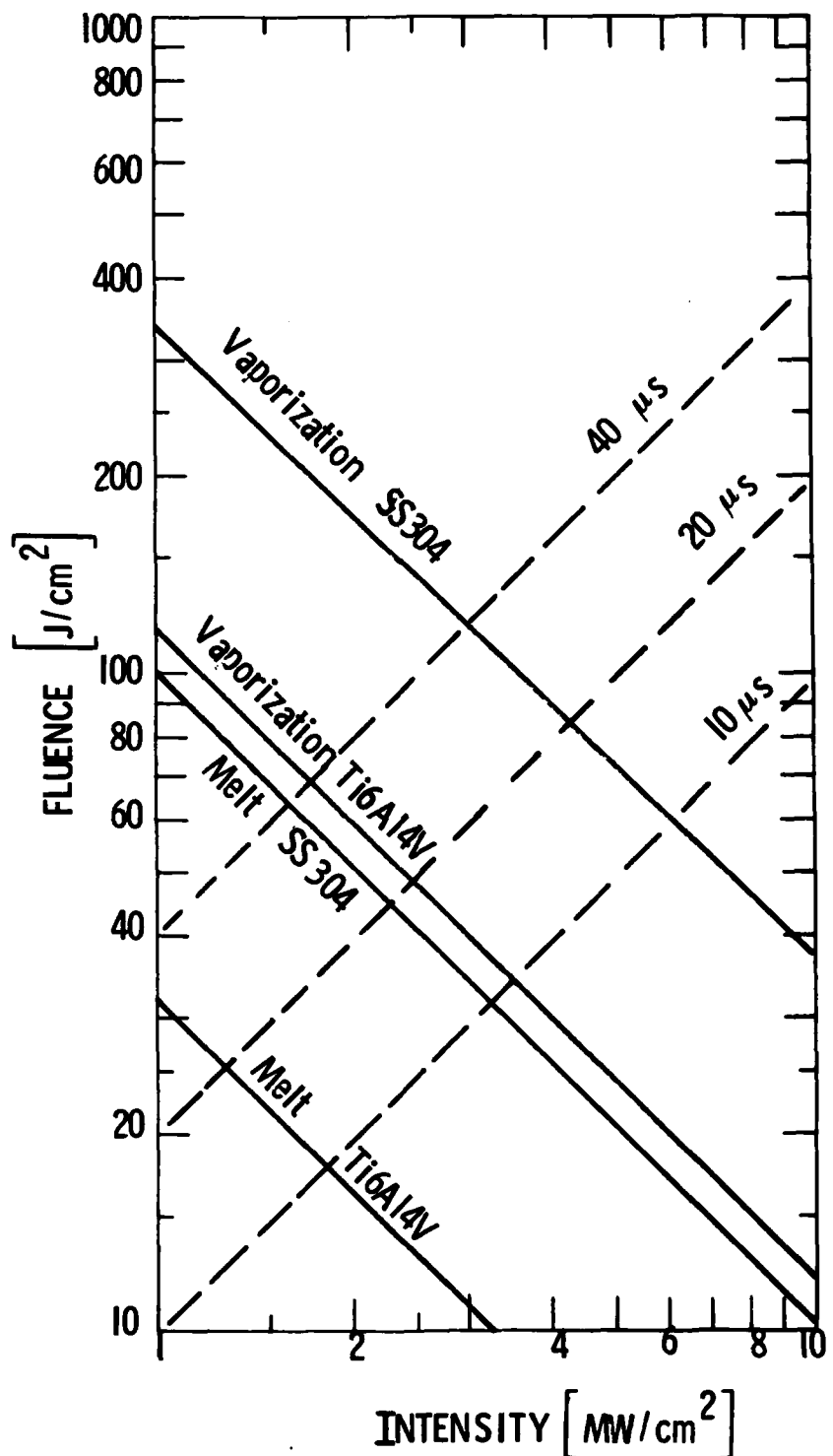
Fig. 16.11 Fluence as a Function of Intensity to Raise
Thin Coat of Al to Melting or Vaporization
Temperature for SS 304 and Ti6Al4V Substrates.
Dashed Lines Show Fluence Delivered by Lasers
of Fixed Pulse Time.

355
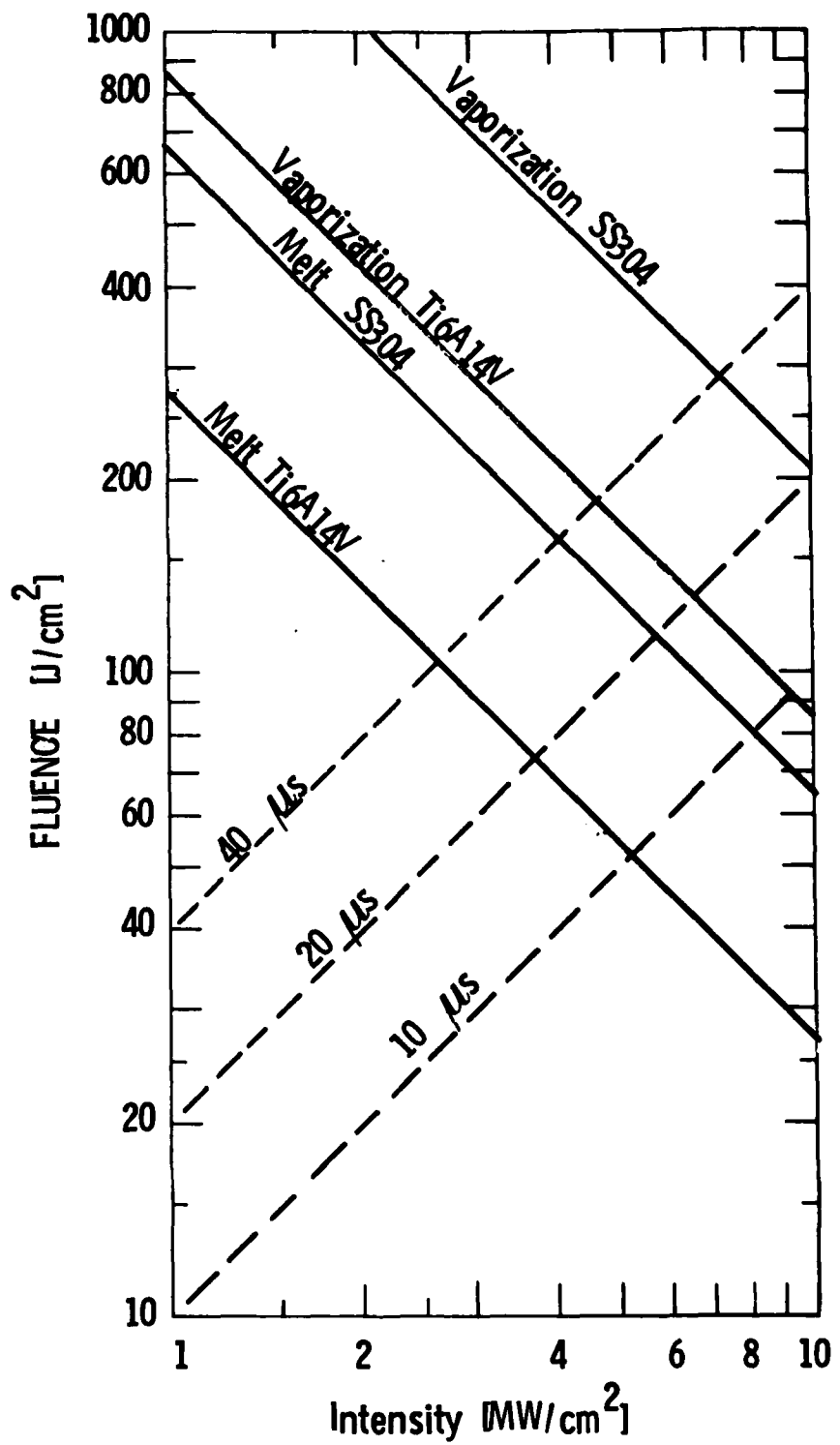
Fig. 16.12   Fluence as Function of Intensity to
Raise Thin Coat of Cu to Melting or
Vaporization for SS 304 and Ti6Al4V
Substrates.   Dashed Lines Show
Fluence Delivered by Lasers of Fixed
Pulse Time.

356

Fig. 16.13

(a) Sketch of Temperature Profile in Target Which has a Coating Over a Substrate.
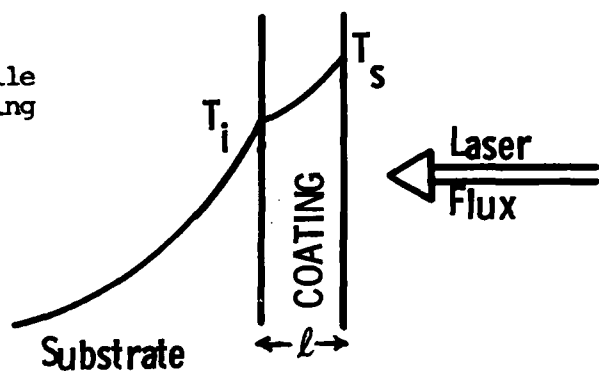
(b) Sketch of Temperature Profile in Substrate Subjected to Heat Flux Given by $I' = F'/t_p$.

$$T_i = 2 I' \sqrt{\frac{t_p}{\pi \rho_s c_s k_s}}$$
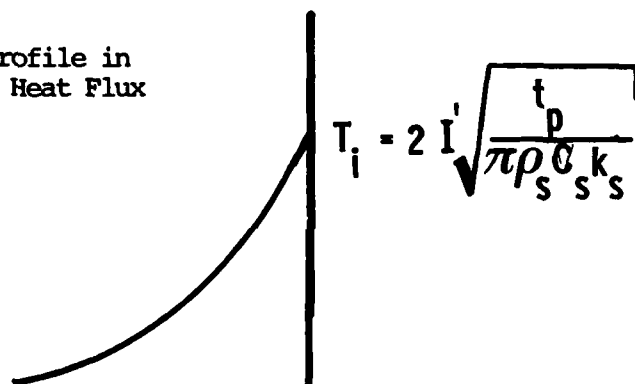
(c) Sketch of Quadratic Temperature Profile in Thin Layer Subjected to Heat Flux αI on Front Surface and Losing Flux I' from Back Surface ($I' << \alpha I$).
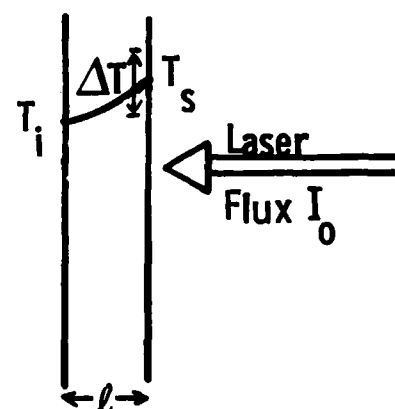
$$\Delta T = T_s - T_i \approx \alpha I \, \ell/2k$$

$$(\alpha I - I') t_p = \rho c \ell \left[T_s - \frac{2 \Delta T}{3} \right]$$

approximated as a parabolic profile. This approximation is very good when the thermal conductivity of the coating is much greater than that of the substrate, and when $\kappa t/\ell^2 \geq .3$ where ℓ is the thickness of the coating, κ is the thermal diffusivity of the coating, and t is the time involved. For a one mil thick coating of aluminum the approximation is good whenever t is longer than 3 μ sec. The temperature difference between the front surface and the rear surface is given by

$$T_s - T_i = \frac{\alpha I \ell}{2 k} \quad , \tag{16.24}$$

where T_s is the front surface temperature, α is the absorptivity, I is the laser intensity, and k is the thermal conductivity of the target. Finally, conservation of energy requires that the difference between the absorbed fluence α F and fluence F' transported into the substrate be equal to the thermal sensible heat in the coating;

$$\alpha F - F' = \rho c \ell \left\{ T_i + \frac{T_s - T_i}{3} \right\} \quad , \tag{16.25}$$

where ρ and c are the density and specific heat of the coating material. The set of equations (16.23) - (16.25) is completed by the assertion that the intensities and fluences are related by the laser pulse length τ_p;

$$F = I \tau_p \quad , \tag{16.26}$$

$$F' = I' \tau_p \quad .$$

Calculations have been made of the fluence and intensity required to raise the coating surface to the melt temperature ($T_s = T_m$); the results are presented in Figs. 16.14 and 16.15, where the size of the thinnest coating sufficient to prevent front surface melting is plotted as a function of intensity for several pulse times and several substrate materials. This is a conservative estimate of the coating size needed to protect the substrate from a long series of pulses, since immediate melt removal is assumed. A lower limit on useful coating thickness is determined by the ignition suppression requirements discussed earlier and is of the order of 1/2 micron. For an aluminum coating of typical thickness, say 1 mil, (25.4 μm), no melting occurs for a long string of 10 μsec pulses with intensities up to 9 MW/cm^2 (see Fig. 16.14). If the pulses are 20 μsec long, the 1 mil coating will protect the substrate for intensities up to 5 MW/cm^2, and if the pulses are 40 μsec long, the intensity maximum is 3 MW/cm^2. To achieve these intensities and fluences, the incident pulses are forced to lie outside the enhanced coupling region. Copper is substantially better (see Fig. 16.15); it can foil even a series of 40 μsec pulses at 8 MW/cm^2. The improved performance of copper has two potential drawbacks. The copper coating weighs 3 times as much as an aluminum coating of identical thickness. Moreover, if there are a few defects in the coating, so that plasmas are ignited intermittently, the coupling of the plasma to the copper coated target is expected to be higher than to the aluminum coated target, because copper absorbs the plasma radiation better.

In summary, highly reflective metal coatings appear to offer substantial protection from enhanced coupling, provided, of course, they can be manufactured defect-free and bonded strongly to a substrate.
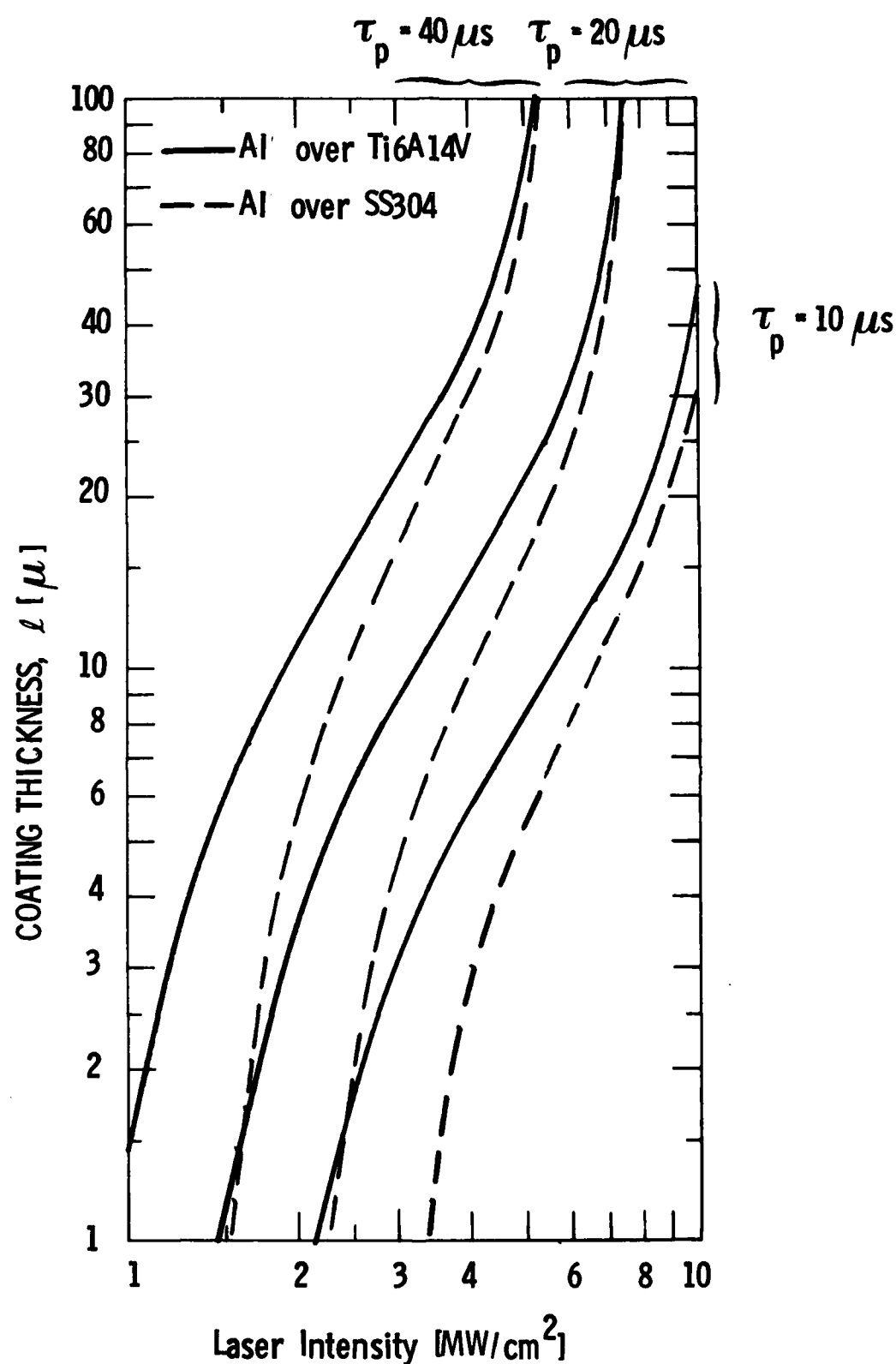
Fig. 16.14 Incident Laser Intensity Required to Melt the
Front Surface of a Layer of Defect-Free Al
of thickness l. Curves are Shown for Two
Different Substrates and Three Different
Pulse Times.

360
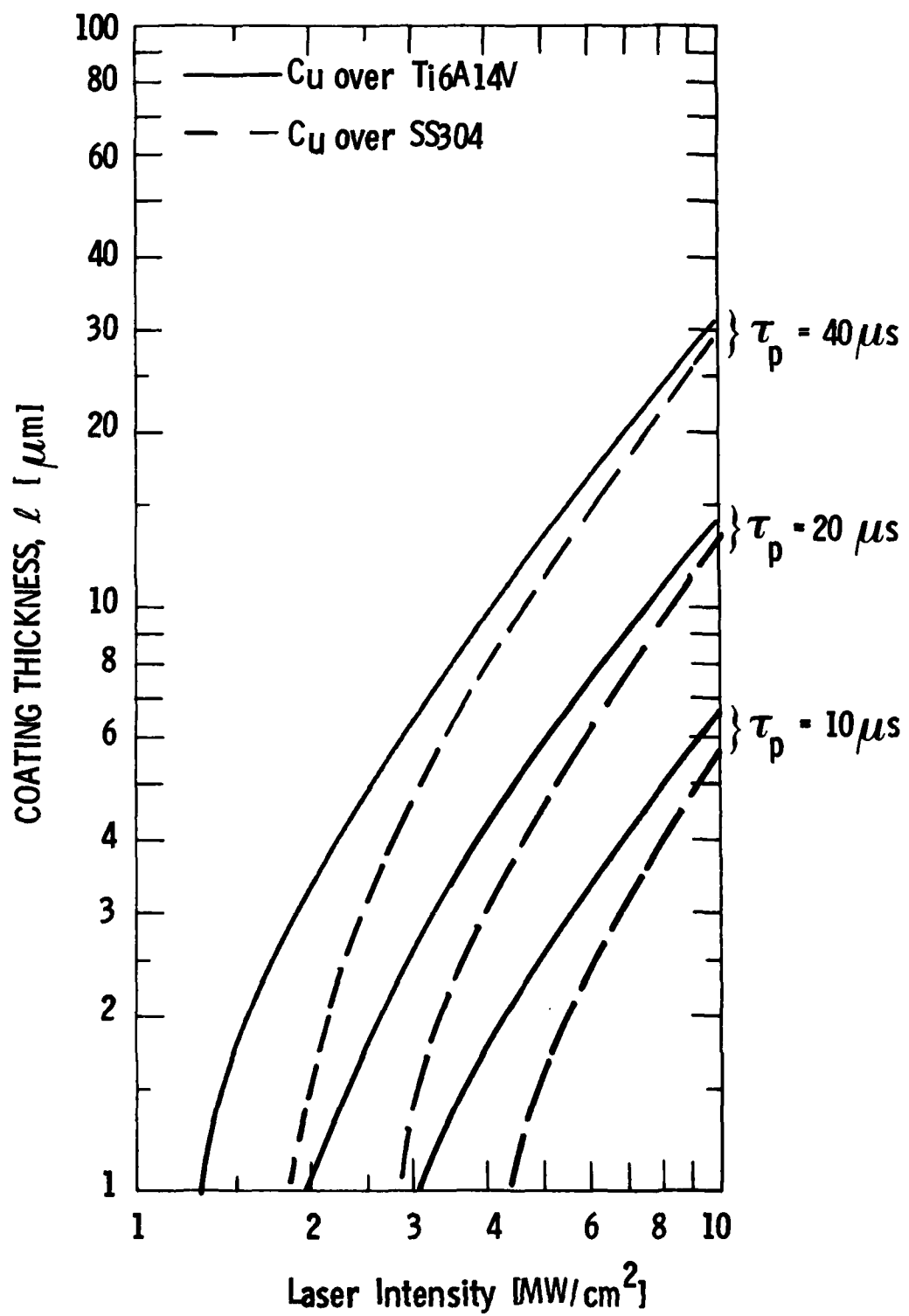
Fig. 16.15 Incident Laser Intensity Required to Melt the Front
Surface of a Layer of Defect-Free Copper of Thickness
l. Curves Shown for Two Different Substrates and
Three Different Pulse Times.

16.6 Transparent Coatings

Over a highly reflective surface such as aluminum, a potential method of preventing ignition is to place a highly transparent material over the surface whose purpose is to prevent the flakes from vaporizing and seeding the air with electrons. Some suggested transparent materials are ZnS, ZnSe, and CaF_2.

Our analysis of the hardening potential of these materials shall be concentrated on identifying criteria that must be met by the candidates. For example, the material must be transparent enough to prevent an appreciable fraction, say 5 percent, of the incident radiation from being absorbed; otherwise, the transparent material acts as an additional heat source. Furthermore, the coating must not initiate breakdown itself, since then its raison d'être is destroyed. The bonding of the material to the substrate must be accomplished in such a manner that it does not cause absorption of radiation, and it must maintain its integrity at high temperature (at least up to the melting point of aluminum).

A summary of some of the properties[20, 21, 22] of the substances mentioned above are listed in Table 16.4. It is found that ZnS and ZnSe both have good transparency, but CaF_2 is an order of magnitude worse. In order for there to be less than 5 percent of the laser energy absorbed in passing through the layer twice, (incident and reflected rays), we require $2kx < .05$, where k is the absorption coefficient of the material and x is the thickness. Therefore, the permitted thickness of ZnS and ZnS· is about .02 cm, whereas the thickness of the CaF_2 layer must be less than 30 microns. The temperatures listed for melting or transition all exceed the melting point of aluminum. Therefore, the critical temperature which must not be exceeded during the interaction with the laser is the melting point of aluminum, $933^{\circ}K$. The

TABLE 16.4

Some Physical Properties of Some Dielectrics.

	CaF_2	ZnS	ZnSe	Ref
$k_{10.6\ \mu}$ [cm^{-1}] (calculated from transmittance)	8.0	1.0	1.2	20
$k\ \left[\dfrac{W}{K\text{-}cm}\right]$	.06 @ 176 C	.11@174 C	.07 @422 C	20
$\rho\ \left[g/cm^3\right]$	3.18	4.1	5.27	20
$C\ \left[\dfrac{J}{g\text{-}k}\right]$	.85 (22)*	.5 (21) (22)		21,22
T_m	1423 C(24) 1360 C(21)		>1100(23) (24)	21,23,24
T(transition	1151 C	1020(22) (23) (24)		22,23,24
Refractive Index @ 10 μm	1.28	2.19	2.40	20

*Ref. in ( )

temperature that the dielectric is expected to reach as a result of this absorption (neglecting conduction and assuming no reflection at the surface) is given by

$$T - T_o = \frac{kIt}{\rho c} \quad , \tag{16.27}$$

where T is the final temperature, T_o is the initial temperature, t is time, I is the laser intensity, k is the absorption coefficient, ρ is the density, and c is the heat capacity. For ZnS, the fluence required to reach the melting point of aluminum is 640 J/cm^2. This exceeds the fluence required to melt the aluminum by intrinsic absorption of the laser, thus, the dielectric coating does not cause the aluminum to melt.

Unless thermal conduction in the overlying dielectric can prohibit the flake vaporization, the bonding between dielectric and aluminum must be sufficiently strong to withstand the pressure of both the vapor production and the subsequent production of small pockets of plasma. Although the pockets will be small and localized, they can exert tremendous pressures. Thermal conduction from the flake into a typical dielectric ($\kappa \approx .03$ cm^2/sec) removes some of the heat from the flake and may prevent the flake from vaporizing. For example, during the gain switched spike which lasts approximately .1 μsec, the depth a thermal wave travels into the dielectric from the flake is approximately .5 μm. If the temperature of the flake is approximately 2700 ^{o}K, the heat flux at the flake surface is approximately 4.8 x 10^7 k where k is the conductivity in W/cm-K For ZnS the heat flux is 5 MW/cm^2. If the aluminum flake has an average absorptivity of .1, this corresponds to the energy supplied by an incident intensity of 50 MW/cm^2. It seems, therefore, that plasma pockets will not occur at low intensities, but small pockets may occur at high intensities, where the intensity in the gain switched spiked exceeds 50 MW/cm^2. Therefore, it is important to have strong bond.

Provided that all the criteria mentioned above can be met, dielectric layers should be able to prevent plasma ignition. There is some evidence, however, that it may be difficult to achieve some of these criteria. Recent experiments[23] in which dielectric stacks were subjected to laser radiation showed that plasma were routinely ignited, and the integrity of the dielectric stack was destroyed. This problem appears to be severe and emphasizes that special care must be exercised to produce defect-free samples.

Even if a defect-free sample is manufactured in an economical manner, the method may not work for reasons quite apart from those examined here. For example, the material may degrade in the atmosphere and, therefore, must be protected. The process of removing the protective coating with a laser may well compromise the homogeneity of the sample, since, undoubtedly, the dielectric is a good absorber of the plasma radiation which is produced during the removal of the protective coating.

16.7 Electron Attaching Gas Injected Into the Boundary Layer

The above mentioned solutions to the plasma inhibition problem depend upon elimination of defects which act as the initial source of electrons for the cascade breakdown. Another approach is to permit the defects to remain, to heat up, and to create electrons, but to curtail the cascade avalanche which is also necessary to produce a LSC wave plasma. Two potential ways of accomplishing this are injection of electron attaching gases into the boundary layer and displacement of the boundary layer with a gas which does not support LSC waves.

The first potential method - injection of electron attaching gases such as SF_6 and WF_6 - will fail if the model of ignition advanced earlier is correct. The ignition process occurs within a distance of a few microns of the surface

and is suspected of being a result of breakdown in aluminum vapor. Small concentrations of an electron attaching gases in the boundary layer cannot prevent the formation and subsequent rapid breakdown of a cloud of aluminum vapor. The limiting step in the breakdown process is the production of the aluminum vapor, not the cascade breakdown. Nor is it expected that electron scavengers can prevent the formation and propagation of a LSC wave in air, since the production of a LSC wave requires, even in the absence of electron scavengers, that the air be heated by conduction and radiation from the hot plasma point to temperatures in the range of 12,000 to 14,000°K before the air can absorb laser energy. At these high temperatures, the electron attaching molecules are expected to be completely disassociated; therefore, they cannot affect the development of the wave. Of course, this conjecture should be examined experimentally, since it depends upon the ignition model which has not been verified, but the experiment should be designed with the above-mentioned likelihood in mind.

16.8 Detaching the Air Boundary Layer

The other potential method of eliminating the production of a LSC wave is to displace the air in the boundary layer with a gas which will not support LSC waves. Since the plasma pockets are initially very close to the target surface, the presence of this gas can isolate the plasma pockets from the air and may thereby prevent LSC wave ignition. This possibility is advanced as a potential mechanism, but we have not examined the concept in detail. Further theoretical work must be expended in this area in order to identify candidate gases. The ability of the gas to attach electrons is not a primary criterion for the candidate gases, however, since once again the initial plasma clouds can heat the gas to well in excess of 10,000°K. Instead, the important features of the gas are expected to be its energy transport

properties and ionization potential. Whatever the nature of the gas, there must be massive blowing in order to displace the air. The massive blowing requirement may well be a crucial factor in the determination of practicality of such a hardening scheme.

16.9 <u>Summary</u>

As a result of the analysis of the suggested approaches to ignition inhibition, we have reached the following tentative conclusions:

1) Mechanical polishing is unattractive, since it does not remove the very thin defects which initiate the plasma.

2) Chemical polishing is better than mechanical polishing. It is expected to be most useful at low intensities, but probably fails at high intensities. Any useful applications are probably limited to Al2024.

3) Surface melting to remove defects probably produces oxide which will ignite the LSC wave. Application is again limited to Al2024.

4) Highly reflective coatings appear to have great potential if defect-free samples can be strongly bonded to the substrate. This approach should be valid for all substrates. There is limited experimental evidence in support of this approach.

5) Use of transparent coatings is fraught with difficulties. Nevertheless, the coatings could function effectively if suitable bonding and ignition-free samples can be produced. However, scant preliminary experimental evidence suggests strongly that it is nearly impossible to eliminate sites which ignite plasma.

6) Electron scavenger injection into the boundary layer is unattractive since it cannot prevent ignition in a target vapor and is equally unlikely to prevent LSC wave maintenance.

7) Massive flowing of a foreign gas to displace the air boundary layer may curtail LSC wave formation. However, suitable gases have not yet been identified, and massive blowing requirements may prove impractical.

The conclusions listed above can serve as preliminary indications of which hardening approaches are likely to be fruitful. It is important, however, that experiments be performed to assess the validity of these conclusions, and that further research on material properties be incorporated into the criteria. The analysis contained in this section can, nevertheless, aid in the design of experiments.

SECTION 17

PLASMA DETACHMENT APPROACHES

In this section we investigate methods of igniting detached plasmas.
Two different physical effects are expected to reduce the enhanced thermal
coupling in this approach: first, the layer of cold air between the plasma
and the target absorbs much of the reradiated plasma radiation and thereby
inhibits radiative transfer of the crucial short wavelength portions of the
spectra; and second, the absence of a wall immediately behind the plasma
permits expansion of the plasma in two directions. Because of this expan-
sion, subsequent cooling of the plasma makes the plasma radiate less effi-
ciently and reduces the pressure. The overall effect is similar to the re-
duction in coupling experienced by pulses that have large values of $\hat{\tau}$.

As a further benefit, an opaque detached plasma absorbs all the in-
cident radiation; therefore, if the coupling via the plasma reradiation is
poor, it is possible for the total coupling to fall below the coupling pre-
dicted by intrinsic absorption of the laser. This is especially advanta-
geous for metals with high intrinsic absorptivity.

It is not known how far from the surface the plasma should be ig-
nited, but a few conservative estimates can be made. An LSC wave ex-
panding away from the target has a velocity of $1 - 2 \times 10^5$ cm/sec. It
is expected that, when expansion occurs in two directions, the velocity
is lower; for definiteness, we choose a value of 10^5 cm/sec. Therefore,
if the plasma is detached 1 cm, for example, it requires 10 μsec for
the wave to reach the surface. Since it is also anticipated that the re-
sultant plasma has poor radiating properties, a 1 cm air gap is probably
sufficient to prevent acceptable thermal coupling, even for laser pulse
lengths substantially longer than 10 μsec. However, should it be de-
sirable to reduce further the radiative coupling, even for long pulse

times such as 40 μsec, a 3 cm gap could be used. This gap cannot be bridged in less than 30 μsecs. Moreover, a 30 μsec pulse is already in the region of $\hat{\tau} > 1$ with the spot sizes expected. Therefore, when the plasma reaches the target, it has already degenerated into a very poorly radiating three-dimensional plasma. Thus, a 3 cm gap represents the maximum gap size necessary for protection of the target at normal incidence.

It is conceivable that gaps smaller than 1 cm may also be adequate to shield the surface since the absorption length of the photo-recombination radiation in air is approximately .01 cm; this is much less than the gap size. However, performance of a small gap is pure conjecture at this time, and it is appropriate to concentrate on conservative gap sizes in the following disucssion.

17.1 Dimpling the Surface

In this approach the surface is covered with concave dimples whose purpose is to reflect the laser radiation to a high intensity focus which causes laser-induced breakdown of the air. From the intensity required for breakdown and from the focusing characteristics of the dimple, it is possible to determine the size of the dimples necessary to achieve breakdown of the air at any given distance above the surface.

The threshold intensity for laser induced breakdown in pure air for 10.6 μm radiation has been calculated by Schlier, Pirri and Reilly,[12] and is shown in Fig. 17.1. For large spot sizes the threshold intensity is approximately 3 to 4 GW/cm^2. However, the breakdown threshold increases slowly if the radius of the high intensity focal region is smaller than .003 cm. The diameter of the dimples required to produce breakdown will be calculated under the assumption that the radius of the high intensity region exceeds .003 cm, an assumption which is justified a posteriori.

If the dimple is a perfect focusing reflector with a square aperture,
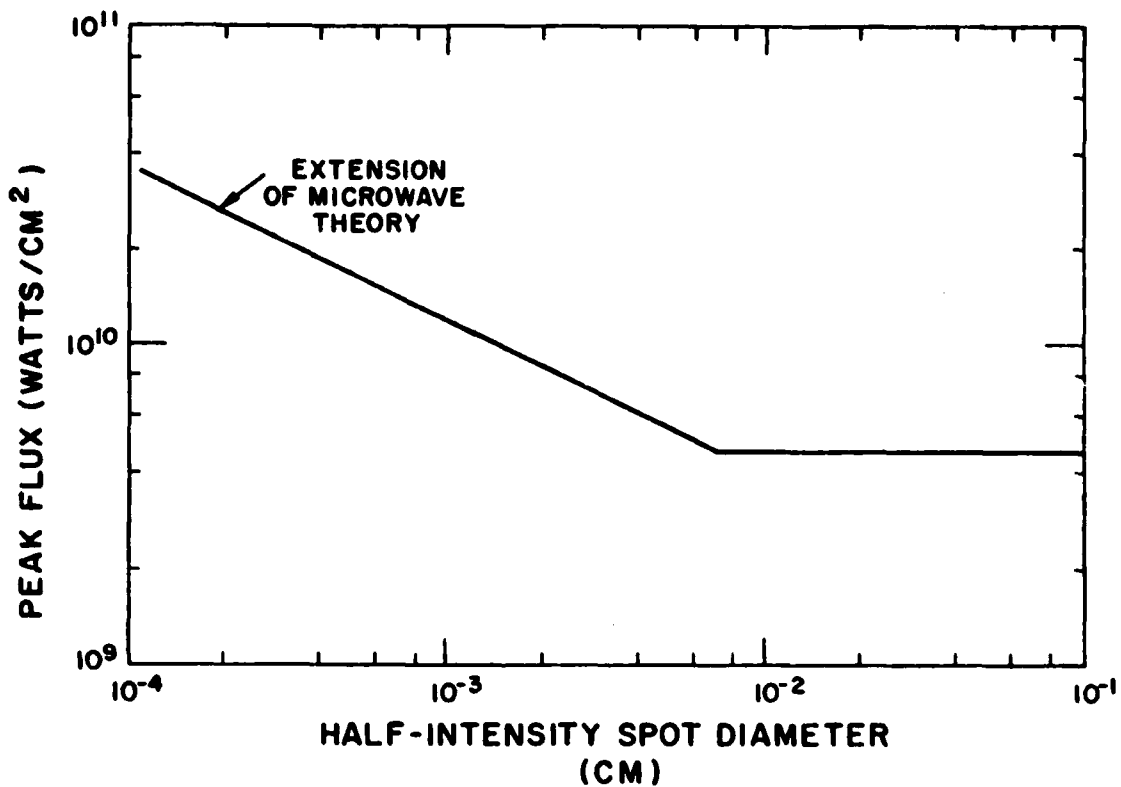
Fig. 17.1 Clean Air Breakdown Threshold vs Beam Diameter at
One Atmosphere Pressure from Ref. 12.

the diffraction limit on the spot radius is given by $\lambda F/D$ where λ is the radiation wavelength, F is the focal length, and D is the width of the aperture. For a spherical aperture, the above expression must be multiplied by a numerical value of 1.22. In general, we shall assume that the relationship between the focal spot radius r and the other parameters is given by

$$r = \frac{c \lambda F}{D} \ , \tag{17.1}$$

where c is the constant chosen to represent the actual focusing capabilities of the dimple. It will be shown later that the required dimple size varies only as the 1/2 power of the constant c and, therefore, the size of the dimple is rather insensitive to the value of c as long as it lies between 1 - 10. The intensity I at the focus is related to the incident intensity I_o by

$$I = I_o \left(\frac{D}{2r}\right)^2 \ . \tag{17.2}$$

Using Eq. (17.1), we find

$$I = I_o \left(\frac{D^2}{2c \lambda F}\right)^2 \ . \tag{17.3}$$

For an incident spike intensity of 20 MW/cm^2 and a breakdown threshold of 4 GW/cm^2, the relationship between D and F for 10.6 μm radiation becomes

$$D = \sqrt{.03 \, cF} \ . \tag{17.4}$$

A plot of D versus F for c = 1 and c=10 is shown in Fig. 17.2. Since we are mainly interested in values of F from 1 to 3 cm for normal incidence, the values of D corresponding to these values of F are listed in Table 17.1. It should be

372
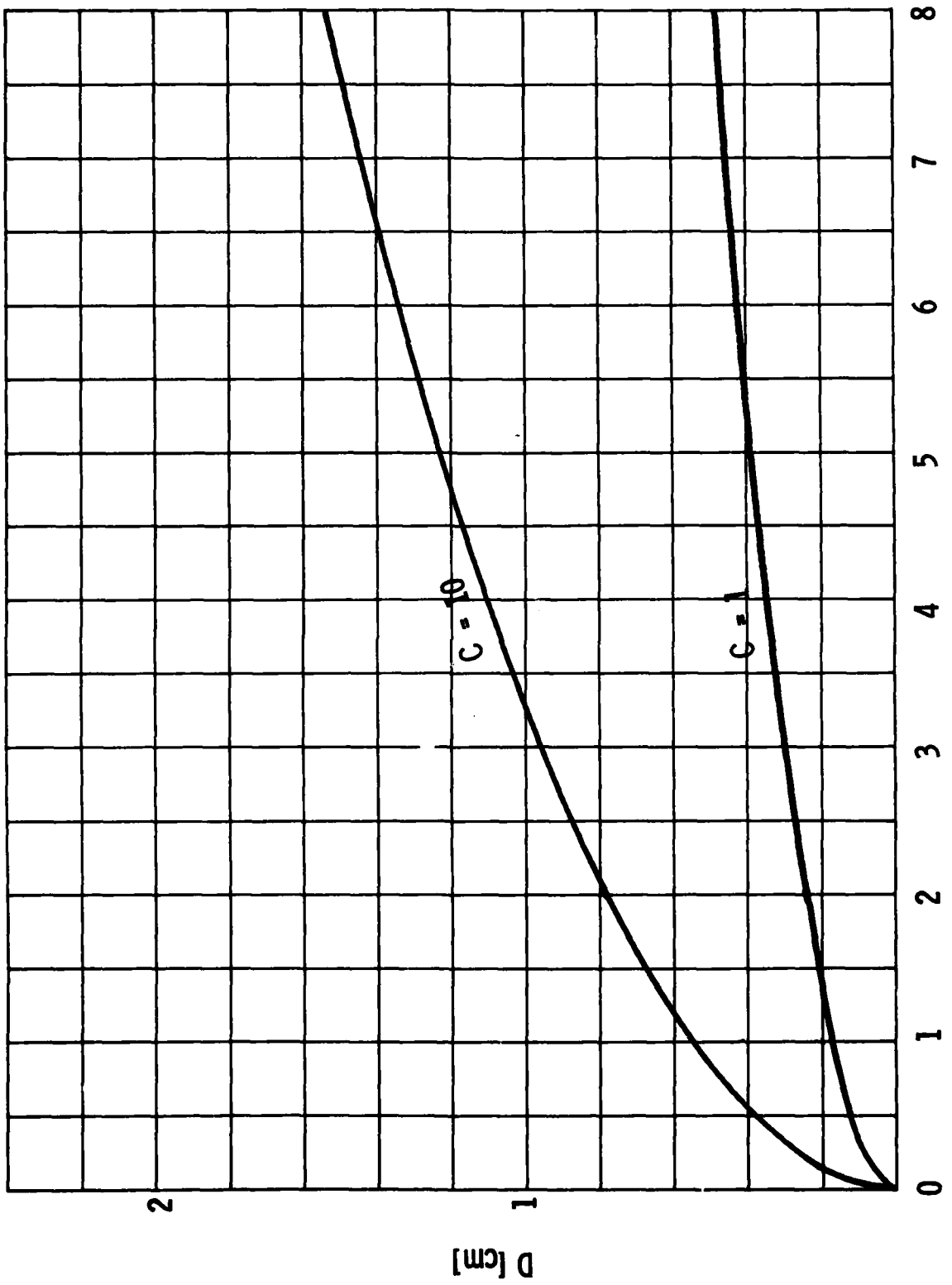
Fig. 17.2 Diameter of Dimple as Function of Focal Length for Two Values of Constant C.

373

TABLE 17.1

Diameter of Dimple Associated with Given Focal Length
For Two Different Choices of C.

F [cm]	1	3
D [cm] (C = 1)	.17	.30
D [cm] (C = 10)	.55	.95

noted from Eq. (17.3) that the diameter depends on the choice of intensity to only the 1/4 power. Therefore, small errors in the choice of I_o and I have practically no effect on the subsequent discussion. Inspection of Table 17.1 shows that as long as the constant c is less than 10, the diameter of a dimple need not exceed 1 cm. The radius of the focal spot is given by

$$r = \frac{\lambda cF}{D} = .035 D \, , \tag{17.5}$$

where we have used Eq. (17.4) to replace cF by $100 D^2/3$. The diffraction limited spot size is greater than .003 cm, the minimum size for breakdown to occur at $I = 4 \times 10^9$ W/cm^2, whenever D is greater than .1 cm. This criteria is met for the spot sizes corresponding to a focal length greater than .5 cm. A cross-section of a spherical dimple for normal incidence focusing is shown in Fig. 17.3. The focal distance F is approximately 1/2 the radius R of the sphere. The depth h of the dimple is found from

$$h = 2F \left(1 - \sqrt{1 - \frac{D^2}{16F^2}} \right),$$

which reduces to $D^2/16F$ for the cases considered here. For c = 10, h is .02 cm, whereas for c = 1, the depth is only .002 cm. Even h = .02 cm is not deep enough to effect the aerodynamics of a Mach 1 missile which is a few meters long because the momentum thickness in the turbulent boundary layer is approximately .1 cm.[24] The only effect the dimple may have is to change, possibly, the point of transition from a laminar boundary layer to a turbulent boundary layer.

Having established the size of the dimple required to ignite a detached plasma, we must determine how quickly the plasma shields the surface, and what the effect is of oblique angles of incidence.

noted from Eq. (17.3) that the diameter depends on the choice of intensity to only the 1/4 power. Therefore, small errors in the choice of I_0 and I have practically no effect on the subsequent discussion. Inspection of Table 17.1 shows that as long as the constant c is less than 10, the diameter of a dimple need not exceed 1 cm. The radius of the focal spot is given by

$$r = \frac{\lambda cF}{D} = .035 D , \qquad (17.5)$$

where we have used Eq. (17.4) to replace cF by $100 D^2/3$. The diffraction limited spot size is greater than .003 cm, the minimum size for breakdown to occur at $I = 4 \times 10^9$ W/cm^2, whenever D is greater than .1 cm. This criteria is met for the spot sizes corresponding to a focal length greater than .5 cm. A cross-section of a spherical dimple for normal incidence focusing is shown in Fig. 17.3. The focal distance F is approximately 1/2 the radius R of the sphere. The depth h of the dimple is found from

$$h = 2F \left(1 - \sqrt{1 - \frac{D^2}{16F^2}} \right),$$

which reduces to $D^2/16F$ for the cases considered here. For c = 10, h is .02 cm, whereas for c = 1, the depth is only .002 cm. Even h = .02 cm is not deep enough to effect the aerodynamics of a Mach 1 missile which is a few meters long because the momentum thickness in the turbulent boundary layer is approximately .1 cm.[24] The only effect the dimple may have is to change, possibly, the point of transition from a laminar boundary layer to a turbulent boundary layer.

Having established the size of the dimple required to ignite a detached plasma, we must determine how quickly the plasma shields the surface, and what the effect is of oblique angles of incidence.

INCIDENT
RAYS

φ_{max}

REFLECTED
RAYS

FOCUS

RADIUS OF
CURVATURE
R

$F \approx R/2$

$h = R (1 - \cos\varphi_{max})$

DIMPLE

D

Diameter of Dimple

Fig. 17.3 Cross-Section of Spherical Focussing Dimple.

The plasma shields the surface when the individual plasma bubbles merge, and when the plasma clouds become opaque. For the maximum size of dimple expected, namely 1 cm in diameter, the plasma cloud need grow only .5 cm to join the adjacent plasma. The growth rate is uncertain; it is a competition between the radial growth of the LSD wave as it travels up the reflected beam and the radial expansion of the plasma cloud produced at the focus. The radial expansion is supported by the incident laser radiation and, therefore, should be similar to an LSC wave rather than an LSD wave. Our analysis shall concentrate on the LSD wave moving axially toward the surface for two reasons: first, the axial LSD wave velocity is higher than the radial LSC wave velocity (which is verified in the following analysis); second, the LSD wave should be opaque to laser radiation, whereas a radially expanding LSC wave may be transparent at the intensities of interest.

The LSD wave plasma travels toward the target at the velocity given by[25]

$$V_{LSD} = [2 (\gamma^2 -1) I / \rho]^{1/3} , \qquad (17.6)$$

where ρ is the density of ambient air ($\rho = 1.2 \times 10^{-3} g/cm^3$), γ is the ratio of specific heats ($\gamma = 1.2$), and I is the laser intensity. For I measured in MW/cm^2, Eq. (17.6) reduces to $V_{LSD} = 2 \times 10^5 I^{1/3}$ [cm/sec]. The expansion time can be roughly estimated by assuming that the reflected laser intensity is given by the conical profile shown in Fig. 17.4. The error in using the conical profile rather than the profile appropriate to diffraction limited focusing is restricted to the region close to the focus. The wave traverses this region quickly, and most of the time is spent in the lower intensity region which is well approximated by Fig. 17.4. The intensity I is a function of the distance z from the laser focus (see Fig. 17.4) and is given by

$$I (z) = I_o (\frac{F}{z})^2 , \qquad (17.7)$$

where I_o is the incident laser intensity and F is the focal length. Then the
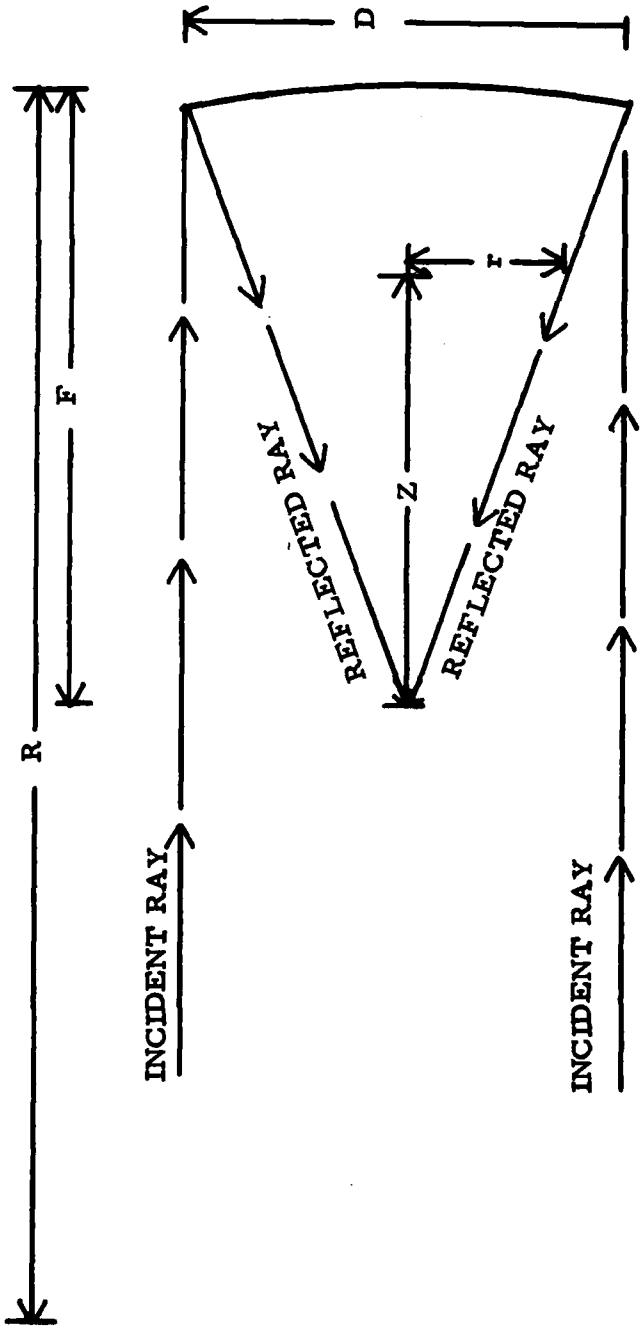
Fig. 17. 4 Conical Shape of Focussed Reflected Radiation (Neglects Diffraction Effects).

378

velocity as a function of z is

$$V(z) = 2 \times 10^5 \left[I_o \, [\mathrm{MW/cm^2}] \right]^{1/3} \left(\frac{F}{z} \right)^{2/3} \mathrm{cm/sec}. \tag{17.8}$$

The growth in the radial direction is then given by

$$\frac{dr}{dt} = \frac{D}{2F} V(z) = 2 \times 10^5 \, I_o^{1/3} \frac{D}{2F} \left(\frac{D}{2r} \right)^{2/3}. \tag{17.9}$$

Integration of this expression yields

$$\frac{2r}{D} = I_o^{1/5} \left(\frac{2 \times 10^5 t}{F} \right)^{3/5}. \tag{17.10}$$

To cover the complete spot at this rate of growth requires approximately $5 \, F \, I^{-1/3}$ microseconds if the incident intensity is measured in $\mathrm{MW/cm^2}$. For $F = 3$ cm and $I = 1 \, \mathrm{MW/cm^2}$, the time is 15 microseconds. This is an extremely long time. Moreover, the LSD wave approximation breaks down as the intensity drops below $4 \, \mathrm{MW/cm^2}$. Shielding of the whole target is impractical, at least for large values of F and low intensities.

However, it may not be necessary to shield the whole target. The main requirement is to prevent the formation of a small $\widehat{T}$ plasma at this surface. Ignition at a number of sites can destroy the ability to form a uniform plasma adjacent to the target. Consider Fig. 17.5 which shows the detached plasma configuration when plasmas have expanded 1/4 of the way to the adjacent ignition site. If a plasma is ignited at the surface in the unshielded zone, say at point A in Fig. 17.5, the coupling via plasma reradiation from the surface plasma is expected to be low because the surface plasma can rapidly expand laterally into the regions of the surface which are shielded from the laser by the detached plasmas. Therefore, it is appropriate to calculate the time to cover a fraction of the dimple, say 1/4 of the area. From
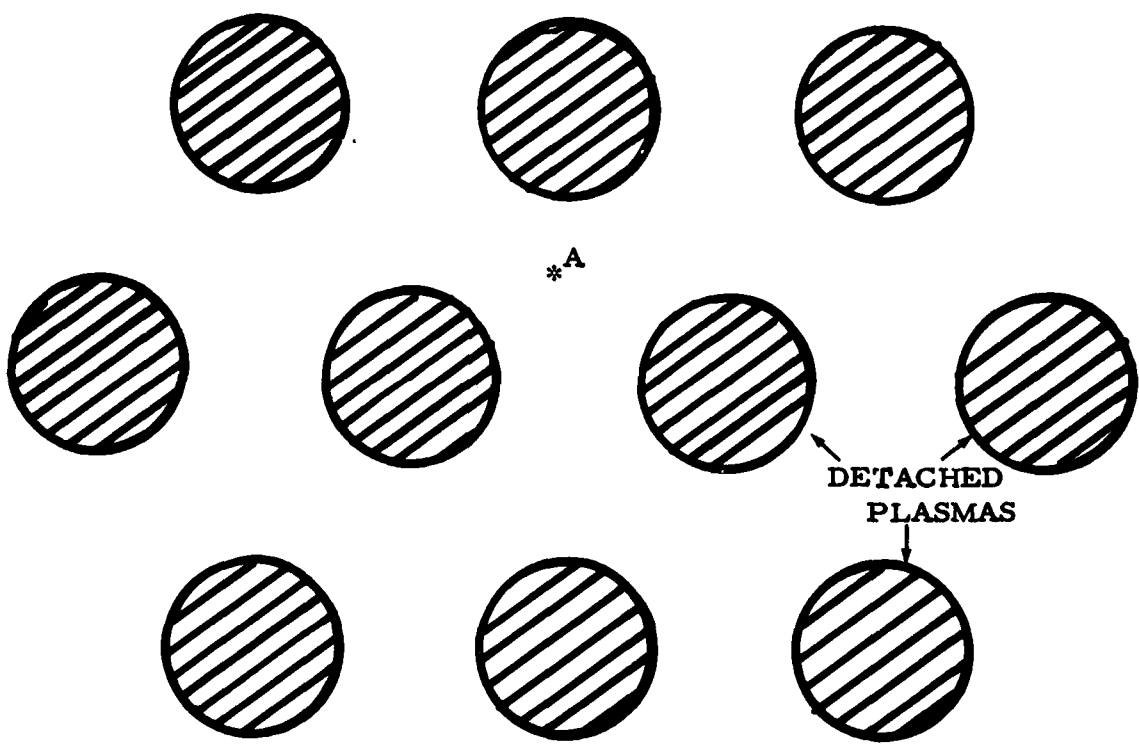
Fig. 17.5 Configuration of Detached Plasmas When Plasmas Have
Expanded .25 of Distance to Nearest Ignition Site.

Eq. (17.10) we find that the time required to cover a quarter of the dimple is roughly $1.6 \, F \, I^{-1/3} \, \mu sec$ for I measured in MW/cm^2. This corresponds to only $5 \, \mu sec$ at $1 \, MW/cm^2$ and $3 \, \mu sec$ at $3 \, MW/cm^2$. Therefore, the plasma can be forced to be effectively a large $\hat{T}$ plasma with little or no coupling. We conclude that the plasma formed in this manner has a strong likelihood of disrupting the coupling via plasma reradiation, even though the coupling cannot be eliminated completely.

Finally, it is important to study the behavior of this system when the beam is no longer incident at normal angles. Spherical mirrors are subject to a variety of aberrations, including spherical aberration, coma, and astigmatism.[26, 27] Spherical aberration can be defined as the longitudinal variation of the focal point (for normal incidence radiation) as a function of the aperture size (dimple diameter). The radius of the focal region as a result of this variation can be calculated from third order theory[27] to be

$$ r = \frac{FD^3}{256 \, F^2} . \tag{17.11} $$

This radius is smaller than the diffraction limited spot size for $10.6 \, \mu m$ radiation whenever

$$ D < 4.2 \, F^{3/4} \tag{17.12} $$

which is always true for the dimples considered here. Spherical aberration is not a problem.

Coma is the variation of magnification (image size) with aperture for light rays incident at an angle to the axis of symmetry. Figure 17.6 illustrates the appearance of a cross-section of the focal region because of coma.

Astigmatism is a focusing defect which occurs because a group of light rays incident on a spherical reflector at an angle to the axis focus
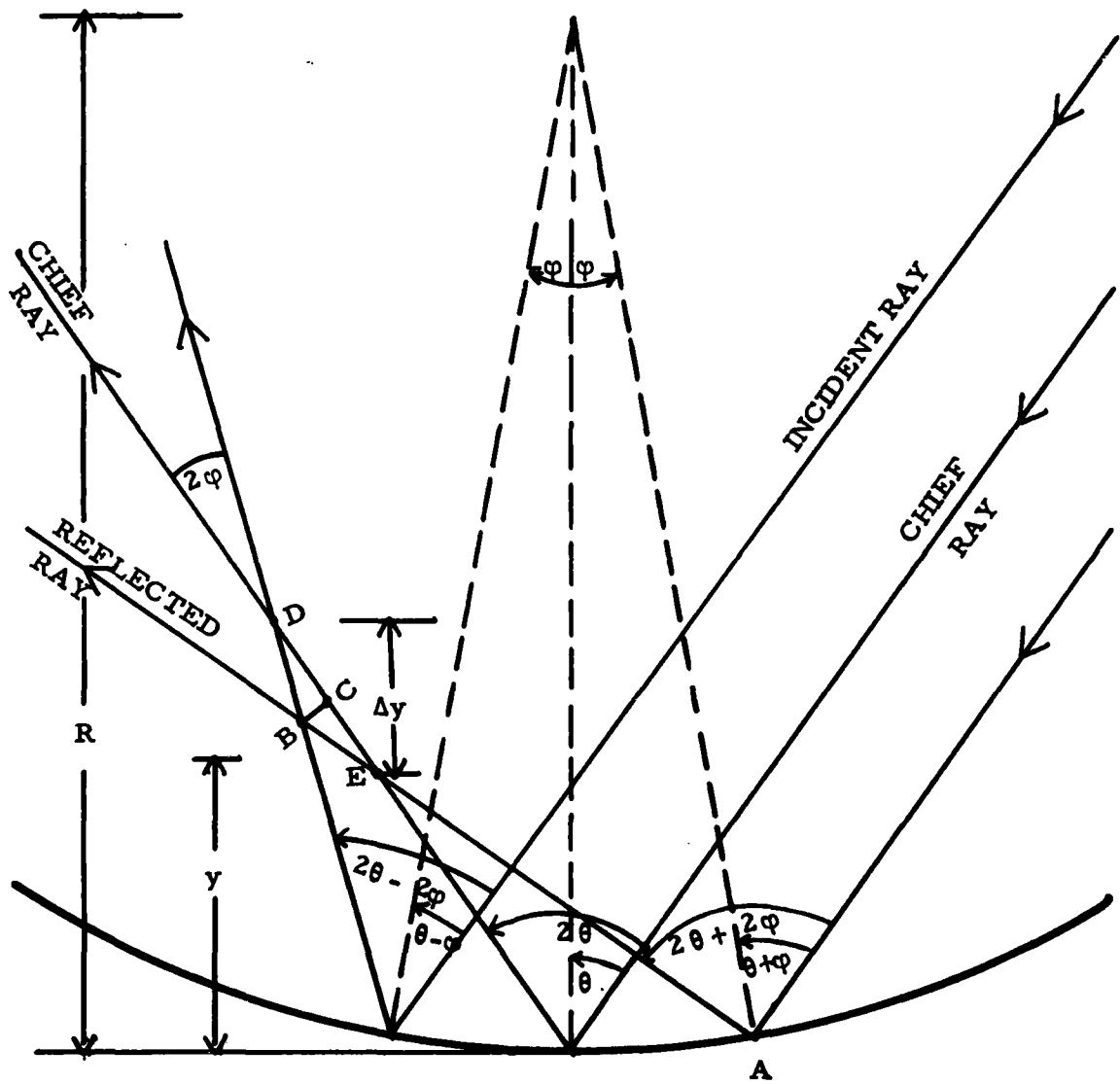
Fig. 17.6 Cross-Section of Dimple Showing Focussing of Rays
Incident at Angle θ.

at different points depending upon the plane in which the incident rays lie. This effect is illustrated in Fig. 17.7. The chief ray is the ray reflected from the center of the spherical reflector. The tangential plane is the plane which contains both the chief ray and the axis of symmetry, whereas the sagittal plane contains the chief ray and is perpendicular to the tangential plane. The astigmatic image of the laser source is a line in the sagittal plane at a distance F_T from the reflector and a line in the tangential plane at a different distance F_S.

We shall analyze coma and astigmatism separately. Because large angles of incidence are expected to be of interest, it is appropriate to use ray tracing to examine the features rather than using the third order theory (ray tracing expanded to third order in all angles).

The radiation reflected at large angles of incidence is not focused as tightly by the spherical dimple as it is for normal incidence because of coma. An estimate of the size of the focal volume can be made by using ray tracing techniques with no diffraction effects included. Consider Fig. 17.6 which shows three rays incident in the tangential plane of a spherical dimple, the angle of incidence is θ. The ray reflected at the center of the dimple is the chief ray. The other rays can be designated by the angle φ that a line drawn from the center of curvature to the point of reflection makes with the axis of symmetry (see Fig. 17.6). The ray which strikes the surface on the right hand side at an angular distance of φ is reflected through an angle of $2\theta + 2\varphi$. In other words, the ray which strikes the target at A is reflected at an angle of 2φ with respect to the rays reflected at the center ($\varphi = 0$). Geometrical considerations can be used to determine the distance y above the surface that the intersection of the chief ray ($\varphi = 0$) and the ray reflected at φ occurs. In terms of the radius R of the spherical dimple, the angle of incidence θ of the laser beam, and the angle φ which defines the ray, the distance y above the surface is given by
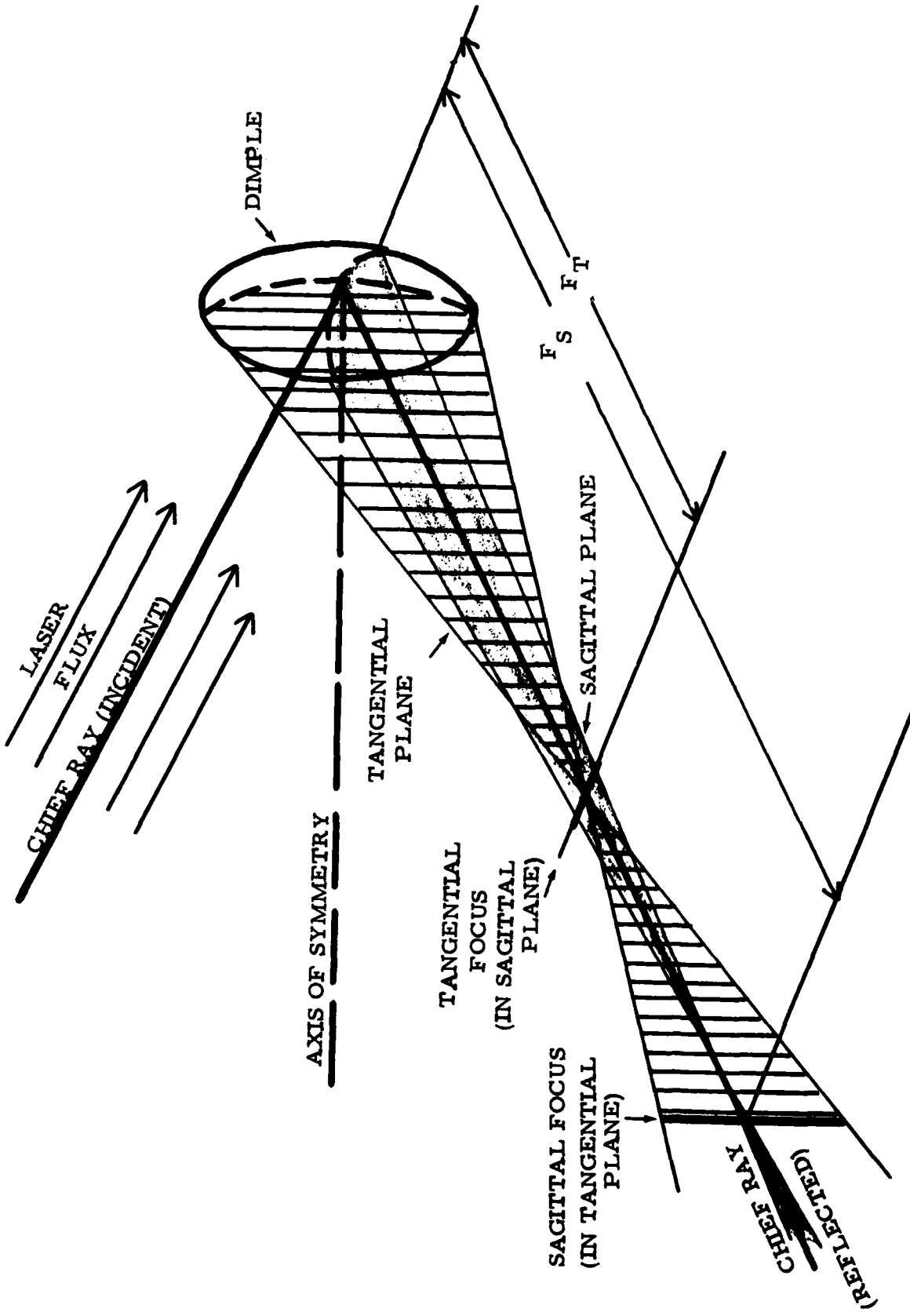
Fig. 17.7 Astigmatism – Showing Different Focussing Points in Tangential and Sagittal Planes.

$$\frac{y}{R} = \frac{\sin \varphi + (1 - \cos \varphi) \tan (\theta + 2 \varphi)}{\tan (\theta + 2 \varphi) - \tan \theta} \qquad (17.13)$$

This ratio is plotted in Fig. 17.8 for two values of φ. Note that except for a small region near $\theta = 0$, the value of y increases as φ is decreased at fixed θ. (For negative φ, a decrease of φ corresponds to an increase in the absolute value of φ.) Therefore, all reflected rays which strike the surface between φ and $-\varphi$ must cross through the line BC in Fig. 17.6. Note that this line spans the distance between the central ray and the intersection of the rays reflected from φ and $-\varphi$. The length d of the line BC is indicative of the size of the focal volume in the tangential plane due to coma caused by a spherical dimple. Under the assumption that φ is small, the vertical distance Δy between the intersections denoted by D and E in Fig. 17.6 is given by

$$\Delta y = \frac{3 \varphi \sin \theta \cos \theta \ R}{4} \qquad (17.14)$$

and the size of BC can be computed to be

$$d \approx \frac{3 \varphi^2 \sin \theta R}{4} = \frac{3 D^2 \sin \theta}{32 F} \qquad (17.15)$$

where we have used

$$\varphi \approx \frac{D}{4F} \qquad (17.16)$$

and $R \approx 2F$ to obtain Eq. (17.15).

The arguments which led to the above equations are strictly true only for rays which intersect the dimple in the tangential plane (see Fig. 17.7). For rays which are reflected from points displaced a distance δz

Fig. 17.8 Distance Above Surface that Ray Reflected at φ Intersects Chief Ray as Function of Angle of Incidence.
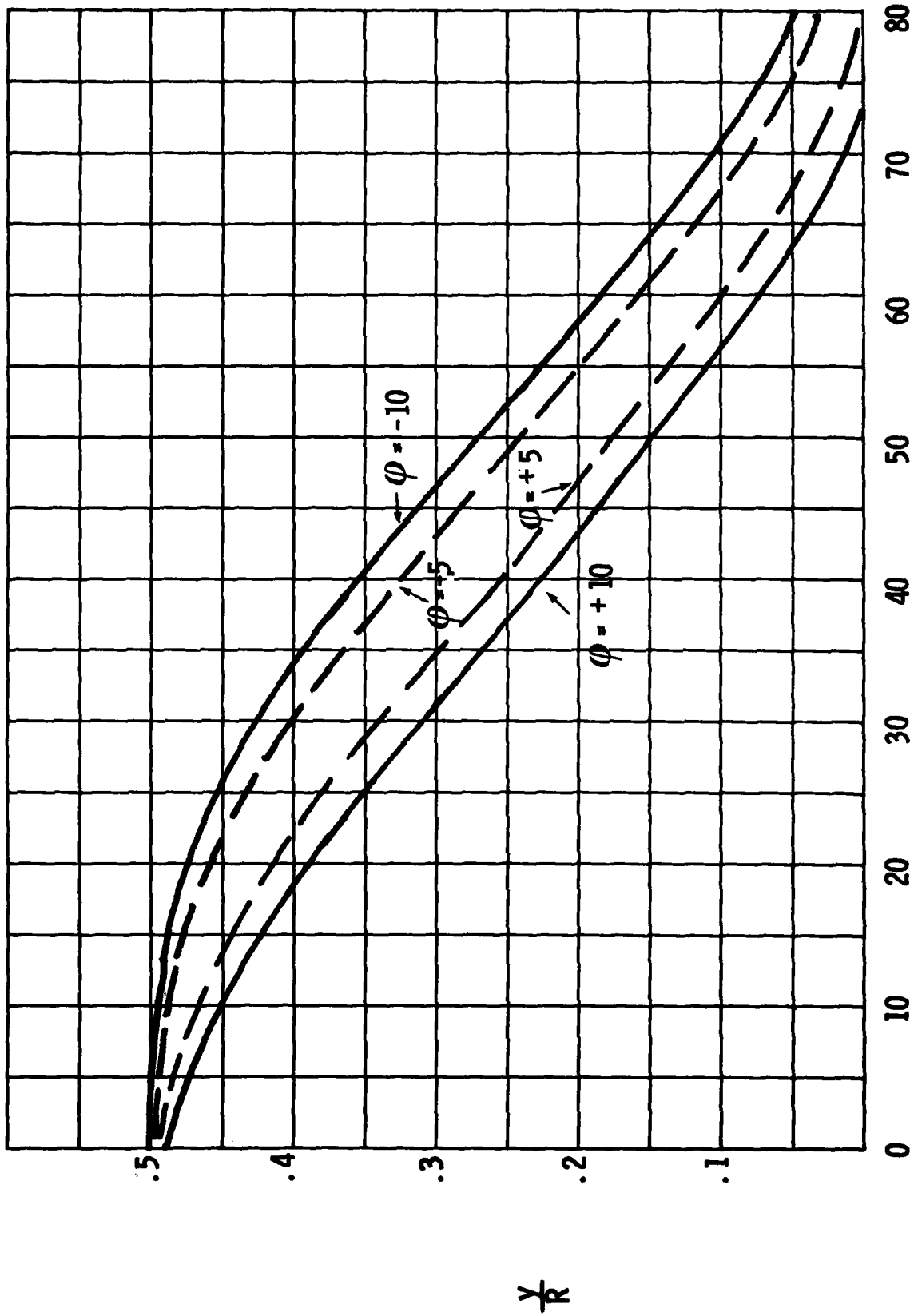
from the intersection of the tangential plane and the dimple, such as the line B B' in Fig. 17.9a, two effects occur. The radius of the cross-sectional arc is changed from R to $\sqrt{R^2 - \delta z^2}$, and the reflected ray no longer remains in a plane parallel to the tangential plane.

The first effect is small. The maximum displacement δz is small compared to R as long as the maximum value of φ is small. Therefore, the effective radius is essentially unchanged from R insofar as the calculation of coma is concerned.

The second effect, focusing of the rays in the sagittal plane, is related to astigmatism. This effect can be dramatized by comparing the distance from the center of the dimple to the focus. The rays in the tangential plane focus at a distance of approximately [28]

$$F_T = F \cos \theta ,$$
(17.17)

as can be seen from Fig. 17.10. The rays in the sagittal plane focus at a distance of approximately

$$F_S = \frac{F}{\cos \theta} ,$$
(17.18)

as shown in Fig. 17.9b. At large angles of incidence the tangential focus approaches the dimple whereas the sagittal focus recedes. (The sagittal focus always occurs in a plane which is a fixed distance away from the dimple as shown in Fig. 17.9c.) Thus a three-dimensional focus cannot be achieved by the spherical dimple for large angles of incidence, and this may well be the dominant effect on the ability of the dimple to cause air breakdown at large angles of incidence.

It is beyond the scope of the analysis performed here to solve in detail the intensity distribution expected in the image formed at large angles. As a worst case, consider the average intensity at the tangential focus. The tangential focus has a width (in the tangential plane) given by d in Eq. (17.15) and a length (in the sagittal plane) of approximately $D \sin^2 \theta$.
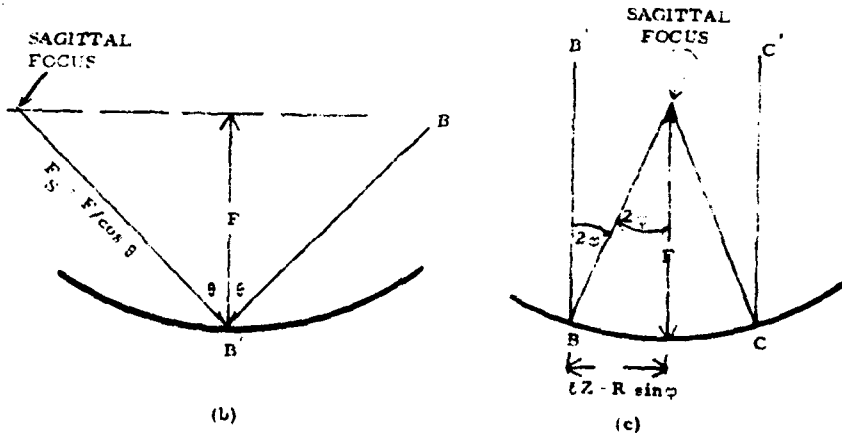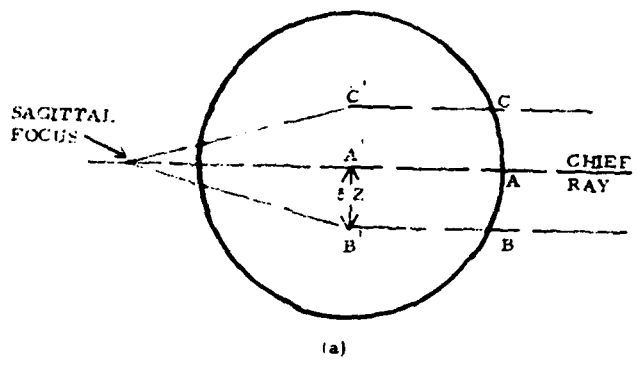
Fig. 17.9 (a) Frontal View of Dimple Sagittal Focus;
(b) Projection Onto Sagittal Plane;
(c) Projection Onto Tangential Plane.
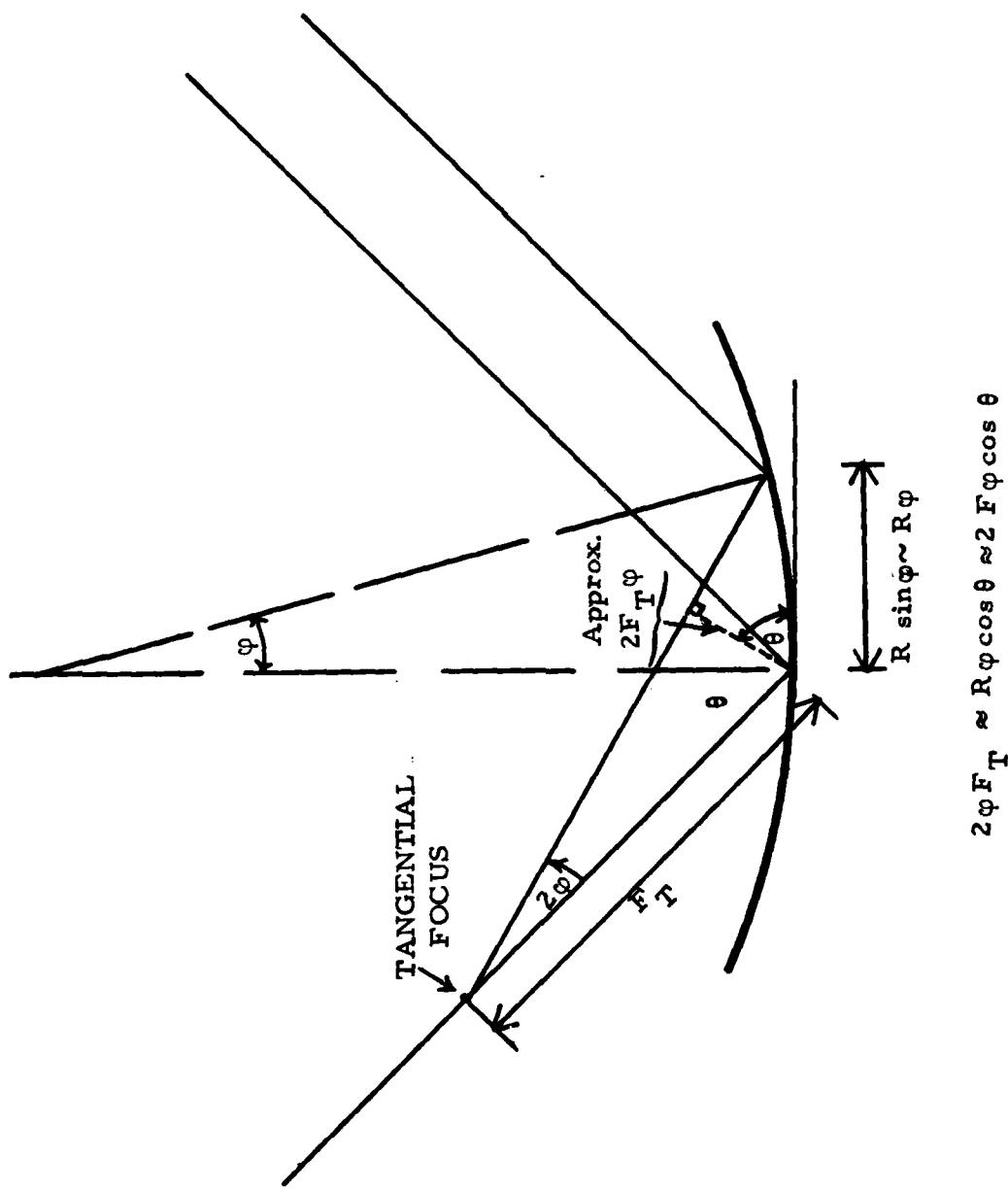
$2\varphi F_T \approx R\varphi\cos\theta \approx 2F\varphi\cos\theta$

Fig. 17.10 Sketch Showing why $F_T \sim F\cos\theta$.

TANGENTIAL FOCUS

2φ

F_T

Approx.
$2F_T\varphi$

$R\sin\varphi \sim R\varphi$

φ

θ

We can now estimate the effects of non-normal incidence on the performance of a dimpled surface as an countermeasure. In Fig. 17.11 the focal region of rays in the tangential plane is shown for $\varphi = 5^{\circ}$ as a function of the angle of incidence θ. As θ is increased, the focus moves closer to the target and closer to the dimple. At extreme angles, roughly those greater than $(90^{\circ} - 2\varphi)$, the dimple no longer focuses in the tangential plane. For an angle of 75°, the focus occurs a vertical distance of .07 F above the target and a total distance of .26 F away from the center of the dimple. Thus, one effect of oblique angles is to reduce the gap between the plasma and the target.

However, it may not be necessary to have as large an air gap at oblique incidence. As the angle of incidence increases, the pressure and the velocity of the LSC wave are decreased and the plasma is less likely to propagate across the small gap. For example, for $F = 3$ cm and $\theta = 75^{\circ}$, the focus should occur about 1/4 cm above the surface. At the reduced intensities expected at this angle, 1/4 cm may well be sufficient to prevent good thermal coupling. Of course, experiments must be performed to test this hypothesis. The important conclusion, however, is that dimples can focus a reasonable distance above the surface in situations in which the angle of incidence is large only if the normal focal distance F is large. Therefore, large values of F are recommended.

For given choice of F, increasing the diameter of the dimple decreases the diffraction limits on the focal volume, but it increases the size of the focal volume attributable to the inability of the spherical dimple to focus at oblique angles. The spherical limits on the focusing increase as D^2 (see Eq. (17.15)); therefore, the average intensity at the focus, as determined by ray tracing, cannot be increased by merely expanding the diameter of the dimple. An optimum size can be defined by equating the size of the focal volume due to spherical defocusing to the diffraction limited focal volume. The diffraction limited value is calculated for normal incidence; the spherical
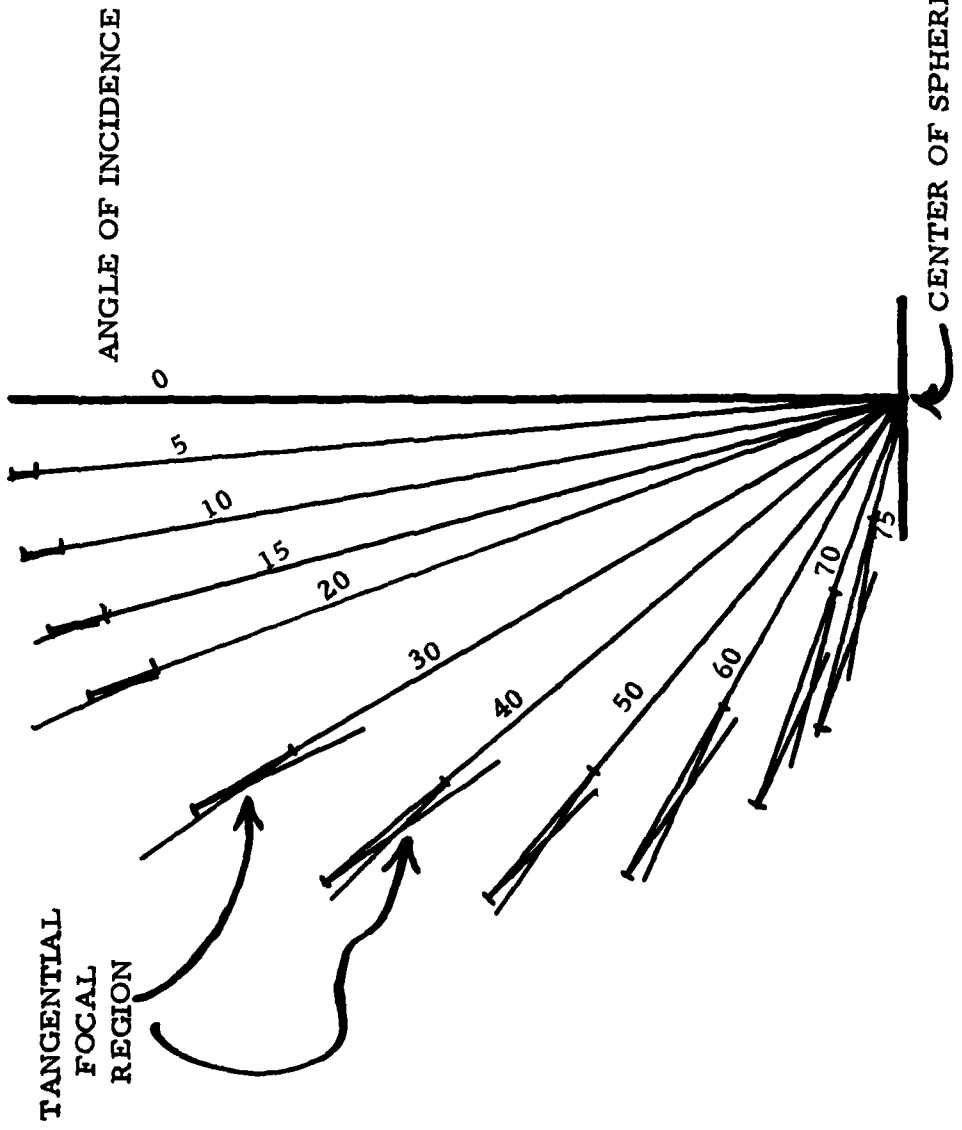
Fig. 17.11 Sketch of Focal Volume for Tangential Focus for Dimple Angular Distance $\varphi = 5°$, as Function of Angle of Incidence.

aberration is determined for the maximum angle of incidence. We find

$$\frac{\lambda F}{D} = \frac{3 D^2 \sin \theta}{64 F} , \qquad (17.19)$$

where λ is the wavelength, F is the focal length, D is the dimple diameter and θ is the angle of incidence. For $\lambda = 10.6\mu$ with a focal length F of 3 cm and an angle of incidence $\theta = 75^{\circ}$, the two effects are equal for D = .6 cm. Either increasing or decreasing the diameter will not increase the average intensity in the focal volume. For an incident spike intensity of 20 MW/cm^2, the effective intensity at the surface of the dimple is approximately 5 MW/cm^2. For diffraction limited focusing with F = 3 cm, the intensity at the focus is estimated to be 1.7×10^{10} W/cm^2 which can easily ignite a plasma. This is appropriate for normal incidence. However, at 75°, little focusing occurs in the sagittal plane and the average intensity is reduced to 3×10^8 MW/cm^2, which cannot ignite a plasma in pure air. The above calculation uses the average intensity over the whole focal region. The intensity of the comatic image is expected to vary over the focal volume. Calculation of the maximum intensity must include diffraction effects and will not be done here. Nevertheless, it is possible that within the image there is a region of intensity high enough to cause breakdown. Moreover, even without enhancement due to high intensity regions in the comatic image, this dimple can ignite a plasma when the angle of incidence is reduced to approximately 60°.

It therefore appears, that a dimple having a diameter of somewhere between .5 to 1 cm and focusing 3 cm above the surface for normal incidence has the potential to ignite detached plasmas for angles of incidence as large as 60°. The dimple may function out to 75° if the intensity maximum in the comatic image is strong enough. More detailed theoretical analyses and experiments must be performed in order to determine the maximum angle of incidence for which the dimple is useful.

Dimpling on the surface appears to have good potential for eliminating the enhanced coupling mechanism. Calculations suggest this approach is feasible even for fairly large angles of incidence, as long as the dimple is designed to focus far enough from the surface.

17.2 Debris Injection

The threshold intensity for breakdown in air containing particulates is several orders of magnitude below the clean air breakdown threshold. Particles from 10 to 100 μm in diameter have been observed to initiate plasmas at intensities of the order of a few MW/cm^2 if the preceding spike is sufficiently strong.[29,30,31] Indeed, breakdown often occurs in front of the target in the repetitively pulsed experiments discussed in Parts I and II of this report. A possible approach to hardening, therefore, is to ignite detached plasmas by injecting appropriate debris into the boundary layer. Once again, the formation of a plasma is expected to protect the surface in a variety of ways. The plasma will absorb the incident radiation, at least over part of the surface. The radiative transfer from the plasma ignited from the debris is expected to be poor because the air gap between the target and the plasma absorbs radiation. Moreover, the rapid gas dynamic cooling due to expansion of the debris ignited plasma in several directions reduces the amount of radiation produced. Finally, any plasma that does form on the surface is expected to have a large effective value of $\hat{T}$ because of the presence of regions which are shielded from the laser; therefore, the radiative transfer from the surface plasma is expected to be minimal.

The experimental results[29,30,31] show that plasma can be ignited by particles of varying composition and size, provided the gain switched spike is sufficiently strong. But it has not been established which composition is most efficient in igniting plasmas; that is, which composition creates plasmas at the lowest intensity and/or smallest particle size. In the following analysis, debris mass densities shall be constructed for a variety of compositions and particle sizes and the consequences of ignition will be explored.

The rate of expansion of the plasma is uncertain, but theoretical estimates[32, 33] suggest that at low intensities, where an LSD wave cannot be sustained, the plasma velocity is at least the speed of sound in the cold air, i. e., 3×10^4 cm/sec. Numerical simulation[34] suggests that LSD waves can be supported above 5 MW/cm^2. Indeed, higher velocities of the order of 2×10^5 to 3×10^5 cm/sec, consistent with LSD wave predictions, have been observed[31, 35] in the initial stages of growth when the laser intensity is high, but for the present purpose, a conservative value is appropriate. Therefore, most of the calculations use the sonic velocity of the ambient air for the plasma expansion rate.

It shall be assumed that whenever the projection of the plasma clouds on the target surface coalesce, insignificant target coupling results. The reasons for the reduction in coupling are the same as discussed in Subsection 17. 1 in conjunction with Fig. 17. 5. First, the plasma clouds ignited by debris in front of the target shield a large fraction of the target from direct laser radiation. Second, any plasma ignited at the surface in the unshielded zones can rapidly expand into the shielded regions (see Fig. 17. 5); therefore, the surface plasma has a large effective value of $\hat{T}$ and its thermal coupling is poor. The reduction in coupling is the combined effect of many particles and is not limited to the absorption characteristics of an individual particle.

The loading of particles can now be related to the time at which the pulse is effectively terminated by the coalescence of the plasma clouds. If the projection of particles on to the target plane represent a surface density of N particles/cm^2, then the time for the plasma clouds to coalesce is given by $1/ (2 V \sqrt{N})$, where V is the velocity of propagation. The time to effective termination of the pulse as a function of N is plotted for two values of velocity V in Fig. 17. 12. The two values of velocity which are used are the sonic velocity 3×10^4 cm/sec^2, which is a conservative estimate, and the velocity of 2×10^5 cm/sec which is observed during the initial stages of growth. Notice that plasma clouds coalesce within 2 μsec for N >70
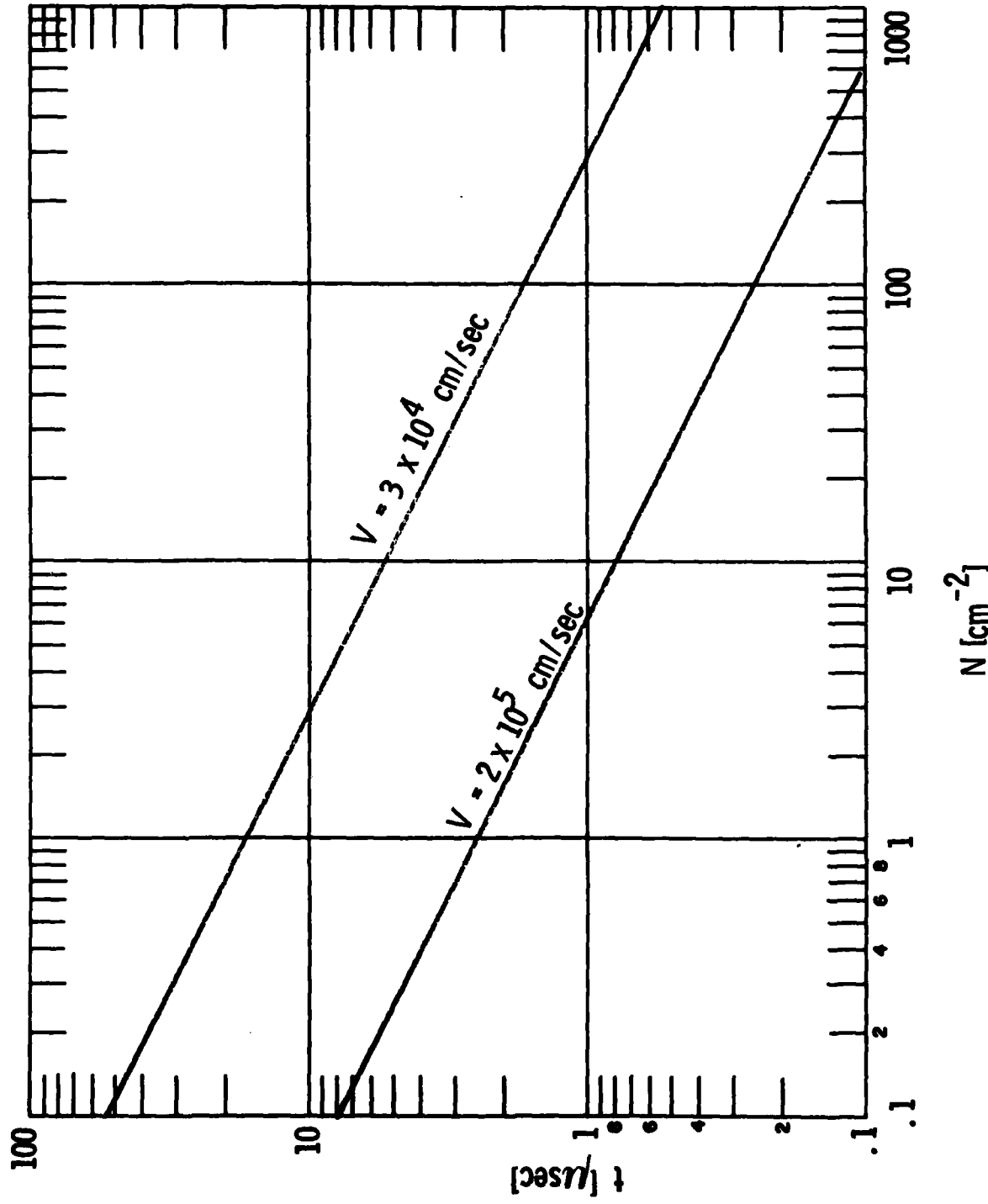
Fig. 17.12 Time to Plasma Coalescence as Function of Particle Surface Density.

particles/cm^2 if the speed of propagation is the sonic velocity. At the higher speed of propagation, it requires only 1.5 particle/cm^2 for the clouds to coalesce within 2 μsec. Hereafter, we shall concentrate on estimates made using the sonic velocity.

The practicality of this hardening approach may well depend on the weight penalty it imposes. The weight depends, of course, upon the particle loading, the particle composition, and the particle diameter D. Mass loading M per unit surface area is given by

$$M = \frac{\pi D^3}{6} \rho N \qquad (17.20)$$

where ρ is the density of the material. The mass loading is shown in Fig. 17.13 for three materials - plexiglass, Al_2O_3, and $CaCO_3$ (which have a density of 1.2, 3.8, and 2.8 gm/cm^3, respectively) and three particle diameters, D = 10, 30 and 50 microns. Plexiglass is the lightest of the group and if it has good ignition characteristics, it is the most attractive candidate for minimizing the weight penalty. However, in terms of weight penalty, the size of particle is far more crucial than the density. The "best" particle is the one which gives good ignition at the smallest size.

In order to make a quantitative estimate of the weight penalty, consider a hypothetical vehicle having a cylindrical shape. The vehicle has a length L of 3m, a radius R of 10 cm, and is travelling at a velocity U equal to 3 x 10^4 cm/sec (Mach one). In order to protect this vehicle from a time t of 5 seconds, the particulate density N must cover an effective surface area of 2 πR Ut instead of the actual surface area of 2 πRL. The effective surface is a factor of Ut/L = 500 larger than the true area. For a weight penalty equivalent to a 1 mil aluminum coating, the mass loading must be less than 1.4 x 10^{-5} gm/cm^2. At a loading of 70 particles/cm^2, it is possible to meet
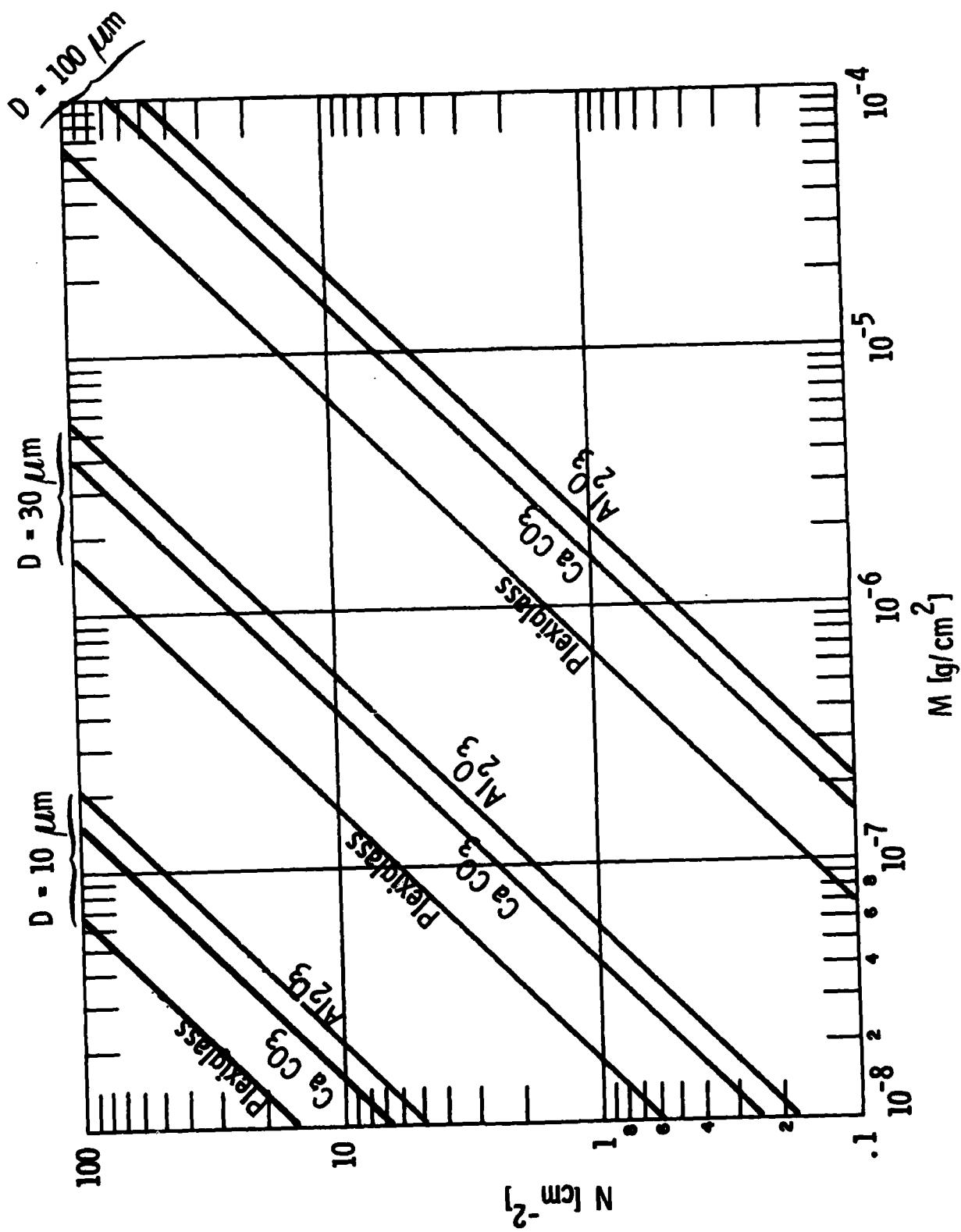
Fig. 17.13 Mass Loading of Particles as Function of Number Density for Various Particle Diameters and Compositions.

397

this criteria with all particulate compositions and particle diameters up to 50 microns. A different criteria is to demand that the total weight penalty be less than 1 kg; this corresponds to a mass loading of 1×10^{-4} gm/cm^2, which is a less stringent criteria. The mass penalty also depends on the plasma expansion velocity U. If the plasma expansion rate is 2×10^{5} cm/sec rather than 3×10^{4} cm/sec, the required particle concentration N is only 1.5/cm^2. At this concentration, particles 100 μm diameter can be used with no significant weight penalty.

There is a question as to whether the plasma formed by ignition of the particle remains opaque; it is important to resolve this issue. Experiments [30,31,35] indicate that a large fraction of the energy will be transmitted through the plasma if the intensity is not high enough. It is difficult to use these experiments to forecast the opacity in the present case. At early time, that is, the first few microseconds, the plasma in the experiment grew rapidly at a rate close to the LSD velocity which is highly suggestive of a strongly absorbing plasma. At later time, however, the growth rate was dramatically reduced. The transition from rapid growth to slow growth coincided approximately with the plasma cloud expansion reaching the edge of the laser beam. It is not known whether or not the transparency of the plasma is related to edge effects. It will be important to establish experimentally the opacity of the clouds in cases where the plasma cloud cannot expand beyond the beam.

In this brief analysis of the potential of debris injection it was shown that the method will probably not impose a huge weight problem and thus has good potential as a hardening technique. However, several details must be studied by experiments. In particular, it is important to establish the minimum laser intensity as a function of particle composition and size for debris-ignited breakdown and also to establish what the minimum laser intensity is for sustaining a strongly absorbing plasma, especially if this intensity is higher than the breakdown threshold.

17.3 Electron Injection

Another approach to igniting plasmas is to seed the air in front of the target with electrons by electron injection. However, as mentioned earlier, the initial concentration of electrons appears to have little to do with the non-equilibrium cascade breakdown unless the concentration is sufficiently high to cause electron-ion inverse Bremsstrahlung to be the chief absorption mechanism. Electron-ion inverse Bremsstrahlung does not dominate unless the ion concentration is larger than 1% of the neutral concentration; in short, there must be approximately 3×10^{17} electrons/cm^3.

An estimate of the number of electrons produced by energetic electrons passing through air[36] is given in Table 17.2 and Fig. 17.14. Precise predictions of electron density require detailed numerical calculation; for preliminary examinations, however, order of magnitude estimates are sufficient. An electron-ion pair is produced for each 35 eV of initial electron energy. A 100 keV electron will produce approximately 135 electrons/cm^3 for the first few cms of its flight. As its energy drops, electron production rate increases (see Fig. 17.11). The total range of the 100 keV beam is approximately 13 cm. The electron cloud can be modeled roughly as spherical cloud of radius 6.5 cm and the total volume which the electrons occupy is approximately 1150 cm^3. To obtain an average electron density of 3×10^{17} electrons/cm^3, which is required for electron-ion inverse Bremsstrahlung to cause breakdown at intensities below 2 GW/cm^2, the cloud must contain total of 3.5×10^{20} electrons.

The current required to maintain this concentration of electrons can be estimated by balancing the electron production rate with the electron recombination rate. At the high densities anticipated, the dominant recombination process is three body recombination involving two electrons and an ion; this can be approximated by

TABLE 17.2

Electron Degradation Properties. V = 32 kV (from Ref. 37)

Gas	Molecular Weight gms/mole	Stopping Power MeV-cm^2/gm	Range gm/cm^2	Energy Per Ion Pair eV
He	4	9.1	2.0×10^{-3}	41.9
N_2	28	8.1	2.1×10^{-3}	34.4
Ar	40	6.2	3.0×10^{-3}	26.1
CO_2	44	8.1	2.2×10^{-3}	——
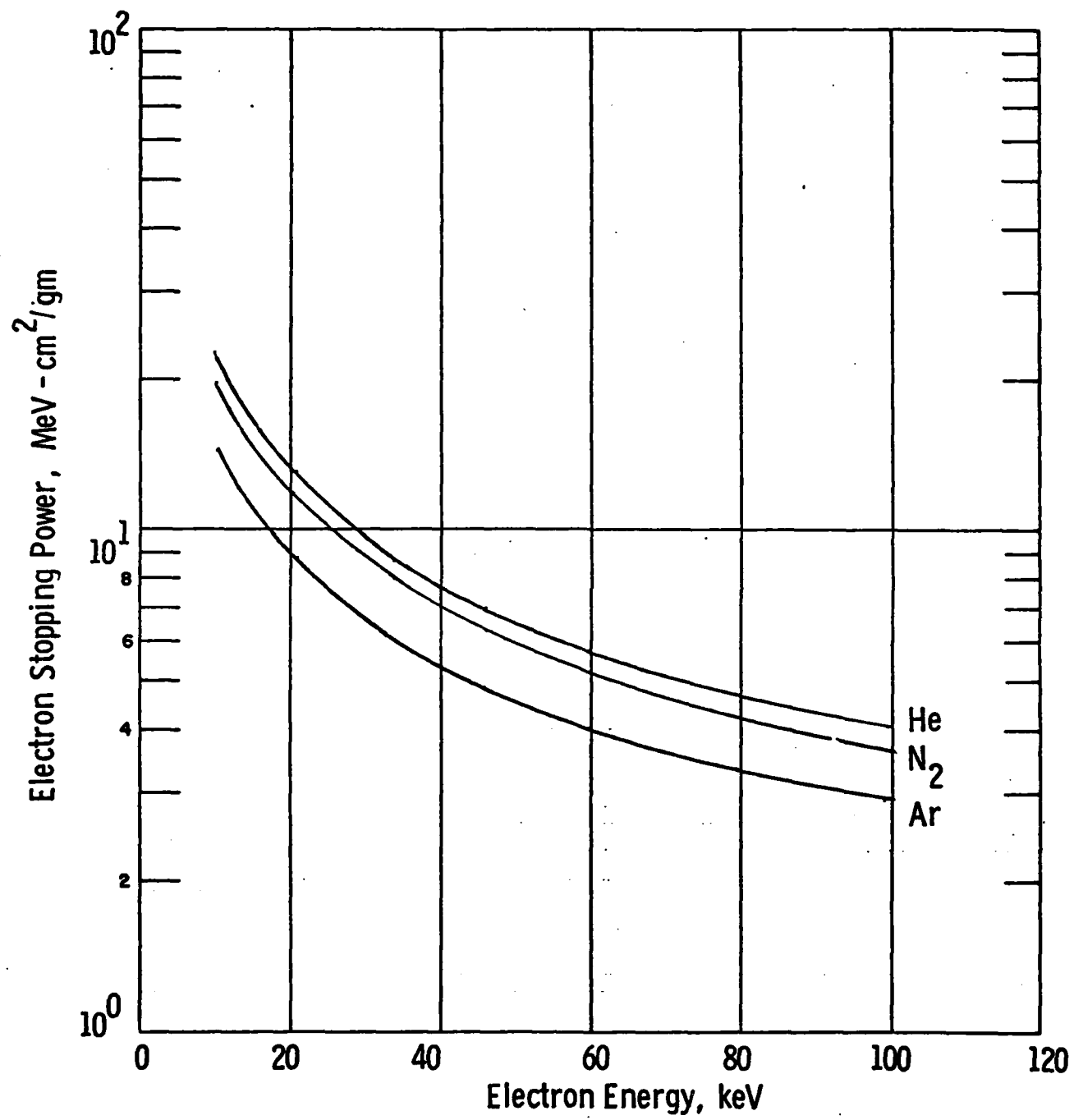
Fig. 17.14 Electron Stopping Power vs. Electron
Energy for He, N_2, Ar (from Ref. 37)

$$\left(\frac{dn_e}{dt}\right)_{recomb.} = b\, n_e^2 \ , \qquad\qquad (17.21)$$

where n_e is the electron concentration and b is the recombination coefficient which is roughly given by[37]

$$b = \frac{5.2 \times 10^{-23}}{(T/10^3)^{9/2}}\ n_e \ . \qquad\qquad (17.22)$$

The recombination rate increases as the temperature drops. Even with steady-state electron temperatures of 5000°K (in the absence of an external laser field) it takes only 10^{-9} sec. for an electron to recombine in a plasma which has $n_e = 3 \times 10^{17}$ cm^{-3}. Thus to maintain 3×10^{17} electrons/cm^3 throughout the cloud for time periods longer than a few nanoseconds requires a current of 3.5×10^{29} electron/sec or 5.5×10^{10} amps. The foregoing calculations indicate that electron injection is not feasible for large area coverage It may, however, be possible to employ electron injection to protect a very limited area, but that possibility will not be explored further here.

17.4 Summary

Igniting a detached plasma possesses several attractive features insofar as hardening is concerned. It is capable of reducing significantly coupling via radiative transport from the plasma and it should also shield the surface from the incident laser so that there will be no coupling by virtue of intrinsic absorption. The analysis of the three suggested methods for igniting the plasma has led to the following conclusions:

(1) Dimpling the surface to focus the reflective beam appears to have good potential, especially for highly reflective metals such as aluminum. This approach should perform well even at reasonably large angles of incidence such as 60°. A typical dimple size should be

. 6 cm in diameter with a focal distance of 3 cm. In the analysis the intensity was averaged over the complete comatic image; however, if the peak intensity within the image is significantly higher than the average value, the dimple may work for angles as large as 75°.

(2) Injecting debris into the boundary layer is efficient in terms of mass penalty for short time engagements. The main uncertainties are the intensity threshold required to create a plasma and the opacity of the plasma. These issues must be resolved by experimental work and further theoretical modeling.

(3) Injection of electrons into the boundary layer will not create a plasma unless enormous electron concentrations are achieved. These concentrations cannot be maintained over large areas with practical electron beams; therefore, electron injection is not an attractive hardening candidate.

SECTION 18

LSD IGNITION APPROACHES

Another method of interfering with coupling via plasma radiative trans-
fer is to induce the plasma to become an LSC wave rather than an LSC wave.
In the discussion of the enhanced coupling mechanism (see Sec. 15), the
upper limit for the intensity in the enhanced coupling region was associated
with the transition from an LSC wave to an LSD wave. LSD waves charac-
teristically move much faster than LSC waves, and ingest new air into the
wave at a much higher rate. The absorbed laser energy is expended in heat-
ing large quantities of gas to moderate temperature rather than heating small
quantities to high temperature. Moreover, since the gas particles behind the
LSD wave are dragged away from the target by the wave, there is further cool-
ing of the gas behind the LSD wave by virtue of this expansion. Since radi-
ation from the plasma gas increases rapidly with temperature, the hot LSC
wave radiates profusely whereas the colder LSD wave radiates poorly.
Secondly, because of the expansion, the surface pressure generated by the
LSD wave falls below the value predicted for the LSC wave. Therefore, ig-
nition of an LSD wave can reduce both thermal coupling and mechanical
coupling.

In this section, we examine the possibility of inducing the plasma to
form an LSD wave by seeding an easily ionized metal atom into the air. The
manner in which these atoms are introduced into the air is left open for the
moment, although injection into the boundary layer and seeding the metal
into an ablative coating are possibilities. This study examines, rather, the
concentration of metal atoms in the boundary layer necessary to produce the
LSD wave.

In the following discussion we deal exclusively with Cs. The energy
states of Cs and their degeneracies are listed in Table 18.1. The ionization
potential, I_{Cs}, of cesium is 3.893 eV. The fraction of the cesium which is
ionized, denoted by α, can be calculated by using the Saha equation[38]

TABLE 18.1

States of Cesium.

Energy Level [cm^{-1}]		Degeneracy
CsI	0	2
	11750	6
	14550	10
	18535	2
	21850	6
CsII	0	1
	107550	8

$$\frac{\alpha^2}{1-\alpha} = \frac{2}{n_{Cs}} \left(\frac{2\pi M_e k}{h^2}\right)^{3/2} \frac{U_+}{U_0} \exp\left(\frac{-I_{Cs}}{kT}\right) , \quad (18.1)$$

where U_+ and U_0 are the electronic partition functions of the ion and neutral cesium atoms, respectively, T is the temperature, k is the Boltzmann constant, M_e is the mass of the electron, h is the Planck constant and n_{Cs} is the number density of Cs particles (neutrals and atoms). The electronic degeneracy function is defined as

$$U_j \equiv \sum_{\substack{\text{states } i \\ \text{of species } j}} g_i \exp\left(\frac{-E_i}{kT}\right) , \quad (18.2)$$

where the degeneracy factor g_i and the energies E_i are the levels of CsI and CsII as listed in Table 18.1.

To determine LSD wave maintenance thresholds, the structure of the wave is broken into a precursor shock followed by a weak deflagration. Whether or not the LSD wave will be maintained depends crucially on the density of electrons immediately behind the shock. It is assumed that the cesium will be only a small fraction of the composition of the gas, so that the LSD wave, should it exist, will have a temperature, pressure, and velocity characteristic of an air LSD wave. Therefore, given any laser intensity, it is possible to determine the speed of the wave from Eq. (17.6) and the strength of the precursor shock from air shock tables.[39] The density of the air ρ_s immediately behind the strong precursor shock is well known to be

$$\frac{\rho_s}{\rho_0} = \frac{\gamma+1}{\gamma-1} = 6 , \quad (18.3)$$

where ρ_0 is the density of the undisturbed air and γ is the specific heat ratio ($\gamma = 1.4$). Therefore, the initial concentration of the cesium atoms behind the shock is $1.6 \times 10^{20} f$ [cm^{-3}], where f is the relative concentration of cesium atoms with respect to the molecules of the air species. A plot of α for various temperatures is shown in Fig. 18.1 for cesium concentrations f of .005, .01, .02, and .05.

Two types of inverse Bremsstrahlung occur, electron-ion Bremsstrahlung involving cesium ions and electron-neutral Bremsstrahlung involving both cesium neutrals and air neutrals. Neutral cesium is only a small fraction of the gas so it is neglected for first order estimates. The electron-ion inverse Bremsstrahlung is given by the standard Kramer formula[40] with a Gaunt factor of 1.3 and the neutral Bremsstrahlung involving N_2 and O_2 can be expressed in an analogous way by using the empirically determined values of Z^2 of Taylor and Caledonia.[14] The final expression for the absorption coefficient at temperature T is found to be

$$k_L' = \left(1 - e\left(-\frac{1357.4}{T}\right)\right) \frac{5.57 \times 10^8 \, \alpha f}{\sqrt{T}} \left\{\alpha f + .012\right\}, \qquad (18.4)$$

where a factor of $(1 - \exp^{-1357.4/T})$ is included to compensate for stimulated emission. The absorption coefficient is plotted in Fig. 18.2 as a function of temperature for various values of f.

Without doing a much more detailed analysis of the deflagration wave, we cannot determine the minimum value of k_L' required to sustain a LSD wave. However, experience with air indicates that the initial absorption coefficient tends to dominate the ability of the wave to maintain itself. As soon as the gas is heated slightly, the electron concentration increases dramatically and, therefore, the absorption coefficient also increases strongly. As a rough estimate, an absorption coefficient of 10, corresponding to an absorption length of 1 mm, is chosen as the minimum value of k_L' needed to sustain an LSD wave.
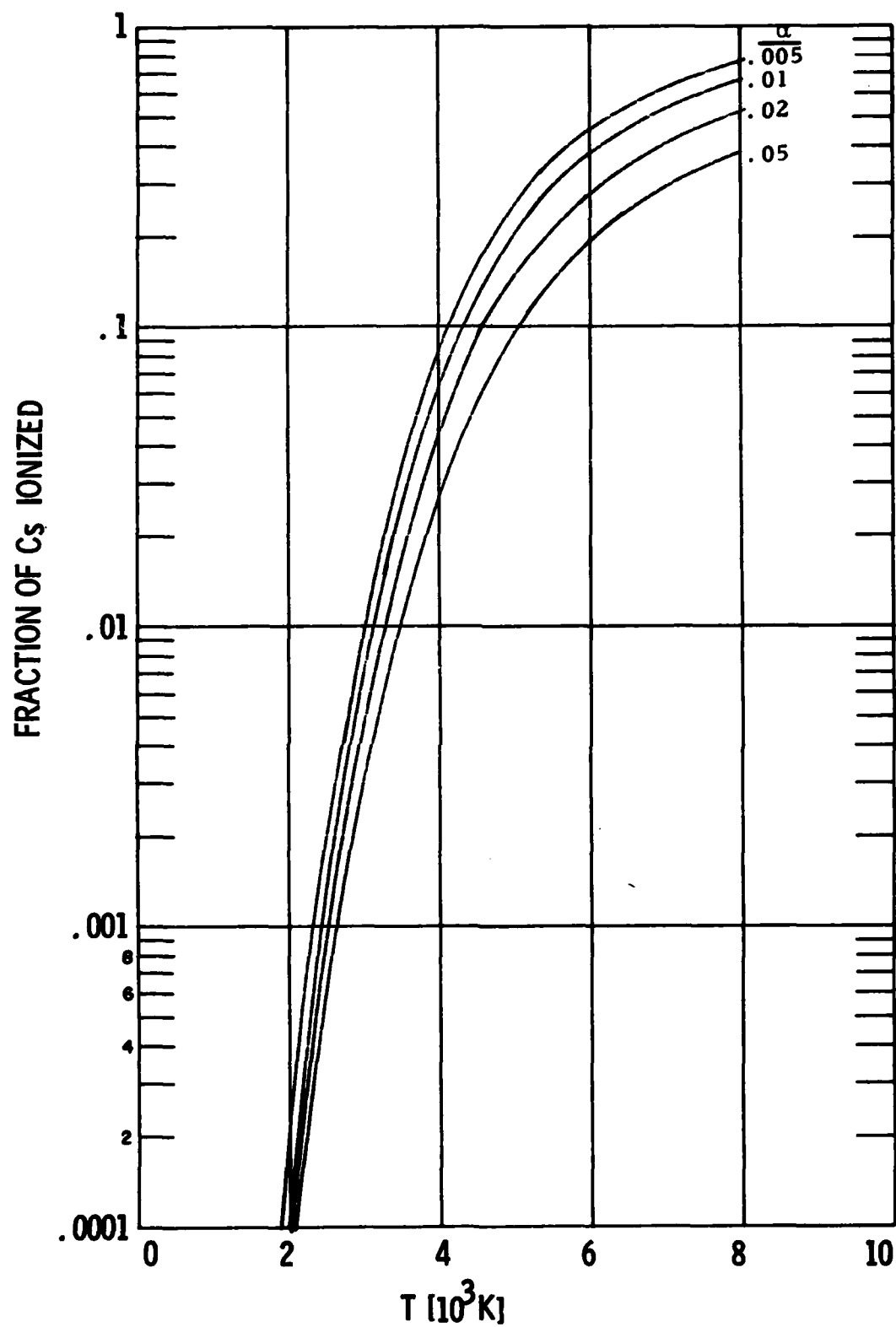
Fig. 18.1 Fraction of Cesium Ionized vs. Temperature for
Various Seed Fractions.
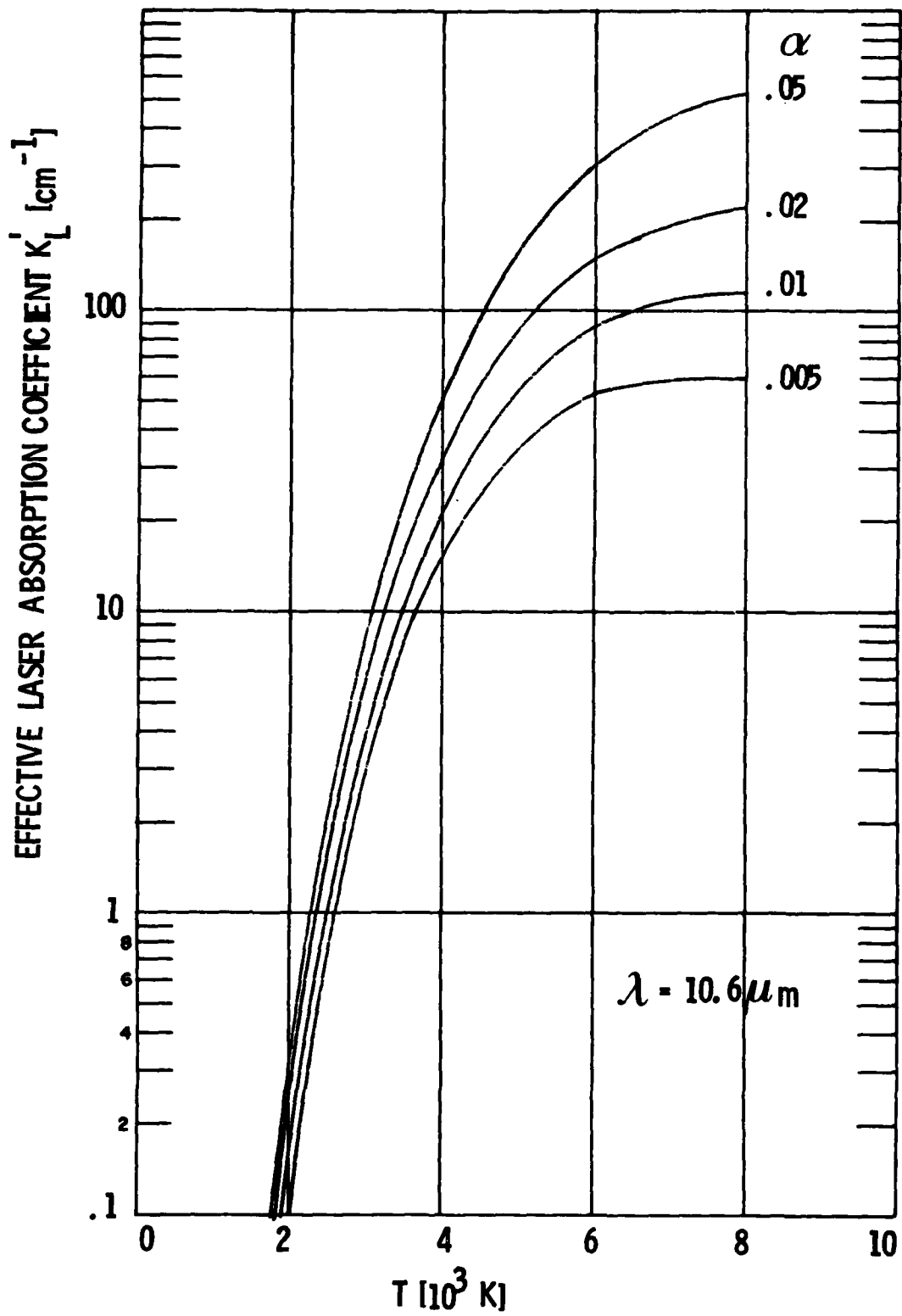
Fig. 18.2 Laser Absorption Coefficient vs. Gas Temperature
for Various Seed Fractions of Cesium.

Table 18.2 lists, for three laser intensities, the velocity V of the LSD wave, the temperature T_{sh} of the air behind the shock, the temperature T_{LSD} of the LSD wave, and the absorption coefficient both in the precursor shock and in the LSD wave. At 2 MW/cm^2, an LSD wave is probably formed, since the absorption occurs in less than 1 mm. At 1 MW/cm^2, the absorption length for all cases considered is greater than 1 mm, so an LSD wave probably does not form. At the intermediate intensity of 1.5 MW/cm^2, the higher concentrations absorb rapidly enough to support the LSD wave whereas the lower concentrations are marginal. The ability to sustain the wave depends more strongly on the laser intensity than it does on the concentration of cesium. The threshold intensity appears to lie between 1 to 2 MW/cm^2.

It is probably sufficient to seed only a small layer of the gas with cesium; once the cool LSD wave is adjacent to the surface, any subsequent formation of a hot LSC wave further away from the surface will not lead to radiative energy transport through the cooler layer to the surface. A seeded layer one centimeter thick should be more than adequate to shield the target.

For the hypothetical vehicle considered in subsection 17.2, which has an effective area of 1×10^7 cm^2, a mass of 600 gms of cesium is required to obtain a one percent concentration of C_s seed throughout a one centimeter thick layer. For these estimates of the required cesium concentration and layer thickness the weight penalty is not prohibitive.

A potential problem with this concept is that it may enhance coupling at low intensities, below 1 MW/cm^2. It may also lower the ignition threshold, thereby creating an extremely efficient coupling mechanisms for lasers operating at intensites below the normal enhanced coupling region.

The theoretical analysis presented above shows that it is plausible that a concentration of one to two percent cesium will create LSD waves in air at laser intensities above 1.5 MW/cm^2. This amount of cesium does not impose

TABLE 18.2

Characteristics of LSD Waves in Air Seeded With Cs.

I [MW/cm^2]	V [mm/sec]	T_{sH} [K]	T_{LSD} [K]	k_L' [cm^{-1}] $\alpha = .005$	$\alpha = .01$	$\alpha = .02$	$\alpha = .05$
1	2.50	2730		1.5	2	3	4.5
			3700	10.5	14	22	36
1.5	2.86	3570		8.5	11.5	17	25
			4300	20	30	45	80
2	3.15	3780		11	15	24	36
			4800	30	45	72	114

a large mass penalty. However, the details of how to achieve the seeding are, as yet, unstudied. Furthermore, experiments and more detailed theoretical analysis are required to test the adequacy of these simple estimates.

SECTION 19
CONCLUSIONS

In the three preceding sections, the potential of various approaches to hardening metals to repetitively pulsed lasers has been analyzed. Examination revealed weaknesses in several of the proposed approaches, revealed important areas of uncertainty in others, and identified some very favorable approaches. Experiments and more detailed analysis should be undertaken to resolve the important issues and confirm the predictions.

As a result of the analysis, the most attractive schemes are:

1. The use of reflective metal coatings to inhibit ignition.

2. Dimpling the surface to create a shielding, detached plasma.

A number of schemes are less attractive, either because the analysis showed them to be marginal, or because there are unresolved questions about some of the important physical phenomena. Included in this group are:

3. Chemical polishing which is expected to work at low intensities.

4. Transparent coatings which will work only if they do not ignite
   a plasma.

5. Displacement of the boundary layer by a gas which will not maintain an LSC wave. This gas has not yet been identified.

6. Plasma detachment by debris injection. The threshold intensity
   and the plasma opacity for this method have not yet been identified.

7. LSD ignition by seeding the boundary layer with cesium. The threshold intensity for LSD ignition has not been established.

The following approaches appear to have serious deficiencies and to be unworkable in the forms studied:

8. Mechanical polishing, which does not eliminate small defects.

9. Electron scavenger injection. The cascade breakdown is not
   the determining factor of plasma formation.

10. Plasma detachment by electron injection. Enormous electron currents are required to induce air breakdown at the intensities envisaged.

REFERENCES AND FOOTNOTES - PART III

1. A. N. Pirri, R. G. Root and P. K. S. Wu, "Plasma Energy Transfer to Metal Surfaces Irradiated by Pulsed Lasers," AIAA Journal, 16, 1296 (1978).

2. A. N. Pirri, R. G. Root and P. K. S. Wu, "Analytical Laser/Material Interaction Investigations," Physical Sciences, Inc. Woburn, MA, TR-104, September 1977.

3. P. D. Thomas and H. M. Musal, "A Theoretical Study of Laser-Target Interaction," Lockheed Missiles & Space Company, Inc., Palo Alto, CA, LMSC-D352890, August 1973.

4. J. T. Schriempf, "Response of Material to Laser Radiation: A Short Course," Naval Research Laboratory, Washington, D. C., NRL 7728, July 1974.

5. C. T. Walters, R. H. Barnes, and R. E. Beverly, III, "An Investigation of Mechanisms of Initiation of Laser-Supported Absorption (LSA) Waves," Battelle Columbus Laboratories, Columbus, OH, Contract No. DAAHC 1-73-C-0776, September 1975.

6. Lloyd P. Smith, "Thermionic Emission," in Handbook of Physics, Ed. E. U. Condon and Hugh Odishaw, 2nd ed. (McGraw-Hill Book Company, Inc., New York, 1958). pp. 8-76.

7. Herbert B. Michaelson, "Electron Work Functions of the Elements," in Handbook of the Tables for Applied Engineering Science, Ed. Ray E. Bolz and George L. Tuve (The Chemical Rubber Co., Cleveland, OH, 1970). p. 250.

8. P. D. Thomas, H. M. Musal and Y. S. Chou, "Laser Beam Interaction - Part II," Lockheed Missiles & Space Company, Inc., Palo Alto, CA, LMSC-D403747, August 1974.

9. P. D. Thomas and H. M. Musal, "A Theoretical Study of Laser-Target Interaction," Lockheed Missiles & Space Company, Palo Alto, CA, LMSC-D313142, December 1972.

10. Ref. 5.

REFERENCES AND FOOTNOTES - PART III(Cont.)

11. Ref. 8.

12. Robert E. Schlier, Anthony N. Pirri and Dennis J. Reilly, "Air Breakdown Studies," Air Force Weapons Laboratory, Kirtland Air Force Base, NM, AFWL-TR-72-74, February 1973.

13. R. D. Hake, Jr. and A. V. Phelps, "Momentum-Transfer and Inelastic-Collision Cross-Sections for Electrons in O_2, CO, and CO_2," Physical Review 158, 70 (1967).

14. R. L. Taylor and G. Caledonia, "Experimental Determination of the Cross-Sections for Neutral Bremsstrahlung - II. High Temperature Air Species -- O, N and N_2," Journal of Quantitative Spectroscopy and Radiative Transfer 9, 681 (1969).

15. Ref. 3.

16. R. G. Root, P. K. S. Wu and A. N. Pirri, "Theoretical Study of Laser-Induced Breakdown in Particle-Contaminated Air," Physical Sciences Inc., Woburn, MA, TR-91, May 1977.

17. A. A. Boni, F. Y. Su, P. D. Thomas and H. M. Musal, "Theoretical Study of Laser-Target Interactions," Science Applications Incorporated, La Jolla, CA, SAI77-567LJ, May 1977.

18. Steve Lyon, presentation of JANAF Pulsed Laser Effect Technical Steering Committee Meeting, November 15, 1978.

19. Ref. 3.

20. "Condensed Data for KODAK IRTRAN Infrared Optical Materials," Kodak Pamphlet No. U-71, May 1975.

21. William L. Wolfe, "Optical Materials," in Handbook of Military Infrared Technology, Ed. William L. Wolfe (Office of Naval Research, Department of the Navy, Washington, D.C., 1965).

22. Gessner G. Hawley, The Condensed Chemical Dictionary, 8th ed. (Van Nostrand Reinhold Company, New York, 1971).

23. Ref. 18.

REFERENCES AND FOOTNOTES - PART III(Cont.)

24. M. L. Finson, Physical Sciences Inc., personal communication, 1979.

25. Yu. P. Raizer, Soviet Physics - JETP, <u>31</u>, 1148 (1970).

26. Francis A. Jenkins and Harvey E. White, <u>Fundamentals of Optics</u>, 3rd ed., (McGraw-Hill Book Company, Inc., New York, 1957).

27. Warren J. Smith, "Image Formation: Geometrical and Physical Optics," in <u>Handbook of Optics</u>, Ed. Walter G. Driscoll and William Vaughan (McGraw-Hill Book Company, New York, 1978).

28. Ref. 26, p. 95.

29. Ref. 12.

30. D. E. Lencioni, presentation at HELREG Subpanel Propagation Meeting, November 18, 1975, MITRE Corporation, Bedford, MA.

31. J. Reilly, P. Singh and G. Weyl, "Multiple Pulse Laser Propagation Through Atmospheric Dusts at 10.6 Microns," AIAA Paper 77-697, presented at AIAA 10th Fluid & Plasmadynamics Conference, Albuquerque, NM, June 1977.

32. Ref. 16.

33. P. K. Wu and A. N. Pirri, "The Dynamics of Air Plasma Growth in a 10.6 µm Laser Beam," AIAA Paper 78-176, presented at AIAA 16th Aerospace Sciences Meeting, Huntsville, AL, January 1978.

34. A. Edwards and J. A. Fleck, Jr., "Two-Dimensional Modeling of Aerosal Induced Breakdown in Air," Paper distributed at AIAA Conference, Cambridge, MA, October 31-November 2, 1978. Preprint UCRL-81840.

35. P. I. Singh, "Experiments on Aerosal Induced Breakdown by Pulsed Lasers," AIAA Paper 79-0249, presented at 17th Aerospace Sciences Meeting, New Orleans, LA, January 1979.

REFERENCES AND FOOTNOTES - PART III(Cont.)

36.   Randall E. Murphy, Floyd H. Cook, G. E. Caledonia, and B. D. Green, "Infrared Fluorescence of Electron Irradiated CO_2 in the Presence of N_2, Ar and He, " Air Force Geophysics Laboratory, Hanscom AFB, MA, AFGL-TR-77-0205, September 1977.

37.   Ya. B. Zel'dovich and Yu, P. Raizer, Physics of Shock Waves and High-Temperature Hydrodynamic Phenomena, Ed. Wallace D. Hayes and Ronald F. Probstein, Vol. I (Academic Press, New York, 1966), p. 407.

38.   Ref. 37, p. 194.

39.   Saul Feldman, "Hypersonic Gas Dynamic Charts for Equilibrium Air, " Avco Research Laboratory, Everett, MA, RR-40, January 1957.

40.   Ref. 37, p. 259.

Commander Defense Technical Information Center ATTN: DDC-TCA Cameron Station Alexandria, VA 22134	2 copies
DARPA (STO) ATTN: Dr. R. C. Sepucha 1400 Wilson Blvd Arlington, VA 22209	1 copy
Director Defense Advanced Research Projects Agency ATTN: Director, Laser Division 1400 Wilson Blvd Arlington, VA 22209	1 copy
Director Institute for Defense Analysis ATTN: Classified Library Dr. R. G. Finke 400 Army Navy Drive Arlington, VA 22202	1 copy
Director Institute for Defense Analysis ATTN: Classified Library Dr. J. Ross 400 Army Navy Drive Arlington, VA 22202	1 copy
Office of Under Secretary of Defense for Research and Engineering ATTN: Director Space and Advanced Systems The Pentagon Washington, D. C. 20301	1 copy
Commander U. S. Army Harry Diamond Labs. ATTN: DRXDO-TI 2800 Powder Mill Road Adelphi, MD 20783	1 copy
Commander U. S. Army Mobility Equipment Research & Development Command ATTN: Tech Document Center, Bldg 315, DRSME-RZT Fort Belvoir, VA 22060	1 copy
Department of the Army HQDA ATTN: DAMA-WSN-T, Pellegrini Washington, D. C. 20310	1 copy
Department of the Army, HQDA ATTN: DAMA-WS, McCorkle Washington, D. C. 20310	1 copy

DISTRIBUTION LIST
FOR CONTRACT DAAK40-78-C-0010 (Cont.)

Department of the Army, HQDA   1 copy
ATTN: DAMA-AR, Garker
Washington, D.C.   20310

Department of the Army, HQDA   1 copy
ATTN: DAMA-RAA, LTC Narius
Washington, D.C.   20310

Director   1 copy
U.S. Army Advanced BMD Tech. Ctr.
ATTN: ATC-T, A. Carmichael
P.O. Box 1500
Huntsville, AL   35807

Director, U. S. Army Advanced BMD Tech Ctr   1 copy
ATTN: ATC-O, J. Hagefstration
P.O. Box 1500
Huntsville, AL   35807

Director   1 copy
USAMSAA
ATTN: DRXSY-AAF, D. Smith
Aberdeen Proving Ground, MD   21005

Director   1 copy
USAMSAA
ATTN: DRXSY-AAA, A. Henderson
Aberdeen Proving Ground, MD   21005

US Army Ballistic Research Lab   1 copy
ATTN: DRDAR-BLV/Mr. J.H. McNeilly
Aberdeen Proving Ground, MD   21005

US Army Ballistic Research Lab   1 copy
ATTN: DRDAR-BLV/Mr. J. Evans
Aberdeen Proving Ground, MD   21005

U.S. Army Materials & Mechanics   1 copy
Research Center
ATTN: DRXMR-RA(T.V. Hynes)
Watertown, MA   02172

U.S. Army Materials & Mechanics
Research Center
ATTN: DRXMR-RA(R. Fitzpatrick)
Watertown, MA   02172

U.S. Army Missile Research & Development Command   1 copy
ATTN: DRSMI-RHE/Mr. R. Mitchell
Redstone Arsenal, AL   35809

US Army Missile Research & Development Command ATTN: DRSMI-RH/Col W.R. DeLeuil Redstone Arsenal, AL 35809	1 copy
US Army Missile Research & Development Command ATTN: DRSMI-RHC/Dr. R.W. Conrad Redstone Arsenal, AL 35809	1 copy
Naval Research Laboratory ATTN: Dr. J.T. Schriempf/Code 6330 Washington, D.C. 20375	1 copy
Naval Research Laboratory ATTN: Dr. J. MacCallum/Code 1409 Washington, D.C. 20375	1 copy
Naval Research Laboratory ATTN: Dr. R. Wenzel Washington, D.C. 20375	
Naval Research Laboratory ATTN: Dr. A. Schindler/Code 6000 Washington, D.C. 20375	1 copy
Naval Research Laboratory ATTN: Dr. R. Stegman/Code 6333 Washington, D.C. 20375	1 copy
Naval Research Laboratory ATTN: Dr. F. Patten/Code 6003 Washington, D.C. 20375	1 copy
Naval Research Laboratory ATTN: Dr. S.K. Searles/Code 5540 Washington, D.C. 20375	1 copy
Naval Research Laboratory ATTN: Dr. D. Lewis/Code 6360 Washington, D.C. 20375	1 copy
Naval Sea Systems Command ATTN: PMS-405, Mr. A.L. Stoessell Washington, D.C. 20362	1 copy
Naval Sea Systems Command ATTN: PMS-405, CPT A. Skolnick Washington, D.C. 20362	1 copy
Office of Naval Research ATTN: Dr. F. Quelle 555 Summer Street Boston, MA 02110	1 copy

DISTRIBUTION LIST
FOR CONTRACT DAAK40-78-C-0010 (Cont.)

Office of Naval Research ATTN: Dr. W.J. Condell(421) 800 N. Quincy Street Arlington, VA 22217	1 copy

Superintendent
U.S. Naval Postgraduate School
ATTN: Department of Physics & Chemistry
        Prof. J.R. Neighbours
        Library, Code 2124
Monterey, CA   93940
	1 copy

AFAPL (SFH/Mr. T. Hogan) Wright-Patterson AFB, OH 45433	1 copy
AFML (LPJ/Mr. G. Denman) Wright-Patterson AFB, OH 45433	1 copy
AFML (LPJ/Dr. S. Lyon) Wright-Patterson AFB, OH 45433	1 copy

AFWL   (AREE/Dr. R. Rudder)   1 copy
         (AREE/Dr. W. Laughlin)   1 copy
         (AREE/Capt. Hastings)   1 copy
         (AREP/LtCol R. Grotbeck)   1 copy
         (AREA/Lt R. Malseed)   1 copy
         (ARLO/Lt Col K. Jungling)   1 copy
         (ARAC/Dr. P. J. Ortwerth)   1 copy
Kirtland AFB, NM 87117

AFIT/ENY ATTN: Dr. Peter Torvik Wright-Patterson AFB, OH 45433	1 copy
Aerospace Corporation ATTN: Dr. R. Hofland 2350 E. El Segundo Blvd. El Segundo, CA 90245	1 copy
Aerospace Corporation ATTN: Dr. J. Whittier 2350 E. El Segundo Blvd. El Segundo, CA 90245	1 copy
Avco Everett Research Laboratory ATTN: Dr. E. Bressel 2385 Revere Beach Parkway Everett, MA 02149	1 copy
Avco Everett Research Laboratory ATTN: Dr. J. Woodroffe 2385 Revere Beach Parkway Everett, MA 02149	1 copy

Avco Everett Research Laboratory   1 copy
ATTN: Dr. T. Cronburg
2385 Revere Beach Parkway
Everett, MA 02149

Director   1 copy
Lawrence Livermore Laboratory
ATTN: Dr. J. Emmett, L-555
P. O. Box 808
Livermore, CA 94550

General Electric Company   1 copy
Space Division
ATTN: Mr. W. J. East
Valley Forge Space Center
P. O. Box 8555
Philadelphia, PA 19101

General Electric Company   1 copy
Re-entry and Environmental Systems Division
ATTN: Mr. Winter, Rm 2534
3198 Chestnut Street
Philadelphia, PA 19101

General Electric Company   1 copy
Re-entry and Environmental Systems Division
ATTN: Mr. D. Rich, Rm 6045
3198 Chestnut Street
Philadelphia, PA 19101

General Research Corporation   1 copy
ATTN: Dr. G. K. Warmbrod
Huntsville, AL 35807

George Mason University   1 copy
ATTN: Dr. R. Cozzens
School of Engineering
Fairfax, VA 22030

Lockheed Missile & Space Co.   1 copy
ATTN: Dr. M. Bina
Org 52-05, Bldg 573
P. O. Box 504
Sunnyvale, CA 94086

Massachusetts Institute of Technology   1 copy
Lincoln Laboratory
ATTN: Dr. L. Marquet
P. O. Box 73
Lexington, MA 02173

Massachusetts Institute of Technology   1 copy
Lincoln Laboratory
ATTN: Dr. Rediker
P. O. Box 73
Lexington, MA 02173

Massachusetts Institute of Technology   1 copy
Lincoln Laboratory
ATTN: Dr. S. Edelberg
P.O. Box 73
Lexington, MA   02173

Massachusetts Institute of Technology   1 copy
Lincoln Laboratory
ATTN: Dr. V. Reis
P.O. Box 73
Lexington, MA   02173

McDonnell Douglas Astronautics Company   1 copy
ATTN: Dr. W. Bozich
5301 Bolsa Avenue
Huntington Beach, CA   92647

McDonnell Douglas Corporation   1 copy
ATTN: Dr. T. Ender
P.O. Box 516
St. Louis, MO   63166

Mitre Corporation   1 copy
ATTN: Mr. N. Harmon
       RS 62 and Middlesex Turnpike
P.O. Box 208
Bedford, MA   01730

National Bureau of Standards   1 copy
ATTN: Dr. E. Johnson
Electromagnetic Technology Division
Code 724.02
Boulder, CO   80303

Northrop Corporation   1 copy
Northrop Research and Technology Center
One Research Park
Palos Verdes Peninsula, CA   90274

Physical Sciences Inc.   1 copy
ATTN: Dr. A. Pirri
30 Commerce Way
Woburn, MA   01801

Physical Sciences Inc.   1 copy
ATTN: Dr. R. Root
30 Commerce Way
Woburn, MA   01810

R&D Associates   1 copy
ATTN: Dr. R. Hundley
P.O. Box 9695
Marina Del Rey, CA   90291

R&D Associates   1 copy
ATTN: Dr. D. Gakenheimer
P. O. Box 9695
Marina Del Rey, CA 90291

Science Applications, Inc.   1 copy
ATTN: Dr. A. Boni
P. O. Box 2351
La Jolla, CA 92038

Science Applications, Inc.   1 copy
ATTN: Dr. W. Wilson
P. O. Box 2351
La Jolla, CA 92038

Science Applications, Inc.   1 copy
ATTN: F. G. Gebhardt
3 Preston Court
Bedford, MA 01730

Science Applications, Inc.   1 copy
ATTN: K. Farro
2361 Jefferson Davis Highway
Arlington, VA 22202

Science Applications, Inc.   1 copy
ATTN: J. Kaplan
2361 Jefferson Davis Highway
Arlington, VA 22202

Science Applications, Inc.   1 copy
ATTN: Mr. H. Ford
6600 Powers Ferry Road, Suite 220
Atlanta, GA 30339

Science Applications, Inc.   1 copy
ATTN: Dr. R. Binkowski
2201 San Pedro
Suite 214
Albuquerque, NM 87110

Stanford Research Institute   1 copy
ATTN: Dr. B. S. Holmes
333 Ravenswood Avenue
Menlo Park, CA 94025

Textron Incorporated   1 copy
Bell Helicopter Textron
P. O. Box 482
Fort Worth, TX 76101

The Boeing Company   1 copy
ATTN: Dr. R. B. Hall
P. O. Box 1707
7755 East Marginal Way
Seattle, Washington 98124

TRW Systems Group   1 copy
ATTN: DR. R. Aprahamian
One Space Park
Redondo Beach, CA   90278

TRW Systems Group   1 copy
ATTN: Mr. P. Bhutta
One Space Park
Redondo Beach, CA   90278

W.J. Schafer Associates, Inc.   1 copy
ATTN: DR. T.Norwood
1901 North Fort Myer Drive
Suite 800
Arlington, VA   22209

W.J. Schafer Associates, Inc.   1 copy
ATTN: Dr. J. Reilly
10 Lakeside Office Park
Wakefield, MA   01880

W.J. Schafer Associates, Inc.   1 copy
ATTN: Dr. Bouche
10 Lakeside Office Park
Wakefield, MA   01880

Hughes Aircraft Company   1 copy
ATTN: James E. Robin
Culver City, CA   90230